

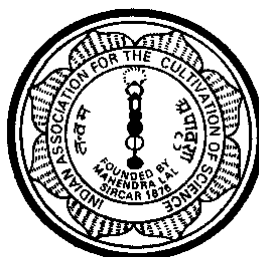
**OPTOELECTRONIC APPLICATIONS AND  
SPINTRONIC ASPECTS OF METAL HALIDE  
PEROVSKITES**

*A thesis submitted for the degree of*  
**Doctor of Philosophy (Science)**

of

Jadavpur University

2022



BY

**ABHISHEK MAITI**

SCHOOL OF PHYSICAL SCIENCES

INDIAN ASSOCIATION FOR THE CULTIVATION OF SCIENCE

JADAVPUR, KOLKATA 700 032, INDIA





*Dedicated  
In Loving Memory  
of  
My Grandfather*

*Nikhil Baran Jana*



## চিত্ত যেথা ভয়শূন্য

চিত্ত যেথা ভয়শূন্য, উচ্চ যেথা শির,  
জ্ঞান যেথা মুক্ত, যেথা গৃহের প্রাচীর  
আপন প্রাঙ্গণতলে দিবস-শবরী  
বসুধারে রাখে নাই খন্ড ক্ষুদ্র করি,  
যেথা বাক্য হৃদয়ের উৎসমুখ হতে  
উচ্ছসিয়া উঠে, যেথা নির্বীরিত স্রোতে  
দেশে দেশে দিশে দিশে কর্মধারা ধায়  
অজস্র সহস্রবিধ চরিতার্থতায়-  
যেথা তুচ্ছ আচারের মরুবালুরাশি  
বিচারের স্রোতঃপথ ফেলে নাই গ্রাসি,  
পৌরুষে করেনি শতধা; নিত্য যেথা  
তুমি সর্ব-কর্ম চিন্তা-আনন্দের নেতা-  
নিজ হস্তে নির্দয় আঘাত করি, পিতঃ,  
ভারতেরে সেই স্বর্গে করো জাগরিতা॥

—বিশ্বকবি রবীন্দ্রনাথ ঠাকুর (নৈবেদ্য হতে সংগ্রহীত)



# WHERE THE MIND IS WITHOUT FEAR

WHERE THE MIND IS WITHOUT FEAR AND THE HEAD IS HELD HIGH

WHERE KNOWLEDGE IS FREE

WHERE THE WORLD HAS NOT BEEN BROKEN UP INTO FRAGMENTS

BY NARROW DOMESTIC WALLS

WHERE WORDS COME OUT FROM THE DEPTH OF TRUTH

WHERE TIRELESS STRIVING STRETCHES ITS ARMS TOWARDS PERFECTION

WHERE THE CLEAR STREAM OF REASON HAS NOT LOST ITS WAY

INTO THE DREARY DESERT SAND OF DEAD HABIT

WHERE THE MIND IS LED FORWARD BY THEE

INTO EVER-WIDENING THOUGHT AND ACTION

INTO THAT HEAVEN OF FREEDOM, MY FATHER, LET MY COUNTRY AWAKE.

(ENGLISH TRANSLATION BY RABINDRANATH TAGORE)





INDIAN ASSOCIATION FOR THE CULTIVATION OF SCIENCE  
इंडियन एसोसियेशन फर दि काल्टिवेशन आफ साइंस

From:  
Prof. Amlan J. Pal, *FNA, FNAE, FASc, FNASc*  
JC Bose National Fellow  
School of Physical Sciences

Jadavpur,  
Kolkata 700 032,  
INDIA

**Certificate from the Supervisor**

This is to certify that the thesis entitled "Optoelectronic Applications and Spintronic Aspects of Metal Halide Perovskites" submitted by Sri Abhishek Maiti, who got his name registered on September 20, 2018 for the award of Ph.D. (Science) degree of Jadavpur University, is absolutely based upon his own work and under my supervision and that neither this thesis nor any part of it has been submitted for any degree/diploma or any other academic award anywhere before.

August 2022

*Amlan J. Pal*  
25/8/2022  
(Amlan J. Pal)

**Professor Amlan J. Pal**  
Department of Solid State Physics  
Indian Association for the  
Cultivation of Science  
Jadavpur, Kolkata 700 032





# Acknowledgements

---

As this beautiful journey is coming to an end, I remember the memories of countless ventures in the last five years, the lessons I have learned, and the ups and downs in the pathway of my doctoral research at the School of Physical Sciences, Indian Association for the Cultivation of Science (IACS), from 2018 to 2022. Over these years, I've had the opportunity to carry out my research work in a very friendly and encouraging environment. While writing the thesis, I would like to take this as an opportunity to express my gratitude to all who made this journey wonderful.

First and foremost, I would like to express my sincere gratitude to my supervisor, Prof. Amlan J. Pal for providing me the opportunity to work in his laboratory. I am truly inspired by his way of teaching, scientific thinking, and research philosophy. I would like to thank him for training me on how a research problem could be chosen, solved, and presented in style. His aspiring guidance, continuous day-to-day support in my research activities, countless opportunities, enthusiasm, and immense knowledge to point out numerous pitfalls in my thinking made it possible to write this dissertation. More than these, his working style and ideology towards life would have a great positive impact on my future.

I am also thankful to the Indian Association for the Cultivation of Science for providing all the facilities to carry out this work. I would like to acknowledge INSPIRE fellowship, Department of Science & Technology (DST), India for financial assistance.

I would like to thank my senior lab members, Dr. Biswajit Kundu, Dr. Soumyo Chatterjee, Dr. Hrishikesh Bhunia, Dr. Arnab Banerjee, Dr. Gautam Paul, and Dr. Salma Khatun for helping me to learn different instruments and conduct several joint experiments with me. I acknowledge my fellow lab mates and juniors, Raja Chakraborty, Subham Paramanik, Soirik Dan, Arpan Bera, and Sourav Mukherjee for their cooperation in keeping a friendly atmosphere in the lab. I am also thankful to Dr. Lekha P. for her cooperation and valuable suggestions from time to time. I especially acknowledge Dr. Uttam Kumar Ghorai for inspiring me always, Dr. Sudipto Bera for his help to learn

---

several scanning probe-related techniques, and Dr. Rini Ganguly for her efforts to train me in LabVIEW programming. I would like to express sincere thanks to the central scientific service (CSS) of IACS for allowing me to carry out several measurements. I would like to also acknowledge the research group of Prof. Tarun Kumar Mandal, School of Chemical Sciences, IACS, for allowing me to access the lab facility which was needed for the synthesis of some materials. In this regard, I would also like to thank Prof. Pradipta Panchadhyayee, PK College, Contai for his mentorship in my career.

I thank my lovely friends at IACS, Amaresh, Tamal, Pradeepta, Sujan, Satya, Subhajit, Suman, Biswajit, Shameek, Sourav, Shantanu, Ayan Da, Subharaj Da, Jayjit Da, and Anupam Da for their support in professional and personal life throughout the last five years.

I would like to thank Prof. Oleg Kolosov for allowing me to work as an international visiting student under his supervision at Lancaster University (LU), United Kingdom (UK), under the Newton Bhabha Ph.D. placement scheme. I thank DST and British Council for financial assistance during my stay in the UK. I thank my fellow lab mates at Lancaster, Dr. Rajasekhar Medapalli, Dr. Khushboo Agarwal, Dr. Yue Chen, and Sergio Gonzalez Munoz for their support in Prof. Kolosov's lab.

I thank my fiancée Shreya for her continuous support and inspiration throughout my life. She stayed by my side to share happy and troublesome moments of my journey toward the Ph.D. I wish to thank my younger brother Arijit for his support, concerns, and encouraging comments on my work. I am also thankful to my grandmother Mrs. Manimala Jana for her endless love and support. Above all, I offer my deepest gratitude to my mother, Mrs. Aparna Maiti, and father, Mr. Amit Kumar Maiti, for their love, sacrifice, encouragement, and support towards what I have achieved in my life. To finish, I want to acknowledge my grandfather, Late Nikhil Baran Jana who was a great teacher and always inspired me to pursue an academic career.

IACS, Kolkata.

August, 2022

(Abhishek Maiti)

# Contents

---

<i>Synopsis</i>	<i>i-vi</i>
<i>List of Publications</i>	<i>vii-ix</i>
<b>Chapter 1: Introduction</b>	<b>1-50</b>
1.1. Metal Halide Perovskites ( $ABX_3$ ): State-of-the-Art	1
1.2. Introduction to Different Metal Halide Perovskites	3
1.2.1. Methylammonium Lead Iodide ( $MAPbI_3$ )	3
1.2.1.1. Crystal Structures and Phases	3
1.2.1.2. Chemical Bonding and Interaction	6
1.2.2. Perovskites beyond $MAPbI_3$ : Substitution Strategies	6
1.2.2.1. A-Site Substitution	7
1.2.2.2. B-Site Substitution	10
1.2.2.3. X-Site Substitution	13
1.3. Electronic Band-Structures	16
1.4. Optoelectronic Properties of Metal Halide Perovskites	19
1.4.1. Optical Properties	20
1.4.2. Excitonic Character	21
1.4.3. Electronic Properties: Charge Transport	22
1.4.4. Defect Physics: Ion Migration and Recombination	24
1.4.5. Hot Carriers	26
1.4.6. Edge States	27
1.5. Spintronic Properties of Metal Halide Perovskites	28
1.5.1. The Emergence of Spin-Orbit Coupling (SOC)	28
1.5.2. Rashba and Dresselhaus Effect	29
1.5.3. Spin Triplet Formation	31
1.5.4. Magnetic Response and Magneto-Optical Phenomena	32
1.5.5. Chirality-Induced Spintronic Properties	34

1.6.	Device Applications	35
1.6.1.	Solar Cells	35
1.6.2.	Photodetectors	37
1.6.3.	Light Emitting Diodes	39
1.6.4.	Spintronic Devices	39
1.7.	Scopes and Objectives of the Doctoral Research	41
1.8.	References	42
 <b>Chapter 2: Experimental Methods</b>		<b>51-86</b>
2.1.	Materials	51
2.2.	Synthesis of Materials	52
2.2.1.	Thin Films through Spin Coating	52
2.2.2.	Nanostructures through Chemical Exfoliation	54
2.3.	Basic Characterization Techniques	54
2.3.1.	Optical Absorption Spectroscopy	55
2.3.2.	Circular Dichroism Spectroscopy	56
2.3.3.	Photoluminescence Spectroscopy	57
2.3.4.	Raman Spectroscopy	59
2.3.5.	X-Ray Diffraction	60
2.3.6.	X-Ray Photoelectron Spectroscopy	62
2.3.7.	Scanning Electron Microscopy	64
2.3.8.	Transmission Electron Microscopy	65
2.4.	Advanced Characterizations: Scanning Probe Microscopy	67
2.4.1.	Scanning Tunneling Microscopy	68
2.4.1.1.	Scanning Tunneling Spectroscopy	71
2.4.1.2.	Spin-Polarized Scanning Tunneling Spectroscopy	72
2.4.1.3.	Differential Conductance ( $dI/dV$ ) Imaging	74
2.4.2.	Atomic Force Microscopy (AFM)	74
2.4.3.	Kelvin Probe Force Microscopy (KPFM)	76

---

2.4.4. Conducting Atomic Force Microscopy (c-AFM)	78
2.5. Fabrication of Devices	79
2.6. Characterization of Devices	81
2.6.1. Solar Cells	81
2.6.2. Polarized Light Detectors	82
2.7. References	83

**Chapter 3: Ternary Halide Perovskites: Detrimental Role of Defects** **87-110**

3.1. Introduction	87
3.2. Experimental	89
3.2.1. Materials	89
3.2.2. Formation of MA <sub>3</sub> Bi <sub>2</sub> I <sub>9</sub> and Cs <sub>3</sub> Bi <sub>2</sub> I <sub>9</sub> Thin Films	89
3.2.3. Fabrication of Devices	90
3.3. Results and Discussion	91
3.3.1. Characterization of Materials	91
3.3.2. STS of Cs <sub>3</sub> Bi <sub>2</sub> I <sub>9</sub> and the Defect States	94
3.3.3. STS of (CH <sub>3</sub> NH <sub>3</sub> ) <sub>3</sub> Bi <sub>2</sub> I <sub>9</sub> and the Defect States	101
3.3.4. Defect States in A <sub>3</sub> Bi <sub>2</sub> I <sub>9</sub> and Solar Cell Parameters	104
3.4. Conclusions	106
3.5. References	107

**Chapter 4: Double Perovskites: Introducing Cationic Order** **111-134**

4.1. Introduction	112
4.2. Experimental	114
4.2.1. Materials	114
4.2.2. Synthesis of Pristine Cs <sub>2</sub> AgBiBr <sub>6</sub> Crystallites	114
4.2.3. Synthesis of Ordered Cs <sub>2</sub> AgBiBr <sub>6</sub> Crystallites	115
4.2.4. Formation of Cs <sub>2</sub> AgBiBr <sub>6</sub> Thin Films	115
4.2.5. Fabrication and Characterization of Devices	115

---

4.3.	Results and Discussion	116
4.3.1	Introducing Cation-Ordering in Cs <sub>2</sub> AgBiBr <sub>6</sub>	116
4.3.2.	Structural Characterization to Study Cation-Ordering	118
4.3.3.	Influence of Cation-Ordering on Raman Modes	119
4.3.4.	Optical Characteristics	121
4.3.5.	Band-Edges and Transport Gap through STS	123
4.3.6.	Surface Potential and Local Current Mapping	126
4.3.7.	Photovoltaic Performance	128
4.4.	Conclusions	129
4.5.	References	130
<b>Chapter 5: Quasi-2D Ruddlesden-Popper (RP) Perovskite: How Edge Matters</b>		
5.1.	Introduction	136
5.2.	Experimental	138
5.2.1.	Materials	138
5.2.2.	Synthesis of Perovskites	138
5.3.	Results and Discussions	140
5.3.1.	Characterization of Quasi-2D RP Perovskites	140
5.3.2.	Band-Mapping through Scanning Tunneling Spectroscopy	141
5.3.3.	Edge State in BA <sub>2</sub> MA <sub>2</sub> Pb <sub>3</sub> I <sub>10</sub> is MAPbI <sub>3</sub>	144
5.3.4.	Edge States in (BA) <sub>2</sub> (MA) <sub>n-1</sub> Pb <sub>n</sub> I <sub>3n+1</sub> and the Mechanism of their Formation	149
5.3.5.	Edge States Driven Exciton Dissociation: An Insight from STS and KPFM	151
5.4.	Conclusions	155
5.5.	References	155

---

<b>Chapter 6: Hybrid Halide Perovskite: Rashba Band Splitting</b>	<b>159-184</b>
6.1. Introduction	159
6.2. Experimental	162
6.2.1. Materials	162
6.2.2. Formation of MAPbI <sub>3</sub> Perovskite Thin Films	162
6.2.3. STS Studies	163
6.3. Results and Discussion	163
6.3.1. Formation of MAPbI <sub>3</sub>	163
6.3.2. STS of MAPbI <sub>3</sub> with a Pt/Ir Tip	165
6.3.3. SP-STS of MAPbI <sub>3</sub> with a Chromium-Coated Tip	167
6.3.4. Origin of Two Pair of Bands in MAPbI <sub>3</sub> : Probing Rashba-Split States through SP-STS	170
6.3.5. Spin-Polarized dI/dV Imaging	175
6.3.6. Rashba Splitting, Inter-domain Spin-Forbidden Transition Model, and Implications in Solar Cells	177
6.4. Conclusions	179
6.5. References	180
<b>Chapter 7: Chiral Perovskites: Spin Photovoltaic Effect</b>	<b>185-208</b>
7.1. Introduction	186
7.2. Experimental	188
7.2.1. Materials	188
7.2.2. Synthesis of Chiral Perovskites and Thin Films	189
7.2.3. Spin-Polarized (Magnetic) Conducting AFM (mC-AFM)	189
7.2.4. Fabrication and Characterization of Devices	190
7.3. Results and Discussion	191
7.3.1. Basic Characterization of Materials	191
7.3.2. Chiroptical Activity under CPL Illumination	193

7.3.3. Spin-Dependent Charge Transport: Chirality-Induced Spin-Selectivity (CISS) Effect	195
7.3.4. Spin-Photovoltaic Response and CPL Detection	199
7.4. Conclusions	205
7.5. References	206
<b>Chapter 8: Concluding Remarks</b>	<b>209-214</b>
8.1. General Conclusions and Summary	209
8.2. Key Findings	211
8.3. Future Prospects	212
8.4. References	214
<b>Appendix</b>	<b>215-272</b>
A. Quantifying Anisotropic Thermal Transport in 2D Perovskite	215
B. Sulfur-Vacancy Passivation in Sb <sub>2</sub> S <sub>3</sub> Thin Films	237
<b>Reprints of Published Articles</b>	<b>273</b>



# Synopsis

---

**Thesis Title:** Optoelectronic Applications and Spintronic Aspects of Metal Halide Perovskites.

**Submitted by:** Abhishek Maiti

In recent years, metal halide perovskites have emerged as a promising field of research themselves. To move forward, the present thesis outlines the fabrication and characterization of a range of perovskite thin films and nanostructures to investigate their optoelectronic and spintronic properties. Primarily, the electronic bands, localized charge/spin transport, and photophysics in different perovskites were investigated through scanning probe microscopic techniques. In addition, a significant effort was devoted to the device physics, in understanding their functionality for optoelectronic and spintronic applications. A brief review of the chapters is given below.

## **Chapter 1. Introduction**

This chapter deliberates the background of existing literature, which motivated the doctoral research work. Throughout the chapter, the overarching goal is to provide a concise discussion on metal halide perovskites, from their basic composition and structure to the fundamental optoelectronic and spintronic properties. In addition, the progress of different halide perovskite-based optoelectronic and spintronic devices is discussed. At the end of this chapter, the existing challenges and scope of the thesis have been presented.

## **Chapter 2. Experimental Methods**

During this doctoral research, several perovskite compounds, for example, organic-inorganic hybrid halide perovskite, bismuth-based ternary halide perovskite, double perovskite, quasi-2D Ruddlesden-Popper perovskite, and chiral perovskites were synthesized and characterized. In this chapter, the procedures followed to form and characterize such perovskite thin films and nanostructures have been discussed, followed by the fabrication of different photovoltaic devices and their characterization.

**Chapter 3. Ternary Halide Perovskites: Detrimental Role of Defects**

In this chapter, the role of defects on band-edges of bismuth-based ternary halide perovskites ( $A_3Bi_2I_9$ ) formed with cesium and methylammonium (MA) ions at the *A*-site has been studied to investigate the charge transport phenomena towards photovoltaic applications. A range of precursor-stoichiometries was considered leading to different reaction environments. In  $Cs_3Bi_2I_9$ , the intrinsic defects formed during the synthesis of the perovskites affect the materials' band-energies as observed through scanning tunneling spectroscopy (STS). Fermi energy of the perovskites could be seen to remain closer to the valence band (VB) as compared to the conduction band (CB) inferring their *p*-type nature of conductivities. Acceptor-type defects having the least formation energy was considered to result in the *p*-type behavior. Upon a variation in the precursor stoichiometry in forming the perovskites, STS studies evidenced a decrease in the band gap of the materials formed with  $BiI_3$ -rich precursors. The change in band-energies occurred due to the formation of deep defects above the VB-edge responsible for the poor photovoltaic performance of heterojunction solar cells. In contrast, the transport gap of  $(CH_3NH_3)_3Bi_2I_9$  was found to be independent of the precursor stoichiometry due to their defect-tolerant nature. As a result, the hybrid perovskite exhibited a superior charge transport and higher short circuit current compared to the inorganic one during the photovoltaic performance.

**Chapter 4. Double Perovskites: Introducing Cationic Order**

In this chapter, the role of cation-ordering in double perovskite solar cells ( $Cs_2AgBiBr_6$  to be specific) has been investigated for efficient charge transport in photovoltaic devices. In spite of environmental stability and non-toxic merits, the performance  $Cs_2AgBiBr_6$  has not excelled due to their large indirect bandgap, low absorption of the solar spectrum, and more importantly hurdles in carrier transport processes due to disordered cations namely silver and bismuth. A large number of intrinsic defects and self-trapped excitons (STE) appear in the double perovskite due to a disordered arrangement of Ag/Bi octahedra in the perovskite lattice. In this direction, a

ligand-assisted film-fabrication method was investigated through the use of phenethylammonium bromide (PEABr) to regulate the cation-ordering in the system towards an improved carrier conduction process. While the cation ordering was verified from X-ray diffraction studies and Raman spectroscopy, a reduction in the defect density and an inhibition of STE-formation was witnessed from optical spectroscopy. The transport gap, as obtained from scanning tunneling spectroscopy (STS) and density of states (DOS) spectra thereof, was found to increase suggesting defect-states to become suppressed. The effect of cationic ordering towards an efficient carrier transport in the ordered lattice of  $\text{Cs}_2\text{AgBiBr}_6$  was also manifested in Kelvin probe force microscopy and conductive atomic force microscopy. Finally, a fair improvement in photovoltaic parameters was observed in devices based on the ordered double perovskite.

### **Chapter 5. Quasi-2D Ruddlesden-Popper Lead Halide Perovskites: How edge Matters**

In this work, a band-mapping technique is introduced to investigate the low-energy edge states in quasi-2D Ruddlesden-Popper (RP) perovskites,  $(\text{BA})_2(\text{MA})_{n-1}\text{Pb}_n\text{I}_{3n+1}$  through a localized mode of measurement, namely scanning tunneling spectroscopy. The local intrinsic band structure revealed the formation of 3D  $\text{CH}_3\text{NH}_3\text{PbI}_3$  (MAPbI<sub>3</sub>) at the edges of the quasi-2D perovskites. The band-mapping process, introduced at the edge and the interior regions of their nanosheets, inferred the presence of a low-energy 3D phase at the periphery; for the thin films, the 3D phase could be seen to form at grain boundaries. The presence of MAPbI<sub>3</sub> at the edges or grain boundaries of quasi-2D perovskites and thereby a self-forming type-II band-alignment in  $\text{BA}_2\text{MA}_2\text{Pb}_3\text{I}_{10}$  ( $n = 3$ ) has been the rationale behind achieving high efficiency in solar cells based on the material, although it has a large exciton binding energy. Kelvin probe force microscopy under illumination conditions yielded a higher surface photovoltage at the edges compared to the interior and supported the inference of internal exciton dissociation as a result of the in-situ type-II band-alignment in the quasi-2D RP perovskites.

**Chapter 6: Hybrid Halide Perovskite: Rashba Band Splitting**

This chapter reports an experimental observation of Rashba splitting in methylammonium lead iodide (MAPbI<sub>3</sub>). Such non-trivial Rashba split band structure is unprecedentedly important for superior optoelectronic and spintronic applications of the compound. Because of a large spin-orbit coupling parameter in the non-centrosymmetric material, both the bands were predicted to split having two different spin-textures leading to two different  $Z$ -components of total angular momentum ( $J_z$ ). Spin-polarized scanning tunneling spectroscopy was employed to probe only one type of  $J_z$ -matched bands throughout the film;  $dI/dV$  spectra recorded at many different points of a film however allowed also to monitor both the Rashba split-levels and also deliberated on their spin-textures. It was observed that the bands split in such a manner that the conduction and valence bands closer to the Fermi energy have the same type of spin-textures (a spin-allowed transition model). Still, a low recombination rate of photogenerated carriers in MAPbI<sub>3</sub> was analyzed by considering Wannier-type excitons, molecular nature of spin-domains from  $dI/dV$  images, and therefore a spin-forbidden nature of interdomain transitions.

**Chapter 7. Chiral Perovskites: Spin Photovoltaic Effect**

In this chapter, a pair of lead-free chiral perovskites have been introduced for the detection of circularly polarized light (CPL). The organic-inorganic hybrid perovskites have an integration of a bismuth-based inorganic framework and a chiral organic sublattice ( $R/S$ -methylbenzylammonium) which introduces chirality into the entire compound. The chiroptical activities of the perovskites under CPL illumination evidence generation of spin-polarized carriers. However, their absorption anisotropy under different CPL illumination was low; the density of photogenerated carriers under the two CPLs was hence mostly similar. Interestingly, due to the intrinsic chirality of the compounds, the perovskites exhibited chirality-induced spin-selectivity (CISS) allowing the transport of one type of spin-half state while blocking the other type. A high value of spin-polarization in the current along the out-of-plane direction was observed in these

lead-free perovskites (as compared to conventional chiral compounds) due to their lower-dimensional form to make them suitable for CPL detection. Accordingly, a spin-dependent photovoltaic effect was observed in the vertical heterojunction devices; the photocurrent response was different under left- and right-handed CPL illuminations resulting in photocurrent anisotropy. As a result, the polarization states of CPL photons could readily be detected by investigating the anisotropic current response of the photodetector devices. While a self-powered CPL detector showed a limited (but one of the highest to date) anisotropy factor of 0.3 due to possible spin-flips during the transport process, the factor rose to 0.6 under bias prompting extension of the effective spin-diffusion length.

## **Chapter 8. Concluding Remarks**

This chapter contains the concluding remarks and the key findings of the doctoral research work as presented in the thesis. In addition, it also discusses the development of new perovskite materials and the prospects of the research field.

## **Appendix A. Quantifying Anisotropic Thermal Transport in 2D Perovskite**

In this work, the anisotropic thermal transport in two-dimensional (2D) perovskite (phenethylammonium lead iodide) nanolayers has been investigated through a novel measurement technique called cross-sectional scanning thermal microscopy (xSThM). In this method, a target perovskite layer on a substrate was polished obliquely with an Ar ion beam to create a low angle wedge with nanoscale roughness followed by high vacuum SThM to obtain the thermal conductance map as a function of local 2D material thickness. The experimentally obtained data was processed with an analytical model validated by the finite elemental analysis simulation to quantify the in-plane ( $k_{l,xy}$ ) and cross-plane thermal conductivities ( $k_{l,z}$ ) of the 2D perovskite from a single set of measurements with nanoscale resolution. An ultra-low thermal conductivity ( $k_l = 0.25 \pm 0.05 \text{ Wm}^{-1}\text{K}^{-1}$ ) for the 2D perovskite was obtained along with an anisotropy

---

( $k_{l,xy} = 0.45 \pm 0.05 \text{ Wm}^{-1}\text{K}^{-1}$  and  $k_{l,z} = 0.13 \pm 0.05 \text{ Wm}^{-1}\text{K}^{-1}$ ) associated with the unique structure of the perovskite and different phonon lifetimes and group velocities for in-plane and out-of-plane directions. The results that are available for the first time, are essential for the thermal management of 2D perovskite-based optoelectronic devices, and potential thermoelectric applications of these materials.

### **Appendix B. Sulfur-Vacancy Passivation in $\text{Sb}_2\text{S}_3$ Thin Films**

In this work, a modified two-step sequential deposition method has been developed to form  $\text{Sb}_2\text{S}_3$  thin films. In contrast to the conventional chemical bath deposition (CBD) route, this sequential deposition approach allowed passivation of sulfur-vacancies in  $\text{Sb}_2\text{S}_3$  through control over precursor-stoichiometry (S/Sb ratio) during the film-formation. An in-depth characterization of the chalcogenide thin films was made upon passivation of the vacancies. While a sulfur-deficient composition led to the formation of donor-like sulfur vacancies, a sulfur-rich stoichiometry passivated such vacancies followed by the creation of sulfur antisite defects in the chalcogenide. Scanning tunneling spectroscopy and thereby density of states allowed locating individual band-energies and their dependence on defect-passivation. A strong dependence of optical bandgap and surface morphology of the  $\text{Sb}_2\text{S}_3$  layer on the precursor stoichiometry was evidenced in this study and an optimized balance between the parameters was estimated for a slightly sulfur-rich composition (S/Sb ratio of 1.2). Interestingly, the photovoltaic parameters of Cu:NiO/ $\text{Sb}_2\text{S}_3$ /PCBM planar heterojunctions excelled at the predicted stoichiometry yielding a power conversion efficiency of 3.02% along with a significantly high open-circuit voltage of 0.8 V. This effort thus provides new insights into the influence of defect-passivation on solar cell characteristics based on solution-processed  $\text{Sb}_2\text{S}_3$  thin-films.

# List of Publications

---

## Journal Publications Included in This Thesis

### *Research Articles*

1. Band-Edges of Bismuth-Based Ternary Halide Perovskites ( $A_3Bi_2I_9$ ) through Scanning Tunneling Spectroscopy vis-à-vis Impact of Defects in Limiting the Performance of Solar Cells.  
**Abhishek Maiti**, Goutam Paul, Hrishikesh Bhunia, Amlan J. Pal  
*Solar Energy Materials & Solar Cells* 2019, **200**, 109942.
2. Sulfur-Vacancy Passivation in Solution-Processed  $Sb_2S_3$  Thin Films: Influence on Photovoltaic Interfaces.  
**Abhishek Maiti**, Soumyo Chatterjee, Amlan J. Pal  
*ACS Applied Energy Materials* 2020, **3**, 810-821.
3. Rashba Band Splitting in  $CH_3NH_3PbI_3$ : An Insight from Spin-Polarized Scanning Tunneling Spectroscopy.  
**Abhishek Maiti**, Salma Khatun, Amlan J. Pal  
*Nano Letters* 2020, **20**, 292-299.
4. Effect of Cation Occupancy Ordering in Double Perovskites to Overcome Hurdles in Carrier Transport:  $Cs_2AgBiBr_6$  as a Case Study  
**Abhishek Maiti**, Amlan J. Pal  
*Journal of Physical Chemistry C* 2021, **125**, 16324-16333.
5. Spin-Selective Charge Transport in Lead-Free Chiral Perovskites: The Key towards High-Anisotropy in Circularly-Polarized Light Detection  
**Abhishek Maiti**, Amlan J. Pal  
(Communicated)
6. Quasi-2D Ruddlesden-Popper Lead Halide Perovskite: How Edge Matters  
**Abhishek Maiti**, Amlan J. Pal  
(Communicated)
7. Quantifying Anisotropic Thermal Transport in 2D Perovskite  
**Abhishek Maiti**, Khushboo Agarwal, Sergio Gonzalez Munoz, Oleg. V. Kolosov  
(Communicated)

*Review Articles*

8. Role of Defects and their Passivation in Hybrid Halide Perovskites towards Solar Cell Applications.  
**Abhishek Maiti**, Soumyo Chatterjee, Lekha Peedikakkandy, Amlan J. Pal  
*Solar RRL* 2020, **4**, 2000505.
9. Carrier Recombination in  $\text{CH}_3\text{NH}_3\text{PbI}_3$ : Why is it a Slow Process?  
**Abhishek Maiti**, Amlan J. Pal  
*Reports on Progress in Physics* 2022, **85**, 024501.

Journal Publications not Included in This Thesis

10. Bowing of Transport Gap in Hybrid Halide Perovskite Alloys ( $\text{CH}_3\text{NH}_3\text{Sn}_{1-x}\text{Pb}_x\text{I}_3$ ): Which Band is Responsible?  
Salma Khatun, **Abhishek Maiti**, Amlan J. Pal  
*Applied Physics Letters* 2020, **116**, 012104.
11. Role of Individual Bands in the Unusual Temperature-Dependent Bandgap of  $\text{CH}_3\text{NH}_3\text{PbI}_3$   
Salma Khatun, **Abhishek Maiti**, Amlan J. Pal  
*The Journal of Physical Chemistry C* 2020, **124**, 19841-19848.
12. Large Resistive Switching and Artificial Synaptic Behaviors in Layered  $\text{Cs}_3\text{Sb}_2\text{I}_9$  Lead-Free Perovskite Memory Devices  
Subham Paramanik, **Abhishek Maiti**, Soumyo Chatterjee, Amlan J. Pal  
*Advanced Electronic Materials* 2021, **7**, 2100237.
13. Origin of Bandgap Bowing in  $\text{Cs}_2\text{Na}_{1-x}\text{Ag}_x\text{BiCl}_6$  Double Perovskite Solid-State Alloys: A Paradigm through Scanning Tunneling Spectroscopy  
Soirik Dan, **Abhishek Maiti**, Soumyo Chatterjee, Amlan J. Pal  
*Journal of Physics: Condensed Matter* 2021, **33**, 245703.
14. Defect Passivation of  $\text{Mn}^{2+}$ -Doped  $\text{CsPbCl}_3$  Perovskite Nanocrystals as Probed by Scanning Tunneling Spectroscopy: Towards Boosting Emission Efficiencies  
Raja Chakraborty, **Abhishek Maiti**, Uttam Kumar Ghorai, Amlan J. Pal  
*ACS Applied Nano Materials* 2021, **4**, 10155-10163.
15. Energy Landscape in Silver-Bismuth-Iodide Rudorffites: Combining Scanning Tunneling Spectroscopy and Kelvin Probe Force Microscopy  
Arpan Bera, Subham Paramanik, **Abhishek Maiti**, Amlan J. Pal  
*Physical Review Materials* 2021, **5**, 095404.



### Conference Proceedings (Oral and Poster Presentations)

1. Band Engineering of Bismuth based Ternary Halide Perovskite through Precursor Stoichiometry  
*Poster Presentation, ICPHPV 2020, IIT Delhi, India.*
2. Rashba Band Splitting in  $\text{CH}_3\text{NH}_3\text{PbI}_3$ : An Insight from Spin-Polarized Scanning Tunneling Spectroscopy.  
*Poster Presentation, Winter School 2020, JNCASR, India (Virtual).*
3. Rashba Band Splitting in  $\text{CH}_3\text{NH}_3\text{PbI}_3$ : An Insight from Spin-Polarized Scanning Tunneling Spectroscopy.  
*Oral Presentation, EESTER 2020, SRM University, IIT Madras, and Uppsala University, India and Sweden (Virtual).*
4. Observation of Rashba Band Splitting in Methylammonium Lead Iodide through Spin-Polarized Scanning Tunneling Spectroscopy.  
*Poster Presentation, MRS Fall Meeting 2020, MIT, USA (Virtual).*
5. Methylammonium Lead Iodide: Slow Recombination Unveiled.  
*Oral Presentation, WNCST 2021, VIT, India (Virtual).*

### Awards during PhD

1. Newton Bhabha PhD Placement Program during September 2021 to January 2022 at Lancaster University, UK.  
*DST and British Council, India and UK (2021).*
2. ACS Omega Best Oral Presentation Award  
*WNCST, VIT, India (2021).*
3. Best Oral Presentation Award  
*EESTER, SRM University, IIT Madras, and Uppsala University, India and Sweden (2020).*



# Chapter 1

## Introduction

*This chapter deliberates the background of existing literature that motivates this doctoral research work towards the optoelectronic applications and spintronic aspects of metal halide perovskites. Throughout the chapter, the overarching goal is to provide a concise discussion on metal halide perovskites, from their basic composition and structure to the fundamental and emerging optoelectronic and spintronic properties, and the progress of different halide perovskite-based optoelectronic and spintronic devices. At the end of this chapter, the existing challenges and scope of the thesis have been discussed.*

### **1.1. Metal Halide Perovskites ( $ABX_3$ ): State-of-the-Art**

In recent years, metal halide perovskites with organic-inorganic hybrid structures have gained widespread attention as an emerging class of materials [1]. Such compounds combine the advantages of both organic and inorganic moieties. Primarily, the organic sub-lattice provides structural diversity and flexibility to the compound. On the other hand, bandgap tunability, superior charge transport, and exclusive magnetic and dielectric properties come from the inorganic counterpart [2]. In the early days, perovskites specifically represented oxide-based inorganic materials, possessing the crystal structure of  $ABO_3$ , such as calcium titanate ( $CaTiO_3$ ) or barium titanate ( $BaTiO_3$ ) [3]. In 1978, the first generation of halide-based organic-inorganic perovskites such as  $MAPbX_3$  (MA= methylammonium,  $X= Cl, Br, \text{ and } I$ ) was explored [4]. However, they did not receive much attention initially, due to a lack of clarity on their potential applications in field-effect transistors (FET) and organic light-emitting diodes (OLEDs). The unprecedented potential of this unique class of compounds in modern-day material

science, especially in the energy-related application was first discovered in 2009 by Miyasaka and co-workers when they introduced  $\text{MAPbI}_3$  as absorber material in dye-sensitized solar cell (DSSC) devices [5]. Since then, the research thirst has been amplified and the state-of-the-art power conversion efficiency (PCE) of perovskite solar cells (PSCs) exceeded 24% in a decade surpassing the efficiency achieved in single-crystalline silicon solar cells [6]. In addition, the solution-processability of the material reveals the enormous potential of PSCs to be the low-cost photovoltaic (PV) technology in the future. However, the ambient instability of the material along with the presence of toxic lead could be a potential roadblock for their future applications [7]. In this direction, research focus has been shifted towards the development of other solution processed perovskites such as all-inorganic halide perovskites [8], two-dimensional (2D) Ruddlesden-Popper (RP) and Dion-Jacobson (DJ) hybrid halide perovskites [9], bismuth and antimony based ternary halide perovskites [10], and double perovskites [11] with tailored functionality and better ambient stability.

It may be noted that the solution-processed synthesis and crystallization kinetics of such perovskite materials contain a lot of chemistry and materials engineering. On the flip side, characterization and further device application are associated with strong backgrounds in physics. Such multidisciplinary nature of perovskite research has attracted a large community of researchers around the world to shed light on several unique properties of these compounds for their applications beyond solar cells. As a result, metal halide perovskites have prompted a further expansion in other optoelectronic devices as well including photodetectors [12], optical and photonic memory devices [13], and light-emitting diodes (LEDs) [14]. In addition to their excellent optoelectronics properties, these perovskites possess an unprecedented potential for several spintronics technologies [15]. The discovery of several spin-related phenomena originated from spin-orbit coupling (SOC) in the compound [16]. For example, giant Rashba band splitting [17], spin-triplet formation [18], different magneto-optical phenomena [19], and polarized light-related effects [20] indicate that additional usage of the spin degrees of freedom.

In this chapter, the composition and chemical structure of different perovskite materials have been discussed along with their physical properties. Different applications of such materials in optoelectronic and spintronic devices (to date) have also been deliberated. In the final section, the remaining challenges and the scope of the doctoral research work have been presented.

## 1.2. Introduction to Different Metal Halide Perovskites

As mentioned earlier, hybrid halide perovskites are denoted by a general perovskite structure of  $ABX_3$ , in which  $A$  and  $B$  represent an organic monovalent cation and bivalent metal cation, respectively, and  $X$  is a halide anion. Because of its excellent properties, the most remarkable material of this series, that is  $\text{MAPbI}_3$  ( $A = \text{MA}^+$ ,  $B = \text{Pb}^{2+}$ , and  $X = \text{I}$ ), is considered a prototype of such a class of materials. However, several spin-offs of this prototype can be achieved through substitutional doping at each of the crystallographic sites. In this section, we have discussed their basic crystal structure, different phases, chemical bonding of the hybrid halide perovskite  $\text{MAPbI}_3$ , and finally the routes to achieve different perovskite materials from the parent compound.

### 1.2.1. Methylammonium Lead Iodide ( $\text{MAPbI}_3$ )

#### 1.2.1.1. Crystal Structures and Phases

The crystal structure of  $\text{MAPbI}_3$  (Figure 1.1a) belongs to the general structure of  $ABX_3$  which is comprised of an array of corner-sharing  $BX_6$  octahedra where the  $A$ -site cation situates inside the octahedral cavities [1]. To evaluate the geometric stability of any perovskite structure, the Goldschmidt tolerance factor has been defined [21] as:

$$t = \frac{R_A + R_X}{\sqrt{2}(R_B + R_X)} \quad (1.1)$$

where, the effective ionic radii of  $A$ ,  $B$ , and  $X$  ions are denoted as  $R_A$ ,  $R_B$ , and  $R_X$ , respectively. Ideally, the crystal structure of a perovskite should be cubic for a near-unity value of  $t = 1$ . However, a cubic perovskite structure can be sustained when  $t$

ranges between 0.9 and 1.0 (semi-empirically). On the other hand, the deviation of  $t$  would result in structural distortion and the formation of lower symmetry phases with tetragonal and orthorhombic crystal structures. It is imperative to state that the value of  $t$  in the archetypal MAPbI<sub>3</sub> (MA<sup>+</sup> = 1.8 Å, Pb<sup>2+</sup> = 1.32 Å, and I<sup>-</sup> = 2.06 Å) is found to be 0.81 signifying a tetragonal structure ( $\beta$ -phase) [22]. A change in different crystal structures and phases can be envisaged through two different approaches:

(i) *Substitutional Doping Induced Phase Engineering*: Substitutional doping at three different sites of the compound will lead to different ABX<sub>3</sub> (MAPbI<sub>3</sub>) derivatives having different phases. Although the details of substitutional doping will be discussed in a later section, here a portion of the topic has been deliberated to understand the effect of doping on MAPbI<sub>3</sub> towards phase engineering (Figure 1.1b) [23]. First of all, the distortion of the perovskite lattice can be accomplished by introducing a smaller size  $A$ -site cation (Cs: cesium) which would lower the  $t$  value ( $< 0.89$ ) resulting in a lower symmetry crystal structure such as tetragonal ( $\beta$ -phase) or orthorhombic ( $\gamma$ -phase) phases. In contrast, a large  $A$ -site cation (FA: formamidinium) increases  $t$  to achieve a higher crystal symmetry of cubic ( $\alpha$ -phase). However, a very large-sized  $A$ -cation (PEA: phenethylammonium, BA: butylammonium) could not be “tolerated” in this structure since the value of  $t$  become very large ( $t > 1$ ). Such substitution affects the dimensionality of the perovskite crystal and low-dimensional 2D Ruddlesden-Popper (RP) or Dion-Jacobson (DJ) phases will be formed [9]. On the other hand, substitutional doping at the  $X$ -site, from I<sup>-</sup> to Cl<sup>-</sup> (through Br<sup>-</sup>), will gradually increase the value of  $t$  indicating a higher crystal symmetry. Similarly, homo-valent doping of Sn<sup>2+</sup> and Ge<sup>2+</sup> will also increase  $t$  resulting in a cubic phase. It may be noted that Sn<sup>2+</sup> and Ge<sup>2+</sup> are the most promising two candidates that can be projected for homo-valent doping at  $B$ -site, although Sn<sup>2+</sup> is known to oxidize to Sn<sup>4+</sup>.

(ii) *Variable Temperature Phase Engineering*: Temperature is an external stimulus that can act as a driving force for the phase transformation in perovskite materials (Figure. 1.1c) [24]. As mentioned earlier, MAPbI<sub>3</sub> exhibits a tetragonal crystal structure ( $\beta$ -phase) at room temperature [22]. At higher temperatures, the disorder of

MA<sup>+</sup> cations initiates a lattice distortion that finally results in the phase transition to the cubic crystal structure ( $\alpha$ -phase) at 330 K. Similarly, the crystal structure becomes orthorhombic ( $\gamma$ -phase) below 160 K. Along with the rotation of MA molecules, such phase transitions are also related to the tilting of the [PbI<sub>6</sub>]<sup>4-</sup> octahedra. Interestingly, such temperature-dependent phase transition has been observed in other perovskites as well [24]. For example, in CsPbI<sub>3</sub>, FAPbI<sub>3</sub>, and CsSnI<sub>3</sub>, an additional non-perovskite  $\delta$ -phase has been also observed that is vulnerable to the stability of the compound [25]. It may be concluded that all of these phase transitions can influence the electronic bands which would result in tailored functionalities for optoelectronic and spintronic applications.

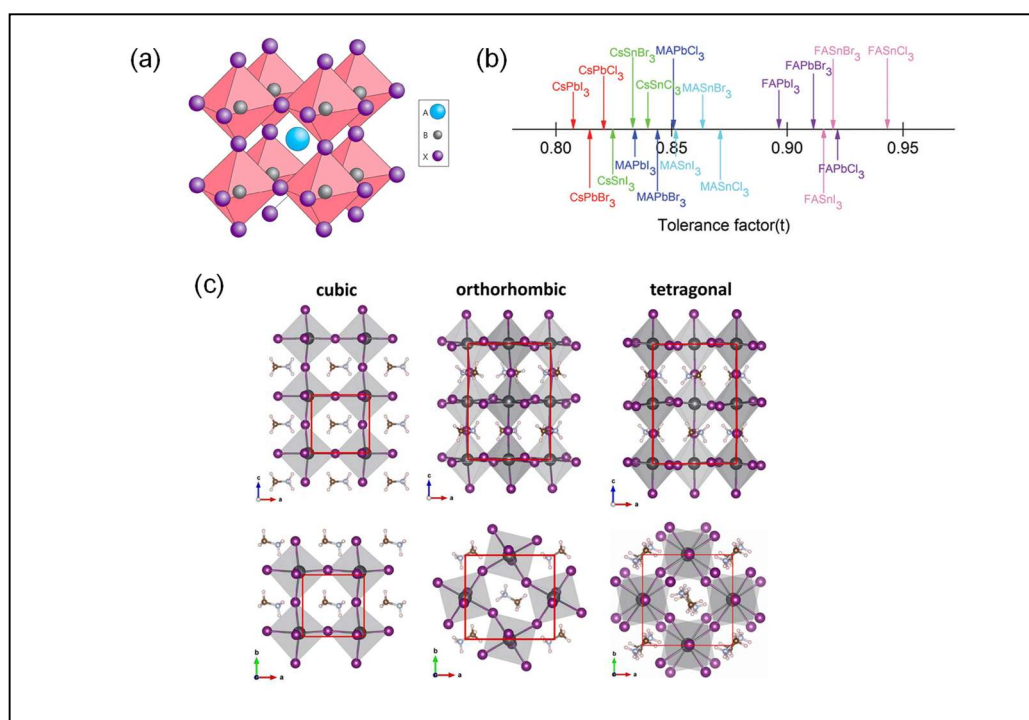


**Figure 1.1.** (a) Schematic representation of the perovskite crystal structure. (b) Tolerance factor of a series of halide perovskites. Reprinted from Ref [23], Copyright Royal Society of Chemistry 2018. (c) Different crystal structures of archetypal MAPbI<sub>3</sub> perovskite. Reprinted from Ref [24], Copyright Elsevier 2019.

### 1.2.1.2. Chemical Bonding and Interaction

The crystal lattice of MAPbI<sub>3</sub> can be separated into two sub-lattices with organic moieties (MA) and an inorganic network (PbI<sub>6</sub>) with endless bonding connectivity. The inorganic sub-lattice is three-dimensional (3D) whereas the organic counterpart is considered zero-dimensional (0D) due to its molecular nature. Although the metal core (Pb) of the inorganic sub-lattice does not make any direct bond with the carbon atoms of an organic moiety, a large number of interactions ensue between them [26]. Primarily, the interactions between the individual PbI<sub>6</sub> octahedra in the inorganic network are mixed ionic and covalent and they predominantly interact with the *A*-site molecular cation through Coulomb interaction. This interaction is originated from the oppositely charged nature of the two sublattices where the Born effective charges of PbI<sub>6</sub> octahedra and MA molecule are equivalent to four times the electronic charge and unity of protonic charge, respectively. In addition, a large static dielectric constant is associated with both the inorganic (2.89 D) and organic sub-lattices (2.29 D) [27]. Hence, another major interaction between the organic cation and the inorganic framework is their dipole-dipole interactions along with an electrostatic communication that originated from the charge-dipole interaction. In addition, both the lattices can interact with each other through hydrogen bonding as well [28].

These interactions are found to affect the molecular orientation of the molecule and lattice distortion resulting in the appearance of novel functionalities. As an example, the interplay between different interactions influences the octahedra tilting and the orientation of the organic cation which is believed to be one of the crucial factors behind several fundamental and emerging properties of the perovskite compounds.

### 1.2.2. Perovskites beyond MAPbI<sub>3</sub>: Substitution Strategies

Undoubtedly, MAPbI<sub>3</sub> is the most remarkable associate of the metal halide perovskite family. However, there exist challenges regarding the ambient stability of the compound. Moreover, the toxicity of the compound due to the presence of lead is another concern behind its potential commercialization [7,29]. In this direction, several



other perovskites are also explored beyond this archetypal material that can be obtained through substitutions or doping at different sites of MAPbI<sub>3</sub> (Figure 1.2). Such substitution strategies do not only promote the stability of the perovskite but also result in the tuning of their mechanical, optical, electronic, spintronic, and thermal properties towards novel functionalities. In this section, both homo-valent (valence state of the dopant is the same as the pristine) and hetero-valent substitutions (valence state of the dopant is different compared to the pristine) will be discussed.

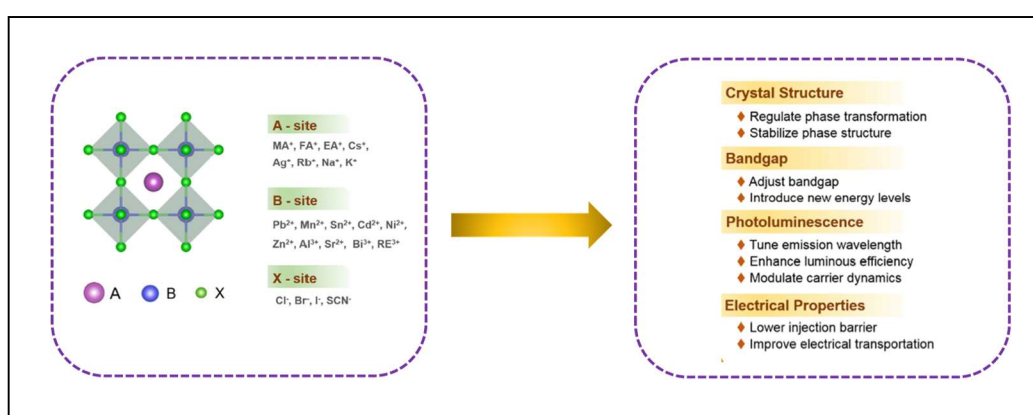


**Figure 1.2.** Schematic representation of substitutional doping approaches at different sites of the prototype  $ABX_3$  (MAPbI<sub>3</sub>). Some part of the image has been adapted from [30] with permission.

### 1.2.2.1. A-Site Substitution

The A-site of MAPbI<sub>3</sub> is occupied by the singly-protonated MA<sup>+</sup> cation. Based on the size of the A-site cation, different crystal structures can be achieved (Figure 1.3a) [31]. Here, the most suitable alternative is indeed FA<sup>+</sup> (FA: formamidinium) to replace MA<sup>+</sup> in this structure. In addition, the larger size of FA<sup>+</sup> seems promising for the formation of a higher symmetry perovskite crystal structure. Moreover, FAPbI<sub>3</sub> shows a comparatively smaller bandgap ( $E_g = 1.48$  eV) closest to the Shockley-Queisser limit [32]. Hence, FAPbI<sub>3</sub> is a more promising material for photovoltaic applications compared to MAPbI<sub>3</sub>. However, the environmental stability of FAPbI<sub>3</sub> is even poorer than MAPbI<sub>3</sub> [33]. It has been observed that FAPbI<sub>3</sub> ( $\alpha$ -phase) quickly degrades to a

non-perovskite crystal structure ( $\delta$ -phase) at ambient conditions. In this direction, the mixed  $A$ -site perovskite compounds are envisaged such as  $\text{MA}_{1-x}\text{FA}_x\text{PbI}_3$  [34]. These compounds possess superior optoelectronic properties induced by  $\text{FA}^+$  with better ambient stability. Similarly,  $\text{Cs}^+$  is another choice at the  $A$ -site for the fabrication of all-inorganic metal halide perovskites ( $\text{CsPbI}_3$ ) [8,35]. Although the thermal phase stability of all-inorganic perovskites is better than the organic-inorganic hybrid ones, it has been found that they lack some of the novel functionalities for further optoelectronic and spintronic applications [35]. Hence, it can be stated that the presence of organic moiety at the  $A$ -site of perovskite is very important. Nonetheless, all these  $A$ -site cations have their own merits and demerits; as a result, the best way out is indeed to use all the three cations at  $A$ -site through doping/alloying [36]. These triple cation perovskites would possess superior thermal phase stability ( $\text{Cs}^+$  cation), a suitable bandgap close to the Shockley-Queisser limit ( $\text{FA}^+$  cation), and the novel optical, electronic, and charge transport properties ( $\text{MA}^+$  cation) making them an outstanding choice for different device applications. It may be added that in addition to the abovementioned cations,  $\text{GA}^+$  ( $\text{GA}$ : guanidinium) and  $\text{Rb}^+$  have been also employed at the  $A$ -site to enhance the stability further and to improve the morphology and grain sizes of the perovskite films [37].

It may be noted that the previous discussion is restricted to those cations only that have a comparable effective ionic radius to  $\text{MA}^+$ . As a result, all the derived perovskites have a  $\text{MAPbI}_3$ -like 3D crystal structure. Interestingly, a very large organic cation can increase the space between inorganic octahedra leading to the formation of 2D layered perovskite structures. Primarily these 2D perovskites can be classified into two categories namely Ruddlesden-Popper (RP) and Dion-Jacobson phases. In general, the 2D-RP perovskites are described with a generic formula of  $A_2B_{n-1}Pb_nX_{3n+1}$ ; where  $A$  represents a large aliphatic or aromatic substituted ammonium spacer cation such as butylamine ( $\text{BA}^+$ ) or phenethylamine ( $\text{PEA}^+$ ) and  $B$  denotes a small organic cation for example  $\text{MA}^+$  or  $\text{FA}^+$ , and  $X$  is a halide anion; in addition, the integer  $n$  indicates the number of perovskite layers between two successive organic spacer cations (Figure

1.3b) [38]. On the other hand, the DJ phase has a unique stacking of inorganic layers as they are laid exactly on top of each other. These materials adopt a general formula of  $A'B_{n-1}Pb_nX_{3n+1}$  where  $A'$  represents a template cation such as  $(3\text{-AMP})^{2+}$  (AMP: amino-methylpiperidinium),  $B$  denotes a small organic cation for example  $\text{MA}^+$  or  $\text{FA}^+$ , and  $X$  is a halide anion [39]. The advantages of the 2D perovskites are indeed their exceptional material stability as the bulky spacer cations are hydrophobic thus endowing excellent moisture stability. However, these large organic cations have an insulating nature, which would result in a sacrifice of cross-plane transport [29]. Moreover, due to a strong quantum and dielectric confinement, it would sacrifice the optoelectronic properties by increasing the exciton binding energy and thereby lowering the efficiency [40]. Once these issues are solved and the toxicity of Pb can be stepped aside, these materials should be considered as a true alternative to  $\text{MAPbI}_3$  in perovskite optoelectronics [9].

Based on the above discussion, it is imperative to state that the effect of  $A$ -site substitution is more significant in modulating the stability of the compound rather than tailoring its intrinsic optoelectronic properties. However, the picture is not the same for the spintronic properties of the material. Although, most of the novel spin-related phenomena originate due to the spin-orbit coupling (SOC) associated with Pb and are not directly related to the  $A$ -site cation, recently, a new way has been developed to increase the spin functionality of perovskites through  $A$ -site cation engineering. In this direction, left-handed ( $S$ ) and right-handed ( $R$ ) chiral cations, for example,  $R/S$ -MBA (MBA: methylbenzylammonium) are introduced at the  $A$ -site to introduce chiroptical phenomena in the perovskites (Figure 1.3c) [41]. The chiroptical activity of the perovskites is reported to enhance the spin properties of the perovskites by creating an imbalance of spin population in the bands. Moreover, the introduction of the chiral molecules paves the way for spin-selective charge transport which is known as chirality-induced spin selectivity [42]. Although this is at a very premature stage, it is envisaged that such material will open a new direction in perovskite-based spintronics. Several cutting-edge device technologies such as spin-polarized photodetectors, spin LEDs, and

spin memory devices might emerge with the development of such chiral perovskites. All these devices would work under zero magnetic field [43].

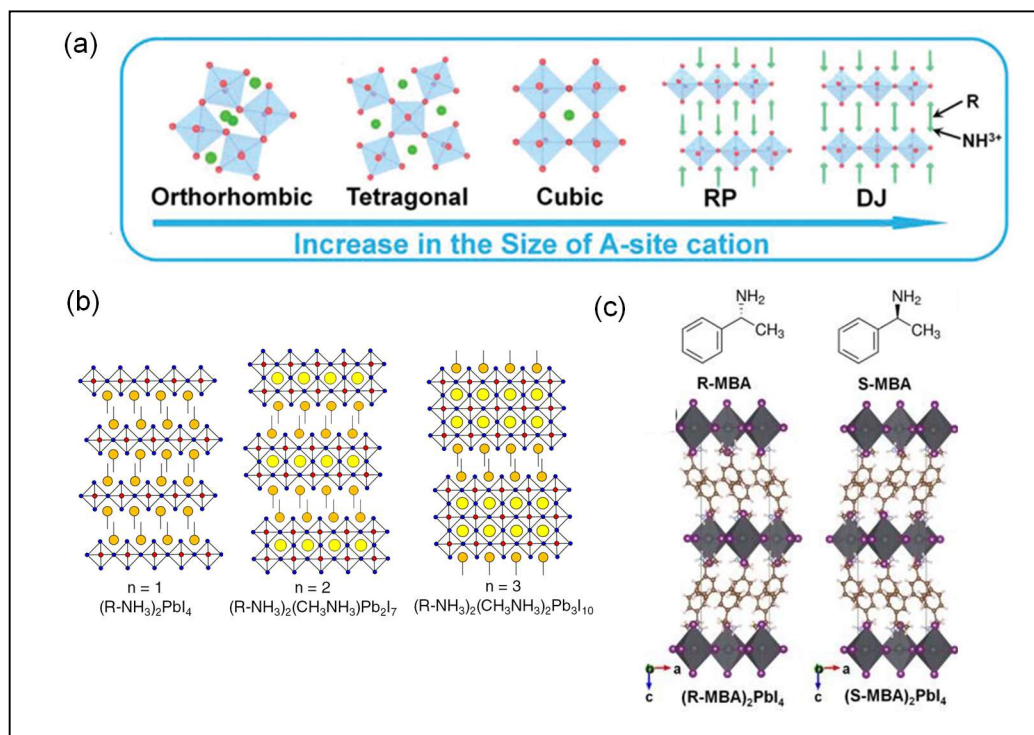


**Figure 1.3.** (a) Possible perovskite structures were obtained through different A-site cations in  $MAPbI_3$ . Reprinted from Ref [31], Copyright Wiley VCH 2020. (b) Schematic structure of layer number dependent 2D perovskites. (c) Structure of chiral perovskites. Reprinted from Ref [41], Copyright Royal Society of Chemistry.

### 1.2.2.2. B-Site Substitution

In search of novel perovskites beyond  $MAPbI_3$ , B-site substitution seems to be most important as the metal-site has a substantial contribution in forming the band-edges and electronic properties thereby [44]. Moreover, like the A-site cation, substitution at B-site reduces the toxicity of the perovskites by replacing the lead. In this direction, both homo-valent and hetero-valent substitutions have been attempted to date based on Goldschmidt's tolerance factor ( $t$ ) as discussed earlier (Equation 1.1).

(i) *Homo-valent Substitution*: Ideally, most of the elements having an oxidation state of +2 are potential candidates for homo-valent substitution of lead in metal hybrid halide perovskite unless  $t$  deviates significantly from its limiting values. Such homo-valent elements could be short-listed from the periodic table for the replacement of toxic lead (Figure 1.4a) [29]. First of all,  $\text{Sn}^{2+}$  and  $\text{Ge}^{2+}$  from group-14 (same group of  $\text{Pb}^{2+}$ ) could be considered the most suitable candidates for such homo-valent substitutions as they possess similar electronic configurations. However, despite being non-toxic, both  $A\text{SnX}_3$  and  $A\text{GeX}_3$  have a critical concern regarding their stability independent of the choice of  $A$ - and  $X$ -site compositions [45]. Moreover, as all the novel optoelectronic (electronic band structure) and spintronic (spin-orbit coupling) properties are related to Pb, such derived perovskite would lose most of these properties as well. For the same reason, although several alkaline earth metals ( $\text{Mg}^{2+}$ ,  $\text{Sr}^{2+}$ ,  $\text{Ca}^{2+}$ ) have been introduced as dopants, they are found to be incapable of showing novel optoelectronic properties [46]. Additionally, a complete replacement of all  $\text{Pb}^{2+}$  with these alkaline earth metals is not possible as the derived compounds are not thermodynamically stable. A similar conclusion can be drawn for transition metals ( $\text{Mn}^{2+}$ ,  $\text{Zn}^{2+}$ ,  $\text{Cu}^{2+}$ ) as well. Despite being good candidates at the  $B$ -site for homo-valent substitutions, the as-obtained perovskites will result in insignificant functionalities. However, doping of  $\text{Mn}^{2+}$  in all-inorganic perovskites ( $A = \text{Cs}^+$ ,  $\text{Rb}^+$ ) is found to be significant for solid-state lighting applications [47].

(ii) *Hetero-valent Substitution*: Based on the above-mentioned discussion, it may be concluded that although replacement of  $\text{Pb}^{2+}$  at the metal site through homo-valent substitution reduces the toxicity of the compounds, all of these resultant perovskites lack the superior optoelectronic and spintronic properties of the Pb-based perovskites and most of them are even more unstable compared to the parent compound making this approach insignificant. In this direction, hetero-valent substitutions are endeavored and found to be more beneficial [48]. It may be noted that several attempts are made to dope monovalent ( $\text{Ag}^+$ ,  $\text{Cu}^+$ ), trivalent ( $\text{Bi}^{3+}$ ,  $\text{In}^{3+}$ ,  $\text{Au}^{3+}$ ,  $\text{Sb}^{3+}$ ), and tetravalent ( $\text{Sn}^{4+}$ ,  $\text{Ti}^{4+}$ ) elements [49]. Although doping of these elements alters the

electronic band structure and tunes the optoelectronic and spintronic properties of the perovskites, it does not change the 3D crystal structure of the parent  $ABX_3$  significantly. Moreover, the strategy of doping is not practically suitable to enhance the stability of the compound. In this direction, the complete substitution of  $Pb^{2+}$  is important to derive new perovskite compounds through a combinatorial approach (Figure 1.4b) [50].

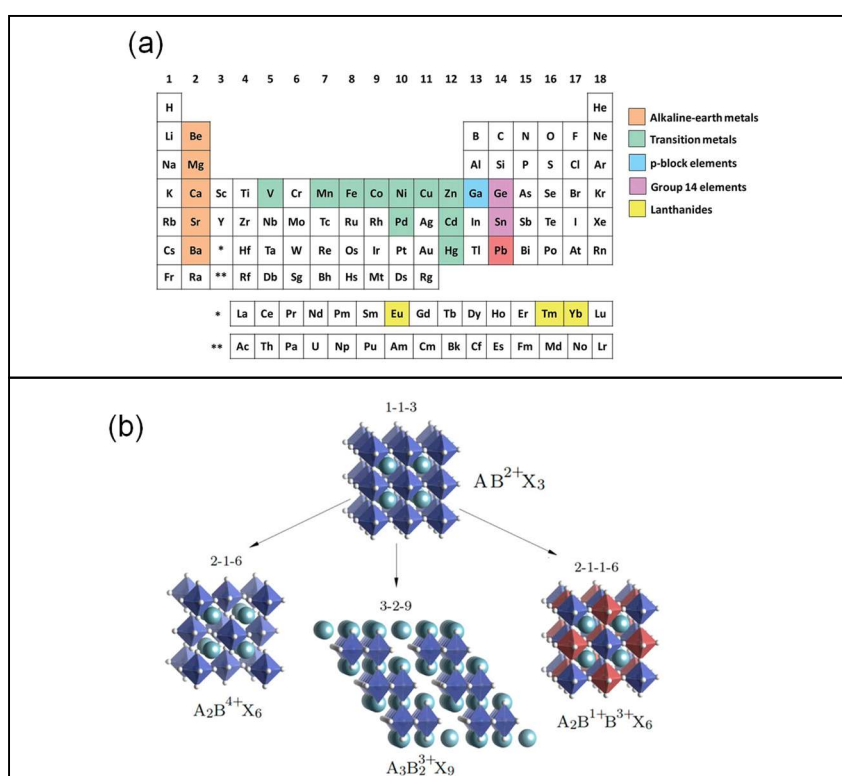


**Figure 1.4.** (a) Possible homo-valent elements from the periodic table towards the replacement of toxic lead at B-site. Reprinted from Ref [29], Copyright Royal Society of Chemistry. (b) Schematic representation of combinatorial approach to derive several perovskites from the parent structure through hetero-valent substitutions. Reprinted from Ref [50], Copyright Royal Society of Chemistry 2017.

In this direction, a few (sub) classes of perovskites can be constructed such as ternary halide perovskites, double perovskites, and defect order perovskites. In contrast to the previous case, all of these non-toxic perovskite derivatives possess superior

environmental stability with moderate performance in the devices. First of all, the replacement of all the  $B^{2+}$  in the  $ABX_3$  structure with a trivalent element will lead to  $A_3B_2^{3+}X_9$  for the charge balancing. In this direction, two suitable candidates are  $\text{Bi}^{3+}$  and  $\text{Sb}^{3+}$  as they have the same electronic configuration ( $ns$ ) and also similar atomic numbers (spin-orbit coupling) [10]. The choice of  $A$ -site cation is irrelevant as both hybrid and all inorganic ternary halide perovskites can be achieved. Hence, it is expected that such perovskites would possess novel optoelectronic and spintronic properties similar to the prototype  $\text{MAPbI}_3$ . However, these ternary halide perovskites possess a low dimensional structure (0D and 2D), as a result, superior transport properties of the 3D perovskites would be missing [51]. To resolve the issue, 3D lead-free perovskites are envisioned when a tetravalent substitution occurs. Under these circumstances, charge neutrality is balanced by either one monovalent ( $\text{Ag}^+$ ) and one trivalent ( $\text{Bi}^{3+}$ ,  $\text{In}^{3+}$ ) cation or completely by one tetravalent cation ( $\text{Sn}^{4+}$ ). The first approach would lead to the formation of double perovskites with the  $A_2B^+B^{3+}X_6$  structure. These compounds possess a 3D network similar to the  $ABX_3$  perovskites with alternate  $B^+$ - and  $B^{3+}$ -site octahedra. Alike the ternary halide perovskites, MA- and I-based double perovskites ( $\text{MA}_2\text{AgBiI}_6$ ) are not thermodynamically stable [52] and only all-inorganic double perovskites are demonstrated mostly in literature. In this regard, the most important material is  $\text{Cs}_2\text{AgBiBr}_6$ ; although a few Cl-based double perovskites ( $\text{Cs}_2\text{AgInCl}_6$ ) are also considered in this regard [11]. On the other hand, when charge neutrality is balanced by one tetravalent cation, defect-ordered perovskites with  $A_2BX_6$  are formed where a percentage of the metal sites seems to be replaced by “vacancies”. It is similar to the 3D double perovskites where one of the B-site octahedra is replaced by vacancies/defects. One such derived perovskite is  $\text{Cs}_2\text{SnX}_6$  or  $\text{MA}_2\text{SnX}_6$  [53,54].

### 1.2.2.3. X-Site Substitution

Alike  $A$ -site and  $B$ -site,  $X$ -site substitution does not have any significant role in resolving the toxicity and stability issues. However, this kind of substitution is indeed important for bandgap engineering, morphology improvement, superior carrier

dynamics, better charge transport, and so forth [55-57]. It may be noted that the valence band (VB) of  $\text{MAPbX}_3$  is composed of Pb ( $s$ ) and I ( $p$ ) antibonding characteristics. On the other hand, the conduction band (CB) is formed by the Pb ( $p$ ) states [58]. As such a change at the  $X$ -site from Cl to Br to I results in a change in the valence orbitals from  $3p$  to  $4p$  to  $5p$  accordingly. As a result, a bandgap narrowing is expected monotonically from Cl to Br to I. In this way, the optical properties of the perovskites can be tuned over a wide range of wavelength ranges. It may be noted that the bandgap of  $\text{MAPbBr}_3$  is 2.3 eV while it is 3.11 eV for  $\text{MAPbCl}_3$  [59]. Incorporation of Br and Cl at the  $X$ -site was found to be beneficial as these derived perovskites can form an energy barrier that confines electrons inhibiting the accumulation of charge carriers at the interface and back-transfer recombination [24]. Hence, similar to triple cation perovskites, mixed anion perovskites are also explored to improve the device performance[56]. These mixed halide perovskites are imperative for the energy level alignment with different materials and superior device performance thereby. Moreover, these mixed cation perovskites promote better film morphology with large size crystal grains which is vital for superior charge transport [55]. In addition to the mixed halogens, small molecular ionic moieties such as thiocyanate (SCN) and beryllium tetrafluoride ( $\text{BF}_4$ ) can also be envisaged at the  $X$ -site as dopants [60,61]. The electrical conductivity of the perovskites increases with the incorporation of these molecules. The effect of  $X$ -site substitution is similar for all of the derived perovskites as well as discussed in the previous sections.

In summary, different perovskites have been described in this section in light of their composition, crystal structure, chemical bonding, and so forth. Starting from the parent  $\text{ABX}_3$  several perovskite derivatives can be derived with the substitution of  $A$ -,  $B$ -, and  $X$ -site of the pristine compound. All of them have some advantages and disadvantages regarding toxicity, phase stability, material dimensionality, and functionalities which have been compiled (Table 1.1) along with their applications in devices.



**Table 1.1.** Different metal halide perovskites and their potential applications.

Class of	Compounds	Advantages	Disadvantages	Major Applications
<b>Perovskites</b>				
<b>Hybrid Halide Perovskites</b>	MAPbX <sub>3</sub> (X= I, Br, Cl)	Superior Performance	Stability, Toxicity	Solar Cells, Photodetectors, Spintronic Devices, Memory Devices.
	FAPbX <sub>3</sub> (X= I, Br, Cl)	Superior Performance	Stability, Toxicity	Solar Cells, Detectors, Spintronic Devices, Memory Devices.
	MASnX <sub>3</sub> (X= I, Br, Cl)	Non-Toxic	Stability, Performance	Solar Cells, Memory Devices
<b>All Inorganic Perovskites</b>	CsPbX <sub>3</sub> (X= I, Br, Cl)	Stability	Toxicity, Performance	LEDs, Spintronic Devices.
	RbPbX <sub>3</sub> (X= I, Br, Cl)	Stability	Toxicity, Performance	LEDs.
<b>Mixed Cation Perovskites</b>	(CMF)Pb(I Br) <sub>3</sub> (CMF)Pb(I Br) <sub>3</sub> = Cs <sub>x</sub> (MA <sub>0.17</sub> FA <sub>0.83</sub> ) <sub>(1-x)</sub> Pb(I <sub>0.83</sub> Br <sub>0.17</sub> ) <sub>3</sub>	Stability, Performance	Toxicity	Solar Cells, Photodetectors.
<b>Ternary Halide Perovskites</b>	MA <sub>3</sub> Bi <sub>2</sub> X <sub>9</sub> (X= I, Br, Cl)	Stability, Non-Toxic	Performance	Solar Cells, Photodetectors.
	MA <sub>3</sub> Sb <sub>2</sub> X <sub>9</sub> (X= I, Br, Cl)	Stability, Non-Toxic	Performance	Solar Cells, Photodetectors.
	Cs <sub>3</sub> Bi <sub>2</sub> X <sub>9</sub> (X= I, Br, Cl)	Stability, Non-Toxic	Performance	Solar Cells, Photodetectors, LEDs, and Memory devices.
	Cs <sub>3</sub> Sb <sub>2</sub> X <sub>9</sub> (X= I, Br, Cl)	Stability, Non-Toxic	Performance	Solar Cells, Photodetectors, LEDs, and Memory devices.
	Cs <sub>2</sub> AgBiBr <sub>6</sub>	Stability, Non-Toxic	Performance	Solar Cells, Photodetectors, LEDs, and Memory devices.
<b>Defect-Ordered Double Perovskites</b>	Cs <sub>2</sub> SnX <sub>6</sub> (X= I, Br, Cl)	Stability, Non-Toxic	Performance	Solar Cells, Photodetectors, LEDs, and Memory devices.

<b>2D Perovskites</b>	$A_2B_{n-1}Pb_nX_{3n+1}$ ( $A=$ PEA, BA $B=$ MA, FA)	Stability, Performance	Toxic	Solar Cells, Photodetectors, LEDs, Spintronic Devices, and Memory devices.
<b>Lead-Free 2D Perovskites</b>	$Cs_2CuBr_4$ $Cs_2CuBr_4$ $Cs_2SnI_4$ $MA_2SnI_4$	Stability, Non-Toxic	Performance	Solar Cells, Photodetectors, LEDs, Spintronic Devices, and Memory devices.
<b>Rudorffites</b>	$A_mB_nI_{m+3n}$	Stability, Non-Toxic	Performance	Solar Cells, Photodetectors.
<b>Chiral Perovskites</b>	$(R/S-MBA)_2PbI_4$ $(R/S-MBA)_2BiBr_5$	Spin-Related Phenomena Spin-Related Phenomena, Non- Toxic	Toxic -	Spintronic Devices, Opto- Spintronic Devices. Spintronic Devices, Opto- Spintronic Devices.

### 1.3. Electronic Band-Structures

With a brief knowledge of different metal halide perovskites with their composition and structure, the optoelectronic and spintronic properties of these materials are going to be discussed now. However, before proceeding in that direction, it is imperative to discuss their electronic band structure as several remarkable properties such as the nature of bandgap, optical characteristics, transport parameters, recombination dynamics, and spin-related features of the materials are associated with it [62]. In this direction, the formation of bands has been discussed in the prototype  $MAPbI_3$ . After that, the discussion is shifted to how different substitutions at the different sites of  $MAPbI_3$  affect the electronic bands. This, in turn, would explain the formation of bands in several other perovskites beyond  $MAPbI_3$  such as all-inorganic perovskites ( $CsPbCl_3$ ), ternary halide perovskites ( $MA_3Bi_2I_9$ ,  $Cs_3Bi_2I_9$ ), double perovskites ( $Cs_2AgBiBr_6$ ,  $Cs_2AgInCl_6$ ), and 2D RP perovskites. It is needless to state that these materials are not only associated with the doctoral research work but also cover all of the sub-classes of the perovskite family.

(i) *Band-Structure in  $MAPbI_3$* : It may be noted that the presence of Pb at the B-site is most significant towards achieving interesting properties in the material because

it has 6s electrons acting as lone pair below the valence band (VB) edge [24]. Moreover, the strong SOC of Pb induces spin-splitting resulting in a spin-polarized band structure of the compound [63]. The density of states (DOS) calculations has suggested that the VB-edge of this archetypal perovskite compound (MAPbI<sub>3</sub>) is constructed with antibonding orbitals of Pb (6s) and I (5p). On the other hand, the conduction band (CB) edge is primarily formed with an occupied Pb (6p) orbital leading to both the covalent and ionic (dual) nature of the electronic band structures (Figure 1.5) [62]. Moreover, both the band edges reside at the corner (*R*-point) in the momentum space resulting in a direct nature of the bandgap.

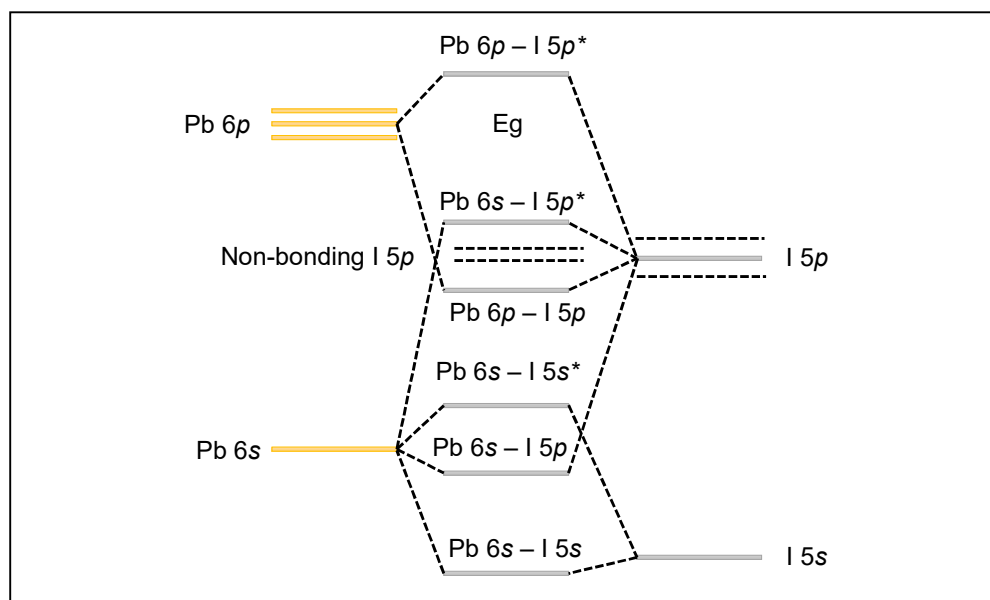


**Figure 1.5.** Band formation in MAPbI<sub>3</sub> perovskite compound. Redrawn and adapted from Ref [62], Copyright Springer 2016.

(ii) *Band-Structure of Perovskites beyond MAPbI<sub>3</sub>*: As such MA<sup>+</sup> at the *A*-site has not any direct contributions in forming the bands in MAPbI<sub>3</sub> [58]. Hence, the band structure of different *A*-site substituted perovskites (3D), such as CsPbI<sub>3</sub> or FAPbI<sub>3</sub>, own a similar band structure. However, the presence of organic moiety in the perovskite

lattice influences the electronic band structure by distorting the inorganic lattice [64]. As an example, the rotations of the organic molecule may create a “dynamical” position of the CB-edge leading to the formation of an electron basin around the high-symmetry point in the momentum space to influence several electronic properties in the material. Moreover, the steric effect of the organic moiety impacts the electrostatic background in terms of charge donation to the inorganic network [65]. In contrast, substitution at the *X*-site would tune the electronic bands (VB-edge); for this reason, the bandgap is changed from MAPbI<sub>3</sub> to MAPbCl<sub>3</sub> through MAPbBr<sub>3</sub>. As mentioned earlier, the presence of Pb is most significant while analyzing the electronic band structure. Partial doping or complete substitution also alters both the band edges meaningfully. Notably, as most of the relativistic features (associated with SOC) originate from the high-*Z* element (Pb), a replacement by a low-*Z* element (Sn) would result in the loss of these features. However, most of the lead-free derived perovskite structures, such as ternary halide perovskites (MA<sub>3</sub>Bi<sub>2</sub>I<sub>9</sub>, Cs<sub>3</sub>Bi<sub>2</sub>I<sub>9</sub>) and double perovskites (Cs<sub>2</sub>AgBiBr<sub>6</sub>) contain Bi which keeps the remarkable SOC related effects in the bands. The involvement of different atomic orbitals to form the band edges of a series of perovskite materials has been summarized in Table 1.2.

In this direction, an investigation of the band structure of 2D RP perovskites also attracts a sizable attention. It may be noted that they have a multiple quantum well-like band structure due to their structure in which the perovskite layers act as quantum wells and the large size spacer cations (PEA<sup>+</sup>, BA<sup>+</sup>) represent barriers due to their insulating nature. In these 2D perovskites, the formation of VB- and CB-edges are similar to 3D MAPbI<sub>3</sub>. Here, the major difference is that the formerly degenerate bands (appeared from Pb, and I orbitals) of MAPbI<sub>3</sub> split in the 2D RP perovskites resulting in sub-bands governed by the number of layers. Under these circumstances, both the band-edges are found to be localized in a particular domain of individual perovskite slabs. To be specific the CB-edge remains close to that of those [PbI<sub>6</sub>] layers nearer to the spacer cations and VB-edge at the central [PbI<sub>6</sub>] layers [9]. Such a multiple quantum well

nature is significant as it gives rise to dielectric and quantum confinement effects [66,67].

**Table 1.2.** Summary of band formations, bandgap, bandgap nature, and relativistic effect (spin-orbit coupling) of different metal halide perovskites used in this research work.

Perovskites	VB-Edge	CB-Edge	Bandgap	Nature	SOC	Ref
MAPbI <sub>3</sub>	I (5p)	Pb (6p)	1.55	Direct	Strong	[64,65]
MASnI <sub>3</sub>	I (5p)	I (5p), Sn(5p)	1.40	Direct	Low	[64]
CsPbCl <sub>3</sub>	Cl (3p)	Pb (6p)	3.00	Direct	Strong	[47]
MA <sub>3</sub> Bi <sub>2</sub> I <sub>9</sub>	I (5p)	Bi (6p)	2.15	Direct	Strong	[51]
Cs <sub>3</sub> Bi <sub>2</sub> I <sub>9</sub>	I (5p)	Bi (6p)	2.03	Direct	Strong	[51]
Cs <sub>3</sub> Sb <sub>2</sub> I <sub>9</sub>	I (5p)	Sb (5p)	2.15	Direct	Low	[67]
Cs <sub>2</sub> AgBiBr <sub>6</sub>	Br (4p) Ag (4d)	Bi (6p)	2.00	Indirect	Strong	[66]
Cs <sub>2</sub> AgBiCl <sub>6</sub>	Ag (4d) Cl (3p)	Bi (6p) Cl (3p)	2.69	Indirect	Strong	[62]
(BA) <sub>2</sub> PbI <sub>4</sub>	I (5p)	Pb (6p)	2.20	Direct	Strong	[38]
(BA) <sub>2</sub> MAPb <sub>2</sub> I <sub>7</sub>	I (5p)	Pb (6p)	2.05	Direct	Strong	[38]
(BA) <sub>2</sub> MA <sub>2</sub> Pb <sub>3</sub> I <sub>10</sub>	I (5p)	Pb (6p)	1.90	Direct	Strong	[38]

## 1.4. Optoelectronic Properties of Metal Halide Perovskites

With the knowledge of band structures, the optoelectronic properties of different metal halide perovskites would be deliberated in this section. It may be noted that the unique optoelectronic properties of perovskites are originated from several interesting optical (suitable optical bandgap, high absorption coefficient, direct bandgap nature, and excitonic character) and electronic properties (small electron and hole effective mass, high mobility, slow recombination, and large diffusion length) of the compounds. Similar to the discussion of band structures, these properties would be discussed primarily considering MAPbI<sub>3</sub> as a reference followed by a discussion of how they are changed in the other derived perovskites, for example, ternary halide perovskites (MA<sub>3</sub>Bi<sub>2</sub>I<sub>9</sub>, Cs<sub>3</sub>Bi<sub>2</sub>I<sub>9</sub>, Cs<sub>3</sub>Sb<sub>2</sub>I<sub>9</sub>), double perovskites (Cs<sub>2</sub>AgBiBr<sub>6</sub>), and quasi-2D perovskites (RP phase). In addition, a few novel phenomena (hot carriers and edge states) would be discussed; although these are not common in all perovskites, they have

a significant role in achieving superior optoelectronic applications from certain perovskite systems [68,69].

### 1.4.1. Optical Properties

Most of the metal halide perovskites exhibit strong optical absorption in the visible region. Interestingly, their absorption coefficient is very high ( $\sim 10^5 \text{ cm}^{-1}$ ) enabling a sufficient amount of light absorption by a thin layer of such materials [70]. In general, optical absorption in a material is explained considering the Fermi Golden rule which is further correlated with (i) transition probability of electrons governed by the transition matrix associated with VB to CB energy levels and (ii) the joint DOS measuring the total number of such transitions [71]. As a result, optical absorption in perovskites is majorly related to the band structures as described in the previous section. It may be noted that due to an indirect bandgap, transition probability would be lower resulting in lower absorption of light for a given thickness. Hence, most of the perovskites possessing a direct bandgap need a thinner absorber layer compared to silicon (indirect bandgap) in photovoltaic devices to facilitate sufficient light absorption.

The strong optical absorption in prototype  $\text{MAPbI}_3$  originated from the large optical transitions in the bands. As explained earlier, CB is formed mainly with the unoccupied Pb ( $6p$ ) orbitals whereas VB is derived from the I ( $5p$ ) and Pb ( $6s$ ) orbitals [58,63,72]. Hence, both inter-atomic and intra-atomic transitions are possibly associated with I ( $p$ )  $\rightarrow$  Pb ( $p$ ) and Pb ( $s$ )  $\rightarrow$  Pb ( $p$ ), respectively. In addition, as VB and CB are situated at the same value in momentum space due to the direct nature of the bandgap, it will promote strong optical absorption in a thin layer. Now, similar optical absorption will be observed in different  $A$ -site substituted perovskites, such as  $\text{FAPbI}_3$  and  $\text{CsPbI}_3$ , as the band structure and transition probability would remain the same. In this direction,  $B$ -site substituted  $\text{MASnI}_3$  or  $X$ -site substituted  $\text{MAPbBr}_3$  and  $\text{CsPbCl}_3$  will indeed alter the transition probability and joint DOS; as such these changes are almost negligible resulting in a little change in optical absorption coefficient and thereby the absorbance. However, all these derived perovskites have a different bandgap; as a result, the absorption will occur at different wavelengths resulting in bandgap tunability.

This strong optical absorption is a common feature for other derived perovskites as well beyond the  $ABX_3$  structure. The ternary halide perovskites ( $MA_3Bi_2I_9$ ,  $Cs_3Bi_2I_9$ ) also possess similar optical transitions for their direct bandgap nature and involvement of similar Bi orbitals [10]. In contrast, the double perovskites ( $Cs_2AgBiBr_6$ ) possess indirect bandgap [11]. As a result, they need a thicker absorber layer for their optoelectronic (photovoltaic) applications. On the other hand, the optical properties of 2D RP perovskites are almost similar to the  $MAPbI_3$ -based perovskites [9].

### 1.4.2. Excitonic Character

Absorption of a photon in halide perovskite results in the generation of exciton which is a quasi-particle made of electron and hole bonded by Coulomb force. In photovoltaic devices, dissociation of excitons into free carriers has been considered a prerequisite. In this regard, exciton binding energy ( $E_b$ ) in  $MAPbI_3$  is found to be small (15 meV) making them suitable for solar cell applications [73]. As  $MAPbI_3$  possesses a large dielectric constant,  $E_b$  can be expressed in light of the Wannier exciton model:

$$E_b = \frac{13.6 m^*}{\epsilon_r^2} \quad (1.2)$$

where,  $m^*$  and  $\epsilon_r$  represent the reduced mass of exciton and the dielectric constant, respectively [74]. Now the total dielectric constant could be deconvoluted into three components as follows

$$\epsilon_r = \epsilon_{pol} + \epsilon_{vib} + \epsilon_{dip} \quad (1.3)$$

where  $\epsilon_{pol}$  appears from the polarizable electron density,  $\epsilon_{vib}$  denotes the vibrational contribution, and  $\epsilon_{dip}$  signifies the dipolar contribution [24]. It may be noted that as  $MAPbI_3$  consists of elements of high atomic number (Pb, I),  $\epsilon_r$  (~20) in this material is mostly governed by the first term ( $\epsilon_{pol}$ ) along with a secondary contribution from the third term ( $\epsilon_{dip}$ ). As a result, a change at the  $A$ -site by  $Cs^+$  or  $FA^+$  would not significantly change the  $\epsilon_r$  and  $E_b$  of the compounds. However, a little increase in  $E_b$  in all-inorganic perovskites ( $CsPbI_3$ ) is expected as  $\epsilon_r$  decreases due to the loss of molecular framework and  $\epsilon_{dip}$  term thereby. On the other hand, a replacement of  $X$ -site cation will lead to a

change in  $\epsilon_{\text{pol}}$ . Under these circumstances,  $\epsilon_r$  would be decreased from I<sup>-</sup> to Cl<sup>-</sup> through Br<sup>-</sup> to increase  $E_b$  accordingly. Similarly, one can predict the change of  $E_b$  upon *B*-site substitution. As an example, in  $\text{MASnI}_3$ , a decrease of  $\epsilon_r$  is expected as Sn has a lower atomic number than Pb resulting in an increase of  $E_b$ . Interestingly,  $E_b$  also depends on the quantum confinement and dielectric confinement effect. As an example, in 2D perovskites obtained through *A*-site cation engineering, the scenario becomes different and  $E_b$  increases primarily due to a dielectric confinement effect [75,76]. Similarly, in lead-free perovskites (beyond  $\text{MAPbI}_3$ ), such as ternary halide perovskites ( $\text{MA}_3\text{Bi}_2\text{I}_9$ ), although there are heavier elements,  $E_b$  is still very large due to the strong quantum confinement effect originating from the 0D structure. On the other hand,  $E_b$  is comparatively lesser in double perovskites ( $\text{Cs}_2\text{AgBiBr}_6$ ) due to their 3D structure.

### 1.4.3. Electronic Properties: Charge Transport

In a semiconductor, superior charge transport signifies the efficient flow of electrons/holes and their control. Efficient transport of charge carriers generated after the dissociation of excitons is critical for the operation of perovskite-based photovoltaic devices (solar cells, photodetectors). In this direction, achieving a high efficiency in such devices depends on their excellent transport properties [77]. These materials own small carrier effective mass, long carrier lifetime and diffusion length, high mobility, and ambipolar conductivity [78]. They all contribute jointly towards the efficient charge transport in optoelectronic devices.

Primarily, the effective mass ( $m^*$ ) of electrons and holes is imperative in determining an efficient transport role. Mathematically,  $m^*$  has been expressed as

$$m^* = \hbar^2 \left[ \frac{\partial^2 \epsilon(k)}{\partial k^2} \right]^{-1} \quad (1.4)$$

where  $\hbar$  is the reduced Planck constant and  $\epsilon(k)$  is the energy dispersion relation function associated with the band edges as a function of momentum ( $k$ ). It may be noted that a much dispersive nature of the band edges signifies a smaller effective mass. Interestingly, in  $\text{MAPbI}_3$  perovskite, the VB- and CB-edges are formed with Pb (*s*) and I



( $p$ ) orbitals, and Pb ( $p$ ) orbitals respectively. The strong coupling between  $s$  and  $p$  orbitals makes the VB-edge dispersive. On the other hand, involvement of the heavy  $p$  orbitals of Pb results in a much dispersive CB edge too. As a result,  $m^*$  for both the carriers (electron in CB and hole in VB) are small in MAPbI<sub>3</sub>. More importantly,  $m^*$  is at the same level for both electrons and holes in this compound signifying a similar ability of transport (ambipolarity). The effective mass of charge carriers determines the charge carrier mobility ( $\mu$ ). The mobility of MAPbI<sub>3</sub> is 100 cm<sup>2</sup> V<sup>-1</sup> s<sup>-1</sup> as obtained from Hall effect measurements [78]. In this direction, the other important parameters are carrier lifetime and diffusion length in governing efficient charge transport. It has been found that the carrier lifetime and diffusion length in MAPbI<sub>3</sub> is significantly large originating from a slow recombination process. Several microscopic phenomena, such as defect tolerance nature, presence of ferroelectric domains, polaron formation, Rashba effect in both bands, and photon recycling are also being considered. *A detailed discussion about these interesting processes can be found in a review article written during this doctoral research which is attached at the end of this thesis (preprints) [79].* Hence, the joint contribution of low carrier effective mass, long carrier lifetime and diffusion length, high mobility, and ambipolar conductivity make carrier transport superior in the prototype MAPbI<sub>3</sub>.

Now, it will be intriguing to see to what extent this efficient charge transport sustains in other derived perovskites. Because of this, it is customary to mention that the presence of organic moiety is important behind the slow recombination process and thereby the long carrier lifetime and diffusion length. As a result, although the superior transport could be observed in FAPbI<sub>3</sub>, it diminishes to some extent in all inorganic (CsPbI<sub>3</sub>) perovskites [8]. In addition, the 3D network of the inorganic lattice is also important in efficient charge transport acting as continuous pathways. In this direction, charge transport in ternary halide perovskites (MA<sub>3</sub>Bi<sub>2</sub>I<sub>9</sub>, Cs<sub>3</sub>Bi<sub>2</sub>I<sub>9</sub>, MA<sub>3</sub>Sb<sub>2</sub>I<sub>9</sub>, Cs<sub>3</sub>Sb<sub>2</sub>I<sub>9</sub>) suffers major problems owing to their 0D dimer-like structure [10]. As a result, despite their other suitable optoelectronic properties, the device performance of these materials has not excelled yet and the current research theme is focused on the dimensionality

engineering of these materials. Moreover, like MAPbI<sub>3</sub> most of these ternary halide perovskites, especially the inorganic ones, are not defect tolerant and non-radiative recombination also limits the charge transport [80]. In contrast, the double perovskites (Cs<sub>2</sub>AgBiBr<sub>6</sub>) possess a 3D framework to exhibit better charge transport but the presence of defects originating from the cation disorder such perovskites also confine the charge transport [11]. Although, 2D RP perovskites possess most of the superior optoelectronic properties in MAPbI<sub>3</sub>, charge transport in these perovskites is not as superior as their 3D counterpart. It may be recalled that in the 2D perovskites, long-chain spacer cations create an insulating barrier resulting in poor charge transport [29]. Hence, it may be concluded that although the superior optical properties sustain in most of the other perovskites beyond MAPbI<sub>3</sub>, the electronic properties, particularly charge transport gets hampered on a serious note resulting in poor performance in optoelectronic devices such as solar cells. *In this direction, a significant part of the thesis (related to the optoelectronic applications of metal halide perovskite) is focused on the investigation of poor charge transport in different lead-free perovskites and the strategies to improve it [51,81].*

#### **1.4.4. Defect Physics: Ion Migration and Recombination**

Most of the metal halide perovskites are synthesized through a crude solution process approach. Hence, the presence of a large number of defects and/or imperfections are inevitable in atomic-scale (point-defect), nanoscale (structural disorder), and micro-scale (grain boundary defects), respectively. Some of the commonly formed defects in metal halide perovskites are presented in Figure 1.6. The topic of defect physics in metal halide perovskites is vast and hard to discuss thoroughly in this context. *However, a detailed analysis could be found in another review article written during this doctoral research and is being attached to the reprint section [82].* This article discusses different types of defects, their characterization techniques, their detrimental roles, and different routes to passivate them. Here, in this section, a precise

discussion would be deliberated focusing on the role of defects in MAPbI<sub>3</sub> and other perovskites in their optoelectronic properties.

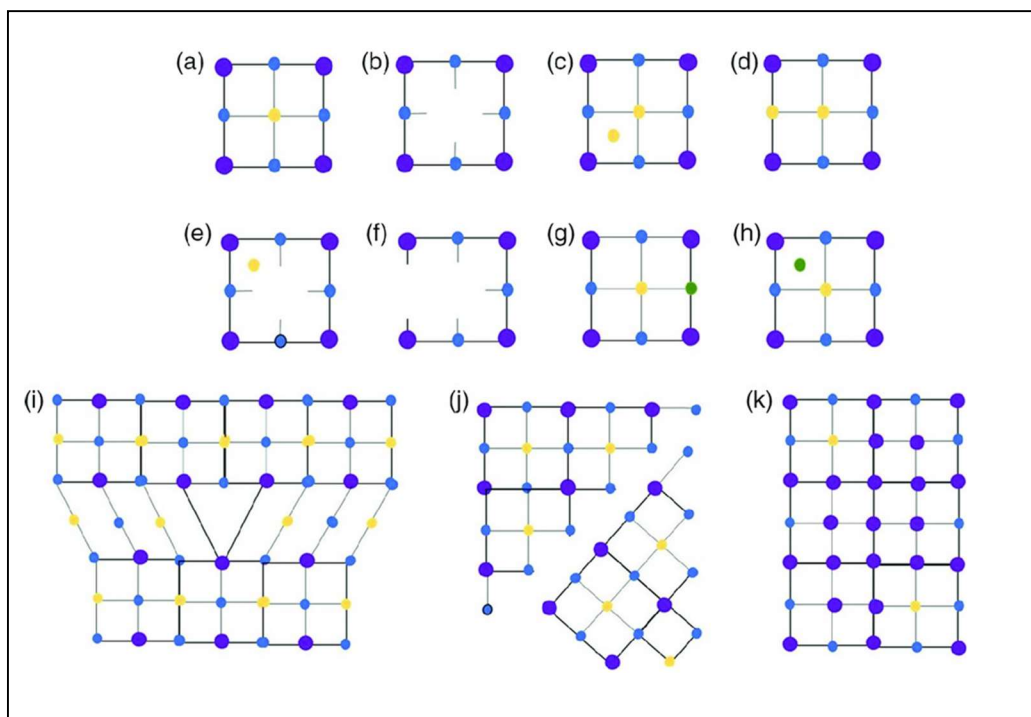


**Figure 1.6.** Schematic representation of different types of defects in metal halide perovskites. *a)* A perfect perovskite lattice, *b)* vacancy at the A-site, *c)* an interstitial defect, *d)* an antisite substitution (an A-ion occupying an X-site), *e)* Frenkel defects, *f)* Schottky defects, *g)* substitutional impurity, *h)* interstitial impurity, *i)* edge dislocation, *j)* grain boundary, and *k)* precipitate.

The defect physics in metal halide perovskites are crucial for their optoelectronic applications as recombination dynamics, and thereby lifetime and diffusion length are determined by them. To be specific, such point defect sites and/or induced impurities can act as a non-radiative recombination center resulting in an impeded transport of the charge carriers. Interestingly, in the prototype MAPbI<sub>3</sub>, it has been found that although the donor-like and acceptor-like traps may lead to the doping type-change within the material, the bandgap remains invariant [80]. Previous

computational investigations have highlighted the formation energies for the point defects in various forms including the site vacancies ( $V_{MA}$ ,  $V_{Pb}$ , and  $V_I$ ), interstitials ( $MA_i$ ,  $Pb_i$ , and  $I_i$ ), anti-site substitutions ( $MA_I$ ,  $Pb_I$ ,  $I_{MA}$ , and  $I_{Pb}$ ), and cation substitutions ( $MA_{Pb}$  and  $Pb_{MA}$ ). The vacancies and interstitials are the most common defects present in the halide perovskite, which can further introduce shallow states within the bandgap and influence charge behavior. However, they are not so detrimental to their optoelectronic properties leading to a defect-tolerant nature in contrast to ternary halide and double perovskites. However, the coexistence of ion/vacancy migration, each procedure within the photovoltaic process including the photo-generated electron-hole pairs, electron-hole separation, recombination, conduction, and extraction will be mutually affected, making the system even more complex [83]. In this case, the electron and hole wavefunctions could be localized at the grain boundaries and additional phonon modes can be generated. Such an electron-phonon coupling effect will result in a higher rate of non-radiative recombination [84]. However, the low activation energy of defects and modest ionic diffusion coefficients of different charged defects ions in halide perovskite has inspired worldwide research in nonvolatile memory and switchable photovoltaics [13,85].

### 1.4.5. Hot Carriers

According to the Boltzmann distribution, hot carriers denote charge carriers having preliminary kinetic energy over  $kT$  above the band-edges [86]. Such hot carriers are generated through a successive thermalization of photo-generated (above bandgap) charge carriers at a non-equilibrium condition. Generally, within a small timescale (picoseconds) these hot carriers reach their equilibrium with the lattice through cooling. Such cooling is generally governed by different spontaneous processes such as Auger recombination, electron-phonon scattering, and so forth [87]. Moreover, an ultra-low thermal conductivity is also required for the slow hot carrier cooling. In Figure 1.7a, the mechanism of hot carriers cooling has been presented at the VB- and CB-edges. Notably, slower hot carrier cooling is imperative to extract the additional energy from

the hot carriers [88]. With the aid of this extra energy, several optoelectronic technologies including hot-carrier solar cells exceeding the Shockley-Queisser limit can be envisaged [87]. In this direction, although the origin of hot carrier cooling is controversial, a prolonged cooling time has been discovered in metal halide perovskite. As such, the topic of hot carriers is not directly related to the scope of the thesis but to unleash the full potential of these materials in optoelectronics, such properties are very much significant.

#### 1.4.6. Edge States

Based on the discussions till now, it is more or less clear that the presence of lead is very much important for the superior optoelectronic properties of metal halide perovskites. So, the prime concern should be the stability enhancement of such compounds keeping lead in the structure [9]. In this direction, quasi-2D RP perovskites with quantum-well-like structures exhibit excellent optoelectronic properties with better stability. For example, the power conversion efficiency in such solar cell devices has reached 15% with a better operation time compared to MAPbI<sub>3</sub> [38]. However, such high performance is surprising because of the high exciton binding energy of 2D perovskites appearing due to the quantum confinement effect [69,75,89,90]. In contrast to conventional organic semiconductors, no intentional donor-acceptor architecture is even required to facilitate exciton dissociation in the RP perovskites. This apparent anomaly of exciton dissociation and superior optoelectronic properties in the 2D-RP phase has been explained by considering the existence of lower energy edge states having different optoelectronic properties as compared to the interior region (Figure 1.7b). It is predicted that excitons are dissociated at the edges of perovskites. However, the formation mechanism of edge states, their spatial extent, and more importantly the mechanism of exciton dissociation is still under investigation. *In this context, significant work has been carried out during this doctoral research to reveal this anomaly.*

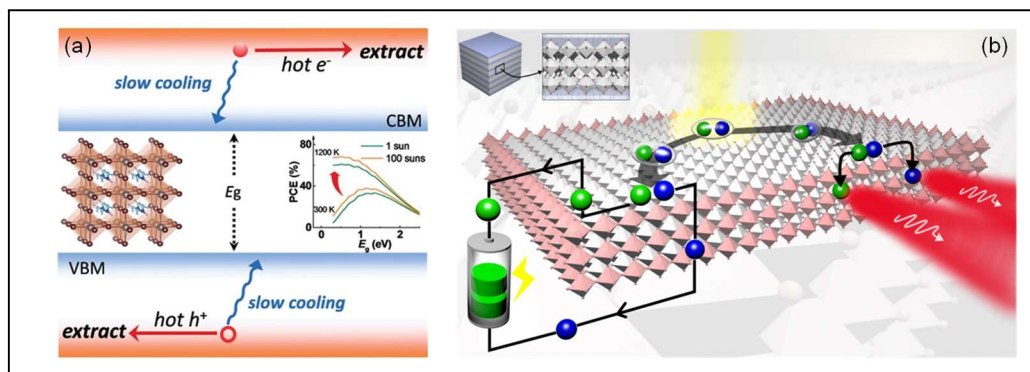


**Figure 1.7.** (a) Schematic representation of hot carrier cooling in perovskite. Reprinted from Ref [88], Copyright Wiley VCH 2018. (b) Edge state-driven exciton dissociation in 2D perovskites.

Picture courtesy [www.phys.org](http://www.phys.org).

## 1.5. Spintronic Properties of Metal Halide Perovskites

As mentioned earlier, hybrid halide perovskites are also suitable for several spintronic applications. Numerous spin-related optoelectronic properties have been explored in metal halide perovskites such as triplet formation, spin selective optical Stark effect, different magneto-optical phenomena, and polarized light-related effects [91]. Most of these novel spintronic properties originate from a strong SOC. In this section, after providing the origin of SOC in these compounds, several spintronic properties of metal halide perovskites would be discussed.

### 1.5.1. The Emergence of Spin-Orbit Coupling (SOC)

It may be noted that most of the metal halide perovskites contain heavy elements with high atomic numbers ( $Z$ ) such as Pb ( $Z = 82$ ), Bi ( $Z = 83$ ), and I ( $Z = 53$ ). Due to their high  $Z$ , a spin-orbit coupling parameter is induced spontaneously ( $\text{SOC} \sim Z^4$ ) in these compounds. Such strong SOC influences several optical and electronic (transport) properties such as bandgap, the strength of optical oscillators, the effective mass of the carriers, and so forth [15]. Moreover, a SOC-induced change of symmetry at conduction band minimum affects the electron-phonon coupling processes and Auger

recombination [24]. Similar to the optoelectronic properties several spin-related phenomena in metal halide perovskites appear due to the strong SOC. Primarily, SOC in a non-centrosymmetric perovskite splits the conduction and valence band resulting in a Rashba and Dresselhaus effect [63,92]. This SOC-induced effect is considered the driving force for several perovskite-based spintronic devices. Moreover, spin-triplet formations, complex light emissions, and different magnetic responses are governed by SOC in the perovskite compounds. In the next sections, these SOC-related effects are discussed. In contrast to most of the optoelectronic properties, these effects should be found in various perovskites beyond the prototype MAPbI<sub>3</sub>; especially, lead-free bismuth-based ( $Z = 83$ ) perovskites such as ternary halide perovskites (MA<sub>3</sub>Bi<sub>2</sub>I<sub>9</sub>) and double perovskites (Cs<sub>2</sub>AgBiBr<sub>6</sub>) would be a suitable choice in this regard. Moreover, the non-centrosymmetric 2D perovskites (containing lead) are also very promising with similar SOC (superior spintronic properties thereby) and better stability [93].

### 1.5.2. Rashba and Dresselhaus Effect

The Rashba and Dresselhaus effect is defined as a momentum-dependent spin-splitting of the spin bands around the band-extrema in momentum space ( $k$ -space). Such a splitting in the bands of metal halide perovskites appears from the large SOC arising out of high- $Z$ -elements in the compound along with a lack of centrosymmetry appearing due to a tilted PbI<sub>6</sub> octahedral. Due to the Rashba and Dresselhaus effect, an effective magnetic field is generated that removes the spin degeneracy resulting in a spin splitting (Figure 1.8). As a result, spin polarization occurs even in the nonmagnetic compound. Such a phenomenon was first demonstrated in the archetypal MAPbI<sub>3</sub> [91]. Although, the effects are similar, a significant difference between Rashba and Dresselhaus effects is their different types of symmetry breaking. Rashba effect originates from a site inversion asymmetry whereas the Dresselhaus effect occurs due to the bulk inversion asymmetry [94]. Previously, the Rashba effect in MAPbI<sub>3</sub> has been indirectly verified through circularly polarized light (CPL) induced pump-probe measurements and angle-resolved photoelectron spectroscopy [17]. *In this direction, a direct method for the*

observation of this spin-splitting has been also developed during this doctoral research through spin-polarized scanning tunneling spectroscopy [63]. The amount of the splitting could be measured with the splitting parameter as follows

$$\alpha = \frac{2E_0}{k_0} \quad (1.5)$$

where  $E_0$  is the amplitude of band splitting and  $k_0$  is the shift between two split bands in the  $k$ -space. According to the previous reports, the splitting energy and splitting parameter are found to be significantly high. Such a large splitting is beneficial as it can slow down the carrier recombination leading to a high carrier lifetime [92]. Due to the nonidentical nature of splitting in the two bands, photogenerated carriers find themselves effectively in an indirect bandgap in the momentum space and hence become long-lived. In this regard, *this doctoral research work deliberates an interesting description of this slow recombination process* [79]. The spin-polarized band structure of the material reveals that the inner pair of split levels ( $VB_1$  and  $CB_1$ ) possess similar kinds of spin texture or spin states. In addition, it has been found that the individual molecules act like single-spin domains [63]. Under this situation, two types of recombination could be possible namely interdomain and intradomain recombination. Practically, due to the presence of Wannier exciton where electrons and holes reside in different molecules, the major recombination process should be interdomain in nature. However, due to the spin-forbidden nature of this process, recombination becomes restricted in this material.

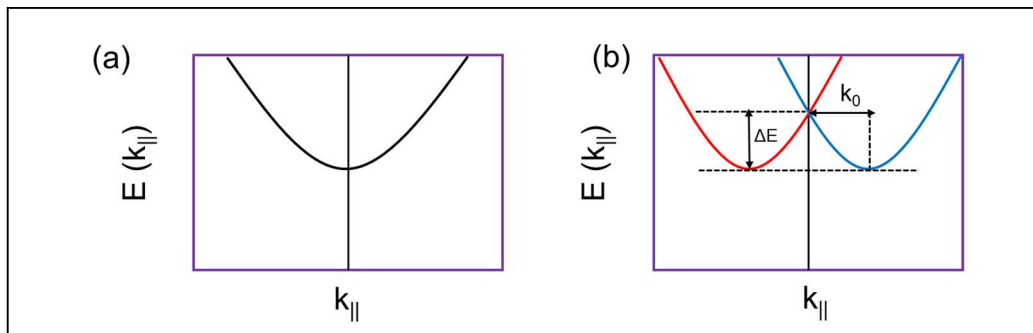


**Figure 1.8.** (a-b) Bands with and without Rashba splitting.



In addition, Rashba splitting along with several other spin-related phenomena associated with the generation, detection, and modulation of spin currents could open new avenues in spintronics. For example, coupling of Rashba splitting with spin Hall effect (spin current generation), Edelstein effect (conversion of charge to spin), and spin galvanic effect (detection of spin) might be useful for the design of highly efficient spin hall effect (SHE) transistors, spin field-effect transistors (spin-FET), spin logic devices, Stern-Gerlach spin-filters, and so on [94]. Finally, it would be useful to point out some of the newly proposed findings related to the Rashba effect beyond archetypal  $ABX_3$ . Recently, the Rashba effect has been observed in layered 2D perovskites along with a layer dependence of the effect. Both theoretical and experimental results exhibited that Rashba band splitting occurs for even numbers of inorganic layers [93]. Moreover, the Rashba effect is also expected in various lead-free perovskites such as ternary halide perovskites ( $MA_3Bi_2I_9$ ) due to the presence of high-Z elements in the compounds.

### 1.5.3. Spin Triplet Formation

Polarized light interaction produces spin pairs (electron/hole pair) in metal halide perovskites. Circularly polarized light ( $\sigma^+$ ) produces parallel spin states whereas linear excitation ( $\sigma^+ + \sigma^-$ ) generates antiparallel spin states (Figure 1.9a) [16]. The parallel and antiparallel pairs form triplet ( $2S+1=3$ ) and singlet ( $2S+1=1$ ) products respectively where  $S$  denotes the total spin of the pair. The presence of triplet products is beneficial in metal halide perovskites as the recombination is slower in triplets compared to the singlets. Even for unpolarized photoexcitation, triplets can be formed due to the strong SOC. Under this situation, the generally formed singlets can turn into triplets as well through an intersystem crossing phenomenon that involves both dissociation and recombination (Figure 1.9b) [92]. This transition of singlets into longer-lived triplet states is also considered a major aspect of the high carrier lifetime of the material. A long lifetime of triplet states can be directly correlated to the proposition of the Rashba effect associated slow recombination process. The effective orbital angular momentum in the triplet states would be larger than in the singlet states. As a result, the Rashba

splitting would be amplified in the bands involving triplet states. It may be recalled that a larger Rashba splitting promotes less allowed recombination. Hence, the stability of the triplet states would be larger compared to the singlet states.

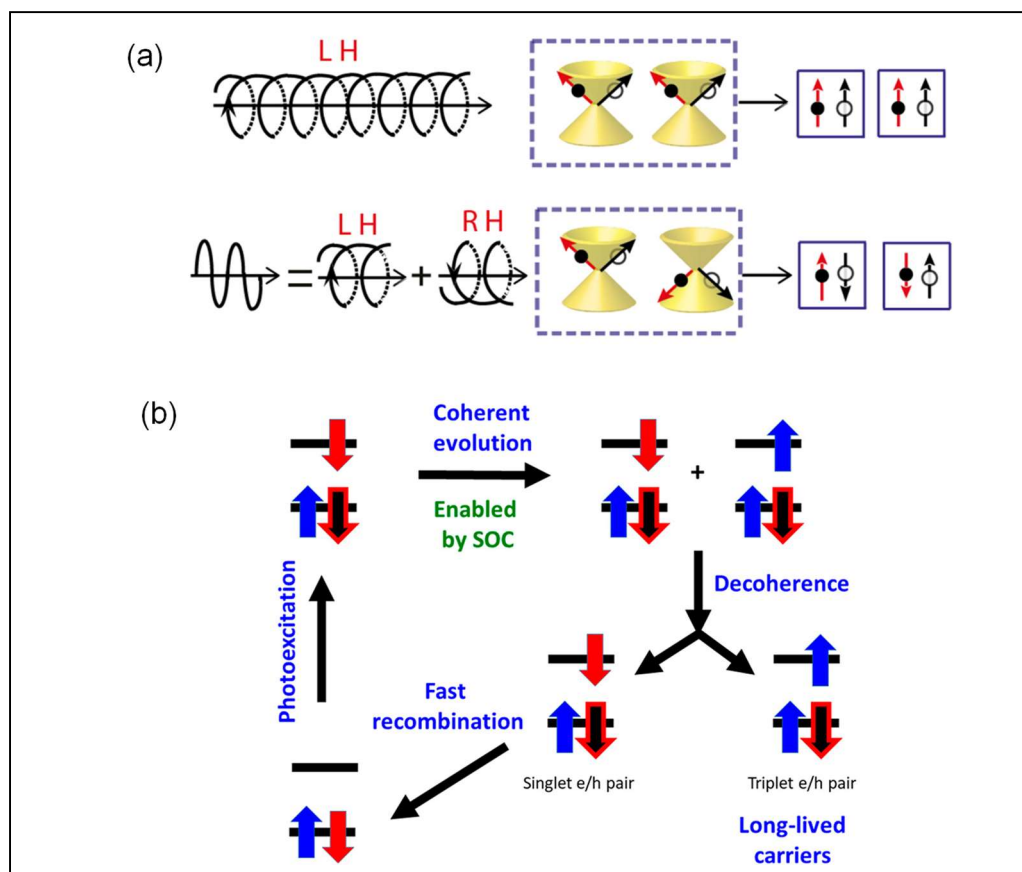


**Figure 1.9.** (a) Generation of triplet and singlet pair formation by circularly and linearly polarized light. Reprinted from Ref [16], Copyright Elsevier 2017. (b) The internal conversion process and generation of long-lived triplet pairs under (unpolarized) photoexcitation. Reprinted from Ref [92], Copyright American Chemical Society 2018.

#### 1.5.4. Magnetic Response and Magneto-Optical Phenomena

The application of an external magnetic field in metal halide perovskites can induce a series of interesting spin-related effects such as magnetoresistance,

magnetocapacitance, magneto-photoconductivity, magneto-photoluminescence, and magneto-electroluminescence [15,91]. The density (population) of photoexcited spin-pairs possessing both singlet and triplet configurations can be altered with the application of an external magnetic field which changes the characters of spin-sublevels as discussed in the spin-pair manifold. As a result, the rate of spin-mixing or crossover can be tuned resulting in a modulation of their (spin-pairs) steady-state populations [24]. In this direction, a detailed description of this process has been demonstrated by Zheng et al (Figure 1.10) [19]. They proposed that the spin-pair species could undergo a precession between singlet and triplet configurations depending on the magnitude of the magnetic field and most importantly the difference between the  $g$ -factor of electron and hole in a particular spin-pair species ( $\Delta g$ ).

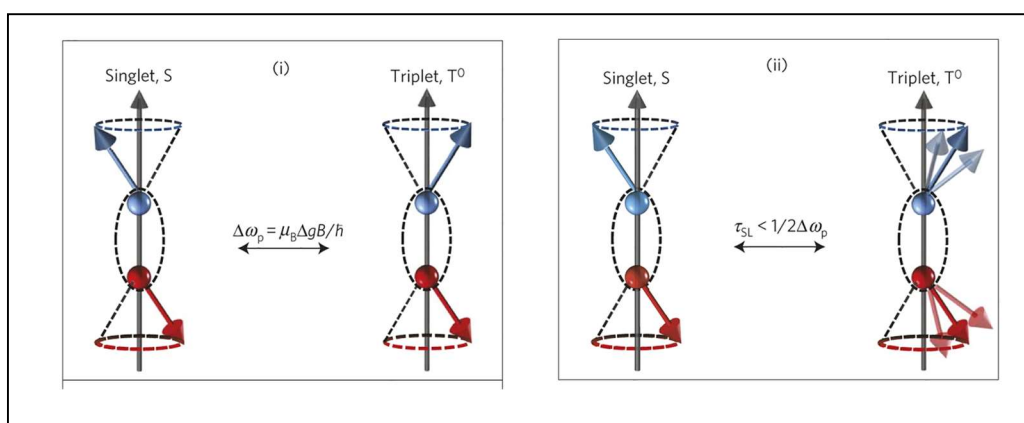


**Figure 1.10.** Spin mixing between electrons and holes when spin relaxation is much slower (upper) or faster (bottom) than spin intercrossing. Reprinted from Ref [19], Copyright Springer Nature 2015.

Under this situation, the large SOC effects would shorten the spin-lattice relaxation time ( $\tau_{SL}$ ) of the spin-pair species. It may be noted that  $\tau_{SL}$  is even shorter than the timescale associated with the field-induced population changes among the sublevels of spin-pairs. In this direction, the spin precession frequency difference between the spin of a pair can be expressed as:

$$\Delta\omega_P = \frac{\mu_B \Delta g B}{\hbar} \quad (1.6)$$

where  $\mu_B$  is the Bohr magneton and  $B$  denotes the strength of the magnetic field. Such frequency difference would be induced when the state is crossing between the singlet and the triplet. Consequently, a magnetic field-induced photocurrent, photoluminescence, and electroluminescence would be observed.

### 1.5.5. Chirality-Induced Spintronic Properties

Recently, an interesting avenue has been discovered to enhance the spintronic properties of metal halide perovskites by introducing a chiral organic sub-lattice into the entire hybrid system [43]. Chirality is considered an important structural property of certain materials in which right-handed (*R*: Rectus) and left-handed (*S*: Sinister) chiral compounds possess identical chemical conformation but cannot be superimposed with each other by a mirror transformation resulting in a loss of inversion symmetry. Chiral perovskites can be used in the injection and detection of spin signals. On the other hand, the combination of the spin-filtering effect has opened a new research domain, called chiro-spintronics or chiral-based spintronics [42]. As discussed earlier, achiral perovskites also exhibit promising spin-related properties due to the presence of strong spin-orbit coupling, large Rashba splitting, and long spin lifetimes. However, such an application can only be envisaged with the use of a magnetic field to generate a sufficiently large concentration of spin-polarized electron-hole pairs. On the other hand, chiral perovskites inherently enable spin-polarized absorption and emission. As a result, it can be stated that chiral perovskites are the missing link that can integrate the optoelectronic and spintronic properties of metal halide perovskites easily towards advanced devices. *In this direction, an effort was made during the research work by introducing a pair of novel chiral perovskites and a proper methodology of device fabrication to detect the polarization states of CPL photons with the highest accuracy.*

## 1.6. Device Applications

While the most significant application of metal halide perovskites is in solar cells, these materials have also exhibited excellent performance in a wide range of other applications, such as photodetectors, light-emitting diodes, resistive switching devices, gas sensors, and spintronic devices. However, considering the scope of the thesis and related research work, the advancements of different optoelectronic and spintronic devices have been discussed in the following.

### 1.6.1. Solar Cells

Primarily, metal halide perovskites were introduced as an absorber layer in dye-sensitized solar cells by Miyasaka and co-workers [5]. In such devices, the perovskite was adsorbed on a  $\text{TiO}_2$  layer. The perovskite layer absorbs light having a suitable wavelength matching the bandgap and facilitates photoexcitation. The photogenerated electrons in the perovskite layer are then transferred into the CB of  $\text{TiO}_2$  and finally transported to the fluorinated tin oxide (FTO) electrode. Next, the electrons drift in the outer circuit to the counter electrode (cathode) and are associated with the oxidized species of electrolyte typically required in this sensitization concept. However, in contrast to the principle of such solar cells, later studies suggest that the photogenerated charge carriers (both electrons and holes) could be transported through the perovskite medium itself without any semiconducting scaffold resulting in an exploration of the potential of perovskites in *n-i-p* and *p-i-n* solar cells [77]. These different architectures are illustrated in Figure 1.11a. In both cases, the perovskite acts as an intrinsic absorber layer sandwiched between two selective contacts (*p* and *n*). Generally, in the first structure (*n-i-p*),  $\text{TiO}_2$  (compact or mesoporous layer) is widely used as an *n*-type electron transport layer (ETL), perovskite works as the intrinsic (*i*) absorber layer, and a spiro-OMeTAD (an organic molecule) is employed as the *p*-type hole transport layer (HTL). On the other hand, the *p-i-n* structure is fabricated with the inverted geometry where the intrinsic perovskite is sandwiched between a *p*-type material (for example,

PEDOT: PSS) at the bottom and an *n*-type layer (for example, PCBM) at the top. With the rapid advancement of both material and device engineering including perovskite film formation (Figure 1.11b) and selecting the suitable choice of the carrier transport layer, the power conversion efficiency has reached 25% in MAPbI<sub>3</sub>-based solar cells (Figure 1.11c).

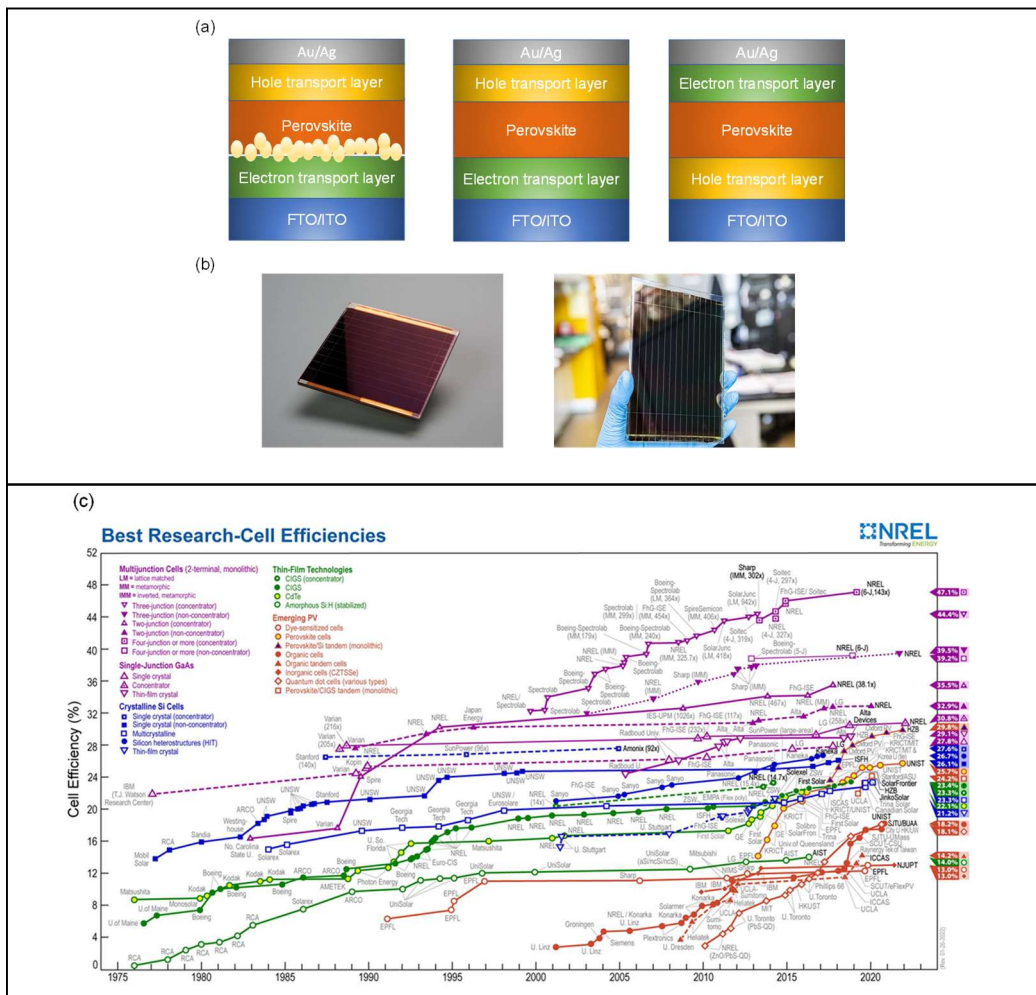


**Figure 1.11.** (a) Different device architecture of metal halide perovskite. (b) Digital images of perovskite solar cells. Picture courtesy [www.pv-magazine.com](http://www.pv-magazine.com) and National Renewable Energy Laboratory (NREL). (c) Efficiency chart of metal halide perovskites as published by NREL.

However, due to the instability of the compounds and toxicity of lead, research direction has shifted towards other perovskite derivatives as well. In this direction, all inorganic perovskites, 2D-RP perovskites, and lead-free perovskites have emerged over the years [7-11]. The performance of solar cell devices based on these materials is presented in Table 1.3 with a comparison to the parent compound. Moreover, it may be noted that now perovskites are used in tandem solar cell architecture with Si and other compounds [1].

**Table 1.3.** Summary of solar cell performance of different metal halide perovskites.

Perovskites	Device Architecture	PCE (%)	Ref
MAPbI <sub>3</sub>	FTO/c-TiO <sub>2</sub> /Perovskite/Spiro/Au	21	[97]
MASnI <sub>3</sub>	FTO/TiO <sub>2</sub> /MASnI <sub>3</sub> /C/Au	6	[98]
FAPbI <sub>3</sub>	FTO/SnO <sub>2</sub> /Perovskite/Spiro/Ag	22	[99]
CsPbCl <sub>3</sub>	ITO/NiO <sub>x</sub> /Perovskite/ZnO/C <sub>60</sub> /Ag	16	[100]
Cs <sub>3</sub> Bi <sub>2</sub> I <sub>9</sub>	FTO/c-TiO <sub>2</sub> /Cs <sub>3</sub> Bi <sub>2</sub> I <sub>9</sub> /CuI/Au	3	[101]
Cs <sub>3</sub> Sb <sub>2</sub> I <sub>9</sub>	ITO/PEDOT:PSS/Perovskite/PMMA/WS <sub>2</sub> /Al	3	[102]
Cs <sub>2</sub> AgBiBr <sub>6</sub>	FTO/c-TiO <sub>2</sub> /Perovskite/Dye/Spiro/Ag	3	[103]
Quasi-2D	FTO/c-TiO <sub>2</sub> /Perovskite/Spiro/Au	17	[104]

FTO: fluorine-doped tin oxide, c-TiO<sub>2</sub>: compact TiO<sub>2</sub>, spiro: spiro-OMeTAD, Au: gold, PTAA: Poly[bis(4-phenyl)(2,4,6-trimethylphenyl)amine] PMMA: poly(methyl methacrylate).

### 1.6.2. Photodetectors

It is indeed true that the research field of perovskite optoelectronics is mostly dominated by solar cells. However, the amazing optical and electronic properties of

perovskites also make them suitable for advanced applications in detecting light signals [95]. Perovskites can absorb light effectively in a broadband range. Due to a high absorption coefficient, the absorption of light and yield of photogenerated carriers become significantly high. Moreover, the charge carrier mobility is found to be high. As a result, perovskites show immense potential for sensitive, reliable, and fast photodetection [12]. A wide range of sensing regions has been demonstrated from ultraviolet-visible-near infrared (UV-Vis-NIR) to gamma and X-ray photons (Figure 1.12) [96]. These materials with different forms, such as polycrystalline thin films, nano-particles, and single crystals, have exhibited promising performance with significantly high responsivity, detectivity, and response speed. It is expected that a combination of different perovskites (hybrid halides, all inorganic, bismuth-based ternary halides, and double perovskites), with a range of various optoelectronic properties such as bandgap, mobility, carrier lifetime, and so on would replace the commercial silicon-based photodetectors in future [97].

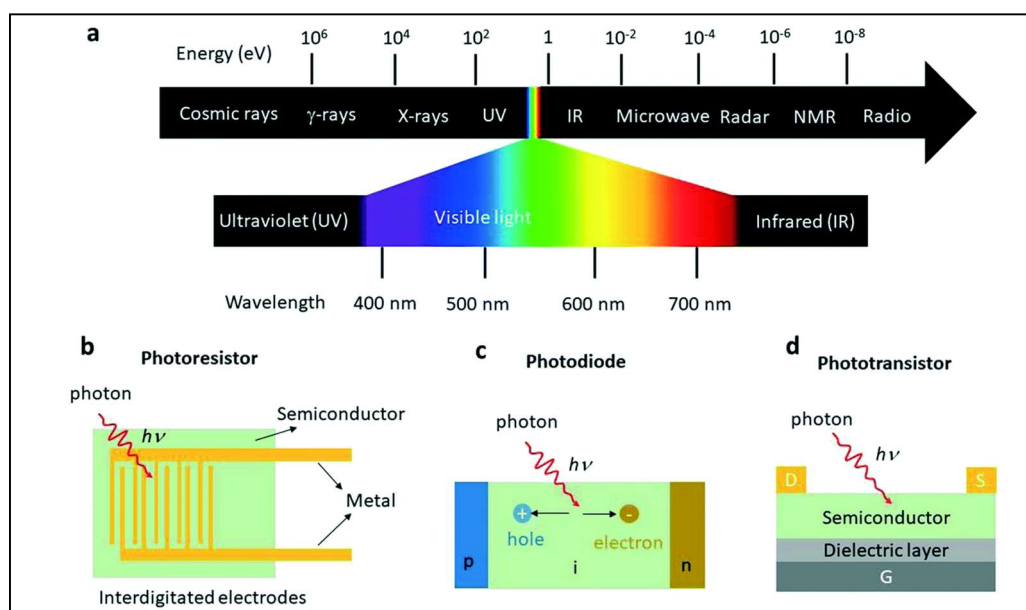


**Figure 1.12.** Different device architecture of metal halide perovskite. Reproduced from Ref [96].

Copyright Royal Society of Chemistry 2018.



### 1.6.3. Light Emitting Diodes (LEDs)

It is often argued that the generation of power in a solar cell is a reverse operation of a LED [97]. As a result, an efficient solar cell should be a bright LED as well. Halide perovskite LEDs, particularly the all-inorganic perovskites ( $\text{CsPbX}_3$ ,  $X = \text{I}, \text{Br}, \text{Cl}$ ) have exhibited extraordinary performance with luminance values up to  $91\,000 \text{ cd m}^{-2}$  whereas their external quantum efficiencies (EQEs) are almost 12% [14]. The most significant aspect of perovskite LEDs is indeed their emission color tunability from blue to green or red. This can be easily done by replacing the halide anions from Cl to I through Br. Hence, perovskites are also suitable for their use in white LEDs [98]. Such high performance of perovskite LEDs is originated from some of the intrinsic properties of the wonder material. For example, their low defect density, high photoluminescence quantum yield (PLQY), and efficient charge transport can be considered. Notwithstanding, perovskite LEDs combine the advantages of organic LEDs and quantum dot LEDs making them suitable for next-generation lighting systems. Besides the all-inorganic perovskites, several other perovskites belonging to the double perovskites ( $\text{Cs}_2\text{AgInCl}_6$ ), the 2D RP phase ( $\text{PEA}_2\text{PbI}_4$ ,  $\text{BA}_2\text{PbI}_4$ ), and other perovskite derivatives such as ( $\text{Cs}_3\text{Cu}_2\text{I}_5$  and  $\text{CsCu}_2\text{I}_3$ ), have also gained immense attention [99,100]. In addition, the light-emitting properties in devices can be modulated and enhanced by different techniques such as Mn-doping, self-trapped exciton (STEs) engineering, and so forth.

It may be noted that no significant work has been carried out in this doctoral thesis associated with the light-emitting applications of perovskite materials. However, considering the enormous interest in perovskite LEDs, a contemporary discussion has been devoted to this section.

### 1.6.4. Spintronic Devices

Besides the abovementioned optical devices, metal halide perovskites are also suitable for spintronic applications due to their large spin diffusion length. In contrast to

the optoelectronics-related research, the field of spintronic is comparatively new and most of the studies are still limited to the lead-based organic-inorganic hybrid halide perovskites. Although bismuth-based perovskites should exhibit similar spintronic properties, such reports are yet to be appeared in the literature. In this section, advancements in different perovskite-based spintronic devices are reviewed, such as spin-valve devices, quantum computing devices, spin-filters, and spin switches [91]. Moreover, by combining the optoelectronic and spintronic properties of metal halide perovskites, the potentials of several integrated opto-spintronic devices have been discussed.

(i) *Spin Valve Devices*: To unleash the potential of perovskite-based spintronic devices, the primary interest should be the realization of electrical spin injection in metal halide perovskites from ferromagnetic electrodes. Recently, spin-polarized carrier injection has been demonstrated in  $\text{MAPbBr}_3$  using a vertical spin-valve device [101]. This device is consisted of a perovskite interlayer sandwiched between two magnetic materials. The electrical resistance can be changed between two states depending on the alignment of the magnetization. Such a resistance change is instigated by the giant magnetoresistance effect. In addition, the spin lifetimes of the carriers could be measured by applying an external magnetic field in the vertical direction with respect to the injected spin carriers.

(ii) *Spin-Filter Devices*: Spin filtering devices are one of the most important maneuvers in spintronics. Due to the presence of the Rashba effect, metal halide perovskites possess different spin channels allowing them to act as spin filters with ferromagnetic electrodes and applied to the external field. In this direction, such spin filtering effects can also be observed in chiral perovskites. Due to the intrinsic chirality-induced spin selectivity phenomena, they can act as in-situ spin filters.

(iii) *Quantum Computing Devices*: Most interestingly, metal halide perovskites are excellent candidates for quantum computation due to the large spin selective optical Stark effect where the absorption can be controlled by changing the polarization states of incident photons [102]. Such a precise level of control recommends unprecedented

opportunity to use the spin states as spin qubits. However, the real-world problem of this concept is their small spin coherence time at room temperature. As a result, it is not possible to carry out numerous independent operations. Such operation at low temperature, where the coherence time would be increased, might be possible.

(v) *Integrated Opto-Spintronic Devices*: Finally, integrated opto-spintronic devices are envisaged combining the superior optoelectronic and spintronic properties of metal halide perovskites. Especially, spin-polarized photodetectors and spin-polarized LEDs have gained immense interest when operating under a magnetic field. Recently, such operations have been demonstrated even without the applications of magnetic fields. As mentioned earlier, this has been possible by incorporating chiral ligands in the structure of metal halide perovskites [43].

## 1.7. Scopes and Objectives of the Doctoral Research

The objective of this doctoral thesis has two facets: optoelectronics and spintronics features of metal halide perovskites. In the first part of the thesis, the research was focused on the optoelectronic applications of several perovskite materials. It may be noted that despite the success of  $ABX_3$  ( $\text{MAPbI}_3$ ) based perovskites in optoelectronics, to be specific in photovoltaics, numerous issues can be found in perovskite-based devices. One of the major problems with this type of material is its environmental stability, especially with moisture, oxygen, UV radiation, and heat [7]. Moreover, these highly efficient perovskite optoelectronic devices contain toxic lead. In addition, hysteresis phenomenon in the current vs voltage characteristics is observed in photovoltaic devices. It may be noted that the phenomenon of non-identical current-voltage characteristics in the two-sweep direction are known as hysteresis and results in an ambiguity in the efficiency of the devices [24]. Hysteresis in these devices appears for several reasons: scan speed and direction, light soaking history, and presence of interfaces with transport layers. To overcome these issues, there are immense scopes to determine alternate materials in the field of perovskite-based optoelectronics. Hence, the research work of this doctoral thesis was focused to investigate the optoelectronic

properties of different perovskite compounds beyond the parent  $ABX_3$  structure. In this direction, three possible perovskite derivatives were investigated as potential alternatives, namely bismuth-based ternary halide perovskites ( $MA_3Bi_2I_9$ ,  $Cs_3Bi_2I_9$ ), double perovskite ( $Cs_2AgBiBr_6$ ), and 2D RP perovskites ( $BA_2MA_2Pb_3I_{10}$ ). In a nutshell, this part of the research work addresses one focal question: “*Can we envisage an alternate perovskite photovoltaic material beyond  $MAPbI_3$  for viable applications with better stability and probably less toxicity?*”

In the next part of the thesis, spintronic aspects of these materials were investigated that are closely associated with their optoelectronic properties. Based on the discussion associated with the spintronic properties of metal halide perovskites, it is clear that the origin of most of the novel spin properties is allied with a Rashba effect. However, proper experimental verification was still lacking in the literature. In this direction, one of the most significant goals of this doctoral thesis was to verify Rashba splitting experimentally. Next, the research work was focused on the spin-selective charge transport in perovskite materials without the presence of a magnetic field. In this regard, chirality was induced into the perovskite structure through chiral ligands. The intrinsic chirality-induced spin selectivity enables spin-dependent charge transport in the lead-free chiral perovskites. Finally, another pivotal question was addressed: “*Can we integrate optoelectronic and spintronic properties of metal halide perovskites for next-generation opto-spintronic devices?*”

## 1.8. References

- [1] A. K. Jena, A. Kulkarni, and T. Miyasaka, *Chem. Rev.* **119**, 3036 (2019).
- [2] J. Y. Kim, J.-W. Lee, H. S. Jung, H. Shin, and N.-G. Park, *Chem. Rev.* **120**, 7867 (2020).
- [3] M. Kubicek, A. H. Bork, and J. L. M. Rupp, *J. Mater. Chem. A* **5**, 11983 (2017).
- [4] D. Weber, *Zeitschrift für Naturforschung B* **33**, 1443 (1978).

- 
- [5] A. Kojima, K. Teshima, Y. Shirai, and T. Miyasaka, *J. Am. Chem. Soc.* **131**, 6050 (2009).
- [6] J. Jeong, M. Kim, J. Seo, H. Z. Lu, P. Ahlawat, A. Mishra, Y. G. Yang, M. A. Hope, F. T. Eickemeyer, Y. J. Yoon, I. W. Choi, B. P. Darwich, S. J. Choi, Y. Jo, J. H. Lee, B. Walker, S. M. Zakeeruddin, L. Emsley, U. Rothlisberger, A. Hagfeldt, D. S. Kim, M. Gratzel, and J. Y. Kim, *Nature* **592**, 381 (2021).
- [7] Y. G. Rong, Y. Hu, A. Y. Mei, H. R. Tan, M. I. Saidaminov, S. I. Seok, M. D. McGehee, E. H. Sargent, and H. W. Han, *Science* **361**, eaat8235 (2018).
- [8] W. C. Xiang and W. Tress, *Adv. Mater.* **31**, 1902851 (2019).
- [9] F. Zhang, H. P. Lu, J. H. Tong, J. J. Berry, M. C. Beard, and K. Zhu, *Energy Environ. Sci.* **13**, 1154 (2020).
- [10] Z. X. Jin, Z. Zhang, J. W. Xiu, H. S. Song, T. Gatti, and Z. B. He, *J. Mater. Chem. A* **8**, 16166 (2020).
- [11] L. Chu, W. Ahmad, W. Liu, J. Yang, R. Zhang, Y. Sun, J. P. Yang, and X. A. Li, *Nano-Micro Lett.* **11**, 16 (2019).
- [12] G. Li, Y. Wang, L. Huang, and W. Sun, *ACS Appl. Electron. Mater.* **4**, 1485 (2022).
- [13] K. J. Kang, W. Hu, and X. S. Tang, *J. Phys. Chem. Lett.* **12**, 11673 (2021).
- [14] Q. Van Le, H. W. Jang, and S. Y. Kim, *Small Methods* **2**, 1700419 (2018).
- [15] A. Privitera, M. Righetto, F. Cacialli, and M. K. Riede, *Adv. Opt. Mater.* **9**, 2100215 (2021).
- [16] J. Zhang, T. Wu, J. S. Duan, M. Ahmadi, F. Y. Jiang, Y. H. Zhou, and B. Hu, *Nano Energy* **38**, 297 (2017).
- [17] D. Niesner, M. Wilhelm, I. Levchuk, A. Osvet, S. Shrestha, M. Batentschuk, C. Brabec, and T. Fauster, *Phys. Rev. Lett.* **117**, 126401 (2016).
- [18] M. A. Becker, R. Vaxenburg, G. Nedelcu, P. C. Sercel, A. Shabaev, M. J. Mehl, J. G. Michopoulos, S. G. Lambrakos, N. Bernstein, J. L. Lyons, T. Stoferle, R. F. Mahrt, M. V. Kovalenko, D. J. Norris, G. Raino, and A. L. Efros, *Nature* **553**, 189 (2018).

- 
- [19] C. Zhang, D. Sun, C. X. Sheng, Y. X. Zhai, K. Mielczarek, A. Zakhidov, and Z. V. Vardeny, *Nat. Phys.* **11**, 428 (2015).
- [20] Y. Yang, M. J. Yang, K. Zhu, J. C. Johnson, J. J. Berry, J. van de Lagemaat, and M. C. Beard, *Nat. Commun.* **7**, 12613 (2016).
- [21] G. Kieslich, S. J. Sun, and A. K. Cheetham, *Chem. Sci.* **6**, 3430 (2015).
- [22] P. S. Whitfield, N. Herron, W. E. Guise, K. Page, Y. Q. Cheng, I. Milas, and M. K. Crawford, *Sci. Rep.* **6**, 35685 (2016).
- [23] Z. H. Zhu, Q. Sun, Z. P. Zhang, J. Dai, G. C. Xing, S. Z. Li, X. Huang, and W. Huang, *J. Mater. Chem. C* **6**, 10121 (2018).
- [24] K. Wang, D. Yang, C. C. Wu, M. Sanghadasa, and S. Priya, *Prog. Mater. Sci.* **106**, 100580 (2019).
- [25] S. J. Jiang, Y. L. Luan, J. I. Jang, T. Baikie, X. Huang, R. P. Li, F. O. Saouma, Z. W. Wang, T. J. White, and J. Y. Fang, *J. Am. Chem. Soc.* **140**, 13952 (2018).
- [26] A. K. Cheetham, C. N. R. Rao, and R. K. Feller, *Chem. Commun.* **11**, 4780 (2006).
- [27] J. M. Frost, K. T. Butler, F. Brivio, C. H. Hendon, M. van Schilfhaarde, and A. Walsh, *Nano Lett.* **14**, 2584 (2014).
- [28] A. Varadwaj, P. R. Varadwaj, and K. Yamashita, *J. Comput. Chem.* **38**, 2802 (2017).
- [29] S. Chatterjee and A. J. Pal, *J. Mater. Chem. A* **6**, 3793 (2018).
- [30] L. Xu, S. Yuan, H. Zeng, and J. Song, *Mater. Today Nano* **6**, 100036 (2019).
- [31] W. Gao, C. Chen, C. Ran, H. Zheng, H. Dong, Y. Xia, Y. Chen, and W. Huang, *Adv. Funct. Mater.* **30**, 2000794 (2020).
- [32] G. E. Eperon, S. D. Stranks, C. Menelaou, M. B. Johnston, L. M. Herz, and H. J. Snaith, *Energy Environ. Sci.* **7**, 982 (2014).
- [33] J. W. Lee, D. H. Kim, H. S. Kim, S. W. Seo, S. M. Cho, and N. G. Park, *Adv. Energy Mater.* **5**, 1501310 (2015).
- [34] N. Pellet, P. Gao, G. Gregori, T. Y. Yang, M. K. Nazeeruddin, J. Maier, and M. Gratzel, *Angew. Chem.-Int. Edit.* **53**, 3151 (2014).

- [35] T. Miyasaka, A. Kulkarni, G. M. Kim, S. Oz, and A. K. Jena, *Adv. Energy Mater.* **10**, 1902500 (2020).
- [36] M. Saliba, T. Matsui, J. Y. Seo, K. Domanski, J. P. Correa-Baena, M. K. Nazeeruddin, S. M. Zakeeruddin, W. Tress, A. Abate, A. Hagfeldt, and M. Gratzel, *Energy Environ. Sci.* **9**, 1989 (2016).
- [37] A. D. Jodlowski, C. Roldan-Carmona, G. Grancini, M. Salado, M. Ralaiarisoa, S. Ahmad, N. Koch, L. Camacho, G. de Miguel, and M. K. Nazeeruddin, *Nat. Energy* **2**, 972 (2017).
- [38] L. L. Mao, C. C. Stoumpos, and M. G. Kanatzidis, *J. Am. Chem. Soc.* **141**, 1171 (2019).
- [39] H. Y. Fu, *J. Mater. Chem. C* **9**, 6378 (2021).
- [40] B. Cai, X. M. Li, Y. Gu, M. Harb, J. H. Li, M. Q. Xie, F. Cao, J. Z. Song, S. L. Zhang, L. Cavallo, and H. B. Zeng, *Sci. China-Mater.* **60**, 811 (2017).
- [41] J. Ahn, E. Lee, J. Tan, W. Yang, B. Kim, and J. Moon, *Mater. Horiz.* **4**, 851 (2017).
- [42] H. P. Lu, J. Y. Wang, C. X. Xiao, X. Pan, X. H. Chen, R. Brunecky, J. J. Berry, K. Zhu, M. C. Beard, and Z. V. Vardeny, *Sci. Adv.* **5**, eaay0571 (2019).
- [43] G. K. Long, R. Sabatini, M. I. Saidaminov, G. Lakhwani, A. Rasmita, X. G. Liu, E. H. Sargent, and W. B. Gao, *Nat. Rev. Mater.* **5**, 423 (2020).
- [44] Q. Ou, X. Bao, Y. Zhang, H. Shao, G. Xing, X. Li, L. Shao, and Q. Bao, *Nano Mater. Sc.* **1**, 268 (2019).
- [45] G. E. Eperon and D. S. Ginger, *ACS Energy Lett.* **2**, 1190 (2017).
- [46] M. R. Filip and F. Giustino, *J. Phys. Chem. C* **120**, 166 (2016).
- [47] R. Chakraborty, A. Maiti, U. K. Ghorai, and A. J. Pal, *ACS Appl. Nano Mater.* **4**, 10155 (2021).
- [48] S. F. Hoefler, G. Trimmel, and T. Rath, *Mon. Chem.* **148**, 795 (2017).
- [49] K. Z. Du, X. M. Wang, Q. W. Han, Y. F. Yan, and D. B. Mitzi, *ACS Energy Lett.* **2**, 2486 (2017).
- [50] P. V. Kamat, J. Bisquert, and J. Buriak, *ACS Energy Lett.* **2**, 904 (2017).

- 
- [51] A. Maiti, G. Paul, H. Bhunia, and A. J. Pal, *Sol. Energy Mater. Sol. Cells* **200**, 109941, (2019).
- [52] D. Han, T. Zhang, M. L. Huang, D. Y. Sun, M. H. Du, and S. Y. Chen, *APL Mater.* **6**, 084902 (2018).
- [53] S. Ullah, J. Wang, P. Yang, L. Liu, J. Khan, S.-E. Yang, T. Xia, H. Guo, and Y. Chen, *Sol. RRL* **5**, 2000830 (2021).
- [54] A. E. Maughan, A. M. Ganose, D. O. Scanlon, and J. R. Neilson, *Chem. Mat.* **31**, 1184 (2019).
- [55] C. H. Lu, G. V. Biesold, Y. J. Liu, Z. T. Kang, and Z. Q. Lin, *Chem. Soc. Rev.* **49**, 4953 (2020).
- [56] E. Mosconi, A. Amat, M. K. Nazeeruddin, M. Gratzel, and F. De Angelis, *J. Phys. Chem. C* **117**, 13902 (2013).
- [57] B. Suarez, V. Gonzalez-Pedro, T. S. Ripolles, R. S. Sanchez, L. Otero, and I. Mora-Sero, *J. Phys. Chem. Lett.* **5**, 1628 (2014).
- [58] R. Prasanna, A. Gold-Parker, T. Leijtens, B. Conings, A. Babayigit, H. G. Boyen, M. F. Toney, and M. D. McGehee, *J. Am. Chem. Soc.* **139**, 11117 (2017).
- [59] M.-C. Tang, H. X. Dang, S. Lee, D. Barrit, R. Munir, K. Wang, R. Li, D.-M. Smilgies, S. De Wolf, D.-Y. Kim, T. D. Anthopoulos, and A. Amassian, *Sol. RRL* **5**, 2000718 (2021).
- [60] S. Nagane, U. Bansode, O. Game, S. Chhatre, and S. Ogale, *Chem. Commun.* **50**, 9741 (2014).
- [61] C. H. Hendon, R. X. Yang, L. A. Burton, and A. Walsh, *J. Mater. Chem. A* **3**, 9067 (2015).
- [62] S. Andalibi, A. Rostami, G. Darvish, and M. K. Moravvej-Farshi, *Opt. Quant. Electron.* **48**, 258 (2016).
- [63] A. Maiti, S. Khatun, and A. J. Pal, *Nano Lett.* **20**, 292 (2020).
- [64] Y. F. Miao, Y. T. Chen, H. R. Chen, X. T. Wang, and Y. X. Zhao, *Chem. Sci.* **12**, 7231 (2021).



- 
- [65] C. Motta, F. El-Mellouhi, S. Kais, N. Tabet, F. Alharbi, and S. Sanvito, *Nat. Commun.* **6**, 7026 (2015).
- [66] B. Cheng, T. Y. Li, P. Maity, P. C. Wei, D. Nordlund, K. T. Ho, D. H. Lien, C. H. Lin, R. Z. Liang, X. H. Miao, I. A. Ajia, J. Yin, D. Sokaras, A. Javey, I. S. Roqan, O. F. Mohammed, and J. H. He, *Commun. Phys.* **1**, 80 (2018).
- [67] Q. Wang, X. D. Liu, Y. H. Qiu, K. Chen, L. Zhou, and Q. Q. Wang, *AIP Adv.* **8**, 025108 (2018).
- [68] J. H. Fu, Q. Xu, G. F. Han, B. Wu, C. H. A. Huan, M. L. Leek, and T. C. Sum, *Nat. Commun.* **8**, 1300 (2017).
- [69] K. Wang, C. C. Wu, Y. Y. Jiang, D. Yang, and S. Priya, *Sci. Adv.* **5**, eaau3241 (2019).
- [70] J. S. Manser, J. A. Christians, and P. V. Kamat, *Chem. Rev.* **116**, 12956 (2016).
- [71] P. A. M. Dirac and N. H. D. Bohr, *Proc. R. Soc. Lond.* **114**, 243 (1927).
- [72] S. Khatun, A. Maiti, and A. J. Pal, *Appl. Phys. Lett.* **116**, 012104 (2020).
- [73] A. Miyata, A. Mitioglu, P. Plochocka, O. Portugall, J. T. W. Wang, S. D. Stranks, H. J. Snaith, and R. J. Nicholas, *Nat. Phys.* **11**, 582 (2015).
- [74] M. Baranowski and P. Plochocka, *Adv. Energy Mater.* **10**, 1903659 (2020).
- [75] Z. S. Zhang, W. H. Fang, R. Long, and O. V. Prezhdo, *J. Am. Chem. Soc.* **141**, 15557 (2019).
- [76] E. D. Kinigstein, H. Tsai, W. Nie, J.-C. Blancon, K. G. Yager, K. Appavoo, J. Even, M. G. Kanatzidis, A. D. Mohite, and M. Y. Sfeir, *ACS Materials Lett.* **2**, 1360 (2020).
- [77] W. J. Yin, J. H. Yang, J. Kang, Y. F. Yan, and S. H. Wei, *J. Mater. Chem. A* **3**, 8926 (2015).
- [78] L. M. Herz, *ACS Energy Lett.* **2**, 1539 (2017).
- [79] A. Maiti and A. J. Pal, *Rep. Prog. Phys.* **85**, 024501 (2022).
- [80] K. X. Steirer, P. Schulz, G. Teeter, V. Stevanovic, M. Yang, K. Zhu, and J. J. Berry, *ACS Energy Lett.* **1**, 360 (2016).
- [81] A. Maiti and A. J. Pal, *J. Phys. Chem. C* **125**, 16324 (2021).

- 
- [82] A. Maiti, S. Chatterjee, L. Peedikakkandy, and A. J. Pal, *Sol. RRL* **4**, 2000505 (2020).
- [83] F. Wang, S. Bai, W. Tress, A. Hagfeldt, and F. Gao, *npj Flex. Electron.* **2**, 22 (2018).
- [84] A. D. Wright, C. Verdi, R. L. Milot, G. E. Eperon, M. A. Perez-Osorio, H. J. Snaith, F. Giustino, M. B. Johnston, and L. M. Herz, *Nat. Commun.* **7**, 11755 (2016).
- [85] S. Paramanik, A. Maiti, S. Chatterjee, and A. J. Pal, *Adv. Electron. Mater.* **8**, 2100237 (2022).
- [86] D. Konig, K. Casalenuovo, Y. Takeda, G. Conibeer, J. F. Guillemoles, R. Patterson, L. M. Huang, and M. A. Green, *Physica E* **42**, 2862 (2010).
- [87] S. Kahmann and M. A. Loi, *J. Mater. Chem. C* **7**, 2471 (2019).
- [88] M. Li, J. Fu, Q. Xu, and T. C. Sum, *Adv. Mater.* **31**, 1802486 (2019).
- [89] E. Z. Shi, S. B. Deng, B. Yuan, Y. Gao, Akriti, L. Yuan, C. S. Davis, D. Zemlyanov, Y. Yu, L. B. Huang, and L. T. Dou, *ACS Nano* **13**, 1635 (2019).
- [90] C. Y. Zhao, W. M. Tian, J. Leng, Y. Zhao, and S. Y. Jin, *J. Phys. Chem. Lett.* **10**, 3950 (2019).
- [91] K. Liao, X. Y. Hu, Y. K. Cheng, Z. C. Yu, Y. X. Xue, Y. Chen, and Q. H. Gong, *Adv. Opt. Mater.* **7**, 1900350 (2019).
- [92] W. Li, L. J. Zhou, O. V. Prezhdo, and A. V. Akimov, *ACS Energy Lett.* **3**, 2159 (2018).
- [93] Y. X. Zhai, S. Baniya, C. Zhang, J. W. Li, P. Haney, C. X. Sheng, E. Ehrenfreund, and Z. V. Vardeny, *Sci. Adv.* **3**, e1700704 (2017).
- [94] M. Kepenekian and J. Even, *J. Phys. Chem. Lett.* **8**, 3362 (2017).
- [95] M. Ahmadi, T. Wu, and B. Hu, *Adv. Mater.* **29**, 1605242 (2017).
- [96] F. Yao, P. Gui, Q. Zhang, and Q. Lin, *Mol. Syst. Des. Eng.* **3**, 702 (2018).
- [97] Y. Zhang, Y. Ma, Y. Wang, X. Zhang, C. Zuo, L. Shen, and L. Ding, *Adv. Mater.* **33**, 2006691 (2021).
- [98] S. Adjokatse, H. H. Fang, and M. A. Loi, *Mater. Today* **20**, 413 (2017).

- [99] L. Zhang, C. J. Sun, T. W. He, Y. Z. Jiang, J. L. Wei, Y. M. Huang, and M. J. Yuan, *Light-Sci. Appl.* **10**, 61 (2021).
- [100] X. Li, X. P. Gao, X. T. Zhang, X. Y. Shen, M. Lu, J. L. Wu, Z. F. Shi, V. L. Colvin, J. H. Hu, X. Bai, W. L. W. Yu, and Y. Zhang, *Adv. Sci.* **8**, 2003334 (2021).
- [101] J. Wang, C. Zhang, H. Liu, R. McLaughlin, Y. Zhai, S. R. Vardeny, X. Liu, S. McGill, D. Semenov, H. Guo, R. Tsuchikawa, V. V. Deshpande, D. Sun, and Z. V. Vardeny, *Nat. Commun.* **10**, 129 (2019).
- [102] Y. L. Li, S. He, X. Luo, X. Lu, and K. F. Wu, *J. Phys. Chem. Lett.* **11**, 3594 (2020).

This page is intentionally left blank.

# Chapter 2

## Experimental Methods

*During this doctoral research, the deceiving goal was to investigate different metal halide perovskites for optoelectronic and spintronic applications. In this direction, several perovskite compounds such as organic-inorganic hybrid halide perovskites, bismuth-based ternary halide perovskites, double perovskites, quasi-2D Ruddlesden-Popper perovskites, and chiral perovskites were fabricated and characterized. In this chapter, the procedures followed to form and characterize such perovskite thin films and nanostructures have been discussed followed by the fabrication of different photovoltaic devices and their characterization.*

### 2.1. Materials

To optimize the performance of an optoelectronic device, especially solar cells and photodetectors to excel, it is critical to select the active materials with suitable bandgap, high absorption coefficient, low trap-state density, long carrier lifetime, and diffusion length [1]. On the flip side, it is desired that the material is non-toxic and stable in ambient conditions. It is also expected that such materials are formed with earth-abundant elements and thereby have a low cost. In this direction, although organic-inorganic hybrid halide perovskite (MAPbI<sub>3</sub>) has established its worth, the difficulties associated with the stability and toxicity of the compound are still considered a major concern [2,3]. Herein, the potential of three major perovskite derivatives was investigated during the doctoral research as an alternative to MAPbI<sub>3</sub>-based photovoltaic devices. Hence, materials such as bismuth-based ternary halide perovskites (Cs<sub>3</sub>Bi<sub>2</sub>I<sub>9</sub>, MA<sub>3</sub>Bi<sub>2</sub>I<sub>9</sub>), double perovskites (Cs<sub>2</sub>AgBiBr<sub>6</sub>), and a quasi-2D Ruddlesden-Popper (RP) perovskite

( $\text{BA}_2\text{MA}_2\text{Pb}_3\text{I}_{10}$ ) were formed and characterized. On the other hand, the potential of this class of materials in the research field of spintronic has been studied in the prototype  $\text{MAPbI}_3$ . Finally, an attempt was made to combine the superior optoelectronic and spintronic properties of metal halide perovskites where a new class of metal halide perovskite with chiral moiety ( $R/S\text{-MBA}_4\text{Bi}_2\text{Br}_{10}$ ) was fabricated and investigated towards their spin-optoelectronic device applications. In this section, the fabrication and characterization of these materials in their thin film or nanostructure form have been discussed followed by some of their device applications.

## 2.2. Synthesis of Materials

First of all, the fabrication of several perovskite thin films and nanostructure have been discussed. In particular, the materials were formed through spin coating (thin film) and chemical exfoliation methods (nanostructure). It may be noted that such methods are inexpensive and simple yet suitable for high-quality sample preparation.

### 2.2.1. Thin Films through Spin Coating

Spin coating is considered one of the most commonly used solution-processed film fabrication techniques [4]. High-quality perovskite thin films ranging from a few nanometers to a few microns in thickness could be cast through the spin coating on a range of substrates. A schematic representation of the spin-coating method along with the original instrumentation is presented in Figure 2.1. In this low-cost method, the substrate (glass, quartz, indium tin oxide (ITO)-coated glass, Si) is covered with the precursor solution followed by rotation at a particular speed. An even covering could be achieved due to the centripetal force arising from the rotation and the surface tension of the solution that pulls the liquid. When the solvent evaporates, the desired film of the material is formed on the substrate. Sometimes annealing is needed further for the complete evaporation of the solvent. Here, the thickness of the film could be controlled easily by changing the spin speed and concentration of the precursor solution. To be specific, the

thickness of the film could be increased with a more concentrated solution and vice versa. On the other hand, the typical thickness of the film is proportional to the inverse of the square root of the spinning speed. The uniformity of the film is found to be dependent on the surface tension of the solvent used with respect to the substrate surface. In addition, the solvent evaporation rate is also considered important to determine the uniformity and surface morphology.

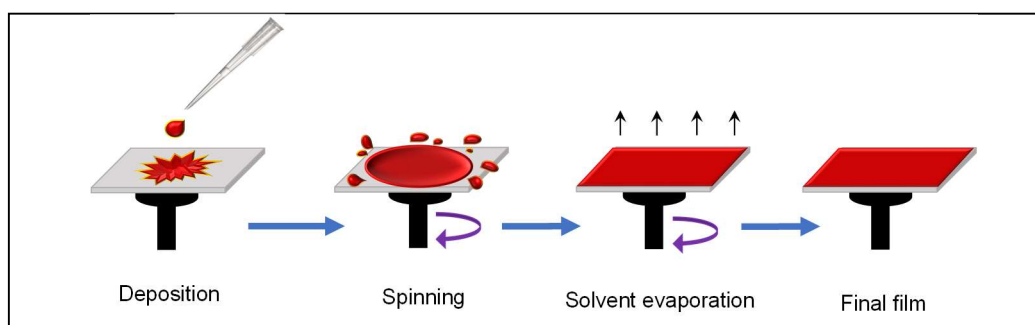


*Figure 2.1. A schematic representation of the spin coating method.*

In this doctoral research work, a one-step spin-coating method was adopted to fabricate thin films of different perovskite-based active layers. All of the films were formed inside a glove box (unless mentioned) with oxygen and moisture level below 0.1-1.0 ppm. First of all, a single precursor solution was prepared with a desired stoichiometry of the individual component. For example,  $\text{CH}_3\text{NH}_3\text{I}$  (MAI) and  $\text{PbI}_2$  were mixed in anhydrous N, N-dimethylformamide (DMF) with an equimolar ratio to form the thin film of  $\text{MAPbI}_3$ . Then the solution was stirred overnight at 70 °C inside the glovebox. The substrates (glass, quartz, ITO-coated glass, Si) were cleaned and subjected to UVO treatment before the film fabrication. The perovskite layer was then cast through the spin coating process at a particular speed followed by annealing at 150 °C. However, to further improve the film quality by controlling the nucleation and growth, several techniques were adopted such as antisolvent treatment, vacuum-assisted solvent evaporation, recrystallization, two-step film fabrication, hot-casting, and so forth [5].

Apart from the fabrication of perovskite thin film as active material in devices, several charge-transporting layers such as poly(3,4-ethylenedioxythiophene) polystyrene sulfonate (PEDOT: PSS), Cu-doped NiO, and [6,6]-phenyl-C61-butyric acid methyl ester (PCBM) were also prepared from their precursor solution with optimized concentration and desired thickness thereby.

### 2.2.2. Nanostructures through Chemical Exfoliation

Similar to the thin film, perovskite nanostructure was formed through chemical routes as well. To be particular, nanosheets of different  $BA_2MA_{n-1}Pb_nI_{3n+1}$  (BA= butylammonium, MA= methylammonium) quasi-2D RP perovskite was prepared through a very well-known synthesis route [6]. A perovskite precursor solution was freshly prepared by dissolving 0.2 mmol of BAI, 0.2 mmol MAI and 0.3 mmol of  $PbI_2$  in 1 mL of DMF inside a glovebox. For the synthesis of phase pure nanosheets, 15  $\mu$ L of the precursor solution was quickly dropped into 10 mL of toluene under a vigorous stirring condition, and the nanosheets were obtained after centrifugation at 7,000 rpm for 1 min. In addition, the  $MAPbI_3$  nanosheets were also prepared following the same protocol from a mixed precursor solution of 0.1 mmol of MAI and 0.1 mmol of  $PbI_2$ .

## 2.3. Basic Characterization Techniques

Before proceeding to the applications of these materials in optoelectronic and spintronic devices, it is important to characterize them properly. In this direction, to understand the optical properties, crystal structure, composition, surface morphology, and so on, the perovskite materials were characterized through several standard characterization techniques. The details of these techniques focusing on their working principle and instrumentation have been discussed below. At first, the basic characterization techniques are discussed followed by some advanced scanning probe-related characterization tools to investigate their band structure, localized charge (spin) transport, and photophysics.



### 2.3.1. Optical Absorption Spectroscopy

Optical absorption spectroscopy is a spectroscopic technique that is employed to determine the bandgap of semiconductor materials. It measures the transmittance and thereby absorbance of electromagnetic radiation by a material over a certain range of the selected spectral region of measurement as a function of wavelength. To acquire the absorption spectra of a sample, a spectrophotometer is employed that records the intensity of light passing through the sample ( $I$ ) to that through a reference ( $I_0$ ). In principle, the ratio of these two intensities ( $I/I_0$ ) is considered as transmittance (%  $T$ ) of that material. From transmittance, absorbance ( $A$ ) and absorption coefficient ( $\alpha$ ) are evaluated

$$A = 2 - \log (\% T) \quad (2.1)$$

$$\alpha = \frac{A}{bc} \quad (2.2)$$

where  $b$  denotes the path length and  $c$  is the concentration of the solution. In the case of thin film samples, the thickness of the material is considered instead of  $bc$ . Now, the bandgap of the material could be derived by a simple formulation called Tauc's method. Typically, in the Tauc plot, the variation of  $(ah\nu)^{1/r}$  is plotted with respect to the energy ( $h\nu$ ) of the incident photon. It may be noted that the value of  $r$  depends on the nature of the bandgap; to be specific the values are 1/2 or 2 for direct and indirect transitions, respectively. In this way, a distinct linear regime could be found denoting the absorption onset. The optical bandgap of the material is obtained after extrapolating this linear region to the energy axis [7].

During this doctoral work, absorption spectroscopy of all the perovskite was carried out as a routine characterization method. Two different spectrophotometers were used over two distinct spectral regions although their basic working principle was identical (Figure 2.2). For characterization of perovskites having optical absorption in the UV-visible region, Shimadzu UV-VIS-2550 spectrometer was employed. On the other hand, a Cary 5000 spectrophotometer (Agilent Technologies) was preferred for the measurements in the UV-visible-NIR region.

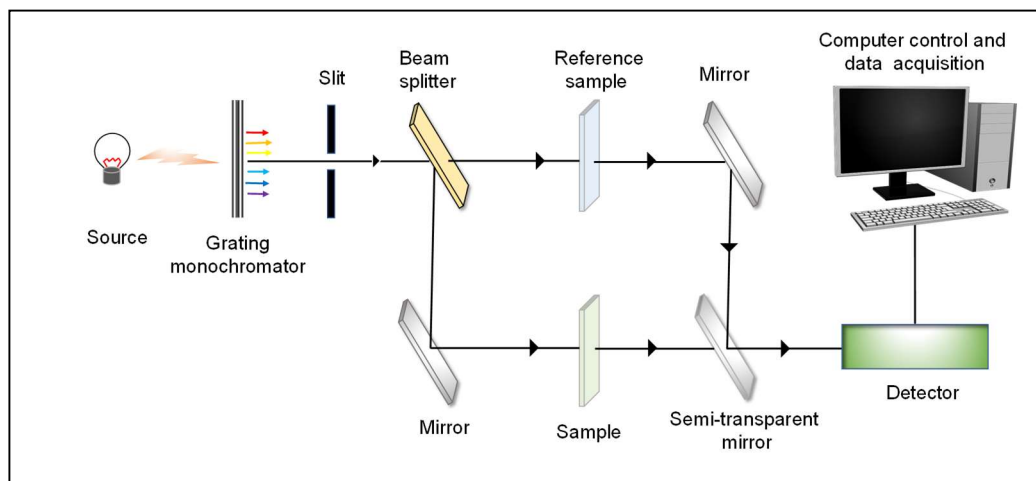


**Figure 2.2.** A schematic representation of the spectrophotometer.

The spectrophotometer is primarily composed of a source of illumination, a grating monochromator, a beam splitter, three mirrors, and a detector. As the source of illumination, a Xenon lamp is used and the beam of light is passed through a grating monochromator which is placed in front of the source. The resulting monochromatic light is then divided into two parts using a beam splitter so that it can simultaneously pass through the sample and the reference. However, in this process, a phase difference is generated inevitably between these light beams which are counterbalanced by placing reflecting mirrors in the path of beams. Finally, a detector compares the intensity ratio of these two beams and converts it to the absorbance of the perovskite at a particular wavelength. Subsequently, the next wavelength is passed by the grating to continue the measurement over a range of wavelengths covering the desired region of study to yield the entire optical absorption spectra through software.

### 2.3.2. Circular Dichroism Spectroscopy

Circular dichroism (CD) spectroscopy is a method that measures the difference in absorbance of light absorption under the right-(RCP) and left-circularly polarized (LCP) light in contrast to the absorbance of isotropic light as discussed in the previous

section. If a compound allows the passage of LCP and RCP through it with different velocities due to the different refractive indices it is called optical rotation or circular birefringence. The variation of optical rotation as a function of wavelength is called optical rotary dispersion (ORD). On the other hand, when RCP and LCP are absorbed differently due to the difference in their extinction coefficients at some wavelengths, it is called CD [8].

In this research work, the chiral perovskites were additionally characterized by circular dichroism spectroscopy. The chiral response of the perovskites was recorded in the transmission geometry by a Jasco J-1500 CD spectrometer with the thin film being placed in the beam path. The CD spectra were monitored in the range of desired wavelengths. The obtained CD signal was calculated by an internal algorithm with the use of the relation:

$$CD = \Delta A \left( \frac{\ln 10}{4} \right) \left( \frac{180000}{\pi} \right) \quad (2.3)$$

where  $\Delta A$  is the difference in the optical density (OD) between LCP and RCP illuminations [9].

### **2.3.3. Photoluminescence Spectroscopy**

The bandgap of the materials can be probed through another optical method called photoluminescence (PL) spectroscopy. It is a non-destructive technique based on an important optical phenomenon called photoluminescence in which the PL active material absorbs photons of appropriate energy and then emits light [10]. In principle, the electrons present in such materials with a direct bandgap are excited by the incident photons and make a transition to an excited state. When these electrons transit from the higher energy levels to the equilibrium level, they lose the excess energy in the form of characteristic emissions (Figure 2.3). In PL spectroscopy, this emission is recorded as a function of wavelength resulting in a characteristic PL spectrum of the corresponding material.

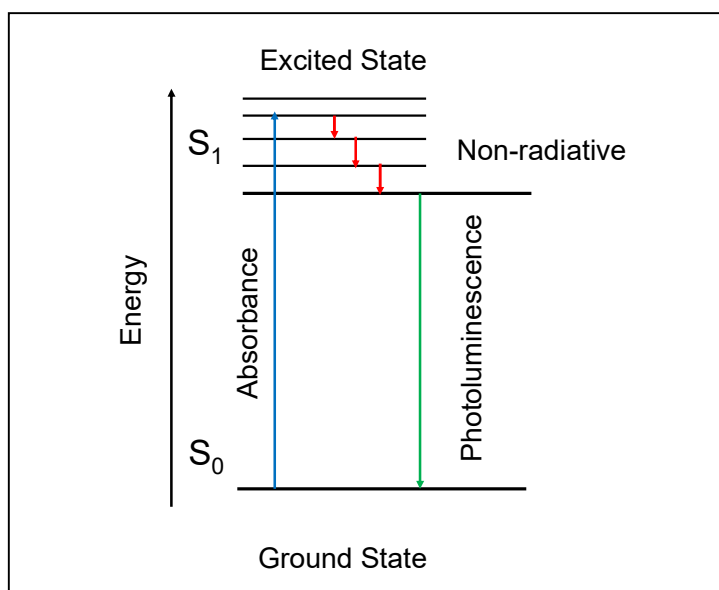


**Figure 2.3.** Mechanism of photoluminescence process between two electronic states.

Considering the LED applications of metal halide perovskites, it is important to study the PL spectra of these compounds [11]. However, as the focus of this thesis is not directly related to the LED applications, during this research tenure, some of the perovskite materials were investigated through PL spectroscopy for their basic characterization. A Horiba Jobin Yvon Fluoromax 4P spectrofluorometer was used in the UV-vis range. The spectrofluorometer consisted of a light source, a couple of gratings, and finally a detector (Figure 2.4). As a source of illumination, a Xenon lamp was used. The gratings were used as excitation and emission monochromators. The first grating acting as an excitation monochromator was positioned at a fixed place in front of the light source to select the desired excitation wavelength. Monochromatic light passed through a slit and subsequently, excited the sample. Similarly, to disperse the emission of the sample another grating was employed working as an emission monochromator. Finally, a detector was used to count the photons and the characteristic PL spectra were recorded by the software.

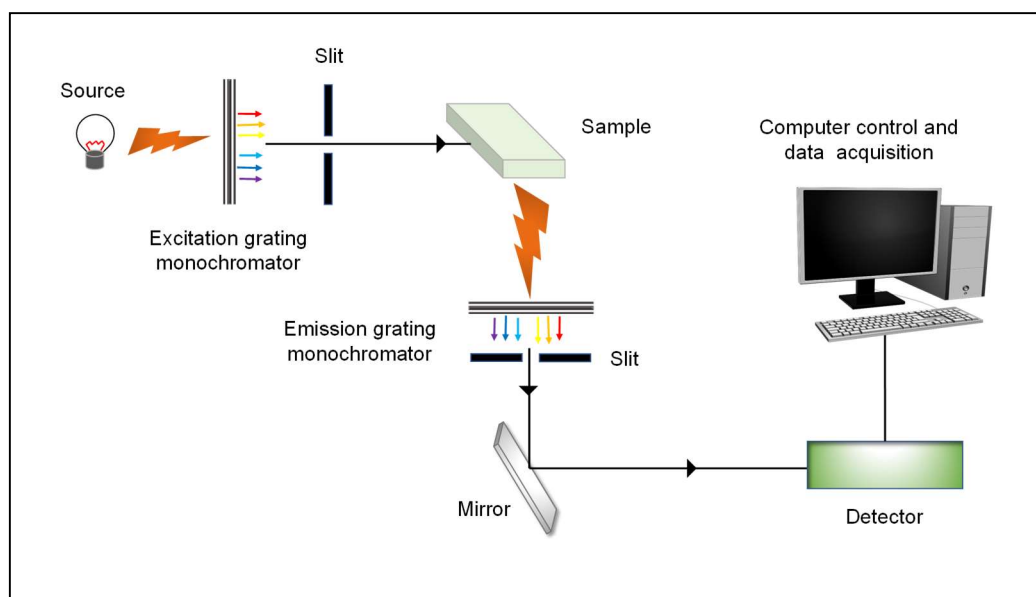


**Figure 2.4.** A schematic representation of the spectrofluorometer.

### 2.3.4. Raman Spectroscopy

Raman spectroscopy is considered an important technique that provides a structural fingerprint of any sample by investigating its vibronic modes [12]. Raman spectroscopy is based on a basic physical phenomenon of inelastic scattering of monochromatic light and material. To be specific, it is a light-matter interaction between the electric field of the incident photon and the electron cloud of the material under test. In this process, the energy of the photons changes to higher or lower energy due to the interaction of incident photons with molecular vibrations and phonons. As a result, essential information about the vibrational modes of the materials is obtained.

The schematic representation of the Raman spectrometer is presented in Figure 2.5. Generally, the sample under study is illuminated with a highly monochromatic light in the Raman spectrometer. Now, a lens is used to collect the electromagnetic radiation from the sample fed to a monochromator. To filter the particular contribution appearing from elastic scattering, a filter is used at that particular wavelength. In this direction, a

notch filter or a bandpass filter is used, Finally, the residual radiation is collected by a detector.

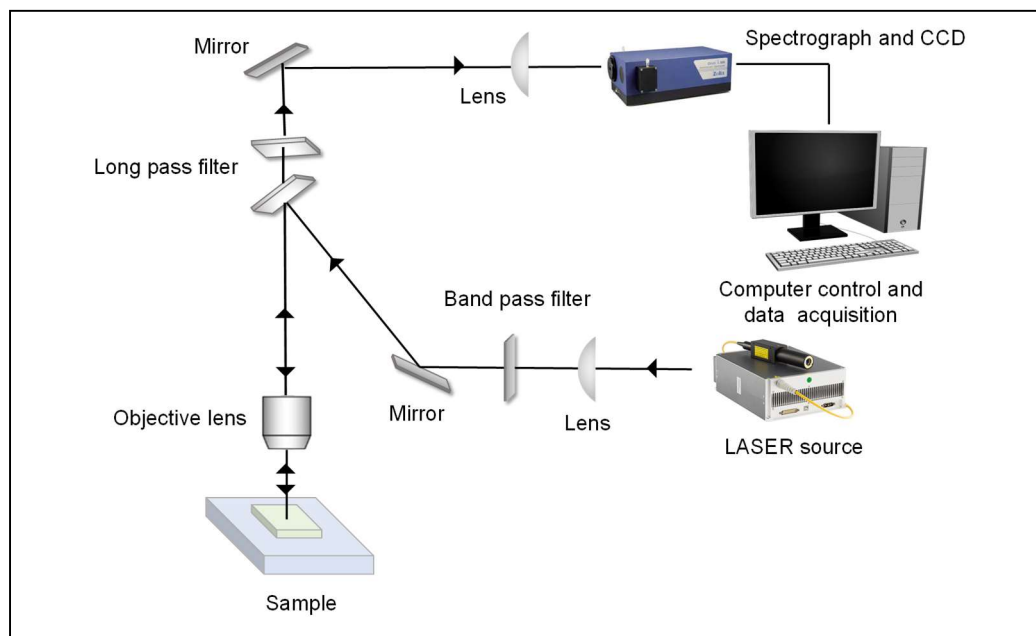


*Figure 2.5. A schematic representation of the Raman spectrometer.*

In this research tenure, several perovskite materials were characterized with a Horiba Jobin-Yvon Raman triple grating spectrometer system (model number T64000). In most of the cases, a 514 nm excitation from the Spectra-Physics laser source (model number Stabilite 2017) was used.

### 2.3.5. X-Ray Diffraction

To ensure the crystal structure and phase purity of any material X-ray diffraction patterns are considered a fingerprint [13]. It may be noted that the atoms in a crystal are arranged regularly as different sets of planes having a specific interval of spacing depending on the structure. When high-energy X-ray waves interact with atoms, it is scattered. In other words, it may be stated that it is reflected from a particular set of crystal

planes. These reflected waves interfere constructively in a particular direction governed by the Bragg's law

$$2d \sin \theta = n\lambda \quad (2.4)$$

where  $d$  represents the spacing between crystal planes,  $\theta$  denotes the incident angle of the wave,  $n$  is an integer, and  $\lambda$  is the wavelength of probing-ray (Figure 2.6) [14].

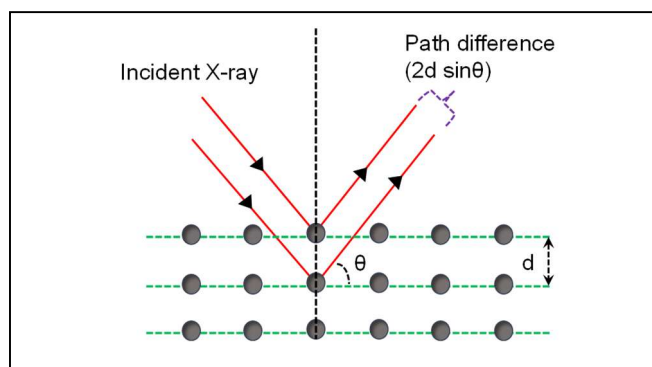


**Figure 2.6.** Schematic representation of X-ray diffraction phenomena illustrating Bragg's equation.

In this direction, X-rays are most suitable as their wavelength is comparable to the spacing between crystal planes. The reflected beam is captured by a detector that moves over a range of  $2\theta$  angle. As a result, all of the diffracted X-rays coming from every possible diffraction direction are detected to generate the X-ray diffraction pattern as a function of the  $2\theta$  angle. Now, a crystalline material has a characteristic X-ray diffraction pattern due to its unique crystal spacing. Identification of the diffraction peaks in terms of  $d$ -spacings permits the characterization of materials. During this doctoral research, XRD measurements were carried out as a mandatory characterization of all the metal halide perovskites used further. Either a Rigaku SmartLab X-ray diffractometer or Bruker D8 advanced X-ray powder diffractometer was used with Cu-K $\alpha$  (1.54 Å) as the incident radiation. Irrespective of the model, both the diffractometers consisted of three basic elements: an X-ray tube, a sample holder, and an X-ray detector (Figure 2.7).

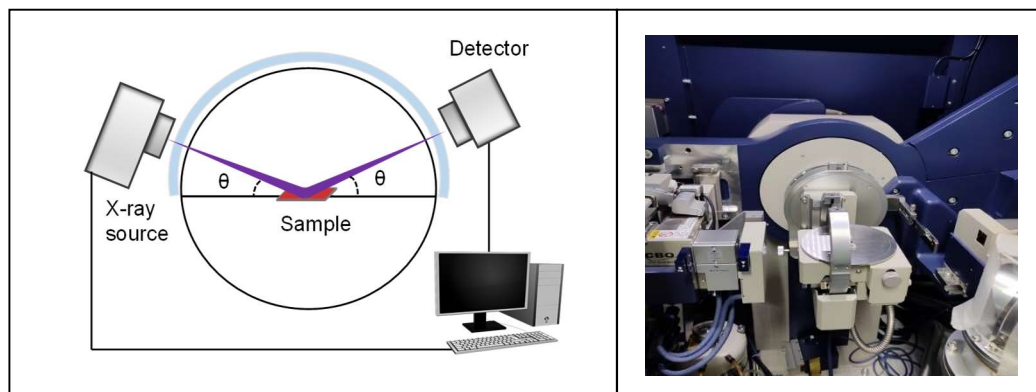


**Figure 2.7.** Schematic representation of X-ray diffractometer (left panel) along with the digital image of the original instrument (right panel).

### 2.3.6. X-Ray Photoelectron Spectroscopy

The chemical composition of the surface of a material can be probed with an analytical surface characterization procedure called X-ray photoelectron spectroscopy, commonly known as XPS. However, the surface properties are associated to several factors such as moisture and oxygen [15]. As a result, XPS characterization is performed in an ultra-high vacuum. The working principle of XPS measurement is governed by a fundamental process: the interaction between electrons and the incident X-ray [16]. Originally an electron, exposed to X-ray scattering, is evicted from the core possessing specific kinetic energy interrelated with the binding energy of the electron to the core. This phenomenon is often termed Compton scattering. As a consequence, a hole is created; however, due to the instability of these newly created holes, another electron from the core comes and occupies the vacant position (hole). To conserve the resultant energy, an Auger electron is released from the core having kinetic energy associated with the respective binding energy (Figure 2.8).



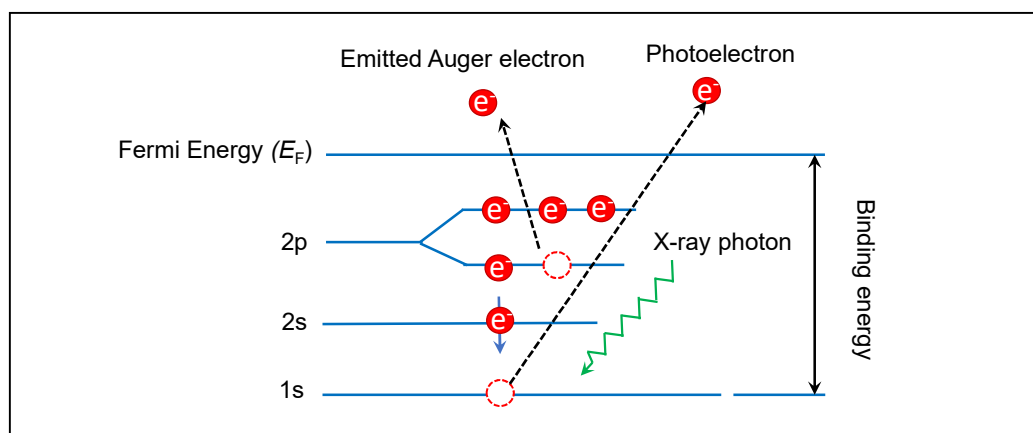


**Figure 2.8.** Mechanism of the XPS technique on an atomic scale.

It may be noted that every electron has a unique binding energy. Moreover, it belongs to a certain element along with a certain valence state. Hence, to identify the elemental composition, the energies of the emitted electrons could be used. By using the relation of conservation of energy, the entire process can be described as following

$$E_{\text{photon}} = E_{\text{Binding}} + E_{\text{Kinetic}} + \varphi \quad (2.5)$$

where, the first term on the left-hand side represents the energy of the incident photon; the first two terms on the right-hand side represent the binding and kinetic energy of the electron, and  $\varphi$  signifies the work function of the material [17]. In this research tenure, an Omicron XPS instrument (Serial no. 0571) was used for XPS characterization of perovskite samples. A schematic diagram of a typical X-ray photoelectron spectrometer has been presented in Figure 2.9. The experiments were carried out under UHV conditions, achieved through several pumps, such as the turbo molecular pump, ion pump, and titanium sublimation pump.

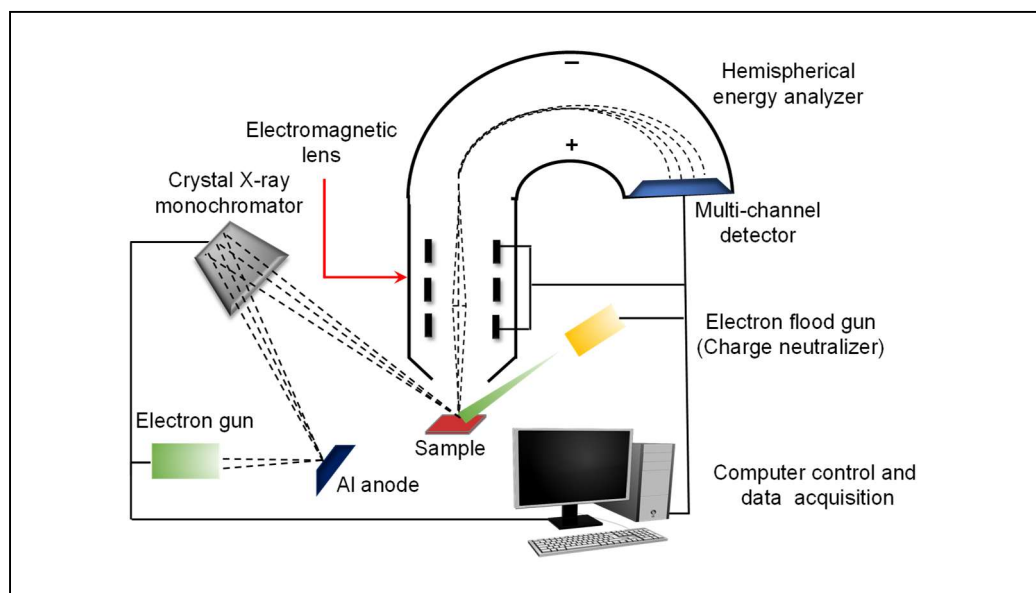


**Figure 2.9.** Schematic diagram of an X-ray photoelectron spectrometer.

### 2.3.7. Scanning Electron Microscopy

The morphology of a material, especially in its thin film form, can be obtained from scanning electron microscopy (SEM). In addition, SEM is used to gain information about the crystalline structure and chemical composition of solid samples [18]. In general, data are collected at a specific area situated at the surface of the sample. In this process, a two-dimensional (2D) image is produced that infers the spatial variations of the surface and associated properties. A schematic diagram of SEM instrumentation is presented in Figure 2.10 along with a discussion of its working principle [19].

A beam of electrons is produced by the filament fitted inside the SEM. A series of anodes and condenser lenses are used to accelerate and collimate these electrons. As such these accelerated electrons interact with the sample under investigation resulting in a deceleration of them. In this process, their kinetic energy is dissipated and several signals are produced due to electron-sample interactions including secondary electrons, backscattered electrons (BSE), diffracted backscattered electrons (DBSE), photons (characteristic X-rays), and heat. However, to extract the image of a sample, secondary

electrons and BSE are generally used. To be specific, secondary electrons generate the morphology and topography of the sample surface. On the other hand, BSE determines the contrasts appearing due to the multiphase samples. In addition, characteristic X-rays are utilized to determine the elemental composition of samples. This surface analytic process is termed energy dispersive X-ray analysis or EDXA. Since, electrons cannot travel through the air, the experiments are carried out under a high vacuum. During this doctoral research, a JEOL JSM model 6700F field emission scanning electron microscope was used to obtain SEM images of the perovskite materials.

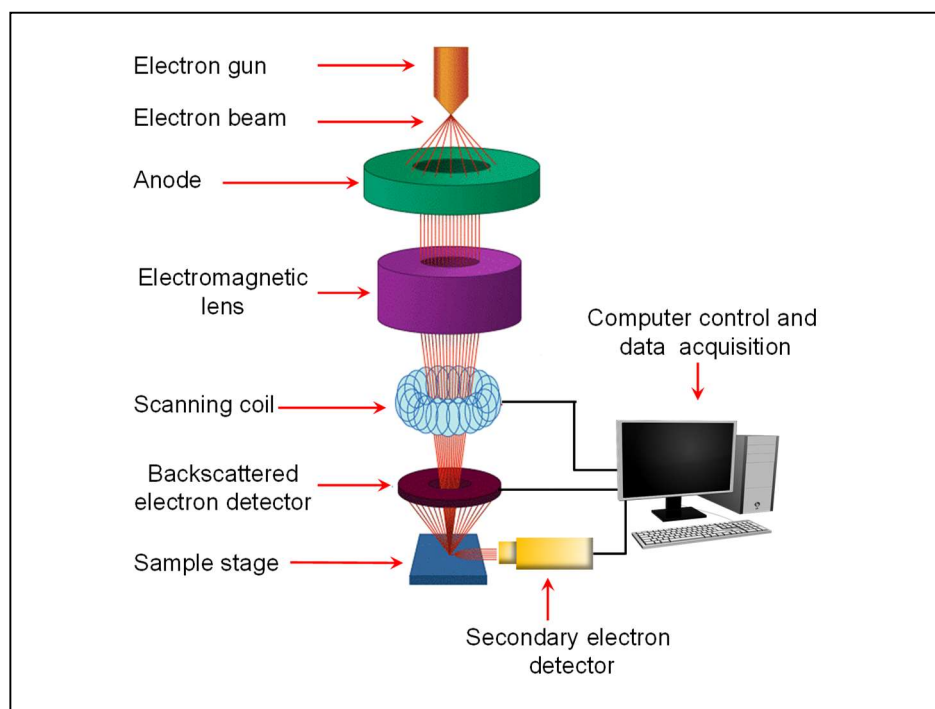


**Figure 2.10.** Schematic diagram of a field emission scanning electron microscope (FE-SEM) instrument. Reproduced with permission from [19].

### 2.3.8. Transmission Electron Microscopy

In modern science, transmission electron microscopy (TEM) is considered a major analytical technique to obtain high-resolution images of very small samples such

as nanomaterials. In this method, the image of the sample is formed with the aid of high-energy electrons. It may be stated that the principle of TEM is based on a direct consequence of wave-particle duality and the Abbe diffraction limit [20]. In general, the resolving power of a microscope is proportional to the wavelength ( $\lambda$ ) of the photon used to probe it, to be precise,  $d \approx \lambda/2$  where  $d$  is the resolvable size of the feature. For example, the smallest possible resolution of an optical microscope is  $\sim 200$  nm. On the other hand, according to de Broglie's hypothesis, the wavelength ( $\lambda$ ) of an electron having energy  $eV$  is

$$\lambda = \frac{h}{\sqrt{2meV}} \quad (2.6)$$

where  $h$  denotes the Planck constant,  $e$  and  $m$  represent elementary charge and rest mass of an electron, respectively. As a result, the use of high-energy electrons with an energy of 100 kV can increase the limit of resolution of TEM to probe nanomaterials. Similar to SEM, a high vacuum is required as electrons cannot travel through air. In Figure 2.11, the basic components of a TEM have been represented [19].

A filament, normally made of LaB<sub>6</sub> or W, is used to produce electrons; they are accelerated by a voltage of the order of 100 - 300 keV by a series of anodes placed inside the main microscope. Condenser lenses (magnetic) are used to collimate and focus these accelerated electrons onto the sample under investigation. The beam is partially transmitted and partially diffracted based on the angle of incidence and thickness of the sample. The transmitted beam passes through a magnetic objective lens. Finally, an objective lens is used to form a focused image of the specimen through the collection of these transmitted electrons. In addition, a projector lens is used to magnify the image further. This image is viewed on a fluorescent screen and a computer monitor. If images are formed by small-angle scattered electrons, they are called "bright-field" TEM images. On the other hand, images are produced by high-angle scattered electrons, they are termed "dark-field" TEM images. It may be noted that the resolution of the TEM is greater than that of the SEM. Typically it can resolve up to the order of 0.2 nm. During the research tenure, a JEOL TEM (JEM-2100) was used to characterize perovskite nanostructures.

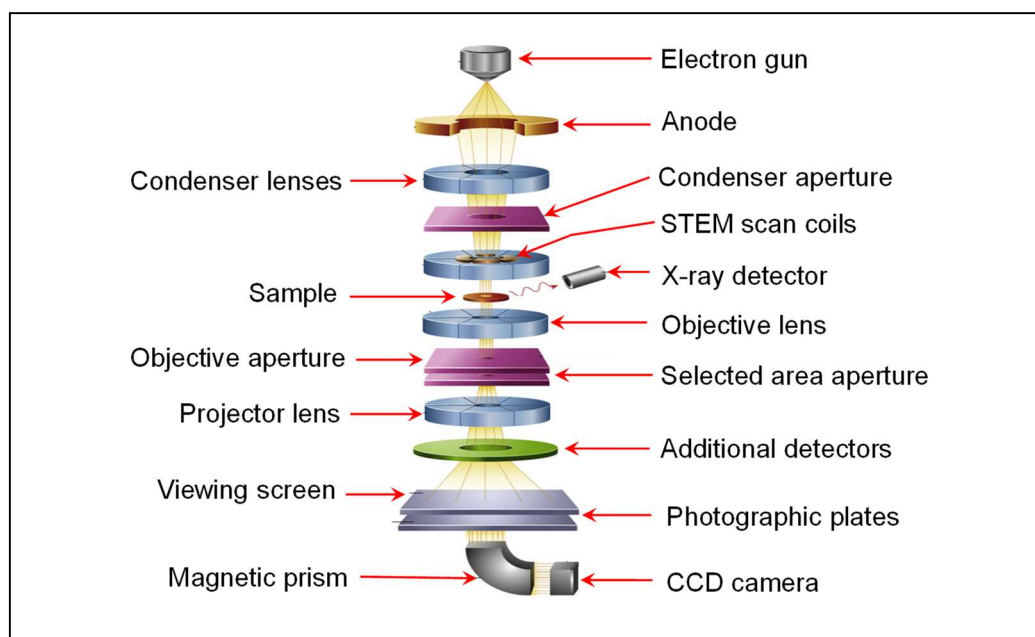


**Figure 2.11.** (a) Schematic diagram of transmission electron microscope (TEM) instrument. Reproduced with permission from [19].

## 2.4. Advanced Characterizations: Scanning Probe Microscopy

During the research tenure, most of the perovskite materials were characterized through advanced scanning probe microscopy techniques. Such cutting-edge microscopic methods possess unprecedented opportunities to investigate the local scale optoelectronic and spintronic properties of perovskite materials such as the band structure, charge/spin transport, and photophysics [21]. It may be noted that scanning probe microscopy does not denote any single microscopic method; rather it is a general class of several measurement techniques such as scanning tunneling microscopy/spectroscopy (STM/S), spin-polarized scanning tunneling spectroscopy (SP-STs), atomic force microscopy (AFM), Kelvin probe force microscopy (KPFM), conducting atomic force microscopy (C-AFM), magnetic conducting atomic force microscopy (mC-AFM), and so on. In this

section, the mechanism, working principle, and instrumentation of these methods have been discussed.

### 2.4.1. Scanning Tunneling Microscopy

Scanning tunneling microscopy is a prevailing scanning probe technique to obtain a high-resolution image of a conducting sample surface at the atomic scale [22]. In this method, a metallic tip is brought close to a sample with a gap of a few angstroms. This small gap acts as a tunnel barrier and electrons can travel from tip to sample or vice versa through a quantum mechanical tunneling process. The schematic diagram and energy band illustration of the STM tunnel junction has been presented in Figure. 2.12.

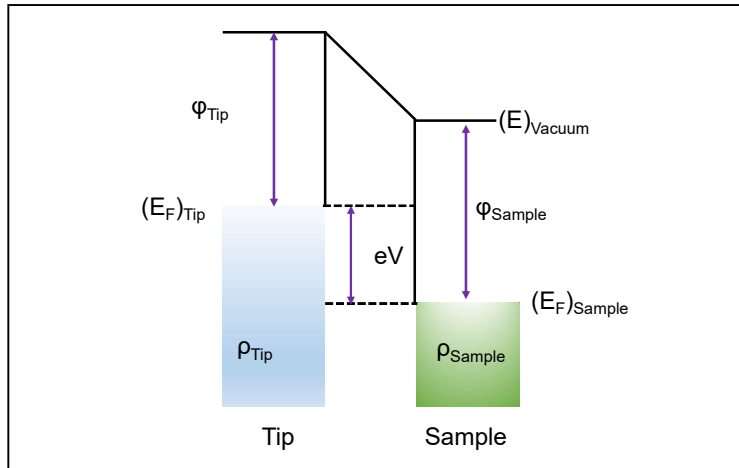


**Figure 2.12.** Schematic illustration of STM tunnel junction.

Based on Wentzel-Kramers-Brillouin (WKB) approximation, the transmission coefficient ( $T$ ) of electrons, associated with tunneling can be written as

$$T \propto \exp \left[ -\frac{4\pi d}{h} \sqrt{2m_e \left( \phi + \frac{eV}{2} - E \right)} \right] \quad (2.7)$$

where  $d$  denotes the separation between tip and sample,  $m_e$  and  $E$  represent mass and energy of the electron, respectively,  $h$  is the Planck constant, and  $e$  signifies the electronic

charge. The average height of the potential barrier has been represented as  $\varphi = \varphi_{Tip} + \varphi_{Metal}$ . Now, the tunneling current stated as

$$I_t(V) \propto \int_{E_F}^{E_F+eV} \rho_{Tip}(E - eV) \rho_{Sample}(E) T(d, E, eV) dE \quad (2.8)$$

where  $\rho_{Tip}$  and  $\rho_{Sample}$  denote the density of states (DOS) of tip and sample, respectively. As such DOS of the tip remains constant, hence tunneling current mostly depends on the DOS of the sample and the separation between tip and sample [23]. As a result, STM has unprecedented merit to probe both the information associated with the sample height (topography) and energy levels (band-edges) related to DOS. It may be noted that ideally, electrons tunnel without any loss of energy; hence it is considered a elastic tunneling process.

The instrumentation of an STM has been presented in Figure. 2.13a. It consists of an atomically resolved tip, a piezoelectric motor to move the tip along the  $z$ -direction, a positioning system to control the movement of the tip along the  $x$ - $y$  direction, a current amplifier, a feedback system along with a computer to produce an STM image while tracking the trace of tip over a particular area of scanning. In addition, vibration isolation systems, ultra-high vacuum (UHV), and cryostat to maintain low temperature are used to reduce noise and obtain stable tunneling current. Moreover, lock-in amplifiers are employed to acquire DOS without much electrical noise.

The topographic image of a sample has been recorded in two different modes, commonly known as constant current mode and constant height mode (Figure. 2.13b) [24]. In constant current mode, the tunneling current remains constant by employing a feedback loop that controls the tip-sample distance. The topography of the sample is obtained by internal software that monitors the vertical position of the tip at each point of scanning. In contrast, the tip-sample distance remains constant in constant height mode. Generally, this mode is performed by disabling the feedback circuit associated with the tunneling current measurement and the tunneling current is recorded with respect to the lateral position ( $x, y$ ) to construct the topography of the sample. Although the scanning speed of the constant height mode is higher than the constant current mode, chances of

tip-crashing are involved. To overcome this problem, additional feedback might be used to monitor the constant height by adjusting the tunneling current.

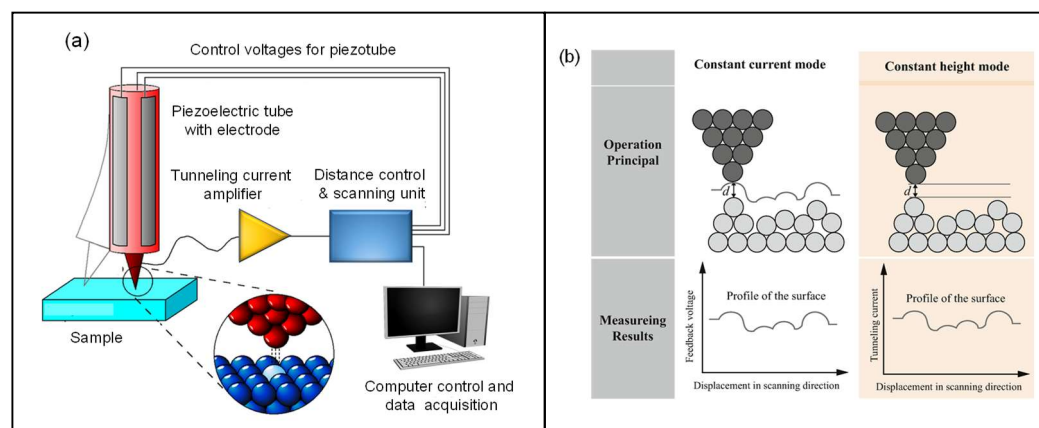


**Figure 2.13.** (a) Schematic diagram of STM instrument. Reproduced from Wikipedia. (b) Different modes of STM operations. Reprinted with permission from [24], Copyright Springer 2019.

During this doctoral research work, a Nanosurf EasyScan2 and variable temperature Pan-style flow-type UHV-STM of M/s RHK Technology was used to investigate the perovskite materials (Figure. 2.14). The Nanosurf EasyScan2 STM was operated in ambient conditions and placed on a vibration isolation table. On the other hand, RHK Pan-style STM functioned under a UHV condition ( $10^{-10}$  Torr). A combination of pumping system consisting of a turbo molecular pump, an ion pump, and a titanium sublimation pump (TSP) was used to achieve such low pressure inside the STM main chamber. Moreover, low-temperature measurements were performed with the aid of a cryostat and a Lakeshore temperature controller (model no 335). Such low-temperature measurements were carried out by using liquid nitrogen (up to 77 K) which was transferred to the STM cryostat through a standard transfer line. Generally, metal probes, such as Pt/Ir tips were formed by a mechanically cut. In addition, tip cleaning pulses were applied during measurements to modify the tip apex which is monitored in



an oscilloscope. In spin-polarized STS-related measurements, commercially purchased Cr-coated W tips were used.



**Figure 2.14.** Digital image of (a) ambient (left panel) and (b) UHV STM (right panels) instruments used during this doctoral research.

### 2.4.1.1. Scanning Tunneling Spectroscopy (STS)

The application of STM is not limited to high-resolution imaging only. The spectroscopic mode of STM, commonly known as scanning tunneling spectroscopy (STS) has been used to study several important properties of a conducting material [25]. The tunneling current ( $I_t$ ) is governed by two interrelated parameters (Equation 2.8), the separation between the tip-sample ( $d$ ) and the applied bias ( $V$ ). Hence, three types of spectroscopies are performed through STS by fixing one parameter so that the relation between the other two could be established. These spectroscopic measurement modes are: (i)  $I$ - $V$  spectroscopy to probe the band edges of the material, (b)  $V$ - $d$  spectroscopy to study electronic levels above the vacuum barrier (in the field emission regime), and (iii)  $I$ - $d$  characteristics to determine the local work function. However, the most commonly used spectroscopic technique is indeed  $I$ - $V$  spectroscopy where the feedback loop remains disabled to maintain a constant tip sample separation,  $d$ . With the tip being fixed at a specific height, the applied voltage is ramped over a chosen range to record the tunneling

current. The obtained differential tunnel conductance ( $dI/dV$ ) as a function of swept voltages is plotted. It may be noted that  $dI/dV$  as a function of  $V$  can be expressed as:

$$\begin{aligned} \frac{dI_t}{dV} I_t(V) \propto & \rho_{Tip}(E_F) \rho_{Sample}(E_F + eV) T(d, E_F + eV, eV) + \int_{E_F}^{E_F + eV} \rho_{Tip}(E - \\ & eV) \rho_{Sample}(E) \frac{dT(d, E, eV)}{dV} dE + \int_{E_F}^{E_F + eV} \frac{d\rho_{Tip}(E - eV)}{dV} \rho_{Tip}(E - \\ & eV) \rho_{Sample}(E) T(d, E, eV) dE \end{aligned} \quad (2.9)$$

Assuming both  $\rho_t$  and  $T$  constant, the expression is simplified to:

$$\frac{dI_t}{dV} I_t(V) \propto \rho_{Tip}(E_F) \rho_{Sample}(E_F + eV) T(d, E_F + eV, eV) \quad (2.10)$$

Hence,  $dI/dV$  is approximately proportional to the local DOS of the sample surface at a particular energy  $eV$ . Although,  $dI/dV$  can be achieved by simple mathematical treatment, for a precise measurement the signal is recorded with the aid of a lock-in amplifier. In this direction, a sinusoidal behavior in the tunneling current is added by applying a sinusoidal voltage ( $V_{AC}$ ) with high-frequency and small amplitude along with a constant DC bias ( $V_{DC}$ ). Mathematically, this modulated current for a signal  $V_{AC} = V_m \sin(\omega t)$  can be expressed in a Taylor series form:

$$I(V_b + V_m \sin(\omega t)) \approx I(V_{bias}) + \frac{dI(V_b)}{dV} V_m \sin(\omega t) + \frac{d^2 I(V_b)}{dV^2} V_m^2 \sin^2(\omega t) + \dots \quad (2.11)$$

As such, the lock-in amplifier extracts the first harmonic frequency and  $dI/dV$  which is proportional to it. In a  $dI/dV$  spectrum, if the bias is applied to the tip, first peaks at positive and negative voltage regions represent the valence band maximum (VBM) and conduction band minimum (CBM), respectively. On the other hand, if bias is applied to the sample, this thumb rule becomes the opposite. Similarly, it is also possible to detect the second harmonic ( $d^2I/dV^2$ ) that can be used to probe the vibrational states of a material. It may be added as a disclaimer that the frequency of the modulated signal should be higher than the cut-off frequency of the feedback loop.

### 2.4.1.2. Spin-Polarized Scanning Tunneling Spectroscopy

Spin-polarized scanning tunneling microscopy (SP-STM) and spectroscopy (SP-STs) are advanced characterization techniques to investigate the spin-states of a material

with high spatial resolution [26]. The scheme of spin-polarized electron tunneling has been presented in Figure 2.15 where the tunneling current is governed by the local magnetization ( $m_s$  and  $m_t$ ) of the tip and the sample.

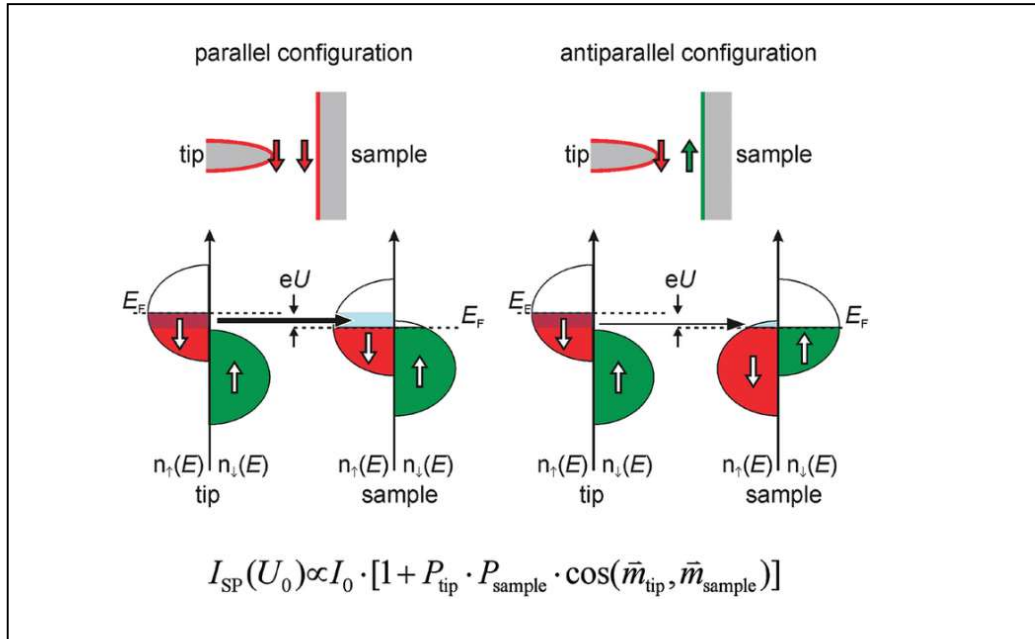


**Figure 2.15.** Schematic representation of electron tunneling during SP-STM. Reprinted with permission from [26].

In addition, an external magnetic field is applied to control  $m_s$  and  $m_t$ . Theoretically, the DOS of a magnetic material is split into up-spin ( $\uparrow$ ) and down-spin ( $\downarrow$ ) for the exchange interaction. In this direction, spin-polarization could be defined as:

$$P(E) = \frac{n_{\uparrow}(E) - n_{\downarrow}(E)}{n_{\uparrow}(E) + n_{\downarrow}(E)} \quad (2.12)$$

Under these circumstances, differential tunnel conductance ( $dI/dV$ ) could be written as:

$$\frac{dI}{dV}(d, V) \propto n_t \cdot n_s(d, E_F + eV) + m_t \cdot m_s(d, E_F + eV) \quad (2.13)$$

Although, there are several complex methods to carry out SP-STM measurements with a ferromagnetic tip, in this doctoral research work, a simpler method of SP-STM was

introduced with antiferromagnetic tip. The details of which could be found later (*Chapter 6*).

### **2.4.1.3. Differential Conductance ( $dI/dV$ ) Imaging**

Differential conductance ( $dI/dV$ ) imaging is an advanced technique that can map the energy distribution of the DOS of the material at particular energy [27,28]. It is considered a combination of imaging and spectroscopic modes of STM. In the imaging mode of STM, either the distance between the tip and the sample or the tunneling current remains fixed as a set point and the variation of the other is recorded to construct the topography. However, in  $dI/dV$  imaging the tip first records and constructs the smallest region of the topography and gets stopped at that position to measure DOS ( $dI/dV$ ). As discussed earlier, the bias voltage is modulated by a small sinusoidal voltage, the period of which is much shorter than the time constant of the feedback loop. In this way, at each point, modulation of tunneling current,  $dI$  is measured and divided by  $dV$  to obtain a pixel of  $dI/dV$  image. In this way, by plotting  $dI/dV$  at a given DC bias as a function of the lateral position the spatial variation of DOS could be acquired. So, the  $dI/dV$  image reflects the density of electrons at any particular energy as a function of position on the surface. The DOS at a particular energy level of the sample can be understood from the color contrast difference. This interesting technique is used to investigate heterostructures of two or three materials with respect to their DOS. Moreover, this method can also be used to identify the molecular orientation and magnetic spin domains.

### **2.4.2. Atomic Force Microscopy (AFM)**

In modern nanoscience, AFM is also an important scanning probe microscopic technique apart from STM. It may be noted that STM measurements could be carried out for conducting samples only. However, AFM does not have this limitation and can be used to analyze the surface of almost every type of samples such as polymers, ceramics, glass, and biological samples [29]. The resolution of this measurement is varied from micrometer to a fraction of a nanometer. It allows for studying several physical properties

including size, morphology, and roughness of a sample. Moreover, statistical information such as size, surface area, and volume distributions are obtained from AFM topographies. In Figure 2.16, a schematic diagram of an AFM system has been presented. It is built with different components such as a cantilever tip, a scanner, a laser source, a photodetector, feedback control, and a data processor. Similar to STM, the tip is brought to the vicinity of the sample to acquire the topography of the surface. Based on the nature of the surface, AFM can function in either contact or non-contact mode. In principle, AFM works in a repulsive tip-sample force regime during the contact mode measurements. Under this situation, the tip remains either in contact or intermittent contact with the surface of the sample. However, in the contact mode, several other interactions hinder high-resolution imaging. Hence, a non-contact mode of imaging is also used where the AFM tip functions in the attractive force regime and is oscillating in the close vicinity of the sample surface. In this mode, no tip-sample physical contact is made. In the contact mode, the interaction force between the tip and the sample generates a static deflection of the tip-cantilever system. As a result, it is also termed static force mode. On the other hand, in non-contact or dynamic force mode, the interaction force modulates the amplitude, frequency, or phase of the cantilever oscillation. However, an interaction between the tip and the sample would result in a deflection of the cantilever irrespective of the operating mode. Primarily, this is monitored by the reflection of a laser ray falling on the top of the cantilever. This reflected laser beam is detected by a four-quadrant photodetector. Finally, this signal is used to construct the surface topography of the sample with the help of a feedback circuit and software.

In addition, the thickness of a thin film is measured by using the AFM. In this direction, a film under investigation is scratched deliberately followed by scanning over the scratch; the thickness of the thin film is determined from a line profile analysis. During this doctoral research work, a Nanosurf easyScan2 AFM and Nanosurf Flex AFM were employed to characterize the morphology and thickness of different perovskites thin films. In most cases, NCLR tips were used with a force constant of 48 N/m. It may be

noted that the merit of AFM was not limited to investigating the morphology and thickness of a sample.

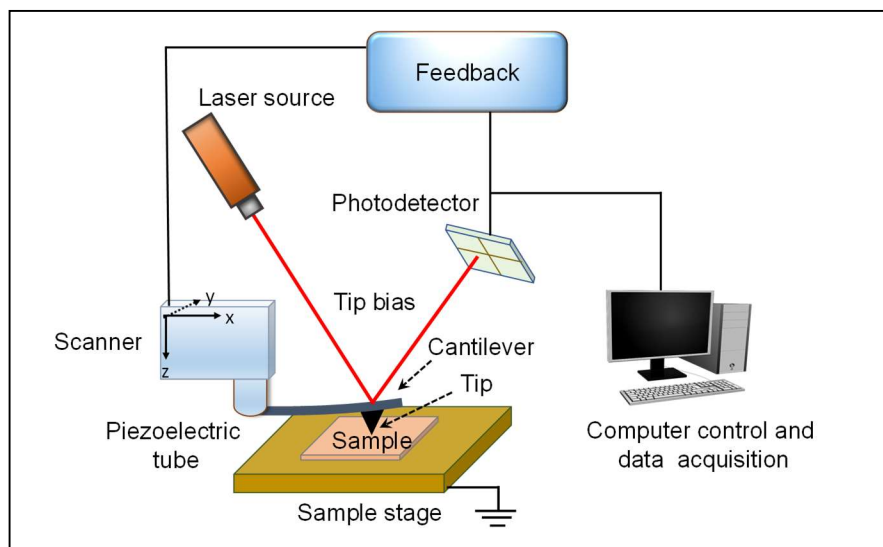


*Figure 2.16 Schematic diagram of AFM setup.*

Apart from these two purposes, several other properties of a sample can be studied at their local scale making it one of the strongest characterization tools in modern science. With a modification and proper choice of the tip, AFM can be used to study the mechanical (ultrasonic force microscopy), electrical (electrostatic force microscopy, Kelvin probe force microscopy, piezoelectric force microscopy, conducting atomic force microscopy), thermal (scanning thermal microscopy), and magnetic (magnetic force microscopy) properties of several samples. However, based on the work carried out in this thesis, the discussion is limited only to Kelvin probe force microscopy and conducting atomic force microscopy.

### **2.4.3. Kelvin Probe Force Microscopy (KPFM)**

Kelvin probe force microscopy (KPFM) is a modified form of AFM that determines the local contact potential difference (CPD) between the tip and sample

through a conducting tip. KPFM is widely considered an exclusive method to investigate electronic and electrical properties of semiconductor surfaces [30]. Since the KPFM is an extension of AFM, the preliminary working mechanism and instrumentation of both techniques are similar. However, additional components are used in KPFM to detect electrical signals.

When a conducting tip is brought close to the sample, an electrical force is generated due to the differences in their work functions. In Figure 2.17, the schematic diagram of the KPFM system has been presented. An electrical contact between the tip and the sample allows the flow of electrons until an equilibrium is established through the alignments of Fermi levels. Subsequently, excess charges appear on the tip and sample surface resulting in a development of a voltage difference, which known as CPD and defined as:

$$CPD = \frac{\phi_{Tip} - \phi_{Sample}}{e} \quad (2.13)$$

where  $\phi_{Tip}$  and  $\phi_{Sample}$  denote the work functions of the tip and sample, respectively and  $e$  represents the electronic charge.

The magnitude of CPD is obtained by applying an AC voltage ( $V_{AC}$ ) and a DC voltage ( $V_{DC}$ ) to the tip, where  $V_{AC}$  creates an oscillation in the tip. In this process, additional oscillating components are induced by the electrostatic force between the tip and the sample resulting in a change in amplitude, frequency, and phase of the oscillation of the tip. Upon applying  $V_{DC}$  to the tip, such additional components are nullified. However,  $V_{DC}$  could be applied to the sample as well. In principle, the magnitude of  $V_{DC}$  should be equal to CPD. However, its sign depends on whether it is applied to the tip or sample. KPFM is performed in dynamic force mode or tapping mode through either amplitude modulation (AM) or frequency modulation (FM). In the first case, the change in the amplitude of the cantilever oscillation originating from the electrostatic interaction between the tip and the sample is monitored to measure the CPD; to be precise the amount of  $V_{DC}$  (applied to the tip) required to nullify the change in amplitude denotes the CPD. On the flip side, the frequency of cantilever oscillation is monitored in FM mode to measure the CPD. Estimation of work function through Equation 2.13 has been

considered as one of the most important applications of KPFM with a tip of known work function. It may be noted that KPFM is used to image potential distributions on the surface of a sample with sub-nanometer resolution. Such measurements are important to investigate the local electrical behavior of any hidden phase in a material. During this doctoral research, a Nanosurf Flex AFM was used to carry out KPFM measurements of perovskite samples with the aid of a Multi75EG (Pt/Cr) conducting tip.

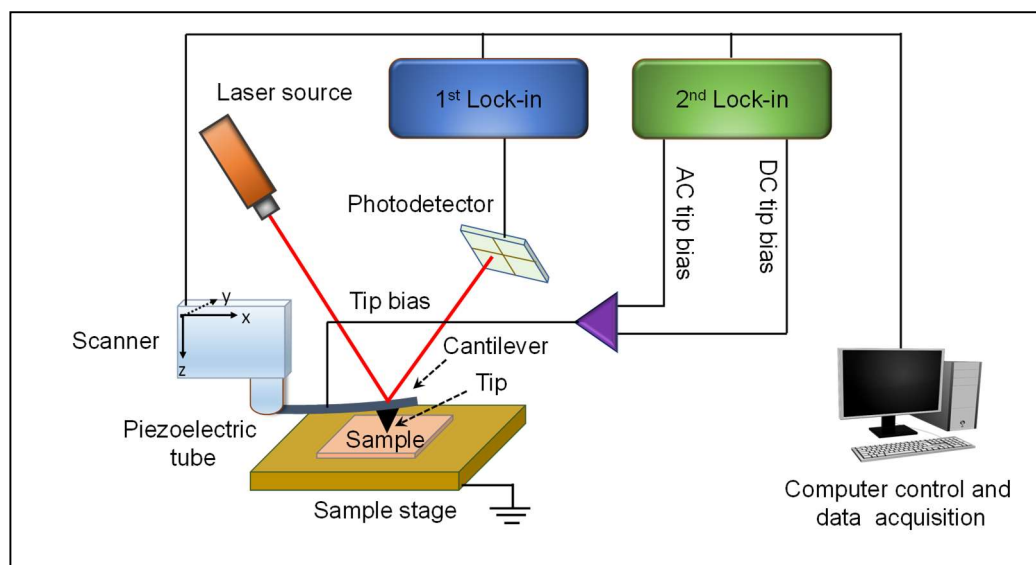


*Figure 2.17. Schematic diagram of KPFM measurement.*

#### 2.4.4. Conducting Atomic Force Microscopy (C-AFM)

Conductive atomic force microscopy (C-AFM) is considered an important tool to understand the local scale current conduction in a material with high spatial resolution [31]. In this research tenure, C-AFM was carried out to study the optoelectronic and spintronic properties of metal halide perovskites in the nanoscale. With the aid of this modified atomic force microscopy-based technique, the topography and the electric current flow through a contact point between the tip and the surface can be simultaneously recorded. In C-AFM, a conductive tip is used in contact mode to scan the surface of the sample. A current image is generated by applying a particular voltage between the tip and



the sample. The topography of the sample is attributed to the general principle of AFM as discussed earlier (monitoring the deflection of the cantilever). However, the current map is obtained by enabling a current-voltage pre-amplifier. As both the topography and current maps are recorded simultaneously from a particular area of the sample under investigation, the electrical features of the sample, for example, conductivity, at a local scale can be investigated. In addition, by enabling the spectroscopic mode, the local current versus voltage ( $I$ - $V$ ) characteristics can be obtained at the desired location very precisely, such as grain and grain boundaries. In particular, the contact is made by moving the tip to a specific position acquired in the topographic image, and local currents are recorded by ramping the voltage. Moreover, this technique can be extended for spin-polarized measurements by using pre-magnetized ferromagnetic tips.

During this research tenure, C-AFM was carried out in the contact mode of a Nanosurf FlexAFM system at ambient. Generally, a PPP-CONTPt (Pt/Ir) was used with a force constant ranging between 0.02-0.77 N/m. In addition, spin-polarized (magnetic) conductive atomic force microscopy (mC-AFM) was carried out with a ferromagnetic Bruker MESP-V2 (Co-Cr) tip having a spring constant of 3 N/m. The tip could be pre-magnetized (either up or down), by applying a strong magnetic field. Current versus voltage ( $I$ - $V$ ) characteristics were acquired by ramping the voltage from -2.5 to +2.5 V. To do so, a bias was applied to the sample deposited on an indium tin oxide (ITO) coated substrate electrodes with respect to the tip.

## **2.5. Fabrication of Devices**

Fabrication of solar cells and photodetectors in this research tenure was carried out in inert conditions inside a glove box. Typically, all the devices were formed on patterned transparent indium tin oxide (ITO) which served the purpose of light entering electrodes in the devices. The ITO substrates had a width of 1/8", a sheet resistance of ~15  $\Omega$ /sq, and a work function of 4.8 eV. Before forming the subsequent active layers, the ITO substrates were cleaned following a usual protocol of ultrasonic cleaning in a range

of liquids, then were dried under airflow, and finally treated with ultraviolet ozone (UVO) to remove the hydrocarbons from the substrate surface for intimate contact with the immediate layer. The different parts of the devices were discussed below:

(i) *Absorber layer*: A *p-i-n*-architecture was designed to fabricate perovskite-based solar cells and photodetectors. In this sandwiched structure, the perovskite acted as an absorber layer which was formed through a spin-coating process.

(ii) *Charge transport layer*: In addition to the active layers, charge transport layers were also cast for better charge transport in the devices. During this doctoral research, all of the photovoltaic devices had an inverted device structure (*p-i-n*). Hence, before forming the perovskite layer, a *p*-type hole transport layer (HTL) was cast. Based on the band alignment, either Cu-doped NiO or PEDOT: PSS was selected to serve the purpose. For Cu-doped NiO, the coated substrates were subjected to a short UVO treatment. The perovskite layer was then formed following the solution-based routes mentioned earlier. After that, an *n*-type electron-transport layer (ETL) was formed on top of the perovskite layer. It should be kept in mind that the precursor solution of the ETL must not contain any solvent that might dissolve the perovskite active layer. In addition, all the active layers were subjected to appropriate annealing steps to remove the excess solvents from the films.

(iii) *Top electrode deposition*: As the top electrode, aluminum was thermally evaporated through a proper shadow mask at a precisely controlled deposition rate. The aluminum strips were also around 1/8' wide and 100 nm thick. Thus, the active area of the devices was mostly 10 mm<sup>2</sup>. Ultra-pure aluminum wires (purity 99.999%) were purchased from Optical Filters and Sigma Aldrich Chemical Company. The wire was kept under an inert condition to prevent an oxidation of aluminum. In this method, the device was kept in a vacuum chamber (base pressure 10<sup>-6</sup> Torr). The Al wire was generally kept in a conducting filament or boat, directly below the substrate at a fixed vertical distance. The evaporation of Al and the rate of deposition are controlled by the flow of the current through the filament. A monitor made with a quartz crystal and placed close to the substrate, kept a track of the rate of deposition and thickness of the deposited film with

the help of the piezoelectric effect of the crystal. The change in the mass of the crystal was electronically converted to obtain the thickness and the rate of the aluminium deposition.

## **2.6. Characterization of Devices**

The photovoltaic devices (solar cells and photodetectors) fabricated in this doctoral research tenure were characterized by current-voltage ( $I$ - $V$ ) characteristics under both dark and illuminated conditions. For the spin-photovoltaic devices  $I$ - $V$  characteristics were recorded under left- and right-handed circularly polarized light. These processes are discussed below.

### **2.6.1. Solar Cells**

To quantify the power conversion efficiency (PCE) of solar cells, the most important characterization technique is indeed the measurement of their current-voltage ( $I$ - $V$ ) characteristics. In this direction, vertical heterojunction (sandwiched) devices were positioned in an inert environment of the glove box (Figure 2.18). It may be noted that an inert environment is beneficial to avoid the oxidation of the aluminum top electrodes. To connect the electrodes (ITO and Al) of such vertical heterostructure devices, micro-positioners with pressure-loaded spring probes were used. The  $I$ - $V$  characteristics were recorded through a Keithley 2636A electrometer controlled by LabTracer software. As a source of illumination, a Solar Simulator (Newport-Oriel Sol3A) attached with an AM1.5 filter was used. To be specific, the  $I$ - $V$  characteristics were measured with a voltage sweep from -2.0 to +2.0 V in both forward and reverse directions. To avoid any influence of adjacent areas or cells, regions outside the cell under inspection were covered. The devices were illuminated with a typical illumination intensity of 100 mW/cm<sup>2</sup> (1 sun) from the ITO side.  $I$ - $V$  characteristics under dark were recorded with a similar methodology, only in absence of any illumination.



**Figure 2.18.** Practical set-up of solar cell measurements inside the glove box.

### 2.6.2. Polarized Light Detectors

To investigate the response of chiral perovskites under circularly polarized light (CPL),  $I$ - $V$  characteristics of the devices were recorded under left (LCP) and right-handed polarized (RCP) illumination in a shielded vacuum chamber fitted with a quartz window (Figure 2.19). As a source of excitation, a high-intensity solar simulator (TriSOL; OAI instruments, USA) was used. Monochromatic light was obtained by passing the light through an Oriel Cornerstone monochromator (model 130). Circularly polarized light was filtered by using a quarter-wave plate followed by a linear polarizer. The state of polarization (LCP or RCP) was determined by changing the angle of the quarter-wave plate.  $I$ - $V$  responses under LCP and RCP were recorded through a Keithley 2636A source meter controlled by LabTracer software. In addition, the time-dependent photocurrent response was recorded at zero bias by using a Keithley 617 electrometer controlled by LabVIEW commands. For intensity-dependent measurements, the intensity (in terms of power density) of light illumination was controlled using a series of integrated neutral density filters and measured accordingly by a power meter (model 1918C; Newport Corp, USA).

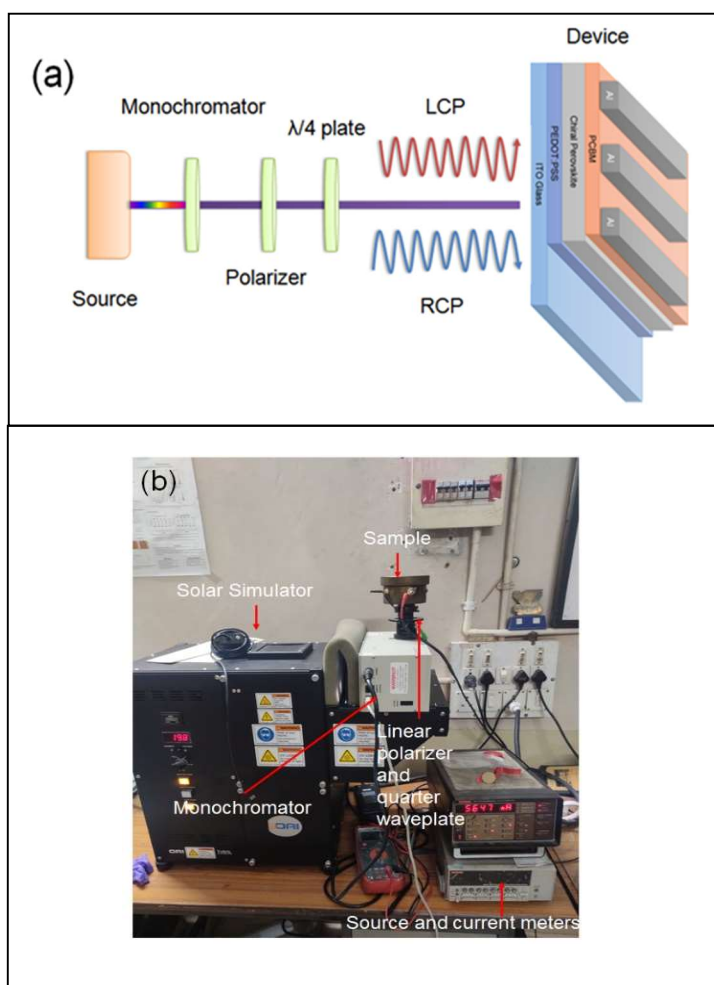


**Figure 2.19.** (a) Schematic diagram and (b) the practical setup of polarized light detection.

## 2.7. References

- [1] P. K. Nayak, S. Mahesh, H. J. Snaith, and D. Cahen, *Nat. Rev. Mater.* **4**, 269 (2019).
- [2] A. K. Jena, A. Kulkarni, and T. Miyasaka, *Chem. Rev.* **119**, 3036 (2019).
- [3] J. P. Correa-Baena, M. Saliba, T. Buonassisi, M. Gratzel, A. Abate, W. Tress, and A. Hagfeldt, *Science* **358**, 739 (2017).

- 
- [4] N. Sahu, B. Parija, and S. Panigrahi, *Indian J. Phys.* **83**, 493 (2009).
- [5] Z. Chen, P. He, D. Wu, C. Chen, M. Mujahid, Y. Li, and Y. Duan, *Front. Mater.* **8**, 723169 (2021).
- [6] L. Zhu, H. Zhang, Q. Lu, Y. Wang, Z. Deng, Y. Hu, Z. Lou, Q. Cui, Y. Hou, and F. Teng, *J. Mater. Chem. C* **6**, 3945 (2018).
- [7] J. Tauc, *Mater. Res. Bull.* **3**, 37 (1968).
- [8] B. Ranjbar and P. Gill, *Chem. Biol. Drug. Des.* **74**, 101 (2009).
- [9] J. Hao, H. P. Lu, L. L. Mao, X. H. Chen, M. C. Beard, and J. L. Blackburn, *ACS Nano* **15**, 7608 (2021).
- [10] A. Jablonski, *Nature* **131**, 839 (1933).
- [11] T. Kirchartz, J. A. Marquez, M. Stolterfoht, and T. Unold, *Adv. Energy Mater.* **10**, 1904134 (2020).
- [12] P. J. Hendra and P. M. Stratton, *Chem. Rev.* **69**, 325 (1969).
- [13] A. A. Bunaciu, E. G. Udristioiu, and H. Y. Aboul-Enein, *Crit. Rev. Anal. Chem.* **45**, 289 (2015).
- [14] W. H. Bragg and W. L. Bragg, *Proc. R. Soc. Lond.* **88**, 428 (1913).
- [15] G. Greczynski and L. Hultman, *Prog. Mater. Sci.* **107**, 100591 (2020).
- [16] C. S. Fadley, *J. Electron Spectrosc. Relat. Phenom.* **178**, 2 (2010).
- [17] C. R. Brundle and B. V. Crist, *J. Vac. Sci. Technol. A* **38**, 041001 (2020).
- [18] Y. Z. Zheng, D. J. Cosgrove, and G. Ning, *Microsc. microanal.* **23**, 1048 (2017).
- [19] B. J. Inkson, in *Materials Characterization Using Nondestructive Evaluation (NDE) Methods*, edited by G. Hübschen, I. Altpeter, R. Tschuncky, and H.-G. Herrmann (Woodhead Publishing, 2016), p. 17.
- [20] D. B. Williams and C. B. Carter, in *Transmission Electron Microscopy: A Textbook for Materials Science*, edited by D. B. Williams, and C. B. Carter (Springer US, Boston, MA, 1996), pp. 3.
- [21] J. Hieulle, C. Stecker, R. Ohmann, L. K. Ono, and Y. Qi, *Small Methods* **2**, 1700295 (2018).
- [22] G. Binnig and H. Rohrer, *Surf. Sci.* **126**, 236 (1983).

- [23] G. Binnig, H. Rohrer, C. Gerber, and E. Weibel, *Phys. Rev. Lett.* **49**, 57 (1982).
- [24] F. Fang and B. Ju, in *CIRP Encyclopedia of Production Engineering*, edited by L. Laperrière (Springer Berlin Heidelberg, Berlin, Heidelberg, 2014), pp. 1090.
- [25] H. J. W. Zandvliet and A. van Houselt, *Annu. Rev. Anal. Chem.* **2**, 37 (2009).
- [26] M. Bode, *Rep. Prog. Phys.* **66**, 523 (2003).
- [27] B. Kundu, A. Bera, and A. J. Pal, *Nanotechnology* **28**, 095705 (2017).
- [28] G. Paul, B. Kundu, and A. J. Pal, *Org. Electron.* **59**, 27 (2018).
- [29] F. J. Giessibl, *Rev. Mod. Phys.* **75**, 949 (2003).
- [30] W. Melitz, J. Shen, A. C. Kummel, and S. Lee, *Surf. Sci. Rep.* **66**, 1 (2011).
- [31] P. Klapetek, in *Quantitative Data Processing in Scanning Probe Microscopy*, edited by P. Klapetek (William Andrew Publishing, 2013), pp. 221.

This page is intentionally left blank.



# Chapter 3

## Ternary Halide Perovskites: Detrimental Role of Defects

*In this chapter, we have studied the role of defects on the band-edges of bismuth-based ternary halide perovskites ( $A_3\text{Bi}_2\text{I}_9$ ) formed with cesium and methylammonium (MA) ions at the A-site. We consider a range of precursor-stoichiometries leading to different reaction environments. The intrinsic defects formed during the perovskite formation affect the materials' band-energies. We introduce scanning tunneling spectroscopy (STS) to probe the band-edges. Fermi energy of the perovskites could be seen to remain always closer to the valence band (VB) as compared to the conduction band (CB) inferring their p-type nature. Acceptor-type defects having the least formation energy have been considered to result in the p-type behavior. Upon a variation in the precursor-stoichiometry in forming the perovskites, STS studies evidence a decrease in the band gap of the materials formed with  $\text{BiI}_3$ -rich precursors. The change in band-energies occurs due to the formation of deep defects above the VB-edge; a shift in the CB-edge towards the Fermi energy is due to a change in the contribution of  $\text{Bi}(p)$  orbitals which form the CB of the perovskite. With methylammonium at the singly-protonated site, the material becomes defect-tolerant as evidenced by the absence of deep-level defects and an improvement in the parameters of solar cells formed with  $(\text{CH}_3\text{NH}_3)_3\text{Bi}_2\text{I}_9$ .*

### 3.1. Introduction

Over the years, research on hybrid halide perovskite materials, which are suitable for solar cells, has progressed from the initial methylammonium lead triiodide

( $\text{CH}_3\text{NH}_3\text{PbI}_3$ , alias MAPI) to a range of directions [1-4]. Multication [5], metal-substitution [6,7], and mixed-halide approaches [8-10] separately or in conjunction were considered in the  $AMX_3$  structure, where  $A$  and  $M$  represent a monovalent and a bivalent cation, respectively, and  $X$  symbolizes a halide. Since a complete replacement of lead from the MAPI structure did not retain the uniqueness of MAPI in terms of a high level of defect tolerance towards its optoelectronic properties [11,12], small exciton binding energies [13], excellent carrier mobilities leading to long charge carrier diffusion lengths [14], and minority carrier lifetime [15], the focus has therefore been shifted towards solution-processed materials beyond  $AMX_3$ . In this direction, interestingly through combinatorial approaches, double perovskites in the form of  $A_2B'B''X_6$  with  $B'$  and  $B''$  being a monovalent and a trivalent metal respectively, or trivalent metal ( $B$ ) based perovskites ( $A_3B_2X_9$ ) are being considered [2,16-19]. Beyond them, layered materials in the form of Ruddlesden-Popper, Aurivillius, and Dion-Jacobson phases are also being envisaged in perovskite solar cells [20].

In the  $A_3B_2X_9$  structure,  $\text{Bi}^{3+}$  and  $\text{Sb}^{3+}$  are especially being considered at the  $B$ -site due to their isoelectronic configuration ( $s^2p^0$ ) as in lead ions ( $\text{Pb}^{2+}$ ), which is believed to be responsible for the unique optoelectronic properties of MAPI or lead-based similar perovskites [21]. The device performance with these trivalent metal-based perovskites has however not excelled primarily due to a wider band gap leading to a large decrease in the achievable efficiency ( $\eta$ ) as per the Shockley-Queisser limit [16,22-24]. Also, the presence of isolated face-shared  $\text{BiI}_6$  octahedra framework (0D) rather than three-dimensional corner-shared  $\text{PbI}_6$  octahedra of MAPI that is known to be responsible for high carrier mobilities through the 3D framework has been another parameter for the truncated efficiency in these 0D systems [25,26].

Although some of the above mentioned issues can be circumvented through materials engineering, it is pertinent to know about the defects which may inevitably form in the material during growth processes. While the defects having energies outside the gap may not have an adverse effect, the deep-level defects forming within the band gap will have a crucial impact on the materials' optoelectronic properties, since the

defect sites can then act as recombination or trapping centers hindering carrier transports for efficient charge collection [27]. It is hence extremely pertinent to identify the defect states along with their energies responsible for a low  $\eta$  in  $A_3B_2X_9$ -based solar cells and thereby possible remedies to passivate the defects. In this work, we introduce scanning tunneling spectroscopy (STS) to understand the presence of defects in bismuth-based ternary halide perovskite systems. The spectroscopy would provide the energy-dependent density of states (DOS) and hence both the band-edges of the perovskites under the influence of defects. We have varied the precursor-stoichiometry in forming  $A_3Bi_2I_9$  ( $A = Cs^+$  and  $CH_3NH_3^+$ ) that in turn changed the reaction environment and thereby only control defect-formation. The range of materials has hence provided a platform to study the role of defects on the band-edges, which are of extreme relevance in designing heterojunction solar cells while retaining the chemical composition of the perovskite.

## **3.2. Experimental**

### **3.2.1. Materials**

Methylammonium iodide ( $CH_3NH_3I$ , 99%) was purchased from Dyesol Limited, Australia, cesium iodide ( $CsI$ , 99.9%), bismuth triiodide ( $BiI_3$ , 99.9%), and anhydrous N, N-dimethylformamide (DMF, 99%) were purchased from Sigma-Aldrich Chemical Company. The materials, stored in a nitrogen-filled glove box with moisture and oxygen level below  $< 0.1$  ppm, were used without further purification.

### **3.2.2. Formation of $MA_3Bi_2I_9$ and $Cs_3Bi_2I_9$ Thin Films**

To cast the perovskites in their thin film form, we adopted a usual one-step solution method, which was based on the co-deposition of both the organic and inorganic precursors from a single solution [28]. A one-step method was followed in lieu of a two-step one to maintain the same degree of structural control on crystallization during the conversion process. In this method, the desired amount of  $CsI$

or  $\text{CH}_3\text{NH}_3\text{I}$  (MAI) and  $\text{BiI}_3$  in DMF were stirred overnight in a glove box at  $70\text{ }^\circ\text{C}$  to dissolve the precursors thoroughly. The molar ratio of CsI (or MAI) to  $\text{BiI}_3$  was tuned from 1.5:1.0 to 1.0:1.5 to obtain a range of perovskites formed with CsI (MAI)-rich to  $\text{BiI}_3$ -rich precursors. The mixed solution was spun on pre-heated ( $70\text{ }^\circ\text{C}$ ) substrates at 2500 rpm for 30 s; at the tenth second, 0.5 mL of warm ( $80\text{ }^\circ\text{C}$ ) chlorobenzene was spun as a protocol for antisolvent treatment, which is known to improve the film-morphology, instead of additive-assisted crystallization [29]. The film was annealed at  $100\text{ }^\circ\text{C}$  for 15 min (30 min for  $\text{CH}_3\text{NH}_3$ -based perovskites) inside the glove box for conversion to  $\text{Cs}_3\text{Bi}_2\text{I}_9$  ( $\text{MA}_3\text{Bi}_2\text{I}_9$ ) perovskite phase. For optical characterization, the thin films were formed on quartz substrates; for STS studies, the same solution of the precursors was spun on arsenic-doped silicon wafers (HF treated) having a resistivity of 3-10  $\text{m}\Omega\cdot\text{cm}$  at a higher rpm, so that the film was ultrathin enough which is necessary for characterization in a scanning tunneling microscope (STM). Since certain physical properties of the perovskite may depend to some extent, on the film thickness or the nature of the substrate used, we have used one set of film-deposition protocols necessary for each measurement method. This allowed us to compare each parameter of all the perovskites formed with a range of precursor-stoichiometries.

### 3.2.3. Fabrication of Devices

Fluorine-doped tin oxide (FTO) coated glass substrates were used for solar cell fabrication. The substrates were cleaned through a usual protocol using soap water, deionized water, acetone, and 2-propanol in sequence followed by UV-ozone (UVO) treatment for 20 min. To form heterostructures, a copper-doped nickel oxide ( $\text{Cu@NiO}$ ) layer was first deposited as a hole-transport layer (HTL) through a sol-gel process [30]. The process included annealing at  $425\text{ }^\circ\text{C}$  for 15 min followed by a short UVO treatment. The precursors to form the active perovskite layer were then spun on  $\text{Cu@NiO}$  coated FTO substrates inside the glove box; the thin films of the precursors were then annealed as per the protocol (*vide supra*). Finally, as an electron-transport layer (ETL), ZnO nanoparticles formed through a hydrothermal method and dispersed

in chlorobenzene (20 mg/mL) were spun at 3000 rpm for 30 s followed by annealing at 100 °C for 20 min [31]. To complete the device fabrication process, aluminum (Al) electrodes were thermally deposited as strips orthogonal to FTO ones in a vacuum chamber, which was inside the glove box system. The active area of the cells was 10 mm<sup>2</sup>.

### **3.3. Results and Discussion**

#### **3.3.1. Characterization of Materials**

Depending on the moiety at the *A*-site, bismuth-based ternary halide perovskites ( $A_3\text{Bi}_2\text{I}_9$ ) as such have a band gap of 2 eV and above [32]. In Figure 3.1, we have presented optical absorption spectra and their corresponding Tauc plots for the two sets of perovskites formed with a range of precursor-stoichiometries or reaction environments. Considering the inaccuracies in deriving optical band gap from Tauc plots, we have used the results to compare the optical band gap from bismuth-based ternary halide perovskites formed with a range of precursor-stoichiometries. The gap could be found to depend on the stoichiometry of the precursors, with which the perovskites were formed. With the optical gap of the respective materials being enlisted in Table 3.1, the gap could be seen to decrease when a perovskite material was formed with imbalanced precursors. Here, the gap must have become altered due to a change in one or both of the bands which are prone to defects in these ternary perovskites (as opposed to MAPI). That is, defect species having the least formation energy may have formed and modified the band-edge(s) and accordingly the gap. Since the optical spectroscopy provides a combined effect of (shift in) both the band-edges and is a rough estimate of the gap, we hence have introduced scanning tunneling spectroscopy (in a later section) to deliberate on the effect of precursor-stoichiometry on band-edges separately and thereby transport gap of such low-dimensional materials under the influence of different synthesis conditions.

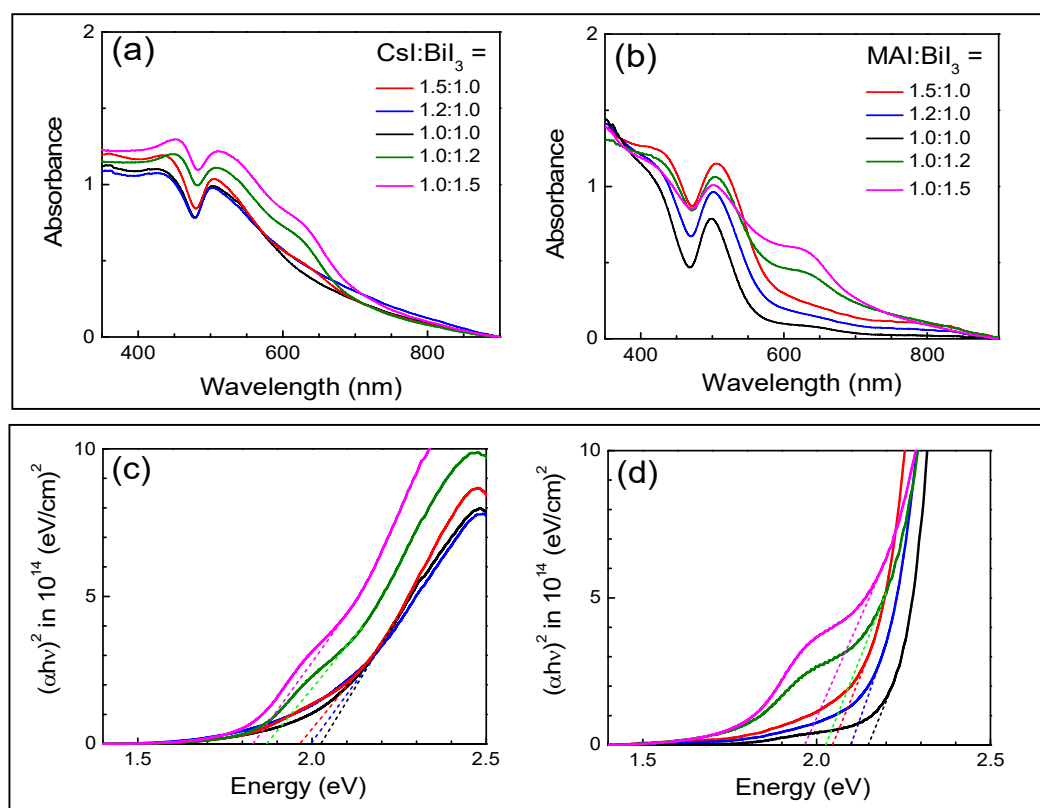


**Figure 3.1.** (a-b) Optical absorption spectra (upper panel) and (c-d) corresponding Tauc plots (lower panel) of  $\text{Cs}_3\text{Bi}_2\text{I}_9$  and  $\text{MA}_3\text{Bi}_2\text{I}_9$  respectively, formed with different precursor-stoichiometries as mentioned in the legends.

**Table 3.1.** The optical gap of  $\text{Cs}_3\text{Bi}_2\text{I}_9$  and  $\text{MA}_3\text{Bi}_2\text{I}_9$  formed with different precursor-stoichiometries.

Material	Optical gap of $\text{Cs}_3\text{Bi}_2\text{I}_9$ and $\text{MA}_3\text{Bi}_2\text{I}_9$ in eV				
	CsI (or MAI) : BiI <sub>3</sub> ratio of the precursors				
	1.5:1.0	1.2:1.0	1.0:1.0	1.0:1.2	1.0:1.5
$\text{Cs}_3\text{Bi}_2\text{I}_9$	1.96	2.00	2.03	1.87	1.84
$\text{MA}_3\text{Bi}_2\text{I}_9$	2.04	2.10	2.15	2.03	1.97

Since hybrid halide perovskites are known to exhibit strong optical absorption in the visible region, optical spectroscopy is often inadequate to establish the phase purity of the materials. We hence characterized the perovskites from the viewpoint of crystal structures; XRD patterns of the two sets of perovskites were recorded accordingly (Figure 3.2).

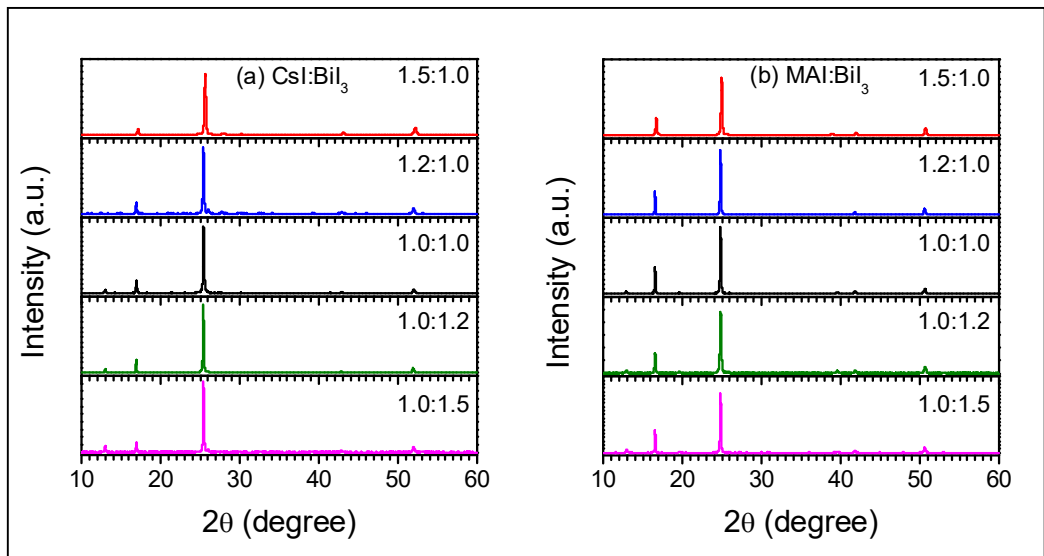


**Figure 3.2.** XRD patterns of (a)  $Cs_3Bi_2I_9$  and (b)  $MA_3Bi_2I_9$  formed with different precursor-stoichiometries as mentioned in the legends.

Perovskites with a particular *A*-cation exhibited diffraction peaks at appropriate positions corresponding to only that particular perovskite ensuring a complete conversion during the annealing process. For example, XRD patterns of as-prepared  $Cs_3Bi_2I_9$  thin films exhibited sharp diffraction peaks at  $16.9^\circ$  and  $25.4^\circ$ , which corresponded to (004) and (006) planes of the hexagonal crystal, respectively, and matched well with the literature evidencing formation of phase-pure  $Cs_3Bi_2I_9$  [19,33]. A higher intensity of the  $25.4^\circ$  peak implies that the solution-processed film had a preferred orientation along its (006) crystal plane. With increasing  $BiI_3$  content in the precursors, an additional peak appeared at  $12.9^\circ$ , which represents residual  $BiI_3$  in the

perovskite films [34]. For the methylammonium (MA)-based perovskites ( $\text{MA}_3\text{Bi}_2\text{I}_9$ ), the characteristic peaks of (004) and (006) planes appeared at  $16.6^\circ$  and  $24.8^\circ$ , respectively [34]. Alike  $\text{Cs}_3\text{Bi}_2\text{I}_9$ , the  $\text{BiI}_3$ -rich phase of  $\text{MA}_3\text{Bi}_2\text{I}_9$  had a signature of unreacted  $\text{BiI}_3$  in terms of a peak at  $12.9^\circ$ . By comparing the intensity of the peak at  $12.9^\circ$ , which represents the residual  $\text{BiI}_3$ , it can be stated that  $\text{CH}_3\text{NH}_3\text{I}$  has a better reactivity with  $\text{BiI}_3$  as compared to that of  $\text{CsI}$  with the same triiodide.

### 3.3.2. STS of $\text{Cs}_3\text{Bi}_2\text{I}_9$ and the Defect States

With the phase purity of the materials being substantiated, we proceeded to analyze the band-edges of the materials. We accordingly recorded STS of  $\text{Cs}_3\text{Bi}_2\text{I}_9$  and  $\text{MA}_3\text{Bi}_2\text{I}_9$  formed with different precursor-stoichiometries. Measurements on each of the materials in their ultrathin-film form provided differential tunnel conductance spectra ( $dI/dV$  versus  $V$ ) and thereby their DOS and band-edges. For each material, measurements at different points have been summed up as histograms of CB and VB-energies. The topographies of the samples are presented in Figure 3.3. All the images were recorded in a constant current mode. The typical  $dI/dV$  spectrum and CB and VB energy-histograms of several  $\text{Cs}_3\text{Bi}_2\text{I}_9$  samples formed with different precursors stoichiometry are shown in Figure 3.4. The  $dI/dV$  spectrum shows peaks on either side of 0 V, at which Fermi energy ( $E_F$ ) is aligned. Since the bias was applied to the tip, the first peak at a positive voltage closest to 0 V implied the withdrawal of electrons from the perovskite material and hence its VB-edge. The first peak in the other bias direction similarly denoted the injection of electrons and hence the CB-edge of the semiconductor. For example, the  $dI/dV$  spectrum and the histograms of a sample formed with balanced precursor stoichiometry show that the VB- and CB-energies are located at 0.96 eV below  $E_F$  and 1.05 eV above the  $E_F$ , respectively. As compared to the CB-edge, the VB turned out to be closer to the Fermi energy denoting a  $p$ -type nature of  $\text{Cs}_3\text{Bi}_2\text{I}_9$ .

A non-intrinsic nature in the perovskite formed with stoichiometrically-balanced precursors implies the presence of point defects in the system [24,35]. As such, possible point defects in  $\text{Cs}_3\text{Bi}_2\text{I}_9$  can be classified broadly into two types:



acceptor-like and donor-like; and they will naturally affect the Fermi energy of the semiconductors in an opposing manner. While the acceptor-like defects would originate due to cation vacancies ( $V_{Cs}$ ,  $V_{Bi}$ ), iodine interstitial ( $I_i$ ), Cs on Bi substitution ( $Cs_{Bi}$ ), and antisite substitutions, namely iodide on cation ( $I_{Cs}$ ,  $I_{Bi}$ ), the source of donor-like defects could be iodine-vacancies ( $V_I$ ), cation interstitials ( $Cs_i$ ,  $Bi_i$ ), Bi on Cs substitution ( $Bi_{Cs}$ ), and cation on iodide antisite-substitutions ( $Cs_I$ ,  $Bi_I$ ) (Table 3.2).

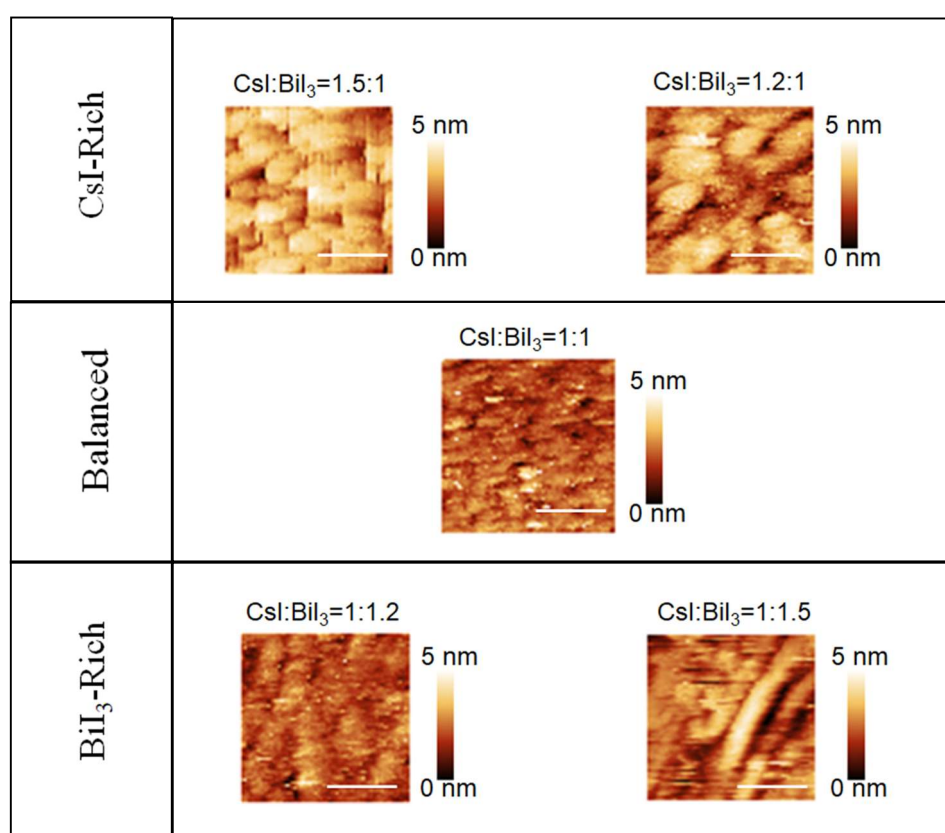


**Figure 3.3.** STM topographies of a few representative  $Cs_3Bi_2I_9$  thin films formed with different precursor-stoichiometries as mentioned in the legends. The scale in the topographies is 50 nm.

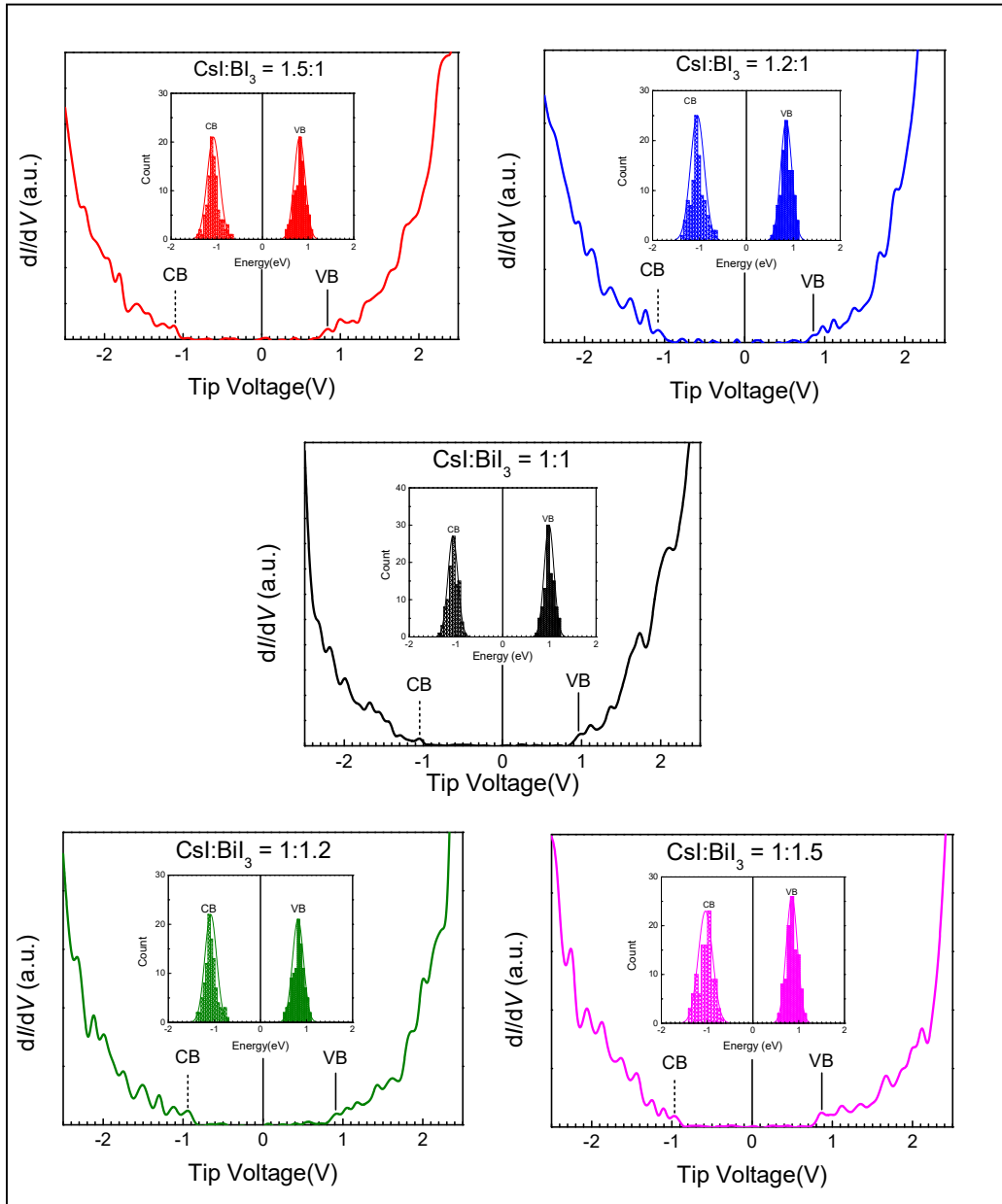


**Figure 3.4.** The typical STS spectrum (upper panel) and histograms of CB and VB-edges (lower panel) of  $\text{Cs}_3\text{Bi}_2\text{I}_9$  formed through different precursor stoichiometry.

**Table 3.2.** List of all possible vacancies formed in  $\text{Cs}_3\text{Bi}_2\text{I}_9$  with CsI-rich and  $\text{BiI}_3$ -rich precursors and their effect on electronic band positions. For each type of vacancy, the one represented in bold has the least formation energy [24].

<b><math>\text{Cs}_3\text{Bi}_2\text{I}_9</math> Formed with</b>	<b>Effect on Electronic Band-Positions</b>	
	Acceptor-like (p-type)	Donor-like (n-type)
<b>CsI-Rich Precursors</b>	Cation vacancies ( $V_{\text{Bi}}$ )	Cation on iodide substitutions ( $\text{Cs}_\text{I}$ )
	<b>Cs on Bi substitution (<math>\text{Cs}_{\text{Bi}}</math>)</b>	<b>Cation interstitials (<math>\text{Cs}_\text{i}</math>)</b>
	Iodide on cation antisite substitution ( $\text{I}_{\text{Bi}}$ )	Iodine-vacancy ( $V_\text{I}$ )
	<b>Iodine interstitial (<math>\text{I}_\text{i}</math>)</b>	
	Cation vacancies ( $V_{\text{Cs}}$ )	Cation on iodide substitutions ( $\text{Bi}_\text{i}$ )
<b><math>\text{BiI}_3</math>-Rich Precursors</b>	<b>Iodide on cation antisite substitution (<math>\text{I}_{\text{Cs}}</math>)</b>	<b>Cation interstitials (<math>\text{Bi}_\text{i}</math>)</b>
	Iodine interstitial ( $\text{I}_\text{i}$ )	Bi on Cs substitution ( $\text{Bi}_{\text{Cs}}$ )
		<b>Iodine-vacancy (<math>V_\text{I}</math>)</b>

The  $p$ -type nature in the perovskite formed with stoichiometrically-balanced precursors, in general, should imply that amongst the 12 possible point defects (Table 3.2), the formation energy of an acceptor-like defect is the least. When we compare the formation energies of all the point defects, we find that donor-type  $V_\text{I}$  and acceptor-type  $\text{Cs}_{\text{Bi}}$  defects have similar and least formation energy [24]. Formation of  $\text{Cs}_{\text{Bi}}$  point-defects has a higher possibility in the perovskite reacted with stoichiometrically-balanced precursors, since a presence of unreacted  $\text{BiI}_3$  was observed in the XRD pattern allowing cesium-ions to occupy the vacant bismuth sites. That is, the unreacted bismuth salt in effect paved perovskite-formation in an environment of CsI-rich precursors leaving the bismuth vacancies to fill in sequence by cesium-ions ( $\text{Cs}_{\text{Bi}}$ ), and hence we have obtained a  $p$ -type nature in the system instead of an  $n$ -type behavior.

Similarly, we extended the discussion to the other perovskites formed with different stoichiometry. Their energy levels obtained from the histograms have been

collated in Figure 3.5. Additionally, in Table 3.3, we have presented the band edges and correspondingly the band gap of the materials for comparison. The results show that (1) the nature of conductivity of the perovskite remained *p*-type when the compounds were formed through different precursor-stoichiometries and (2) the gap decreased when the perovskites were formed with imbalanced precursors, that is, in both CsI-rich and BiI<sub>3</sub>-rich conditions. It may be restated that the type of defects prevalent in compounds formed through different precursor-stoichiometries could be understood from the relative location of Fermi energy with respect to the two band-edges since these two categories of defects would push the Fermi energy towards either band-edges.

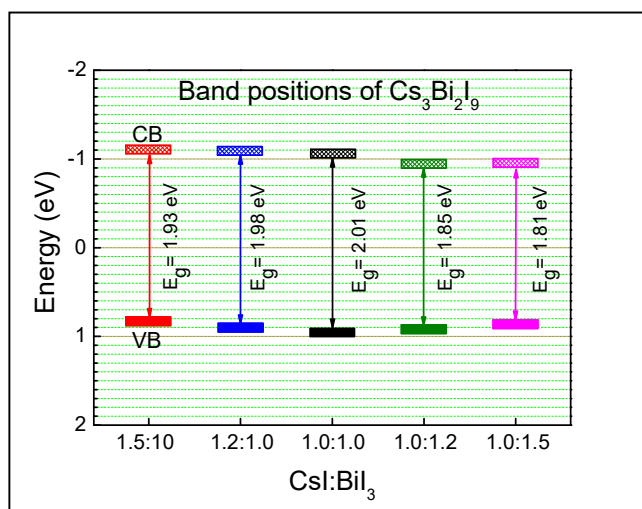


**Figure 3.5.** Band positions of  $Cs_3Bi_2I_9$  formed with different stoichiometric ratios of the precursors, namely CsI and BiI<sub>3</sub>.

The perovskites formed with CsI-rich or with BiI<sub>3</sub>-rich precursors remained *p*-type in nature to the same extent. That is, in perovskites formed with CsI-rich precursors, Cs<sub>Bi</sub> vacancies continued to dominate in addition to some other acceptor-like vacancies, such as I<sub>Bi</sub> and V<sub>Bi</sub> having a formation energy a little higher than that of Cs<sub>Bi</sub>. If we look at the formation energies of defects in the perovskite formed with BiI<sub>3</sub>-rich precursors (Table 3.2), we find that the energy for iodine-vacancy (V<sub>I</sub>) is the least; due

to the donor-like nature of such vacancies, they should have transformed the material to an *n*-type. Since the BiI<sub>3</sub> in a BiI<sub>3</sub>-rich environment has left a larger fraction of unreacted triiodide salt in the perovskite, the unreacted precursor may also affect the nature of conductivity. It may be noted that BiI<sub>3</sub> possesses a strong *p*-type character [24]. The *p*-type nature of BiI<sub>3</sub> may hence have counterbalanced or passivated the effect of donor-like iodine-vacancies leading to the formation of nearly intrinsic or subtle *p*-type in Cs<sub>3</sub>Bi<sub>2</sub>I<sub>9</sub> formed with a BiI<sub>3</sub>-rich environment. The results are in contrast to CH<sub>3</sub>NH<sub>3</sub>PbI<sub>3</sub> (MAPI) in which a variation in the precursor-stoichiometry had transformed the perovskite material from *p*-type (CH<sub>3</sub>NH<sub>3</sub>I-rich) to *n*-type (PbI<sub>2</sub>-rich) without any change in the band gap [36-38].

**Table 3.3.** CB and VB edges of Cs<sub>3</sub>Bi<sub>2</sub>I<sub>9</sub> formed with different precursor-stoichiometries and comparison of their optical and transport gaps.

Precursor-Stoichiometry, CsI:BiI <sub>3</sub>	CB (eV)	VB (eV)	Band Gap (eV)	Optical Gap (eV)
1.5:1.0	-1.10	0.83	1.93	1.96
1.2:1.0	-1.08	0.90	1.98	2.00
1.0:1.0	-1.05	0.96	2.01	2.03
1.0:1.2	-0.93	0.92	1.85	1.87
1.0:1.5	-0.95	0.86	1.81	1.84

Although the precursor-stoichiometry did not affect the nature of conductivity in the perovskites, band-positions have been found to respond in a large manner (Table 3.3). The gap shrunk from 2.01 eV (balanced condition) to 1.93 eV (CsI-rich environment) and to 1.81 eV (BiI<sub>3</sub>-rich environment). The optical gap has also decreased with a similar trend, although to a lesser extent. Additionally, amongst the band-energies, the VB-edge should represent the deep Cs<sub>Bi</sub>-defects forming above the actual VB [24]. In perovskites formed with BiI<sub>3</sub>-rich precursors, band-positions of the unreacted *p*-type BiI<sub>3</sub> have affected the VB-edge by pushing it towards the  $E_F$ .

Regarding the CB, we shall have to look at the orbitals that are responsible for the formation of the band in  $\text{Cs}_3\text{Bi}_2\text{I}_9$ . CB is known to be formed with a mixture of I( $s$ ), I( $p$ ), and Bi( $p$ ) orbitals [35]. The perovskites formed with increasingly more  $\text{BiI}_3$  precursors should hence offer a higher overlap between bismuth and iodine orbitals leading the bands to move towards the Fermi energy and correspondingly shrinking the band gap. Due to the presence of defect-states above the VB, orbitals responsible for VB did not affect the band-edge. Even if we keep the defect-states aside, we note that the VB is contributed by I( $p$ ) and Bi( $s$ ) orbitals; the band hence becomes more tolerant to the precursor-stoichiometry, since the  $s$ -orbitals are known to have a lesser influence on a band than the  $p$ -orbitals which offer a higher spin-orbit coupling. Also, due to the antibonding characteristics of VB [24], the possibility of VB-derivative formation close to the edge can be ruled out. These hence corroborate that the change in VB-edge occurred due to the formation of deep-level defect-states.

If we compare the optical and transport gap of the materials, we find that the optical gap was slightly higher than the transport one (Table 3.3). As such, a contrasting trend was expected due to the involvement of exciton binding energy in optical spectroscopy. Our results hence further support that defect states were probed here as the VB-edge in bismuth-based hybrid halide perovskites.

Since we have made many STS measurements leading to CB- and VB-energies on each material, we could estimate the spreading or dispersion of the energies as full-width at half-maxima (FWHM) of their histograms (Table 3.4). For all the materials, unlike MAPI, the CB- was more dispersed than the VB-energy implying a higher effective mass of carriers and thereby hindering the devices' optoelectronic performances [39]. The histogram of VB-energy appeared asymmetric with the distribution extending more towards the  $E_F$ . Asymmetric histograms of this type support the thesis of deep-level defect states forming above the VB in these systems.

**Table 3.4.** FWHM of CB and VB edges and band gap of  $\text{Cs}_3\text{Bi}_2\text{I}_9$  formed with different precursor-stoichiometries.

Precursor-Stoichiometry, $\text{CsI}:\text{BiI}_3$	(FWHM) of CB	(FWHM) of VB
1.5:1.0	0.34	0.29
1.2:1.0	0.33	0.28
1.0:1.0	0.26	0.24
1.0:1.2	0.31	0.27
1.0:1.5	0.37	0.30

### 3.3.3. STS of $(\text{CH}_3\text{NH}_3)_3\text{Bi}_2\text{I}_9$ and the Defect States

We have extended the work by characterizing  $\text{MA}_3\text{Bi}_2\text{I}_9$  formed with different precursor-stoichiometries between MAI and  $\text{BiI}_3$ . The STM topographies were presented in Figure 3.6.

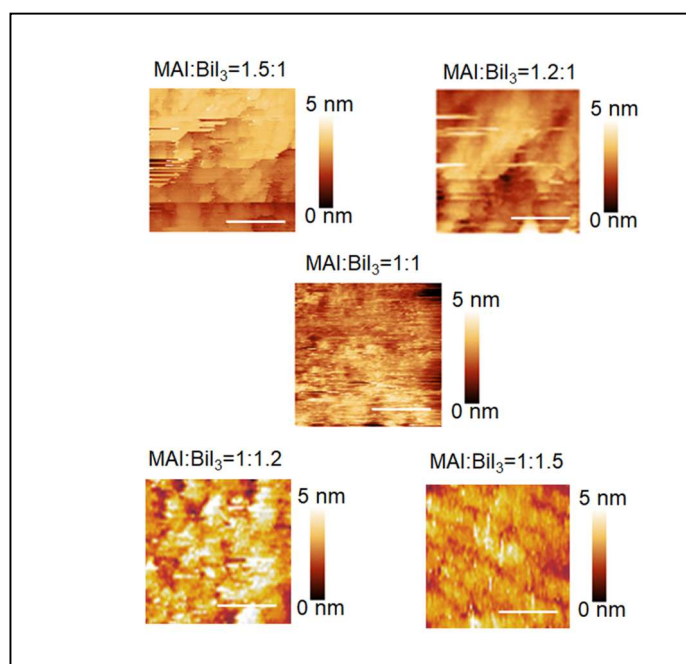


**Figure 3.6.** STM topographies of  $\text{Cs}_3\text{Bi}_2\text{I}_9$  samples formed through different precursor stoichiometry. The scale bar is 50 nm.

The  $dI/dV$  spectra and corresponding histogram of band energies were shown in Figure 3.7.

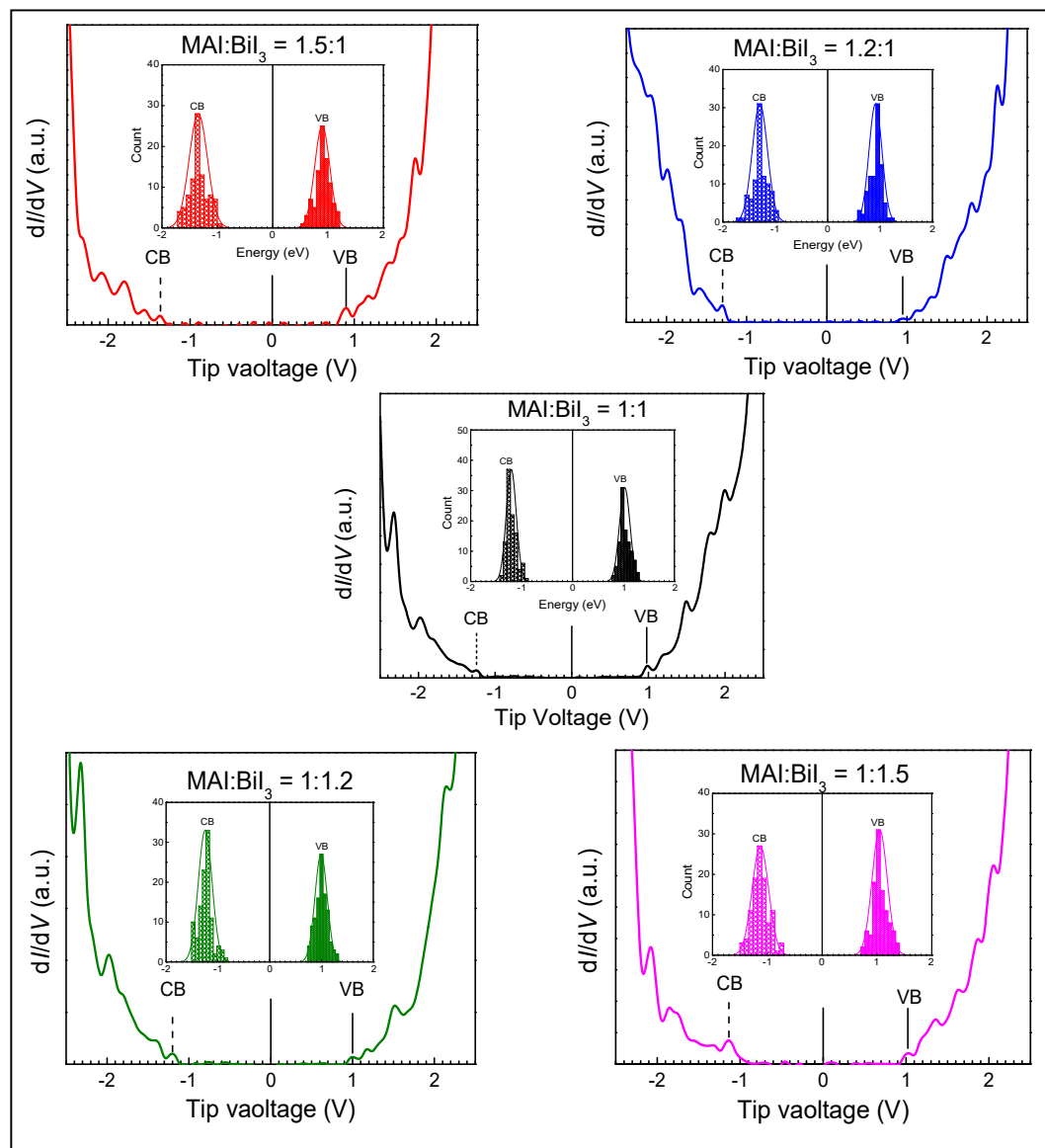


**Figure 3.7.** Typical STS spectrum and histograms of CB and VB-edges of  $Cs_3Bi_2I_9$  formed through different precursor stoichiometry as mentioned in the legends.



First of all, STS studies of  $\text{MA}_3\text{Bi}_2\text{I}_9$  formed with stoichiometrically-balanced precursors exhibited  $p$ -type character. Upon variation in the precursor stoichiometry, the gap did not respond largely; Fermi energy could be seen to shift away from the VB-edge (Figure 3.8). The  $p$ -type perovskite formed with MAI-rich precursors turned into near-intrinsic when the material was formed with  $\text{BiI}_3$ -rich precursors. If we compare the optical and transport gaps (Table 3.5) derived from STS studies, we find that the former was always lesser than the latter one. Such a nature, which is in contrast to the results in  $\text{Cs}_3\text{Bi}_2\text{I}_9$ , that is, the occurrence of deep-level defects above VB, implies the involvement of exciton binding energy in the optical gap and the absence of any mid-gap defect states in  $\text{MA}_3\text{Bi}_2\text{I}_9$ . The non-intrinsic nature of  $\text{MA}_3\text{Bi}_2\text{I}_9$  formed with stoichiometrically-balanced precursors and the invariance of band gap upon a variation in the stoichiometry hence implies the formation of shallow-level defects outside the gap. The  $p$ -nature of the material and a shift in Fermi energy towards the VB in systems formed with MAI-rich precursors further indicate that acceptor-like defects are forming in  $\text{MA}_3\text{Bi}_2\text{I}_9$ . In perovskites reacted with excess- $\text{BiI}_3$ , the  $p$ -nature of the salt could be seen to influence band-edges of the material like  $\text{Cs}_3\text{Bi}_2\text{I}_9$  synthesized under a similar condition.

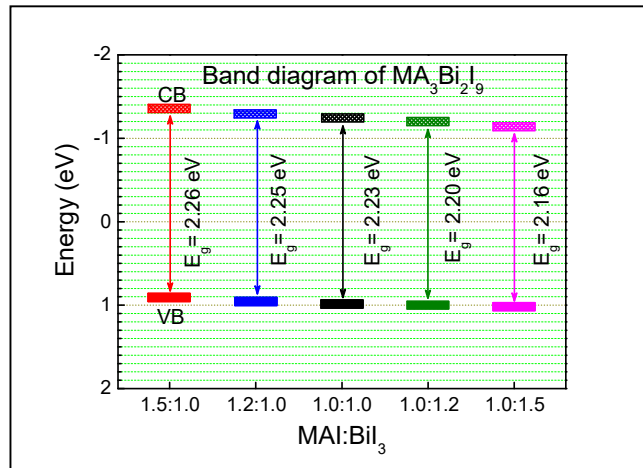


**Figure 3.8.** Band positions of  $\text{MA}_3\text{Bi}_2\text{I}_9$  formed with different stoichiometric ratios of the precursors, namely MAI and  $\text{BiI}_3$ .

**Table 3.5.** CB and VB edges of MA<sub>3</sub>Bi<sub>2</sub>I<sub>9</sub> formed with different precursor-stoichiometries and comparison of their optical and transport gaps.

Precursor-Stoichiometry, MAI:BiI <sub>3</sub>	CB (eV)	VB (eV)	Band Gap (eV)	Optical Gap (eV)
1.5:1.0	-1.36	0.90	2.26	2.04
1.2:1.0	-1.30	0.95	2.25	2.10
1.0:1.0	-1.25	0.98	2.23	2.15
1.0:1.2	-1.20	1.00	2.20	2.03
1.0:1.5	-1.14	1.02	2.16	1.97

Since CB in A<sub>3</sub>Bi<sub>2</sub>I<sub>9</sub> is known to be formed with a mixture of I(*s*), I(*p*), and Bi(*p*) orbitals, the singly-protonated ion at the *A*-site should have little influence on its formation. That is, like Cs<sub>3</sub>Bi<sub>2</sub>I<sub>9</sub>, the CB in MA<sub>3</sub>Bi<sub>2</sub>I<sub>9</sub> formed with BiI<sub>3</sub>-rich precursors moved towards the Fermi energy due to a higher overlap between bismuth and iodine orbitals. In MA<sub>3</sub>Bi<sub>2</sub>I<sub>9</sub>, the change in VB is now observable due to an absence of mid-gap defect-states, since the VB is contributed by the *p*-orbitals of I and the *s*-orbitals of Bi. It may be restated that in Cs<sub>3</sub>Bi<sub>2</sub>I<sub>9</sub>, the original shift in VB was marred by an appearance of deep-level defect-states above the VB. The results in MA<sub>3</sub>Bi<sub>2</sub>I<sub>9</sub> further substantiate the formation of defect-states in cesium-based bismuth ternary halide perovskites.

### 3.3.4. Defect States in A<sub>3</sub>Bi<sub>2</sub>I<sub>9</sub> and Solar Cell Parameters

Notwithstanding the unfavorable issues of trivalent metal-based perovskites, such as wider band gap and isolated face-shared BiI<sub>6</sub> octahedra framework implying lower-dimensional nature rather than 3D corner-shared PbI<sub>6</sub> octahedra of MAPbI<sub>3</sub>, the effect of defect states in A<sub>3</sub>Bi<sub>2</sub>I<sub>9</sub> can be seen to be reflected in photovoltaic properties. We have fabricated heterojunction devices based on bismuth-based halide perovskites with stoichiometrically-balanced precursors and characterized them to study their photovoltaic performances. The devices were formed with Cu@NiO and ZnO as a hole-

and electron-transport layers, respectively, so that a type-II band-alignment is formed at both the interfaces (Figure 3.9).

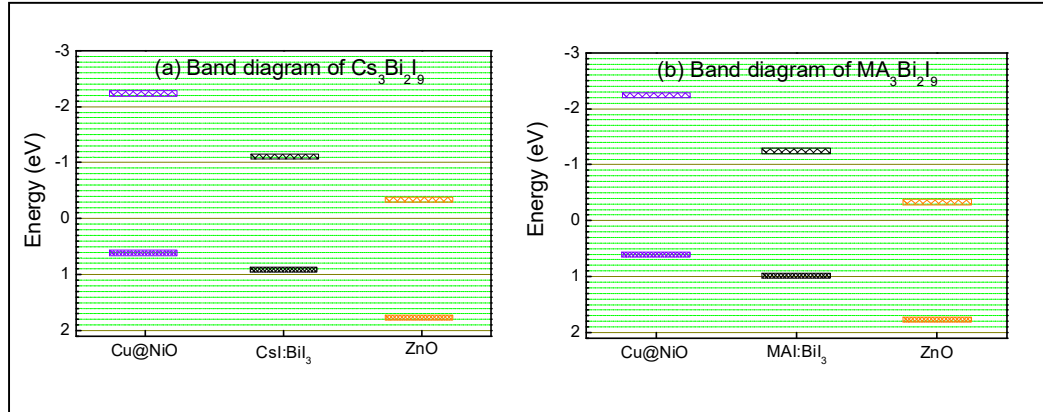


**Figure 3.9.** Type-II band alignment of (a) Cu: NiO/ $\text{Cs}_3\text{Bi}_2\text{I}_9/\text{ZnO}$  and (b) Cu: NiO/ $\text{MA}_3\text{Bi}_2\text{I}_9/\text{ZnO}$  heterojunctions.

The devices based on both cesium and methylammonium first of all exhibited rectifying  $I$ - $V$  characteristics under dark conditions (Figure. 3.10). We hence expected that the devices would demonstrate photovoltaic properties under illumination. The characteristics under light were not impressive due to a large band gap of the active material and also a high exciton binding energy in the perovskite (around 200-300 meV) [40]. When we compare the characteristics of the devices based on  $\text{Cs}_3\text{Bi}_2\text{I}_9$  and  $\text{MA}_3\text{Bi}_2\text{I}_9$ , we observe that the performance of  $\text{Cs}_3\text{Bi}_2\text{I}_9$  was inferior to that of  $\text{MA}_3\text{Bi}_2\text{I}_9$ -based devices. The  $\eta$  improved to 0.36 in (deep) defect-free  $\text{MA}_3\text{Bi}_2\text{I}_9$  as compared to  $\text{Cs}_3\text{Bi}_2\text{I}_9$  containing acceptor-like deep-level defects. The defect levels provide a route for recombination loss in solar cells; the shunt resistance calculated from  $I$ - $V$  characteristics under illumination accordingly could be seen to increase upon defect-passivation. The results hence again support the formation of defect-states in cesium-based bismuth ternary halide perovskites and indicate a necessity of defect-passivation while fabricating solar cells.

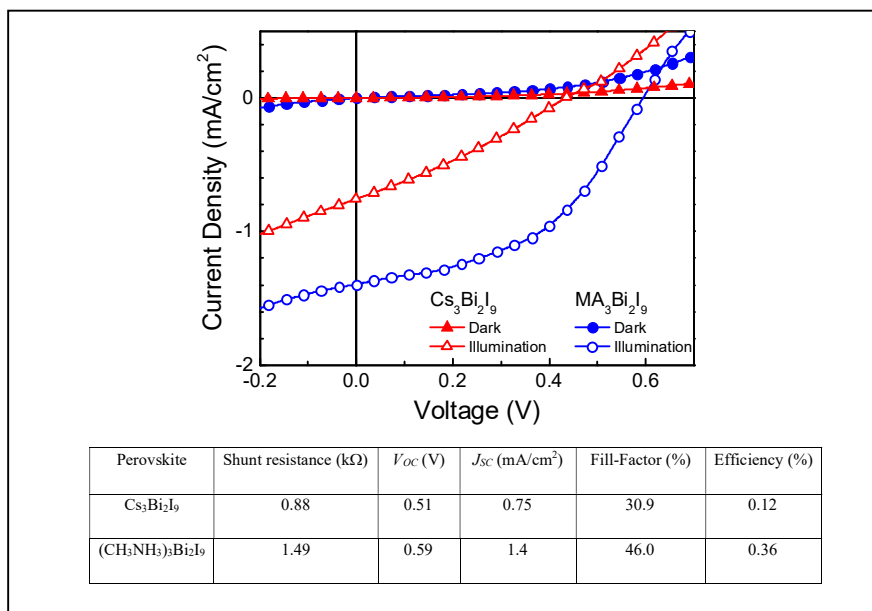


**Figure 3.10.** Current-voltage characteristics of Cs<sub>3</sub>Bi<sub>2</sub>I<sub>9</sub> and MA<sub>3</sub>Bi<sub>2</sub>I<sub>9</sub> based devices under dark and 1 sun illumination conditions. The lower part shows a comparison of photovoltaic parameters between these two perovskites.

### 3.4. Conclusions

In conclusion, we have established the presence of defect-states in Cs<sub>3</sub>Bi<sub>2</sub>I<sub>9</sub> perovskites through STS and inferred them to be primarily responsible for their poor photovoltaic performance. We have formed and characterized bismuth-based ternary halide perovskites with precursors having different stoichiometries. At the *A*-site, we have considered cesium and methylammonium ions in forming the perovskites. When we focused on the band-edges of Cs<sub>3</sub>Bi<sub>2</sub>I<sub>9</sub> through STS, we observed that the materials were *p*-type due to the acceptor nature of the defects above the VB-band. The STS studies further showed that the band gap of the cesium-based perovskites decreased from 2.01 to 1.81 eV when they were formed with BiI<sub>3</sub>-rich precursors. The decrease in the gap was due to the formation of mid-gap defects affecting the VB band and also perturbing the Bi(*p*) orbitals and thereby the CB edge. With methylammonium at the *A*-

sites, defect-formation was not facile due to the defect-tolerant nature of MA-based perovskites. A comparison of photovoltaic performances in devices based on  $\text{Cs}_3\text{Bi}_2\text{I}_9$  and  $\text{MA}_3\text{Bi}_2\text{I}_9$  supported the formation of mid-gap defects in the former material.

### 3.5. References

- [1] Q. X. Fu, X. L. Tang, B. Huang, T. Hu, L. C. Tan, L. Chen, and Y. W. Chen, *Adv. Sci.* **5**, 1700387 (2018).
- [2] A. M. Ganose, C. N. Savory, and D. O. Scanlon, *Chem. Commun.* **53**, 20 (2016).
- [3] Z. Li, T. R. Klein, D. H. Kim, M. J. Yang, J. J. Berry, M. van Hest, and K. Zhu, *Nat. Rev. Mater.* **3**, 18017 (2018).
- [4] J. Lei, F. Gao, H. X. Wang, J. Li, J. X. Jiang, X. Wu, R. R. Gao, Z. Yang, and S. Z. Liu, *Sol. Energy Mater. Sol. Cells* **187**, 1 (2018).
- [5] M. Saliba, T. Matsui, J. Y. Seo, K. Domanski, J. P. Correa-Baena, M. K. Nazeeruddin, S. M. Zakeeruddin, W. Tress, A. Abate, A. Hagfeldt, and M. Gratzel, *Energy Environ. Sci.* **9**, 1989 (2016).
- [6] L. G. Li, F. Zhang, Y. Y. Hao, Q. J. Sun, Z. F. Li, H. Wang, Y. X. Cui, and F. R. Zhu, *J. Mater. Chem. C* **5**, 2360 (2017).
- [7] G. R. Berdiyrov, M. E. Madjet, and F. El-Mellouhi, *Sol. Energy Mater. Sol. Cells* **170**, 8 (2017).
- [8] L. K. Ono, E. J. Juarez-Perez, and Y. B. Qi, *ACS Applied Materials & Interfaces* **9**, 30197 (2017).
- [9] H. Y. Zhang, C. Zhao, D. Li, H. Guo, F. Y. Liao, W. Cao, X. B. Niu, and Y. Y. Zhao, *J. Mater. Chem. A* **7**, 2804 (2019).
- [10] B. Yang, M. Wang, X. F. Hu, T. W. Zhou, and Z. G. Zang, *Nano Energy* **57**, 718 (2019).
- [11] K. X. Steirer, P. Schulz, G. Teeter, V. Stevanovic, M. Yang, K. Zhu, and J. J. Berry, *ACS Energy Lett.* **1**, 360 (2016).

- 
- [12] Z. N. Bi, X. Rodriguez-Martinez, C. Aranda, E. Pascual-San-Jose, A. R. Goni, M. Campoy-Quiles, and A. Guerrero, *J. Mater. Chem. A* **6**, 19085 (2018).
- [13] V. D’Innocenzo, G. Grancini, M. J. P. Alcocer, A. R. S. Kandada, S. D. Stranks, M. M. Lee, H. J. Snaith, and A. Petrozza, *Nat. Commun.* **5**, 3586 (2014).
- [14] G. C. Xing, N. Mathews, S. Y. Sun, S. S. Lim, Y. M. Lam, M. Gratzel, S. Mhaisalkar, and T. C. Sum, *Science* **342**, 344 (2013).
- [15] P. Azarhoosh, S. McKechnie, J. M. Frost, A. Walsh, and M. van Schilfgaarde, *APL Mater.* **4**, 091501 (2016).
- [16] B. W. Park, B. Philippe, X. L. Zhang, H. Rensmo, G. Boschloo, and E. M. J. Johansson, *Adv. Mater.* **27**, 6806 (2015).
- [17] C. N. Savory, A. Walsh, and D. O. Scanlon, *ACS Energy Lett.* **1**, 949 (2016).
- [18] M. Pantaler, K. T. Cho, V. I. E. Queloz, I. G. Benito, C. Fettkenhauer, I. Anusca, M. K. Nazeeruddin, D. C. Lupascu, and G. Grancini, *ACS Energy Lett.* **3**, 1781 (2018).
- [19] F. Bai, Y. H. Hu, Y. Q. Hu, T. Qiu, X. L. Miao, and S. F. Zhang, *Sol. Energy Mater. Sol. Cells* **184**, 15 (2018).
- [20] X. Q. Zhang, G. Wu, S. D. Yang, W. F. Fu, Z. Q. Zhang, C. Chen, W. Q. Liu, J. L. Yan, W. T. Yang, and H. Z. Chen, *Small* **13**, 1700611 (2017).
- [21] M. H. Du, *J. Mater. Chem. A* **2**, 9091 (2014).
- [22] T. Singh, A. Kulkarni, M. Ikegami, and T. Miyasaka, *ACS Applied Materials & Interfaces* **8**, 14542 (2016).
- [23] M. Abulikemu, S. Ould-Chikh, X. H. Miao, E. Alarousu, B. Murali, G. O. N. Ndjawa, J. Barbe, A. El Labban, A. Amassiana, and S. Del Gobbo, *J. Mater. Chem. A* **4**, 12504 (2016).
- [24] B. Ghosh, S. Chakraborty, H. Wei, C. Guet, S. Z. Li, S. Mhaisalkar, and N. Mathews, *J. Phys. Chem. C* **121**, 17062 (2017).
- [25] C. S. Ni, G. Hedley, J. Payne, V. Svrcek, C. McDonald, L. K. Jagadamma, P. Edwards, R. Martin, G. Jain, D. Carolan, D. Mariotti, P. Maguire, I. Samuel, and J. Irvine, *Nat. Commun.* **8**, 170 (2017).

- [26] H. Hu, B. H. Dong, and W. Zhang, *J. Mater. Chem. A* **5**, 11436 (2017).
- [27] C. M. Sutter-Fella, D. W. Miller, Q. P. Ngo, E. T. Roe, F. M. Toma, I. D. Sharp, M. C. Lonergan, and A. Javey, *ACS Energy Lett.* **2**, 709 (2017).
- [28] B. Ghosh, B. Wu, H. K. Mulmudi, C. Guet, K. Weber, T. C. Sum, S. G. Mhaisalkar, and N. Mathews, *ACS Appl. Mater. Interfaces* **10**, 35000 (2018).
- [29] Y. L. Wang, S. W. Liu, Q. Zeng, R. Wang, W. J. Qin, H. Q. Cao, L. Y. Yang, L. Li, S. G. Yin, and F. L. Zhang, *Sol. Energy Mater. Sol. Cells* **188**, 140 (2018).
- [30] K. H. Kim, C. Takahashi, Y. Abe, and M. Kawamura, *Optik* **125**, 2899 (2014).
- [31] X. Fang, J. H. Li, D. X. Zhao, D. Z. Shen, B. H. Li, and X. H. Wang, *J. Phys. Chem. C* **113**, 21208 (2009).
- [32] A. J. Lehner, D. H. Fabini, H. A. Evans, C. A. Hebert, S. R. Smock, J. Hu, H. B. Wang, M. L. Chabinyk, and R. Seshadri, *Chem. Mat.* **27**, 7137 (2015).
- [33] M. B. Johansson, H. M. Zhu, and E. M. J. Johansson, *J. Phys. Chem. Lett.* **7**, 3467 (2016).
- [34] C. F. Lan, J. T. Luo, S. Zhao, C. Zhang, W. G. Liu, S. Z. Hayase, and T. L. Ma, *J. Alloy. Compd.* **701**, 834 (2017).
- [35] D. Phuyal, S. M. Jain, B. Philippe, M. B. Johansson, M. Pazoki, J. Kullgren, K. O. Kvashnina, M. Klintonberg, E. M. J. Johansson, S. M. Butorin, O. Karis, and H. Rensmo, *J. Mater. Chem. A* **6**, 9498 (2018).
- [36] J. Kim, S.-H. Lee, J. H. Lee, and K.-H. Hong, *Phys. Chem. Chem. Phys.* **5**, 1312 (2014).
- [37] W.-J. Yin, T. Shi, and Y. Yan, *Appl. Phys. Lett.* **104**, 063903 (2014).
- [38] G. Paul, S. Chatterjee, H. Bhunia, and A. J. Pal, *J. Phys. Chem. C* **122**, 20194 (2018).
- [39] G. Giorgi, J. I. Fujisawa, H. Segawa, and K. Yamashita, *J. Phys. Chem. Lett.* **4**, 4213 (2013).
- [40] Z. Zhang, X. W. Li, X. H. Xia, Z. Wang, Z. B. Huang, B. L. Lei, and Y. Gao, *J. Phys. Chem. Lett.* **8**, 4300 (2017).

This page is intentionally left blank.



# Chapter 4

## Double Perovskites: Introducing Cationic Order

*Despite environmental stability and toxic-free merits, the performance of double perovskite solar cells ( $\text{Cs}_2\text{AgBiBr}_6$  to be specific) has not excelled due to their large indirect bandgap, low absorption of the solar spectrum, and more importantly hurdles in carrier transport processes. A large number of intrinsic defects and self-trapped excitons (STE) appear in the double perovskite due to a disordered arrangement of Ag/Bi octahedra in the perovskite lattice. In this work, we have investigated the role of cation-ordering in  $\text{Cs}_2\text{AgBiBr}_6$  through the use of phenethylammonium bromide (PEABr) in the precursor towards suppression of STEs and deep-level defect-states, such as antisite defects of  $\text{Ag}^+/\text{Bi}^{3+}$ , for an improved carrier conduction process. While the cation ordering has been verified from X-ray diffraction studies and Raman spectroscopy, a reduction in the defect density and an inhibition of STE-formation have been witnessed from optical spectroscopy. The transport gap, as obtained from scanning tunneling spectroscopy (STS) and density of states (DOS) spectra thereof, has been found to increase suggesting defect-states become suppressed. The effect of cation-ordering towards an efficient carrier transport in the ordered lattice of  $\text{Cs}_2\text{AgBiBr}_6$  has been manifested in Kelvin probe force microscopy and conductive atomic force microscopy. Finally, a fair improvement in photovoltaic parameters was observed in devices based on the ordered double perovskite.*

## 4.1. Introduction

Lead-free double perovskites have recently emerged as a potential alternative to the hybrid halide perovskite ( $\text{CH}_3\text{NH}_3\text{PbI}_3$ ) due to their environmental stability and toxic-free merits [1-4]. This new class of double perovskites (elpasolite) is designed through a combinatorial approach by substituting two bivalent lead ions ( $\text{Pb}^{2+}$ ) with a monovalent and a trivalent cation to balance the overall charge distribution in the compound [5-7]. These double perovskites possess a face-centered cubic rock-salt crystal structure ( $\text{Fm}\bar{3}\text{m}$  space group) and corner-sharing octahedra of the two cations in alternate. This group of materials has received widespread attention as promising candidates for optoelectronic applications due to a low effective mass of electrons and holes, a decent carrier lifetime, micro-sized grains, a high crystallinity, and overall environmental stability [2,4,8-10].

In the class of lead-free double perovskites, silver-bismuth combination ( $\text{Cs}_2\text{AgBiBr}_6$ ) with an alternate  $[\text{AgBr}_6]^{5-}$  and  $[\text{BiBr}_6]^{3-}$  octahedra have received initial importance for solar cell applications. Photovoltaic performance of  $\text{Cs}_2\text{AgBiBr}_6$  has however not surpassed (compared to  $\text{CH}_3\text{NH}_3\text{PbI}_3$ ) primarily due to their large indirect bandgap and thereby a reduced absorption of visible light and more importantly a correlated effect of low carrier mobility and an inefficient carrier transport through the perovskite lattice [11,12]. Although the bandgap can be lowered through materials engineering upon the introduction of suitable dopants [13,14], a remedy to overcome the hurdles in the charge transport process remained a roadblock.

In general, cation ordering in double perovskites plays an important role in the emergence of novel electronic and magnetic properties [15-17]. In an ideally-ordered  $\text{Cs}_2\text{AgBiBr}_6$  double perovskite structure, each  $[\text{AgBr}_6]^{5-}$  octahedron should be surrounded by six corner-sharing  $[\text{BiBr}_6]^{3-}$  octahedra and vice versa [2,18]. Due to the solution-based synthesis route of the double perovskite from cation-precursors, namely  $\text{AgBr}$  and  $\text{BiBr}_3$ , the formation of a disordered phase with a random arrangement of  $[\text{AgBr}_6]^{5-}$  and  $[\text{BiBr}_6]^{3-}$  octahedra is inevitable and energetically favorable as well [19,20]. In a disordered lattice,  $[\text{BiBr}_6]^{3-}$  and  $[\text{AgBr}_6]^{5-}$  octahedra are located randomly

enhancing the electrostatic repulsion between two neighboring octahedra locally and thereby distorting the crystalline structure. Under such a situation, due to a strong electron-phonon interaction, the photogenerated charge carriers would be self-trapped at the distorted states arising out from a large Jahn-Teller (JT) like distortion of the disordered octahedra [21]. Hence, self-trapped excitons (STEs) are formed leading to poor charge transport in the double perovskite lattice [20,22]. In addition, a disorder in cation-occupancies leads to silver at bismuth ( $\text{Ag}_{\text{Bi}}$ ) antisite-defects with deep transition levels inside the bandgap providing recombination pathways for photogenerated carriers [1,23].

Because of this, achieving a cation-ordering in the lattice of double perovskites would be a promising pathway to suppress the formation of STEs and mid-gap defect-states. Through first principle calculations, Yang et al. proposed that a very high temperature of synthesis can induce a better ordering in the lattice [19]; however, such a strategy is almost improbable to be applied in practice. In double perovskite oxides, the incorporation of different ligands/polymers as site-selective binders has been followed in achieving spontaneous cationic ordering in their thin films (polymer-assisted deposition, PAD) [24,25]. A similar strategy has been used in double perovskite single crystals ( $\text{Cs}_2\text{AgBiBr}_6$ ) towards control over in-situ cationic ordering through the incorporation of phenethylammonium bromide (PEABr) and considered previously for applications in X-Ray detectors [20]; with the addition of PEABr in the precursor, selective coordination between functionalized phenyl and ammonium ions with the two inorganic cations ( $\text{Ag}^+$  and  $\text{Bi}^{3+}$ , respectively) promotes a better ordering in the lattice [20].

With this background information, we have introduced the process of cationic ordering in solar cells based on the double perovskite. We envisaged that an improved cation-ordering in the double perovskite, upon suppression of STE formation and passivation of defect-states, would facilitate charge transports and thereby would improve photovoltaic parameters in devices based on the perovskite. While the effect of cation-ordering toward suppressing the formation of STEs, has been investigated by

evaluating the Huang-Rhys factor (S) as obtained from a combination of electronic absorption spectroscopy, photoluminescence spectroscopy, and Raman spectroscopy, the transport gap derived from scanning tunneling spectroscopy (STS) and density of states (DOS) spectra evidenced that the ordering process suppressed the formation of deep-level defects. Finally, a large improvement in the photovoltaic parameters of devices was found in the ordered Cs<sub>2</sub>AgBiBr<sub>6</sub> double perovskites.

## 4.2. Experimental

### 4.2.1. Materials

Cesium bromide (CsBr, 99.9%), silver bromide (AgBr, 99.9%), bismuth bromide (BiBr<sub>3</sub>, 99.9%), hydrobromic acid (HBr, 48 wt%) in water, hydrofluoric acid (HF, 48 wt%) in water, dimethyl sulfoxide (DMSO, 99.9%), 1-phenylethylamine (PEA), anhydrous N, N-dimethylformamide (DMF, 99.8%), 2-propanol, chlorobenzene (CB, 99%), poly(3,4-ethylenedioxythiophene) polystyrene sulfonate (PEDOT: PSS), and bathocuproine (BCP, 96%) were purchased from Sigma Aldrich Chemical Co. Phenyl-C61-butyric acid methyl ester (PCBM, 99%) was procured from M/s SES Research, Houston, TX. Except for HBr, HF, PEA, and PEDOT: PSS, the rest of the compounds were stored in a nitrogen-filled glovebox with both oxygen and moisture levels below 0.1 ppm.

### 4.2.2. Synthesis of Pristine Cs<sub>2</sub>AgBiBr<sub>6</sub> Crystallites

Crystalline powder of Cs<sub>2</sub>AgBiBr<sub>6</sub> was prepared by following a standard route as proposed by Igbari et al [26]. In this process, 213 mg of CsBr, 94 mg of AgBr, and 225 mg of BiBr<sub>3</sub> (2:1:1) were first dissolved in 20 mL of HBr. The solution was stirred in a fume-hood at 125 °C for almost three hours until half of the solvent evaporated. The as-prepared solution was then cooled overnight to room temperature in a dark environment. Orange-colored crystalline powders of Cs<sub>2</sub>AgBiBr<sub>6</sub> were finally obtained by decanting the excess solution followed by drying in an oven at 50 °C for 24 h.

### **4.2.3. Synthesis of Ordered Cs<sub>2</sub>AgBiBr<sub>6</sub> Crystallites**

Following a reported route [27], PEABr powder was prepared and added to the HBr solution at the desired concentration (2, 4, 6, 8, and 10 mol%) and the above-mentioned synthesis route was followed.

### **4.2.4. Formation of Cs<sub>2</sub>AgBiBr<sub>6</sub> Thin Films**

The Cs<sub>2</sub>AgBiBr<sub>6</sub> crystalline powder was dissolved in a stoichiometric (1:1) mixture of DMF and DMSO at 70 °C to form a light-yellow precursor solution (0.8 M) which was spun on properly cleaned substrates inside a glove box at 1000 rpm for 10 s followed by ramping to 3500 rpm for 30 s. Anti-solvent treatment was performed by adding 0.5 mL of chlorobenzene to the film at the twentieth second of the spin-coating process. After that, the film was rapidly moved to the low-pressure antechamber of the glove box followed by pumping for aging. Finally, the films were annealed for a while (5 min) at an optimized temperature of 280 °C inside the glove box. For STS studies, ultra-thin films were cast on highly-doped Si(111) substrates (arsenic-doped, *n*-type) having a resistivity of 3-10 mΩ·cm at a higher rpm (4500 rpm for 30 s); the silicon substrates were treated with HF before use through a standard protocol in removing the oxide layer [28].

### **4.2.5. Fabrication and Characterization of Devices**

Heterojunction solar cells were fabricated on indium tin oxide (ITO) coated glass substrates which were first cleaned following a usual procedure and treated with UV-ozone (UVO) for 20 min. After that, a layer of PEDOT: PSS was spun at 3000 rpm for 60 s followed by annealing at 150 °C to form a hole-transport layer (HTL). The substrates were then transferred to the glove box. A layer of the double perovskite was then cast through the previously-mentioned film-deposition process. As an electron-transport layer (ETL), PCBM was spun at 2500 rpm for 30 s from a stock solution in chlorobenzene (20 mg/mL) and annealed at 100 °C. Finally, an ultrathin film of BCP

dissolved in IPA solution (0.5 mg/mL) was cast at 4000 rpm for 30 s as a buffer layer, which was annealed at 100 °C. The process of device fabrication was completed by depositing 100 nm thick aluminum (Al) strips (orthogonal to the ITO strips) as the top electrode through thermal evaporation in a vacuum chamber ( $10^{-6}$  mbar) fitted to the glove box. An active area of the cells was 10 mm<sup>2</sup>. Current-voltage (*I-V*) characteristics of the sandwiched heterojunction devices were recorded with a Keithley 2636A electrometer under dark and 1 sun illumination conditions. All the measurements were carried out in the inert environment of the glove box. Contacts were made with pressure-loaded gold probes with the respective electrodes. A 300 W solar simulator (Newport-Oriel Sol3A) coupled with an AM1.5 filter was used as a source of illumination.

## 4.3. Results and Discussion

### 4.3.1. Introducing Cation-Ordering in Cs<sub>2</sub>AgBiBr<sub>6</sub>

Poor solubility of the silver salt in polar aprotic solutions such as DMF or DMSO has been a major concern to achieve high-quality and phase-pure Cs<sub>2</sub>AgBiBr<sub>6</sub> perovskite thin films [18,29]. Gao and coworkers have recently developed a new strategy to overcome this drawback; Cs<sub>2</sub>AgBiBr<sub>6</sub> was first formed in HBr solution followed by spin-casting of the compound in a DMF: DMSO solution [30]. Igbari et al. demonstrated the advantages of this method over vacuum-deposition in forming phase-pure and near-stoichiometric Cs<sub>2</sub>AgBiBr<sub>6</sub> thin films [26]. However, during the synthesis of Cs<sub>2</sub>AgBiBr<sub>6</sub> following the above-mentioned methods, the formation of disordered arrangements of silver and bismuth octahedra in the perovskite compound and silver at bismuth (Ag<sub>Bi</sub>) antisite-defects were common and energetically favorable even under an excess HBr-rich growth condition [31]. Such disordered arrangements of Ag<sup>+</sup> and Bi<sup>3+</sup> in the perovskite compound prompt a large JT-kind distortion in the lattice leading to strong electron-phonon interaction and simultaneous self-trapping of excitons in the distorted Cs<sub>2</sub>AgBiBr<sub>6</sub> [20,21,32]. Under this circumstance, both generation and

transport of charge carriers get impeded resulting in a poor short-circuit current density in solar cells.

In this direction, the incorporation of  $\text{PEA}^+$  as ligands during the synthesis can be an effective strategy to promote cation-occupancy-ordering in the system. According to previous reports, the ligand activity of  $\text{PEA}^+$  can be used to bind  $\text{Ag}^+/\text{Bi}^{3+}$  in a regular arrangement as phenyl and ammonium groups of  $\text{PEA}^+$  possess the ability to make selective coordination with  $\text{Bi}^{3+}$  and  $\text{Ag}^+$ , respectively [20]. To state in detail, the  $\pi$ -electron clouds of the phenyl group present in  $\text{PEA}^+$  prefer to form bonds with  $\sigma^*$  orbital of bismuth halide due to a push-electron-induced mechanism; on the other hand, the ammonium group of  $\text{PEA}^+$  bonds with  $\text{Ag}^+$  through a non-covalent intermolecular force in forming a  $\text{PEA-AgBr}_2$  complex [33]. Such a preferred linkage occurs since the distance between the phenyl and ammonium groups is about 6.4 Å in  $\text{PEA}^+$ , which is similar to the distance between  $\text{Ag}^+$  and  $\text{Bi}^{3+}$  ions in a  $\text{Cs}_2\text{AgBiBr}_6$  lattice (6.5 Å) [20]. Consequently,  $\text{Ag}^+$  and  $\text{Bi}^{3+}$  in a lattice would be arranged regularly through the selective coordination ability of  $\text{PEA}^+$  ligand to finally form an ordered double perovskite phase. However, after the formation of ordered  $\text{Cs}_2\text{AgBiBr}_6$ , the ligands would still be attached to the compound with coordinate bonds [34,35]. Upon dissolution of the ordered double perovskite crystals in DMF/DMSO mixed solvent, as a step for film-casting, these  $\text{PEA}^+$  ligands would remain in the solution. During the re-crystallization process, the ligands would further bind the  $\text{Ag}^+$  and  $\text{Bi}^{3+}$  ions to promote order. Finally, these  $\text{PEA}^+$  ligands would desorb upon annealing at a high temperature (280 °C) leaving an ordered arrangement of Ag/Bi octahedra in the perovskite thin films. It may be stated that the quantity of  $\text{PEA}^+$ -ligands that can be harvested from the surface may not match the actual feed ratio used during the growth of the crystals. This interesting scientific issue can further be addressed from the modeling of reaction kinetics which is beyond the scope of this work.

### 4.3.2. Structural Characterization to Study Cation-Ordering

Evaluation of XRD patterns is a straightforward and well-documented approach to quantitatively estimating the cation ordering in a double perovskite [36]. According to the previous report,  $\text{Cs}_2\text{AgBiBr}_6$  belongs to  $\text{Fm}\bar{3}\text{m}$  space group (FCC) [2]; the crystal structure demonstrates that both (111) and (022) planes do not follow the conventional extinction law. However, in the primary cubic structure, the (111) plane would be extinctive with respect to the extinction law [36]. Under the circumstances, in case of a complete disorder of  $\text{Bi}^{3+}$  and  $\text{Ag}^+$ , the (111) plane can be considered as an extinctive one. Hence, evaluation of two super-lattice reflections with adjacent normal lattice reflection viz the intensities of (111) and (022) planes is a straightforward method to study the extent of ordering in the double perovskite; a higher ratio between the intensities of (111) and (022) planes,  $(I_{111}/I_{022})$  infers a better ordering of the Ag/Bi octahedra and presence of fewer antisite defects as well [36]. In Figure 4.1a, we have presented the evolution of XRD patterns with an increasing concentration of  $\text{PEA}^+$ . As shown in Figure 4.1b, the intensity of (111) plane relative to the one of (022) could be seen to increase with an increase of  $\text{PEA}^+$ -concentration supporting an improvement of ordering in silver and bismuth occupancies. Moreover, the full width at half maximum (FWHM) of the pattern referring to the (111) plane could be found to decrease upon an increase in the  $\text{PEA}^+$  concentration; such behavior implies an enhanced crystallinity and a lesser density  $\text{Ag}_{\text{Bi}}$  defects. The observed change in the XRD patterns of perovskite thin films is in consistent with the report on single crystals as well [20].

It is necessary to mention that doping of  $\text{PEA}^+$  in the lattice can be ruled out from XRD studies. Although it stays at the surface of the crystallites through coordination bonds, its presence in the final thin films is unlikely due to the high annealing temperature. In addition, the formation of  $\text{PEA}^+$ -based lower-dimensional systems at the grain boundaries has also been ruled out [37]. In the XRD patterns of  $\text{Cs}_2\text{AgBiBr}_6$  (Figure 4.1a), we did not observe any characteristic peaks of  $\text{PEA}_4\text{AgBiBr}_8$  evidencing the absence of  $\text{PEA}^+$  in the double perovskite [20].



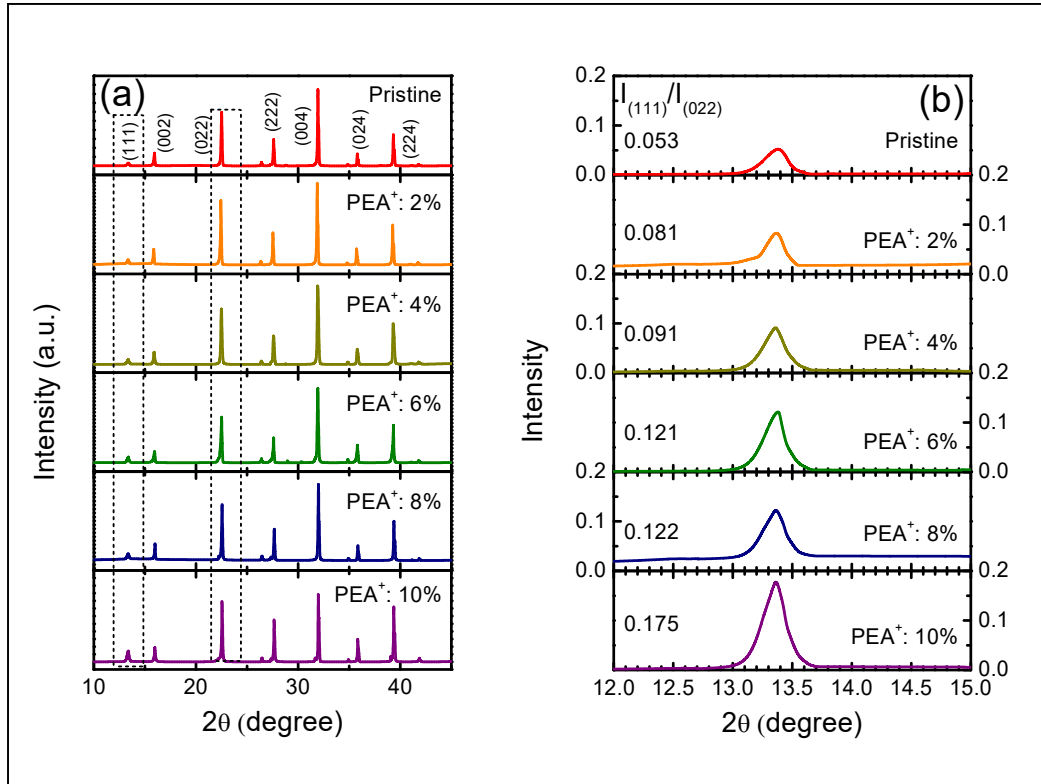


**Figure 4.1.** (a) Evolution of XRD patterns of  $\text{Cs}_2\text{AgBiBr}_6$  upon addition of  $\text{PEA}^+$ . (b) Peak representing the (111) plane with respect to the intensity of (022) plane.

### 4.3.3. Influence of Cation-Ordering on Raman Modes

We have studied Raman modes of the ordered and disordered  $\text{Cs}_2\text{AgBiBr}_6$  (Figure 4.2a). Along with the investigation of cation ordering, phonon energies can also be calculated from such measurements. The room temperature Raman spectrum of the pristine disordered system was dominated by a peak at  $180\text{ cm}^{-1}$  which is assigned to a longitudinal optical (LO) phonon mode  $A_{1g}$  coupled with the symmetric stretching vibration of Br around a Bi atom. In addition, two less-intense peaks were also observed at  $139\text{ cm}^{-1}$  and  $74\text{ cm}^{-1}$ . The peak at  $139\text{ cm}^{-1}$  is considered as  $E_g$  mode related to the asymmetric stretching vibrations of Br around a Bi atom. On the other hand, the  $T_{2g}$

mode appearing at  $74\text{ cm}^{-1}$  could be correlated to the scissoring motion of Cs around Br atoms [38,39]. Schematic representations of the vibrations have been presented in Figure 4.2b. Although the influence of  $\text{PEA}^+$ -induced ordering was found to be significant for all the Raman modes, based on conventional practice, we have limited our discussion only to the most intense  $A_{1g}$  mode at  $180\text{ cm}^{-1}$  since the energy of the LO phonon was considered for further discussion in a later section.

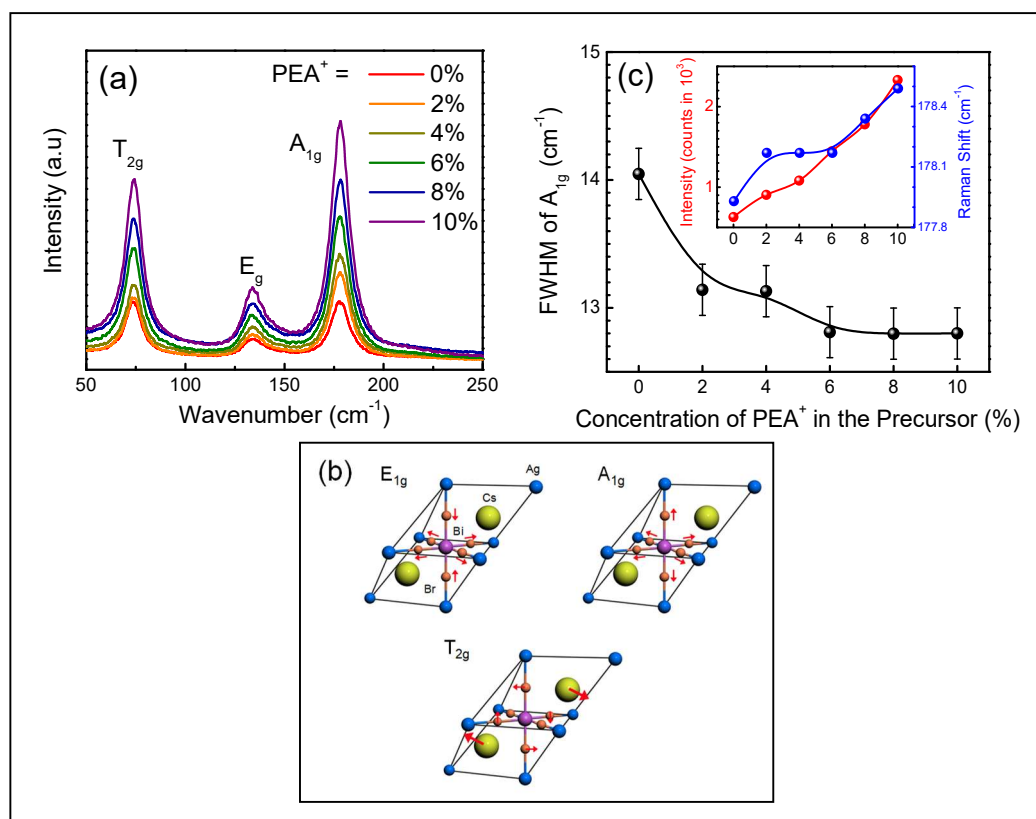


**Figure 4.2.** (a) Raman spectra of  $\text{Cs}_2\text{AgBiBr}_6$  upon addition of different  $\text{PEA}^+$ -content. (b) Schematic representation of the Raman modes. (c) Comparison of FWHM of the  $A_{1g}$  mode as a function of  $\text{PEA}^+$ -concentration; inset shows intensity and Raman shift of the mode.

In Figure 4.2c, the intensity, FWHM, and also energy of the peak as a function of  $\text{PEA}^+$  concentration have been presented. A sharp increase in peak intensity and a

narrowing of the peaks were observed; the figure also shows a little shift of the LO mode towards the higher energy with an increase in the PEA<sup>+</sup>-concentration. Such an observation has also been found in some other quaternary semiconductor systems (kesterites) supporting the inference of increasing order in the cation occupancy [40].

#### 4.3.4. Optical Characteristics

We then proceeded to record optical absorption spectra of the disordered and ordered thin films as a function of PEA<sup>+</sup>-concentration. All the compounds showed a characteristic peak at ~440 nm confirming the formation of the double perovskite (Figure 4.3a) [1,11]. A little blue shift was observed with increasing PEA<sup>+</sup>-concentration that could be correlated to an enhanced cation-ordering in the double perovskite. A similar observation was previously reported in the literature in other semiconductors where the light absorption threshold was significantly higher in an ordered system than that in the disordered one and an increase in the bandgap upon a decrease in the defect density [19,23,41]. The optical bandgap of all the compounds was estimated from their Tauc plots (Inset).

A detailed analysis of STE formation and PEA<sup>+</sup>-induced cation-ordering in the lattice has been carried out from optical characteristics. The broad PL (Figure 4.3b) and a large Stokes shift between optical absorption and PL spectra can be considered characteristic signatures of a disordered double perovskite (Figure 4.3c). The formation of STEs due to the distortion can intensively constrain exciton dissociation and thereby hinder carrier transport [20,21]. In this section, we have studied the effect of increasing Ag<sup>+</sup>/Bi<sup>3+</sup> cation-ordering on reducing the formation of STE states as a function of PEA<sup>+</sup>-concentration. The effect of a strong electron-phonon coupling responsible for a large distortion of the crystalline lattice can be quantitatively measured by the Huang-Rhys factor ( $S$ ) which is derived from the following equation [39,42]

$$\text{Stokes Shift} = (2S - 1)E_{\text{Phonon}} \quad (4.1)$$

where  $E_{\text{Phonon}}$  represents the energy of the most intense A<sub>1g</sub> mode. As presented in Table 4.1, the derived value of  $S$  has been found to decrease with an increasing concentration

of  $\text{PEA}^+$ . Such a lowering of  $S$  can be considered as a direct consequence of the restricted formation of STEs due to a high ordering in cation occupancies [20].

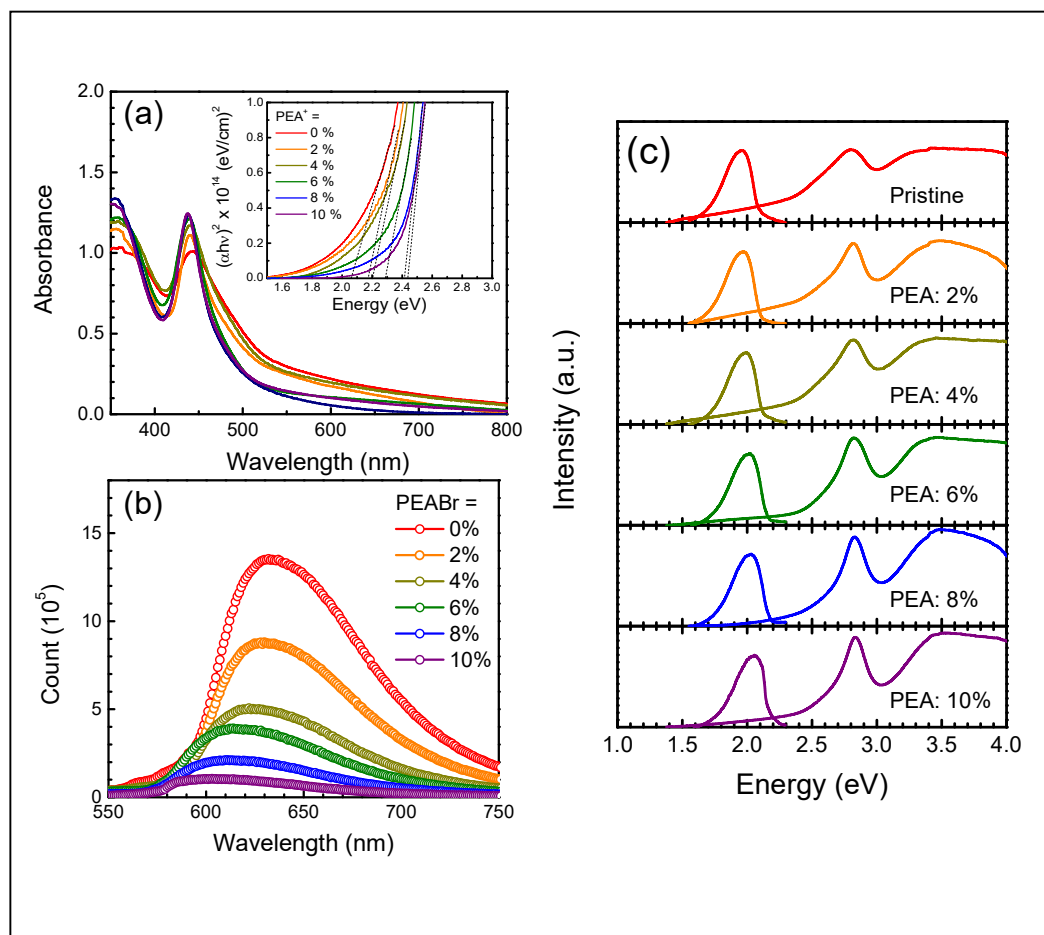


**Figure 4.3.** Evolution of the (a) absorption (b) emission spectra. (c) Derivation of Stokes shift as a function of  $\text{PEA}^+$ -concentration (with normalized PL spectra).

**Table 4.1.** Calculation of Huang-Rhys factor (S) with  $E_{\text{phonon}} = 22.1 \pm 0.1$  meV as a function of PEA<sup>+</sup>-concentration.

PEA <sup>+</sup> -Concentration	Stokes Shift (meV)	Huang-Rhys Factor (S)
0	840 ± 5	19.6 ± 0.2
2	840 ± 5	19.5 ± 0.2
4	830 ± 5	19.3 ± 0.2
6	810 ± 5	18.8 ± 0.2
8	800 ± 5	18.6 ± 0.2
10	770 ± 5	17.9 ± 0.2

### 4.3.5. Band-Edges and Transport Gap through STS

The influence of cation-ordering on the band-edges of Cs<sub>2</sub>AgBiBr<sub>6</sub> and thereby their transport gap has been studied from STM/S characterization. Valence band (VB) and conduction band (CB) edges with respect to Fermi energy ( $E_F$ ) of the double perovskite in its disordered and ordered phases could be located from differential tunnel conductance spectra ( $dI/dV$ ) or density of states (DOS). Since the bias was applied to the tip, the first peak in the positive voltage region of a DOS spectrum closest to 0 V inferred the extraction of electrons and hence the energy of the VB-edge. Likewise, the energy of the first peak in the negative voltage region of a  $dI/dV$  plot implied the injection of electrons into the compound and hence the location of the CB-edge [23]. The characteristic  $dI/dV$  spectra of the disordered and ordered double perovskite compounds are presented in Figure 4.4, along with a few topographies. As STS is recorded in an extremely localized mode,  $dI/dV$  spectra were measured at numerous regions on the surface of each ultra-thin film. From each of these measurements, VB- and CB-edges were located to finally draw a histogram of their energies (insets of each  $dI/dV$  spectra). The edges obtained from the peaks of histograms inferred a *p*-type conductivity in the double perovskite, as their VB could be found to be closer to  $E_F$  (at 0 V) as compared to the relative energy of the CB. Such a *p*-type nature of the double perovskite has been previously predicted by considering the presence of acceptor-like

silver-vacancies ( $V_{Ag}$ ) and silver at bismuth ( $Ag_{Bi}$ ) antisite-defects having low formation energy [23].

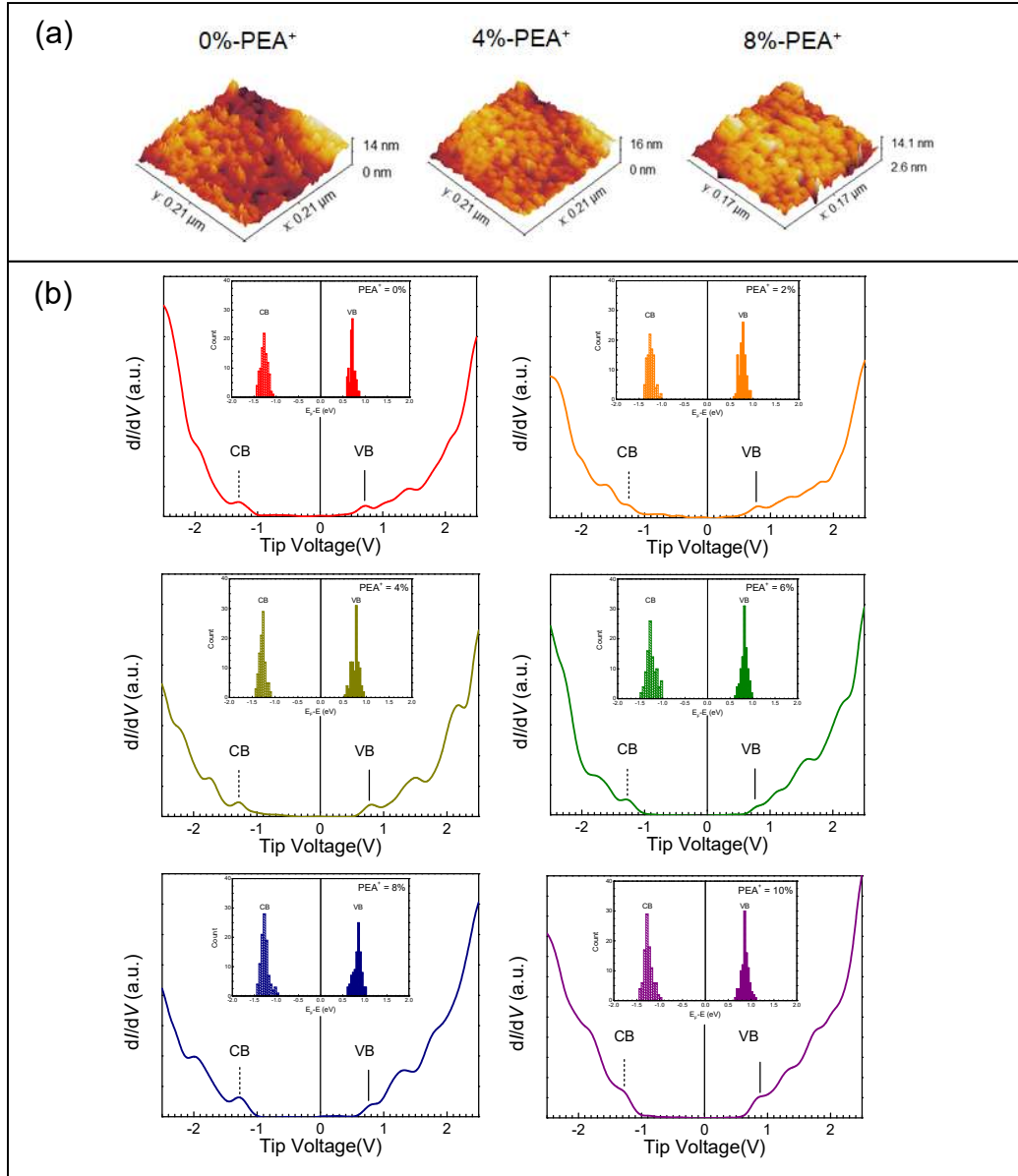


**Figure 4.4.** (a) STM topography of some of the representative sample (upper panel). (b)  $dI/dV$  versus tip voltage plots and histograms of BV- and CB-energies as a function of PEA<sup>+</sup>-concentration mentioned in the legends (lower panel).

Band-edges of the double perovskites can be seen to be heavily influenced by the extent of cation-ordering in the compound. Upon the formation of the  $\text{PEA}^+$ -induced ordered phase, the VB-edge is found to move away from the Fermi energy leading to an increase in the transport gap; the CB-edge remained almost unchanged. A much larger change in the VB as compared to the CB can be explained by considering the involvement of different atomic orbitals in forming the two bands. In  $\text{Cs}_2\text{AgBiBr}_6$  double perovskite, the unoccupied CB is generally formed with Bi(6p) orbitals, whereas the VB is composed of a mixture of Br(4p), Ag(4d), and Bi(6p) orbitals. A  $\text{PEA}^+$ -induced ordering would hence promote hybridization between the Ag(4d) and Bi(6p) orbitals leading to a significant increase in the overlap integral and a rise in the occupied VB state without affecting the CB energy [23,43]. The strong  $p$ -type nature of the disordered double perovskite has reduced with an increase in the  $\text{PEA}^+$ -concentration at the precursor suggesting a lesser density of antisite-defects in the ordered system (Figure 4.5). The transport gap in the ordered double perovskite (like the optical bandgap) hence increased upon the formation of an ordered lattice.

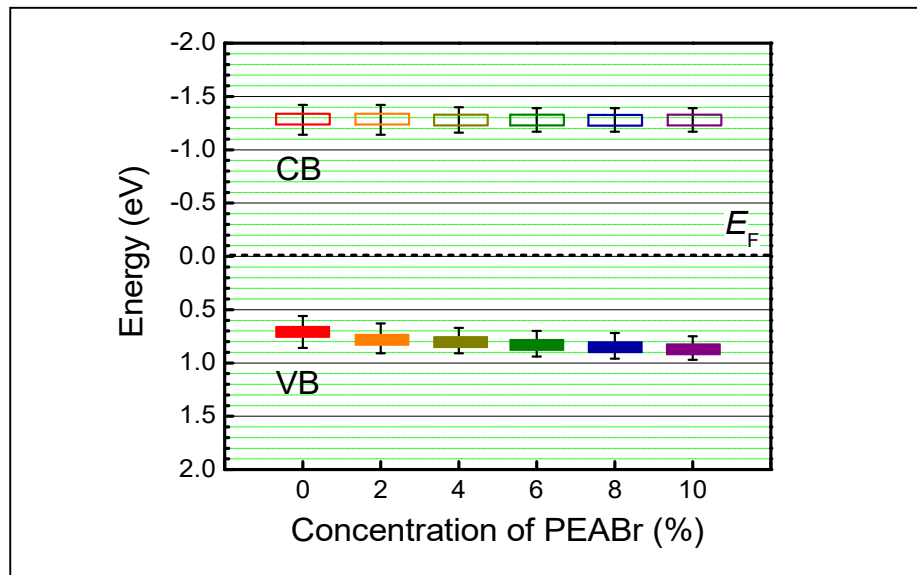


Figure 4.5. Band-edges of  $\text{Cs}_2\text{AgBiBr}_6$  double perovskites as a function of  $\text{PEA}^+$ -concentration.

### 4.3.6. Surface Potential and Local Current Mapping

To study the role of cation-ordering in an efficient carrier transport process, we have further carried out a series of measurements at the local scale. Kelvin probe force microscopy (KPFM) images were recorded to measure the surface potential distribution of the disordered and ordered double perovskite films. As such, surface work function is considered crucial in semiconducting thin films towards optoelectronic applications as it influences electronic transports by tuning Fermi energy across metal-semiconductor interfaces. To study the role of cation-ordering in double perovskite thin-films on the transport process, we have mapped the contact potential difference (CPD) for the disordered and the ordered films in an identical experimental condition. As observed from the CPD map presented in the upper panel of Figure 4.6 along with the topography of the surface, the CPD value increased from  $80 \pm 10$  to  $120 \pm 10$  mV when an ordering was developed in the perovskite. A larger CPD value in an ordered perovskite infers an extraction and transfer of more charge carriers to the surface due to a suppression of STE formation [44]. In other words, fewer defect-states on the path of charge transport to electrodes (in the ordered structure) would result in a better charge accumulation and a larger CPD value [45,46]. Since it may be argued that a change in CPD would lead to a shift of Fermi energy itself, the FWHM can be a better-suited parameter in probing defect-states; a reduction in the FWHM of the surface potential distribution would definitively imply a lesser defect concentration upon cationic-ordering in the double perovskite.

To study the improvement of charge transport in the ordered perovskite lattice with respect to the disordered one, C-AFM measurements were carried out at the local scale. Identical film thicknesses were considered for the measurements, so that a thickness-induced variation in resistance may not prompt a change in the local conductivity. With a bias voltage of 1.0 V being applied, the resulting current was measured and mapped throughout the surface along with the topography (lower panel of Figure 4.6). When the current on the surface was analyzed by drawing their distribution, we observed an increase in the average value of local current due to an improvement in



the conductivity of the ordered system. Here, the improved conductivity occurred due to a lowering of the defect density. The results hence infer an efficient charge transport due to lesser defects-densities in the  $\text{Cs}_2\text{AgBiBr}_6$  double perovskite with the cations being ordered in alternate.

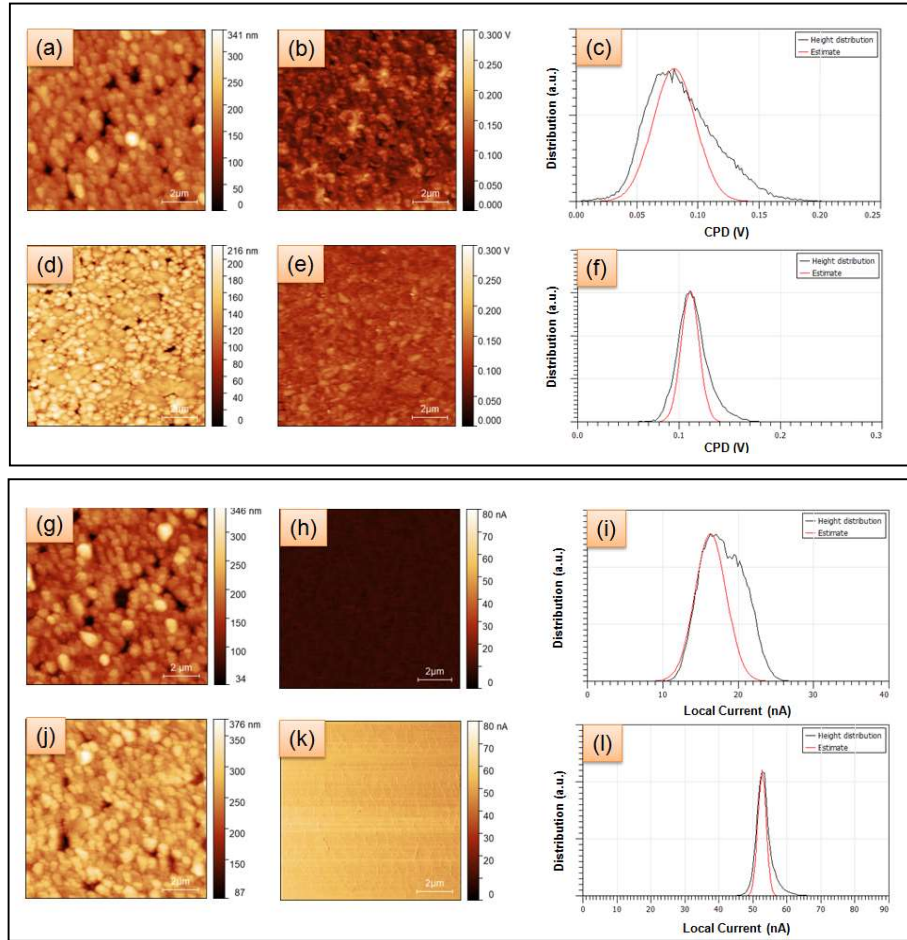


**Figure 4.6.** Upper panel: (a) Topography, (b) CPD map, and (c) statistical distribution of CPD for the disordered  $\text{Cs}_2\text{AgBiBr}_6$  thin films. Such plots for the ordered  $\text{Cs}_2\text{AgBiBr}_6$  films are shown in (d) through (f).

Lower panel: (g) Topography, (h) local current map, and (i) statistical distribution of local current for the disordered  $\text{Cs}_2\text{AgBiBr}_6$  thin films. Such plots for the ordered  $\text{Cs}_2\text{AgBiBr}_6$  films are shown in (j) through (l).

### 4.3.7. Photovoltaic Performance

We finally proceeded to study the influence of cation-ordering on the photovoltaic properties of inverted heterojunction solar cells based on  $\text{Cs}_2\text{AgBiBr}_6$  double perovskite thin films. Sandwiched heterojunction devices were fabricated (ITO/PEDOT: PSS/ $\text{Cs}_2\text{AgBiBr}_6$ /PCBM/BCP/Al) where both the electron transport layer (ETL) and hole transport layer (HTL) formed a type-II band alignment with the active material as observed from STS band diagram. A very thin layer of BCP was formed as a buffer layer to protect the PCBM layer. In Figure 4.7a, we have presented the current-voltage ( $I$ - $V$ ) characteristics of the heterojunction devices;  $\text{Cs}_2\text{AgBiBr}_6$  in the devices were formed with different concentrations of PEABr in the precursor. Photovoltaic parameters obtained under 1 sun illumination have been collated in Table 4.2.

As cation-ordering in the double perovskite facilitates carrier transport processes by suppressing the STE effect and passivating antisite defects, an improvement of photovoltaic parameters was observed as a function of  $\text{PEA}^+$  concentration. An improvement in the open-circuit voltage ( $V_{\text{OC}}$ ) was observed due to an increase in the transport gap and a decrease in defect densities as observed from STS studies. While the increase in  $V_{\text{OC}}$  was from 0.95 to 1.08 V, the increase of short-circuit current density ( $J_{\text{SC}}$ ) was large (from 1.17 to 2.76  $\text{mA}/\text{cm}^2$ ) leading to a substantial augmentation in PCE from 0.43 to 1.78 % with a gradual increase in the PEABr-content at the precursor. A further increment in the PEABr concentration ( $>6$  %) adversely affected the  $J_{\text{SC}}$  owing to a widening in the bandgap (Figure 4.7b). Fill-factor of the cells showed evidence of improvement implying lesser carrier recombination in devices based on ordered  $\text{Cs}_2\text{AgBiBr}_6$  thin films. Hence, as presented in Table 4.2, the PCE of the cells could be optimized with the PEABr-content in the precursor. Although to the best of our knowledge, this is the highest  $V_{\text{OC}}$  achieved so far in a double perovskite solar cell, the PCE value however remained a little low leaving routes for further improvement through proper band-engineering with carrier-transport materials.

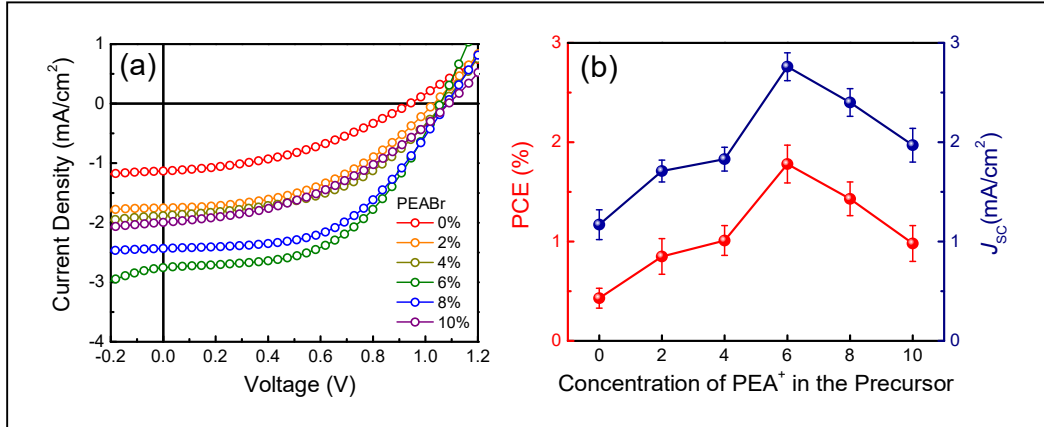


**Figure 4.7.** (a) Current-voltage characteristics of PEDOT:PSS/Cs<sub>2</sub>AgBiBr<sub>6</sub>/PCBM/BCP heterojunctions under 1 sun illumination; Cs<sub>2</sub>AgBiBr<sub>6</sub> was formed with different PEA<sup>+</sup>-concentrations. (b) Variation of  $J_{sc}$  and PCE with the PEA<sup>+</sup>-content in the precursor.

**Table 4.2.** Photovoltaic parameters of PEDOT: PSS/Cs<sub>2</sub>AgBiBr<sub>6</sub>/PCBM/BCP/Al heterojunctions under 1 sun illumination; PEA<sup>+</sup>-concentration in forming Cs<sub>2</sub>AgBiBr<sub>6</sub> is quoted in the first column.

PEA <sup>+</sup> -Concentration (%)	V <sub>oc</sub> (V)	J <sub>sc</sub> (mA/cm <sup>2</sup> )	Fill Factor (%)	PCE (%)
0	0.95 ± 0.02	1.17 ± 0.15	38 ± 2	0.43 ± 0.10
2	1.03 ± 0.02	1.71 ± 0.11	48 ± 3	0.85 ± 0.18
4	1.06 ± 0.02	1.83 ± 0.12	52 ± 3	1.01 ± 0.15
6	1.06 ± 0.02	2.76 ± 0.14	61 ± 3	1.78 ± 0.19
8	1.08 ± 0.02	2.40 ± 0.14	55 ± 2	1.43 ± 0.17
10	1.08 ± 0.02	1.97 ± 0.17	46 ± 3	0.98 ± 0.18

#### 4.4. Conclusions

In conclusion, we have investigated the effect of cation-ordering in Cs<sub>2</sub>AgBiBr<sub>6</sub> double perovskite through the incorporation of phenethylammonium bromide (PEABr) on conduction processes. Ordering of the [AgBr<sub>6</sub>]<sup>5-</sup> and [BiBr<sub>6</sub>]<sup>3-</sup> octahedra in the perovskite occurred due to selective coordination between functionalized phenyl and

ammonium ions in  $\text{PEA}^+$  with the inorganic  $\text{Ag}^+$  and  $\text{Bi}^{3+}$  ions, respectively. An improvement in the ordering of the two cations (silver and bismuth) was evidenced by XRD studies and Raman spectroscopy. Such an ordering has widened the bandgap of the perovskite due to a decrease in  $\text{Ag}_{\text{Bi}}$  antisite defect density and suppression of self-trapped excitons (STEs) appearing out of Jahn-Teller (JT) like distortions in the disordered double perovskite. The suppression of STE formation was confirmed by witnessing shrinkage of the Huang Rhys factor in the ordered lattice. From scanning tunneling spectroscopy studies, a lower concentration of defects has been manifested as a shift of VB away from the Fermi energy. Local surface potential and conductivity measurements through KPFM and C-AFM inferred an efficient carrier transport as well in cationic-ordered compounds. Finally, suppression of STE formation and an efficient carrier transport provided a large improvement in the photovoltaic parameters of devices based on the  $\text{Cs}_2\text{AgBiBr}_6$  double perovskite.

## 4.5. References

- [1] E. Greul, M. L. Petrus, A. Binek, P. Docampo, and T. Bein, *J. Mater. Chem. A* **5**, 19972 (2017).
- [2] E. T. McClure, M. R. Ball, W. Windl, and P. M. Woodward, *Chem. Mater.* **28**, 1348 (2016).
- [3] W. C. Pan, H. D. Wu, J. J. Luo, Z. Z. Deng, C. Ge, C. Chen, X. W. Jiang, W. J. Yin, G. D. Niu, L. J. Zhu, L. X. Yin, Y. Zhou, Q. G. Xie, X. X. Ke, M. L. Sui, and J. Tang, *Nat. Photonics* **11**, 726 (2017).
- [4] A. H. Slavney, T. Hu, A. M. Lindenberg, and H. I. Karunadasa, *J. Am. Chem. Soc.* **138**, 2138 (2016).
- [5] P. V. Kamat, J. Bisquert, and J. Buriak, *ACS Energy Lett.* **2**, 904 (2017).
- [6] Z. W. Xiao, Z. N. Song, and Y. F. Yan, *Adv. Mater.* **31**, 1803792 (2019).
- [7] J. Klarbring, O. Hellman, I. A. Abrikosov, and S. I. Simak, *Phys. Rev. Lett.* **125**, 045701 (2020).
- [8] S. Chatterjee and A. J. Pal, *J. Mater. Chem. A* **6**, 3793 (2018).

- [9] R. M. Nie, R. R. Sumukam, S. H. Reddy, M. Banavoth, and S. I. Seok, *Energy Environ. Sci.* **13**, 2363 (2020).
- [10] G. Volonakis, M. R. Filip, A. A. Haghighirad, N. Sakai, B. Wenger, H. J. Snaith, and F. Giustino, *J. Phys. Chem. Lett.* **7**, 1254 (2016).
- [11] W. Y. Gao, C. X. Ran, J. Xi, B. Jiao, W. W. Zhang, M. C. Wu, X. Hou, and Z. X. Wu, *ChemPhysChem* **19**, 1696 (2018).
- [12] C. N. Savory, A. Walsh, and D. O. Scanlon, *ACS Energy Lett.* **1**, 949 (2016).
- [13] A. Karmakar, M. S. Dodd, S. Agnihotri, E. Ravera, and V. K. Michaelis, *Chem. Mater.* **30**, 8280 (2018).
- [14] Z. H. Zhang, C. C. Wu, D. Wang, G. H. Liu, Q. H. Zhang, W. Luo, X. Qi, X. Guo, Y. Q. Zhang, Y. N. Lao, B. Qu, L. X. Xiao, and Z. J. Chen, *Org. Electron.* **74**, 204 (2019).
- [15] C. Meneghini, S. Ray, F. Liscio, F. Bardelli, S. Mobilio, and D. D. Sarma, *Phys. Rev. Lett.* **103**, 046403 (2009).
- [16] G. M. McNally, A. M. Arévalo-López, F. Guillou, P. Manuel, and J. P. Attfield, *Phys. Rev. Mater.* **4**, 064408 (2020).
- [17] A. Paul and T. Birol, *Phys. Rev. Res.* **2**, 033156 (2020).
- [18] J. Kim, H. Kim, M. Chandran, S. C. Lee, S. H. Im, and K. H. Hong, *APL Mater.* **6**, 084903 (2018).
- [19] Y. Yang, F. Gao, S. W. Gao, and S. H. Wei, *J. Mater. Chem. A* **6**, 14949 (2018).
- [20] W. N. Yuan, G. D. Niu, Y. M. Xian, H. D. Wu, H. M. Wang, H. Yin, P. Liu, W. Z. Li, and J. D. Fan, *Adv. Funct. Mater.* **29**, 1900234 (2019).
- [21] J. J. Luo, X. M. Wang, S. R. Li, J. Liu, Y. M. Guo, G. D. Niu, L. Yao, Y. H. Fu, L. Gao, Q. S. Dong, C. Y. Zhao, M. Y. Leng, F. S. Ma, W. X. Liang, L. D. Wang, S. Y. Jin, J. B. Han, L. J. Zhang, J. Etheridge, J. B. Wang, Y. F. Yan, E. H. Sargent, and J. Tang, *Nature* **563**, 541 (2018).

- 
- [22] G. Longo, S. Mahesh, L. R. V. Buizza, A. D. Wright, A. J. Ramadan, M. Abdi-Jalebi, P. K. Nayak, L. M. Herz, and H. J. Snaith, *ACS Energy Lett.* **5**, 2200 (2020).
- [23] A. Maiti, S. Chatterjee, L. Peedikakkandy, and A. J. Pal, *Sol. RRL* **4**, 2000505 (2020).
- [24] H. L. Wang, J. Gazquez, C. Frontera, M. F. Chisholm, A. Pomar, B. Martinez, and N. Mestres, *NPG Asia Mater.* **11**, 44 (2019).
- [25] H. L. Wang, C. Frontera, J. Herrero-Martin, A. Pomar, P. Roura, B. Martinez, and N. Mestres, *Chem.-Eur. J.* **26**, 9338 (2020).
- [26] F. Igbari, R. Wang, Z. K. Wang, X. J. Ma, Q. Wang, K. L. Wang, Y. Zhang, L. S. Liao, and Y. Yang, *Nano Lett.* **19**, 2066 (2019).
- [27] M. Y. Ban, Y. T. Zou, J. P. H. Rivett, Y. G. Yang, T. H. Thomas, Y. S. Tan, T. Song, X. Y. Gao, D. Credington, F. Deschler, H. Sirringhaus, and B. Q. Sun, *Nat. Commun.* **9**, 3892 (2018).
- [28] S. Bera, J. Kolay, P. Pramanik, A. Bhattacharyya, and R. Mukhopadhyay, *J. Mater. Chem. C* **7**, 9038 (2019).
- [29] A. Kulkarni, A. K. Jena, M. Ikegami, and T. Miyasaka, *Chem. Commun.* **55**, 4031 (2019).
- [30] J. Yang, C. X. Bao, W. H. Ning, B. Wu, F. X. Ji, Z. B. Yan, Y. T. Tao, J. M. Liu, T. C. Sum, S. Bai, J. P. Wang, W. Huang, W. J. Zhang, and F. Gao, *Adv. Opt. Mater.* **7**, 1801732 (2019).
- [31] Z. W. Xiao, W. W. Meng, and Y. F. Yan, *ChemSusChem* **9**, 2628 (2016).
- [32] R. Kentsch, M. Scholz, J. Horn, D. Schlettwein, K. Oum, and T. Lenzer, *J. Phys. Chem. C* **122**, 25940 (2018).
- [33] W. Clegg, M. R. J. Elsegood, R. J. Errington, G. A. Fisher, and N. C. Norman, *J. Mater. Chem.* **4**, 891 (1994).
- [34] A. Heuer-Jungemann, N. Feliu, I. Bakaimi, M. Hamaly, A. Alkilany, I. Chakraborty, A. Masood, M. F. Casula, A. Kostopoulou, E. Oh, K. Susumu, M.

- H. Stewart, I. L. Medintz, E. Stratakis, W. J. Parak, and A. G. Kanaras, *Chem. Rev.* **119**, 4819 (2019).
- [35] T. Wang, Y. P. Fu, L. R. Jin, S. B. Deng, D. X. Pan, L. Dong, S. Jin, and L. B. Huang, *J. Am. Chem. Soc.* **142**, 16254 (2020).
- [36] T. W. Lim, S. D. Kim, K. D. Sung, Y. M. Rhyim, H. Jeon, J. Yun, K. H. Kim, K. M. Song, S. Lee, S. Y. Chung, M. Choi, and S. Y. Choi, *Sci. Rep.* **6**, 19746 (2016).
- [37] D. Lee, J. S. Yun, J. Kim, A. M. Soufiani, S. Chen, Y. Cho, X. F. Deng, J. Seidel, S. J. Huang, and A. W. Y. Ho-Baillie, *ACS Energy Lett.* **3**, 647 (2018).
- [38] P. Pistor, M. Meyns, M. Guc, H. C. Wang, M. A. L. Marques, X. Alcobe, A. Cabot, and V. Izquierdo-Roca, *Scr. Mater.* **184**, 24 (2020).
- [39] S. J. Zelewski, J. M. Urban, A. Surrente, D. K. Maude, A. Kuc, L. Schade, R. D. Johnson, M. Dollmann, P. K. Nayak, H. J. Snaith, R. Kudrawiec, R. J. Nicholas, P. Plochocka, and M. Baranowski, *J. Mater. Chem. C* **7**, 8350 (2019).
- [40] K. Rudisch, A. Davydova, C. Platzer-Bjorkman, and J. Scragg, *J. Appl. Phys.* **123**, 161558 (2018).
- [41] F. Gao, Y. Zhao, and J. B. You, *Adv. Energy Mater.* **10**, 1902650 (2020).
- [42] M. de Jong, L. Seijo, A. Meijerink, and F. T. Rabouw, *Phys. Chem. Chem. Phys.* **17**, 16959 (2015).
- [43] K. Z. Du, W. W. Meng, X. M. Wang, Y. F. Yan, and D. B. Mitzi, *Angew. Chem.-Int. Edit.* **56**, 8158 (2017).
- [44] X. N. Qi, F. R. Tan, Y. Y. Gao, T. L. Wu, R. Liu, C. Dong, G. T. Yue, S. J. Li, and L. S. Zhang, *Appl. Phys. Lett.* **115**, 192105 (2019).
- [45] J. S. Yun, A. Ho-Baillie, S. J. Huang, S. H. Woo, Y. Heo, J. Seidel, F. Z. Huang, Y. B. Cheng, and M. A. Green, *J. Phys. Chem. Lett.* **6**, 875 (2015).
- [46] J. J. Li, J. Y. Ma, J. S. Hu, D. Wang, and L. J. Wan, *ACS Appl. Mater. Interfaces* **8**, 26002 (2016).

This page is intentionally left blank.



# Chapter 5

## Quasi-2D Ruddlesden-Popper Lead Halide Perovskites: How Edge Matters

*In this work, we have introduced a band-mapping technique to investigate the low-energy edge states in quasi-2D Ruddlesden-Popper (RP) perovskites,  $(BA)_2(MA)_{n-1}Pb_nI_{3n+1}$  through a localized mode of measurement, namely scanning tunneling spectroscopy. The local intrinsic band structure reveals the formation of 3D  $CH_3NH_3PbI_3$  (MAPbI<sub>3</sub>) at the edges of the quasi-2D perovskites. The band-mapping process, introduced at the edge and the interior regions of their nanosheets, inferred the presence of a low-energy 3D phase at the periphery; for the thin films, the 3D phase could be seen to form at grain boundaries. The presence of MAPbI<sub>3</sub> at the edges or grain boundaries of quasi-2D perovskites and thereby a self-forming type-II band-alignment in  $BA_2MA_2Pb_3I_{10}$  ( $n = 3$ ) has been the rationale behind achieving high efficiency in solar cells based on the material, although it has a large exciton binding energy. Kelvin probe force microscopy under illumination conditions yielded a higher surface photovoltage at the edges compared to the interior and supported the inference of internal exciton dissociation as a result of the in-situ type-II band-alignment in the quasi-2D RP perovskites.*

## 5.1. Introduction

As an emerging class of two-dimensional (2D) materials, Ruddlesden-Popper (RP) hybrid halide perovskites have gained widespread attention in recent years owing to their novel electronic and photophysical properties [1-4]. In general, the quasi-2D RP perovskites are described with a generic formula of  $A_2B_{n-1}M_nX_{3n+1}$  where  $A$  represents a large aliphatic or aromatic substituted ammonium spacer cation, such as butylamine (BA) or phenethylamine (PEA),  $B$  denotes a small organic cation like methylammonium (MA) or formamidinium (FA),  $M$  is a divalent metal cation, and  $X$  is a halide. In addition, the integer  $n$  indicates the number of perovskite layers between two successive organic spacers. This particular class of quantum-well-like materials exhibits excellent power conversion efficiency (PCE) in solar cells, despite a large exciton binding energy originating from strong quantum as well as dielectric confinement effects at room temperature [5-7]. In contrast to conventional organic solar cell structures, no intentional donor-acceptor architecture is even required for exciton dissociation in photovoltaic devices based on the RP perovskites [8]. This apparent contradiction between a large exciton binding energy in the materials and superior photovoltaic properties has been explained by considering the existence of lower energy states at the edges as compared to the interior region; exciton dissociation hence becomes an efficient process through the edge states of the materials [9-11].

Several intrinsic and extrinsic mechanisms for the rationale of edge-state-formation in quasi-2D RP perovskites have been proposed [10,12,13], prompting researchers to become even more curious and seek a proper identification technique(s). Although the conventional optical methods, including confocal fluorescence microscopy and time-resolved measurements, have successfully demonstrated the existence of edge states and somewhat different photophysics at the edge than those at the interior, the methods, due to the diffraction limit at the nanoscale, have faced restrictions in resolving the structure of edge states and thereby understanding their origin. On the other hand, while high-resolution transmission electron microscopy (TEM), scanning electron microscopy (SEM), and atomic force microscopy (AFM) have revealed some

minor morphological and structural differences at the edge and the interior [10,14,15], no definite structures could be identified by the microscopies to infer the formation of edge states having distinctly different electronic properties than those at the interior of the compounds. More importantly, proper experimental results to conclusively evidence the role of edge states and to infer the mechanism of efficient exciton dissociation are yet to be reported.

In order to shed further light on the origin of edge states and the abovementioned exciton dissociation processes, it would be intriguing to resolve the edge and the interior of these compounds energetically. As such, a surface analytical technique like scanning tunneling microscopy/spectroscopy (STM/S) at its extreme localized mode is useful for the estimation of band-energies over conventional methods, such as optical spectroscopy, cyclic voltammetry (CV), ultraviolet photoelectron spectroscopy (UPS), and so forth. The local density of states (LDOS) of a semiconductor with a high spatial and energetic resolution can hence be probed through STS [16-20].

In this letter, we have employed STS-based localized band-mapping approach to estimate the conduction (CB) and valence band (VB) energies along the edges to the interior of different quasi-2D RP perovskites, with a special emphasis on the archetypal compound  $\text{BA}_2\text{MA}_2\text{Pb}_3\text{I}_{10}$  ( $n = 3$ ). Needless to state, this material has been considered as a prototype having an edge state and characteristic edge emission [9-11]. Upon band-mapping through STS and supplemented studies through controlled X-ray diffraction (XRD) patterns, we have conclusively evidenced that these surface localized states are composed of their 3D ( $n = \infty$ ) counterpart,  $\text{MAPbI}_3$ . The results have been independently verified both in nanosheets and in thin films; in the latter case, the grain boundaries are analogous to the edge states. We have further carried out Kelvin probe force microscopy (KPFM) under illumination in the more realistic hot cast thin films, which are suitable for large area device applications, and have observed a higher contact potential difference (CPD) at the grain boundaries compared to the grain interiors. Based on STS and KPFM measurements, we could visualize the formation of an in-situ

type-II band alignment at the interface between the edge and the interior of  $\text{BA}_2\text{MA}_2\text{Pb}_3\text{I}_{10}$ . The built-in potential of such self-formed  $pn$  junctions would naturally facilitate exciton dissociation at the grain boundaries towards yielding improved solar cell efficiencies.

## 5.2. Experimental

### 5.2.1. Materials

Butylammonium iodide (BAI, 99.9%), lead (II) iodide ( $\text{PbI}_2$ , 99%), N, N-anhydrous-dimethylformamide (DMF, 99%), dimethyl sulfoxide (DMSO, 99%), and toluene were purchased from Sigma-Aldrich Chemical Co. Methylammonium iodide (MAI, 99.9%) was purchased from Great Cell Solar Limited. The materials were stored in a nitrogen-filled glovebox with an oxygen and moisture level below 0.5 ppm.

### 5.2.2. Synthesis of Perovskites and Scanning Probe Microscopy

Nanosheets and thin films of  $(\text{BA})_2\text{MA}_2\text{Pb}_3\text{I}_{10}$  quasi-2D RP perovskite were prepared through a reported synthesis route [21]. A precursor solution was freshly prepared by dissolving 0.2 mol of BAI, 0.2 mol of MAI, and 0.3 mol of  $\text{PbI}_2$  in 1 mL of DMF inside a glovebox through an overnight stirring process. To cast thin films, the precursor solution was spun at 2500 rpm for 30 s followed by annealing at 80 °C for 10 min. The films on glass or quartz substrates were characterized by recording XRD patterns and optical absorption spectroscopy. For STS, a thinner film was cast on Si (111) substrate (arsenic doped,  $n$ -type) from a 10-times-diluted precursor solution at an increased spinning speed of 4000 rpm followed by a similar annealing process. Before the film fabrication, Si wafers were treated with HF to remove the  $\text{SiO}_2$  layer and a final resistivity of 3-10  $\text{m}\Omega\cdot\text{cm}$  was obtained. For the growth of nanosheets, 15  $\mu\text{L}$  of the same precursor solution was quickly dropped into 20 mL of toluene under a vigorous stirring condition. The nanosheets were separated through centrifugation at 7,000 rpm for 1 min. The size of the nanosheets was varied by changing the centrifugation speed

(*vide infra*). To record STS of the nanosheets, they were drop-cast on freshly-cleaved highly oriented pyrolytic graphite (HOPG) surfaces.

For the preparation of other perovskites, we varied the ratio of BAI, MAI, and  $\text{PbI}_2$  in the precursor solution as stated below (Table 5.1):

**Table 5.1.** Precursor stoichiometry to form different quasi-2D perovskites

Perovskite	BAI (mol)	MAI (mol)	$\text{PbI}_2$ (mol)
$\text{BA}_2\text{PbI}_4$	0.2	0.0	0.1
$\text{BA}_2\text{MAPb}_2\text{I}_7$	0.2	0.1	0.2
$\text{BA}_2\text{MA}_2\text{Pb}_3\text{I}_{10}$	0.2	0.2	0.3
$\text{MAPbI}_3$	0.0	0.1	0.1

Since high-quality compact films were needed for KPFM measurements, we adopted a modified film casting process, namely hot-casting method [8], to deposit  $\text{BA}_2\text{MA}_2\text{Pb}_3\text{I}_{10}$  films. In this process, the precursor solution was prepared by dissolving 0.2 mmol of BAI, 0.2 mmol of MAI, and 0.3 mmol of  $\text{PbI}_2$  in 1 mL of mixed DMF:DMSO solvent (97:3) inside a glovebox. Pre-cleaned indium tin oxide (ITO) coated glass substrates with a surface resistance of 15  $\Omega$ /square were used for film formation. The substrates were pre-heated to 60 °C for 10 min. The precursor solution was then spun at a speed of 3000 rpm for 20 s followed by annealing at 100 °C for 10 min.

STS measurements were carried out with a Nanosurf Easy-Scan 2 STM; atomically-pointed tips were formed through an oblique cut of a Pt/Ir (80%:20%) wire having a 0.25 mm diameter. A bias was applied to the tip with a set point for approach (of STM-tip) being 0.5 nA at 2.0 V. KPFM measurements were carried out with a Nanosurf Flex-AFM with a Multi75E-G (Pt/Ir-coated) tip in an amplitude-modulated single pass mode. For measurements under illumination, a green (532 nm) laser was used having a power density of 300 mW/cm<sup>2</sup>. It may be noted that this wavelength is suitable for photogeneration of carriers in the material. More importantly, the wavelength is different to the near infrared laser (840 nm) associated with the feedback

loop of AFM. The beam was pointed at the sample at an angle so that it was not blocked by the probe.

## 5.3. Results and Discussions

### 5.3.1. Characterization of Quasi-2D RP Perovskites

The nanosheets and thin films of  $(\text{BA})_2(\text{MA})_{n-1}\text{Pb}_n\text{I}_{3n+1}$  with  $n = 3$ , that is  $\text{BA}_2\text{MA}_2\text{Pb}_3\text{I}_{10}$  were synthesized by following a well-documented solution process approach [21], which has been described in the experimental section. The phase purity of the as-prepared nanosheets and thin films of  $\text{BA}_2\text{MA}_2\text{Pb}_3\text{I}_{10}$  was confirmed through conventional characterization techniques, such as X-ray diffraction (XRD) measurements and optical absorption spectroscopy (Figure 5.1).

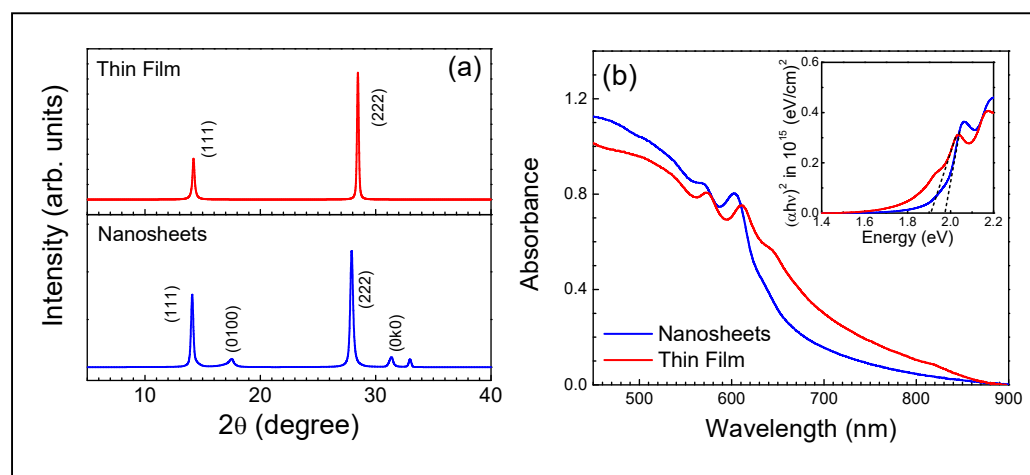


**Figure 5.1.** (a) XRD patterns and (b) optical absorbance spectra with Tauc plots (inset) of  $\text{BA}_2\text{MA}_2\text{Pb}_3\text{I}_{10}$  quasi-2D perovskite with its thin film and nanosheet forms.

The diffraction patterns were indexed and found to match well with the previous reports [22,23]. The excitonic feature at 610 nm could be observed in thin films; the feature exhibited a blue shift in the nanosheets due to its lower dimension.

### **5.3.2. Band-Mapping through Scanning Tunneling Spectroscopy**

In order to visualize the edge states in quasi-2D RP perovskite and also investigate their origin, we have derived the electronic energy levels of the material through a localized mode of measurement with an STM tip. In this localized spectroscopic mode, we characterized  $\text{BA}_2\text{MA}_2\text{Pb}_3\text{I}_{10}$  perovskite in its nanosheet and thin film forms. Primarily, our objective was to estimate the conduction and valence bands (CB and VB, respectively) in the material at different points on the nanosheets and thin films. Tunneling current versus voltage ( $I$ - $V$ ) characteristics were recorded after positioning the STM tip above the nanosheet or a thin film and thereafter disabling the scanning and feedback controls. As differential tunnel conductance ( $dI/dV$ ) at an energy  $E$  is proportional to the density of states (DOS) of the sample, that is  $dI/dV \propto \text{DOS}_{\text{Sample}}(E_F - E)$ , where  $E_F$  represents the Fermi energy of the semiconductor, we could locate the band-edges from the DOS spectra. Here, the band energies are derived with respect to  $E_F$  which is aligned at 0 V along with the work functions of the tip and the substrate-electrode. Since the bias was applied to the tip with respect to the substrate-electrode, the first peak at the negative voltage region, at which electrons could be injected from the tip to the semiconductor, denoted the location of the CB-edge. Similarly, the first peak at the positive voltage denoted the VB-edge at which electrons could be withdrawn from the quasi-2D RP perovskites.

Our first task was to locate a suitable nanosheet, preferably with an ultrathin thickness suitable for a quantum tunneling process. A TEM image and an STM topography of such a nanosheet have been presented in Figures 5.2a-b. The lateral size of the nanosheet was 1  $\mu\text{m}$  (Figure 5.2a) with a thickness of 3 nm (Figure 5.2b) inferring their ultrathin nature [24,25]. As our emphasis was to derive the electronic states of the nanosheets, we recorded STS along a line initiating from the bare HOPG (highly oriented pyrolytic graphite) electrode to the interior of the perovskite nanosheet (Figure 5.2c). In other words, DOS spectra were recorded as the tip stepped towards the interior from outside the edge. Measurements were carried out along many such lines.

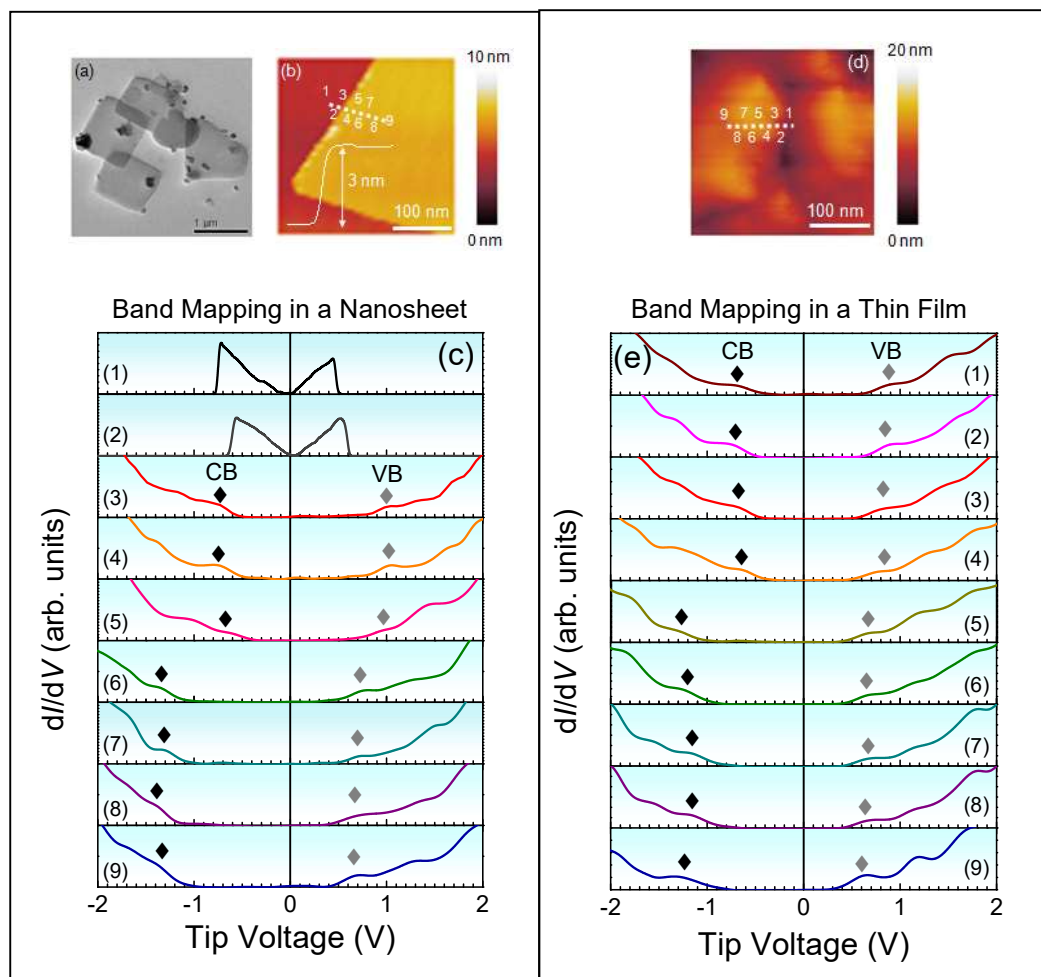


**Figure 5.2.** Left panel (nanosheet): (a) A TEM image and (b) an STM topography of  $BA_2MA_2Pb_3I_{10}$  nanosheet. The latter image was recorded in a constant current mode. (c)  $dI/dV$  spectra at different points on the nanosheet as marked on the topography. Right panel (thin film): (d) An STM topography and (e)  $dI/dV$  spectra at different points.

For the initial points,  $dI/dV$  spectra exhibited the typical metallic signature with zero DOS at 0 V or  $E_F$  originating from the substrate electrode (HOPG). Now, with the gradual inching forward of the tip towards the nanosheet, the energy levels of the compound could be identified. The tip finally progressed to probe the interior of the



BA<sub>2</sub>MA<sub>2</sub>Pb<sub>3</sub>I<sub>10</sub> nanosheet. Interestingly, we observed characteristically different  $dI/dV$  spectra at the periphery (edge) and the interior of the nanosheet. In particular, the edge of the nanosheet exhibited CB- and VB-energies at -0.69 and 0.97 eV, respectively, from the  $E_F$  with a transport gap of 1.66 eV and  $n$ -type conductivity, since the CB-edge was closer to the  $E_F$  as compared to the VB. At the interior, a different set of CB- and VB-energies (with respect to  $E_F$ ) were obtained at -1.29 eV and 0.71 eV, respectively, with a transport gap of 2.00 eV. The VB at the interior turned out to be closer to the  $E_F$  than the CB and thus inferring a  $p$ -type conductivity at the interior. These results more importantly infer that the edges of the compound possessed a lower transport gap as compared to the interior.

In a similar fashion, we mapped the energies of a thin film of BA<sub>2</sub>MA<sub>2</sub>Pb<sub>3</sub>I<sub>10</sub> along a line covering the boundary and interior of a grain. We chose a clear grain for this purpose. In Figure 5.2d, we have presented an STM topography of such a grain where detailed tunneling current measurements were carried out. Alike the results from a nanosheet, we obtained different sets of energy levels at the grain boundary and at the grain interiors (Figure 5.2e). In particular, the grain boundaries of the thin film exhibited CB- and VB-energies at -0.64 and 0.86 eV (with respect to  $E_F$ ), respectively, with a transport gap of 1.50 eV and an  $n$ -type conductivity. On the other hand, at the grain interior, a different set of CB- and VB-energies were obtained at -1.27 eV and 0.65 eV with a transport gap of 1.92 eV and a  $p$ -type conductivity. We have collated the band energies of the samples at different positions of the nanosheet and thin film to draw the band diagram (Figure 5.3). The overall results hence show that the edge of a nanosheet or the boundary of a grain in thin films always had a lower transport gap as compared to the respective interior of the halide perovskite.

It would be intriguing to know the length scale over which the edge-state extends towards the interior. In this direction, STS, due to its extent of localization in measurements, would be able to determine the precise width of the edge states towards the interior [26]. Accordingly, from Figure 5.3, we have observed that the edge state is

extended by about 30 nm from the extreme edge of the nanosheet to the interior. For thin films, the edge-state could be seen to be extended by about 40 nm.

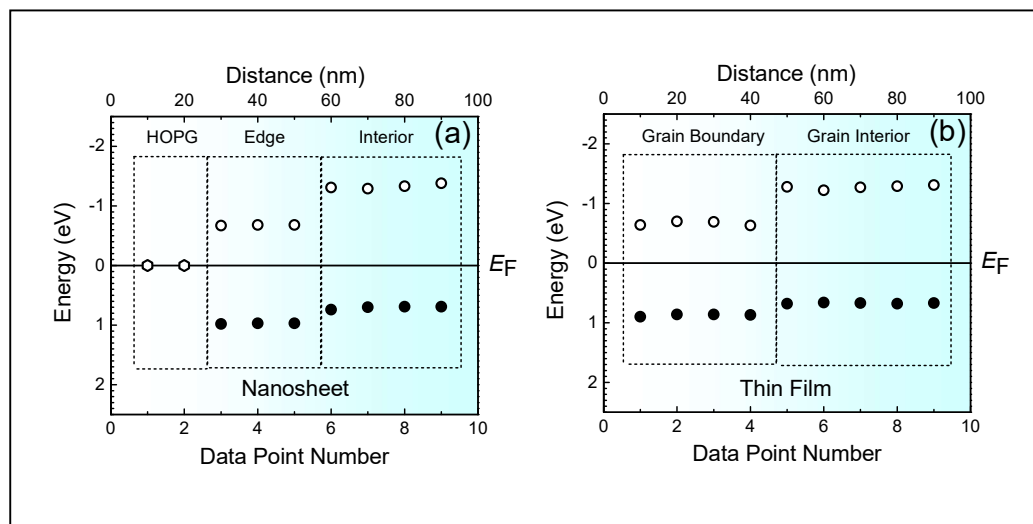


**Figure 5.3.** Mapping of the energy levels along the line on (a) the nanosheet and (b) a grain in a thin film of  $BA_2MA_2Pb_3I_{10}$  with the Fermi energy being aligned at 0 V.

### 5.3.3. Edge State in $BA_2MA_2Pb_3I_{10}$ is $MAPbI_3$

It is quite interesting to comment on the value of the transport gap at the edge. A transport gap of 1.50 eV and associated  $n$ -type conductivity are typical signatures of  $MAPbI_3$ . The energy of CB and VB from  $E_F$  also matches the respective values of the perovskite. It is hence tempting to infer that  $MAPbI_3$  was formed at the edges of  $BA_2MA_2Pb_3I_{10}$ . We accordingly carried out a set of control experiments. We first of all recorded STS of  $MAPbI_3$  nanosheets and thin films formed separately, that is the 3D counterpart of quasi-2D RP perovskites with a general formula of  $(BA)_2(MA)_{n-1}Pb_nI_{3n+1}$  ( $n = \infty$ ) [27]. The phase purity of the nanosheets and thin films of  $MAPbI_3$  has been confirmed through XRD and optical absorption spectroscopy (Figure 5.4). Similar to the quasi-2D perovskite, XRD patterns of  $MAPbI_3$  were recorded in its thin film and nanosheet forms. Both the XRD patterns were indexed and found to match well with the literature [28]. We have also presented their optical absorption spectra. The bandgap of

the samples was calculated from their respective Tauc plots; they matched well with the literature [28]. A similar blue-shift was observed in the nanosheets of the perovskite.

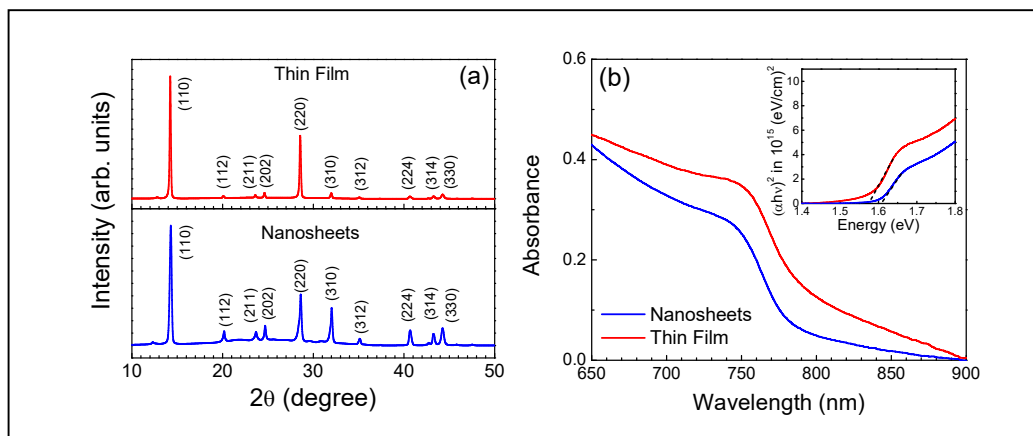


**Figure 5.4.** (a) XRD patterns and (b) optical absorbance spectra with Tauc plots (inset) of MAPbI<sub>3</sub> perovskite with its thin film and nanosheet forms.

Their STM topographies along with a TEM image of the nanosheet (thin film) are shown in Figures 5.5a-b. While the TEM image depicts the shape and size of the MAPbI<sub>3</sub> nanosheet, the STM topography shows the regions where the STS measurements were carried out. The advantages of the localized mode of measurements in STS allowed us to choose clean regions for such studies. In contrast to the results from the quasi-2D RP perovskite (Figure 5.2), the  $dI/dV$  spectra of MAPbI<sub>3</sub> yielded the same energy levels at the edge and the interior of the nanosheet (Figure 5.5d). When STS was recorded at the grain interior and the grain boundary of a thin film, identical  $dI/dV$  spectra were obtained in both cases (Figure 5.5e). The obtained CB and VB edges of the nanosheet were -0.72 and 0.92 eV from  $E_F$ , respectively, with a transport gap of 1.64 eV and an  $n$ -type character. The corresponding energies obtained in thin films were -0.65 and 0.90 eV, respectively, with a transport gap of 1.55 eV. All these values are well-documented and considered to be the signature of MAPbI<sub>3</sub> [28,29]. They also matched the energy levels obtained from the edge of the nanosheet (and grain boundary

of thin films) of the quasi-2D RP perovskite (Table 5.2). We hence conclude that the edge of  $\text{BA}_2\text{MA}_2\text{Pb}_3\text{I}_{10}$  perovskite contains the 3D perovskite, that is  $\text{MAPbI}_3$ .

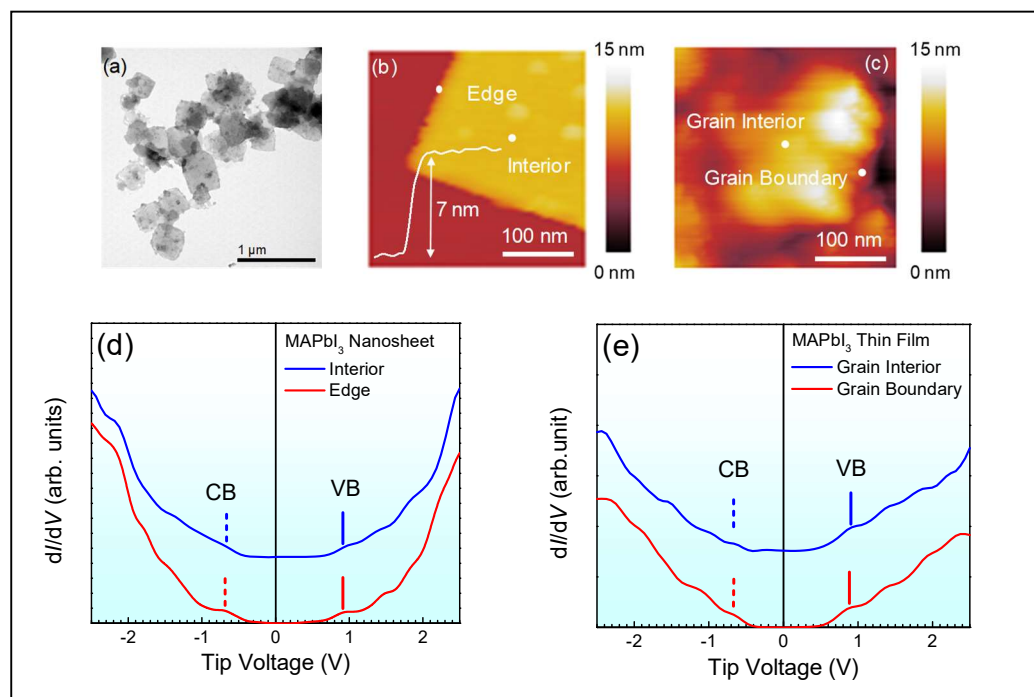


**Figure 5.5.** (a) TEM image and (b) STM topography of a  $\text{MAPbI}_3$  nanosheet. (c) STM topography of a domain in a thin film of  $\text{MAPbI}_3$ . (d) Differential tunnel conductance ( $dI/dV$ ) spectra at the interior and the edge of the nanosheet, as marked in the topography. (e)  $dI/dV$  spectra recorded on the grain-interior and the grain boundary of the domain, as marked in the topography. A Y-offset has been added in the  $dI/dV$  spectrum at the interior for the clarity of presentation.

**Table 5.2.** Localized energy levels and transport gap of a quasi-2D RP perovskite and MAPbI<sub>3</sub> in their nanosheet and thin film forms at different regions as observed from STS-based band-mapping measurements. All the band-edge energies are with respect to  $E_F$ .

Form	Quasi-2D Perovskite, BA <sub>2</sub> MA <sub>2</sub> Pb <sub>3</sub> I <sub>10</sub>				3D Perovskite, MAPbI <sub>3</sub>			
	Region	E <sub>V</sub> (eV)	E <sub>C</sub> (eV)	Transport gap (eV)	Region	E <sub>V</sub> (eV)	E <sub>C</sub> (eV)	Transport gap (eV)
Nanosheets	Edge	0.97	-0.69	1.66	Edge			
	Interior	0.71	-1.29	2.00	Interior	0.92	-0.72	1.64
Thin Films	Boundary	0.86	-0.64	1.50	Boundary			
	Interior	0.65	-1.27	1.92	Interior	0.90	-0.65	1.55

In order to validate the proposition, XRD measurements were carried out further. It may be noted that XRD is considered to be a reliable technique to identify the presence of any hidden phase/structure in a thin film. However, the XRD pattern of as prepared BA<sub>2</sub>MA<sub>2</sub>Pb<sub>3</sub>I<sub>10</sub> did not show any sign of MAPbI<sub>3</sub> (Figure 5.6a); here, the nanosheets were collected at a centrifugation speed of 7000 rpm. This is due to the fact that the contribution of the edge would be too small as compared to the area of the interior in a typical nanosheet having a lateral dimension of 1 μm. Since the edge-to-interior area ratio would be higher in smaller-sized nanosheets, we isolated nanosheets from the supernatants at different stages of increasing centrifugation speed and recorded XRD patterns of the residues collected in succession. The pattern of the nanosheets collected at a higher speed of 10000 rpm from the supernatant collected after the previous stage of centrifugation (at a lower speed of 7000 rpm) is shown in Figure 5.6a (middle panel). A clear signature of MAPbI<sub>3</sub> could be observed in this XRD pattern. In fact, the intensity of the signature peaks could be seen to increase in patterns of the residues collected at higher speeds up to 14000 rpm (Figures 5.6b-c). In the lower panel of Figure 5.6a, we have presented a pattern obtained from MAPbI<sub>3</sub> nanosheets for

comparison. From the analysis of the results from STM/S and XRD patterns, we could hence confirm that MAPbI<sub>3</sub> was formed at the edge of BA<sub>2</sub>MA<sub>2</sub>Pb<sub>3</sub>I<sub>10</sub>.

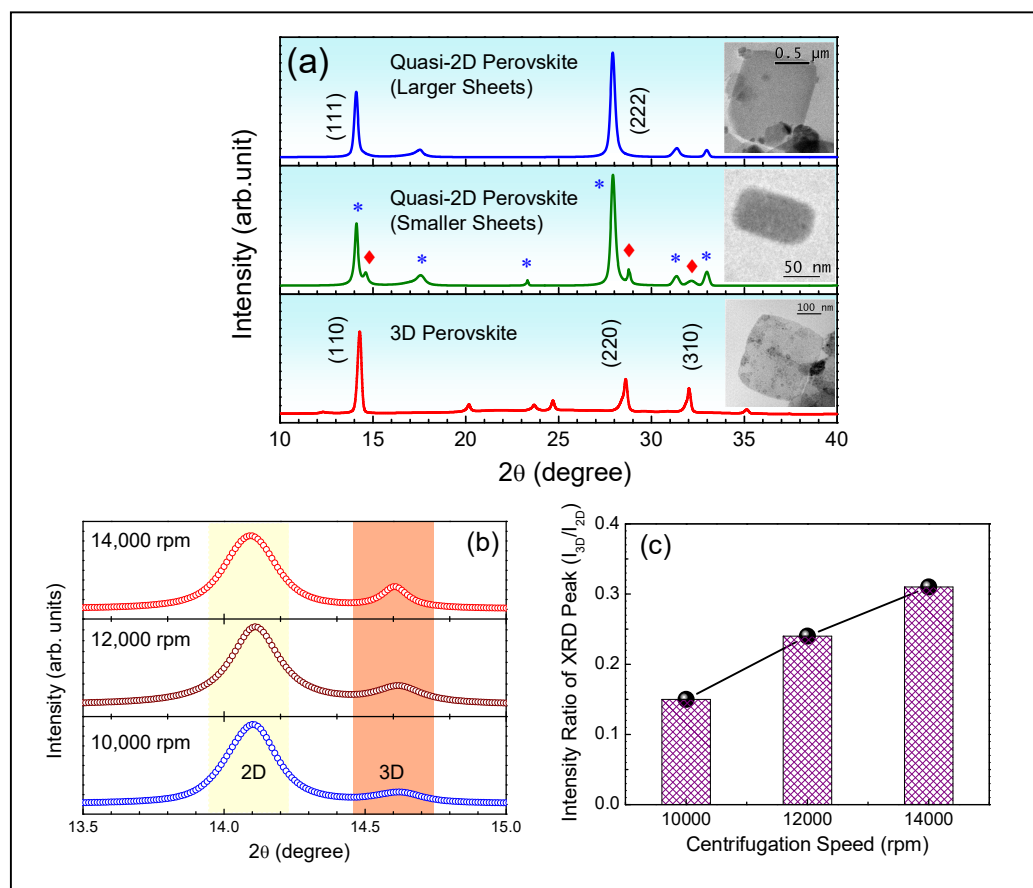


**Figure 5.6.** (a) XRD patterns of quasi-2D RP nanosheets of different sizes as collected under a centrifugation speed of 7000 and 1000 rpm (vide supra), and of the MAPbI<sub>3</sub> perovskite. The signature peaks of 3D MAPbI<sub>3</sub> have been marked in the pattern observed for the smaller nanosheets of the quasi-2D RP. The star and diamond marks represent the peaks corresponding to BA<sub>2</sub>MA<sub>2</sub>Pb<sub>3</sub>I<sub>10</sub> and MAPbI<sub>3</sub>, respectively. (b) XRD patterns and (c) intensity ratio of 3D/2D XRD peaks of different BA<sub>2</sub>MA<sub>2</sub>Pb<sub>3</sub>I<sub>10</sub> nanosheets as a function of centrifugation speed.

### 5.3.4. Edge States in $(\text{BA})_2(\text{MA})_{n-1}\text{Pb}_n\text{I}_{3n+1}$ and the Mechanism of their Formation

In the following, we shed light on the mechanism of  $\text{MAPbI}_3$  formation at the edge of  $\text{BA}_2\text{MA}_2\text{Pb}_3\text{I}_{10}$  (Figure 5.7). When RP perovskites are exposed to humid air, both BA and MA can interact with water through the formation of hydrogen bonds. Since the size of the BA spacer molecule is larger than MA, the former has a much weaker interaction with the lead halide octahedron frame. The BA moieties can hence become coupled with water molecules easily and finally get washed away, resulting in a loss of BA in the perovskite [10,30,31]. The availability of MA moieties and a loss of BA led to the formation of  $\text{MAPbI}_3$  at the edges of  $\text{BA}_2\text{MA}_2\text{Pb}_3\text{I}_{10}$ .

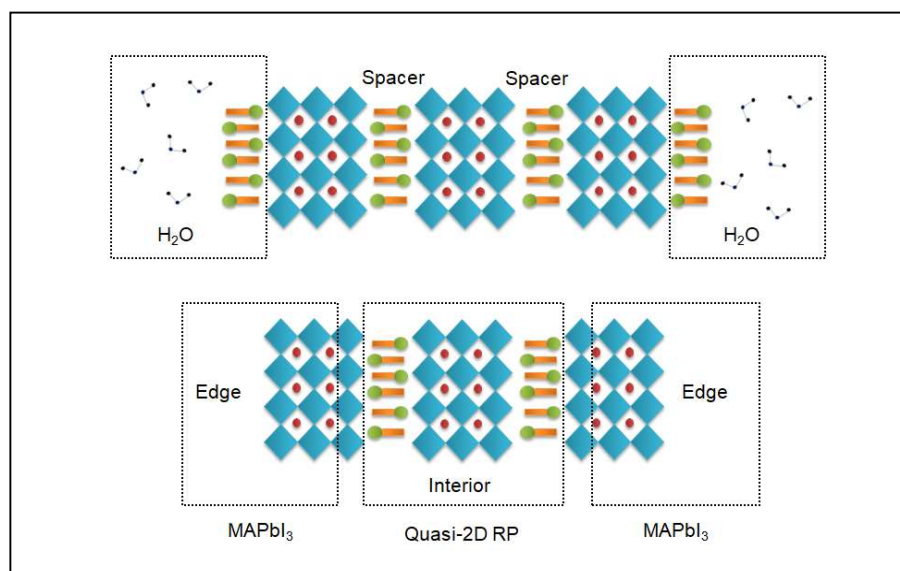


**Figure 5.7.** Mechanism of 3D  $\text{MAPbI}_3$  formation at the edges of quasi-2D RP perovskites.

The compound with  $n = 1$ , that is  $\text{BA}_2\text{PbI}_4$  hence did not result in an edge state due to the absence of the MA moiety (Figure 5.8) and thereby resulted in inefficient solar cells [1,2]. Edge states in the form of  $\text{MAPbI}_3$  should thereby exist in the RP series, that is  $(\text{BA})_2(\text{MA})_{n-1}\text{Pb}_n\text{I}_{3n+1}$  with  $n > 1$ .

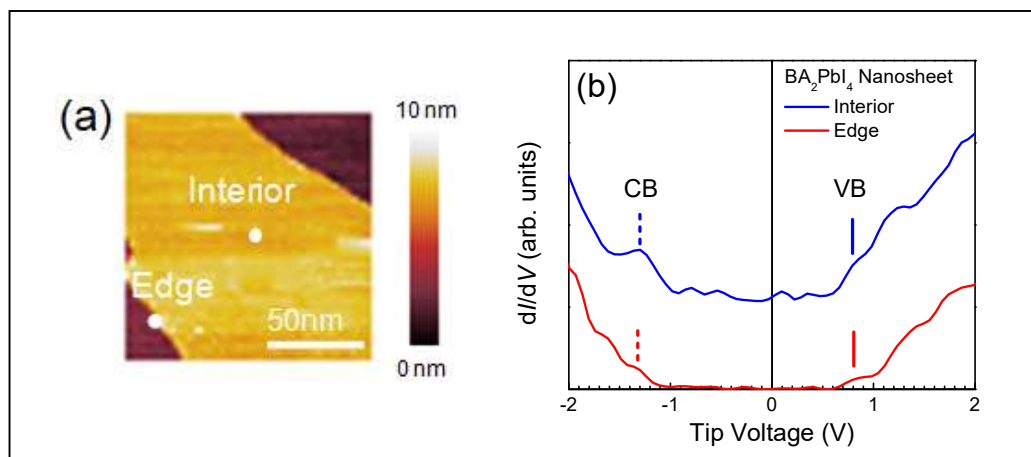


**Figure 5.8.** (a) STM topography of a  $BA_2PbI_4$  nanosheet. (b) Differential tunnel conductance ( $dI/dV$ ) spectra recorded at the interior and at the edge of the nanosheet as marked by white dots on the topography. This material did not show a presence of edge states.

We carried out a similar set of experiments in  $(BA)_2(MA)_{n-1}Pb_nI_{3n+1}$  with  $n = 2$  as well. According to theoretical predictions, an edge state should exist in  $BA_2MAPb_2I_7$  [13]. When we carried out band mapping measurements in the compound (Figure 5.9), we indeed observed the presence of  $MAPbI_3$  at the edges. The transport gap at the interior of  $BA_2MAPb_2I_7$  was 2.07 eV with an  $n$ -type conductivity. The edge being  $MAPbI_3$  with a transport gap of 1.50 eV and also an  $n$ -type conductivity, a type-I band-alignment formed at the interface between the interior and the edge of  $BA_2MAPb_2I_7$  nanosheets. Such a band-alignment is naturally unfavorable for dissociation of photogenerated excitons and thereby had led to inefficient solar cells based on  $BA_2MAPb_2I_7$  [32] as compared to that with  $BA_2MA_2Pb_3I_{10}$  which exhibited an in-situ type-II alignment (*vide infra*). The type-I band-alignment in  $BA_2MAPb_2I_7$  may however be the rationale for efficient lighting applications [33].



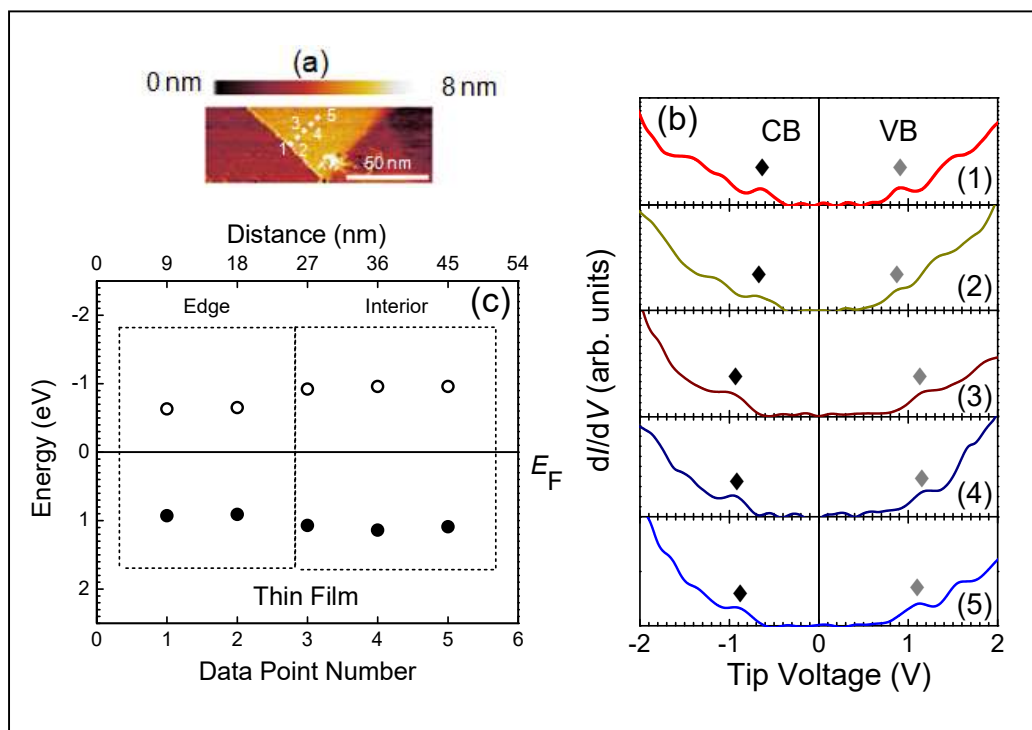


**Figure 5.9.** (a) STM topography of  $BA_2MAPb_2I_7$  nanosheet. (b) Differential tunnel conductance ( $dI/dV$ ) spectra recorded at the interior and the edge of the nanosheet along a line (as shown in the topography). (c) Band diagram evidencing the presence of an in-situ type-I band alignment at the interface between the interior and the edge of  $BA_2MAPb_2I_7$ .

### 5.3.5. Edge States Driven Exciton Dissociation: An Insight from STS and KPFM

Quasi-2D RP perovskites have emerged as a potential candidate to circumvent the stability issue of the traditional hybrid halide perovskite, namely MAPbI<sub>3</sub> in solar cell applications [34]. It may be noted that the PCE of a specific quasi-2D RP has reached over 21% making them a true alternative to MAPbI<sub>3</sub> with significantly higher operational stability [35]. Such a high efficiency in devices based on the quasi-2D RP is quite unusual considering the high binding energy of around 150-200 meV in the materials [5-7]. Although edge states are reported to be responsible for an efficient

internal exciton dissociation, a proper mechanism for the manner in which the edge states are involved is yet to be formulated and supported by experimental evidence. The mapping of the band diagram, as obtained from STS measurements, provides a clear picture in this direction. The STS recorded at the interior and at the edge of a nanosheet (or at the grain interior and the grain boundary of a domain in thin films) shows that a type-II band-alignment is formed at the interface between the quasi-2D RP ( $\text{BA}_2\text{MA}_2\text{Pb}_3\text{I}_{10}$ ) and 3D ( $\text{MAPbI}_3$ ) perovskites (Table 5.2). The band offsets are higher than the exciton binding energy, indicating the ability of such self-forming heterojunctions to dissociate photogenerated excitons in the materials. With the exciton diffusion length in this compound being about 100 nm, which is moreover comparable to the grain size [9], and a lower bandgap of  $\text{MAPbI}_3$  compared to 2D RP perovskite, most of the photogenerated excitons will be transferred to the edge (grain boundary). Upon such a transfer, the built-in potential of the *pn* junction would facilitate efficient charge separation at room temperature, preventing a carrier recombination process (Figure 5.10a).

To validate this conjecture, we further carried out Kelvin probe force microscopy (KPFM) studies of  $\text{BA}_2\text{MA}_2\text{Pb}_3\text{I}_{10}$  thin films under green (532 nm) laser illumination. It may be noted that this wavelength is suitable for photogeneration of carriers in the material. More importantly, the wavelength is different as compared to the near infrared laser (840 nm) associated with the feedback loop of AFM. In principle, KPFM measures the voltage required to balance the electrostatic force generated between the AFM tip and the sample surface; therefore, a net contact potential difference (CPD) is obtained between the tip and the perovskite surface on ITO [36]. The results obtained from high resolution KPFM measurements have been presented in Figure 5.10b along with the topography. We have also added the KPFM map of the area and the corresponding line profile analysis under dark and illumination conditions. The grain boundaries have been marked with “1” and “2” in the figures. Ideally, the CPD value should be uniform in the grain including the grain boundary of a particular thin film, since it corresponds to the work function difference between the tip and sample,

( $\phi_{\text{Tip}} - \phi_{\text{Sample}}$ ). However, the CPD profile of the quasi-2D perovskite under a dark condition shows a lower CPD at the grain boundary compared to that at the interior, with a potential difference of 30 mV. Such a difference in CPD points towards the presence of two different perovskite materials, namely  $\text{BA}_2\text{MA}_2\text{Pb}_3\text{I}_{10}$  with *p*-type conductivity and  $\text{MAPbI}_3$  having an *n*-type at the interior and at the boundary, respectively. It may be counter argued that a surface roughness may lead to different CPDs during the KPFM measurements; the roughness of the film, as marked by an asterisk symbol (\*), did not influence the CPD significantly. Hence, it can be inferred that the change in CPD at the boundary and at the interior has originated due to a *pn*-junction formed at the interface between the interior and the edge of a grain.

We then measured the CPD on the same domain upon illumination. We observed the opposite nature of CPDs at the grain boundary and at the grain interior: the CPD at the boundary has become higher as compared to that at the interior, with a CPD difference of 40 mV. The KPFM results under illumination hence infer that a surface photovoltage ( $\text{SPV} = \text{CPD}_{\text{Light}} - \text{CPD}_{\text{Dark}}$ ) amounting to 70 mV had originated only at the grain boundary as a result of charge generation. In fact, the SPV at the grain interior was tending to zero implying that the separation of photogenerated carriers occurred only at the grain boundaries. This observation could further be supported with the aid of STS band diagram, which indicates a band bending across the grain boundaries appearing at the self-forming *pn* junctions. As a result, with the exciton diffusion length of this material being high (100 nm), excitons formed upon illumination would diffuse to the edges, followed by charge carrier separation at the grain boundaries.

A similar KPFM investigation was carried out on  $\text{MAPbI}_3$  thin films (Figure 5.10c). In contrast to the quasi-2D RP perovskite, a near-identical CPD was observed at the grain and the grain boundary of  $\text{MAPbI}_3$ ; the grain boundaries have been marked with “3” and “4” in the figures. A little variation was observed due to the presence of charged defects at the grain boundaries and an upward band bending [37]. Interestingly, the average CPD value matches well to that at the grain boundary of quasi-2D RP perovskites, inferring again the formation of  $\text{MAPbI}_3$  at the edges. Upon illumination,

the CPD value in a domain of a MAPbI<sub>3</sub> thin film increased uniformly due to exciton dissociation across the domain in a homogeneous manner. As a result, a similar SPV appeared on the grain interior and grain boundaries. We can thereby conclude that the presence of grain boundaries is beneficial in the solar cell applications of quasi-2D RP perovskites as the SPV has been high at the edges. The findings also suggest that a proper edge-engineering strategy in quasi-2D perovskites, namely (BA)<sub>2</sub>(MA)<sub>*n*-1</sub>Pb<sub>*n*</sub>I<sub>3*n*+1</sub> with *n* > 1 can result in efficient exciton dissociation and thereby enhance their solar cell activities.

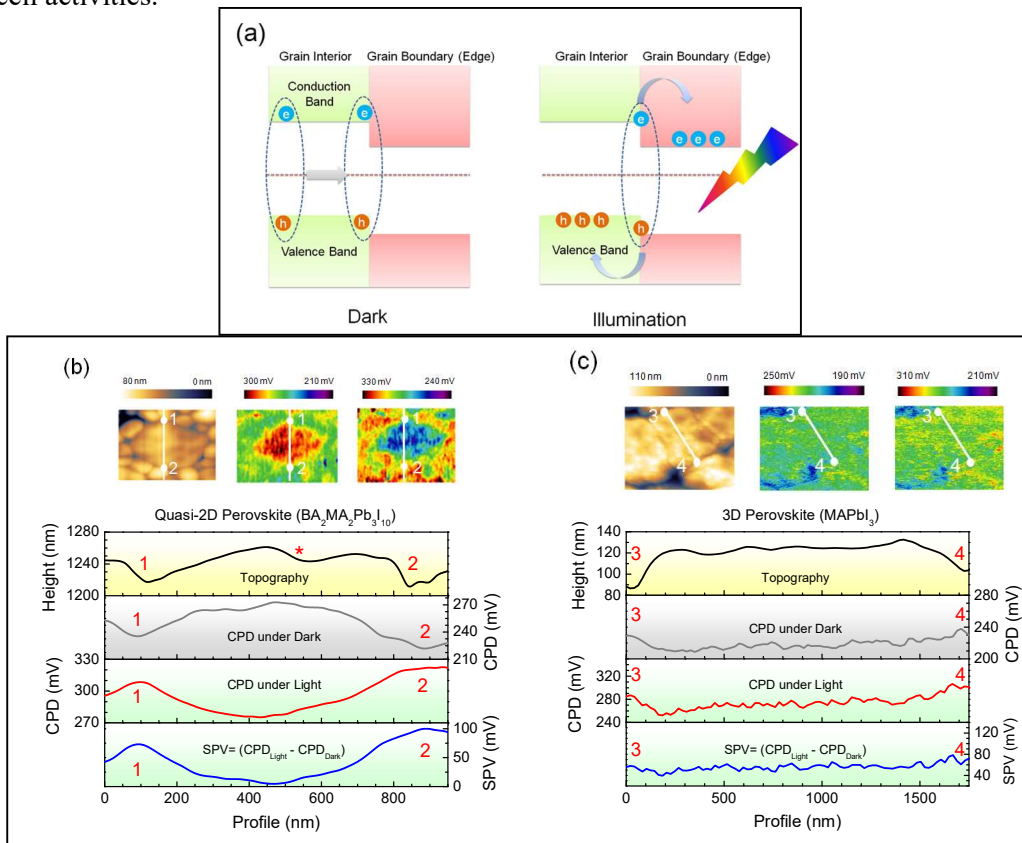


**Figure 5.10.** (a) Proposed mechanism of exciton dissociation through the self-formed pn-junction between quasi-2D RP and 3D (MAPbI<sub>3</sub>) perovskites. Topography and CPD mapping under dark and illumination conditions in (b) quasi-2D (left panel) and (c) 3D perovskites (right panel). The profile analysis of different parameters (as mentioned in the legends) has been carried out through a line as shown in the topographies.

## 5.4. Conclusions

In this letter, we have shown that MAPbI<sub>3</sub> is formed at the edges of quasi-2D RP perovskites, (BA)<sub>2</sub>(MA)<sub>*n*-1</sub>Pb<sub>*n*</sub>I<sub>3*n*+1</sub> with *n* > 1. We have characterized nanosheets and thin films of the perovskites with a special emphasis on BA<sub>2</sub>MA<sub>2</sub>Pb<sub>3</sub>I<sub>10</sub> through STS in a localized mode. We have obtained low energy states and an *n*-type conductivity, which are signatures of MAPbI<sub>3</sub>, at the edges of nanosheets and at the grain boundaries in thin films of the RP perovskites. In comparison, the interiors of the nanosheets and grains have returned a *p*-type conductivity and a wider transport gap, which are representative of BA<sub>2</sub>MA<sub>2</sub>Pb<sub>3</sub>I<sub>10</sub>. The RP perovskites have thereby possessed a self-forming type-II band-alignment at the interface between the interior and the edge, comprising of a quasi-2D and 3D MAPbI<sub>3</sub> perovskites, respectively. Such a band-alignment with an adequate band-offset has been ripe for internal exciton dissociation in the RP perovskites. We further carried out KPFM measurements under dark and illumination conditions and observed higher CPD at the grain boundaries compared to that at the grain interior. With the aid of STS, KPFM, and controlled XRD studies, we have conclusively evidenced the formation of MAPbI<sub>3</sub> at the edge of RP perovskites with an in-situ *pn*-junction, which could be the rationale for achieving high-efficiency in solar cells based on the quasi-2D materials.

## 5.5. References

- [1] L. Pedesseau, D. Saponi, B. Traore, R. Robles, H. H. Fang, M. A. Loi, H. H. Tsai, W. Y. Nie, J. C. Blancon, A. Neukirch, S. Tretiak, A. D. Mohite, C. Katan, J. Even, and M. Kepenekian, *ACS Nano* **10**, 9776 (2016).
- [2] Y. N. Chen, Y. Sun, J. J. Peng, J. H. Tang, K. B. Zheng, and Z. Q. Liang, *Adv. Mater.* **30**, 1703487 (2018).
- [3] L. Mao, C. C. Stoumpos, and M. G. Kanatzidis, *J. Am. Chem. Soc.* **141**, 1171 (2019).

- 
- [4] C. Liang, H. Gu, Y. Xia, Z. Wang, X. Liu, J. Xia, S. Zuo, Y. Hu, X. Gao, W. Hui, L. Chao, T. Niu, M. Fang, H. Lu, H. Dong, H. Yu, S. Chen, X. Ran, L. Song, B. Li, J. Zhang, Y. Peng, G. Shao, J. Wang, Y. Chen, G. Xing, and W. Huang, *Nat. Energy* **6**, 38 (2021).
- [5] O. Yaffe, A. Chernikov, Z. M. Norman, Y. Zhong, A. Velauthapillai, A. van der Zande, J. S. Owen, and T. F. Heinz, *Phys. Rev. B* **92**, 045414 (2015).
- [6] R. L. Milot, R. J. Sutton, G. E. Eperon, A. A. Haghighirad, J. M. Hardigree, L. Miranda, H. J. Snaith, M. B. Johnston, and L. M. Herz, *Nano Lett.* **16**, 7001 (2016).
- [7] C. Katan, N. Mercier, and J. Even, *Chem. Rev.* **119**, 3140 (2019).
- [8] E. D. Kinigstein, H. Tsai, W. Nie, J.-C. Blancon, K. G. Yager, K. Appavoo, J. Even, M. G. Kanatzidis, A. D. Mohite, and M. Y. Sfeir, *ACS Materials Lett.* **2**, 1360 (2020).
- [9] J. C. Blancon, H. Tsai, W. Nie, C. C. Stoumpos, L. Pedesseau, C. Katan, M. Kepenekian, C. M. M. Soe, K. Appavoo, M. Y. Sfeir, S. Tretiak, P. M. Ajayan, M. G. Kanatzidis, J. Even, J. J. Crochet, and A. D. Mohite, *Science* **355**, 1288 (2017).
- [10] E. Z. Shi, S. B. Deng, B. Yuan, Y. Gao, Akriti, L. Yuan, C. S. Davis, D. Zemlyanov, Y. Yu, L. B. Huang, and L. T. Dou, *ACS Nano* **13**, 1635 (2019).
- [11] Z. S. Zhang, W. H. Fang, R. Long, and O. V. Prezhdo, *J. Am. Chem. Soc.* **141**, 15557 (2019).
- [12] M. Kepenekian, B. Traore, J. C. Blancon, L. Pedesseau, H. Tsai, W. Y. Nie, C. C. Stoumpos, M. G. Kanatzidis, J. Even, A. D. Mohite, S. Tretiak, and C. Katan, *Nano Lett.* **18**, 5603 (2018).
- [13] J. Hong, D. Prendergast, and L. Z. Tan, *Nano Lett.* **21**, 182 (2021).
- [14] K. Wang, C. C. Wu, Y. Y. Jiang, D. Yang, and S. Priya, *Sci. Adv.* **5**, eaau3241 (2019).
- [15] J. Bao and V. G. Hadjiev, *Nano-Micro Lett.* **11**, 26 (2019).

- [16] M.-C. Shih, B.-C. Huang, C.-C. Lin, S.-S. Li, H.-A. Chen, Y.-P. Chiu, and C.-W. Chen, *Nano Lett.* **13**, 2387 (2013).
- [17] A. Bera, S. Dey, and A. J. Pal, *Nano Lett.* **14**, 2000 (2014).
- [18] U. Dasgupta, A. Bera, and A. J. Pal, *ACS Energy Lett.* **2**, 582 (2017).
- [19] L. Qiu, S. He, L. K. Ono, and Y. Qi, *Adv. Energy Mater.* **10**, 1902726 (2020).
- [20] S. Sahare, P. Ghoderao, S. B. Khan, Y. Chan, and S.-L. Lee, *Nanoscale* **12**, 15970 (2020).
- [21] L. Zhu, H. Zhang, Q. Lu, Y. Wang, Z. Deng, Y. Hu, Z. Lou, Q. Cui, Y. Hou, and F. Teng, *J. Mater. Chem. C* **6**, 3945 (2018).
- [22] A. S. Tutantsev, E. I. Marchenko, N. N. Udalova, S. A. Fateev, E. A. Goodilin, and A. B. Tarasov, *Nanomaterials* **11**, 3333 (2021).
- [23] M. Rahil, R. M. Ansari, C. Prakash, S. S. Islam, A. Dixit, and S. Ahmad, *Sci. Rep.* **12**, 2176 (2022).
- [24] W. Niu, A. Eiden, G. V. Prakash, and J. J. Baumberg, *Appl. Phys. Lett.* **104**, 171111 (2014).
- [25] C. M. M. Soe, G. P. Nagabhushana, R. Shivaramaiah, H. H. Tsai, W. Y. Nie, J. C. Blancon, F. Melkonyan, D. H. Cao, B. Traore, L. Pedesseau, M. Kepenekian, C. Katan, J. Even, T. J. Marks, A. Navrotsky, A. D. Mohite, C. C. Stoumpos, and M. G. Kanatzidis, *Proc. Natl. Acad. Sci. U. S. A.* **116**, 58 (2019).
- [26] S. Khatun, A. Banerjee, and A. J. Pal, *Nanoscale* **11**, 3591 (2019).
- [27] C. C. Stoumpos, D. H. Cao, D. J. Clark, J. Young, J. M. Rondinelli, J. I. Jang, J. T. Hupp, and M. G. Kanatzidis, *Chem. Mater.* **28**, 2852 (2016).
- [28] A. Maiti, S. Khatun, and A. J. Pal, *Nano Lett.* **20**, 292 (2020).
- [29] L. M. She, M. Z. Liu, and D. Y. Zhong, *ACS Nano* **10**, 1126 (2016).
- [30] C. Y. Zhao, W. M. Tian, J. Leng, Y. Zhao, and S. Y. Jin, *J. Phys. Chem. Lett.* **10**, 3950 (2019).
- [31] Z. Qin, S. Dai, C. C. Gajjela, C. Wang, V. G. Hadjiev, G. Yang, J. Li, X. Zhong, Z. Tang, Y. Yao, A. M. Guloy, R. Reddy, D. Mayerich, L. Deng, Q. Yu,

- 
- G. Feng, H. A. Calderon, F. C. Robles Hernandez, Z. M. Wang, and J. Bao, *Chem. Mater.* **32**, 5009 (2020).
- [32] H. Kheirabadi, H. Abdizadeh, and M. R. Golobostanfard, *ACS Appl. Energy Mater.* **4**, 394 (2021).
- [33] H. Tsai, W. Y. Nie, J. C. Blancon, C. C. Stoumpos, C. M. M. Soe, J. Yoo, J. Crochet, S. Tretiak, J. Even, A. Sadhanala, G. Azzellino, R. Brenes, P. M. Ajayan, V. Bulovic, S. D. Stranks, R. H. Friend, M. G. Kanatzidis, and A. D. Mohite, *Adv. Mater.* **30**, 1704217 (2018).
- [34] Y. Yang, F. Gao, S. W. Gao, and S. H. Wei, *J. Mater. Chem. A* **6**, 14949 (2018).
- [35] M. Shao, T. Bie, P. Yang, Y. R. Gao, X. Jin, F. He, N. Zheng, Y. Yu, and X. L. Zhang, *Adv. Mater.* **34**, 2107211 (2022).
- [36] J. S. Yun, A. Ho-Baillie, S. J. Huang, S. H. Woo, Y. Heo, J. Seidel, F. Z. Huang, Y. B. Cheng, and M. A. Green, *J. Phys. Chem. Lett.* **6**, 875 (2015).
- [37] A. Krishna, H. Zhang, Z. W. Zhou, T. Gallet, M. Dankl, O. Ouellette, F. T. Eickemeyer, F. Fu, S. Sanchez, M. Mensi, S. M. Zakeeruddin, U. Rothlisberger, G. N. M. Reddy, A. Redinger, M. Gratzel, and A. Hagfeldt, *Energy Environ. Sci.* **14**, 5552 (2021).



# Chapter 6

## Hybrid Halide Perovskite: Rashba Band Splitting

*We report an experimental observation of Rashba splitting in methylammonium lead iodide (MAPbI<sub>3</sub>). Due to a large spin-orbit coupling parameter in the non-centrosymmetric material, both the bands were predicted to split having two different spin-textures leading to two different Z-component of total angular momentum ( $J_z$ ). We use spin-polarized scanning tunneling spectroscopy to probe only one type of  $J_z$ -matched bands throughout the film;  $dI/dV$  spectra recorded at many different points of a film however allow us to spot both the Rashba split-levels and also deliberate on their spin-textures. We observe that the bands split in such a manner that the conduction and valence bands closer to the Fermi energy have the same type of spin-textures (a spin-allowed transition model). Still, a low recombination rate of photogenerated carriers in MAPbI<sub>3</sub> has been analyzed by considering Wannier-type excitons, molecular nature of spin-domains from  $dI/dV$  images, and therefore a spin-forbidden nature of inter-domain transition.*

### 6.1. Introduction

Although methylammonium lead iodide (MAPbI<sub>3</sub>) is well-known for its efficient solar-cell activities [1-3], it possesses more interesting properties than can be envisaged in a single conventional semiconductor [4]. A suitable bandgap as per Shockley-Queisser limit [5,6], a high extinction coefficient in the visible wavelength region, a low exciton binding energy for efficient charge separation [7], an in-built electric dipole arising out of the methylammonium ion presumably facilitating exciton

dissociation [8], a long carrier lifetime [9-11], high and ambipolar carrier mobility due to a smaller electron and hole effective masses [12,13], and so forth are some of the commonly-mentioned unique properties of this wonder material. Although such properties are indeed desired in a solar cell material, the most surprising feature of MAPbI<sub>3</sub> is a low recombination rate of photogenerated carriers [14-16]. The rate is as low as five orders of magnitude lower than the predicted Langevin limit in spite of defects and impurities in MAPbI<sub>3</sub> that may form in a solution-processed film [9]; this is in a clear contrast to conventional semiconductors, in which defects form in spite of best efforts during the growth process in a best possible environment and act as carrier recombination sites limiting the carrier lifetime and diffusion length.

A low recombination rate of photogenerated carriers in MAPbI<sub>3</sub> enhancing the carrier lifetime and thereby diffusion length is believed to occur due to Rashba effect [17,18]. The effect drives a spin-splitting leading to a spin-polarization even in a nonmagnetic system like MAPbI<sub>3</sub>. The effect occurs due to a large spin-orbit coupling (SOC) arising out of high-Z elements (lead and iodine) in the compound along with a lack of centrosymmetry appearing due to a tilted PbI<sub>6</sub> octahedra and rotating electric dipoles of the organic ions leading to an effective magnetic field and thereby lifting the Kramer's spin-degeneracy of the electrons [19-21]. In the momentum ( $\mathbf{k}$ ) space, a  $\mathbf{k}$ -dependent spin-splitting of the bands around the band-extrema hence occurs [22]. Splitting for the two bands are however non-identical resulting in an indirect nature of the bandgap.

Upon photoexcitation, the carriers then reside at band extrema having different points in  $\mathbf{k}$ -space. That is, due to a momentum-offset of conduction band (CB) minimum and valence band (VB) maximum, the electrons and holes are in different  $\mathbf{k}$ -space; they in effect find themselves in an indirect bandgap semiconductor and their recombination, which requires a preservation of  $\mathbf{k}$ , turns out to be a slow process [23,24]. Regarding the spin-rotation or spin-texture ( $\chi$ ) of the two split levels, two schools of thought persist among theoreticians: (1) the spin-allowed transition model [25] and (2) the spin-forbidden transition model [17]. In the spin-allowed transition

model, CB and VB having a similar type of spin-texture reside closer to the Fermi energy; although recombination of photoexcited carriers is apparently possible due to spin-allowed nature of the transition, a slow recombination is considered to be due to the presence of ferroelectric domains, passivation of defects, pressure-driven change of structure, and formation of large polarons [25,26]. In the spin-forbidden transition model, after spin-split, the CB and VB closer to the Fermi energy have opposing spin-textures. A recombination between electrons in CB-minimum and holes in VB-maximum is hence a spin-forbidden process leading to a low recombination rate and thereby an enhanced carrier lifetime and a longer diffusion length [17,18].

So far, a few experimental evidence of the Rashba splitting in a bromide-based perovskite ( $\text{MaPbBr}_3$ ) has been reported from angle-resolved photoemission spectroscopy measurements; the measurement method has provided information on the occupied states only [27]. Giovanni et al. have confirmed the presence of Rashba-split band structures in  $\text{MAPbI}_3$  by using a pump-probe method [28]. There are reports describing non-observation of Rashba splitting into certain phases of the perovskite as well making the topic under debate [21,26]. A clear experimental evidence of CB-splitting would hence be truly interesting in lead-based hybrid-halide perovskites since the quantum of splitting into the unoccupied states has been predicted to be more than that in the VB [19,29]. Since the bands after Rashba splitting is spin-selective and (due to a strong SOC in the perovskite system) should be viewed in terms of the Z-component of total angular momentum ( $J_z$ ), tunneling of electrons would necessitate conservation of  $J_z$  instead. This is, tunneling processes in strong SOC systems involve conservation of  $J_z$  in lieu of orbital or spin angular momentum separately [30-32]. We have therefore introduced spin-polarized scanning tunneling spectroscopy (SP-STs), which provides unique opportunities to experimentally probe  $J_z$ -matched Rashba-split bands in  $\text{MAPbI}_3$  and to comment on the spin-states of the two split-levels. Our work may further shed light on the debate and the rationale for a low recombination rate in hybrid halide perovskite materials.

## 6.2. Experimental

### 6.2.1. Materials

Lead (II) iodide ( $\text{PbI}_2$ , 99%), and N, N-dimethylformamide (DMF, 99.8%) were purchased from Sigma Aldrich Chemical Company. Methylammonium iodide (MAI, 99.9%) was purchased from Dyesol Limited. The materials were stored in a nitrogen-filled glovebox with both oxygen and moisture level below 0.1 ppm and were used without further treatment.

### 6.2.2. Formation of $\text{MAPbI}_3$ Perovskite Thin Films and Characterization

Thin films of  $\text{MAPbI}_3$  were formed through a conventional solution-process approach following a usual one-step method which is based on the co-deposition of both the organic and inorganic components. The precursor solution was formed by thorough mixing of stoichiometric  $\text{CH}_3\text{NH}_3\text{I}$  and  $\text{PbI}_2$  in DMF under an overnight stirring process at 70 °C inside the glovebox. The solution was then spun at 2500 rpm for 30 s on pre-heated (70 °C) substrates suitable for different measurements. The films were annealed 100 °C for 20 min to complete the conversion to the perovskite phase. For STS measurements, ultra-thin films were spun at 4000 rpm for 30 s on highly-doped Si(111) substrates (arsenic-doped, *n*-type) having a resistivity of 3-10 m $\Omega$ -cm. Before that, the wafers were treated with HF to remove the native oxide layer. The one-step method moreover led to limited  $\text{CH}_3\text{NH}_3\text{I}$ - and  $\text{PbI}_2$ -rich regions in the perovskite films. The use of a magnetic substrate was avoided since it is known to induce a substrate-induced exchange splitting and thereby hide a Rashba spin-splitting [33].

The thin films were characterized by X-ray diffraction (XRD) patterns and optical absorption and Raman spectroscopy. The measurements were conducted with a Rigaku Smart Lab X-Ray Diffractometer (Cu  $K\alpha$  radiation = 1.5406 Å), UV-vis-NIR spectrophotometer (Cary 5000, Agilent Technologies), and Horiba Jobin Yvon Raman

triple-grating spectrometer system (model number T64000) using 532.0 nm excitation from a diode-pumped solid-state (DPSS) laser.

### **6.2.3. STS Studies**

STS studies of MAPbI<sub>3</sub> were carried out in an ultrahigh-vacuum scanning tunneling microscope (UHV-STM) with a chamber pressure of  $2 \times 10^{-10}$  Torr. The perovskite films with a thickness of around 10 nm were quickly transferred from the glovebox to the load-lock chamber of the STM; they were transferred to the main chamber following a usual protocol. Extremely sharp STM tips were formed through an acute mechanical cut of the Pt:Ir wire (80%:20%) and used for the measurement. For spin-polarized STS (SP-STS), chromium-coated (15 nm) silver/gallium (Ag<sub>2</sub>Ga) nanoneedles, coaxial at the tip of a tungsten wire (0.25 mm), were used. Such tips, (bought from Nauga Needles LLC.) were antiferromagnetic in nature allowing injection of spin-polarized electrons. The temperature of both tips and films was maintained at 80 K during STS studies to enable efficient spin-polarized electron-tunneling process while retaining the non-centrosymmetric phase of the compound [21]. For approach of the tip, a bias of 1.5 V was applied through a feedback-loop; three different currents (100, 200, and 300 pA) were targeted to achieve to obtain different set-points or electron-tunneling conditions. At each set-condition, differential tunnel conductance ( $dI/dV$ ) versus voltage characteristics was recorded with a lock-in amplifier; parameters for the amplifier were 16 mV rms and 1.15 kHz. DC bias was applied to the substrate with respect to the tip.  $dI/dV$  “images” of the films were recorded through scanning of  $dI/dV$  over a small region; feedback-loop was turned off during the scanning and  $dI/dV$  imaging processes.

## **6.3. Results and Discussions**

### **6.3.1. Formation of MAPbI<sub>3</sub>**

To confirm formation of MAPbI<sub>3</sub> in phase-pure form, we have characterized the material through conventional thin film characterization techniques (Figure 6.1).

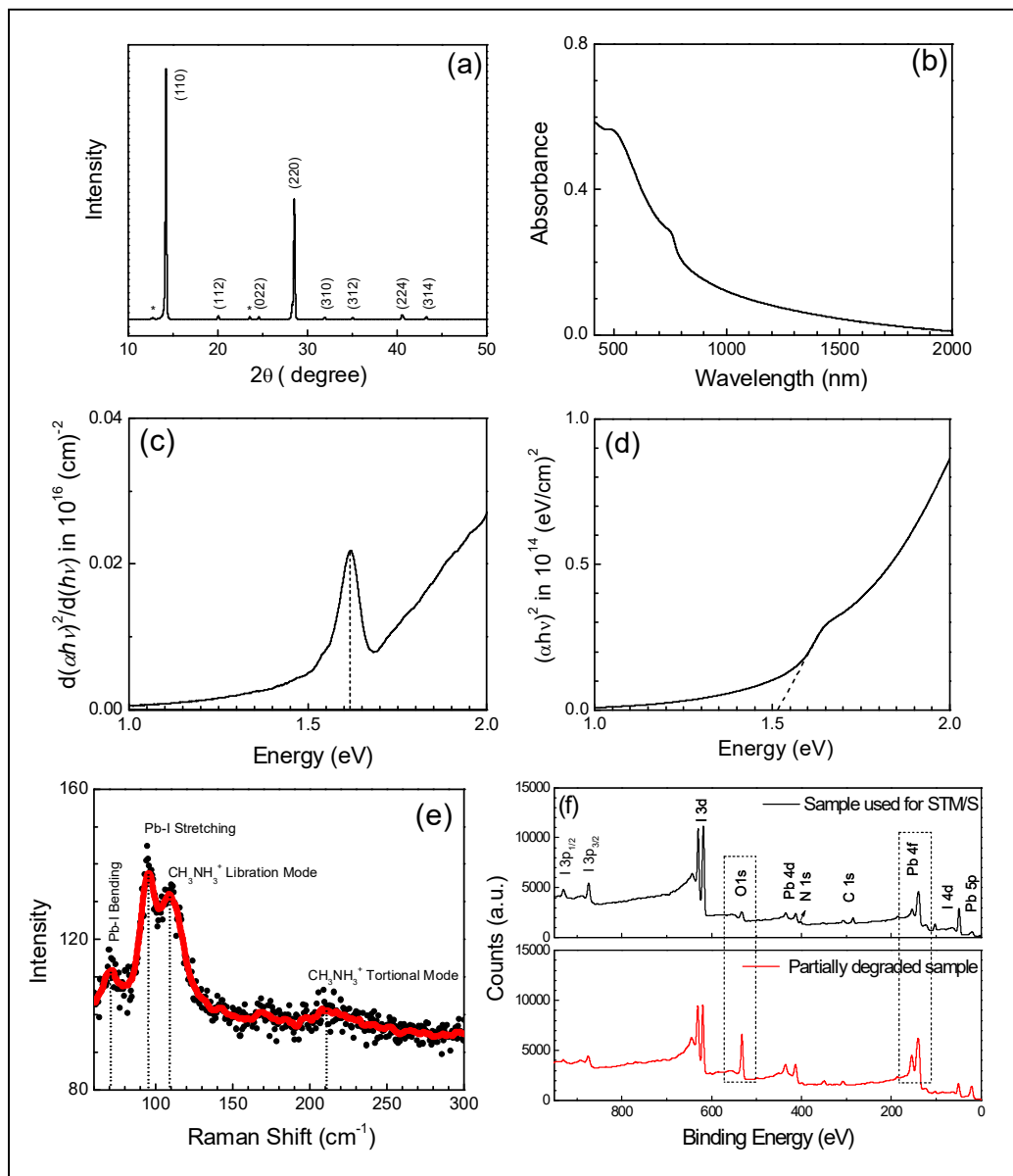


**Figure 6.1.** (a) XRD pattern, (b) optical absorption spectrum, (c)  $d[(\alpha h\nu)^2]/d(h\nu)^2$  versus energy plot of the material (d) Tauc plot estimating the optical band gap, (e) Raman spectrum of MAPbI<sub>3</sub> thin film, and (f) XPS results of two films. In (a), lattice planes have been marked; the asterisks (\*) indicate patterns due to unreacted PbI<sub>2</sub>.

The X-ray diffraction (XRD) pattern yielded the characteristic (110) peak of the perovskite at an appropriate position indicating formation of a tetragonal phase at room temperature [34]. The respective optical absorption spectrum similarly showed two dominant and distinct photoinduced peaks located at around 490 and 740 nm which are characteristics of the material synthesized in N,N-dimethylformamide (DMF) solvent [13] along with a long Urbach tail implying presence of defects [35]. Optical bandgap of the perovskite was estimated from the  $d(ah\nu)^2/d(h\nu)$  versus energy (and Tauc plots); the obtained value of 1.62 (1.52) eV matched well with the reported results [6]. The thin films were in addition characterized by recording Raman spectra of the compound. A couple of modes in the low-frequency range (70 and 95  $\text{cm}^{-1}$ ) were observed. These are the characteristic modes of the inorganic cage and corresponded to the bending and stretching vibrations of the Pb–I bond, respectively. The bands at 107 and 241  $\text{cm}^{-1}$  similarly could be associated to the vibrations of the  $\text{CH}_3\text{NH}_3^+$  cations and the torsional modes confirming formation of the hybrid halide perovskite in a phase-pure form [36]. X-ray photoelectron spectroscopy (XPS) studies inferred little or no degradation during a quick-transfer to the scanning tunneling microscope (STM) chamber [37].

### **6.3.2. STS of $\text{MAPbI}_3$ with a Pt/Ir Tip**

In Figure 6.2a, we have presented typical  $dI/dV$  versus sample voltage plots of the material recorded with a conventional Pt/Ir tip along with a topography. Plots for three set-points representing different tip-to-sample distances are also shown. Since  $dI/dV$  has a correspondence to the density of states (DOS) spectrum and the bias in the scanning tunneling microscope (STM) was applied to the perovskite with respect to the tip, the first peak in the positive voltage closest to 0 V implied injection of electrons and hence the location of CB. The similar peak in the negative voltage implied withdrawal of electrons and thereby the VB of the semiconductor [38]. Both the peaks are with respect to the Fermi energy ( $E_F$ ) of the semiconductor that is aligned to 0 V. The spectra showed that the CB- and VB-energies were at 0.57 and 0.96 eV, respectively, away from  $E_F$  leading to a transport gap of 1.53 eV, which matched well with the literature

[6]. The band energies tallied the results from films grown through a vacuum deposition method [39]; the energies along with the results from XPS studies imply little contamination during the transfer to the STM chamber (*vide supra*). The small variation in the bandgap value was due to some level of arbitrariness in the method of locating a band in different measurements [40,41]. When the band-edges obtained from spectra recorded at different tip-to-sample distances were compared, the CB- and VB-energies could be found to be independent of the tunneling condition. Subsequent peaks, which appeared in both bias directions of a  $dI/dV$  spectrum, arose due to probing of higher levels. The results hence infer that the range of tip-to-sample separations used in recording STS measurements did not influence the band-edges of the semiconductor.

Since STS is an extremely localized mode of measurement, we have recorded  $dI/dV$  spectra at a large number of points on the films and also at all the three tunnel conditions or tip-to-sample separations. In each of the more than 600  $dI/dV$  spectra, we have identified CB and VB edges to finally draw a histogram of the two band-energies (Figure 6.2b). Number of bins in a histogram was set to the square root of the measurement-points; the method is commonly termed as a square-root choice. The histograms of band-energies show that the CB was always closer to the Fermi energy than the VB inferring a clear *n*-type behavior of the perovskite. Such a nature of conductivity in MAPbI<sub>3</sub>, when formed with stoichiometric content of CH<sub>3</sub>NH<sub>3</sub>I and PbI<sub>2</sub>, is in fact known to appear due to iodine-vacancies present in the perovskite; the vacancies can be passivated when the perovskite is formed with PbI<sub>2</sub>-rich precursors [42-44]. The histograms show a symmetric distribution of nearly equal full width at half maximum (FWHM). It may be stated that band-energies of a semiconductor obtained from  $dI/dV$  spectra as such exhibit a distribution [45,46]; in MAPbI<sub>3</sub>, the histogram of CB and VB-edges may have originated due to presence of grains and grain-boundaries in the solution-cast film (inset of Figure 6.2a) as well as CH<sub>3</sub>NH<sub>3</sub>I-rich and PbI<sub>2</sub>-rich regions in the ultra-thin layer. In the STM topography, we did not achieve an atomic resolution which is observed if a single crystal after an in-situ cleaving or films grown through vacuum co-deposition method are imaged [39,47].



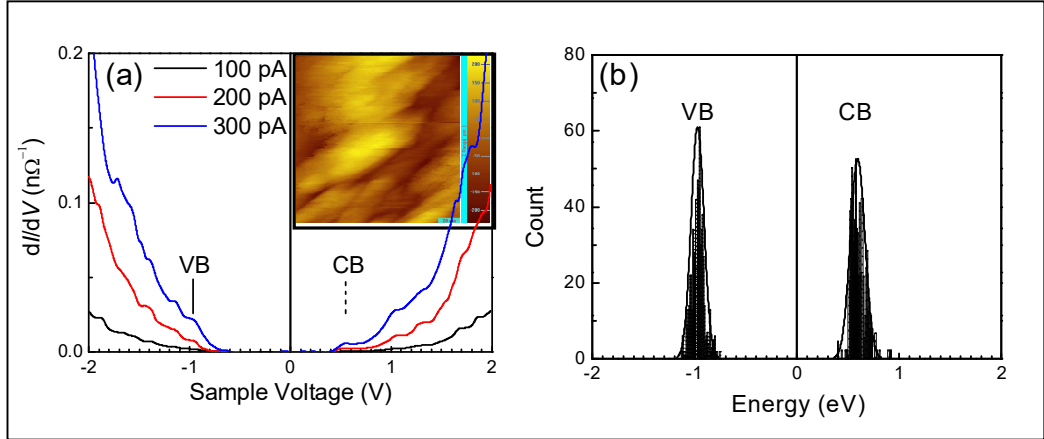


**Figure 6.2.** (a)  $dI/dV$  spectra of MAPbI<sub>3</sub> thin films recorded with a Pt/Ir tip at three tip-approach conditions and (b) histograms of band-energies. Inset of (a) shows a topographic image of the film; while the scale bar in the image represents 20 nm, the height scale of the image is 0.4 nm.

### 6.3.3. SP-STs of MAPbI<sub>3</sub> with a Chromium-Coated Tip

We then proceeded to characterize the same film with a chromium-coated antiferromagnetic tip to record SP-STs. With an injection of spin-polarized electrons, the spectroscopy provides unprecedented opportunities to garner information on the spin-texture of the split-bands which may be referred to as bands having  $J_Z = +1/2$  and  $J_Z = -1/2$  [48,49]. The involvement of  $J_Z$  during the tunneling of spin-polarized electrons is due to the fact that the total angular momentum  $J = L + S$  arising out of a strong spin-orbit interaction term  $L.S$  will have to be the proper eigenvalue at the band-edges [30-32]; the band structure upon Rashba splitting will hence look like the one presented in Figure 6.3a [48]. Here, a  $J_Z = +1/2$  band can be built through ( $L_Z = 0$  and  $S_Z = +1/2$ ) and ( $L_Z = +1$  and  $S_Z = -1/2$ ), which can be viewed to possess a particular spin-texture (say  $\chi = +1$ ). Similarly, a  $J_Z = -1/2$  band can be considered to have formed through ( $L_Z = 0$  and  $S_Z = -1/2$ ) and ( $L_Z = -1$  and  $S_Z = +1/2$ ) with another spin-texture ( $\chi = -1$ ). That is, a particular  $J_Z$  band (say  $J_Z = -1/2$ ) is formed through a partial  $S_Z = +1/2$  band (red trace) and a part of  $S_Z = -1/2$  band (blue trace) in our Figure 6.3a.

Since we have had no prior knowledge about the spin-states of the material at the point of measurement and a spin-equilibrium must exist at the macroscopic scale of the film, we have recorded SP-STs at many different points with the chromium-coated antiferromagnetic tip. In Figure 6.3b, we have presented the topographic image recorded with the spin-polarized tip. The large number of  $dI/dV$  spectra could be classified into two broad types; one typical spectrum from each the two-types of  $dI/dV$  spectra are shown in Figure 6.3c. When we look for CB- and VB-energies in the two types of  $dI/dV$  spectra, we observe two sets of bands. The two  $dI/dV$  spectra may apparently imply two different materials in the film. It may however be recalled that the same film yielded only one CB and one VB when probed with a Pt/Ir tip. Therefore, the two sets of bands appearing in SP-STs must be due to presence of two domains in the films that were invisible by the Pt/Ir tip. The two CB-energies arising out of the two types of domains are widely separated (as large as 300 meV); the two VBs are less split. Since each  $dI/dV$  spectrum was recorded in both bias directions at a single sweep, we could correlate CBs and VBs. If we compare the band-edges of a domain with those of the other, we find that both the energies are either nearer (red-trace in Figure 6.3c) or farther to  $E_F$  (blue trace in Figure 6.3c). They presumably represent band-energies in the two types of domains. When the band-edges were compared in each set, the CB- and VB-energies could be found to be independent of the tunneling condition.

In each of the 600-odd  $dI/dV$  spectra often recorded with different tip-approach conditions of the antiferromagnetic tip, we have identified the CB- and VB-edges and finally collated the energies in the form of histograms (Figure 6.3d). The histogram for CB-energies could be seen to exhibit two clear peaks. The bands may be marked as  $CB_1$  and  $CB_2$  having energies at 0.60 and 0.99 eV, respectively, away from the Fermi energy. Presence of two peaks in the VB was not as apparent as in the CB; since each  $dI/dV$  spectrum provided the energies in pair, that is measurement of CB- and VB-edges are correlated, we could separate out  $VB_1$  and  $VB_2$  corresponding to  $CB_1$  and  $CB_2$ , respectively. We then could draw two distributions in the VB-histogram as well; the separation between the two VBs turned out to be 150 meV. The histograms too infer

that CB- and VB-energies can be either nearer (CB<sub>1</sub> and VB<sub>1</sub>) or farther (CB<sub>2</sub> and VB<sub>2</sub>) to  $E_F$ . That is, the two band-edges split in such a manner that CB<sub>1</sub> and VB<sub>1</sub> are closer to  $E_F$  whereas CB<sub>2</sub> and VB<sub>2</sub> remained away from  $E_F$ .

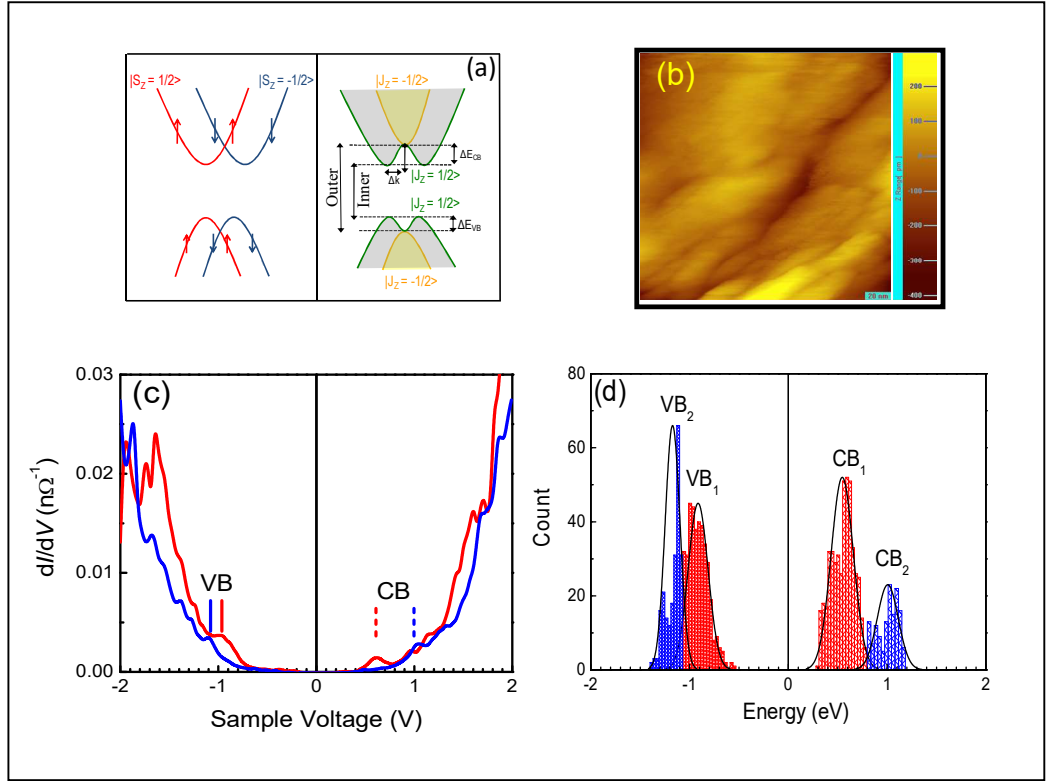


**Figure 6.3.** (a) Schematic representation of Rashba-split bands considering spin angular momentum (left panel) and total angular momentum (right panel). (b) STM topography where the measurement was carried out. (c) Two representative  $dI/dV$  spectra of MAPbI<sub>3</sub> thin films recorded with a chromium-coated antiferromagnetic tip and (d) histogram of band-energies.

It may be recalled that the same film when probed with spin-random electrons (Pt/Ir tip) yielded just one CB- and VB-energies in the histogram. In Figure 6.4a, we have compared a typical  $dI/dV$  spectrum with a Pt/Ir tip with the two sets of spectra obtained with a chromium-coated antiferromagnetic tip. The band-positions of MAPbI<sub>3</sub> obtained for both the tips have been plotted in Figure 6.4b in the form of a band

diagram. A comparison of the band-edges obtained from the two types of tips show that the CB- and VB-energies with a Pt/Ir tip matched the inner pair of energies derived with the chromium-coated tip; that is, with the spin-randomness of injected electrons from the Pt/Ir tip, it always probed the CB- and VB-edges, which had band-energies closer to the  $E_F$  (Figure 6.4b).

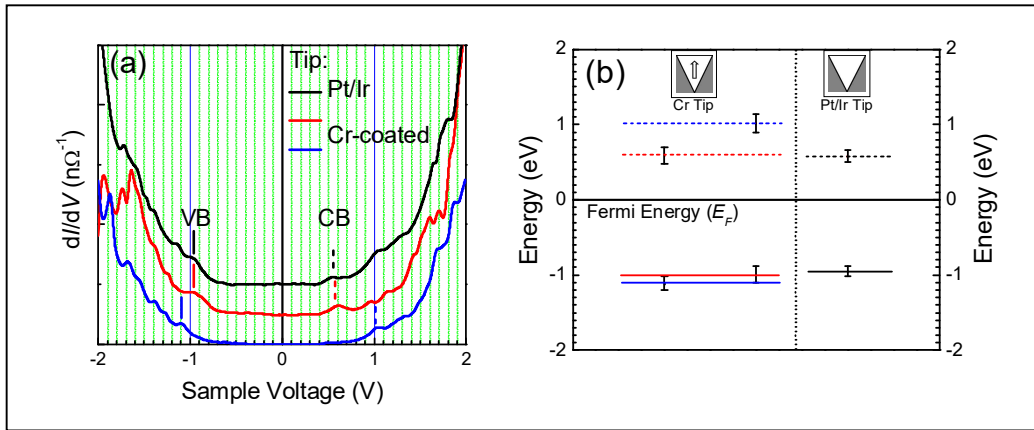


**Figure 6.4.** (a) Comparison of  $dI/dV$  spectra of  $\text{MAPbI}_3$  recorded with a Pt/Ir tip and a chromium-coated antiferromagnetic tip. A Y-offset has been added for clarity of presentation. (b) Band-energies of  $\text{MAPbI}_3$  obtained from the  $dI/dV$  spectra and histograms for the two types of STM-tips.

### 6.3.4. Origin of Two Pair of Bands in $\text{MAPbI}_3$ : Probing Rashba-Split States through SP-STs

Appearance of two pairs of band-edges in a  $\text{MAPbI}_3$  film under the eye of spin-polarized electrons is indeed an interesting observation. Two pairs of band-edges in a single film infer those two domains based on different spin-textures existed in the thin film. As such, the perovskite is known to possess a strong spin-orbit coupling (SOC) due to the presence of high- $Z$  elements in the compound. The SOC parameter, in conjunction with a lack of centrosymmetry on a local scale, can lead to an effective magnetic field and thereby lifting of Kramer's spin-degeneracy of the electrons (Rashba effect) leading to band-splitting in terms of spin-textures [19-21]. It may be stated that

spin-textures are in general used for optical transitions and charge carrier dynamics involving excitons and hence both CB- and VB-energies simultaneously;  $Z$ -component of total angular momentum ( $J_z$ ), on the other hand, is considered and should be conserved when only one band (CB or VB) is probed at a time through injection or withdrawal of electrons, respectively [30-32,48].

In the schematic representation of Rashba-split bands (Figure 6.5), we identified them to possess  $Z$ -component of total angular momentum  $J_z$  of  $-1/2$  and  $+1/2$  implying a spin-texture  $\chi$  of  $-1$  and  $+1$ , respectively. The splitting in VB was smaller than that of CB; this implies that the VB maximum and CB minimum will be at different positions in the  $\mathbf{k}$ -space leading to the formation of an indirect bandgap semiconductor. Here the VB is formed with a major contribution from I( $5p$ ) atomic orbital along with minor involvements from Pb( $6s$ ) and Pb( $6p$ ), whereas the CB arises majorly from Pb( $6p$ ) with a small involvement of I( $5p$ ) orbital. The CB should therefore undergo a larger Rashba splitting due to a higher  $Z$  of lead than that of iodine [19,29]. Also, the CB, which has only a  $p$ -character and hence an orbital angular momentum of  $L = 1$ , in conjunction with a spin angular momentum  $S = 1/2$ , is split into two states with  $J = 1/2$  and  $J = 3/2$  carrying two different total angular momenta ( $J$ ). On the other hand, the  $s$ -character of lead in forming VB with  $L = 0$  is unaffected due to its unique  $J = 1/2$  value [19]; only the  $p$ -character of I( $5p$ ) and Pb( $6p$ ) orbitals hence contributed to the splitting of VB. That is, by considering the SOC parameter of iodine and involvement of I( $5p$ ) orbital in forming the VB, we obtain different  $J$ -values in the VB also. For carrier tunneling, bottom-most CB ( $J = S = 1/2$ ) and top-most VB ( $J = S = 1/2$ ), which are doubly degenerate ( $J_z = \pm 1/2$ ) [48,50], will be of relevance in STS and SP-STs studies.

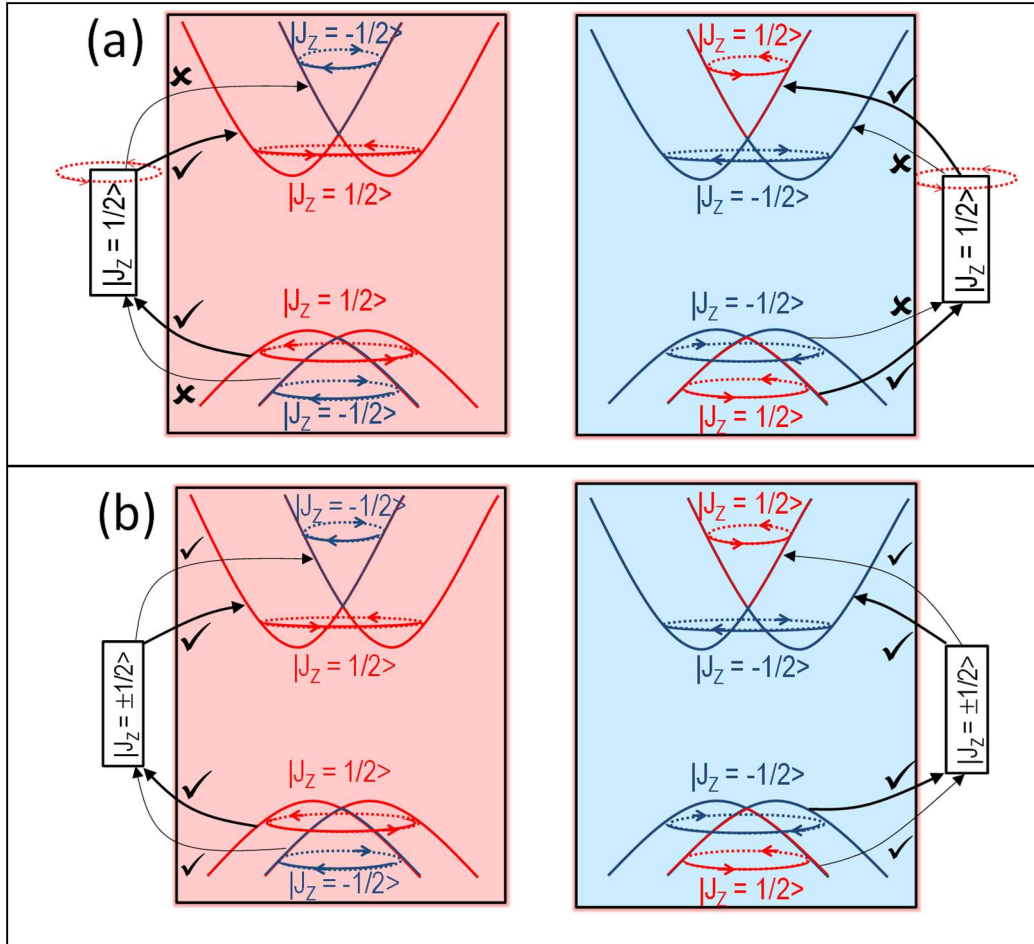


**Figure 6.5.** (a) Schematic representation of electron-tunneling with a chromium coated tip. Rashba band-splitting in two different domains are shown in the left and the right panels. While red-curves represent a  $|J_z = 1/2\rangle$  band, the blue-ones refer to the  $|J_z = -1/2\rangle$  band. A chromium-coated tip ( $L_z = 0$  and  $S_z = 1/2$  due to the  $3d^5 4s^1$  electrons) of SP-STM has been considered to inject up-spin electrons with  $|J_z = 1/2\rangle$ . Thick-arrows indicate tunneling of electrons to the  $J_z$ -matched CB-states and from the matched VB-states. Due to conservation of total angular momentum, tunneling of electrons to/from  $J_z$ -mismatched states (thin-arrows) are not allowed. The two-sets of CB and VB-energies hence appeared due to two types of domains. (b) Schematic representation of electron-tunneling with a Pt/Ir tip. Here both thick- and thin-arrows represent allowed transition to the CB and from the VB.

During tunneling of spin-polarized electrons, time-reversal symmetry dictates that the initial and final state of the tunneling process must possess the same orbital and spin angular momentum. Due to a strong SOC parameter in MAPbI<sub>3</sub>, the two parameters are now coupled together leading to a conservation of  $J_Z$  in lieu of spin or orbital angular momentum, separately. That is, for a tunneling process to a SOC system, the total angular momentum is conserved instead. A spin-change during a tunneling process while conserving  $J_Z$  would have to be absorbed and compensated by an opposite change in the orbital angular momentum leading to the quantum states of tunneling to possess the same total angular momentum eigenvalue (Table 6.1). We may recall that electrons from the chromium-coated tip will have only one value  $J_Z$  which appears due to spin angular momentum of  $4s^1$  electron ( $L_Z = 0$  and  $S_Z = 1/2$ ) [51]; a Pt/Ir tip, on the other hand, will inject both  $J_Z = +1/2$  and  $-1/2$  electrons.

**Table 6.1.**  $L_Z$ ,  $S_Z$ , and  $J_Z$  of states during allowed tunneling processes between a chromium-coated tip and MAPbI<sub>3</sub> through a conservation of total angular momentum.

Tip			Sample			Change During Allowed Tunneling		
$L_Z$	$S_Z$	$J_Z$	$L_Z$	$S_Z$	$J_Z$	$\Delta L_Z$	$\Delta S_Z$	$\Delta J_Z$
0	+1/2	+1/2	0	+1/2	+1/2	0	0	0
			+1	-1/2	+1/2	+1	-1	0
0	-1/2	-1/2	0	-1/2	-1/2	0	0	0
			-1	+1/2	-1/2	-1	+1	0

Since no magnetic field was applied to the material, a spin-equilibrium must occur even in the microscopic scale of the thin film. That is, two possible domains would balance their alignment in the film. Rashba-split bands of the two domains have been represented in the two panes of Figure 6.5a. In each pane, Rashba-split bands have been represented as CB<sub>1</sub> and VB<sub>1</sub> having  $J_Z = +1/2$  and CB<sub>2</sub> and VB<sub>2</sub> with  $J_Z = -1/2$ . That is, the inner CB and VB levels possessed the same  $J_Z$  or spin-textures as proposed

in the spin-allowed transition model [25,26]. When a spin-polarized tip was brought close to the material, tunneling of electrons would occur only when their  $Z$ -component of total angular momenta ( $J_Z$ ) are matched. For example, in a particular domain (left panel of Figure 6.5a), the spin-polarized tip may probe Rashba-split  $CB_1$  and  $VB_1$  which are closer to the  $E_F$  ( $J_Z = +1/2$ ). Similarly, in another domain (right panel of Figure 6.5a), which is anti-parallel to the previous one, the same tip would now probe energies of  $CB_2$  and  $VB_2$  (which are farther to the  $E_F$ ) since they now possess  $J_Z = +1/2$ . Therefore, when SP-STs measurements were made at many different points, two characteristic  $dI/dV$  spectra were obtained; the spectra in Figure 6.3c in fact occur out of schematic representations in the left and right panes of Figure 6.5a.

In Figure 6.5b, we have presented the schematic representation of electron-tunneling with the Pt/Ir tip. Since the tip can now inject/withdraw both types of electrons, half of the electrons find the same CB/VB levels in the two domains as total angular momentum matched states. The Pt/Ir tip simply probed the CB and VB which are nearer to the  $E_F$ , since such a transition is always allowed for one of the two types of electrons injected from the Pt/Ir tip. We hence obtained only one set of band-energies in the  $dI/dV$  spectra of  $MAPbI_3$  film as the CB minimum and the VB maximum. Energy levels obtained with the Pt/Ir tip matched the energies as seen by spin-polarized electrons in one domain (left panel of Figure 6.5a). With a ferromagnetic nickel tip, the same quantum of energy-splitting was observed although the relative position of the bands with respect to the Fermi energy were different due to a different work-function of the metal (Figure 6.6); such a ferromagnetic tip may also introduce stray fields influencing electronic-states of the perovskite.[49]



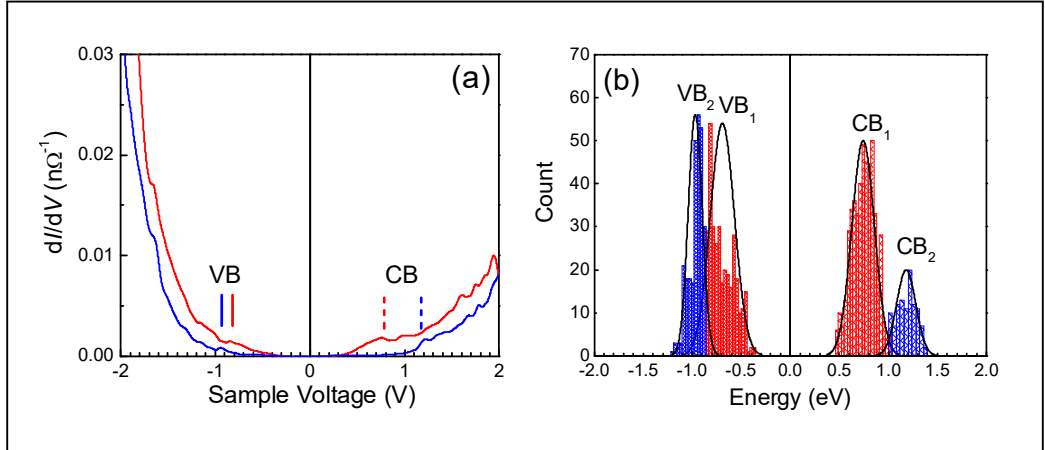


**Figure 6.6.** (a) Two representative  $dI/dV$  spectra of  $\text{MAPbI}_3$  thin films recorded with nickel tip and (b) histogram of band-energies.

### 6.3.5. Spin-Polarized $dI/dV$ Imaging

The analysis of probing Rashba-split states in the perovskite was based on the assumption of spin-equilibrium through two possible domains having different spin-states. It will hence be quite interesting to know or view the spin-states of domains in the material. As such, in  $dI/dV$  images of a film, a material is seen from its energy perspective. With SP-STs and the CB of the material having a larger spin-split, we aimed to probe the spin-states in a domain. That is, the chromium-coated antiferromagnetic tip at a suitable (low) voltage would probe only the domains that have a  $J_Z$ -matched lower-CB. A spin-polarized  $dI/dV$  image was hence recorded at 0.54 V from  $E_F$ , so that the levels only up to that voltage are probed. At such a voltage, the lower of the two CBs (closer to the  $E_F$ ) could be probed, provided the state has a  $J_Z$  matched to that of the spin-polarized electrons; the bias during imaging was kept inadequate, so that the other CB level (away from  $E_F$ ) was never accessed. Neither the CB having a mismatched- $J_Z$  would be probed. Such an image is shown in Figure 6.7a. A high DOS in the image (magenta) implied domains whose lower-CB is  $J_Z$ -matched to

that of the tip. A low DOS similarly indicated the domains whose lower-CB is forbidden for transition. In the spin-polarized  $dI/dV$  image, we find that the two domains were homogeneously distributed. If we look at the scale bar of the image, we notice that the so-called domains may have molecular dimensions. That is, in a  $\text{MAPbI}_3$  film, a molecule itself may have formed a spin-domain.

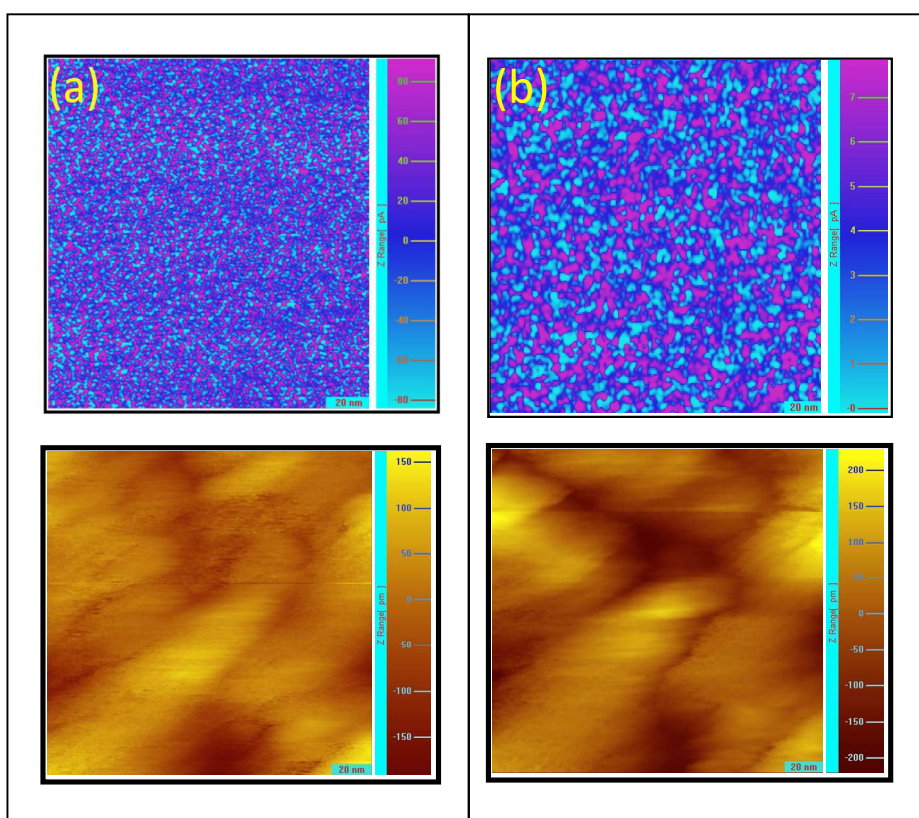


**Figure 6.7.**  $dI/dV$  images of a  $\text{MAPbI}_3$  ultra-thin film recorded (a) with a chromium-coated antiferromagnetic tip to probe the inner and  $J_Z$ -matched CB at 0.54 eV and (b) with a Pt/Ir to probe the CB at 0.54 eV from the  $E_F$ . The SP-STM topographic map of  $\text{MAPbI}_3$  film are also shown where  $dI/dV$  images were recorded.

We also have recorded a  $dI/dV$  image with a Pt/Ir tip at a voltage suitable to probe the CB (Figure 6.7b). With a Pt/Ir tip, a single CB band was available to be

probed by the Pt/It tip all over the film. As compared to the  $dI/dV$  image with a chromium-coated tip, the image with a Pt/Ir tip looked quite homogeneous when a same vertical scale-bar is imagined. A zoomed DOS-scale in the image (Figure 6.7b) allowed us to view the little spatial variation of the electronic properties (not spin related) of the sample that is due to grain boundaries and grain interiors, defects, and inhomogeneity in the film. The grain size obtained in the  $dI/dV$  image with Pt/Ir tip was larger than that when probed with chromium-coated tip. This is due to the fact that domains have almost uniform DOS when energetically seen by the Pt/Ir tip, while the spin-state of a molecule is also read by the chromium-coated tip. The STM topographies of the exact same area, at which  $dI/dV$  images were recorded, are also shown in Figure 6.7 (bottom part). The topographies inferred uniformity of the film-surface. That is, while STM topographies provide only the current-mapping of the surface,  $dI/dV$  images with a spin-polarized tip showed the energy-mapping of the perovskite surface through record of spin-signals as well.

### **6.3.6. Rashba Splitting, Inter-domain Spin-Forbidden Transition Model, and Implications in Solar Cells**

The  $dI/dV$  spectra of  $\text{MAPbI}_3$  recorded with SP-STs have hence provided an experimental observation of Rashba band splitting in the perovskite. Although lowest of the CB and highest of the VB levels have always a matching spin-texture (spin-allowed transition model), the electrons and holes upon photoexcitation would reside in different  $\mathbf{k}$ -space creating an indirect bandgap for recombination. This is due to the fact that the splitting of the two band-edges were different due to involvement of different elements (and hence SOC parameters) in forming the two band-edges. Since the domains have a size of sub-nanometer to a couple of nanometers, quantum of inter-domain recombination should be substantial. For an inter-domain recombination, electrons of a domain and holes in the neighboring domain would have opposing spin-textures; their

radiative recombination would hence be a forbidden process leading to a low recombination rate of photogenerated carriers in MAPbI<sub>3</sub> [14,15,25].

Electrons and holes upon photoexcitation are quite expected to reside in different molecules/domains. Since both the bands of MAPbI<sub>3</sub> are formed through molecular orbitals of the inorganic moieties, the excitons in the perovskite can be considered to be Wannier type [52]; also, due to a large dielectric constant of the material [8], electron-hole pair of an exciton would have a weak Coulomb interaction leading the carriers to reside in different molecules. Instead of intramolecular recombination, intermolecular recombination is hence a likely process in MAPbI<sub>3</sub> if it is not a forbidden transition. With both the bands being Rashba-split, and electrons residing at the CB-minimum of a domain and holes at the VB-maximum of a neighboring domain having opposite  $J_z$  values, intermolecular recombination process will hence be a forbidden transition (Figure 6.8).

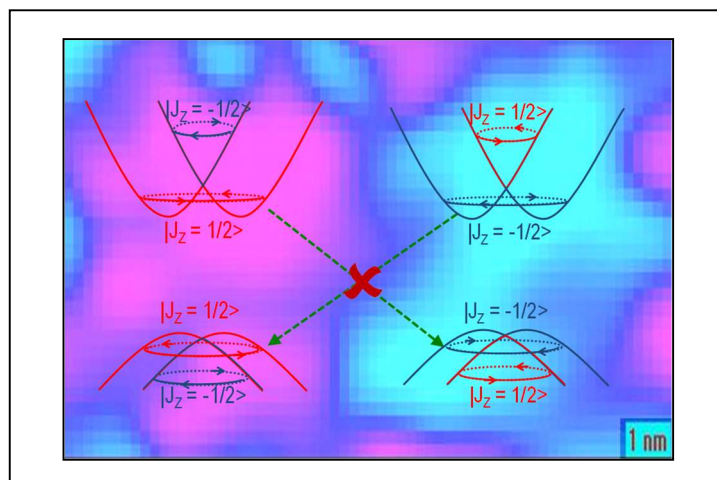


**Figure 6.8.** A schematic representation of Rashba band splitting in two opposing domains. Upon photoexcitation, electrons and holes reside in different positions in the Brillouin zone creating an indirect bandgap and hence led to a slower intra-domain recombination. For inter-domain recombination, electrons of a domain and holes of the neighboring domain do have opposing spin-textures in addition; their radiative recombination is hence a forbidden process (as shown by broken-arrows). Background of the schematic representation is an enlarged section of the  $dI/dV$  image (from Figure 6.7).

Based on the observation of splitting in the two bands, it is tempting to comment on carrier transport in perovskite solar cells. In general, the lowest CB and the highest VB are considered for charge transport through a perovskite and in determining the energy-offset with the carrier-transport layers. With the evidence of splitting of the two bands, both the CBs and both the VBs should in fact be considered while ensuring a type-II band-alignment with the electron- and hole-transport layers for a seamless conduction process. Unless one considers both pair of Rashba-split bands in a perovskite like MAPbI<sub>3</sub> for the conduction process, one would leave those levels from the ambit of charge collection.

## 6.4. Conclusions

We have provided a clear experimental observation of Rashba band splitting in MAPbI<sub>3</sub> that has so far been predicted to occur as a result of a strong SOC parameter and a lack of centrosymmetry in the perovskite. We have elegantly used SP-STs which allows tunneling of spin-polarized electrons to/from only the  $J_z$ -matched bands leaving the mismatched ones invisible. We could observe both the Rashba-split bands, since a spin-equilibrium must occur in the microscopic scale of a film; this necessitated a particular band (say  $J_z = +1/2$ ) to be closer to the Fermi energy in a domain and away from the Fermi energy in the neighboring domain. With the use spin-polarized tip to probe only the  $J_z$ -matched CB and VB throughout the film, we could view both the  $J_z$ -matched split-levels and deliberate on their relative spin-textures as well. We have observed that the two bands split in such a manner that the CB and VB closer to the Fermi energy have the same type of spin-textures; that is, they follow a spin-allowed transition model for carrier recombination. From  $dI/dV$  images of MAPbI<sub>3</sub>, we estimated the dimension of spin-domains to be molecular in size. With Wannier-type of excitons forming in MAPbI<sub>3</sub> upon photoexcitation, the electron and hole would reside in different molecules/domains enforcing only inter-domain recombination; since CB minimum and VB maximum of two neighboring domains have different  $J_z$  values, an

inter-domain transition becomes a forbidden process leading to a low recombination rate of photogenerated carriers in MAPbI<sub>3</sub>.

## 6.5. References

- [1] M. A. Green, A. Ho-Baillie, and H. J. Snaith, *Nat. Photonics* **8**, 506 (2014).
- [2] N. G. Park, M. Gratzel, T. Miyasaka, K. Zhu, and K. Emery, *Nat. Energy* **1**, 16152 (2016).
- [3] M. Saliba, T. Matsui, K. Domanski, J. Y. Seo, A. Ummadisingu, S. M. Zakeeruddin, J. P. Correa-Baena, W. R. Tress, A. Abate, A. Hagfeldt, and M. Gratzel, *Science* **354**, 206 (2016).
- [4] J. S. Manser, J. A. Christians, and P. V. Kamat, *Chem. Rev.* **116**, 12956 (2016).
- [5] W. Shockley and H. J. Queisser, *J. Appl. Phys.* **32**, 510 (1961).
- [6] L. P. Kong, G. Liu, J. Gong, Q. Y. Hu, R. D. Schaller, P. Dera, D. Z. Zhang, Z. X. Liu, W. G. Yang, K. Zhu, Y. Z. Tang, C. Y. Wang, S. H. Wei, T. Xu, and H. K. Mao, *Proc. Natl. Acad. Sci. U. S. A.* **113**, 8910 (2016).
- [7] K. Galkowski, A. Mitioglu, A. Miyata, P. Plochocka, O. Portugall, G. E. Eperon, J. T. W. Wang, T. Stergiopoulos, S. D. Stranks, H. J. Snaith, and R. J. Nicholas, *Energy Environ. Sci.* **9**, 962 (2016).
- [8] S. Govinda, B. P. Kore, M. Bokdam, P. Mahale, A. Kumar, S. Pal, B. Bhattacharyya, J. Lahnsteiner, G. Kresse, C. Franchini, A. Pandey, and D. D. Sarma, *J. Phys. Chem. Lett.* **8**, 4113 (2017).
- [9] C. Wehrenfennig, G. E. Eperon, M. B. Johnston, H. J. Snaith, and L. M. Herz, *Adv. Mater.* **26**, 1584 (2014).
- [10] C. Eames, J. M. Frost, P. R. F. Barnes, B. C. O'Regan, A. Walsh, and M. S. Islam, *Nat. Commun.* **6**, 7497 (2015).
- [11] T. M. Brenner, D. A. Egger, L. Kronik, G. Hodes, and D. Cahen, *Nat. Rev. Mater.* **1**, 15007 (2016).
- [12] A. Miyata, A. Mitioglu, P. Plochocka, O. Portugall, J. T. W. Wang, S. D. Stranks, H. J. Snaith, and R. J. Nicholas, *Nat. Phys.* **11**, 582 (2015).

- [13] G. C. Xing, N. Mathews, S. Y. Sun, S. S. Lim, Y. M. Lam, M. Gratzel, S. Mhaisalkar, and T. C. Sum, *Science* **342**, 344 (2013).
- [14] R. Ihly, A. M. Dowgiallo, M. J. Yang, P. Schulz, N. J. Stanton, O. G. Reid, A. J. Ferguson, K. Zhu, J. J. Berry, and J. L. Blackburn, *Energy Environ. Sci.* **9**, 1439 (2016).
- [15] J.-E. Moser, *Nat. Mater.* **16**, 4 (2016).
- [16] X. Zhang, J. X. Shen, W. N. Wang, and C. G. Van de Walle, *ACS Energy Lett.* **3**, 2329 (2018).
- [17] F. Zheng, L. Z. Tan, S. Liu, and A. M. Rappe, *Nano Lett.* **15**, 7794 (2015).
- [18] Z. G. Yu, *J. Phys. Chem. Lett.* **7**, 3078 (2016).
- [19] M. Kepenekian and J. Even, *J. Phys. Chem. Lett.* **8**, 3362 (2017).
- [20] E. Mosconi, T. Etienne, and F. De Angelis, *J. Phys. Chem. Lett.* **8**, 2247 (2017).
- [21] K. Frohna, T. Deshpande, J. Harter, W. Peng, B. A. Barker, J. B. Neaton, S. G. Louie, O. M. Bakr, D. Hsieh, and M. Bernardi, *Nat. Commun.* **9**, 1829 (2018).
- [22] M. Kepenekian, R. Robles, C. Katan, D. Saponi, L. Pedesseau, and J. Even, *ACS Nano* **9**, 11557 (2015).
- [23] E. M. Hutter, M. C. Gelvez-Rueda, A. Osherov, V. Bulovic, F. C. Grozema, S. D. Stranks, and T. J. Savenije, *Nat. Mater.* **16**, 115 (2017).
- [24] T. Kirchartz and U. Rau, *J. Phys. Chem. Lett.* **8**, 1265 (2017).
- [25] X. Zhang, J. X. Shen, and C. G. Van de Walle, *J. Phys. Chem. Lett.* **9**, 2903 (2018).
- [26] C. Zheng, S. D. Yu, and O. Rubel, *Phys. Rev. Mater.* **2**, 114604 (2018).
- [27] D. Niesner, M. Wilhelm, I. Levchuk, A. Osvet, S. Shrestha, M. Batentschuk, C. Brabec, and T. Fauster, *Phys. Rev. Lett.* **117**, 126401 (2016).
- [28] D. Giovanni, H. Ma, J. Chua, M. Gratzel, R. Ramesh, S. Mhaisalkar, N. Mathews, and T. C. Sum, *Nano Lett.* **15**, 1553 (2015).
- [29] S. B. Hu, H. Gao, Y. T. Qi, Y. X. Tao, Y. L. Li, J. R. Reimers, M. Bokdam, C. Franchini, D. Di Sante, A. Stroppa, and W. Ren, *J. Phys. Chem. C* **121**, 23045 (2017).

- 
- [30] E. M. Chudnovsky, *Phys. Rev. Lett.* **72**, 3433 (1994).
- [31] U. Gennser, M. Schneinert, L. Diehl, S. Tsujino, A. Borak, C. V. Falub, D. Grutzmacher, A. Weber, D. K. Maude, G. Scalari, Y. Campidelli, O. Kermarrec, and D. Bensahl, *Europhys. Lett.* **74**, 882 (2006).
- [32] D. A. Garanin and E. M. Chudnovsky, *Phys. Rev. X* **1**, 011005 (2011).
- [33] T. Warashina, M. Nurmamat, K. Miyamoto, T. Shishidou, M. Taniguchi, A. Kimura, and T. Okuda, *Phys. Rev. B* **94**, 241109 (2016).
- [34] O. J. Weber, B. Charles, and M. T. Weller, *J. Mater. Chem. A* **4**, 15375 (2016).
- [35] T. Wang, B. Daiber, J. M. Frost, S. A. Mann, E. C. Garnett, A. Walsh, and B. Ehrler, *Energy Environ. Sci.* **10**, 509 (2017).
- [36] Z. R. Liang, S. H. Zhang, X. Q. Xu, N. Wang, J. X. Wang, X. Wang, Z. N. Bi, G. Xu, N. Y. Yuan, and J. N. Ding, *RSC Adv.* **5**, 60562 (2015).
- [37] X. F. Tang, M. Brandl, B. May, I. Levchuk, Y. Hou, M. Richter, H. W. Chen, S. Chen, S. Kahmann, A. Osvet, F. Maier, H. P. Steinruck, R. Hock, G. J. Matt, and C. J. Brabec, *J. Mater. Chem. A* **4**, 15896 (2016).
- [38] U. Dasgupta, A. Bera, and A. J. Pal, *ACS Energy Lett.* **2**, 582 (2017).
- [39] L. She, M. Liu, and D. Zhong, *ACS Nano* **10**, 1126 (2015).
- [40] J. Endres, D. A. Egger, M. Kulbak, R. A. Kerner, L. Zhao, S. H. Silver, G. Hodes, B. P. Rand, D. Cahen, L. Kronik, and A. Kahn, *J. Phys. Chem. Lett.* **7**, 2722 (2016).
- [41] C. Li, J. Wei, M. Sato, H. Koike, Z.-Z. Xie, Y.-Q. Li, K. Kanai, S. Kera, N. Ueno, and J.-X. Tang, *ACS Appl. Mater. Interfaces* **8**, 11526 (2016).
- [42] J. Kim, S. H. Lee, J. H. Lee, and K. H. Hong, *J. Phys. Chem. Lett.* **5**, 1312 (2014).
- [43] W. J. Yin, T. T. Shi, and Y. F. Yan, *Appl. Phys. Lett.* **104**, 063903 (2014).
- [44] S. Wang, T. Sakurai, W. Wen, and Y. Qi, *Adv. Mater. Interfaces* **5**, 1800260 (2018).
- [45] D. Marchak, D. Glozman, Y. Vinshtein, S. Jarby, Y. Lereah, O. Cheshnovsky, and Y. Selzer, *Nano Lett.* **12**, 1087 (2012).



- [46] D. C. Milan, J. M. Villalvilla, M. A. Diaz-Garcia, and C. Untiedt, *Appl. Phys. Lett.* **102**, 163307 (2013).
- [47] R. Ohmann, L. K. Ono, H.-S. Kim, H. Lin, M. V. Lee, Y. Li, N.-G. Park, and Y. Qi, *J. Am. Chem. Soc.* **137**, 16049 (2015).
- [48] C. W. Myung, S. Javaid, K. S. Kim, and G. Lee, *ACS Energy Lett.* **3**, 1294 (2018).
- [49] R. Wiesendanger, *Rev. Mod. Phys.* **81**, 1495 (2009).
- [50] Y. Ping and J. Z. Zhang, *J. Phys. Chem. Lett.* **9**, 6103 (2018).
- [51] X. Oudet and G. Lochak, *J. Magn. Magn. Mater.* **65**, 99 (1987).
- [52] L. Q. Phuong, Y. Nakaike, A. Wakamiya, and Y. Kanemitsu, *J. Phys. Chem. Lett.* **7**, 4905 (2016).

This page is intentionally left blank.

# Chapter 7

## Chiral Perovskite: Spin Photovoltaic Effect

*We have introduced a pair of lead-free chiral perovskites toward the detection of circularly polarized light (CPL). The organic-inorganic hybrid perovskites have an integration of a bismuth-based inorganic framework and a chiral organic sub-lattice (R/S-methylbenzylammonium) which introduces chirality into the entire compound. The chiroptical activities of the perovskites under CPL illumination evidence generation of spin-polarized carriers. However, their absorption anisotropy under different CPL illumination is low; the density of photogenerated carriers under the two CPLs is hence mostly similar. Interestingly, due to the intrinsic chirality of the compounds, the perovskites exhibit chirality-induced spin-selectivity (CISS) allowing the transport of one type of spin-half state while blocking the other type. A high value of spin-polarization in the current along the out-of-plane direction has been observed in these lead-free perovskites (as compared to conventional chiral compounds) due to their lower-dimensional form to make them suitable for CPL detection. Accordingly, a spin-dependent photovoltaic effect has been observed in the vertical heterojunction devices; the photocurrent response has been clearly different under left- and right-handed CPL illuminations resulting in photocurrent anisotropy. As a result, the polarization states of CPL photons could readily be detected by investigating the anisotropic current response of the photodetector devices. While a self-powered CPL detector shows a limited (but one of the highest to date) anisotropy factor of 0.3 due to possible spin-flips during the transport process, the factor rose to 0.6 under bias prompting extension of the effective spin-diffusion length.*

## 7.1. Introduction

Together with excellent optoelectronic properties, hybrid halide perovskites have exhibited several spin-related phenomena due to strong spin-orbit coupling (SOC), such as giant Rashba splitting [1-4], spin-triplet formation [5-7], large spin-selective optical Stark effect [8,9], and different magneto-optical properties [10-12]. To enhance the spintronic properties of metal halide perovskites, a chiral organic sub-lattice is introduced to infuse chirality into the entire compound [13-18]. In this regard, chirality is considered an important structural property of certain materials in which right-handed (*R*: rectus) and left-handed (*S*: sinister) chiral compounds possess identical chemical conformation but cannot be superimposed with each other by a mirror transformation resulting in a loss of inversion symmetry [19-21]. Because of the chiroptical activity and superior spintronic properties, chiral perovskites evidenced applications towards circularly polarized light (CPL) detection which is considered in several spin-optoelectronic technologies, such as optical remote sensing, communication of spin-information, quantum computing, quantum cryptography, and quantum optics [13,17,21,22].

In principle, the notion of CPL detection has been developed from the spin-photovoltaic effect where the generation of photocurrent is mostly governed by an imbalance in the generation of the two spin-half states (of electrons/holes) [23,24]. This perception can be considered to distinguish the polarization states of CPL photons; the photocurrent response of those molecules, where chirality could be embedded in their structural property, shows an anisotropic behavior under the right- and left-circularly polarized light (RCP and LCP, respectively) illuminations [25]. Due to their intrinsic chirality-introducing structural properties, thin films of the chiral molecules yield a difference in absorption coefficient towards RCP and LCP illuminations. Accordingly, the density of photogenerated (and spin-polarized) charge carriers as a function of light helicity becomes different in the chiral absorber layer of a device. Such a helicity-dependent photon generation can therefore result in the detection of the polarization information (of a specific CPL photon).

The difference in optical density between RCP and LCP illuminations or the absorption anisotropy of most of the chiral perovskites is however not very large leading to an inadequate difference in the photocurrent under RCP and LCP illuminations. This prompted a search for compounds where the transport is highly spin-selective. In such a scenario, the molecules should satisfy two pre-requisite conditions, such as (1) generation of spin-polarized carriers upon absorption of RCP and LCP in the active layer and (2) selective transport of one type of the spin-polarized charge carriers while blocking the other type, so that the chirality transporting medium acts as an in-situ spin-filter [14,25,26]. An anisotropy in the photocurrent under RCP and LCP illuminations can then be achieved [13,14,17,21,22,25]. With the generation process of spin-polarized carriers is quite natural in chiral compounds, efforts are being made to improve the selectivity of spin-polarized charge transport, which is defined as the spin-polarization of current,  $P$  as:

$$P = \frac{I_{\uparrow} - I_{\downarrow}}{I_{\uparrow} + I_{\downarrow}} \quad (7.1)$$

where,  $I_{\uparrow}$  and  $I_{\downarrow}$  represent the measured currents at a particular voltage for up- and down-spin electrons, respectively. Finally, to quantify the anisotropy of CPL detection, an anisotropy factor of photocurrent response is defined as:

$$g_{\text{current}} = 2 \frac{I_L - I_R}{I_L + I_R} \quad (7.2)$$

where,  $I_L$  and  $I_R$  denote the photocurrent under the LCP and RCP illuminations, respectively [25].

In this direction, a few chiral perovskites fulfilled both the abovementioned conditions. The performance of state-of-the-art CPL detectors based on such perovskites has still not excelled due to low spin-selective charge transport and accordingly a poor anisotropy factor of photocurrent response [17,18,22,27-29]. The spin-selectivity in charge transport, which is known to be originated from the chirality-induced spin-selectivity (CISS) process, remained low due to the use of a lateral device geometry [14,25,26]. It may be noted that CISS occurs mainly for an out-of-plane photocurrent. A high degree of spin-selective transport is hence not achievable in a lateral geometry

involving an in-plane transport making the anisotropy in photocurrent mostly inadequate for the detection of the CPL photons; the absorption anisotropy will hence be the only determining factor in detecting the polarization state.

Herein, we have considered a vertical heterostructure so that spin-selective transport involves out-of-plane photocurrent. In this direction, we have introduced a pair of lead-free chiral perovskites, namely  $(R\text{-MBA})_4\text{Bi}_2\text{Br}_{10}$  and  $(S\text{-MBA})_4\text{Bi}_2\text{Br}_{10}$  towards exhibiting an efficient spin-photovoltaic effect; here MBA represents a methylbenzylammonium cation. These lead-free perovskites have additional advantages over most of the reported perovskites containing high concentrations of lead that could be a potential bottleneck for further applications [13,17,21,22]. Due to their intrinsic chirality-introducing structural properties, the generation of spin-polarized carriers upon absorption of RCP and LCP illuminations is ensured. With a spin-selective charge transport in an out-of-plane direction, the materials having a lower-dimensional structure will act as a superior in-situ spin-filter [14,25,26]. Consequently, the photocurrent response of the chiral perovskites in a vertical geometry under opposite CPL illuminations becomes strongly spin-polarized and can transduce a significantly large anisotropy in electrical signals. Due to a high spin-polarization of current ( $\sim 80\%$ ) in the perovskites, a large anisotropy factor of 0.3 could be achieved which is one of the highest till now in self-powered devices based on chiral perovskites. The factor rose to 0.6 under bias prompting an extension of the spin-diffusion length.

## 7.2. Experimental

### 7.2.1. Materials

$(R)$ -(+)- $\alpha$ -methylbenzylamine ( $R$ -MBA, 98%),  $(S)$ -(-)- $\alpha$ -methylbenzylamine ( $S$ -MBA, 98%),  $(rac)$ -( $\pm$ )- $\alpha$ -methylbenzylamine ( $rac$ -MBA, 98%), bismuth(III) bromide ( $\text{BiBr}_3$ , 99%), poly(3,4-ethylenedioxythiophene) polystyrenesulfonate (PEDOT:PSS),  $N,N$ -anhydrous-dimethyl formamide (DMF, 99%), dimethyl sulfoxide (DMSO, 99%), and 57% aqueous hydrobromic acid (HBr) were purchased from Sigma Aldrich

Chemical Co. Phenyl-C61-butyric acid methyl ester (PCBM, 99%) was procured from M/s SES Research, Houston, TX, USA. While the amines, PEDOT:PSS, and HBr were stored in a refrigerator, BiBr<sub>3</sub>, PMMA, PCBM, and DMF were kept in a nitrogen-filled glovebox where both water and moisture levels were below 0.1 ppm. The other compounds were kept in an ambient condition.

### **7.2.2. Synthesis of the Chiral Perovskite Thin Films**

The chiral perovskites were synthesized following a conventional slow evaporation technique which is typically used for the formation of similar compounds [14,25,30]. To be specific, 0.8 mmol of BiBr<sub>3</sub> (0.359 g) and 1.6 mmol of *R*- or *S*- or *rac*-MBA (0.206 mL) were dissolved in an aqueous solution of 48% HBr (7 mL) and stirred for 15 min. The solutions were heated to 60 °C for 20 min and then allowed to cool down to room temperature. After slow evaporation of the solvent, yellow crystallites were found to form after two days. The crystallites were collected by decanting and ground thoroughly to form powders of the chiral perovskites.

Thin films of *R*-, *S*-, and *rac*-perovskites were cast on different substrates which were cleaned through a conventional protocol (soap water, deionized water, acetone, and isopropanol in sequence in a bath-sonicator, 10 min each) and then treated with UV-ozone for 15 min. The precursor solutions (1 M) of *R*-/*S*-/*rac*-perovskite thin films were prepared inside the glovebox by dissolving the respective chiral perovskite crystallites in DMF. The as-prepared solution was stirred overnight and then spun on the precleaned substrates at 2500 rpm for 30 s. The films were annealed at 80 °C for 10 min to ensure complete evaporation of the solvent and formation of the perovskite phase.

### **7.2.3. Spin-Polarized (Magnetic) Conductive Atomic Force Microscopy (mC-AFM)**

Spin-polarized (magnetic) conductive atomic force microscopy (mC-AFM) was carried out in a contact mode of a Nanosurf FlexAFM with a ferromagnetic Co-Cr tip

(spring constant  $\sim 3$  N/m) which could be pre-magnetized by applying a strong magnetic field. Current versus voltage ( $I$ - $V$ ) characteristics were acquired by ramping the voltage from  $-2.5$  to  $+2.5$  V in 80 steps. The bias was applied to the indium tin oxide (ITO) coated substrate electrode, on which films were deposited, with respect to the tip; the ITO substrate had a surface resistance of  $15 \Omega/\text{square}$ . With the Co-Cr tip being magnetized towards different orientations (up or down), we recorded  $I$ - $V$  characteristics at many different points on the thin films under dark conditions.

#### 7.2.4. Fabrication and Characterization of Devices

The devices were fabricated on patterned ITO-coated glass substrates. The general device architecture was ITO/PEDOT: PSS/chiral perovskite/PCBM/aluminum. A thin film of PEDOT: PSS was spun at 3000 rpm followed by thermal annealing at  $150$  °C in the air for 20 min to form a hole-transport layer (HTL). Each of the  $R$ - $S$ - $rac$ -perovskite solutions was then spun and the films were annealed inside the glovebox. After cooling the film down to room temperature, a 20 mg/mL solution of PCBM in anhydrous chlorobenzene was spun at 2500 rpm and further annealed at  $100$  °C to form an electron-transport layer (ETL). The formation of sandwiched structures was finally completed by thermal evaporation of 100 nm thick aluminum strips (orthogonal to the ITO ones) as the top electrode. Each of the photovoltaic cells had an effective area of  $10 \text{ mm}^2$  as defined by the overlap of ITO and aluminum strips.

The spin-photovoltaic response ( $I$ - $V$  characteristics) of the devices was recorded under CPL illumination by placing the devices in a shielded vacuum chamber that was fitted with a quartz window. As a source of illumination, a high-intensity solar simulator (TriSOL, OAI Instruments, USA) was used. Monochromatic light was obtained with the use of an Oriel Cornerstone monochromator (model 130). Circularly polarized light was obtained by using a quarter waveplate followed by a linear polarizer. The state of polarization (LCP or RCP) was determined by changing the angle of the quarter waveplate to  $45^\circ$  and  $135^\circ$ , respectively.  $I$ - $V$  responses of the devices under LCP and RCP illuminations were recorded with a Keithley 2636A Sourcemeter. In addition, the



time-response of the devices' photocurrent at zero bias was recorded by using a Keithley 617 electrometer. All the instruments were operated through software. For intensity-dependent studies, the power density of light illumination was controlled using a series of integrated neutral density filters; the intensities were measured by a power meter (Newport Corporation, USA, model 1918C).

## **7.3. Results and Discussion**

### **7.3.1. Basic Characterization of Materials**

First of all, we aimed to confirm the formation of the phase-pure lead-free chiral perovskites through conventional characterization techniques. The hybrid structure is formed with two sub-lattices based on organic (MBA)<sup>+</sup> and inorganic [Bi<sub>2</sub>Br<sub>10</sub>]<sup>4+</sup> motifs. In this 0D structure, the bismuth halide octahedra share their edges through two bromines forming the [Bi<sub>2</sub>Br<sub>10</sub>]<sup>4+</sup> dimer. The voids between the dimers are occupied by the organic (MBA)<sup>+</sup> cations which can be either right-handed (*R*) or left-handed (*S*) enantiomer in introducing chirality into the entire hybrid structure through a ligand-to-metal charge transfer (LMCT) principle [27]. Hence, the crystal structures of both *R*- and *S*-perovskites remain identical, although they cannot be superimposed through a mirror transformation [17,18,21]. In Figure 7.1a, XRD patterns of *R*-, *S*-, and *rac*-perovskite thin films have been presented; a series of diffraction peaks corresponding to highly oriented crystal grains could be observed. The experimental results were compared with simulated patterns (CIF data: CCDC 187300-1873001) to confirm the phase purity of the compounds possessing a monoclinic crystal structure with the *P*2<sub>1</sub> space group [30]. However, the *rac*-perovskite thin film crystallizes into an achiral space group *P*2<sub>1</sub>/*c*. It may be also noted that the organic ammonium cation forms asymmetric hydrogen bonding interactions with the [Bi<sub>2</sub>Br<sub>10</sub>]<sup>4+</sup> dimer. These distortions result in the absence of both inversion and mirror symmetry even in the inorganic sublattice which makes the unit cell of the *R*- and *S*-perovskites compound strongly chiral. On the other hand, such asymmetric hydrogen bonding interaction is not present in the *rac*-perovskite.

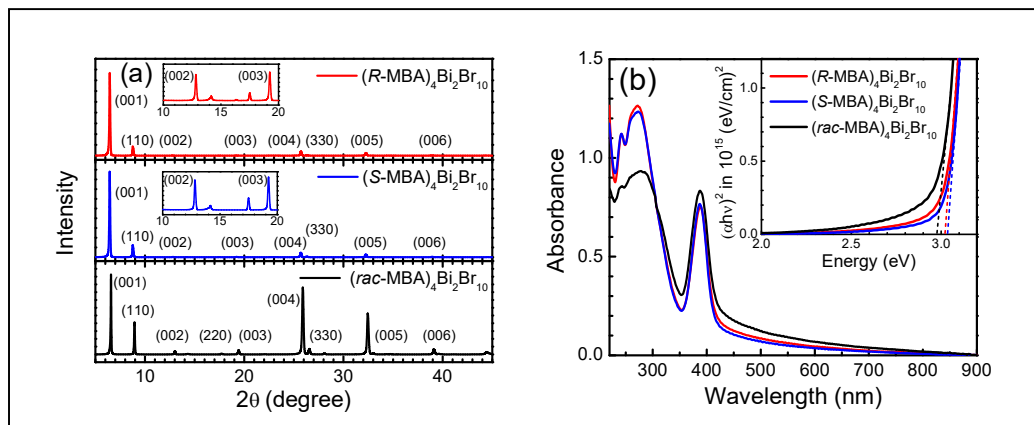


**Figure 7.1.** (a) XRD patterns and (b) optical absorption spectra of  $(R/S/rac\text{-MBA})_4\text{Bi}_2\text{Br}_{10}$  perovskite thin films deposited on quartz substrates. The inset of (b) represents Tauc plots of the materials.

We have further studied the optical absorption spectra of *R*-, *S*-, and *rac*-perovskites (Figure 7.1b). The excitonic feature at 387 nm could be observed in all the compounds that is conventional in other chiral perovskites as well. An additional peak at higher energy ( $\sim 270$  nm) representing an inter-band  $\pi\text{-}\pi^*$  transition of MBA molecules [25,27] was also observed in the absorbance spectra. The optical bandgap of the compounds, as calculated from Tauc plots (inset of Figure 7.1b) was around 3.0 eV and invariant in the three perovskites. On the basis of the abovementioned characterizations and indistinguishable results in *R*-, *S*-, and *rac*-perovskite thin films, we proceeded with the studies of the spin-photovoltaic effect (*vide infra*) which should otherwise not become affected or differ due to a difference in structure and the absorbance of unpolarized light.

### 7.3.2. Chiroptical Activity under CPL Illumination

As conventional optical absorption spectroscopy was inadequate to distinguish these chiral compounds, we proceeded to record their chiroptical response through circular dichroism (CD) spectroscopy under CPL illumination. Due to different absorption coefficients of *R*-, and *S*-perovskite thin films under LCP and RCP light, the chiral perovskites are expected to exhibit an optical anisotropy and consequently facilitate different quantum of light absorption [13,16,25,27]. Theoretically, such a chiroptical response originates from a finite magnetic and electric transition dipole moment, producing a non-zero rotational strength ( $\vec{R}$ ) as expressed by:

$$CD \propto \vec{R} = \text{Im}[\langle \psi_s | \vec{\mu} | \psi_j \rangle \cdot \langle \psi_j | \vec{m} | \psi_s \rangle] = \text{Im} [\mu_{sj} \cdot m_{js}] \quad (7.3)$$

where,  $\psi_s$  and  $\psi_j$  denote the wave functions of the ground and excited states, respectively; the corresponding electric and magnetic transition dipole moments (eigenvalues) are represented as  $\mu_{sj}$  and  $m_{js}$  [27]. As the chiral perovskites do not superimpose with each other by a mirror transformation, the term  $[\mu_{sj} \cdot m_{js}]$  would be non-zero due to a lack of centrosymmetry. A distinct CD response should thereby be obtained in chiral perovskites upon polarized light illumination [17,18,21].

In Figure 7.2a, the CD spectra of the compounds in transmission geometry have been presented. The obtained CD signal was calculated through:

$$CD = \Delta A \left( \frac{\ln 10}{4} \right) \left( \frac{180000}{\pi} \right) \quad (7.4)$$

where,  $\Delta A$  is the difference in the optical density (OD) under the LCP and the RCP illuminations [25]. It may be noted that the chiroptical response of the individual chiral ligands (*R/S*-MBA<sup>+</sup>) appears at high energies (~270 nm) [27]. Hence, the appearance of CD signal near the excitonic peak at 380 nm suggests that there is a chirality transfer from the chiral organic ligands to the inorganic layers through the LMCT principle as mentioned earlier [27]. In contrast, no CD signature was observed in the *rac*-perovskite (Figure 7.2a) due to its centrosymmetric structure. Although the *R*- and *S*- perovskites exhibited CD spectra at the same wavelength, a distinct CPL absorbance anisotropy was

observed in the thin films with opposite polarity (Cotton effect). Such observation suggests that the *R*-perovskite absorbed a larger density of LCP photons than the RCP ones; likewise, the layer of *S*-perovskite absorbed a larger density of RCP photons than the LCP ones.

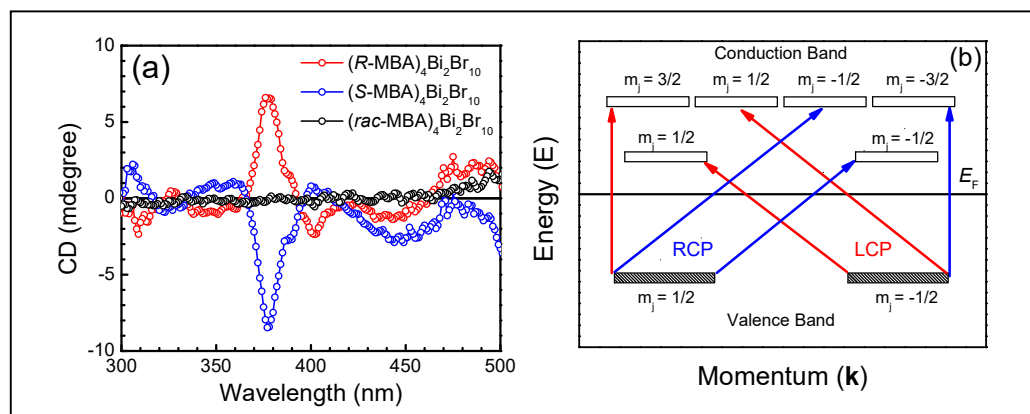


**Figure 7.2.** (a) Circular dichroism (CD) spectra of  $(R/S/rac\text{-}MBA)_4Bi_2Br_{10}$ . The CD polarities of the *R*- and *S*-perovskites are opposite to each other while *rac*-perovskite shows no signature of CD. (b) Proposed optical selection rule and generation of spin-polarized carriers under a RCP and a LCP illumination, respectively. The scheme is independent of the intrinsic chirality of the system.

As the absorption of LCP and RCP illuminations in the chiral perovskites are different, it would generate different exciton densities in an active layer of these compounds upon photoexcitation; that is, the absorbance depends on the chirality of the compound vis-à-vis the polarization states of CPL. Upon exciton dissociation, this would thereby lead to a different density of spin-polarized charge carriers under the LCP and the RCP illumination. Here, we first propose the scheme of spin-polarized carrier generation in the active layers upon CPL illumination based on the optical selection rule (Figure 7.2b). In this regard, it is customary to mention that circularly polarized photons possess a total angular momentum ( $J$ ) of unity ( $\hbar$ ); more specifically, the  $Z$ -component of  $J$ , that is  $J_Z$  of RCP and LCP photons can either be  $+\hbar$  or  $-\hbar$  [27]. When RCP or LCP photons are absorbed by any of the chiral perovskites,  $J_Z$  of the

photons is transferred to the compound; the  $J_z$  of the chiral perovskites is thereby raised or lowered by unity depending on the polarization states of the absorbed CPL. To conserve the total angular momentum, interband transitions would take place followed by the generation of spin-polarized charge carriers. To be specific, a particular chiral perovskite (independent of the chirality) under LCP illumination would yield charge carriers of which 67% will have a spin-up state and 33% will possess a spin-down state. Under RCP illumination, the spin-polarization of photogenerated charge carriers will be reversed: 33% of the carriers will have a spin-up state and 67% of them will have a spin-down state in a chiral perovskite. If a spin-orbit coupling (SOC) parameter due to the presence of a high  $Z$  element (bismuth) is taken into consideration in addition to the chirality-induced breaking of centrosymmetry, a Rashba splitting is indeed expected to occur in the electronic bands [1-4]. However, the analysis of the photogeneration of spin-polarized carriers will remain invariant under such a consideration.

Although the generation of spin-polarized charge carriers would definitely lead to a spin-photovoltaic effect, it is not enough to distinguish the polarization state of CPL photons as the total spin-polarized photocurrent would be the same for both LCP (67% spin-up and 33% spin-down) and RCP (33% spin-up and 67% spin-down) illuminations. In the CD spectra of the chiral perovskites (Figure 7.2a), the absorption anisotropy in the compounds as per Equation (4) is small (0.1%); the CPL photons hence did not produce a large anisotropic signal [25,27]. In this direction, improvement in the anisotropy of CPL detection can be achieved (in terms of significantly large anisotropic current response under the two CPL illuminations) if the transport of one of the two spin-half states is preferred or blocked.

### **7.3.3. Spin-Dependent Charge Transport: Chirality-Induced Spin-Selectivity (CISS) Effect**

In order to restrict the transport of one type of carrier, that is either spin-up or spin-down carriers, CISS is considered to be an important parameter in chiral materials.

Here the chirality of the compound in the charge-transport layer selects one of the two spin-half states for transport while blocking the other [14,25]. Herein, we have investigated the spin-selective charge transport properties of the *R*-, *S*-, and *rac*-perovskite thin films in an out-of-plane direction to show that the resultant current depends strongly on the chirality of the compound in the active layer. That is, we aimed to evidence how a layer of chiral perovskites acts as an in-situ spin-filter.

In this direction, spin-polarized mC-AFM measurements were carried out to demonstrate spin-dependent vertical charge transport in the two chiral perovskites (Figure 7.3a). For each chiral perovskites, two sets of measurements were carried out after the magnetization direction of a tip was made “up” or “down”. The resulting current indicated the vertical charge transport through the chiral perovskite active layer where the helical potential of the chiral center controlled the rate of charge transfer. Since the two measurements had to be made at different points on a film of a chiral perovskite, we eliminated the localized defects (if any) by recording a large number of *I-V* characteristics on the films. The average *I-V*s achieved for *R*-, *S*-, and *rac*-perovskite thin films are shown in Figures 7.3b-d under the two magnetization directions (up or down) of the ferromagnetic tip. For the *R*-perovskite film, we have observed a much higher current when the tip was magnetized in the up-direction as compared to that when the magnetization direction of the tip was “down”. The results infer that spin-up charge carriers are preferentially transferred through the *R*-perovskite film filtering out the spin-down ones. For the *S*-perovskite film, on the other hand, the current was higher when the tip was magnetized in the down-direction implying ease of transport for the spin-down charge carriers. The *rac*-perovskite films did not show any preference towards the transport of the two types of carriers and yielded identical *I-V* characteristics with the two tips (Figure 7.3d). Hence, we conclude that *R*-perovskite possesses the ability to selectively transport spin-up charge carriers, while *S*-perovskite prefers the transport of spin-down carriers. The results, while establishing that the layers of the chiral perovskites acted as a spin-filter due to a spin-selective nature of charge

transport, also paves the path for the detection of polarizability in a circularly-polarized light.

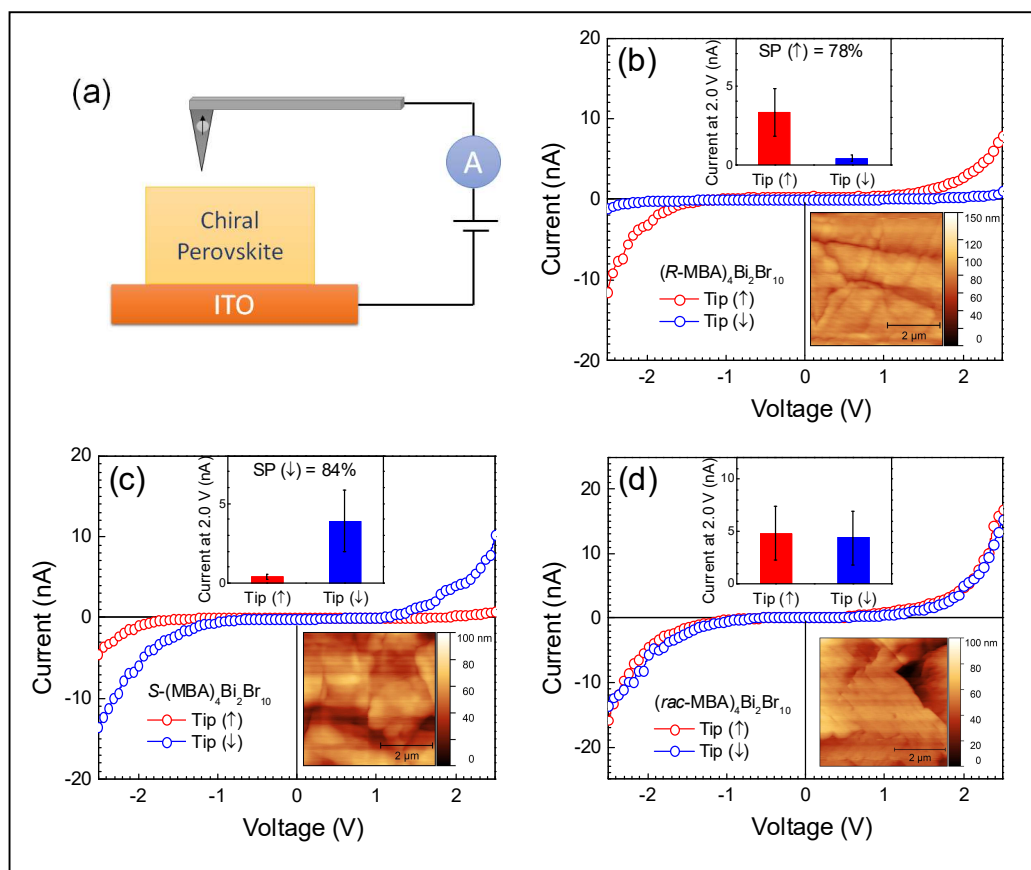


**Figure 7.3.** (a) Schematic representation of *mC*-AFM measurement method to study the spin-selective charge transport. Average current versus voltage characteristics of (b)  $(R\text{-MBA})_4\text{Bi}_2\text{Br}_{10}$ , (c)  $(S\text{-MBA})_4\text{Bi}_2\text{Br}_{10}$ , and (d)  $(rac\text{-MBA})_4\text{Bi}_2\text{Br}_{10}$  perovskites; the probe was magnetized in the upward (red) and downward (blue) directions. The two insets of each graph show (i) a quantitative comparison of current at 2.0 V in deriving spin-polarization (SP) of current and (ii) a representative topography of the films where some measurements were carried out.

Before we proceed in that direction, it is necessary to quantify the out-of-plane spin-selective charge transport, which can be defined as the spin-polarization of current,  $P$ :

$$P = \left( \frac{|I_{\uparrow} - I_{\downarrow}|}{I_{\uparrow} + I_{\downarrow}} \right)_{V=2.0V} \quad (7.5)$$

where,  $I_{\uparrow}$  and  $I_{\downarrow}$  represent the measured currents at 2.0 V when the magnetization of the tip pointed “up” or “down”, respectively. A remarkably high magnitude of  $P$ , around 78% and 84%, was observed for the  $R$ - and the  $S$ -perovskite, respectively. The observed value of spin-polarization is higher than commonly reported chiral compounds and comparable to that of lead-based chiral perovskites [14,26,31]. Primarily, such a high value of spin-polarization originates due to the lower dimensional structure of the bismuth-based chiral perovskites where the chirality per volume will be significantly larger than that in higher dimensional (2D and quasi-2D) chiral perovskites.

When the (little) anisotropy in photocarrier generation in a chiral perovskite is majorly augmented with spin-selective charge transport through the perovskite layer in a sandwiched geometry, the detection of polarizability in a circularly polarized light can truly be envisaged. It may be recalled that in a layer of  $R$ -perovskite, 67% spin-up and 33% spin-down carriers are ideally generated under an LCP illumination in contrast to 33% spin-up and 67% spin-down carriers under an RCP illumination. Now, as transport of spin-up carriers is favorable in the  $R$ -perovskite, it can be stated that spin-up carriers would contribute to yielding higher spin-polarized photocurrent upon an LCP illumination; an RCP illumination in the same chiral compound would result in a significantly less photocurrent and thereby bring forward anisotropy in photocurrent. A device based on a layer of  $S$ -perovskite under RCP illumination would similarly have a higher photocurrent in the external circuit as compared to that under an LCP illumination. Hence, either of the devices should anyway offer anisotropy in photocurrent due to the generation of spin-polarized carriers and spin-selective charge transport.



### 7.3.4. Spin-Photovoltaic Response and CPL Detection

In the light of the abovementioned discussion, the detection of CPL in both the *R*- and the *S*-perovskites has been carried out. For each of the devices, LCP and RCP illuminations were considered. Based on the CD spectra, the distinguishing ability between the RCP and the LCP lights is expected to be at around 380 nm. We accordingly chose a monochromatic (380 nm) RCP or LCP illumination for the measurements. *I-V* characteristics of the devices based on *R*-, *S*-, and *rac*-perovskites were recorded under dark and the two illumination conditions. The intensity of the light was 10.2 mW/cm<sup>2</sup> for both RCP and LCP illuminations. While the device architecture and experimental setup for CPL detection have been illustrated in Figure 7.4a, the *I-V*'s of the three devices have been presented in Figure 7.4b through Figure 7.4d. In devices based on the *R*-perovskite, a higher photocurrent response was observed under an LCP illumination as compared to an RCP one. In contrast, the device based on a layer of *S*-perovskite returned a higher photocurrent response when the illumination was RCP in nature. As the intensity of LCP and RCP light and other physical measurement conditions remained invariant, a difference in photocurrent under LCP and RCP illumination indicated an intrinsic distinguishing ability of the perovskites towards detection of circular polarization of CPL. The anisotropy factors (as defined in Equation 7.2) of *R*- and *S*-perovskites have been presented in the inset of the respective figures; such a high value of the current anisotropy factor indicates the exceptional merit of these chiral perovskites and the device geometry towards the CPL detection. The control experiments with *rac*-perovskites have resulted in a similar *I-V* response for LCP and RCP photons; since no significant difference in the photocurrent response was observed under the two illuminations, we could further conclude that the distinguishable ability of the LCP and RCP photons towards anisotropy of photocurrent originated from the different chirality of the *R*- and *S*-perovskites. Finally, the rationale for achieving anisotropy in the photocurrent output in devices based on the *R* and *S*-perovskites upon LCP (or RCP) illumination and the relative contribution of spin-polarized carriers towards photocurrent generation have been depicted in Table 7.1.

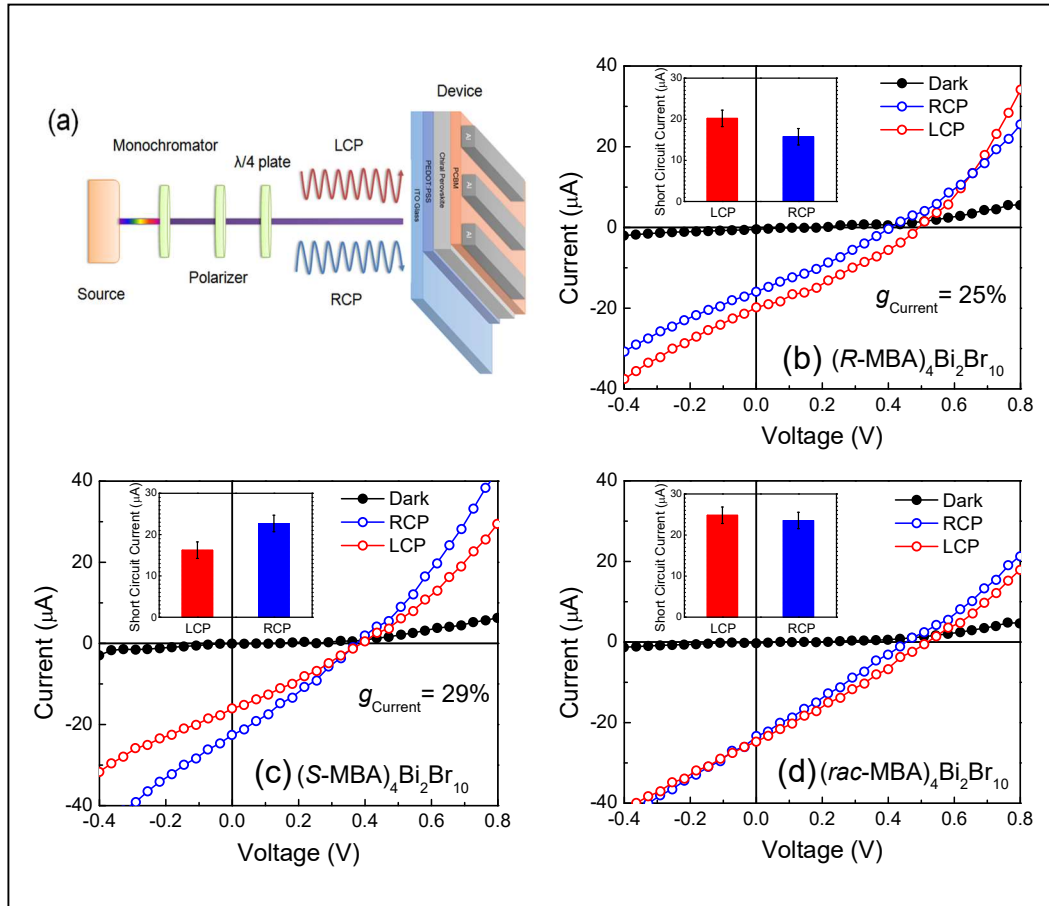


**Figure 7.4.** (a) Schematic representation of the experimental setup for CPL detection. Current versus voltage characteristics of the devices based on (b)  $(R\text{-MBA})_4\text{Bi}_2\text{Br}_{10}$ , (c)  $(S\text{-MBA})_4\text{Bi}_2\text{Br}_{10}$ , and (d)  $(\text{rac-MBA})_4\text{Bi}_2\text{Br}_{10}$  perovskites under dark and RCP and LCP illuminations. Inset of the plots shows quantitative comparison of short-circuit currents; anisotropy factor of the current response,  $|g_{\text{Current}}|$  has been quoted in each inset.

**Table 7.1.** Contribution of the concentration of spin-polarized carriers and spin-selectivity in carrier transport towards photocurrent under different CPL illuminations.

Chiral Perovskite	Polarization state of CPL	Concentration of spin-polarized carriers		Spin-selectivity in carrier transport		Expected photocurrent	CPL sensitivity of the material
		Spin-up (%)	Spin-down (%)	Spin-up	Spin-down		
(R-MBA) <sub>4</sub> Bi <sub>2</sub> Br <sub>10</sub>	RCP	33	66	High	Low	Small	LCP
	LCP	66	33	High	Low	Large	
(S-MBA) <sub>4</sub> Bi <sub>2</sub> Br <sub>10</sub>	RCP	33	66	Low	High	Large	RCP
	LCP	66	33	Low	High	Small	

The devices based on the chiral perovskites under illumination have exhibited a short-circuit current (Figures 7.4b-c) implying the existence of a built-in potential that drove the charge carriers in the photodiodes. Hence, the devices can act as self-powered photodetectors without the need for an additional electric field. In this direction, we have further proceeded to study the zero-bias photocurrent response of the devices,  $I_{ph} = I_{\text{illumination}} - I_{\text{dark}}$  as a function of time vis-à-vis their recyclable response under RCP and LCP illumination, respectively (Figures 7.5a-c). Here  $I_{\text{illumination}}$  and  $I_{\text{dark}}$  represent current under a CPL illumination and dark, respectively. At zero bias, the  $I_{\text{dark}}$  amounts to the current appearing due to the built-in field developed out of the metal electrodes having dissimilar work functions. In addition, responsivity ( $R^*$ ) and detectivity ( $D^*$ ) of such photodetectors were calculated by the following equations and have been presented in Table 7.2:

$$R^* = \frac{I_{ph}}{PA} \quad (6)$$

$$D^* = \frac{R^*}{\left(\frac{2qI_{\text{dark}}}{A}\right)^{\frac{1}{2}}} \quad (7)$$

where  $P$  is the intensity of light (irradiation power density),  $A$  the active area of the devices, and  $q$  is the elementary charge. Based on the performance of previously reported photodetectors based on other chiral perovskites, the responsivity and

detectivity of these devices were found to be comparable [17,21,28]. In addition, the current response, responsivity, and detectivity of the photodetectors were also investigated as a function of light intensity by using a series of neutral density filters (Figure 7.5d-i). The photocurrent increased almost linearly ( $I_{\text{ph}} \propto P^{0.8}$ ) with the illumination intensity since the current is expected to be proportional to the density of photons generated in the device. At high light intensities, a minor deviation from the linearity was observed that may have appeared due to the defects present in the hybrid halide perovskites [32]. The conduction process was hence limited by the carriers generated in the devices upon illumination. The responsivity and detectivity however decreased with the light intensity; such dependence, which is common in other reported devices [33,34], is known to be due to a photogating effect and scattering of more photons at higher illumination intensities.

**Table 7.2.** Comparison of photodetection parameters based on different chiral perovskites at zero bias. The wavelength and intensity of the incident light were 380 nm and 10.2 mW/cm<sup>2</sup> respectively.

Chiral Perovskites	CPL	Photocurrent ( $\mu\text{A}$ )	Responsivity (mA/W)	Detectivity (Jones $\times$ $10^{11}$ )	Anisotropy $ g_{\text{Current}} $
<b>(R-MBA)<sub>4</sub>Bi<sub>2</sub>Br<sub>10</sub></b>	RCP	15.1	14.8	1.5	0.25
	LCP	19.1	18.7	1.6	
<b>(S-MBA)<sub>4</sub>Bi<sub>2</sub>Br<sub>10</sub></b>	RCP	21.5	21.1	2.1	0.29
	LCP	16.1	15.8	1.6	
<b>(rac-MBA)<sub>4</sub>Bi<sub>2</sub>Br<sub>10</sub></b>	RCP	24.7	24.2	2.5	Negligible (0.03)
	LCP	25.5	25.0	2.6	

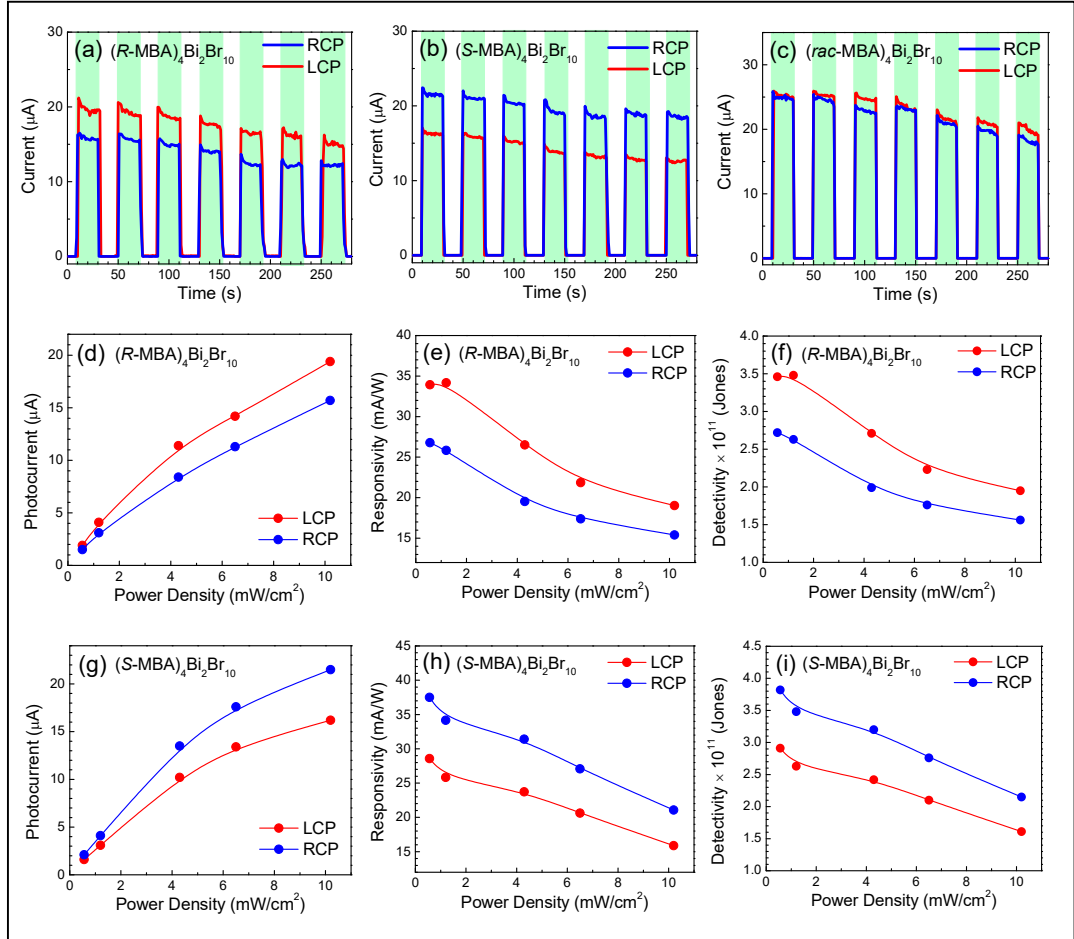


**Figure 7.5.** Variation of the absolute photocurrent in devices based on (a)  $(R-MBA)_4Bi_2Br_{10}$ , (b)  $(S-MBA)_4Bi_2Br_{10}$ , and (c)  $(rac-MBA)_4Bi_2Br_{10}$  under 380 nm RCP and LCP illumination at zero bias as a function of time. Photocurrent response, responsivity, and detectivity of (d-f)  $(R-MBA)_4Bi_2Br_{10}$  and (g-i)  $(S-MBA)_4Bi_2Br_{10}$  perovskites, respectively under LCP and RCP illumination (380 nm) with different light intensities (power densities).

Despite the moderate responsivity and detectivity, the photocurrent anisotropy was found to be significantly high in devices based on both *R*- and *S*-perovskites (Figure 7.6a). It may be recalled that a high value of the current anisotropy factor is considered as the most important figure of merit during the CPL detection. Needless to state, such

high anisotropy originates from a (chirality induced) spin-selective charge transport in the compound; CISS will be much higher in these lower dimensional bismuth-based chiral perovskites due to a larger volume fraction of the chirality compared to the 2D and quasi-2D perovskites. More importantly, the vertical device structure also aids in sustaining such a spin-selective charge transport. Our results hence show that these lead-free chiral perovskites are promising materials for CPL detection in the UV region.

With a high value of the spin-polarization of current,  $P$ , or the current anisotropy under dark conditions (as high as 80% or above), one can expect the photocurrent anisotropy to be high as well. A lower value of the anisotropy in the photocurrent achieved in the device may hence imply that the spin-flips occurred during the carrier transport. That is, the spin diffusion length of the carries limited the photocurrent anisotropy. Although self-powered photodetection has its own merit as the required measurement setup is quite straightforward, we considered the application of an external bias to promote a faster spin transport and thereby larger photocurrent anisotropy which would be beneficial. Here the bias extends the effective spin-diffusion length within the stipulated decay time constant of spin polarization. In this direction, we have derived the variation of photocurrent anisotropy as a function of applied negative voltage where the dark current is practically zero (Figure 7.6b). We have observed that the devices returned a high value of the anisotropy, up to 60%, as the external voltage facilitated faster spin-transport before a spin-flip could take place. It may also be stated that the anisotropy factor is independent of the light intensity (Figure 7.6c). As a result, it is concluded that even for very low intensity of CPL photons, these photodetectors under the application of a bias are quite capable of drawing a significantly large anisotropic photocurrent response at the external circuit leading to the CPL detection.

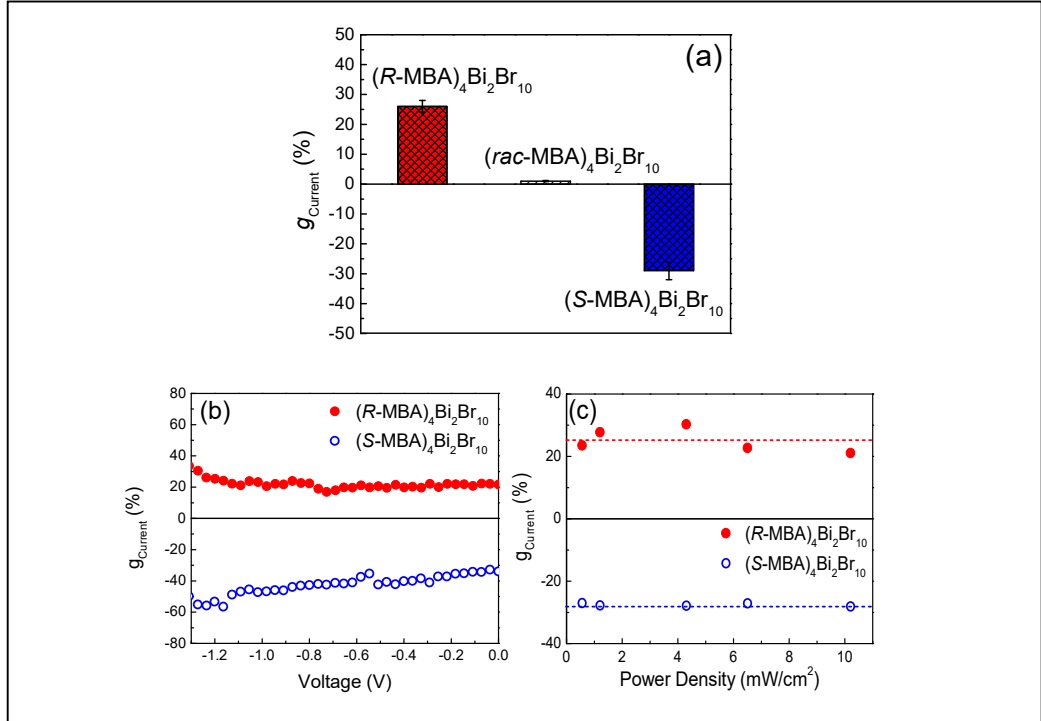


**Figure 7.6.** (a) Photocurrent anisotropy ( $g_{\text{Current}}$ ) of  $(R\text{-MBA})_4\text{Bi}_2\text{Br}_{10}$  and  $(S\text{-MBA})_4\text{Bi}_2\text{Br}_{10}$  perovskites, respectively under LCP and RCP illumination (380 nm) with (b) different applied voltage (intensity of CPL illumination was  $10.2 \text{ mW/cm}^2$ ) and (c) different light intensities (power densities) at zero bias.

## 7.4. Conclusions

In conclusion, we have shown that a pair of bismuth-based lead-free chiral perovskites can act as a CPL detector for the detection of the polarization state of CPL photons. The CPL detection has become possible due to (1) chiroptical activity, that is the generation of spin-polarized carriers as per optical selection rules, and (2) CISS, which is allowing transport of one type of the spin-half states due to the intrinsic chirality in the compounds. With the absorption anisotropy under CPL illumination being low (0.1%) in these perovskites, CPL detection became possible only due to the highly anisotropic out-of-plane charge transport in the chiral perovskites in vertical

heterostructures for the two types of spin-polarized carriers. To evidence the detection of CPL photons, we have characterized the devices under polarized illuminations to derive their photovoltaic responses. The devices based on the *R*-perovskite yielded a higher photocurrent response under an LCP illumination as compared to an RCP one. Likewise, the device based on the *S*-perovskite returned more photocurrent response when the illumination was RCP. The control devices with *rac*-perovskites resulted in a similar *I-V* response for the LCP and RCP photons. The photocurrent anisotropy of the devices based on the *R*- and the *S*-perovskite under zero bias towards CPL detection did not exceed beyond 30% due to a possible spin-flip during the carrier transport. When the devices were operated under a voltage in restricting the spin-flip process, the anisotropy could thereby rise to 60% exhibiting exceptional merit of these chiral perovskites towards CPL detection. This work not only introduces a pair of novel lead-free chiral perovskites but also brings out the unprecedented merit of CISS in vertical heterojunction devices toward the detection of the polarization state of CPL photons.

## 7.5. References

- [1] D. Niesner, M. Wilhelm, I. Levchuk, A. Osvet, S. Shrestha, M. Batentschuk, C. Brabec, and T. Fauster, *Phys. Rev. Lett.* **117**, 126401 (2016).
- [2] C. Zheng, S. D. Yu, and O. Rubel, *Phys. Rev. Mater.* **2**, 114604 (2018).
- [3] Z. Liu, C. Vaswani, X. Yang, X. Zhao, Y. Yao, Z. Song, D. Cheng, Y. Shi, L. Luo, D. H. Mudiyansele, C. Huang, J. M. Park, R. H. J. Kim, J. Zhao, Y. Yan, K. M. Ho, and J. Wang, *Phys. Rev. Lett.* **124**, 157401 (2020).
- [4] Y. Ogawa, H. Tahara, N. Igarashi, Y. Yamada, and Y. Kanemitsu, *Phys. Rev. B* **103**, L081201 (2021).
- [5] M. A. Becker, R. Vaxenburg, G. Nedelcu, P. C. Sercel, A. Shabaev, M. J. Mehl, J. G. Michopoulos, S. G. Lambrakos, N. Bernstein, J. L. Lyons, T. Stoferle, R. F. Mahrt, M. V. Kovalenko, D. J. Norris, G. Raino, and A. L. Efros, *Nature* **553**, 189 (2018).



- [6] W. Li, L. J. Zhou, O. V. Prezhdo, and A. V. Akimov, *ACS Energy Lett.* **3**, 2159 (2018).
- [7] H. Xu, P. Prabhakaran, S. Choi, M. Wang, K.-S. Lee, and B. Hu, *J. Phys. Chem. Lett.* **11**, 1 (2020).
- [8] X. Han, G. F. Zhang, B. Li, C. G. Yang, W. L. Guo, X. Q. Bai, P. Huang, R. Y. Chen, C. B. Qin, J. Y. Hu, Y. F. Ma, H. Z. Zhong, L. T. Xiao, and S. T. Jia, *Small* **16**, 2005435 (2020).
- [9] Y. L. Li, S. He, X. Luo, X. Lu, and K. F. Wu, *J. Phys. Chem. Lett.* **11**, 3594 (2020).
- [10] F. R. Fan, H. Wu, D. Nabok, S. B. Hu, W. Ren, C. Draxl, and A. Stroppa, *J. Am. Chem. Soc.* **139**, 12883 (2017).
- [11] J. Y. Wang, C. Zhang, H. L. Liu, R. McLaughlin, Y. X. Zhai, S. R. Vardeny, X. J. Liu, S. McGill, D. Semenov, H. W. Guo, R. Tsuchikawa, V. V. Deshpande, D. L. Sun, and Z. V. Vardeny, *Nat. Commun.* **10**, 129 (2019).
- [12] A. Privitera, M. Righetto, F. Cacialli, and M. K. Riede, *Adv. Opt. Mater.* **9**, 2100215 (2021).
- [13] C. Chen, L. Gao, W. R. Gao, C. Y. Ge, X. Du, Z. Li, Y. Yang, G. D. Niu, and J. Tang, *Nat. Commun.* **10**, 1927 (2019).
- [14] H. P. Lu, J. Y. Wang, C. X. Xiao, X. Pan, X. H. Chen, R. Brunecky, J. J. Berry, K. Zhu, M. C. Beard, and Z. V. Vardeny, *Sci. Adv.* **5**, eaay0571 (2019).
- [15] J. Q. Ma, C. Fang, C. Chen, L. Jin, J. Q. Wang, S. Wang, J. Tang, and D. H. Li, *ACS Nano* **13**, 3659 (2019).
- [16] J. Ahn, S. Ma, J. Y. Kim, J. Kyhm, W. Yang, J. A. Lim, N. A. Kotov, and J. Moon, *J. Am. Chem. Soc.* **142**, 4206 (2020).
- [17] G. K. Long, R. Sabatini, M. I. Saidaminov, G. Lakhwani, A. Rasmita, X. G. Liu, E. H. Sargent, and W. B. Gao, *Nat. Rev. Mater.* **5**, 423 (2020).
- [18] J. Q. Ma, H. Z. Wang, and D. H. Li, *Adv. Mater.* **33**, 2008785 (2021).
- [19] D. R. Link, G. Natale, R. Shao, J. E. MacLennan, N. A. Clark, E. Korblova, and D. M. Walba, *Science* **278**, 1924 (1997).

- 
- [20] S. Emori, U. Bauer, S. M. Ahn, E. Martinez, and G. S. D. Beach, *Nat. Mater.* **12**, 611 (2013).
- [21] Y. Z. Dong, Y. P. Zhang, X. Y. Li, Y. Q. Feng, H. Zhang, and J. L. Xu, *Small* **15**, 1902237 (2019).
- [22] A. Ishii and T. Miyasaka, *Sci. Adv.* **6**, eabd3274 (2020).
- [23] X. N. Sun, S. Velez, A. Atxabal, A. Bedoya-Pinto, S. Parui, X. W. Zhu, R. Llopis, F. Casanova, and L. E. Hueso, *Science* **357**, 677 (2017).
- [24] K. Bairagi, D. G. Romero, F. Calavalle, S. Catalano, E. Zuccatti, R. Llopis, F. Casanova, and L. E. Hueso, *Adv. Mater.* **32**, 1906908 (2020).
- [25] J. Y. Wang, H. P. Lu, X. Pan, J. W. Xu, H. L. Liu, X. J. Liu, D. R. Khanal, M. F. Toney, M. C. Beard, and Z. V. Vardeny, *ACS Nano* **15**, 588 (2021).
- [26] P. C. Mondal, C. Fontanesi, D. H. Waldeck, and R. Naaman, *Accounts Chem. Res.* **49**, 2560 (2016).
- [27] J. Hao, H. P. Lu, L. L. Mao, X. H. Chen, M. C. Beard, and J. L. Blackburn, *ACS Nano* **15**, 7608 (2021).
- [28] D. Li, X. T. Liu, W. T. Wu, Y. Peng, S. G. Zhao, L. N. Li, M. C. Hong, and J. H. Luo, *Angew. Chem.-Int. Edit.* **60**, 8415 (2021).
- [29] T. Liu, W. Shi, W. Tang, Z. Liu, B. C. Schroeder, O. Fenwick, and M. J. Fuchter, *ACS Nano* **16**, 2682 (2022).
- [30] T. H. Moon, S. J. Oh, and K. M. Ok, *ACS Omega* **3**, 17895 (2018).
- [31] B. P. Bloom, V. Kiran, V. Varade, R. Naaman, and D. H. Waldeck, *Nano Lett.* **16**, 4583 (2016).
- [32] J. M. Ball and A. Petrozza, *Nat. Energy* **1**, 16149 (2016).
- [33] H. H. Fang and W. D. Hu, *Adv. Sci.* **4**, 1700323 (2017).
- [34] C. Xie, C. K. Liu, H. L. Loi, and F. Yan, *Adv. Funct. Mater.* **30**, 1903907 (2020).

# Chapter 8

## Concluding Remarks

*In this chapter, the general conclusion and summary of this doctoral research work have been presented. The originality and key findings are discussed in a nutshell followed by some possible future prospects of the research topic.*

### 8.1. General Conclusions and Summary

The overarching objective of this doctoral thesis was to study the optoelectronic and spintronic properties of several metal halide perovskites towards their device applications. Despite the success of MAPbI<sub>3</sub> in optoelectronics, specifically in photovoltaics, two major concerns could be found. The stability issue of the compound and the toxicity of lead have triggered the research thrust to find alternate materials in the field of perovskite optoelectronics [1,2]. In this context, the motivation of the research work in the first part of the thesis was to address one focal question: “*Is there any alternate perovskite beyond MAPbI<sub>3</sub> for viable photovoltaic applications with better stability and probably less toxicity?*” Three possible perovskite derivatives, beyond ABX<sub>3</sub> structure, were investigated as potential alternatives, namely bismuth-based ternary halide perovskites (MA<sub>3</sub>Bi<sub>2</sub>I<sub>9</sub>, Cs<sub>3</sub>Bi<sub>2</sub>I<sub>9</sub>), double perovskite (Cs<sub>2</sub>AgBiBr<sub>6</sub>), and quasi-2D Ruddlesden-Popper (RP) perovskites (BA<sub>2</sub>MA<sub>2</sub>Pb<sub>3</sub>I<sub>10</sub>). Needless to state, all these materials were reported to be highly stable in ambient condition [3]. The difference which should be noted is that the quasi-2D RP perovskites still contains lead in the crystal lattice in contrast to the ternary halide and double perovskites. Based on fundamental investigations through advanced scanning probe techniques, and practical device applications, it was found that the replacement of lead from the perovskite structure would result in poor charge transport leading to a truncated power conversion efficiency (PCE)

in ternary halide and double perovskite-based photovoltaic devices. To be specific these lead-free perovskites are not as “defect-tolerant” as MAPbI<sub>3</sub>. Although the PCE could be increased to some extent with the aid of material engineering, it is still far behind MAPbI<sub>3</sub> which concludes that role of lead in the perovskite material is crucial for achieving the remarkable optoelectronic properties of hybrid halide perovskite [4]. Hence, the research direction was shifted subsequently to investigate lead-based perovskite materials with *high operational stability*. In this direction, quasi-2D perovskites were already reported promising in terms of their exciting photovoltaic performance and stability [5]. However, their local scale photophysics was not completely understood before. Because of this, an attempt was made to investigate the exciton dissociation mechanism in this material through scanning probe techniques. The results revealed the formation of 3D perovskite at the edges of the quasi-2D RP phase that helps in efficient exciton dissociation.

In the next part of the thesis, spintronic aspects of these materials were investigated. Finally, the goal was to address one pivotal question: “*Can we integrate optoelectronic and spintronic properties of metal halide perovskites for next-generation opto-spintronic devices?*” Notably, most of the novel optoelectronic-related spintronic properties are originated from a spin-orbit coupling (SOC) and Rashba effect in metal halide perovskites [6]. However, proper experimental verification was still lacking in the literature. One of the most significant outcomes of this doctoral thesis was to verify Rashba splitting experimentally in the prototype MAPbI<sub>3</sub> which would be beneficial in the research field of perovskite-based spintronics. In addition, a correlation between optoelectronic and spintronic features of the material was conclusively established for the first time by connecting carrier recombination (optoelectronic) and Rashba splitting (spintronic). Although this study was carried out in the prototype hybrid halide perovskite having stability issues, such a choice was indispensable considering the early stage of the research field. Finally, the research work was stepped forward toward the development and characterization of the opto-spintronic devices where a pair of highly stable lead-free (bismuth-based) chiral perovskites was introduced. In contrast to the optoelectronic properties, spin properties would still sustain in the material due to the presence of strong

SOC. The intrinsic chirality-induced spin selectivity enables spin-dependent charge transport in the chiral perovskites. They were further introduced in spin-photovoltaic devices for the detection of circularly polarized light at zero magnetic fields. In addition, a generalized method was developed to achieve the high performance of such opto-spintronic devices.

## **8.2. Key Findings**

To some extent, these results have laid down the fundamental understanding of optoelectronic and spintronic properties of metal halide perovskites for their device applications. The originality and key findings of the research incorporated in this doctoral thesis have been discussed in this section.

1. Detrimental role of defects in bismuth-based ternary halide perovskites ( $\text{MA}_3\text{Bi}_2\text{I}_9$ ,  $\text{Cs}_3\text{Bi}_2\text{I}_9$ ) was studied through both localized measurements and device applications. In this work, it was concluded that such systems were not suitable for photovoltaic applications. The physics related to defect states are however considered for resistive switching applications. Although this is beyond the scope of this thesis, such an attempt was made in a contributory work [7].
2. The poor charge transport in double perovskite ( $\text{Cs}_2\text{AgBiBr}_6$ ) was studied in this published work. Similar to the bismuth-based ternary halide perovskites, the intrinsic defect states appearing from a cation disorder, were found to be responsible for such truncated transport properties. In this direction, a method was suggested to passivate the defect states by introducing cation ordering. However, the PCE in solar cells was still found inferior compared to the hybrid halide perovskites.
3. The photovoltaic properties of quasi-2D RP perovskites were investigated at a local scale. It may be noted that such perovskites are highly stable in ambient. Hence, amongst all of these alternative perovskites, they are considered as the most promising material to excel in photovoltaics. However, a proper understanding of the exciton dissociation mechanism in such compounds was still

inconclusive. In this direction, a major achievement of the thesis was to shade light on the apparent contradiction of efficient charge separation and strong exciton binding energy in multilayered quasi-2D RP lead halide perovskites. Combining scanning tunneling spectroscopy and Kelvin probe force microscopy we have witnessed the existence of low-energy edge states in this material that helps to dissociate exciton. We have found that most of the open-circuit voltage was generated at the edge (grain boundary).

4. Spin-polarized scanning tunneling spectroscopy was introduced to study Rashba band splitting in hybrid halide perovskite. This finding would be useful for the spintronic applications of metal halide perovskites. Moreover, a correlation between optoelectronic and spintronic features of the material was conclusively established for the first time by connecting carrier recombination and Rashba splitting.

5. The spintronic aspects of metal halide perovskites were established. A pair of lead-free chiral perovskites were synthesized with an integration of a bismuth-based inorganic framework and a chiral organic sub-lattice (*R/S*-methylbenzylammonium). Due to the intrinsic chirality of the compounds, the perovskites exhibited chirality-induced spin-selectivity (CISS) allowing the transport of one type of spin-half state while blocking the other type. These perovskites were introduced for the detection of circularly polarized light at zero magnetic fields. In addition, a generalized method was proposed to achieve the high performance of such opto-spintronic devices.

### 8.3. Future Prospects

The research field of perovskite optoelectronics and spintronics is impressive. Going forward, several potential research directions could be envisaged. In this section, some of the prospects have been envisaged.

### **8.3.1. Optoelectronics**

1. Despite the unprecedented promise of quasi-2D perovskites, a charge transport bottleneck still exists there due to the presence of insulating spacer cations. In this direction, the vertical charge transport of the parent perovskite can be improved by designing new perovskite materials with covalently bound metal-anion networks within the interlayers (linkage) [3].
2. Several interesting properties in different metal halide perovskites can still be envisaged. Although some of them are successfully addressed during the doctoral research, there is still a lot to be investigated such as hot carrier dynamics, electron-phonon scattering, ionic conduction, terahertz response, and so forth [8].
3. The unique optical and ferroelectric properties of quasi-2D perovskites having multiple quantum wells should be investigated further. Such a study might open a new direction in ferroelectric photovoltaics [9].

### **8.3.2. Spintronics**

1. Considering the recent stages of the research field, we studied Rashba splitting in the prototype hybrid halide perovskite. It should be noted that this material is not highly stable in ambient which opens an avenue to search for alternate materials. In this regard, quasi-2D RP perovskites could have been an ideal choice.
2. Designing strategy has to be developed to increase the spin lifetime and diffusion length of different metal halide perovskite, specifically at room temperature.
3. Magnetotransport study of the perovskites should be carried out.
4. The range of polarized light detection has to be extended beyond the UV range through bandgap engineering of chiral perovskites.

5. Fabrication and characterization of advanced spintronic devices such as spin-polarized light-emitting diodes (LED), spin valves, sensors, and so on should be considered.

## 8.4. References

- [1] A. K. Jena, A. Kulkarni, and T. Miyasaka, *Chem. Rev.* **119**, 3036 (2019).
- [2] Y. G. Rong, Y. Hu, A. Y. Mei, H. R. Tan, M. I. Saidaminov, S. I. Seok, M. D. McGehee, E. H. Sargent, and H. W. Han, *Science* **361**, eaat8235 (2018).
- [3] S. Chatterjee and A. J. Pal, *J. Mater. Chem. A* **6**, 3793 (2018).
- [4] Z. X. Jin, Z. Zhang, J. W. Xiu, H. S. Song, T. Gatti, and Z. B. He, *J. Mater. Chem. A* **8**, 16166 (2020).
- [5] F. Zhang, H. P. Lu, J. H. Tong, J. J. Berry, M. C. Beard, and K. Zhu, *Energy Environ. Sci.* **13**, 1154 (2020).
- [6] K. Liao, X. Y. Hu, Y. K. Cheng, Z. C. Yu, Y. X. Xue, Y. Chen, and Q. H. Gong, *Adv. Opt. Mater.* **7**, 1900350 (2019).
- [7] S. Paramanik, A. Maiti, S. Chatterjee, and A. J. Pal, *Adv. Electron. Mater.* **8**, 2100237 (2022).
- [8] K. Wang, D. Yang, C. C. Wu, M. Sanghadasa, and S. Priya, *Prog. Mater. Sci.* **106**, 100580 (2019).
- [9] H. Huang, *Nat. Photonics* **4**, 134 (2010).



# Appendix A

## Quantifying Anisotropic Thermal Transport in 2D Perovskite

*Although, this doctoral research is focussed on the optoelectronic and spintronic applications of metal halide perovskites, it is also important to study their thermal properties considering the thermal management of those devices. In this additional work, the anisotropic thermal transport has been investigated in two-dimensional (2D) perovskite (phenethylammonium lead iodide) nanolayers through a novel measurement technique called cross-sectional scanning thermal microscopy (xSThM). In this method, a target perovskite layer on a substrate was oblique polished with Ar ion beam to create a low angle wedge with nanoscale roughness followed by high vacuum SThM to obtain the thermal conductance map as a function of local 2D material thickness. The experimentally obtained data were processed with analytical model validated by the finite elemental analysis simulation to quantify the in-plane ( $k_{l,xy}$ ) and cross-plane thermal conductivities ( $k_{l,z}$ ) of the 2D perovskite from a single set of measurement with nanoscale resolution. An ultra-low thermal conductivity for the 2D perovskite was obtained along with an anisotropy associated to the unique structure of the perovskite and different phonon lifetimes and group velocities for in-plane and out-of-plane directions. The results that are available for the first time, are essential for the thermal management of 2D perovskite based optoelectronic devices, and for potential thermoelectric applications of these materials.*

## A.1. Introduction

In recent years, Ruddlesden-Popper (RP) hybrid halide perovskites have gained widespread attention as an emerging class of two-dimensional (2D) materials owing to their novel electronic and photo-physical properties [1-5]. This particular class of quantum well like materials exhibiting excellent light emitting and optoelectronic properties is considered as an alternative to their three-dimensional (3D) counterpart [6-8]. The excellent performance of the compound in solar cells, photodetectors and light emitting diodes has been ascribed to many exceptional properties, such as solution-processability [9,10], bandgap tunability [7,11], high extinction coefficient [12,13], high photoluminescence quantum yield (PLQY) [14,15], excitonic effects [1,16-18], and improved ambient stability [19,20]. While the photo-physics and carrier dynamics have been intensively studied [21-23], a much less explored aspect of this exciting class of materials is their thermal properties. A fundamental understanding of different thermal parameters and phonon transport is essential for the proper thermal management of 2D perovskite based existing devices [24], potential thermoelectric applications of these materials [25,26], and development of advanced photovoltaic devices based on the hot phonon bottleneck effect [27,28]. Despite recent reports on the ultra-low thermal conductivity ( $k_l$ ) and underlying phonon transport mechanism, a complete understanding of heat dissipation in 2D perovskite layers remains ambiguous till now due to the limitations of existing thermal characterization techniques [29-31]. As such, the prevailing macroscopic measurement methods are not appropriate for these compounds especially in their thin film form where ballistic heat transport and phonon scattering at the interfaces significantly influence the diffusive heat flow [32]. In this regard, non-destructive scanning thermal microscopy (SThM) approaches may open a novel route to determine local thermal properties of 2D perovskite thin films overcoming the limitations of classical thermal characterization techniques [33-35].

In this work, we measured  $k_l$  of an archetypal 2D perovskite named phenethylammonium lead iodide ((PEA)<sub>2</sub>PbI<sub>4</sub>) through a novel unique tool called cross-sectional scanning thermal microscopy (x-SThM). This microscopic technique is not

only capable for the qualitative thermal imaging of the perovskite with nanoscale resolution to map the local thermal conductance, but also holds the unprecedented opportunity to provide absolute quantitative values of the in-plane ( $k_{l,xy}$ ) and out-of-plane ( $k_{l,z}$ ) components of thermal conductivity via matched analytical model. In this method, a low angle wedge cut in the perovskite thin-films (on Si/SiO<sub>2</sub> substrate) was formed through a beam exit cross sectional polishing (BEXP) followed by high vacuum SThM investigation [36]. As a result, SThM in one map obtains a dependence of the thermal resistance as a function of thickness,  $t$ , replacing the need to create and measure a set of samples of different thickness. The quantitative values of both  $k_{l,xy}$  and  $k_{l,z}$  are then obtained along with interfacial thermal resistance ( $r_{int}$ ) once the experimental data was compared to an appropriate analytical Muzychka-Spièce model, that was independently validated via finite elemental analysis (FEA) simulation [37-39]. To be specific, the measured values of  $k_{l,xy}$  and  $k_{l,z}$  in the material were  $0.45\pm 0.05 \text{ Wm}^{-1}\text{K}^{-1}$  and  $0.13\pm 0.05 \text{ Wm}^{-1}\text{K}^{-1}$ , respectively. Our results also reveal the existence of a thermal anisotropy ( $k_{l,xy}/k_{l,z}\sim 3.4$ ) in the compound that originates in the differences between (in-plane) heat conduction in the continuous inorganic layer versus the out-of-plane heat transport interrupted at the organic-inorganic interfaces. This work provides a novel generic technique to measure quantitative ultra-low value of average thermal conductivity,  $k_l$ , in 2D materials, as well as its deconvolution into anisotropic thermal conductivity components  $k_{l,xy}$  and  $k_{l,z}$  using a single set of measurement. Moreover, this work is beneficial for development of the thermal management strategies for 2D perovskite based optoelectronic devices and also their possible thermoelectric applications.

## **A.2. Materials and Methods**

### **A.2.1. Materials**

Phenethylammonium iodide (PEAI, 99%), lead iodide (PbI<sub>2</sub>, 99%), and anhydrous N, N-dimethyl formamide (DMF, 99.8%) were purchased from Sigma-

Aldrich chemical company. All the materials were kept inside a nitrogen filled glovebox with well-maintained oxygen and moisture levels below 0.1 ppm and used without further purification.

### **A.2.2. Fabrication and Characterization of the Thin Films**

For the fabrication of (PEA)<sub>2</sub>PbI<sub>4</sub> thin films, a precursor solution was prepared by dissolving PEAI (2 M) and PbI<sub>2</sub> (1 M) into DMF solvent. The mixture was stirred continuously at 70 °C to form a clear and homogeneous solution. After that glass and SiO<sub>2</sub>-coated Si substrates (Si/SiO<sub>2</sub>) were cleaned following a usual protocol with ethanol, acetone and isopropyl alcohol for 15 minutes each in a bath-sonicator (37 kHz), followed by a plasma cleaning to remove organic residues. Finally, the precursor solution was spun at 2500 rpm for 30 seconds followed by an annealing of the film at 80 °C for 15 minutes. The perovskite films were characterized through conventional techniques such as X-ray diffraction (XRD), optical absorbance and photoluminescence (PL) spectroscopy to ensure their phase purity. Such measurements were carried out in a Rigaku Smart Lab X-ray diffractometer (Cu K $\alpha$  radiation = 1.5406 Å), Shimadzu UV-vis spectrophotometer and Horiba Jobin Yvon spectrofluorometer (excitation at 405 nm), respectively.

### **A.2.3. Beam Exit Cross Sectional Polishing (BEXP)**

In order to obtain an ultralow wedge like cut in the sample (2D perovskite on Si/SiO<sub>2</sub> substrate), we used the BEXP technique carried out in an EM TIC 3X triple ion beam cutter system (Leica Microsystems). In this technique, the sample was placed on a tilted (5°) stage with respect to the horizontal plane. A shade mask was used in front of the stage so that the cut could be executed on the exposed material by intersecting coplanar argon (Ar) beam coming from three guns. The entire process was executed in high vacuum (10<sup>-5</sup> Torr) through different steps such as warm up of the guns (1 kV, 1

mA, 15 minutes), pre-polishing (5 kV, 2 mA, 15 minutes), nano-cutting or polishing (7 kV, 2.6 mA, 7 hours), and post-polishing (1 kV, 1 mA, 1 hour).

#### **A.2.4. Scanning Thermal Microscopy (SThM)**

After the formation of low angle wedge cut in the sample, it was transferred to high vacuum chamber ( $10^{-6}$  Torr) for SThM measurements. The high vacuum environment is required to avoid additional heat transfer through air and formation of water meniscuses at tip apex affecting the experimental data. The experiments were carried out in a Smena (NT-MDT Spectrum) scanning probe microscope with custom-built SThM electronics. In this system, the thermal probe was composed of a  $\text{Si}_3\text{N}_4$  cantilever with a palladium (Pd) film deposited on it through thermal evaporation. The spring constant of the tip was  $0.4 \text{ Nm}^{-1}$  spring constant with  $<100 \text{ nm}$  tip radius. The probe used a thermal resistive heater and could sense the variations in temperature during the scan over the material [40,41]. The experimental data was fitted with analytical model in MATLAB software. In addition, finite elemental analysis (FEA) simulation was carried out in COMSOL Multiphysics 5.6 software to validate the experimental results.

### **A.3. Results and Discussions**

#### **A.3.1. Characterization of 2D Perovskite**

The crystal structure of  $(\text{PEA})_2\text{PbI}_4$  perovskite reveals that it is formed with alternative stacking of organic spacer layers and the inorganic octahedral slabs (repetition of the structure as shown in Figure A.1a). It may be noted that due to a large size of the bulky spacer cation  $(\text{PEA})^+$ , it could not be “tolerated” in between the cages of inorganic octahedrons ( $[\text{PbI}_4]^{2-}$ ), resulting in a formation of insulating spacer layer depending on intermolecular forces. The large spacer chains are aligned in the out-of-plane direction having covalent bonds (C-C and C-N). In addition, weak van der Waals and electrostatic interactions could be observed between two vertically stacked organic

chains and at the organic-inorganic interfaces. On the other hand, there are strong ionic bonds in the in-plane direction originated from the continuous  $[\text{PbI}_4]^{2-}$  octahedral framework [8,31,42,43].

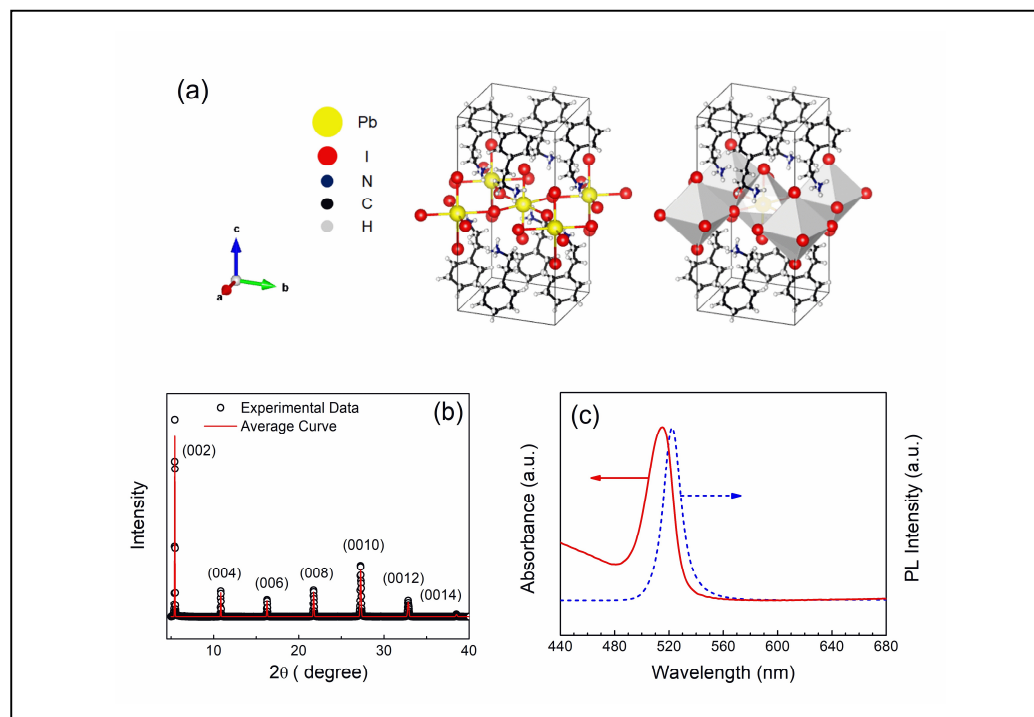


**Figure A.1.** (a) Schematic representations of  $(\text{PEA})_2\text{PbI}_4$  crystal structure. The first one shows the ball-stick model of the crystal. In the second polyhedral model the octahedra are presented. (b-c) XRD patterns, optical absorbance and photoluminescence spectra of the  $(\text{PEA})_2\text{PbI}_4$  thin film.

In order to confirm the phase purity of the thin-film, we have presented X-ray diffraction (XRD) pattern in Figure A.1b. The diffraction pattern is indexed according to previous report and suggests the evolution of strong  $(002l)$  reflection series [44]. Such XRD pattern indicates formation of the film with layers oriented parallel to the substrate preferred along the  $\langle 001 \rangle$  direction [42]. In addition, the optical absorbance and photoluminescence (PL) spectra of the as prepared film are presented in Figure

A.1c, showing a characteristic bandgap of the material around 2.2 eV, typical narrow exciton absorption and emission lines, with a small Stokes shift [45]. Such results confirmed the phase pure formation of the material before proceeding to further measurements.

### **A.3.2. Cross Sectional Scanning Thermal Microscopy (x-SThM)**

After ensuring the purity of the 2D perovskite phase, we proceeded towards the cross-sectioning of the film (fabricated on Si/SiO<sub>2</sub> substrate) through BEXP method to create an easily accessible surface section having wedge like geometry for further x-SThM investigation. In this method, the sample was placed on a tilted (5°) stage with respect to the horizontal plane. A shade mask was used in front of the stage so that the cut could be executed on the exposed material by Ar beams to obtain a wedge-like cut with negligible surface roughness. This technique is called beam-exit cross sectional polishing as the beam exits at a glancing angle to the sample surface to produce the cut with near-atomic roughness and a negligible surface damage [46].

The cross-sectioned 2D perovskite film was then transferred to the high vacuum chamber for SThM measurements that could image the thermal response with high spatial resolution (~50 nm) in contrast to the far-field optical techniques [39,47]. It may be noted that high vacuum is desirable to avoid additional heat transfer through air and formation of water meniscuses at tip apex [41,48,49]. In this setup, the thermal probe was a resistor with electrical resistance  $R_{probe}$  in a Wheatstone bridge circuit with two known resistors ( $R_1$  and  $R_2$ ) and a variable resistor,  $R_3$ . The SThM probe is used as a local heater of the 2D perovskite with a consideration that the heat source is concentrated near the extreme point of the tip apex. When the probe is energised via DC and AC voltage and brought into close contact with the perovskite surface, a heat flow is generated from the tip to sample due to a temperature gradient. This changes the temperature of the probe and hence the resistance of the probe which is monitored as the change of output voltage of the Wheatstone bridge [47].

As the entire sample-system is composed of an assembly of different materials (Si, SiO<sub>2</sub>, and 2D perovskite), the obtained wedge cut provides a perfect platform that includes three different regions and interfaces and can be studied in a single measurement as a function of tip position during SThM characterization. In Figure A.2a, the 3D topography of the cross-sectional surface is presented. It is difficult to identify different materials and interfaces from the topography image due to the near-perfect nano-cross-sectioning via BEXP. At the same time, the deflection and thermal images allow good differentiation of these different layers (Figures A.2b-c). The extracted data (Figure A.2d) revealed the height profile (Z-height) of the layers (SiO<sub>2</sub> and 2D perovskite) as function of tip position,  $x$ , along the section. Due to the dissimilar properties of Si, SiO<sub>2</sub>, and perovskite, a different milling rate is also expected with the Ar beams, that due to the low angle incidence, results in an observable but minor change of angle at the interfaces. Such change is useful to identify different interfaces of the entire sample-system. In addition, a very thin layer of aluminum (Al) was observed at the top of 2D perovskite layer which could be formed during the BEXP cut when the Ar beams exit from the cut sample. At the same time, due to calibration of the scanner, the thickness of the layer is directly measured as a function of the lateral position as described elsewhere with sub-nm precision [36].

Now, during scanning when the tip moves over the wedge cut, contact thermal voltage ( $V_c$ ) could be obtained simultaneously as function of  $t$ , along with the topography as well throughout the cut defined as  $V_c(t)$ ; such thermal signal profile is presented in Figure A.2e. The raw thermal results showed a different voltage contrast of the Si, SiO<sub>2</sub>, and 2D perovskite layers due to different thermal properties of each material. The thermal resistances of different regions over the cut were derived as a function of  $t$  as following [50]:

$$R_x(t) = C_{corr} \frac{V_c(t)}{V_{nc} - V_c(t)} R_P \quad (\text{A.1})$$

where,  $R_P$  represents the probe thermal resistance at high vacuum ( $2.38 \times 10^5 \text{ KW}^{-1}$ ) that was obtained through a calibration [51] and  $C_{corr}$  represents a correction factor that



accounts for the deviation of the approximation that the heat source is concentrated only at the extreme point of the tip apex due to tip geometry [51]. The value of  $V_{nc}$  for the tip out of the contact with the sample is obtained by doing an approach and retract thermal scan over the cut and averaging them. In Figure A.2f, we have presented variation of  $R_x(t)$  at different regions and interfaces through the wedge cut. First of all, we observed stable thermal resistance of Si followed by a clear increase at  $\text{SiO}_2$  inferring an increase of thermal spreading due to a much higher thermal conductivity of Si ( $135 \text{ Wm}^{-1}\text{K}^{-1}$ ) than  $\text{SiO}_2$  ( $1.4 \text{ Wm}^{-1}\text{K}^{-1}$ ) [52,53]. Similarly, the 2D perovskite showed a higher thermal resistance than the  $\text{SiO}_2$  and finally reached a quasi-constant nature at higher thickness. In addition, we witnessed a sudden jump of  $R_x(t)$  at the  $\text{SiO}_2$ -perovskite interface suggesting a high interfacial thermal resistance at the  $\text{SiO}_2$ -perovskite interface. Although, these preliminary observations are consistent with the existing literature regarding the ultra-low thermal conductivity of 2D perovskite [29-31], it is not enough for the quantitative analysis that we now undertake below.

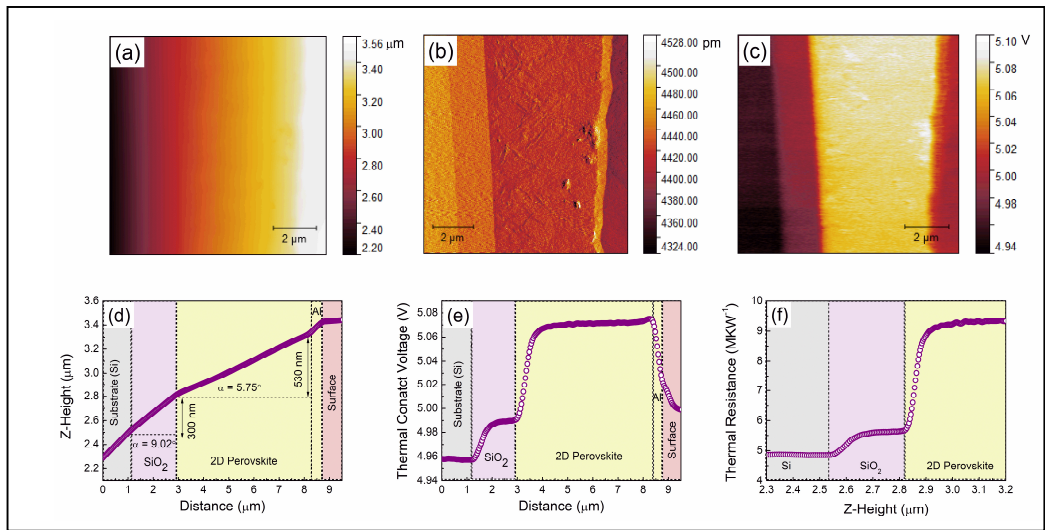


**Figure A.2.** (a) Topography (b) deflection (c) thermal signal image (d) section analysis (e) thermal voltage and (f) variation of thermal resistance at different regions of the BEXP cut sample as mentioned in the plots.

### A.3.3 Analytical Model for SThM Response in Studies of Anisotropic Materials

For the quantitative estimation of thermal conductivity in 2D perovskite, we used an analytical model that describes heat spreading within the layer on a substrate, as mentioned elsewhere [37,38]. It may be recalled that the 2D perovskite film was fabricated on Si substrate having a SiO<sub>2</sub> layer. Hence, the entire system could be represented as a combination of two different heterojunctions (Si/SiO<sub>2</sub> and SiO<sub>2</sub>/2D perovskite) and demonstrated as a layer (top material) with thermal conductivity  $k_l$  on a uniform substrate (bottom material) having a thermal conductivity  $k_s$ . As mentioned earlier, the wedge cut allow us to carry out SThM measurement as a function of  $t$  in a single measurement as effective thickness of the layer under the probe is changed depending on the position of tip. The schematic view of the system has been presented in Figure A.3 in which the arrows represent the direction of heat flow.

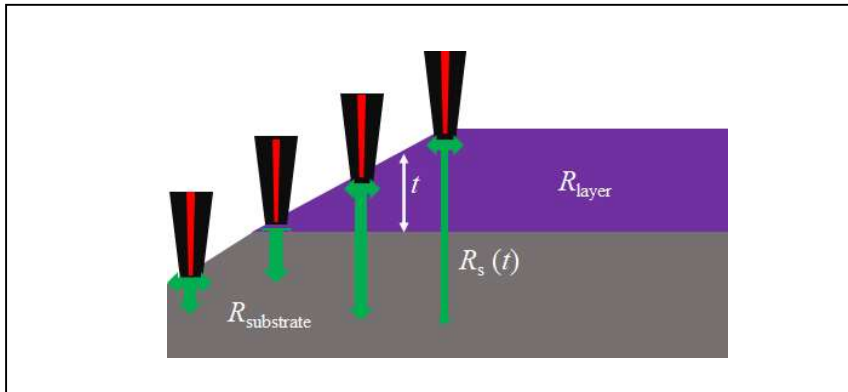


**Figure A.3.** Schematic view of the  $x$ -SThM scanning along the cut sample with increasing thickness.

In order to quantify the thermal properties through this analytical model, we have expressed the total thermal resistance of the “tip-sample system” (Figure A.2f) as a combination of two components connected in series [39] as  $R_x(t) = R_s(t) + R_c$  where  $R_s$  represents the total spreading thermal resistance of the sample and  $R_c$  denotes the contact thermal resistance between the tip and sample. As the experiments were carried

out in vacuum, the contribution of water meniscus conductance has been eliminated [49], and we could consider that  $R_c$  is constant and solely governed by the solid-solid contact thermal resistance depending on the contact radius ( $a$ ) and the thermo-physical properties of the scanned material [35]. Although  $R_c$  is independent of the tip position during scanning, it has a non-zero contribution that should be eliminated as the analytical model describes only the heat spreading within the layer on a substrate [37,38]. In addition, for both heterostructures, at the interfaces the tip-sample contact could be occurring simultaneously touching both materials, resulting in a sudden jump of thermal resistance at the transition point(s), leading to artifacts during fitting. In order to eliminate this, only the data at distance away from the transition point by the contact radius were used, with  $t_l$  denoting the thickness of each consecutive points starting from the point  $t_l = t_0$ . In order to exclude the unknown value of the tip-sample contact resistance,  $R_c$ , the difference between the thermal resistances at thickness  $t_l$  and  $t_0$  was used as follows

$$R_l(t_l) = R_x(t_l) - R_x(0) = R_s(t_l) - R_s(0) + R_c - R_c = R_s(t_l) - R_s(0) \quad (\text{A.2})$$

where,  $R_x(0)$  represents the initial spreading resistance at  $t_0 \rightarrow 0$  nm of thickness and  $R_l(t_l)$  denotes difference of the spreading resistance at each consecutive thickness points above  $t_0$  and the thermal resistance at the point  $t_0$ . Then the final experimental data for both the nanostructure could be interpreted as  $R_l$  as a function of  $t_l$  which is compatible for fitting to the isotropic heat spreading model for  $R_l(t_l)$  described by Muzychka and Spièce [37-39]:

$$R_l(t_l) = \frac{1}{\pi k_l a} \int_0^\infty \left[ \frac{1 + Ke^{-\left(\frac{2xt_{eff}}{a}\right)}}{1 - Ke^{-\left(\frac{2xt_{eff}}{a}\right)}} \right] J_1(x) \sin(x) \frac{dx}{x^2} \quad (\text{A.3})$$

where,  $k_l$  represents the top layer isotropic thermal conductivity and  $J_1$  corresponds to the first order Bessel function. In addition,  $K$  and  $t_{eff}$  are defined as

$$K = \frac{1 - k_l/k_s}{1 + k_l/k_s} \quad \text{and} \quad t_{eff} = t_l + r_{int}k_l \quad (\text{A.4})$$

and  $k_s$  represents the substrate thermal conductivity,  $r_{int}$  denotes the layer-substrate interfacial thermal resistance, and  $t_l$  is the thickness of each layer. While this model is

appropriate when the top layers exhibit inherent isotropic thermal transport, for an anisotropic transport of the top layer it is possible to modify these formulae by transforming  $t_l$  and  $k_l$  as following:

$$t_{l,anis} = \frac{t_l}{\sqrt{\frac{k_{l,z}}{k_{l,xy}}}} \quad \text{and} \quad k_{l,anis} = \sqrt{k_{l,xy}k_{l,z}} \quad (\text{A.5})$$

### A.3.4 Quantitative Analysis of Thermal Conductivity: Fitting Results and FEA Simulation

In order to obtain average thermal conductivity,  $k_{l,anis}$ , of the 2D perovskite layer using the abovementioned model, we applied a two-step fitting due to the need of finding several independent parameters (Equations A.4-5) such as  $a$ ,  $C_{corr}$ ,  $k_{l,xy}$ ,  $k_{l,z}$  and  $r_{int}$ . In the first step, the analytical fitting was carried out in Si/SiO<sub>2</sub> heterostructure considering it as a reference with known values of  $k_s$  ( $k_{Si}$ ) and  $k_l$  ( $k_{SiO_2}$ ) to obtain  $a$  and  $C_{corr}$  as fitting parameters. In the next step, these values were served as known inputs when the model was applied to the SiO<sub>2</sub>/2D perovskite heterostructure to obtain  $k_l$  ( $k_{l,anis}$ ,  $k_{l,xy}$ ,  $k_{l,z}$ ) of 2D perovskite and  $r_{int}$  between SiO<sub>2</sub> and 2D perovskite. In addition, we have validated our fitting results with FEA simulation which is also helpful to qualitatively understand the thermal properties of the system in terms of temperature distribution and heat flow directions.

*Isotropic model fitting for Si/SiO<sub>2</sub> heterojunction:* According to previous studies SiO<sub>2</sub> on Si substrates exhibit an isotropic thermal transport [39,52]. Hence, introducing  $k_s = 130 \text{ Wm}^{-1}\text{K}^{-1}$  and  $k_l = 1.4 \text{ Wm}^{-1}\text{K}^{-1}$  as known parameters during first fitting [52-54], we could extract  $a$  and  $C_{corr}$  along with  $r_{int}$  as fitting parameters by applying the isotropic model (Equations A.3-4). However, before proceeding to the actual refinement of the experimental data, it would be intriguing to understand how each of these fitting parameters govern the overall thermal spreading resistance analytically and theoretically (Figure A.4). In this direction, we formulated a series of forward curves by changing these parameters from both Muzychka-Spièce analytical formulation and FEA

simulation. Such plots are not only useful to obtain a physical idea of how the system is influenced by them but also provides an idea to range the fitting parameters. As an example,  $a$  was found to be located between 50 nm and 60 nm from Muzychka-Spièce approach which is very similar to that one obtained using the FEA simulation through parametric sweep. In a similar way, the possible values of  $r_{int}$  could be anticipated with these two effective approaches. However, from both the studies, we found that the effect  $r_{int}$  at Si-SiO<sub>2</sub> interface is not significant in between  $10^{-9}$  Km<sup>2</sup>W<sup>-1</sup> to  $10^{-15}$  Km<sup>2</sup>W<sup>-1</sup> that has been reported previously. It may be noted that variation of  $C_{corr}$  does not make any physical sense as it is just a scaling factor. Using this approach, a desired goodness of fit was achieved.

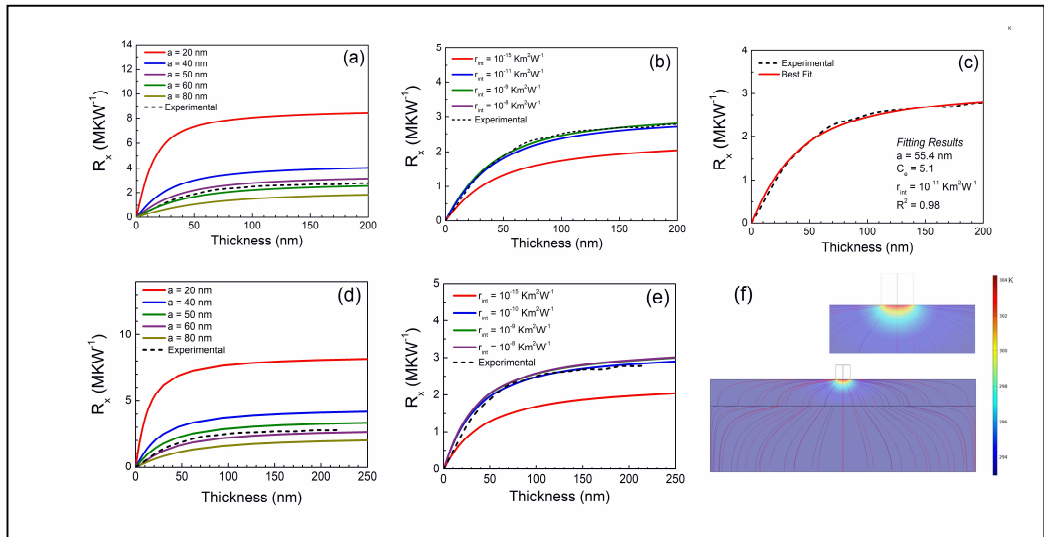


**Figure A.4.** (a-b) Simulated thermal resistance dependence for different  $a$ ,  $r_{int}$ . (c) The fitting plots for Si/SiO<sub>2</sub> heterojunction (analytical model). (d-e) FEA simulated forward plots for different  $a$  and  $r_{int}$ . (f) FEA simulated results of thermal gradient and heat flow at high thickness (inset shows a zoomed in view).

We extracted  $a = 55.4 \pm 0.2$  nm from the fitting which is a good agreement with the specification of the probe with the tip radius  $< 100$  nm. Similarly, we obtained a reasonable value of  $C_{corr} = 5.15$ ; in ideal case this should be unity suggesting that the heat source is concentrated only at the extreme point of the tip apex [51]. Moreover, the

interfacial thermal resistance between Si and SiO<sub>2</sub> ( $r_{Si-Si_2}$ ) was found to be  $\sim 10^{-11}$  Km<sup>2</sup>W<sup>-1</sup>. Finally, these obtained fitting parameters were introduced in a realistic model in COMSOL interface to obtain the idea of thermal transport in this system. In this direction, we mainly proceeded to understand the temperature distribution (colour gradient) and heat flow direction (blue stream lines) in the YZ-direction. As such we depicted the thermal behaviour at two different tip positions indicating two different thicknesses (thick and thin layers). At lower thickness, the temperature gradient was found to be very localized under the tip and did not influence its surroundings creating only a minor temperature difference. Under this situation, mainly  $r_{Si-Si_2}$  restricts the heat transport towards Si resulting in a small thermal gradient.

*Anisotropic model fitting for SiO<sub>2</sub>/2D perovskite heterojunction:* After obtaining the idea of the common parameters from the previous analysis, we could finally use the Muzychka-Spièce model of heat spreading (Equation A.5) for the second heterojunction considering SiO<sub>2</sub> as a substrate and the 2D perovskite as a top layer in order to determine its average thermal conductivity ( $k_{l,anis}$  or  $k_{avg}$ ). Due to the anisotropic layered structure, such 2D perovskites are expected to exhibit anisotropic thermal transport [31]; hence the anisotropic model was considered instead of the isotropic one (Equation A.5). Although, we considered Si/SiO<sub>2</sub> and SiO<sub>2</sub>/2D perovskite as two different heterojunctions during this analytical method, no significant change was expected for  $a$  and  $C_e$  as all three materials (Si/SiO<sub>2</sub>/2D perovskite) were thermally imaged sequentially as a single system under same SThM probe and similar geometrical configuration. Hence, the previously determined values of  $a = 55.4$  nm and  $C_{corr} = 5.15$  along with  $k_s = 1.4$  Wm<sup>-1</sup>K<sup>-1</sup> were used as known inputs during the fitting to obtain  $k_{l,anis}$  ( $k_{avg}$ ) =  $\sqrt{k_{l,xy}k_{l,z}}$ ,  $\Delta_{anis} = \frac{k_{l,xy}}{k_{l,z}}$ , and interfacial thermal resistance between SiO<sub>2</sub> and 2D perovskite ( $r_{intSiO_2-Perovskit}$ ), respectively as fitting parameters and to deconvolute it into  $k_{l,xy}$  and  $k_{l,z}$  finally. However, similar to the Si/SiO<sub>2</sub> heterojunction,

we first generated a series of simulated curves for different  $k_{l,anis}$  ( $k_{avg}$ ) and  $\Delta_{anis}$  to get a preliminary idea about these parameters before the original fitting (Figure. A.5).

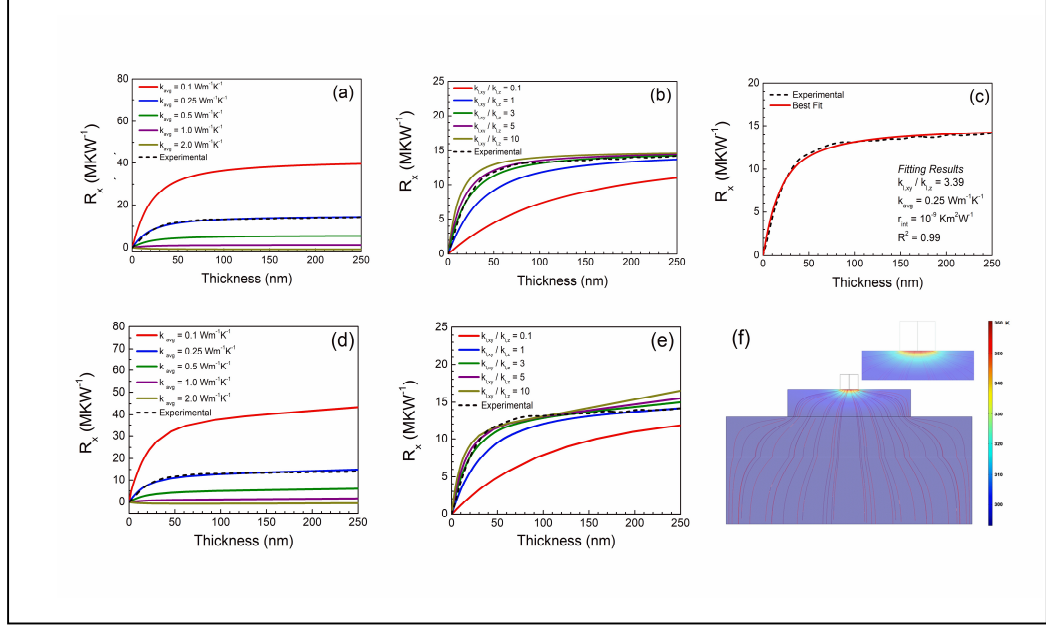


**Figure A.5.** (a-b) Simulated thermal resistance dependence for different  $k_{l,anis}$  ( $k_{avg}$ ) and  $\Delta_{anis}$  ( $\frac{k_{l,xy}}{k_{l,z}}$ ) and (c) the fitting plots for Si/SiO<sub>2</sub> heterojunction (analytical model). (d-e) FEA simulated forward plots for different  $k_{l,anis}$  ( $k_{avg}$ ) and  $\Delta_{anis}$ . ( $\frac{k_{l,xy}}{k_{l,z}}$ ). (f) FEA simulated results of thermal gradient and heat flow (inset shows a zoomed in view).

The results showed that  $k_{l,anis}$  ( $k_{avg}$ ) of the top 2D perovskite layer lies close to  $0.25 \text{ Wm}^{-1}\text{K}^{-1}$ ; such ultra-low value of  $k_l$  is comparable to similar 2D perovskites and its 3D counterpart MAPbI<sub>3</sub> [30,31,33,34,55]. Similarly,  $\Delta_{anis}$  was found to be located in between 2 to 4 which is a good match compared to the recent report of a similar 2D perovskites [31]. We could obtain the precise value of  $k_{l,anis}$  ( $k_{avg}$ ) =  $0.25 \text{ Wm}^{-1}\text{K}^{-1}$  and  $\Delta_{anis} = 3.39$  *vis-à-vis*  $k_{l,xy} = 0.457 \text{ Wm}^{-1}\text{K}^{-1}$  and  $k_{l,z} = 0.135 \text{ Wm}^{-1}\text{K}^{-1}$  after refinement of the experimental data to achieve high agreement with theoretical model in terms of adequate goodness of fit (Table I). It may be concluded that the

independent determination of several thermal parameters in a single experiment became possible, as the measurements were performed for the varied thickness of the sample, which was equivalent to the multiple experiments on the same system (Figure. A.3). Finally, for the validation we introduced these fitting parameters in our FEA model structure similar to the reference sample. We observed a negligible thermal gradient at low thickness in contrast to that for higher thickness where the interface does not influence the heat spreading. Moreover, at higher thickness, the direction of heat flow is also found to be anisotropic having a slightly larger contribution towards the in-plane direction.

### A.3.5. Origin of Anisotropic Thermal Transport in 2D Perovskite

Our study reveals the occurrence of thermal anisotropy in this compound. Such anisotropy in thermal transport can be explained considering the structural landscape of the compound and associated phonon transport (Figure A.6a). As mentioned earlier, in such 2D-RP perovskite, the large PEA chains are aligned in the out-of-plane direction having covalent bonds (C-C and C-N). In addition, weak van der Waals and electrostatic interactions can be found between two vertically stacked organic chains and at the organic-inorganic interfaces. On the other hand, there are strong ionic bonds in the in-plane direction originated from the continuous  $[\text{PbI}_4]^{2-}$  octahedral framework [8,31,42,43]. It may be noted that thermal conductivity can be expressed as  $k_l = \frac{1}{3}C_v v^2 \tau$  where,  $C_v$  represents volumetric heat capacity,  $v$  signifies phonon group velocity and  $\tau$  is phonon lifetime. As such  $C_v$  does not have any directional dependence in contrast to  $v$  and  $\tau$  in governing the anisotropic thermal transport in the compound. Along in-plane direction, presence of continuous  $[\text{PbI}_4]^{2-}$  octahedral framework allows uninterrupted pathways for heat transport [56]. In short, phonons would possess relatively large lifetimes and group velocities within these inorganic layers resulting in a higher thermal conductivity ( $k_{l,xy} = 0.45 \text{ Wm}^{-1}\text{K}^{-1}$ ). In contrast, presence of organic-inorganic interfaces and the weak interactions of two vertically stacked organic chains



would result into scattering of phonons along the out-of-plane direction [43,57]. Hence, thermal transport would be interrupted due to the shorter lifetime and group velocities of phonons leading to comparably lower thermal conductivity along cross plane ( $k_{l,z} = 0.13 \text{ Wm}^{-1}\text{K}^{-1}$ ). In a nutshell, the anisotropy originates mainly due to the antagonism between continuous heat conduction in the inorganic layer along the plane versus the interrupted ones in the cross plane. Our experimental result matches well with the reports of Li et al as obtained from molecular dynamics (MD) simulations of similar 2D perovskite (Figure A.6b). However, the value of  $\Delta_{anis}$  ( $\sim 3.4$ ) is found to be small compared to most of the other layered compounds (Figure A.6c) [58-60]; it may be noted that due to the small volume fraction of the inorganic layers the anisotropy becomes weak.

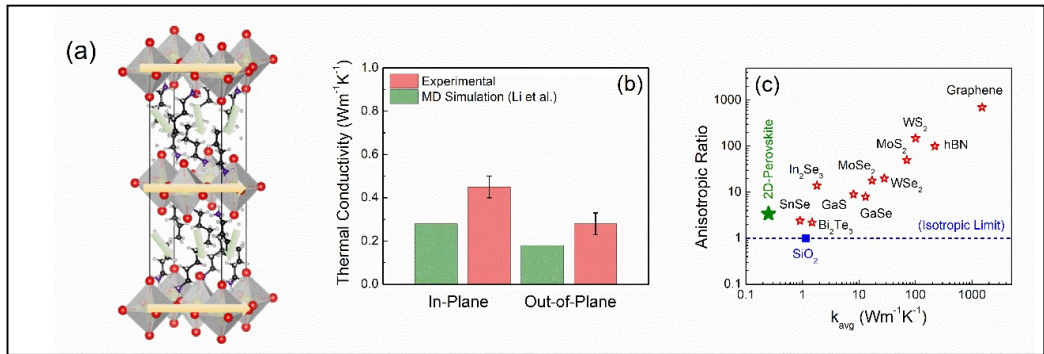


**Figure A.6.** (a) Heat (phonon) conduction pathways in a 2D-RP perovskite along in-plane and out-of-plane directions. (b) Comparison of in-plane and out-of-plane thermal conductivity of  $(\text{PEA})_2\text{PbI}_4$  with respective to MD simulation of similar 2D perovskite [31]. (c) Anisotropic ratio vs average thermal conductivity of 2D-RP perovskite compared to other layered compounds.

## A.4. Conclusions

In this work, we measured thermal transport parameters ( $k_{l,anis}$ ,  $\Delta_{anis}$  vis-à-vis  $k_{l,xy}$ ,  $k_{l,z}$ ) of an archetypal 2D perovskite system of  $(\text{PEA})_2\text{PbI}_4$  thin-films, through xSThM. The low angle nanoscale quality wedge cut of the perovskite thin film on the  $\text{SiO}_2/\text{Si}$  substrate was obtained through the Ar ion BEXP method that allowed to

effectively in one SThM measurement to obtain thermal conductance data for the various thicknesses of all nanoscale layers. The experimentally obtained data were then used to first calibrate the SThM measurements and ultimately with analytical model validated by FEA simulation to directly calculate the absolute values of in-plane and cross-plane anisotropic thermal conductivity  $k_{l,xy}$  and  $k_{l,z}$  of the 2D perovskite finally. We obtained an ultra-low value of average thermal conductivity of this material of ( $k_{avg}$ ) =  $0.25 \pm 0.05 \text{ Wm}^{-1}\text{K}^{-1}$  for the 2D perovskite with an anisotropy factor ( $k_{l,xy}/k_{l,z} \sim 3.4$ ) that we attribute to the unique structure of the perovskite leading to different phonon lifetimes and phonon group velocities along cross-plane and in-plane directions. This work provides new physical insights that would be useful for the thermal management of 2D perovskite based optoelectronic devices and their applications in thermoelectric.

## A.5 References

- [1] J. C. Blancon, H. Tsai, W. Nie, C. C. Stoumpos, L. Pedesseau, C. Katan, M. Kepenekian, C. M. M. Soe, K. Appavoo, M. Y. Sfeir, S. Tretiak, P. M. Ajayan, M. G. Kanatzidis, J. Even, J. J. Crochet, and A. D. Mohite, *Science* **355**, 1288 (2017).
- [2] L. T. Dou, A. B. Wong, Y. Yu, M. L. Lai, N. Kornienko, S. W. Eaton, A. Fu, C. G. Bischak, J. Ma, T. N. Ding, N. S. Ginsberg, L. W. Wang, A. P. Alivisatos, and P. D. Yang, *Science* **349**, 1518 (2015).
- [3] C. R. Kagan, D. B. Mitzi, and C. D. Dimitrakopoulos, *Science* **286**, 945 (1999).
- [4] C. M. M. Soe, C. C. Stoumpos, M. Kepenekian, B. Traore, H. Tsai, W. Y. Nie, B. H. Wang, C. Katan, R. Seshadri, A. D. Mohite, J. Eymann, T. J. Marks, and M. G. Kanatzidis, *J. Am. Chem. Soc.* **139**, 16297 (2017).
- [5] Y. T. Zheng, T. T. Niu, X. Q. Ran, J. Qiu, B. X. Li, Y. D. Xia, Y. H. Chen, and W. Huang, *J. Mater. Chem. A* **7**, 13860 (2019).
- [6] L. Etgar, *Energy Environ. Sci.* **11**, 234 (2018).

- [7] L. L. Mao, C. C. Stoumpos, and M. G. Kanatzidis, *J. Am. Chem. Soc.* **141**, 1171 (2019).
- [8] G. B. Wu, R. Liang, Z. P. Zhang, M. Z. Ge, G. C. Xing, and G. X. Sun, *Small* **17**, 2103514 (2021).
- [9] S. Bellani, A. Bartolotta, A. Agresti, G. Calogero, G. Grancini, A. Di Carlo, E. Kymakis, and F. Bonaccorso, *Chem. Soc. Rev.* **50**, 11870 (2021).
- [10] S. Ghimire and C. Klinker, *Nanoscale* **13**, 12394 (2021).
- [11] M. Pandey, K. W. Jacobsen, and K. S. Thygesen, *J. Phys. Chem. Lett.* **7**, 4346 (2016).
- [12] B. K. Song, J. Hou, H. N. Wang, S. Sidhik, J. S. Miao, H. G. Gu, H. Q. Zhang, S. Y. Liu, Z. Fakhraei, J. Even, J. C. Blancon, A. D. Mohite, and D. Jariwala, *ACS Mater. Lett.* **3**, 148 (2021).
- [13] Y. Zhang, R. Z. Wang, Y. Z. Li, Z. Y. Wang, S. Hu, X. L. Yan, Y. X. Zhai, C. Zhang, and C. X. Sheng, *J. Phys. Chem. Lett.* **10**, 13 (2019).
- [14] L. N. Quan, Y. B. A. Zhao, F. P. G. de Arquer, R. Sabatini, G. Walters, O. Voznyy, R. Comin, Y. Y. Li, J. Z. Fan, H. R. Tan, J. Pan, M. J. Yuan, O. M. Bakr, Z. H. Lu, D. H. Kim, and E. H. Sargent, *Nano Lett.* **17**, 3701 (2017).
- [15] B. Sun, Y. Xu, Y. H. Chen, and W. Huang, *APL Mater.* **8**, 11, 040901 (2020).
- [16] X. Hong, T. Ishihara, and A. V. Nurmikko, *Phys. Rev. B* **45**, 6961 (1992).
- [17] R. Ahumada-Lazo, R. Saran, O. Woolland, Y. P. Jia, M. E. Kyriazi, A. G. Kanaras, D. Binks, and R. J. Curry, *J. Phys. Photonics* **3**, 021002 (2021).
- [18] T. P. Chen, J. X. Lin, C. C. Lin, C. Y. Lin, W. C. Ke, D. Y. Wang, H. S. Hsu, C. C. Chen, and C. W. Chen, *ACS Appl. Mater. Interfaces* **13**, 10279 (2021).
- [19] B. R. Wygant, A. Z. Ye, A. Dolocan, Q. Vu, D. M. Abbot, and C. B. Mullins, *J. Am. Chem. Soc.* **141**, 18170 (2019).
- [20] Y. Yang, F. Gao, S. W. Gao, and S. H. Wei, *J. Mater. Chem. A* **6**, 14949 (2018).
- [21] Z. X. Gan, Y. C. Cheng, W. J. Chen, K. P. Loh, B. H. Jia, and X. M. Wen, *Adv. Sci.* **8**, 2001843 (2021).

- 
- [22] D. Ghosh, D. Acharya, L. Pedesseau, C. Katan, J. Even, S. Tretiak, and A. J. Neukirch, *J. Mater. Chem. A* **8**, 22009 (2020).
- [23] A. Burgos-Caminal, E. Socie, M. E. F. Bouduban, and J. E. Moser, *J. Phys. Chem. Lett.* **11**, 7692 (2020).
- [24] F. T. Pei, N. X. Li, Y. H. Chen, X. X. Niu, Y. Zhang, Z. Y. Guo, Z. J. Huang, H. C. Zai, G. L. Liu, Y. M. Zhang, Y. Bai, X. Zhang, C. Zhu, Q. Chen, Y. Li, and H. P. Zhou, *ACS Energy Lett.* **6**, 3029 (2021).
- [25] S. N. Hsu, W. C. Zhao, Y. Gao, Akriti, M. Segovia, X. F. Xu, B. W. Boudouris, and L. T. Dou, *Nano Lett.* **21**, 7839 (2021).
- [26] S. J. Yang, D. Kim, J. Choi, S. H. Kim, K. Park, S. Ryu, and K. Cho, *Adv. Mater.* **33**, 2102797 (2021).
- [27] X. G. Jia, J. Jiang, Y. Zhang, J. H. Qiu, S. B. Wang, Z. H. Chen, N. Y. Yuan, and J. N. Ding, *Appl. Phys. Lett.* **112**, 143903 (2018).
- [28] F. Sekiguchi, H. Hirori, G. Yumoto, A. Shimazaki, T. Nakamura, A. Wakamiya, and Y. Kanemitsu, *Phys. Rev. Lett.* **126**, 077401 (2021).
- [29] A. D. Christodoulides, P. J. Guo, L. Y. Dai, J. M. Hoffman, X. T. Li, X. B. Zuo, D. Rosenmann, A. Brumberg, M. G. Kanatzidis, R. D. Schaller, and J. A. Malen, *ACS Nano* **15**, 4165 (2021).
- [30] A. Giri, A. Z. Chen, A. Mattoni, K. Aryana, D. Zhang, X. Hu, S. H. Lee, J. J. Choi, and P. E. Hopkins, *Nano Lett.* **20**, 3331 (2020).
- [31] C. Li, H. Ma, T. Y. Li, J. H. Dai, M. A. Rasel, A. Mattoni, A. Alatas, M. G. Thomas, Z. W. Rouse, A. Shragai, S. P. Baker, B. J. Ramshaw, J. P. Feser, D. B. Mitzi, and Z. T. Tian, *Nano Lett.* **21**, 3708 (2021).
- [32] A. Makris, T. Haeger, R. Heiderhoff, and T. Riedl, *RSC Adv.* **6**, 94193 (2016).
- [33] T. Haeger, M. Wilmes, R. Heiderhoff, and T. Riedl, *J. Phys. Chem. Lett.* **10**, 3019 (2019).
- [34] T. Haeger, R. Heiderhoff, and T. Riedl, *J. Mater. Chem. C* **8**, 14289 (2020).
- [35] S. Gomes, A. Assy, and P. O. Chapuis, *Phys. Status Solidi A-Appl. Mat.* **212**, 477 (2015).

- [36] A. J. Robson, I. Grishin, R. J. Young, A. M. Sanchez, O. V. Kolosov, and M. Hayne, *ACS Appl. Mater. Interfaces* **5**, 3241 (2013).
- [37] Y. S. Muzychka, *J. Thermophys. Heat Transf.* **28**, 313 (2014).
- [38] Y. S. Muzychka, M. M. Yovanovich, and J. R. Culham, *J. Thermophys. Heat Transf.* **18**, 45 (2004).
- [39] J. Spiece, C. Evangeli, A. J. Robson, A. El Sachat, L. Haenel, M. I. Alonso, M. Garriga, B. J. Robinson, M. Oehme, J. Schulze, F. Alzina, C. S. Torres, and O. V. Kolosov, *Nanoscale* **13**, 10829 (2021).
- [40] P. D. Tovee and O. V. Kolosov, *Nanotechnology* **24**, 465706 (2013).
- [41] P. D. Tovee, M. E. Pumarol, M. C. Rosamond, R. Jones, M. C. Petty, D. A. Zeze, and O. V. Kolosov, *Phys. Chem. Chem. Phys.* **16**, 1174 (2014).
- [42] J. Yin, R. Naphade, L. G. Arzaluz, J. L. Bredas, O. M. Bakr, and O. F. Mohammed, *ACS Energy Lett.* **5**, 2149 (2020).
- [43] P. J. Guo, C. C. Stoumpos, L. L. Mao, S. Sadasivam, J. B. Ketterson, P. Darancet, M. G. Kanatzidis, and R. D. Schaller, *Nat. Commun.* **9**, 2019 (2018).
- [44] X. Y. Gan, O. Wang, K. Y. Liu, X. J. Du, L. L. Guo, and H. X. Liu, *Sol. Energy Mater. Sol. Cells* **162**, 93 (2017).
- [45] K. Z. Du, Q. Tu, X. Zhang, Q. W. Han, J. Liu, S. Zauscher, and D. B. Mitzi, *Inorg. Chem.* **56**, 9291 (2017).
- [46] O. V. Kolosov, I. Grishin, and R. Jones, *Nanotechnology* **22**, 185702 (2011).
- [47] D. Buckley, Z. R. Kudrynskyi, N. Balakrishnan, T. Vincent, D. Mazumder, E. Castanon, Z. D. Kovalyuk, O. Kolosov, O. Kazakova, A. Tzalenchuk, and A. Patane, *Adv. Funct. Mater.* **31**, 2008967 (2021).
- [48] I. S. Bowen, *Phys. Rev.* **27**, 779 (1926).
- [49] A. Assy and S. Gomes, *Nanotechnology* **26**, 355401 (2015).
- [50] C. Evangeli, J. Spiece, S. Sangtarash, A. J. Molina-Mendoza, M. Mucientes, T. Mueller, C. Lambert, H. Sadeghi, and O. Kolosov, *Adv. Electron. Mater.* **5**, 1900331 (2019).

- 
- [51] J. Spiece, C. Evangeli, K. Lulla, A. Robson, B. Robinson, and O. Kolosov, *J. Appl. Phys.* **124**, 015101 (2018).
- [52] T. Yamane, N. Nagai, S. Katayama, and M. Todoki, *J. Appl. Phys.* **91**, 9772 (2002).
- [53] H. R. Shanks, P. H. Sidles, P. D. Maycock, and G. C. Danielson, *Phys. Rev.* **130**, 1743 (1963).
- [54] F. R. Brotzen, P. J. Loos, and D. P. Brady, *Thin Solid Films* **207**, 197 (1992).
- [55] C. Y. Ge, M. Y. Hu, P. Wu, Q. Tan, Z. Z. Chen, Y. P. Wang, J. Shi, and J. Feng, *J. Phys. Chem. C* **122**, 15973 (2018).
- [56] P. S. Cheng, N. Shulumba, and A. J. Minnich, *Phys. Rev. B* **100**, 094306 (2019).
- [57] W. L. Ong, E. S. O'Brien, P. S. M. Dougherty, D. W. Paley, C. F. Higgs, A. J. H. McGaughey, J. A. Malen, and X. Roy, *Nat. Mater.* **16**, 83 (2017).
- [58] P. Q. Jiang, X. Qian, R. G. Yang, and L. Lindsay, *Phys. Rev. Mater.* **2**, 064005 (2018).
- [59] H. J. Jang, J. D. Wood, C. R. Ryder, M. C. Hersam, and D. G. Cahill, *Adv. Mater.* **27**, 8017 (2015).
- [60] P. Q. Jiang, X. Qian, X. K. Gu, and R. G. Yang, *Adv. Mater.* **29**, 1701068 (2017).

# Appendix B

## Sulfur-Vacancy Passivation in Sb<sub>2</sub>S<sub>3</sub> Thin Films

*In the field of lead-free photovoltaic materials, Sb<sub>2</sub>S<sub>3</sub> is considered a promising material. Hence, in this appendix chapter, we have presented a modified two-step sequential deposition method for forming Sb<sub>2</sub>S<sub>3</sub> thin films. In contrast to the conventional chemical bath deposition (CBD) route, this sequential deposition approach has allowed passivation of sulfur-vacancies in Sb<sub>2</sub>S<sub>3</sub> through control over precursor-stoichiometry (S/Sb ratio) during the film-formation. We have made an in-depth characterization of the chalcogenide thin films upon passivation of the vacancies. While a sulfur-deficient composition led to the formation of donor-like sulfur vacancies, a sulfur-rich stoichiometry passivated such vacancies followed by the creation of sulfur antisite defects in the chalcogenide. Scanning tunneling spectroscopy and thereby density of states allow us to locate individual band-energies and their dependence on defect-passivation. A strong dependence of optical bandgap and surface morphology of the Sb<sub>2</sub>S<sub>3</sub> layer on the precursor stoichiometry has been evidenced in our study and an optimized balance between the parameters is estimated for a slightly sulfur-rich composition (S/Sb ratio of 1.2). Interestingly, the photovoltaic parameters of Cu: NiO/Sb<sub>2</sub>S<sub>3</sub>/PCBM planar heterojunctions excelled at the predicted stoichiometry yielding a power conversion efficiency of 3.02% along with a significantly high open-circuit voltage of 0.8 V. This effort thus provides new insights into the influence of defect-passivation on solar cell characteristics based on solution-processed Sb<sub>2</sub>S<sub>3</sub> thin films.*

## B.1. Introduction

The necessity for low-cost and environmentally-benign materials for high-efficiency solar cell applications has compelled researchers to explore newer photovoltaic materials [1]. Despite the tremendous success of organic-inorganic hybrid lead halide perovskites, novel inorganic semiconductors still attract significant interest owing to their favorable optoelectronic properties [2]. Amongst these materials, antimony trisulfide ( $\text{Sb}_2\text{S}_3$ ) has emerged as a potential solar energy material due to its earth-abundant and nontoxic constituents along with optimal physical properties, such as a suitable direct bandgap (1.7 eV), high absorption coefficient ( $10^5 \text{ cm}^{-1}$  at 450 nm), and a decent stable structure [3-5]. Besides, its existence in a single stable phase having a low melting point ( $\sim 550 \text{ }^\circ\text{C}$ ) aids the formation of  $\text{Sb}_2\text{S}_3$  thin films in a phase-pure and highly-crystalline form [6]. All these properties make  $\text{Sb}_2\text{S}_3$  a potential candidate for its use in stable, efficient, and less-expensive photovoltaic devices [7].

Efforts with  $\text{Sb}_2\text{S}_3$  as a solar energy material have mostly been accounted for the fabrication of solid-state sensitized solar cells having an extremely thin-absorber (ETA) architecture [8,9]. The ETA design is principally derived from dye-sensitized solar cell (DSSC) structures, where a thin absorber layer having a thickness of  $\sim 10 \text{ nm}$  is typically deposited onto a mesoporous  $\text{TiO}_2$  scaffold and the pores are subsequently filled with a hole-transport material (HTM), such as P3HT, CuSCN, or Spiro-OMeTAD [10-12]. The basic advantage behind the realization of such a device structure is faster carrier transfer from the thin absorber-layer to the carrier-selective contacts; however, in practice, such benefits are restricted by carrier-recombination via trap-assisted tunneling [13]. As a result,  $\text{Sb}_2\text{S}_3$ -based ETA solar cells have so far yielded a power conversion efficiency of  $\sim 7.5\%$  which is well below the possibility as per the Shockley Queisser efficiency limit [14]. Improper infiltration of pores in ETA solar cells has been a major roadblock to achieving improved performance in the solar cells [15]. In this respect, the introduction of a planar geometry in such architecture has been projected to be a feasible solution to circumvent the constraint [16]. A compact film having a planar structure not only would reduce the requirement of a large interfacial area for



appreciable photocurrent generation, but it would also moreover prevent interfacial carrier-recombination. Indeed, despite a lower efficiency, planar geometries have so far yielded a higher open-circuit voltage ( $V_{oc}$ ) than that in best-performing ETA cells comprised of the same HTM and Sb<sub>2</sub>S<sub>3</sub> formed through an identical deposition route [17].

The performance of a planar solar cell depends a lot on the quality of the absorber layer. Typically, Sb<sub>2</sub>S<sub>3</sub> thin films are fabricated by the chemical bath deposition (CBD) technique, which is a method elegantly developed by Messina *et al* [18]. Such a route, although convenient and cost-effective, is unfortunately associated with several constraints limiting the performance of devices based on as-grown Sb<sub>2</sub>S<sub>3</sub> films [18,19]. As an alternative to CBD method, spin-coating of different antimony and sulfur-containing precursors was proposed to cast Sb<sub>2</sub>S<sub>3</sub> thin films [3,20]. Such films, when incorporated into a sensitized device structure, have delivered a PCE value of 6.8% [6]. Zheng *et al.* developed a fast solid-gas reaction process to fabricate Sb<sub>2</sub>S<sub>3</sub>-sensitized solar cells with a PCE of 6.27% [21]. While most of the efforts in Sb<sub>2</sub>S<sub>3</sub> solar cells have been carried out in a sensitized architecture, CBD-grown films in most of the planar devices have shown PCE values below 5% which is lower than that in sensitized structures [22,23]. To date, the highest PCE of 5.77% has been reported with films grown by the atomic layer deposition (ALD) method; some of the studies have inferred that the inferior performance of Sb<sub>2</sub>S<sub>3</sub>-based planar heterojunction solar cells could be ascribed to the presence of bulk and surface defects and also a high-resistivity in the films limiting the short-circuit current density ( $J_{sc}$ ) and fill-factor ( $FF$ ) of the devices [24-26]. Hence, to achieve an improved PCE in Sb<sub>2</sub>S<sub>3</sub> planar heterojunction solar cells, it is important to control the intrinsic defects by tuning sulfur vacancies in the material.

In this direction, we have investigated the influence of sulfur vacancies on the photovoltaic properties of antimony trisulfide (Sb<sub>2</sub>S<sub>3</sub>) thin films. We have considered a modified sequential deposition approach to fabricate uniform and phase-pure Sb<sub>2</sub>S<sub>3</sub> thin films; this approach offers not only an alternative to the traditionally used CBD technique but also a precise control over the thickness and composition of the films.

Here, we have tailored the sulfur-vacancies in the as-grown  $\text{Sb}_2\text{S}_3$  films following a couple of routes: precursor stoichiometry and ultraviolet ozone treatment. By monitoring the shift of band-energies through scanning tunneling spectroscopy (STS) and thereof the density of states (DOS) spectra, we aimed to form energy-level optimized planar heterojunctions solar cells with a high open-circuit voltage ( $V_{OC}$ ).

## B.2. Materials and Methods

### B.2.1. Materials

Antimony(III) acetate ( $\text{Sb}(\text{CH}_3\text{COO})_3$ , 99.9%), thiourea  $\text{SC}(\text{NH}_2)_2$ , nickel(II) acetate tetrahydrate ( $\text{Ni}(\text{CH}_3\text{COO})_2 \cdot 4\text{H}_2\text{O}$ , 98%), copper(II) chloride dihydrate ( $\text{CuCl}_2 \cdot 2\text{H}_2\text{O}$ , 99.9%), anhydrous N, N-dimethylformamide (DMF, 99.8%), dimethyl sulfoxide (DMSO, 99.9%), methanol, and diethanolamine were purchased from Sigma Aldrich Chemical Co. Phenyl-C61-butyric acid methyl ester (PCBM, 99%) was procured from M/s SES Research, Houston, TX. The materials were used without further purification.

### B.2.2. Fabrication of $\text{Sb}_2\text{S}_3$ Thin Films through a Two-Step Sequential Deposition Approach

The  $\text{Sb}_2\text{S}_3$  thin films were deposited following a reported solution-based sequential deposition approach with some modifications [3]. Briefly, antimony acetate and thiourea as cationic and anionic precursors were dissolved in DMF and DMSO, respectively, at 70 °C in the desired stoichiometry. To form  $\text{Sb}_2\text{S}_3$  films, the cationic-precursor was first spun on a substrate at 2500 rpm for 30 s followed by a coating of the anionic-precursor at an identical spinning condition. The as-deposited films were then subjected to a two-step annealing process: 100 °C for 10 min followed by 300 °C for 20 min. During such an annealing protocol, the as-deposited transparent and colorless films gradually became yellow and finally a shiny brown while retaining their transparent nature.

To control the sulfur content in Sb<sub>2</sub>S<sub>3</sub> films, the ratio between anionic and cationic precursors varied between 0.6 and 1.4 in steps of 0.2 in forming Sb<sub>2</sub>S<sub>3</sub> in a sulfur-deficient and sulfur-rich condition, respectively. In another approach, films formed through stoichiometrically-balanced precursors (S/Sb = 1.0) were subjected to a UV-ozone (UVO) treatment for 5, 10, 15, or 20 min using a Novascan 4"-UV/Ozone System cleaning unit (model PSDP-UV4T).

### **B.2.3. Formation of Copper-Doped Nickel Oxide Thin Films**

Copper-doped nickel oxide (Cu: NiO) thin films were cast following a routine sol-gel approach [27]. A precursor solution of an optimized concentration was prepared at room temperature by dissolving 0.4 M Ni(OCOCH<sub>3</sub>)<sub>2</sub> with 5 at% CuCl<sub>2</sub> (as doping agent) in methanol which acted as the solvent. Upon complete dissolution, diethanolamine was added drop-wise to the precursor under a vigorous stirring condition. The color of the solution was changed from light-green to light-blue implying the formation of the respective ammine complex. The resulting solution was further stirred for one hour and filtered for further use. Suitable substrates were coated with the solution and annealed at 425 °C for 20 min in an ambient condition leading to thermal decomposition of the ammine complex and the formation of crystalline thin films of Cu: NiO.

### **B.2.4. Characterization of the Chalcogenides**

The materials were characterized through conventional techniques, such as X-ray diffraction (XRD) studies, Raman spectroscopy, X-ray photoelectron spectroscopy (XPS), and optical absorption spectroscopy. The measurements were carried out with a Rigaku Smart Lab X-ray diffractometer (Cu K $\alpha$  radiation,  $\lambda = 1.54 \text{ \AA}$ ), a Horiba Jobin Yvon Raman triple-grating spectrometer system (model number T64000) using a 532.0 nm excitation from a diode-pumped solid-state (DPSS) laser, an Omicron XPS instrument (Serial no. 0571), and a UV-Vis-NIR spectrophotometer (Cary 5000, Agilent

Technologies), respectively. Additionally, band-edges of the materials were probed using scanning tunneling spectroscopy (STS) of ultra-thin films with a Nanosurf Easyscan2 scanning tunneling microscope (STM) under ambient conditions. Highly-doped silicon wafers (both *n*-type and *p*-type with arsenic and boron as dopants, respectively) having a resistivity of 3-10 m $\Omega$ -cm were used as substrates for the studies. The Si substrates were cleaned with HF to remove the oxide layer before usage. Extremely-sharp tips were formed through an acute mechanical cut of a Pt/Ir (80%:20%) wire having a diameter of 0.25  $\mu$ m. During the approach of the tip, a current of 1 nA was set at a bias of 2.0 V, which was applied to the tip. Morphology of the films was recorded with a JEOL JSM-7500F Field Emission Scanning Electron Microscope (FE-SEM) and a Nanosurf Easyscan2 atomic force microscope (AFM) in a non-contact mode.

### B.2.5. Fabrication and Characterization of Devices

While fabricating solar cells, indium tin oxide (ITO) coated glass substrates were cleaned following a standard protocol; they were then subjected to a UV-ozone (UVO) treatment for 20 min. On these treated substrates, a  $\sim$ 40 nm thick hole-transport layer (HTL) of Cu: NiO was formed. The HTL-coated ITO substrates were subjected to a very short UVO treatment of around 3 min. They were then transferred to a nitrogen-filled glove box. The substrates were pre-heated at 70  $^{\circ}$ C for 10 min before depositing a layer of Sb<sub>2</sub>S<sub>3</sub> ( $\sim$ 120 nm) following the two-step sequential deposition process (*vide supra*). As an electron-transport layer (ETL), PCBM was spun at 3000 rpm for 30 s from a 20 mg/mL solution in chlorobenzene. The films were then annealed at 100  $^{\circ}$ C for 10 min. The device fabrication process was completed by depositing 100 nm thick aluminum strips (orthogonal to the ITO ones) as a top electrode through thermal evaporation in a vacuum chamber (10<sup>-6</sup> mbar) fitted inside the glove box. The active area of the cells was 10 mm<sup>2</sup>.

The planar heterojunction devices were characterized by recording current-voltage (*I-V*) characteristics under dark and 1 sun illumination conditions using a

Keithley 2636A electrometer controlled by LabTracer 2.0 software. The measurements were carried out inside the glove box which had both oxygen and moisture content below 0.1 ppm. Contacts with the electrodes were made with pressure-loaded probes. As a source for illumination, a 300 W solar simulator (Newport-Oriel Sol3A) attached with an AM1.5 filter was used. The simulator was placed outside the glove box and the devices were illuminated through a quartz window fitted to the platform of the glove box. To avoid any contribution from neighboring cells or areas outside the cell, regions outside the device under consideration were covered while recording  $I$ - $V$  characteristics under an illumination condition. A Solartron 1260A impedance analyzer was used to record real and imaginary components of complex impedance as a function of frequency; an ac voltage of 10 mV RMS was applied for the impedance measurement with a dc bias of  $V_{OC}$ . The frequency of the test voltage varied between 1 Hz and 10 MHz and ten measurements were made per decade. The external quantum efficiency (EQE) spectrum of the solar cells was recorded with a Horiba Jobin Yvon H20 IR monochromator dispersing the simulated solar illumination; the corresponding photocurrent was measured with a Keithley 486 picoammeter.

## **B.3. Results and Discussions**

### **B.3.1. Importance of Sequential Deposition Approach in Forming Sb<sub>2</sub>S<sub>3</sub> Films**

Over the years, the CBD technique has been the most common synthesis method to fabricate Sb<sub>2</sub>S<sub>3</sub> thin films for photovoltaic applications [10,18,22]. Typically, in the CBD method, a substrate is immersed in a precursor bath to form thin films of non-metallic inorganic semiconductors. The bath contains both cationic and anionic precursors dissolved in a suitable solvent often with an additional complexing agent(s) required to improve the uniformity and crystallinity of the films, and also in controlling thermodynamics and kinetics of the deposition process [28]. Despite such measures, CBD-grown Sb<sub>2</sub>S<sub>3</sub> films lacked the desired phase purity, since the films contain

impurities, such as antimony oxides, hydroxides, or even sulfates [18,29]. Such impurities result in deep traps in  $\text{Sb}_2\text{S}_3$  films and thereby limit the performance of the respective cells. Moreover, the complex reaction mechanism, which includes heterogeneous nucleation and exponential growth of the films at a low temperature ( $\sim 10^\circ\text{C}$ ), demands precise control of processing conditions and eventually hinders reproducibility of the process. It should also be noted that a significantly long time ( $\sim 4$  h) is often needed in the CBD approach to obtain an appropriate thickness which may also affect the phase purity and substrate coverage [30].

In contrast, the sequential deposition process per se through spin-coating is rapid, essentially controls film morphology, and has comparatively easier processability [3]. After sequential deposition of the precursors, the formation of thin films occurs during post-deposition annealing. In this work, we have applied a modified sequential deposition process in forming  $\text{Sb}_2\text{S}_3$  thin films (Figure B.1). The post-deposition annealing was done at a mild temperature of  $100^\circ\text{C}$ ; at this temperature, thiourea decomposes to generate  $\text{H}_2\text{S}$  which reacts rapidly with antimony acetate in forming amorphous  $\text{Sb}_2\text{S}_3$  thin films. The process can in general be noticed through a gradual change in film color from transparent to light-yellow and then to dark-yellow. The crystallinity of the films was achieved after a further rise of the temperature to  $300^\circ\text{C}$  changing the film to dark brown. Interestingly, the rapid nature of the reaction between the precursors effectively prevents the formation of impurities, and thus an improved phase purity in  $\text{Sb}_2\text{S}_3$  thin film is obtained as compared to that in the CBD approach. Such a two-step process additionally offers the liberty to tune the composition by varying the precursor concentrations and the film thickness by the spinning speed. The use of the spin-coating technique furthermore improves the degree of surface coverage of the films. It is worth mentioning here that any additional post-annealing process, such as sulfurization or selenization, is not necessary for this process, since an excess chalcogen can anyway be introduced in thin films by controlling its content in the precursor.

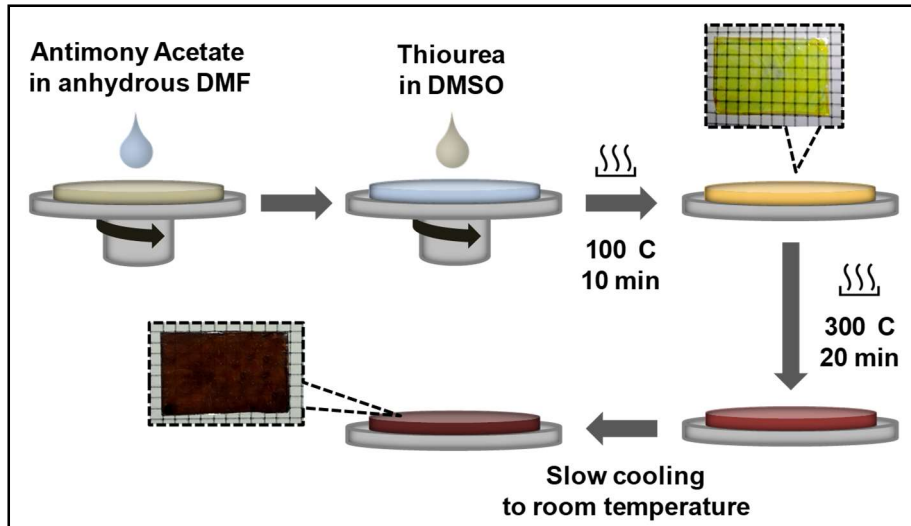


*Figure B.1. Schematic diagram of  $Sb_2S_3$  film fabrication technique through the sequential deposition approach.*

### B.3.2. Characterization of $Sb_2S_3$ Thin Films

Considering the novelty of the film-deposition approach, we first of all aimed to confirm the formation of  $Sb_2S_3$  and its phase purity through conventional thin film characterization methods. In Figure B.2, we have presented the results of  $Sb_2S_3$  thin films formed with a balanced precursor-stoichiometry ( $S/Sb = 1.0$ ). The XRD pattern (Figure B.2a) shows a series of diffraction peaks at appropriate positions (JCPDS #42-1393); the intense peak  $\sim 25^\circ$  matched the diffraction from (130) plane which is the preferred orientation for an orthorhombic stibnite structure of  $Sb_2S_3$  [31]. The intensity of the peaks and their narrow full width at half maxima (FWHM) signifies the high crystallinity of the material, while the absence of additional peaks implied its phase purity. Raman spectrum of  $Sb_2S_3$  films (Figure B.2b) showed the presence of Raman active modes in the form of dominant bands located at 187, 236, 282, and 306  $cm^{-1}$ , which are known to correspond to the orthorhombic phase, alongside, a couple of weak

ones at 126 and 155  $\text{cm}^{-1}$  [32]. The UV-Vis-NIR optical absorption spectrum of  $\text{Sb}_2\text{S}_3$  thin films has been presented in Figure B.2c, which shows a strong absorption over the entire visible region with the absorption onset being located at  $\sim 700$  nm. The band gap of the thin films has been estimated from the following relation considering  $\text{Sb}_2\text{S}_3$  as a direct bandgap semiconductor,

$$\alpha h\nu = C(h\nu - E_g)^{\frac{1}{2}} \quad (\text{B.1})$$

where,  $\alpha$  is the absorption coefficient,  $h\nu$  photon energy, and  $E_g$  is the energy gap. Extrapolating the linear region of the  $(\alpha h\nu)^2$  vs  $h\nu$  plot (inset of Figure B.2c), the bandgap of the film at room temperature could be estimated to be around 1.7 eV, which matches well with the reported results [3].

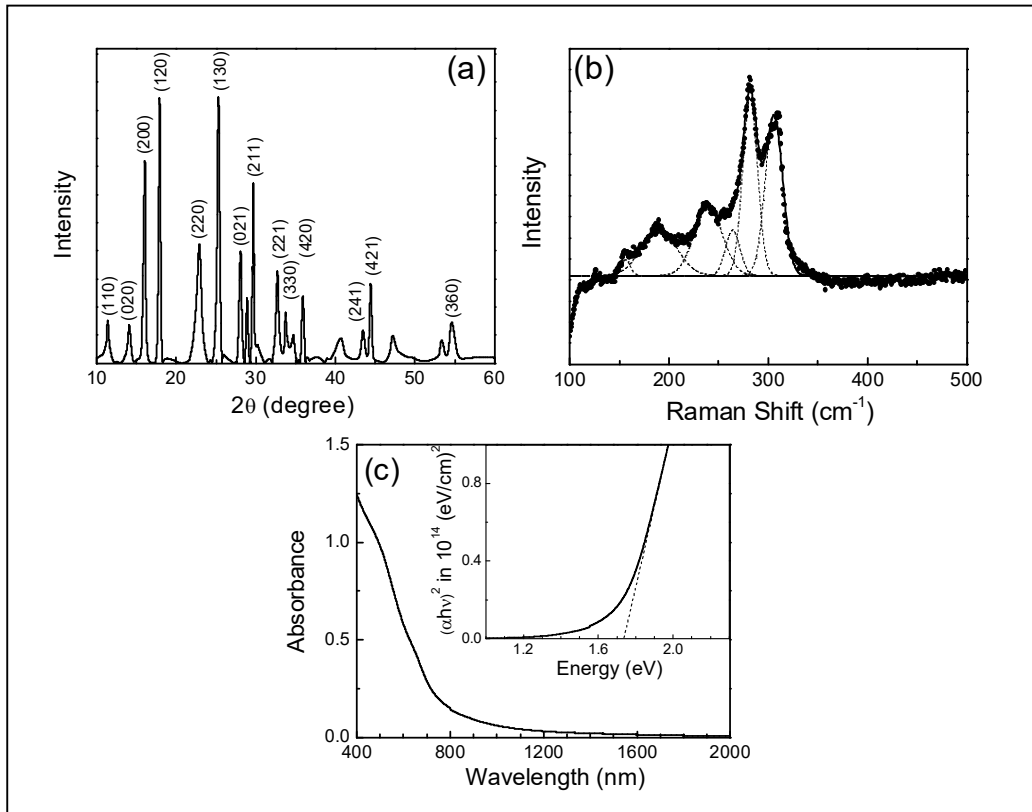


**Figure B.2.** (a) XRD pattern, (b) Raman spectrum, and (c) optical absorption spectrum along with the corresponding Tauc plot (inset) of stoichiometric ( $S/Sb = 1.0$ )  $\text{Sb}_2\text{S}_3$  thin films.



The valence state information of  $Sb_2S_3$  was derived from XPS studies. As presented in Figure B.3a, the survey spectrum of  $Sb_2S_3$  was dominated by a strong presence of antimony and signatures of sulfur and carbon. The peak at 285.0 eV signifying the presence of carbon in the films can be ascribed to be due to usual surface contaminations. We have recorded high-resolution spectra of Sb 3d and S 2p (Figures B.3b-c). In the spectrum of antimony, two peaks at 528.7 and 537.9 eV corresponded to Sb  $3d_{5/2}$  and  $3d_{3/2}$  states, respectively. The separation of the Sb 3d doublet was 9.2 eV indexing a trivalent oxidation state of antimony in the compound [33]. The asymmetric nature of the spectrum showed the presence of a couple of feeble shoulder peaks at 527.8 and 537.1 eV corresponding to the  $Sb^0$  elemental state present in the material [34]. Such a reduction of antimony can be attributed to the ion-induced effect at the time of surface-etching and should not be considered an impurity [35]. The high-resolution spectrum of sulfur showed two overlapped peaks for S  $2p_{3/2}$  and  $2p_{1/2}$  at 159.6 and 160.7 eV, respectively. The S 2p doublet showed an energy separation of 1.1 eV indicating an  $S^{2-}$  oxidation state in the material [33]. The observed binding energy values were in concurrence with the reported data reaffirming the formation of  $Sb_2S_3$  through a solution approach.

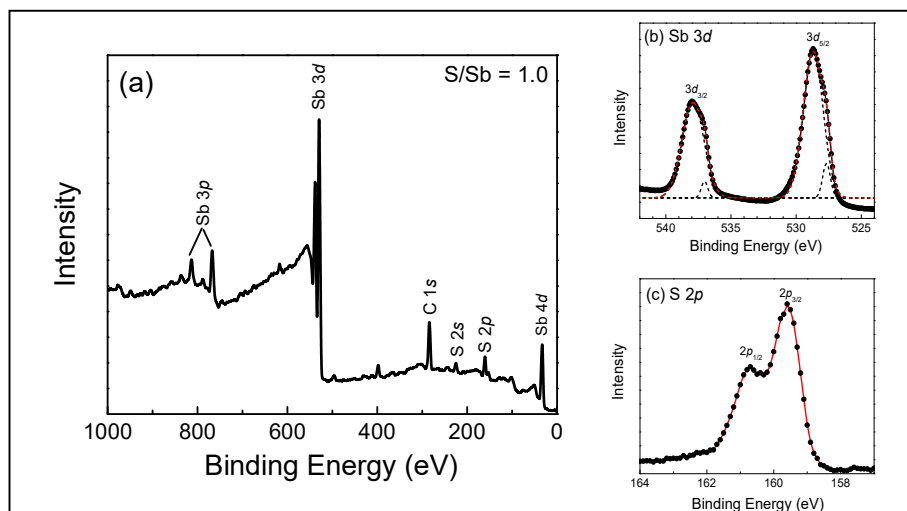


**Figure B.3.** (a) Full range XPS spectrum of  $Sb_2S_3$  thin films with high-resolution spectra of Sb 3d and S 2p states being presented in (b) and (c), respectively.

### B.3.3. Passivation of Sulfur Vacancies in $\text{Sb}_2\text{S}_3$ Thin Films

In a binary chalcogenide compound like  $\text{Sb}_2\text{S}_3$ , six intrinsic defects may exist sulfur and antimony vacancies ( $\text{S}_\text{v}$ ,  $\text{Sb}_\text{v}$ ), sulfur and antimony interstitials ( $\text{S}_\text{i}$ ,  $\text{Sb}_\text{i}$ ), and antisite substitutions ( $\text{Sb}_\text{s}$ ,  $\text{S}_\text{sb}$ ) [36]. The formation energies of the defects depend strongly on the stoichiometry of the precursors. Conversely, the anisotropic nature of  $\text{Sb}_2\text{S}_3$  crystal structure and wide distribution of bond lengths also influence defect formation with their energy level location within or outside the gap [37]. It is however well-accepted that amongst these defects, the energy level of sulfur vacancies ( $\text{S}_\text{v}$ ) is situated within the gap and thereby affects carrier transport or largely instills recombination loss [38]. Extensive efforts were hence made to develop methods in passivating sulfur vacancies in  $\text{Sb}_2\text{S}_3$  through a range of processes, such as thioacetamide post-deposition treatment [14], variation of bath-temperature in CBD approach [39], post-sulfurization (or selenization) [25], and so forth. However, the methods have always brought a restriction or another limiting their efficacy.

The sequential film-deposition approach provides an opportunity to tailor (passivate) sulfur vacancies in  $\text{Sb}_2\text{S}_3$  thin films. In this endeavor, we have considered two different methods: (1) to vary the relative sulfur content (S/Sb) in the precursors in forming both sulfur-rich and sulfur-deficient thin films and (2) to introduce a post-deposition UV-ozone treatment in suppressing the sulfur vacancies by chemisorption of oxygen atoms on the top surface of the thin films. While the former method is applicable in films formed only through a sequential film deposition approach, the latter one has been proved to be more general and effective than the previously reported ones [40].

### B.3.4. Characteristics of $\text{Sb}_2\text{S}_3$ Thin Films: Effect of Vacancy Passivation

In order to tune sulfur vacancies in our  $\text{Sb}_2\text{S}_3$  thin films, we have varied the precursor contents with respect to the stoichiometric condition ( $\text{S}/\text{Sb} = 1.0$ ) in forming

both sulfur-rich ( $S/Sb = 1.2$  and  $1.4$ ) and sulfur-deficient ( $S/Sb = 0.8$  and  $0.6$ ) compositions. The elemental compositions of  $Sb_2S_3$  films were confirmed from EDX analysis (shown in Table B.1).

**Table B.1.** Atomic percentage of sulfur and antimony in  $Sb_2S_3$  thin films having different relative sulfur contents ( $S/Sb$ ).

S/Sb ratio	Atomic % of elements		S/Sb ratio	S/Sb ratio
	S K	Sb L	(Obtained)	(Normalized)
0.6	44.7	55.3	0.8	0.5
0.8	51.8	48.2	1.1	0.7
1.0	59.8	40.2	1.5	1.0
1.2	64.3	35.7	1.8	1.2
1.4	68.4	31.6	2.2	1.4

The XRD patterns of all the vacancy-tuned  $Sb_2S_3$  films evidenced a high degree of crystallinity and a preferred orientation along the (130) plane showing continuance of the orthorhombic phase (Figure B.4a) [31]. The films showed a comparable grain size in the sulfur-deficient to stoichiometric composition whereas a gradual enlargement of the grains in the sulfur-rich conditions was noticed. We further have characterized the vacancy-tuned  $Sb_2S_3$  films by Raman spectroscopy. As presented in Figure B.4b, the spectra revealed the presence of dominant Raman bands at 189.6, 237.9, 281.5, and 309.5  $cm^{-1}$  along with a couple of weak ones at 126 and 155  $cm^{-1}$ . To understand the lattice dynamics of  $Sb_2S_3$ , it is important to recall that the  $Sb_2S_3$  structure is consisted of linked  $SbS_3E$  and  $SbS_5E$  units, where  $E$  refers to the lone electron pair of antimony atoms. Since, in a simplified view, vibrational modes of chalcogenide compounds are usually explained by considering molecular-like units, so, optical phonons of  $Sb_2S_3$  can be partially interpreted as appearing solely from  $SbS_3$  units (without any mention to  $SbS_5$ ). In  $Sb_2S_3$  films formed through conventional techniques, the undistorted  $SbS_3$  units, which have an ideal trigonal pyramidal ( $C_{3v}$ ) symmetry, give rise to four normal

modes of vibration ( $2A_1+2E$ ): symmetric stretching  $\nu_s(A_1)$ , anti-symmetric stretching  $\nu_a(E)$ , symmetric bending  $\delta_s(A_1)$ , and anti-symmetric bending  $\delta_a(E)$  which are both Raman and infrared active, with  $\nu_s > \nu_a$  and  $\delta_s > \delta_{an}$  in general consideration. In the recorded Raman spectra of  $Sb_2S_3$  thin films (Figure B.4b), the band at  $281.5 \text{ cm}^{-1}$  hence corresponds to antisymmetric stretching vibrations  $\nu_a(\text{Sb-S})$ , whereas the band at  $309.5 \text{ cm}^{-1}$  should be attributed to symmetric stretching vibrations  $\nu_s(\text{Sb-S})$ . Similarly, the band at  $189.6$  and  $237.9 \text{ cm}^{-1}$  corresponded to antisymmetric bending vibrations  $\delta_a(\text{S-Sb-S})$  and symmetric bending vibrations  $\delta_s(\text{S-Sb-S})$ , respectively. In addition, the weak bands at  $126$  and  $155 \text{ cm}^{-1}$  could be attributed to  $A_g$  and  $B_{1g}$  modes of vibration, respectively. The Raman shifts obtained from our measurements are in agreement with the reported values [41]. The spectra are mostly dominated by Raman modes at  $281.5$  and  $309.5 \text{ cm}^{-1}$  corresponding to antisymmetric and symmetric Sb-S stretching vibrations in  $Sb_2S_3$ , respectively. A closer inspection of the modes showed that under the influence of precursor stoichiometry, the intensity of the modes changed; the peak corresponding to symmetric stretching gained its intensity with increasing sulfur content in  $Sb_2S_3$  (fewer sulfur vacancies) at the cost of asymmetric stretching mode. Such a change in the peak intensity has also been explained to be due to the absence of sulfur vacancies leading to shorter Sb-S bonds and vice-versa [41].

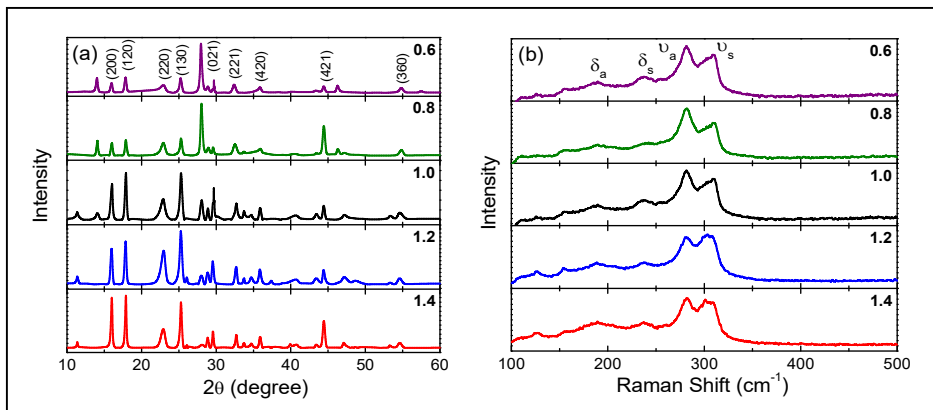


**Figure B.4.** (a) XRD patterns and (b) Raman spectra of vacancy-tailored  $Sb_2S_3$  thin films. Relative sulfur content ( $S/Sb$ ) in the films has been specified in the legend.

Optical absorption spectra of the vacancy-tailored Sb<sub>2</sub>S<sub>3</sub> films having identical thicknesses (~110 nm) were recorded in the UV-Vis-NIR region (Figure B.5); their corresponding Tauc plots have been placed in the inset. All the spectra showed a strong absorbance in the visible region; absorbance intensified further with increased sulfur content in the film. Since, in our sequential deposition approach, sulfurization of the antimony-precursor is done by H<sub>2</sub>S gas produced by the sulfur-precursor thiourea, a lesser amount of thiourea in sulfur-deficient compositions (S/Sb = 0.6 and 0.8) implies an incomplete conversion; a weaker absorbance was hence recorded. With increasing content of thiourea in the precursors, a better conversion was achieved and a higher absorbance was observed in turn. A closer inspection of the spectra, in addition, showed the presence of a tail extending to the longer wavelength region for sulfur-rich compounds indicating a reduction of the bandgap. The respective Tauc plots (inset of Figure B.5) evidenced bandgap narrowing with increasing sulfur content in the films. In Sb<sub>2</sub>S<sub>3</sub>, since both the band-edges are formed by a primary contribution of antimony and sulfur atomic-orbitals, its bandgap depends significantly on the Sb-S orbital overlaps, which would vary with a change in the precursor stoichiometry. The optical bandgap of the binary chalcogenide hence becomes dependent on precursor stoichiometry.

Interestingly, the longer wavelength region of the absorption spectra showed the presence of an apparent background absorbance which might have originated from high surface roughness and thereby scattering of low-energy illumination [42]. It should be noted that, due to the high extinction coefficient of the material, it is extremely difficult to rule out the presence of any impurities, such as phase residues, solely from optical absorption spectroscopy.

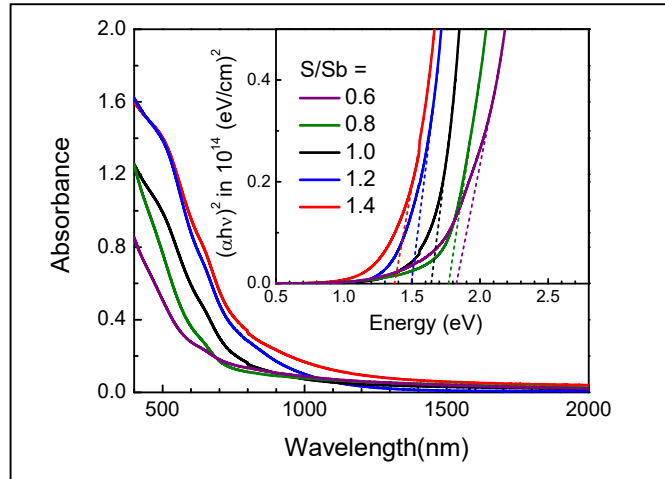


**Figure B.5.** Optical absorption spectra of vacancy-tailored  $Sb_2S_3$  thin films. Inset shows Tauc plots corresponding to the absorption spectra. Relative sulfur content ( $S/Sb$ ) in the films has been specified in the legend.

When the  $Sb_2S_3$  film formed with stoichiometrically-balanced precursors ( $S/Sb = 1.0$ ) was subjected to UV-ozone treatments, suppression of sulfur vacancies takes place through chemisorption of oxygen atoms on the surface of thin films [43]. It is expected that these oxygen atoms formed bonds with antimony and hence, oxidized the metal into impurity phases like  $Sb_2O_3$  [7]. In the present case, we have varied the treatment time up to 20 min in a step of 5 min; the presence of such impurities has however not been manifested in XRD and Raman studies even in the film exposed for 20 min. It can therefore be assumed that the intense peaks of  $Sb_2S_3$  probably have suppressed the oxide signatures. The optical absorption spectra, on the other hand, did not show any marked changes under mild an UVO-treatment (0-10 min); a shift in the edge of absorption towards the longer wavelength was observed when the stoichiometric  $Sb_2S_3$  film was treated for 15 min and above (shown in Figure B.6a). Such a red-shift in the bandgap was also estimated from respective Tauc plots and can be considered to be due to passivation of sulfur vacancies through chemisorption of oxygen atoms (shown in Figure B.6b).

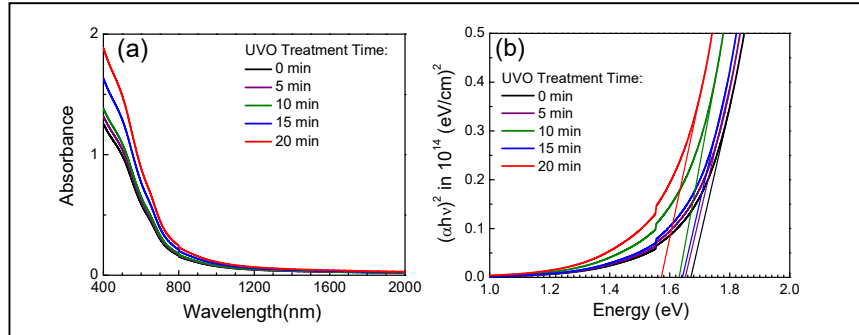


**Figure B.6.** (a) Optical absorption spectra and (b) respective Tauc plots of a stoichiometric  $Sb_2S_3$  thin film under a different duration of UVO treatment.

The evidence of oxygen incorporation in  $Sb_2S_3$  thin films has also been obtained from XPS measurements. Typically, during XPS studies, argon ion bombardment on the sample is carried out to remove traces of oxygen adsorbed from the environment, and as a result, the signature of oxygen can only be obtained if it is incorporated in the bulk of the semiconductor [44]. Interestingly, in the XPS spectra of  $Sb_2S_3$  films with UVO treatment for different lengths of time, the first sign of oxygen could be detected after 15 min of UVO exposure in the form of O 1s peak at a binding energy of 530.9 eV (shown in Figure B.7).

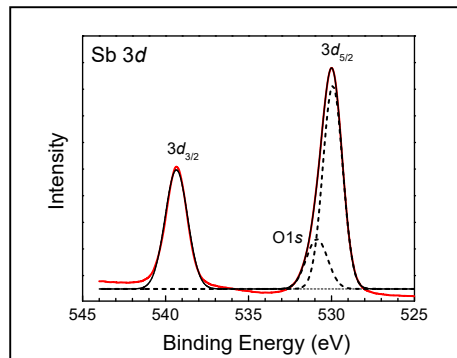


**Figure B.7.** High-resolution XPS spectra of Sb 3d and O 1s states for a stoichiometric ( $S/Sb = 1.0$ )  $Sb_2S_3$  thin film after 15 min of UVO treatment.

### B.3.5. Band-Edges of $\text{Sb}_2\text{S}_3$ Films from Scanning Tunneling Spectroscopy

To study the influence of precursor-stoichiometry on the band-edges of  $\text{Sb}_2\text{S}_3$ , we recorded  $dI/dV$  spectra of the semiconductors that in turn provided their energy-dependent density of states (DOS). The DOS spectra provided energies of valence band (VB) and conduction band (CB) of the material in the form of first peak in either side of the Fermi energy which was aligned at 0 V. With bias being applied to the tip, the first peak at a positive tip voltage implied withdrawal of electrons from the semiconductor and hence denoted the VB-edge of the semiconductor; similarly, the first peak at a negative voltage implied injection of electrons to the CB-edge of the material. Since trap states present within the bandgap also take part in the tunneling process, their signature typically appears nearer to the Fermi energy as compared to the true band-edges [45].

In Figure B.8, we have presented a typical  $dI/dV$  spectrum of an  $\text{Sb}_2\text{S}_3$  film formed with different stoichiometries. To compensate for the localized nature of STS measurements, we have recorded  $dI/dV$  spectra at many different locations on each thin film. From each spectrum, we have identified CB and VB-edges and summed the energies to form a histogram (insets). As evidenced from the  $dI/dV$  spectrum and histogram thereof, the CB-edge of the pristine  $\text{Sb}_2\text{S}_3$  appeared closer to 0 V (Fermi energy) as compared to the VB inferring an *n*-type nature of the semiconductor. The measurements have also yielded a transport gap of 1.78 eV which is a little wider than the optical gap with the energy difference being attributed to the exciton binding energy of the semiconductor. A histogram of the band-edges showed that both the energies have a symmetric distribution. The distribution and a non-intrinsic semiconductor nature observed in pristine  $\text{Sb}_2\text{S}_3$  films can typically be attributed to the presence of defects or disordered states. It can be suggested that exponentially decaying states were present in the gap (band tails). Such states were speculated to arise mainly from sulfur vacancies which are *n*-type or donor in nature [37].



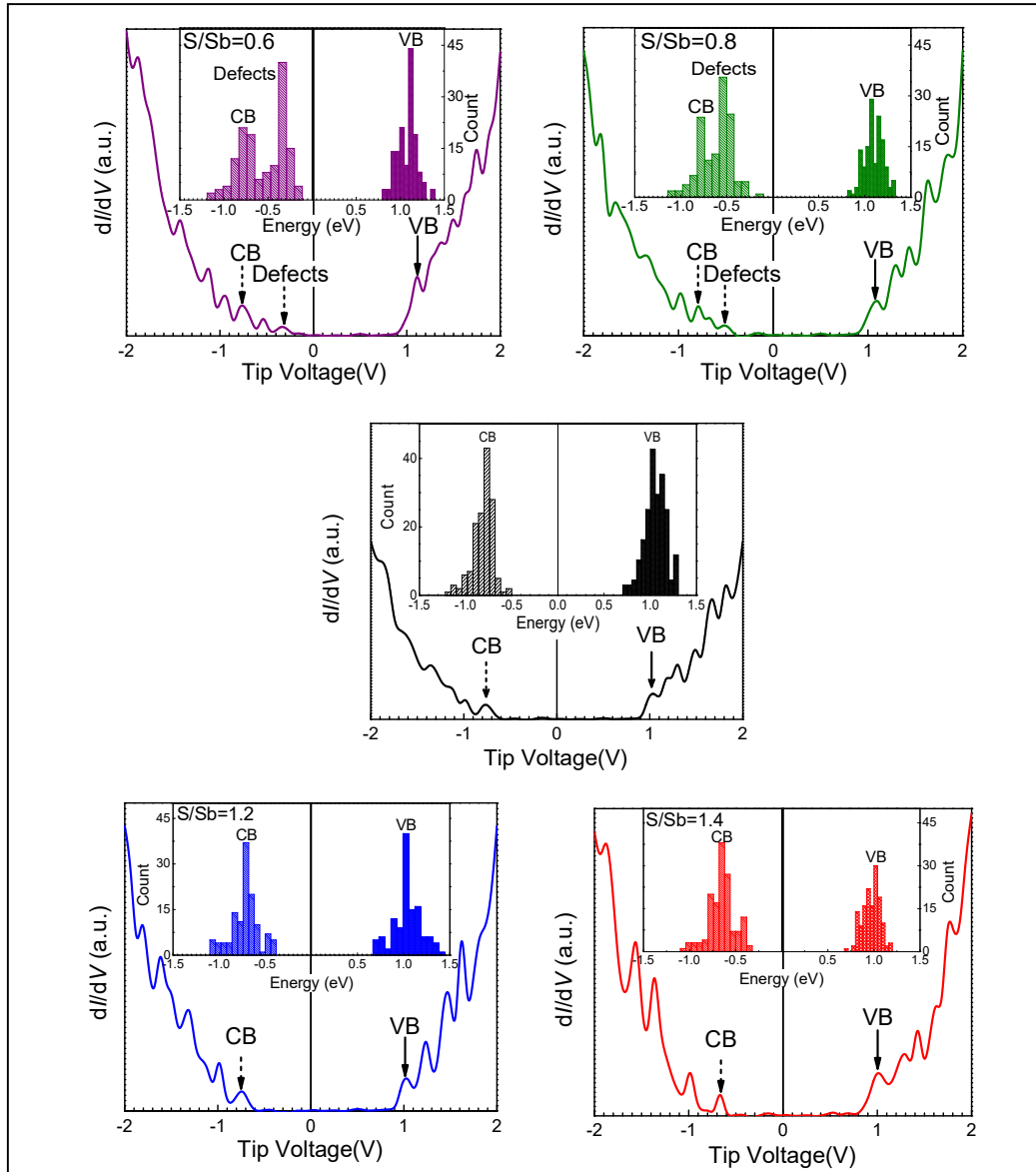


**Figure B.8.**  $dI/dV$  spectrum of different vacancy-tailored  $Sb_2S_3$  thin films. Inset of shows histogram of band-edges.

The  $dI/dV$  characteristics of the vacancy-tuned  $Sb_2S_3$  films showed that with increasing sulfur content from a sulfur-deficient composition ( $S/Sb = 0.6$ ), the transport

gap of  $\text{Sb}_2\text{S}_3$  widened till the relative sulfur content in the semiconductor reached a stoichiometrically-balanced condition ( $\text{S}/\text{Sb} = 1.0$ ). Such a blue shift in the transport gap originated due to a shift of the CB-edge away from the Fermi energy, while the VB-edge remained mostly unaffected under such a variation. In an antimony-rich growth condition, the defect formation is dominated by sulfur vacancies ( $\text{S}_\text{V}$ ) which are typically formed within the bandgap of the material and near the conduction band leading to a strong  $n$ -type electronic conductivity in the semiconductor [37]. Since such mid-gap defect states also contribute to the tunneling current, the transport gap in STS measurements hence appeared to be narrower than the optical bandgap. With increasing sulfur content in the film, the sulfur vacancies become passivated thereby widening of the transport gap was recorded. With further increments in sulfur content ( $\text{S}/\text{Sb} = 1.2$  and  $1.4$ ), the bandgap of  $\text{Sb}_2\text{S}_3$  was found to decrease. Under sulfur-abundance, sulfur antisite defects ( $\text{S}_\text{Sb}$ ) dominated and since such vacancies form also within the bandgap, the transport gap of  $\text{Sb}_2\text{S}_3$  under a sulfur-rich condition decreased [37].

Such a change in the nature and position of defect-states influenced the type of electronic conductivity in  $\text{Sb}_2\text{S}_3$  (Figure B.9). Since the intrinsic  $n$ -type nature in  $\text{Sb}_2\text{S}_3$  films originates due to the formation of deep-level sulfur-vacancies, a sulfur-deficient composition naturally led to the formation of more such vacancies and thereby a stronger  $n$ -type nature was evidenced. In a sulfur-rich condition, on the other hand, passivation of sulfur-vacancies and creation of sulfur-antisite defects is expected to take place, thereby compensating for the  $n$ -type nature.[36] Hence, by varying the precursor-stoichiometry while forming  $\text{Sb}_2\text{S}_3$  thin films through a sequential-deposition approach, it is possible to tune the type of electronic conductivity of the semiconductor from strong  $n$ -type to a mild  $n$ -type nature. Energy and FWHM of the band-edges and transport gap obtained thereof for different  $\text{Sb}_2\text{S}_3$  thin films have been collated in Table B.2.

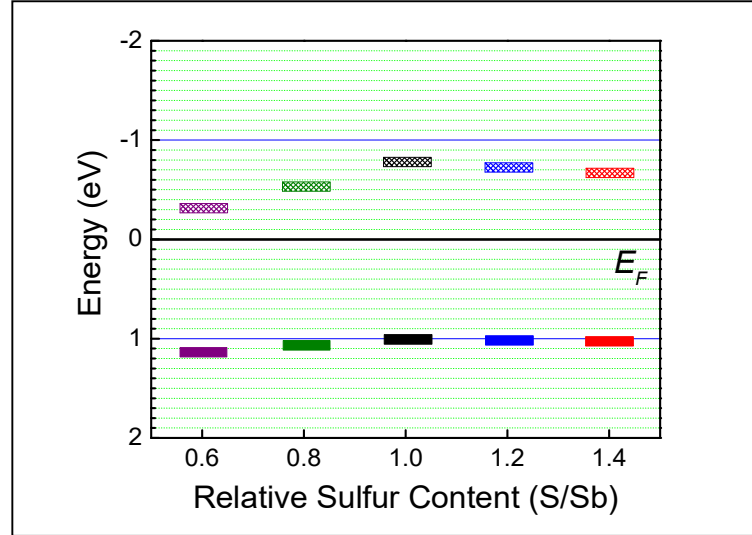


**Figure B.9.** band-edges of different vacancy-tailored  $Sb_2S_3$  thin films.

**Table B.2.** Position and FWHM of the band-edges and transport gap obtained thereof for different relative sulfur content in  $Sb_2S_3$  thin films.

S/Sb ratio	CB with respect to $E_F$		VB with respect to $E_F$		Transport gap (eV)	Optical bandgap (eV)
	Energy (eV)	FWHM (eV)	Energy (eV)	FWHM (eV)		
0.6	-0.32	0.60	1.12	0.26	1.43	1.83
0.8	-0.54	0.39	1.07	0.27	1.61	1.76
1.0	-0.77	0.26	1.01	0.27	1.78	1.67
1.2	-0.72	0.32	1.02	0.26	1.74	1.49
1.4	-0.67	0.33	1.02	0.22	1.69	1.37

The DOS and histogram of band-edges provided further information apart from the VB and CB energies. The histograms were seen to be distributed over the energy scale due to defect or disordered states. The energy distributions were as such symmetric and Gaussian in nature and the FWHM of the distribution can be considered to be a measure of defect or disordered states. Interestingly, after tuning the sulfur

vacancies, the FWHM of only the CB-edge could be seen to be narrowed down, leaving the FWHM of VB mostly unaffected (Table B.2). Such a phenomenon can be explained by considering the orbitals involved in the formation of CB and VB edges of  $\text{Sb}_2\text{S}_3$ . The CB edge in  $\text{Sb}_2\text{S}_3$  is known to be formed with antibonding Sb  $5p$  and S  $3p$  states, whereas the VB edge is comprised of bonding Sb  $5p$ , Sb  $5s$ , and S  $3p$  states. Due to the antibonding nature of orbitals in forming the CB-edge, its energy has a dominant contribution to the bandgap of  $\text{Sb}_2\text{S}_3$  [46] and therefore, while varying the sulfur content in the precursors in forming the films, the shift of the CB-edge was more predominant than the VB. The STS results hence deliberate on the change in two band-edges along with the transport gap of the material formed under different precursor-stoichiometries.

We also studied the influence of UVO treatment on the band-edges of  $\text{Sb}_2\text{S}_3$  thin films (Figure B.10a-d). Since such a treatment suppressed sulfur-vacancies in the semiconductor, the treatment, in turn, modulated the band-edges and transport gap of the binary chalcogenide. Typically, due to the presence of sulfur vacancies, stoichiometric  $\text{Sb}_2\text{S}_3$  shows an  $n$ -type conductivity which has been evidenced by the STS measurements. Upon suppression of the sulfur vacancies through UVO treatment, the VB-edge appeared closer to 0 V (Fermi energy) as compared to the CB-edge inferring a gradual change in the type of conductivity to a mild  $p$ -type (Figure B.10e). The STS studies hence infer that vacancy-engineering in  $\text{Sb}_2\text{S}_3$  thin films is an effective route in lowering its bandgap. It should be noted here that vacancy-engineered modification in the bandgap and also the type of conductivity has recently been reported to be an effective route in modulating band-edges of binary chalcogenides making them suitable in efficient solar cell applications [40].

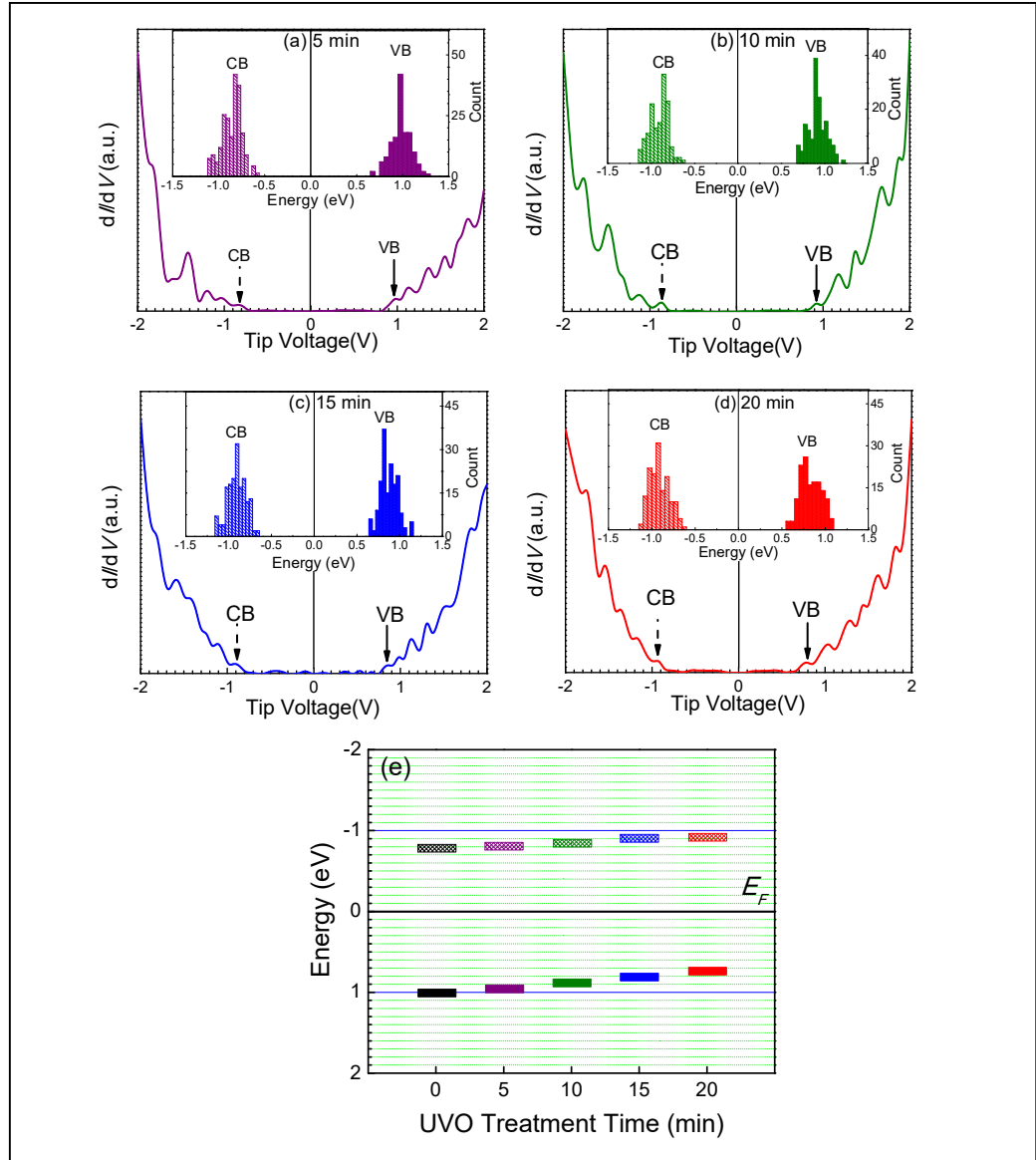


**Figure B.10.** (a)-(d)  $dI/dV$  spectra of  $Sb_2S_3$  thin films under different UVO treatment times and (e) influence of treatment time on the band-edges of  $Sb_2S_3$  thin films. A histogram of CB and VB energies is shown in the inset of (a)-(d).

### S.3.6. Surface Morphology of Vacancy-Tailored $\text{Sb}_2\text{S}_3$ Thin Films

Apart from the bandgap, the morphology of the absorber layer has a governing role in the performance of planar heterojunction solar cells [47]. A tendency of rapid and uncontrollable crystallization during film formation often leads to a rough and inhomogeneous surface morphology affecting the device performance adversely [48]. Typically, the morphology of metal chalcogenides should be affected by a change in precursor stoichiometry and also under a prolonged UVO treatment [49]. We, therefore, recorded AFM images and estimated the root-mean-square (RMS) roughness of such films to study their surface morphology. In Figure B.11a, we have presented AFM topographies of  $\text{Sb}_2\text{S}_3$  thin films formed with different precursor stoichiometries; we have also studied the effect of UVO treatment on  $\text{Sb}_2\text{S}_3$  thin films formed with stoichiometrically balanced precursors (Figure B.11b).

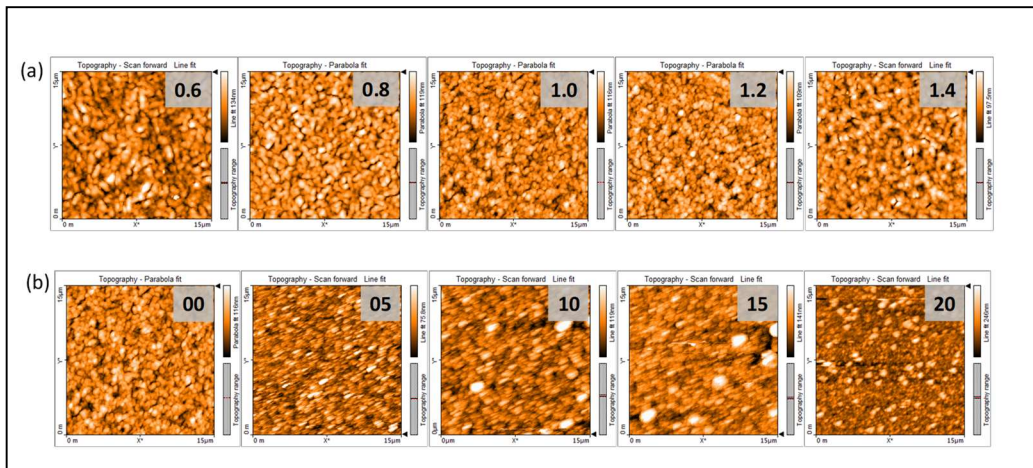


**Figure B.11.** AFM topographies of (a)  $\text{Sb}_2\text{S}_3$  films having different precursor stoichiometries and (b) stoichiometric ( $S/Sb = 1.0$ )  $\text{Sb}_2\text{S}_3$  film under different UVO treatment times as stated in the legends.

RMS roughness of the films was estimated from the morphologies using routine software. In Figure B.12, we have plotted the roughness alongside the optical bandgap for  $\text{Sb}_2\text{S}_3$  thin films formed with different precursor-stoichiometries and also upon UVO

treatment. Morphology of the films was seen to be affected in sulfur-rich conditions. Such a decline in film morphology under highly sulfur-rich conditions can be ascribed to the presence of a large number of byproducts (including  $NH_4SCN$ ,  $NH_3$ , and  $HNCS$ ) in the  $Sb_2S_3$  film that originates from an excess amount of thiourea used during film fabrication [3]. Since  $Sb_2S_3$  decomposes in presence of alkaline materials; the existence of  $NH_3$  affects the film morphology under sulfur-rich conditions. A low sulfur content, on the other hand, may help in maintaining an improved film morphology at the cost of incomplete conversion of the precursors to binary chalcogenides. As can be seen from Figure B.12, the morphology of the vacancy-tailored  $Sb_2S_3$  films degraded in the presence of high sulfur content ( $S/Sb = 1.4$ ) in the precursor. The results hence infer that a balance between bandgap and surface morphology is achieved at a relative sulfur content ( $S/Sb$ ) of 1.2. Similarly, such a correlation has been made for the UVO-treated samples as well.

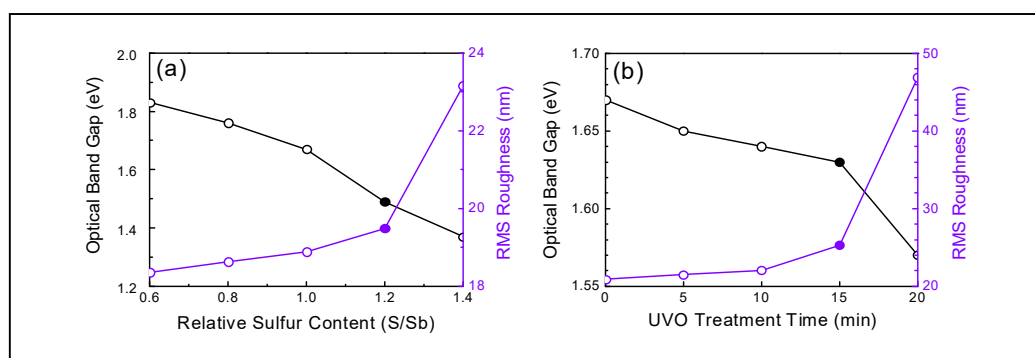


**Figure B.12.** Optimization of (a) precursor stoichiometry and (b) UVO treatment time in  $Sb_2S_3$  thin films on the basis of optical bandgap and surface roughness.

The elemental composition of the vacancy tailored  $Sb_2S_3$  thin films was analyzed through EDX measurement. The atomic% of the elements obtained from such analysis has been placed in Table B.1 (*vide supra*). The analysis evidenced a variation in the composition of the films in accordance with the precursor stoichiometry that in turn supported the degree of control this sequential deposition approach offers.

### S.3.7. Photovoltaic Characteristics

We then proceeded to study the influence of sulfur-vacancy modification on photovoltaic properties of  $\text{Sb}_2\text{S}_3$  thin films in planar heterojunction structures having an inverted (*p-i-n*) geometry. As stated earlier, photovoltaic properties of  $\text{Sb}_2\text{S}_3$  thin films have mostly been studied in a regular (*n-i-p*) sensitized device structure [14,20,29]. The not-so-impressive photovoltaic performance of  $\text{Sb}_2\text{S}_3$  in such efforts can however be attributed to a high resistivity of the binary chalcogenide that originates from both surface-defects and bulk-defects of  $\text{Sb}_2\text{S}_3$  thin films [7]. Although, in contrast, devices based on inverted planar heterojunction structures have several advantages, influence of such intrinsic-defects in dictating the device performance is more crucial [17]. Hence, we aimed to tune these intrinsic defects in  $\text{Sb}_2\text{S}_3$  thin films by varying the stoichiometry (S/Sb ratio) and studying the respective device performance.

In Figure B.13a, we show current-voltage characteristics of vacancy-engineered Cu: NiO/ $\text{Sb}_2\text{S}_3$ /PCBM planar heterojunction devices under 1 sun illumination; photovoltaic parameters of the respective devices have been presented in Table B.3. It should be stated here that, we selected Cu: NiO as a hole-selective layer owing to its wide optical bandgap and chemical inertness under ambient condition along with superior conductivity and hole-mobility. A comparison of device performance based on such vacancy-tailored  $\text{Sb}_2\text{S}_3$  thin films showed an improvement of all the photovoltaic parameters upon passivation of sulfur vacancies to a certain limit beyond which it was counterbalanced by a deterioration of film morphology. Due to a decrease in the optical bandgap of  $\text{Sb}_2\text{S}_3$  with vacancy-passivation, the short-circuit current density ( $J_{SC}$ ) of the solar cells increased gradually to  $9.61 \text{ mA/cm}^2$  in a sulfur-rich stoichiometry (S/Sb = 1.2). Further increment in sulfur content adversely affected the  $J_{SC}$  owing to deterioration in the film morphology. The fill factor of the cells also showed evidence of improvement, i.e. lesser carrier recombination in devices based on defect-passivated  $\text{Sb}_2\text{S}_3$  thin films.



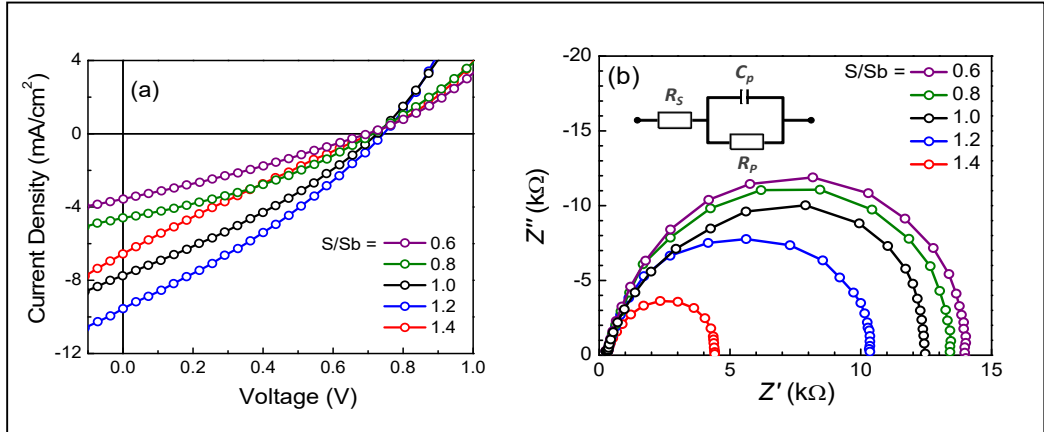


**Figure B.13.** (a) Current-voltage characteristics and (b) Nyquist plots of Cu: NiO/ $\text{Sb}_2\text{S}_3$ /PCBM heterojunctions with different S/Sb ratios under 1 sun illumination. The electrical analog of the device is shown in the inset of (b).

However, the morphological degradation under a high sulfur-rich condition provided carrier recombination pathways and affected the fill-factor in an adverse manner. It should be stated here that the  $J_{SC}$  and fill-factor values recorded in our devices were low due to a high resistivity of  $\text{Sb}_2\text{S}_3$  thin films.  $V_{OC}$  of the cells, on the other hand, was not affected due to the passivation of sulfur-vacancies in  $\text{Sb}_2\text{S}_3$  thin films. Due to an optimized interface with Cu:NiO and PCBM, the  $\text{Sb}_2\text{S}_3$  layer maintained a type-II band-alignment at both the interfaces for all S/Sb ratios leaving the  $V_{OC}$  of the cells mostly unaffected. It is worth mentioning here that  $V_{OC}$  in our devices has been higher than that in devices having different architectures and based on the material formed with other solution-processing methods [3,7,17]. Such an improvement can be attributed to the optimization of precursor stoichiometry leading to a balanced optical bandgap, surface morphology of the  $\text{Sb}_2\text{S}_3$  thin films along with band-alignment with the carrier selective contacts. Due to such changes in photovoltaic parameters, the PCE of the cells also showed a variation with the stoichiometry of the films. The PCE of the cell was optimized to 2.84% at an S/Sb ratio of 1.2, i.e. under a slightly sulfur-rich condition, the  $\text{Sb}_2\text{S}_3$  films showed a better photovoltaic performance. It should be

mentioned here that in a particular batch of device fabrication with an S/Sb ratio of 1.2, the PCE of the cells reached 3.02% with a high  $V_{OC}$  of 0.8 V. The PCE value obtained in our planar heterojunctions is comparable with the reported results on  $Sb_2S_3$  solar cells based on CBD-grown thin films and/or a sensitized device architecture [7]. To check the reproducibility of the device performance, we have fabricated devices with optimized precursor stoichiometry in batches (at least 20 devices) and characterized them under identical conditions. As can be seen from the histogram of device PCE, the devices routinely yielded a PCE of around 2.8%.

To obtain further insights on charge-transfer processes in Cu: NiO/ $Sb_2S_3$ /PCBM heterojunctions with different S/Sb ratios, we have recorded impedance spectra of the respective solar cells under an illumination condition; Nyquist plots for the devices have been presented in Figure B.13b. The plots are dominated by a large distinct semicircle in the low-frequency region which is typically reported for a *pn*-junction. Such single-arc impedance spectra in the low-frequency region are dictated by charge accumulation and recombination within the active layer and can be fitted to an electrical analog containing a parallel combination of the capacitor-resistor network ( $C_P$ - $R_P$ ) connected in series to another resistor ( $R_S$ ) [50]. The parallel and series resistances are typically considered to provide an estimate of layer resistance and interfacial resistance of the device, respectively. When the Nyquist plots were analyzed, a high layer resistance was recorded for the device based on a sulfur deficient  $Sb_2S_3$  layer (S/Sb = 0.6), and as a result, a poor device performance was recorded. With increasing sulfur content (S/Sb ratio) the diameter of the arc started to decrease resulting in a reduction in layer resistance ( $R_P$ ) which can be due to the formation of shunting pathways through the pinholes present in the film having a poor surface morphology. At a high sulfur content (S/Sb = 1.4) a very low layer resistance was recorded that signifies a high degree of carrier recombination in the respective device. The interfacial resistance ( $R_S$ ), on the other hand, being a measure of the contact resistances in the device remained mostly unaltered under variation in stoichiometry. The results of impedance spectroscopy were

hence in concurrence with the morphological studies and device performance of  $Sb_2S_3$  thin films.

**Table B.3.** Photovoltaic parameters and series and shunt resistances of Cu: NiO/ $Sb_2S_3$ /PCBM heterojunctions with different S/Sb ratio under 1 sun illumination. The values within the parentheses indicate respective standard deviations.

S/Sb ratio	$J_{SC}$ (mA/cm <sup>2</sup> )	$V_{OC}$ (V)	Fill factor	PCE (%)	$R_s$ ( $\Omega$ )	$R_p$ (k $\Omega$ )
0.6	3.55 ( $\pm$ 0.31)	0.70 ( $\pm$ 0.09)	0.28 ( $\pm$ 0.05)	0.69 ( $\pm$ 0.19)	303.8 ( $\pm$ 0.2)	13.9 ( $\pm$ 0.1)
0.8	4.59 ( $\pm$ 0.36)	0.71 ( $\pm$ 0.11)	0.34 ( $\pm$ 0.06)	1.10 ( $\pm$ 0.21)	303.5 ( $\pm$ 0.1)	13.4 ( $\pm$ 0.2)
1.0	7.78 ( $\pm$ 0.24)	0.73 ( $\pm$ 0.08)	0.38 ( $\pm$ 0.04)	2.13 ( $\pm$ 0.18)	302.5 ( $\pm$ 0.1)	12.4 ( $\pm$ 0.1)
1.2	9.61 ( $\pm$ 0.21)	0.74 ( $\pm$ 0.08)	0.40 ( $\pm$ 0.04)	2.84 ( $\pm$ 0.11)	305.7 ( $\pm$ 0.2)	10.3 ( $\pm$ 0.1)
1.4	6.50 ( $\pm$ 0.30)	0.71 ( $\pm$ 0.10)	0.32 ( $\pm$ 0.05)	1.48 ( $\pm$ 0.16)	308.9 ( $\pm$ 0.2)	4.4 ( $\pm$ 0.1)

To assure the correctness of our device performance and know the spectral distribution of photocurrent (at 0 V), we have recorded the external quantum efficiency (EQE) spectrum of our champion device (Figure B.14). The evolution of the photocurrent generation efficiency was similar to the analogous optical absorption spectrum of the respective  $Sb_2S_3$  thin film indicating that excitons generated in the chalcogenide layer primarily contributed to the resultant photocurrent. The photocurrent generation in the champion device was comparable to that of the reported sensitized  $Sb_2S_3$  solar cells based on CBD-grown  $Sb_2S_3$  thin films. This proves the effectiveness of using our sequential deposition route for the fabrication of  $Sb_2S_3$  thin films for solar cell applications. The  $J_{SC}$  value was estimated by integrating the overlap of the EQE spectrum with the AM1.5G solar photon flux; the value obtained from the EQE spectrum was 8.68 mA/cm<sup>2</sup>, which was quite close to the  $J_{SC}$  obtained from the  $I-V$  measurement (9.61 mA/cm<sup>2</sup>). We have moreover estimated the optical bandgap from the EQE spectrum as the absorption coefficient at a wavelength has a close relationship with the corresponding EQE value. In the inset of Figure B.14, we have placed the

$[h\nu \ln(1 - EQE)]^2$  versus energy plot; the intercept of the extrapolated linear region with the energy axis provided a bandgap of 1.81 eV for the  $Sb_2S_3$  film with  $S/Sb = 1.2$ . The value was in fair agreement with the optical bandgap (1.49 eV) estimated from the corresponding optical absorption spectrum. The little wider value of the bandgap obtained from the EQE spectrum can be due to possible light absorption in other active layers of the device as well.

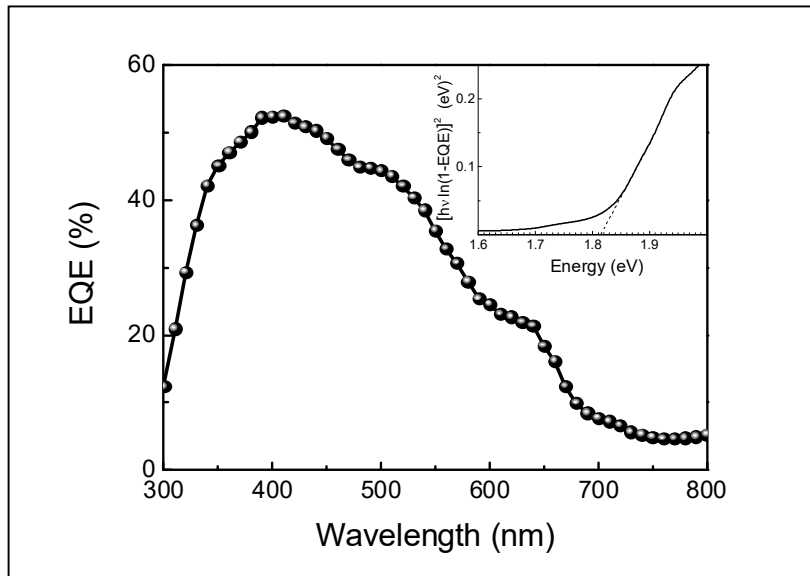


**Figure B.14.** EQE spectrum of Cu: NiO/ $Sb_2S_3$ /PCBM heterojunction with an S/Sb ratio of 1.2. In the inset, a plot of  $[h\nu \ln(1 - EQE)]^2$  versus  $h\nu$  has been placed to determine the optical bandgap.

On the other hand, the performance of heterojunctions based on UVO-treated stoichiometric  $Sb_2S_3$  ( $S/Sb = 1.0$ ) thin films did not show any change till 10 min of treatment. The parameters started to deteriorate afterward and the respective  $I-V$  characteristics under 1 sun illumination have been placed in Figure B.15. In the same plot, we have placed the  $I-V$  characteristics of an untreated device and a comparison of the photovoltaic parameters have been presented in Table B.4. Clearly, performance of the solar cells degraded in all respect after such a UVO treatment which can be ascribed

to the presence of additional oxide-based impurities in the material. Therefore, although such UVO treatment is an effective approach to suppress sulfur vacancies in chalcogenides, it may not a useful route in  $Sb_2S_3$  as a mode to improve solar cell performance.

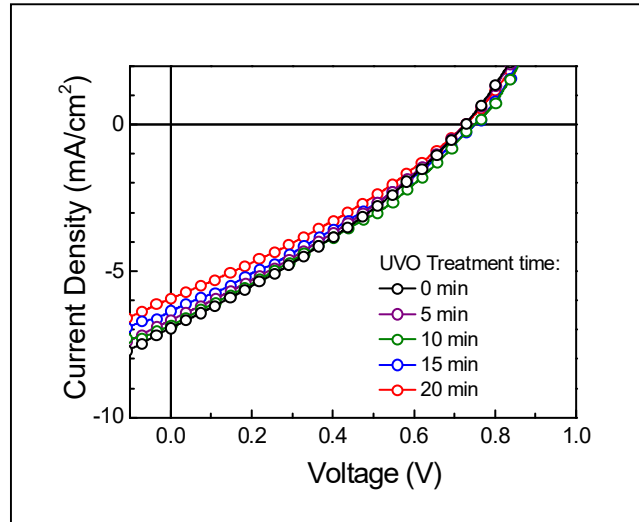


**Figure B.15.** *I-V characteristics of Cu: NiO/Sb<sub>2</sub>S<sub>3</sub>/PCBM heterojunctions with different UVO treatment times under 1 sun illumination.*

**Table B.4.** Photovoltaic parameters of Cu: NiO/Sb<sub>2</sub>S<sub>3</sub>/PCBM heterojunctions with different UVO treatment times under 1 sun illumination.

Treatment time (min)	$J_{SC}$ (mA/cm <sup>2</sup> )	$V_{OC}$ (V)	Fill factor	PCE (%)
0	7.78	0.73	0.38	2.13
5	7.50	0.73	0.39	2.13
10	7.48	0.74	0.38	2.10
15	7.09	0.74	0.36	1.88
20	6.52	0.72	0.34	1.60

## B.4. Conclusions

In conclusion, we have formed  $\text{Sb}_2\text{S}_3$  thin films through a sequential-deposition technique. As opposed to the traditional chemical bath deposition method, this approach allowed possibilities of sulfur-vacancy passivation through a variation in precursor stoichiometry. Sulfur-deficient precursors generated donor-like sulfur-vacancies; sulfur-rich precursors passivated the vacancies and in turn, formed sulfur antisite defects in the semiconductor. The optical bandgap of  $\text{Sb}_2\text{S}_3$  thin films could hence be seen to narrow down with increasing sulfur content in the precursor. From the variation of transport gap as obtained from STS studies and thereby DOS spectra, movement of the conduction band (CB) edge has been found to be responsible for the change in the bandgap. Due to the antibonding nature of antimony-sulfur orbital overlap in forming the CB edge, this particular band has responded majorly under a variation in the precursor-stoichiometry while forming  $\text{Sb}_2\text{S}_3$  thin films. The film-deposition approach in addition offered control over film morphology. Morphological studies revealed that the decrease in bandgap occurred at an expense of film quality; films with an excess sulfur content showed a high surface roughness. Hence, optimization of optical bandgap and surface morphology was estimated showing a balance between the two parameters at an S/Sb ratio of 1.2. Interestingly, the photovoltaic parameters of Cu: NiO/ $\text{Sb}_2\text{S}_3$ /PCBM planar heterojunctions excelled at the predicted stoichiometry yielding a power conversion efficiency of 3.02% along with a significantly high open-circuit voltage of 0.8 V.

## B.5. References

- [1] N. S. Lewis, *Science* **315**, 798 (2007).
- [2] S. Giraldo, Z. Jehl, M. Placidi, V. Izquierdo-Roca, A. Perez-Rodriguez, and E. Saucedo, *Adv. Mater.* **31**, 1806692 (2019).
- [3] L. J. Zhang, C. Y. Wu, W. F. Liu, S. F. Yang, M. T. Wang, T. Chen, and C. F. Zhu, *J. Mater. Chem. A* **6**, 21320 (2018).

- [4] S. H. Im, C. S. Lim, J. A. Chang, Y. H. Lee, N. Maiti, H. J. Kim, M. K. Nazeeruddin, M. Gratzel, and S. I. Seok, *Nano Lett.* **11**, 4789 (2011).
- [5] J. M. Ma, X. C. Duan, J. B. Lian, T. Kim, P. Peng, X. D. Liu, Z. F. Liu, H. B. Li, and W. J. Zheng, *Chem.-Eur. J.* **16**, 13210 (2010).
- [6] R. F. Tang, X. M. Wang, C. H. Jiang, S. Li, G. S. Jiang, S. F. Yang, C. F. Zhu, and T. Chen, *J. Mater. Chem. A* **6**, 16322 (2018).
- [7] R. Kondrotas, C. Chen, and J. Tang, *Joule* **2**, 857 (2018).
- [8] S. Nezu, G. Larramona, C. Chone, A. Jacob, B. Delatouche, D. Pere, and C. Moisan, *J. Phys. Chem. C* **114**, 6854 (2010).
- [9] E. Zimmermann, T. Pfadler, J. Kalb, J. A. Dorman, D. Sommer, G. Hahn, J. Weickert, and L. Schmidt-Mende, *Adv. Sci.* **2**, 1500059 (2015).
- [10] P. P. Boix, Y. H. Lee, F. Fabregat-Santiago, S. H. Im, I. Mora-Sero, J. Bisquert, and S. I. Seok, *ACS Nano* **6**, 873 (2012).
- [11] H. Wedemeyer, J. Michels, R. Chmielowski, S. Bourdais, T. Muto, M. Sugiura, G. Dennler, and J. Bachmann, *Energy Environ. Sci.* **6**, 67 (2013).
- [12] S. J. Moon, Y. Itzhaik, J. H. Yum, S. M. Zakeeruddin, G. Hodes, and M. Gratzel, *J. Phys. Chem. Lett.* **1**, 1524 (2010).
- [13] A. Darga, D. Mencaraglia, C. Longeaud, T. J. Savenije, B. O'Regan, S. Bourdais, T. Muto, B. Delatouche, and G. Dennler, *J. Phys. Chem. C* **117**, 20525 (2013).
- [14] Y. C. Choi, D. U. Lee, J. H. Noh, E. K. Kim, and S. I. Seok, *Adv. Funct. Mater.* **24**, 3587 (2014).
- [15] S. H. Im, H. J. Kim, J. H. Rhee, C. S. Lim, and S. I. Seok, *Energy Environ. Sci.* **4**, 2799 (2011).
- [16] X. Jin, Y. Yuan, C. H. Jiang, H. X. Ju, G. S. Jiang, W. F. Liu, C. F. Zhu, and T. Chen, *Sol. Energy Mater. Sol. Cells* **185**, 542 (2018).
- [17] R. F. Tang, X. M. Wang, C. H. Jiang, S. Li, W. F. Liu, H. X. Ju, S. F. Yang, C. F. Zhu, and T. Chen, *ACS Appl. Mater. Interfaces* **10**, 30314 (2018).
- [18] S. Messina, M. T. S. Nair, and P. K. Nair, *Thin Solid Films* **517**, 2503 (2009).

- 
- [19] N. Maiti, S. H. Im, C. S. Lim, and S. I. Seok, *Dalton Trans.* **41**, 11569 (2012).
- [20] Y. C. Choi and S. I. Seok, *Adv. Funct. Mater.* **25**, 2892 (2015).
- [21] L. Zheng, K. J. Jiang, J. H. Huang, Y. Zhang, B. Bao, X. Q. Zhou, H. J. Wang, B. Guan, L. M. Yang, and Y. L. Song, *J. Mater. Chem. A* **5**, 4791 (2017).
- [22] H. W. Lei, G. Yang, Y. X. Guo, L. B. Xiong, P. L. Qin, X. Dai, X. L. Zheng, W. J. Ke, H. Tao, Z. Chen, B. R. Li, and G. J. Fang, *Phys. Chem. Chem. Phys.* **18**, 16436 (2016).
- [23] Y. O. Mayon, T. P. White, R. P. Wang, Z. Y. Yang, and K. R. Catchpole, *Phys. Status Solidi A-Appl. Mat.* **213**, 108 (2016).
- [24] D. H. Kim, S. J. Lee, M. S. Park, J. K. Kang, J. H. Heo, S. H. Im, and S. J. Sung, *Nanoscale* **6**, 14549 (2014).
- [25] S. J. Yuan, H. Deng, X. K. Yang, C. Hu, J. Khan, W. N. Ye, J. Tang, and H. S. Song, *ACS Photonics* **4**, 2862 (2017).
- [26] E. Cardenas, A. Arato, E. Perez-Tijerina, T. K. Das Roy, G. A. Castillo, and B. Krishnan, *Sol. Energy Mater. Sol. Cells* **93**, 33 (2009).
- [27] K. H. Kim, C. Takahashi, Y. Abe, and M. Kawamura, *Optik* **125**, 2899 (2014).
- [28] P. K. Nair, M. T. S. Nair, V. M. García, O. L. Arenas, A. C. Y. Peña, I. T. Ayala, O. Gomezdaza, A. Sánchez, J. Campos, H. Hu, R. Suárez, and M. E. Rincón, *Sol. Energy Mater. Sol. Cells* **52**, 313 (1998).
- [29] Y. F. Xu, W. Y. Chen, L. H. Hu, X. Pan, S. F. Yang, Q. Shen, and J. Zhu, *J. Alloy. Compd.* **784**, 947 (2019).
- [30] J. Escorcia-Garcia, D. Becerra, M. T. S. Nair, and P. K. Nair, *Thin Solid Films* **569**, 28 (2014).
- [31] J. Escorcia-García, M. Domínguez-Díaz, A. Hernández-Granados, and H. Martínez, *MRS Advances* **3**, 3307 (2018).
- [32] V. Vinayakumar, C. R. O. Hernandez, S. Shaji, D. A. Avellaneda, J. A. A. Martinez, and B. Krishnan, *Mater. Sci. Semicond. Process* **80**, 9 (2018).
- [33] Y. L. Wu, L. Assaud, C. Kryschi, B. Capon, C. Detavernier, L. Santinacci, and J. Bachmann, *J. Mater. Chem. A* **3**, 5971 (2015).



- [34] S. Shaji, L. V. Garcia, S. L. Loredo, B. Krishnan, J. A. A. Martinez, T. K. Das Roy, and D. A. Avellaneda, *Appl. Surf. Sci.* **393**, 369 (2017).
- [35] R. E. Ornelas-Acosta, S. Shaji, D. Avellaneda, G. A. Castillo, T. K. Das Roy, and B. Krishnan, *Mater. Res. Bull.* **61**, 215 (2015).
- [36] L. Guo, B. Zhang, S. Li, Q. Zhang, M. Buettner, L. Li, X. Qian, and F. Yan, *APL Mater.* **7**, 041105 (2019).
- [37] M. A. Tumelero, R. Faccio, and A. A. Pasa, *J. Phys. Chem. C* **120**, 1390 (2016).
- [38] Y. W. Yin, C. Y. Wu, R. F. Tang, C. H. Jiang, G. S. Jiang, W. F. Liu, T. Chen, and C. F. Zhu, *Sci. Bull.* **64**, 136 (2019).
- [39] S. Messina, M. T. S. Nair, and P. K. Nair, *Thin Solid Films* **515**, 5777 (2007).
- [40] B. Peng, G. N. Yu, Y. W. Zhao, Q. Xu, G. C. Xing, X. F. Liu, D. Y. Fu, B. Liu, J. R. S. Tan, W. Tang, H. P. Lu, J. L. Xie, L. J. Deng, T. C. Sum, and K. P. Loh, *ACS Nano* **10**, 6383 (2016).
- [41] R. L. Frost, S. Bahfenne, and E. C. Keeffe, *J. Raman Spectrosc.* **41**, 1779 (2010).
- [42] D. Yang, J. G. Jang, J. Lim, J. K. Lee, S. H. Kim, and J. I. Hong, *ACS Appl. Mater. Interfaces* **8**, 21522 (2016).
- [43] L. Qi, Y. Wang, L. Shen, and Y. H. Wu, *Appl. Phys. Lett.* **108**, 063103 (2016).
- [44] N. Kaufherr and D. Lichtman, *Surf. Sci.* **139**, 347 (1984).
- [45] U. Dasgupta, A. Bera, and A. J. Pal, *ACS Energy Lett.* **2**, 582 (2017).
- [46] T. Ben Nasr, H. Maghraoui-Meherzi, H. Ben Abdallah, and R. Bennaceur, *Physica B* **406**, 287 (2011).
- [47] K. Wang, J. Cheng, X. Yang, R. Hu, L. J. Fu, J. Huang, J. S. Yu, and L. Li, *Nanoscale Res. Lett.* **13**, 270 (2018).
- [48] S. Bae, S. J. Han, T. J. Shin, and W. H. Jo, *J. Mater. Chem. A* **3**, 23964 (2015).
- [49] O. Ramirez, P. Ramasamy, Y. C. Choi, and J. S. Lee, *Chem. Mater.* **31**, 268 (2019).
- [50] J. Bisquert, *J. Phys. Chem. B* **106**, 325 (2002).

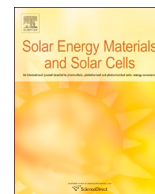
This page is intentionally left blank.

## REPRINTS OF PUBLISHED ARTICLES



## REPRINTS OF PUBLISHED ARTICLES





# Band-edges of bismuth-based ternary halide perovskites ( $A_3Bi_2I_9$ ) through scanning tunneling spectroscopy vis-à-vis impact of defects in limiting the performance of solar cells



Abhishek Maiti, Goutam Paul, Hrishikesh Bhunia, Amlan J. Pal\*

School of Physical Sciences, Indian Association for the Cultivation of Science, Jadavpur, Kolkata, 700032, India

## ARTICLE INFO

### Keywords:

Bismuth-based ternary halide perovskites  
Defects-states and band-energies  
Precursor-stoichiometry

## ABSTRACT

We study the role of defects on the band-edges of bismuth-based ternary halide perovskites ( $A_3Bi_2I_9$ ) formed with cesium and methylammonium (MA) ions at the A-site. We consider a range of precursor-stoichiometries leading to different reaction environments. The intrinsic defects formed during the perovskite formation affect the materials' band-energies. We introduce scanning tunneling spectroscopy (STS) to probe the band-edges. Fermi energy of the perovskites could be seen to remain always closer to valence band (VB) as compared to conduction band (CB) inferring their *p*-type nature. Acceptor-type defects having a least formation energy have been considered to result the *p*-type behavior. Upon a variation in the precursor-stoichiometry in forming the perovskites, STS studies evidence a decrease in the band gap of the materials formed with  $BiI_3$ -rich precursors. The change in band-energies occurs due to formation of deep-defects above the VB-edge; a shift in the CB-edge towards the Fermi energy is due to a change in the contribution of Bi(*p*) orbitals which form the CB of the perovskite. With methylammonium at the singly-protonated site, the material becomes defect-tolerant as evidenced by absence of deep level defects and an improvement in the parameters of solar cells formed with  $(CH_3NH_3)_3Bi_2I_9$ .

## 1. Introduction

Over the years, research on hybrid halide perovskite materials, which are suitable for solar cells, has progressed from the initial methylammonium lead triiodide ( $CH_3NH_3PbI_3$ , alias MAPI) to a range of directions [1–4]. Multication [5], metal-substitution [6,7], and mixed-halide approaches [8–10] separately or in conjunction, were considered in the  $AMX_3$  structure, where *A* and *M* represent a monovalent and a bivalent cation, respectively, and *X* symbolizes a halide. Since a complete replacement of lead from the MAPI structure did not retain the uniqueness of MAPI in terms of a high level in defect tolerance towards its optoelectronic properties [11,12], small exciton binding energies [13], excellent carrier mobilities leading to long charge carrier diffusion lengths [14], and minority carrier lifetime [15], focus has therefore been shifted towards solution-processed materials beyond  $AMX_3$ . In this direction, interestingly through combinatorial approaches, double perovskites in the form of  $A_2B'B'X_6$  with *B'* and *B''* being a monovalent and a trivalent metal respectively, or trivalent metal (*B*) based perovskites ( $A_3B_2X_9$ ) are being considered [2,16–19]. Beyond them, layered materials in the form of Ruddlesden-Popper, Aurivillius, and Dion-Jacobson

phases are also being envisaged in perovskite solar cells [20].

In the  $A_3B_2X_9$  structure,  $Bi^{3+}$  and  $Sb^{3+}$  are specially being considered at the *B*-site due to their isoelectronic configuration ( $s^2p^0$ ) as in lead ions ( $Pb^{2+}$ ), that is believed to be responsible for the unique optoelectronic properties of MAPI or lead-based similar perovskites [21]. The device performance with these trivalent metal based perovskites has however not excelled primarily due to a wider band gap leading to a large decrease in the achievable efficiency ( $\eta$ ) as per the Shockley-Queisser limit [16,22–24]. Also, presence of isolated face-shared  $BiI_6$  octahedra framework (OD) rather than three-dimensional corner-shared  $PbI_6$  octahedra of MAPI that is known to be responsible for high carrier mobilities through the 3D framework has been another parameter for the truncated efficiency in these OD systems [25,26].

Although some of the above-mentioned issues can be circumvented through materials-engineering, it is pertinent to know about the defects which may inevitably form in the material during growth processes. While the defects having energies outside the gap may not have an adverse effect, the deep-level defects forming within the band gap will have a crucial impact on the materials' optoelectronic properties, since the defect-sites can then act as recombination or trapping centers

\* Corresponding author.

E-mail address: [sspajp@iacs.res.in](mailto:sspajp@iacs.res.in) (A.J. Pal).

<https://doi.org/10.1016/j.solmat.2019.109941>

Received 6 March 2019; Received in revised form 3 May 2019; Accepted 10 May 2019

Available online 21 May 2019

0927-0248/ © 2019 Elsevier B.V. All rights reserved.

hindering carrier transports for efficient charge collection [27]. It is hence extremely pertinent to identify the defect states along with their energies responsible for a low  $\eta$  in  $A_3B_2X_9$ -based solar cells and thereby possible remedies to passivate the defects. In this work we introduce scanning tunneling spectroscopy (STS) to understand the presence of defects in bismuth-based ternary halide perovskite systems. The spectroscopy would provide energy-dependent density of states (DOS) and hence both the band-edges of the perovskites under the influence of defects. We have varied the precursor-stoichiometry in forming  $A_3Bi_2I_9$  ( $A = Cs^+$  and  $CH_3NH_3^+$ ) that in turn changed the reaction-environment and thereby only control defect-formation. The range of materials has hence provided a platform to study the role of defects on the band-edges, which are of extreme relevance in designing heterojunction solar cells, while retaining the chemical composition of the perovskite.

## 2. Material and methods

### 2.1. Materials

While methylammonium iodide ( $CH_3NH_3I$ ) was purchased from Dyesol Limited, Australia, cesium iodide (CsI), bismuth triiodide ( $BiI_3$ ), and anhydrous  $N,N$ -dimethylformamide (DMF) were purchased from Sigma-Aldrich Chemical Company. The materials, stored in a nitrogen-filled glove box with moisture and oxygen level below  $< 0.1$  ppm, were used without further purification.

### 2.2. Formation of $MA_3Bi_2I_9$ and $Cs_3Bi_2I_9$ thin-films

To cast the perovskites in their thin-film form, we adopted a usual one-step solution method, which was based on co-deposition of both the organic and inorganic precursors from a single solution [28]. A one-step method was followed in lieu of a two-step one to maintain the same degree of structural control on crystallization during the conversion process. In this method, a desired amount of CsI or  $CH_3NH_3I$  (MAI) and  $BiI_3$  in DMF were stirred overnight in a glove box at  $70^\circ C$  to dissolve the precursors thoroughly. The molar ratio of CsI (or MAI) to  $BiI_3$  was tuned from 1.5:1.0 to 1.0:1.5 to obtain a range of perovskites formed with CsI (MAI)-rich to  $BiI_3$ -rich precursors. The mixed solution was spun on pre-heated ( $70^\circ C$ ) substrates at 2500 rpm for 30 s; at the tenth second, 0.5 mL of warm ( $80^\circ C$ ) chlorobenzene was spun as a protocol for antisolvent treatment, which is known to improve the film-morphology, instead of additive-assisted crystallization [29]. The film was annealed at  $100^\circ C$  for 15 min (30 min for  $CH_3NH_3$ -based perovskites) inside the glove box for conversion to  $Cs_3Bi_2I_9$  ( $MA_3Bi_2I_9$ ) perovskite phase. For optical characterization, the thin-films were formed on quartz substrates; for STS studies, the same solution of the precursors was spun on arsenic-doped silicon wafers having a resistivity of 3–10  $m\Omega cm$  at a higher rpm, so that the film was ultrathin enough which is necessary for characterization in a scanning tunneling microscope (STM). Since certain physical properties of the perovskite may to some extent depend on the film-thickness or the nature of substrate used, we have used one set of film-deposition protocols necessary for each measurement-method. This allowed us to compare each parameter of all the perovskites formed with a range of precursor-stoichiometries.

### 2.3. Characterization of the thin-films

Thin-films of the perovskites were characterized by optical absorption spectroscopy, X-ray diffraction (XRD) patterns, and scanning tunneling spectroscopy (STS). The measurements were executed with a Shimadzu UV-2550 UV-VIS Spectrophotometer, Rigaku Smart Lab X-Ray Diffractometer ( $Cu K_\alpha$  radiation =  $1.5406 \text{ \AA}$ ), and a Nanosurf EasyScan2 STM, respectively.

For STS analysis, the measurements were carried out in ambient condition. STM tips were formed through a mechanical cut of a Pt/Ir (80%:20%) wire having a diameter of 0.25 mm. A voltage of 2.0 V was

applied through a feedback loop to achieve a set current of 1 nA for approach of the tip and to maintain a desired tip-sample separation for tunneling of electrons. To record tunneling current, bias was applied to the tip with respect to the substrate. In the first derivative of tunneling current ( $dI/dV$ ) versus voltage characteristics, which have a correspondence to the density of states (DOS) spectrum of the material, the first peak at a positive and at a negative voltage closest to 0 V implied withdrawal and injection of electrons, respectively, and have hence provided the location of valence band (VB) and conduction band (CB) edges of the material.

### 2.4. Fabrication of devices

Fluorine-doped tin oxide (FTO) coated glass substrates were used for solar cell fabrication. The substrates were cleaned through a usual protocol using soap water, deionized water, acetone, and 2-propanol in sequence followed by UV-ozone (UVO) treatment for 20 min. To form heterostructures, a copper-doped nickel oxide ( $Cu@NiO$ ) layer was first deposited as a hole-transport layer (HTL) through a sol-gel process [30]. The process included an annealing at  $425^\circ C$  for 15 min followed by a short UVO treatment. The precursors to form the active perovskite layer were then spun on  $Cu@NiO$  coated FTO substrates inside the glove box; the thin-films of the precursors were then annealed as per the protocol (vide supra). Finally, as an electron-transport layer (ETL), ZnO nanoparticles formed through a hydrothermal method and dispersed in chlorobenzene (20 mg/mL) were spun at 3000 rpm for 30 s followed by annealing at  $100^\circ C$  for 20 min [31]. To complete the device fabrication process, aluminum (Al) electrodes were thermally deposited as strips orthogonal to FTO ones in a vacuum chamber, which was inside the glove box system. The active area of the cells was  $10 \text{ mm}^2$ .

### 2.5. Characterization of devices

Current-voltage ( $I$ - $V$ ) characteristics of the devices were recorded under dark and 1 sun illumination conditions using a Keithley 2636A electrometer. Electrodes of the devices, which were retained in the glove box, were connected to the electrometer by using three-axes micropositioners coupled with pressure-loaded spring-probe contacts. For measurements under illumination, a solar simulator ( $100 \text{ mW/cm}^2$ ) attached with an AM 1.5 filter was used. Regions outside the cell area were covered to avoid contributions from neighboring areas or cells.

## 3. Results and discussion

### 3.1. Characterization of materials

Depending on the moiety at the A-site, bismuth-based ternary halide perovskites ( $A_3Bi_2I_9$ ) as such have a band gap of 2 eV and above [32]. In Figs. 1 and 2, we have presented optical absorption spectra and their corresponding Tauc plots for the two sets of perovskites formed with a range of precursor-stoichiometries or reaction environment. Considering the inaccuracies in deriving optical band gap from Tauc plots, we have used the results to compare the optical band gap from bismuth-based ternary halide perovskites formed with a range of precursor-stoichiometries. The gap could be found to depend on the stoichiometry of the precursors, with which the perovskites were formed. With optical gap of the respective materials being enlisted in Table 1, the gap could be seen to decrease when a perovskite material was formed with imbalanced precursors. Here, the gap must have become altered due to a change in one or both of the bands which are prone to defects in these ternary perovskites (as opposed to MAPI). That is, defect species having a least formation energy may have formed and modified the band-edge(s) and accordingly the gap. Since the optical spectroscopy provides a combined effect of (shift in) both the band-edges and is a rough estimate of the gap, we hence have introduced scanning tunneling spectroscopy (in a later section) to deliberate on the effect of precursor-stoichiometry on band-edges separately and thereby transport gap of such low-dimensional materials under the influence of different synthesis conditions.



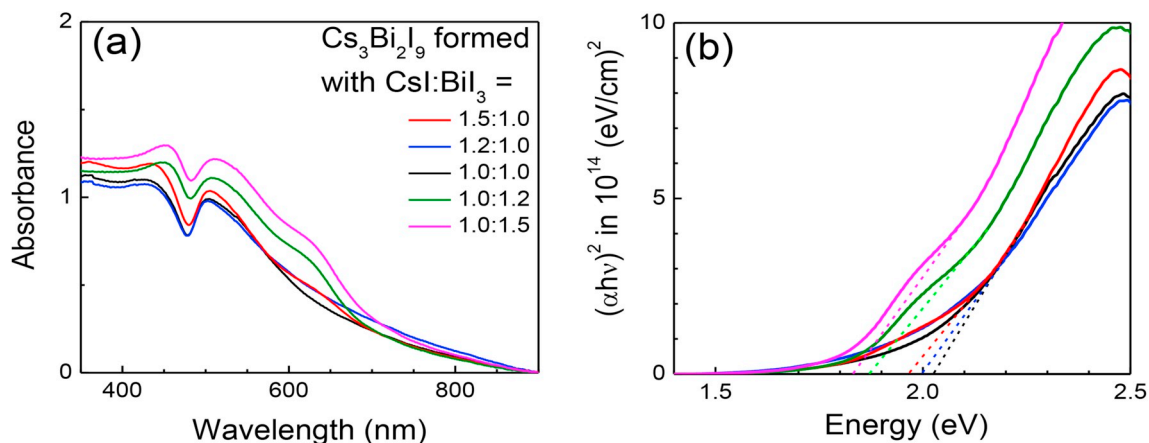


Fig. 1. (a) Optical absorption spectra and (b) corresponding Tauc plots of  $\text{Cs}_3\text{Bi}_2\text{I}_9$  formed with different precursor-stoichiometries.

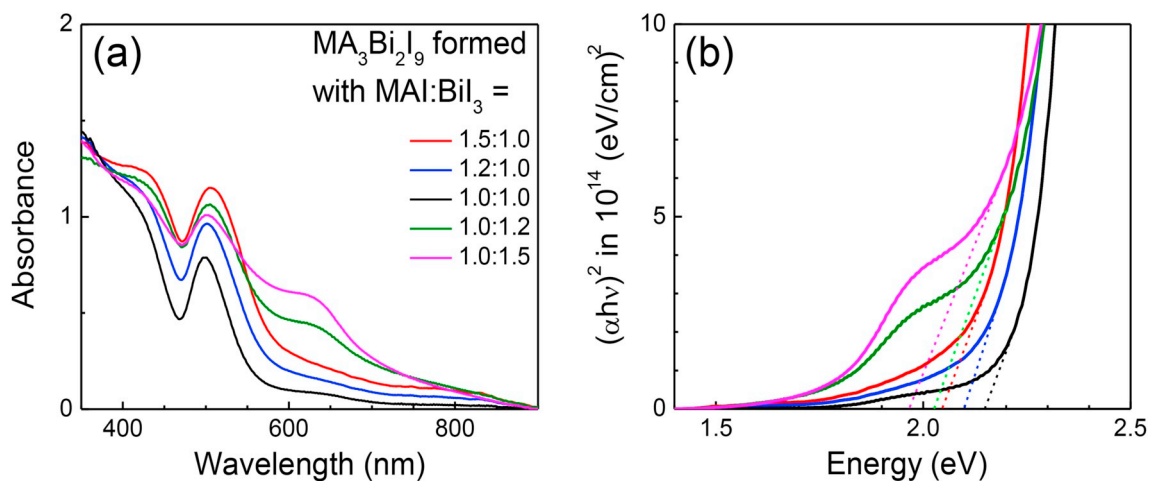


Fig. 2. (a) Optical absorption spectra and (b) corresponding Tauc plots of  $\text{MA}_3\text{Bi}_2\text{I}_9$  formed with different precursor-stoichiometries.

**Table 1**  
Optical gap of  $\text{Cs}_3\text{Bi}_2\text{I}_9$  and  $\text{MA}_3\text{Bi}_2\text{I}_9$  formed with different precursor-stoichiometries.

Material	Optical gap of $\text{Cs}_3\text{Bi}_2\text{I}_9$ and $\text{MA}_3\text{Bi}_2\text{I}_9$ in eV				
	CsI (or MAI): $\text{BiI}_3$ ratio of the precursors				
	1.5:1.0	1.2:1.0	1.0:1.0	1.0:1.2	1.0:1.5
$\text{Cs}_3\text{Bi}_2\text{I}_9$	1.96	2.00	2.03	1.87	1.84
$\text{MA}_3\text{Bi}_2\text{I}_9$	2.04	2.10	2.15	2.03	1.97

Since hybrid halide perovskites are known to exhibit a strong optical absorption in the visible region, optical spectroscopy is often inadequate to establish phase-purity of the materials. We hence characterized the perovskites from the view point of crystal structures; XRD patterns of the two sets of perovskites were recorded accordingly (Fig. 3). Perovskites with a particular A-cation exhibited diffraction peaks at appropriate positions corresponding to only that

particular perovskite ensuring a complete conversion during the annealing process. For example, XRD patterns of as-prepared  $\text{Cs}_3\text{Bi}_2\text{I}_9$  thin-films exhibited sharp diffraction peaks at  $16.9^\circ$  and  $25.4^\circ$ , which corresponded to (004) and (006) planes of the hexagonal crystal, respectively, and matched well with the literature evidencing formation of phase-pure  $\text{Cs}_3\text{Bi}_2\text{I}_9$  [19,33]. A higher intensity of the  $25.4^\circ$  peak implies that the solution-processed film had a preferred orientation along its (006) crystal plane. With increasing  $\text{BiI}_3$  content in the precursors, an additional peak appeared at  $12.9^\circ$ , which represents residual  $\text{BiI}_3$  in the perovskite films [34]. For the methylammonium (MA)-based perovskites ( $\text{MA}_3\text{Bi}_2\text{I}_9$ ), the characteristic peaks of (004) and (006) planes appeared at  $16.6^\circ$  and  $24.8^\circ$ , respectively [34]. Alike  $\text{Cs}_3\text{Bi}_2\text{I}_9$ ,  $\text{BiI}_3$ -rich phase of  $\text{MA}_3\text{Bi}_2\text{I}_9$  had a signature of unreacted  $\text{BiI}_3$  in terms of a peak at  $12.9^\circ$ . By comparing the intensity of the peak at  $12.9^\circ$ , which represents the residual  $\text{BiI}_3$ , it can be stated that  $\text{CH}_3\text{NH}_3\text{I}$  has a better reactivity with  $\text{BiI}_3$  as compared to that of CsI with the same triiodide (Fig. S1 in the Supplementary section).

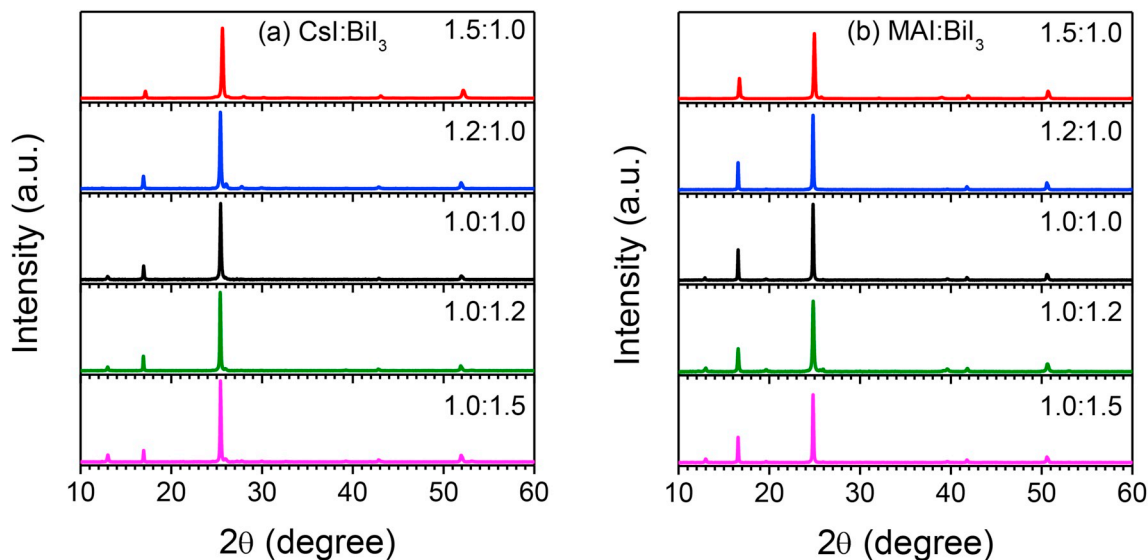


Fig. 3. XRD patterns of (a)  $\text{Cs}_3\text{Bi}_2\text{I}_9$  and (b)  $\text{MA}_3\text{Bi}_2\text{I}_9$  formed with different precursor-stoichiometries.

### 3.2. STS of $\text{Cs}_3\text{Bi}_2\text{I}_9$ and defect states

With phase purity of the materials being substantiated, we proceeded to analyze the band-edges of the materials. We accordingly recorded STS of  $\text{Cs}_3\text{Bi}_2\text{I}_9$  and  $\text{MA}_3\text{Bi}_2\text{I}_9$  formed with different precursor-stoichiometries. Measurements on each of the materials in their ultrathin-film form provided differential tunnel conductance spectra ( $dI/dV$  versus  $V$ ) and thereby their DOS and band-edges. For each material, measurements at different points have been summed up as histogram of CB and VB-energies. A typical  $dI/dV$  spectrum and CB and VB energy-histograms of  $\text{Cs}_3\text{Bi}_2\text{I}_9$  formed with stoichiometrically-balanced precursors are shown in Fig. 4. Inset of Fig. 4a shows the STM topography of a uniform region on which STS were recorded. The  $dI/dV$  spectrum shows peaks on either sides of 0 V, at which Fermi energy ( $E_F$ ) is aligned. Since the bias was applied to the tip, first peak at a positive voltage closest to 0 V implied withdrawal of electrons from the perovskite material and hence it's VB-edge. The first peak in the other bias direction similarly denoted injection of electrons and hence the CB-edge of the semiconductor. The  $dI/dV$  spectrum and the histograms show that the VB and CB energies are located at 0.96 eV below  $E_F$  and 1.05 eV above the  $E_F$ , respectively. As compared to the CB-edge, the VB turned out to be closer to the Fermi denoting a  $p$ -type nature of  $\text{Cs}_3\text{Bi}_2\text{I}_9$ .

A non-intrinsic nature in the perovskite formed with stoichiometrically-balanced precursors implies presence of point-defects in the system [24,35]. As such, possible point-defects in  $\text{Cs}_3\text{Bi}_2\text{I}_9$  can be classified broadly into two-types: acceptor-like and donor-like; and they will naturally affect the Fermi energy of the semiconductors in an opposing manner. While the acceptor-like defects would originate due to cation vacancies ( $V_{\text{Cs}}$ ,  $V_{\text{Bi}}$ ), iodine interstitial ( $I_i$ ), Cs on Bi substitution ( $\text{Cs}_{\text{Bi}}$ ), and antisite substitutions, namely iodide on cation ( $I_{\text{Cs}}$ ,  $I_{\text{Bi}}$ ), source of donor-like defects could be iodine-vacancies ( $V_I$ ), cation interstitials ( $\text{Cs}_i$ ,  $\text{Bi}_i$ ), Bi on Cs substitution ( $\text{Bi}_{\text{Cs}}$ ), and cation on iodide antisite-substitutions ( $\text{Cs}_i$ ,  $\text{Bi}_i$ ) (Table 2). The  $p$ -type nature in the perovskite formed with stoichiometrically-balanced precursors in general should imply that amongst the 12 possible point-defects (Table 2), formation energy of an acceptor-like defect is the least. When we compare formation energies of all the point-defects, we find that a donor-type  $V_I$  and an acceptor-type  $\text{Cs}_{\text{Bi}}$  defects have the similar and least formation energy [24]. Formation of  $\text{Cs}_{\text{Bi}}$  point-defects has a higher possibility in the perovskite reacted with stoichiometrically-balanced precursors, since a presence of unreacted  $\text{BiI}_3$  was observed in the XRD pattern allowing cesium-ions to occupy the vacant bismuth sites. That is, the unreacted bismuth salt in effect paved perovskite-formation in an environment of CsI-rich precursors leaving the bismuth vacancies to fill in sequence by cesium-ions ( $\text{Cs}_{\text{Bi}}$ ) and hence we have obtained a  $p$ -type nature in the system instead of an  $n$ -type behavior.

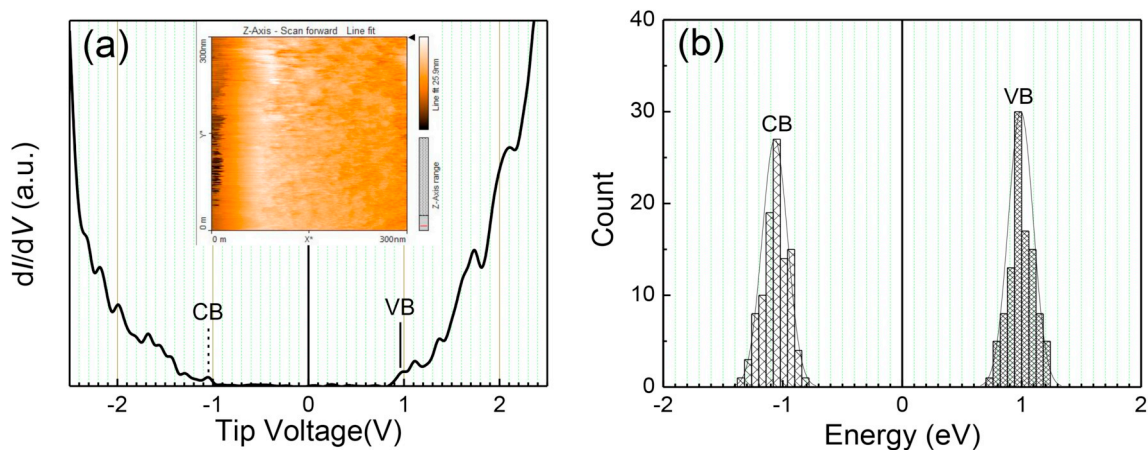


Fig. 4. (a) A typical STS spectrum and (b) histogram of CB and VB-edges of  $\text{Cs}_3\text{Bi}_2\text{I}_9$  formed through stoichiometrically-balanced precursors. Inset of (a) represent a STM topography of 300 nm  $\times$  300 nm region with the line profile being 25.9 nm.

**Table 2**

List of all possible vacancies formed in  $\text{Cs}_3\text{Bi}_2\text{I}_9$  with CsI-rich and  $\text{BiI}_3$ -rich precursors and their effect on electronic band-positions. For each-type of vacancies, the one represented in bold have the least formation energy [24].

$\text{Cs}_3\text{Bi}_2\text{I}_9$ formed with	Effect on electronic band-positions	
	Acceptor-like ( <i>p</i> -type)	Donor-like ( <i>n</i> -type)
CsI-rich precursors	Cation vacancies ( $V_{\text{Bi}}$ )	Cation on iodide substitutions ( $\text{Cs}_i$ )
	<b>Cs on Bi substitution (<math>\text{Cs}_{\text{Bi}}</math>)</b>	Cation interstitials ( $\text{Cs}_i$ )
	Iodide on cation antisite substitution ( $\text{I}_{\text{Bi}}$ )	Iodine-vacancy ( $V_i$ )
$\text{BiI}_3$ -rich precursors	Iodine interstitial ( $\text{I}_i$ )	Cation on iodide substitutions ( $\text{Bi}_i$ )
	Cation vacancies ( $V_{\text{Cs}}$ )	Cation interstitials ( $\text{Bi}_i$ )
	Iodide on cation antisite substitution ( $\text{I}_{\text{Cs}}$ )	Bi on Cs substitution ( $\text{Bi}_{\text{Cs}}$ )
	Iodine interstitial ( $\text{I}_i$ )	<b>Iodine-vacancy (<math>V_i</math>)</b>

In Fig. S2 in the Supplementary section, we have presented typical STS results of  $\text{Cs}_3\text{Bi}_2\text{I}_9$  formed with a range of precursor-stoichiometries. Their energy-levels obtained from the histograms have been collated in Fig. 5. Additionally, in Table 3, we have presented the band-edges and correspondingly the band gap of the materials for comparison. The results show that (1) the nature of conductivity of the perovskite remained *p*-type when the compounds were formed through different precursor-stoichiometries and (2) the gap decreased when the perovskites were formed with imbalanced precursors, that is, in both CsI-rich and  $\text{BiI}_3$ -rich conditions. It may be restated that the type of defects prevalent in compounds formed through different precursor-stoichiometries could be understood from the relative location of Fermi energy with respect to the two band-edges, since these two categories of defects would push the Fermi energy towards either band-edges.

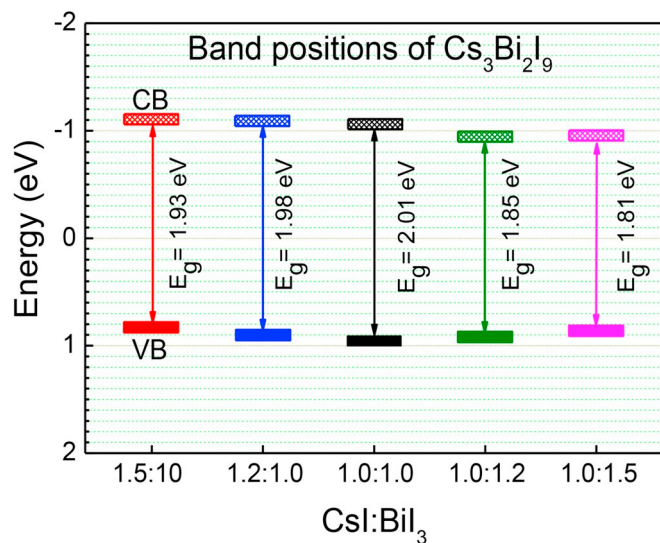


**Fig. 5.** Band positions of  $\text{Cs}_3\text{Bi}_2\text{I}_9$  formed with different stoichiometric ratios of the precursors, namely CsI and  $\text{BiI}_3$ .

**Table 3**

CB and VB edges of  $\text{Cs}_3\text{Bi}_2\text{I}_9$  formed with different precursor-stoichiometries and comparison of their optical and transport gaps.

Precursor-stoichiometry, CsI:BiI <sub>3</sub>	CB (eV)	VB (eV)	Band gap (eV)	Optical gap (eV)
1.5:1.0	-1.10	0.83	1.93	1.96
1.2:1.0	-1.08	0.90	1.98	2.00
1.0:1.0	-1.05	0.96	2.01	2.03
1.0:1.2	-0.93	0.92	1.85	1.87
1.0:1.5	-0.95	0.86	1.81	1.84

The perovskites formed with CsI-rich or with  $\text{BiI}_3$ -rich precursors remained *p*-type in nature to the same extent. That is, in perovskites formed with CsI-rich precursors,  $\text{Cs}_{\text{Bi}}$  vacancies continued to dominate in addition to some other acceptor-like vacancies, such as  $\text{I}_{\text{Bi}}$  and  $V_{\text{Bi}}$  having a formation energy a little higher than that of  $\text{Cs}_{\text{Bi}}$ . If we look at the formation energies of defects in the perovskite formed with  $\text{BiI}_3$ -rich precursors (Table 2), we find that the energy for iodine-vacancy ( $V_i$ ) is the least; due to a donor-like nature of such vacancies, they should have transformed the material to an *n*-type. Since the  $\text{BiI}_3$  in  $\text{BiI}_3$ -rich environment has left a larger fraction of unreacted triiodide salt in the perovskite (as evidenced from XRD patterns of  $\text{BiI}_3$ ), the unreacted precursor may also affect the nature of conductivity. We hence characterized ultrathin-films of  $\text{BiI}_3$  formed separately in the STM. STS of the salt inferred its strong *p*-type character (Fig. S3 in the Supplementary section), as evidenced from the location of CB and VB edges from the Fermi energy. The *p*-type nature of  $\text{BiI}_3$  may hence have counterbalanced or passivated the effect of donor-like iodine-vacancies leading to formation of nearly intrinsic or subtle *p*-type in  $\text{Cs}_3\text{Bi}_2\text{I}_9$  formed with a  $\text{BiI}_3$ -rich environment. The results are in contrast to  $\text{CH}_3\text{NH}_3\text{PbI}_3$  (MAPI) in which a variation in the precursor-stoichiometry had transformed the perovskite material from *p*-type ( $\text{CH}_3\text{NH}_3\text{I}$ -rich) to *n*-type ( $\text{PbI}_2$ -rich) without any change in the band gap [36–38].

Although the precursor-stoichiometry did not affect the nature of conductivity in the perovskites, band-positions have been found to respond in a large manner (Fig. 5 and Table 3). The gap shrunk from 2.01 eV (balanced condition) to 1.93 eV (CsI-rich environment) and to 1.81 eV ( $\text{BiI}_3$ -rich environment). The optical gap has also decreased with a similar trend, although to a lesser extent. Additionally, amongst the band-energies, the VB-edge should represent the deep  $\text{Cs}_{\text{Bi}}$ -defects forming above the actual VB [24]. In perovskites formed with  $\text{BiI}_3$ -rich precursors, band-positions of the unreacted *p*-type  $\text{BiI}_3$  has affected the VB-edge by pushing it towards the  $E_f$ . Regarding the CB, we shall have to look at the orbitals that are responsible for formation of the band in  $\text{Cs}_3\text{Bi}_2\text{I}_9$ . CB is known to be formed with a mixture of  $\text{I}(s)$ ,  $\text{I}(p)$ , and  $\text{Bi}(p)$  orbitals [35]. The perovskites formed with increasingly more  $\text{BiI}_3$  precursors should hence offer a higher overlap between bismuth and iodine orbitals leading the bands to move towards the Fermi energy and correspondingly shrinking of the band gap. Due to the presence of defect-states above the VB, orbitals responsible for VB did not affect the band-edge. Even if we keep the defect-states aside, we note that the VB is contributed by  $\text{I}(p)$  and  $\text{Bi}(s)$  orbitals; the band hence becomes more tolerant to the precursor-stoichiometry, since the *s*-orbitals is known to have a lesser influence on a band than the *p*-orbitals which offer a higher spin-orbit coupling. Also, due to the antibonding characteristics of VB [24], a possibility of VB-derivative formation close to the edge can be ruled out. These hence corroborate that the change in VB-edge occurred due to formation of deep-level defect-states.

If we compare the optical and transport gap of the materials, we find that the optical gap was slightly higher than the transport one (Table 3 and Fig. S4 in the Supplementary section). As such, a contrasting trend was expected due to involvement of exciton binding energy in optical spectroscopy. Our results hence further support that defect states were probed here as the VB-edge in bismuth-based hybrid halide perovskites.

Since we have made many STS measurements leading to CB- and VB-energies on each material, we could estimate the spreading or dispersion of the energies as full-width at half-maxima (FWHM) of their



histograms (Table 4). For all the materials, unlike MAPI, the CB was more dispersed than the VB energy implying a higher effective mass of carriers and thereby hindering the devices' optoelectronic performances [39]. The histogram of VB-energy appeared asymmetric in nature with the distribution extending more towards the  $E_F$ . Asymmetric histograms of this type support the thesis of deep-level defect states forming above the VB in these systems.

**Table 4**

FWHM of CB and VB edges and band gap of  $\text{Cs}_3\text{Bi}_2\text{I}_9$  formed with different precursor-stoichiometries.

Precursor-stoichiometry, CsI:BiI <sub>3</sub>	(FWHM) of CB	(FWHM) of VB
1.5:1.0	0.34	0.29
1.2:1.0	0.33	0.28
1.0:1.0	0.26	0.24
1.0:1.2	0.31	0.27
1.0:1.5	0.37	0.30

### 3.3. STS of $(\text{CH}_3\text{NH}_3)_3\text{Bi}_2\text{I}_9$

We have extended the work by characterizing  $\text{MA}_3\text{Bi}_2\text{I}_9$  formed with different precursor-stoichiometries between MAI and BiI<sub>3</sub>. First of all, STS studies of  $\text{MA}_3\text{Bi}_2\text{I}_9$  formed with stoichiometrically-balanced precursors exhibited *p*-type character (Fig. 6). Upon variation in the precursor-stoichiometry, the gap did not respond in a large manner; Fermi energy could be seen to shift away from the VB-edge (Fig. 7). The *p*-type perovskite formed with MAI-rich precursors turned into near-intrinsic when the material was formed with BiI<sub>3</sub>-rich precursors. While a typical STS spectrum, STM topography of a uniform region, and histogram of band-energies are shown in Fig. 6, the spectra and histograms of all other perovskites are presented in Fig. S2 in the Supplementary section.

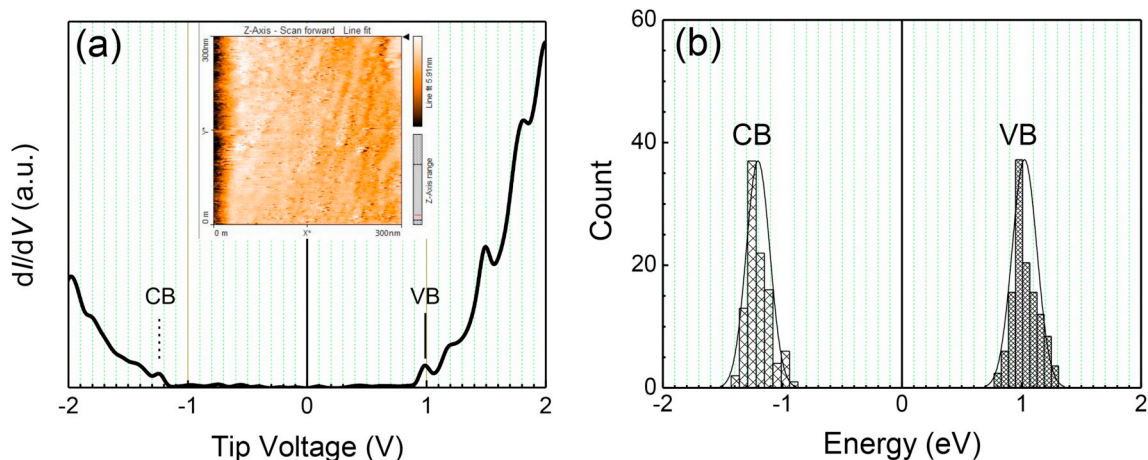


**Fig. 6.** (a) A typical STS spectrum and (b) histogram of CB and VB-edges of  $\text{MA}_3\text{Bi}_2\text{I}_9$  formed through stoichiometrically-balanced precursors. Inset of (a) represent a STM topography of 300 nm × 300 nm region with the line profile being 5.9 nm.

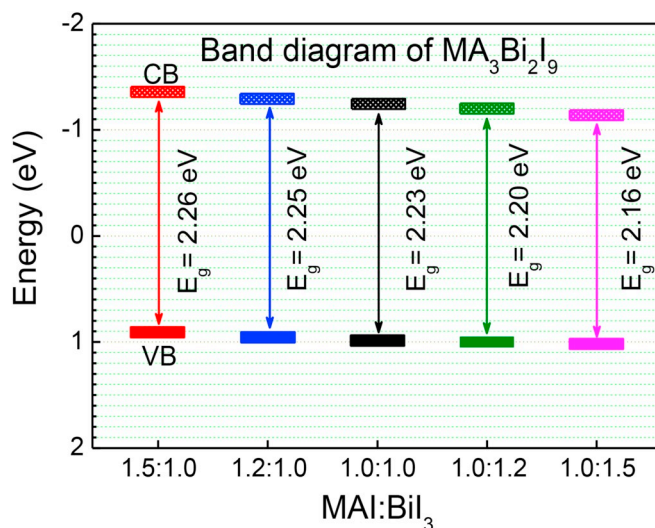


**Fig. 7.** Band positions of  $\text{MA}_3\text{Bi}_2\text{I}_9$  formed with different stoichiometric ratios of the precursors, namely MAI and BiI<sub>3</sub>.

If we compare the optical and transport gaps (Table 5 and Fig. S4 in the Supplementary section) derived from STS studies, we find that the former was always lesser than the latter one. Such a nature, which is in contrast to the results in  $\text{Cs}_3\text{Bi}_2\text{I}_9$ , that is, occurrence of deep-level defects above VB, implies involvement of exciton binding energy in the optical gap and absence of any mid-gap defect states in  $\text{MA}_3\text{Bi}_2\text{I}_9$ . The non-intrinsic nature of  $\text{MA}_3\text{Bi}_2\text{I}_9$  formed with stoichiometrically-balanced precursors and the invariance of band gap upon a variation in the stoichiometry hence imply formation of shallow-level defects outside the gap. The *p*-nature of the material and a shift in Fermi energy towards the VB in systems formed with MAI-rich precursors further

indicate that acceptor-like defects are forming in  $\text{MA}_3\text{Bi}_2\text{I}_9$ . In perovskites reacted with excess- $\text{BiI}_3$ , the  $p$ -nature of the salt could be seen to influence band-edges of the material alike  $\text{Cs}_3\text{Bi}_2\text{I}_9$  synthesized under a similar condition.

**Table 5**

CB and VB edges of  $\text{MA}_3\text{Bi}_2\text{I}_9$  formed with different precursor-stoichiometries and comparison of their optical and transport gaps.

Precursor-stoichiometry, MAI:BiI <sub>3</sub>	CB (eV)	VB (eV)	Band gap (eV)	Optical gap (eV)
1.5:1.0	-1.36	0.90	2.26	2.04
1.2:1.0	-1.30	0.95	2.25	2.10
1.0:1.0	-1.25	0.98	2.23	2.15
1.0:1.2	-1.20	1.00	2.20	2.03
1.0:1.5	-1.14	1.02	2.16	1.97

Since CB in  $\text{A}_3\text{Bi}_2\text{I}_9$  is known to be formed with a mixture of I( $s$ ), I( $p$ ), and Bi( $p$ ) orbitals, the singly-protonated ion at the A-site should have a little influence on its formation. That is, alike  $\text{Cs}_3\text{Bi}_2\text{I}_9$ , the CB in  $\text{MA}_3\text{Bi}_2\text{I}_9$  formed with  $\text{BiI}_3$ -rich precursors moved towards the Fermi energy due to a higher overlap between bismuth and iodine orbitals. In  $\text{MA}_3\text{Bi}_2\text{I}_9$ , the change in VB is now observable due to an absence of mid-gap defect-states, since the VB is contributed by the  $p$ -orbitals of I and the  $s$ -orbitals of Bi, It may be restated that in  $\text{Cs}_3\text{Bi}_2\text{I}_9$ , the original shift in VB was marred by an appearance of deep-level defect-states above the VB. The results in  $\text{MA}_3\text{Bi}_2\text{I}_9$  further substantiate the formation of defect-states in cesium-based bismuth ternary halide perovskites.

### 3.4. Defect-states in $\text{A}_3\text{Bi}_2\text{I}_9$ and solar cell parameters

Notwithstanding the unfavorable issues of trivalent metal based perovskites, such as wider band gap and isolated face-shared  $\text{BiI}_6$  octahedra framework implying lower-dimensional nature rather than 3D corner-shared  $\text{PbI}_6$  octahedra of MAPI, the effect of defect states in  $\text{A}_3\text{Bi}_2\text{I}_9$  can be seen to be reflected in photovoltaic properties. We have fabricated heterojunction devices based on bismuth-based halide perovskites with stoichiometrically-balanced precursors and characterized them to study their photovoltaic performances. The devices were formed with  $\text{Cu@NiO}$  and  $\text{ZnO}$  as hole- and electron-transport layers, respectively, so that a type-II band-alignment is formed at both the interfaces (Fig. S5 in the Supplementary section). The devices based on both cesium and methylammonium first of all exhibited rectifying  $I$ - $V$  characteristics under a dark condition (Fig. 8). We hence expected that the devices would demonstrate photovoltaic properties under illumination. The characteristics under light as presented in Fig. 8, were not impressive due to a large band gap of the active material and also a high exciton binding energy in the perovskite (around 200–300 meV) [40]. When we compare the characteristics of the devices based on  $\text{Cs}_3\text{Bi}_2\text{I}_9$  and  $\text{MA}_3\text{Bi}_2\text{I}_9$ , we observe that the performance of  $\text{Cs}_3\text{Bi}_2\text{I}_9$  was inferior to that of  $\text{MA}_3\text{Bi}_2\text{I}_9$ -based devices. The  $\eta$  improved to 0.36 in (deep) defect-free  $\text{MA}_3\text{Bi}_2\text{I}_9$  as compared to  $\text{Cs}_3\text{Bi}_2\text{I}_9$  containing acceptor-like deep-level defects (Table S1 in the Supplementary section). The defect-levels provide route for recombination loss in solar cells; the shunt resistance calculated from  $I$ - $V$  characteristics under illumination accordingly could be seen to increase upon defect-passivation. The results hence again support the formation of defect-states in cesium based bismuth ternary halide perovskites and indicate a necessity of defect-passivation while fabricating solar cells.

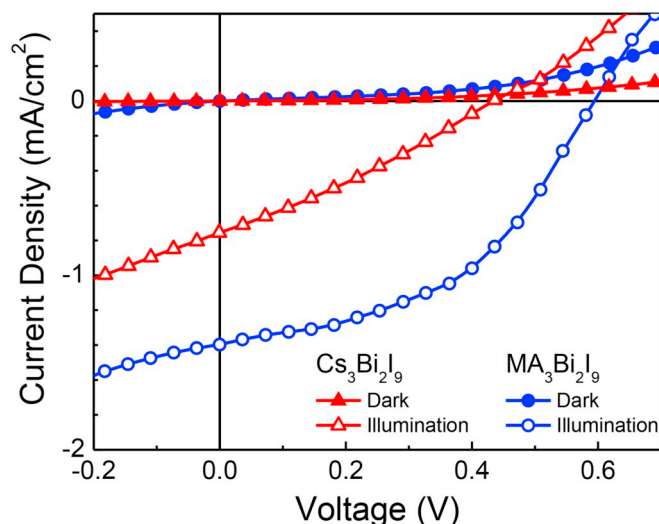


**Fig. 8.** Current-voltage characteristics of  $\text{Cs}_3\text{Bi}_2\text{I}_9$  and  $\text{MA}_3\text{Bi}_2\text{I}_9$  based devices under dark and 1 sun illumination condition.

## 4. Conclusions

In conclusion, we have established presence of defect-states in  $\text{Cs}_3\text{Bi}_2\text{I}_9$  perovskites through STS and inferred them to be primarily responsible for their poor photovoltaic performance. We have formed and characterized bismuth-based ternary halide perovskites with precursors having different stoichiometries. At the A-site, we have considered cesium and methylammonium ions in forming the perovskites. When we focused on the band-edges of  $\text{Cs}_3\text{Bi}_2\text{I}_9$  through STS, we observed that the materials were  $p$ -type due to acceptor-nature of the defects above the VB-band. The STS studies further showed that the band gap of the cesium-based perovskites decreased from 2.01 to 1.81 eV when they were formed with  $\text{BiI}_3$ -rich precursors. The decrease in the gap was due to formation of mid-gap defects affecting the VB band and also perturbing the Bi( $p$ ) orbitals and thereby the CB edge. With methylammonium at the A-sites, defect-formation was not facile due to a defect-tolerant nature of MA-based perovskites. A comparison of photovoltaic performances in devices based on  $\text{Cs}_3\text{Bi}_2\text{I}_9$  and  $\text{MA}_3\text{Bi}_2\text{I}_9$  supported formation of mid-gap defects in the former material.

## Acknowledgments

A.J.P. acknowledges the JC Bose Fellowship (SB/S2/JCB-001/2016) of SERB. A.M. acknowledges the DST INSPIRE Fellowship [IF170922]. G.P. and H.B. acknowledge the CSIR Junior Research Fellowship Numbers 09/080(1042)/2017-EMR-I (Roll No. 523509) and 09/080(0958)/2014-EMR-I (Roll No. 521931), respectively.

## Appendix A. Supplementary data

Supplementary data to this article can be found online at <https://doi.org/10.1016/j.solmat.2019.109941>.

## References

- [1] Q.X. Fu, X.L. Tang, B. Huang, T. Hu, L.C. Tan, L. Chen, Y.W. Chen, Recent progress on the long-term stability of perovskite solar cells, *Adv. Sci.* 5 (2018) 1700387.
- [2] A.M. Ganose, C.N. Savory, D.O. Scanlon, Beyond methylammonium lead iodide: prospects for the emergent field of  $ns^2$  containing solar absorbers, *Chem. Commun.* 53 (2016) 20–44.
- [3] Z. Li, T.R. Klein, D.H. Kim, M.J. Yang, J.J. Berry, M. van Hest, K. Zhu, Scalable fabrication of perovskite solar cells, *Nat. Rev. Mater.* 3 (2018) 18017.

- [4] J. Lei, F. Gao, H.X. Wang, J. Li, J.X. Jiang, X. Wu, R.R. Gao, Z. Yang, S.Z. Liu, Efficient planar CsPbBr<sub>3</sub> perovskite solar cells by dual-source vacuum evaporation, *Sol. Energy Mater. Sol. Cells* 187 (2018) 1–8.
- [5] M. Saliba, T. Matsui, J.Y. Seo, K. Domanski, J.P. Correa-Baena, M.K. Nazeeruddin, S.M. Zakeeruddin, W. Tress, A. Abate, A. Hagfeldt, M. Gratzel, Cesium-containing triple cation perovskite solar cells: improved stability, reproducibility and high efficiency, *Energy Environ. Sci.* 9 (2016) 1989–1997.
- [6] L.G. Li, F. Zhang, Y.Y. Hao, Q.J. Sun, Z.F. Li, H. Wang, Y.X. Cui, F.R. Zhu, High efficiency planar Sn-Pb binary perovskite solar cells: controlled growth of large grains via a one-step solution fabrication process, *J. Mater. Chem. C* 5 (2017) 2360–2367.
- [7] G.R. Berdiyorov, M.E. Madjet, F. El-Mellouhi, Improved electronic transport properties of tin-halide perovskites, *Sol. Energy Mater. Sol. Cells* 170 (2017) 8–12.
- [8] L.K. Ono, E.J. Juarez-Perez, Y.B. Qi, Progress on perovskite materials and solar cells with mixed cations and halide anions, *ACS Appl. Mater. Interfaces* 9 (2017) 30197–30246.
- [9] H.Y. Zhang, C. Zhao, D. Li, H. Guo, F.Y. Liao, W. Cao, X.B. Niu, Y.Y. Zhao, Effects of substrate temperature on the crystallization process and properties of mixed-ion perovskite layers, *J. Mater. Chem.* 7 (2019) 2804–2811.
- [10] B. Yang, M. Wang, X.F. Hu, T.W. Zhou, Z.G. Zang, Highly efficient semitransparent CsPbBr<sub>2</sub> perovskite solar cells via low-temperature processed In<sub>2</sub>S<sub>3</sub> as electron-transport-layer, *Nano Energy* 57 (2019) 718–727.
- [11] K.X. Steirer, P. Schulz, G. Teeter, V. Stevanovic, M. Yang, K. Zhu, J.J. Berry, Defect tolerance in methylammonium lead triiodide perovskite, *ACS Energy Lett* 1 (2016) 360–366.
- [12] Z.N. Bi, X. Rodriguez-Martinez, C. Aranda, E. Pascual-San-Jose, A.R. Goni, M. Campoy-Quiles, X.Q. Xu, A. Guerrero, Defect tolerant perovskite solar cells from blade coated non-toxic solvents, *J. Mater. Chem.* 6 (2018) 19085–19093.
- [13] V. D'Innocenzo, G. Grancini, M.J.P. Alcocer, A.R.S. Kandada, S.D. Stranks, M.M. Lee, G. Lanzani, H.J. Snaith, A. Petrozza, Excitons versus free charges in organo-lead tri-halide perovskites, *Nat. Commun.* 5 (2014) 3586.
- [14] G.C. Xing, N. Mathews, S.Y. Sun, S.S. Lim, Y.M. Lam, M. Gratzel, S. Mhaisalkar, T.C. Sum, Long-range balanced electron- and hole-transport lengths in organic-inorganic CH<sub>3</sub>NH<sub>3</sub>PbI<sub>3</sub>, *Science* 342 (2013) 344–347.
- [15] P. Azarhoosh, S. McKechnie, J.M. Frost, A. Walsh, M. van Schilfgaarde, Research update: relativistic origin of slow electron-hole recombination in hybrid halide perovskite solar cells, *Appl. Mater.* 4 (2016) 091501.
- [16] B.W. Park, B. Philippe, X.L. Zhang, H. Rensmo, G. Boschloo, E.M.J. Johansson, Bismuth based hybrid perovskites A<sub>3</sub>Bi<sub>2</sub>I<sub>9</sub> (A: methylammonium or cesium) for solar cell application, *Adv. Mater.* 27 (2015) 6806–6813.
- [17] C.N. Savory, A. Walsh, D.O. Scanlon, Can Pb-free halide double perovskites support high-efficiency solar cells? *ACS Energy Lett* 1 (2016) 949–955.
- [18] M. Pantaler, K.T. Cho, V.I.E. Quelo, I.G. Benito, C. Fetzkenhauer, I. Anusca, M.K. Nazeeruddin, D.C. Lupascu, G. Grancini, Hysteresis-free lead-free double-perovskite solar cells by interface engineering, *ACS Energy Lett* 3 (2018) 1781–1786.
- [19] F. Bai, Y.H. Hu, Y.Q. Hu, T. Qiu, X.L. Miao, S.F. Zhang, Lead-free, air-stable ultrathin Cs<sub>3</sub>Bi<sub>2</sub>I<sub>9</sub> perovskite nanosheets for solar cells, *Sol. Energy Mater. Sol. Cells* 184 (2018) 15–21.
- [20] X.Q. Zhang, G. Wu, S.D. Yang, W.F. Fu, Z.Q. Zhang, C. Chen, W.Q. Liu, J.L. Yan, W.T. Yang, H.Z. Chen, Vertically oriented 2D layered perovskite solar cells with enhanced efficiency and good stability, *Small* 13 (2017) UNSP 1700611.
- [21] M.H. Du, Efficient carrier transport in halide perovskites: theoretical perspectives, *J. Mater. Chem.* 2 (2014) 9091–9098.
- [22] T. Singh, A. Kulkarni, M. Ikegami, T. Miyasaka, Effect of electron transporting layer on bismuth-based lead-free perovskite (CH<sub>3</sub>NH<sub>3</sub>)<sub>3</sub>Bi<sub>2</sub>I<sub>9</sub> for photovoltaic applications, *ACS Appl. Mater. Interfaces* 8 (2016) 14542–14547.
- [23] M. Abulikemu, S. Ould-Chikh, X.H. Miao, E. Alarousu, B. Murali, G.O.N. Ndjawa, J. Barbe, A. El Labban, A. Amassiana, S. Del Gobbo, Optoelectronic and photovoltaic properties of the air-stable organohalide semiconductor (CH<sub>3</sub>NH<sub>3</sub>)<sub>3</sub>Bi<sub>2</sub>I<sub>9</sub>, *J. Mater. Chem.* 4 (2016) 12504–12515.
- [24] B. Ghosh, S. Chakraborty, H. Wei, C. Guet, S.Z. Li, S. Mhaisalkar, N. Mathews, Poor photovoltaic performance of Cs<sub>3</sub>Bi<sub>2</sub>I<sub>9</sub>: an insight through first-principles calculations, *J. Phys. Chem. C* 121 (2017) 17062–17067.
- [25] C.S. Ni, G. Hedley, J. Payne, V. Svrcek, C. McDonald, L.K. Jagadamma, P. Edwards, R. Martin, G. Jain, D. Carolan, D. Mariotti, P. Maguire, I. Samuel, J. Irvine, Charge carrier localised in zero-dimensional (CH<sub>3</sub>NH<sub>3</sub>)<sub>3</sub>Bi<sub>2</sub>I<sub>9</sub> clusters, *Nat. Commun.* 8 (2017) 170.
- [26] H. Hu, B.H. Dong, W. Zhang, Low-toxic metal halide perovskites: opportunities and future challenges, *J. Mater. Chem.* 5 (2017) 11436–11449.
- [27] C.M. Sutter-Fella, D.W. Miller, Q.P. Ngo, E.T. Roe, F.M. Toma, I.D. Sharp, M.C. Lonergan, A. Javey, Band tailing and deep defect states in CH<sub>3</sub>NH<sub>3</sub>Pb(I<sub>1-x</sub>Br<sub>x</sub>)<sub>3</sub> perovskites as revealed by sub-bandgap photocurrent, *ACS Energy Lett* 2 (2017) 709–715.
- [28] B. Ghosh, B. Wu, H.K. Mulmudi, C. Guet, K. Weber, T.C. Sum, S.G. Mhaisalkar, N. Mathews, Limitations of Cs<sub>3</sub>Bi<sub>2</sub>I<sub>9</sub> as lead-free photovoltaic absorber materials, *ACS Appl. Mater. Interfaces* 10 (2018) 35000–35007.
- [29] Y.L. Wang, S.W. Liu, Q. Zeng, R. Wang, W.J. Qin, H.Q. Cao, L.Y. Yang, L. Li, S.G. Yin, F.L. Zhang, Enhanced performance and stability of inverted planar perovskite solar cells by incorporating 1,6-diaminohexane dihydrochloride additive, *Sol. Energy Mater. Sol. Cells* 188 (2018) 140–148.
- [30] K.H. Kim, C. Takahashi, Y. Abe, M. Kawamura, Effects of Cu doping on nickel oxide thin film prepared by sol-gel solution process, *Optik* 125 (2014) 2899–2901.
- [31] X. Fang, J.H. Li, D.X. Zhao, D.Z. Shen, B.H. Li, X.H. Wang, Phosphorus-doped p-type ZnO nanorods and ZnO nanorod p-n homojunction LED fabricated by hydrothermal method, *J. Phys. Chem. C* 113 (2009) 21208–21212.
- [32] A.J. Lehner, D.H. Fabini, H.A. Evans, C.A. Hebert, S.R. Smock, J. Hu, H.B. Wang, J.W. Zwanziger, M.L. Chabinyr, R. Seshadri, Crystal and electronic structures of complex bismuth iodides A<sub>3</sub>Bi<sub>2</sub>I<sub>9</sub> (A = K, Rb, Cs) related to perovskite: aiding the rational design of photovoltaics, *Chem. Mater.* 27 (2015) 7137–7148.
- [33] M.B. Johansson, H.M. Zhu, E.M.J. Johansson, Extended photo-conversion spectrum in low-toxic bismuth halide perovskite solar cells, *J. Phys. Chem. Lett.* 7 (2016) 3467–3471.
- [34] C.F. Lan, J.T. Luo, S. Zhao, C. Zhang, W.G. Liu, S.Z. Hayase, T.L. Ma, Effect of lead-free (CH<sub>3</sub>NH<sub>3</sub>)<sub>3</sub>Bi<sub>2</sub>I<sub>9</sub> perovskite addition on spectrum absorption and enhanced photovoltaic performance of bismuth triiodide solar cells, *J. Alloy. Comp.* 701 (2017) 834–840.
- [35] D. Phuyal, S.M. Jain, B. Philippe, M.B. Johansson, M. Pazoki, J. Kullgren, K.O. Kvashnina, M. Klintonberg, E.M.J. Johansson, S.M. Butorin, O. Karis, H. Rensmo, The electronic structure and band interface of cesium bismuth iodide on a titania heterostructure using hard X-ray spectroscopy, *J. Mater. Chem.* 6 (2018) 9498–9505.
- [36] J. Kim, S.-H. Lee, J.H. Lee, K.-H. Hong, The role of intrinsic defects in methylammonium lead iodide perovskite, *J. Phys. Chem. Lett.* 5 (2014) 1312–1317.
- [37] W.-J. Yin, T. Shi, Y. Yan, Unusual defect physics in CH<sub>3</sub>NH<sub>3</sub>PbI<sub>3</sub> perovskite solar cell absorber, *Appl. Phys. Lett.* 104 (2014) 063903.
- [38] G. Paul, S. Chatterjee, H. Bhunia, A.J. Pal, Self-doping in hybrid halide perovskites via precursor stoichiometry: to probe the type of conductivity through scanning tunneling spectroscopy, *J. Phys. Chem. C* 122 (2018) 20194–20199.
- [39] G. Giorgi, J.I. Fujisawa, H. Segawa, K. Yamashita, Small photocarrier effective masses featuring ambipolar transport in methylammonium lead iodide perovskite: a density functional analysis, *J. Phys. Chem. Lett.* 4 (2013) 4213–4216.
- [40] Z. Zhang, X.W. Li, X.H. Xia, Z. Wang, Z.B. Huang, B.L. Lei, Y. Gao, High-quality (CH<sub>3</sub>NH<sub>3</sub>)<sub>3</sub>Bi<sub>2</sub>I<sub>9</sub> film-based solar cells: pushing efficiency up to 1.64%, *J. Phys. Chem. Lett.* 8 (2017) 4300–4307.

Supplementary material

Band-edges of bismuth-based ternary halide perovskites ( $A_3\text{Bi}_2\text{I}_9$ ) through scanning tunneling spectroscopy vis-à-vis impact of defects in limiting the performance of solar cells

Abhishek Maiti, Goutam Paul, Hrishikesh Bhunia and Amlan J. Pal\*

*School of Physical Sciences, Indian Association for the Cultivation of Science, Jadavpur, Kolkata 700032, India*

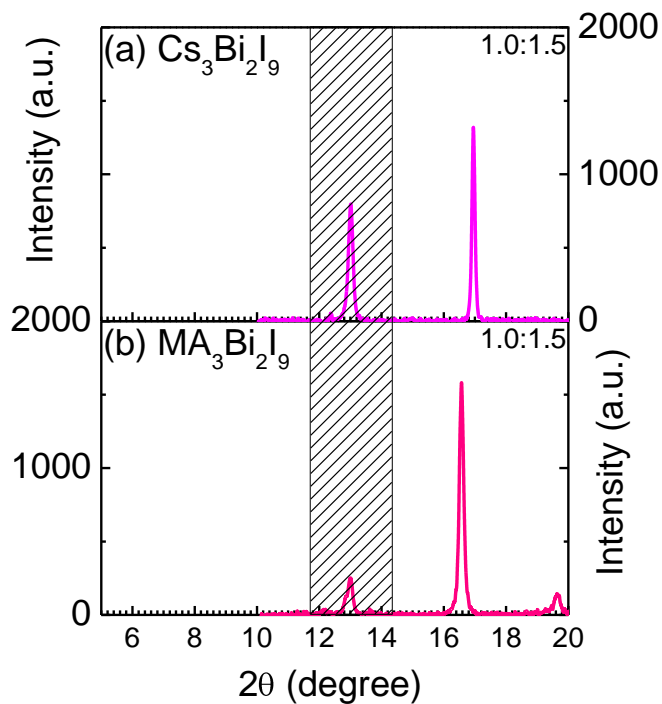


**Fig. S1.** Comparison of XRD peak intensity corresponding to  $\text{BiI}_3$  in  $\text{Cs}_3\text{Bi}_2\text{I}_9$  and  $\text{MA}_3\text{Bi}_2\text{I}_9$  formed with  $\text{BiI}_3$ -rich environment.



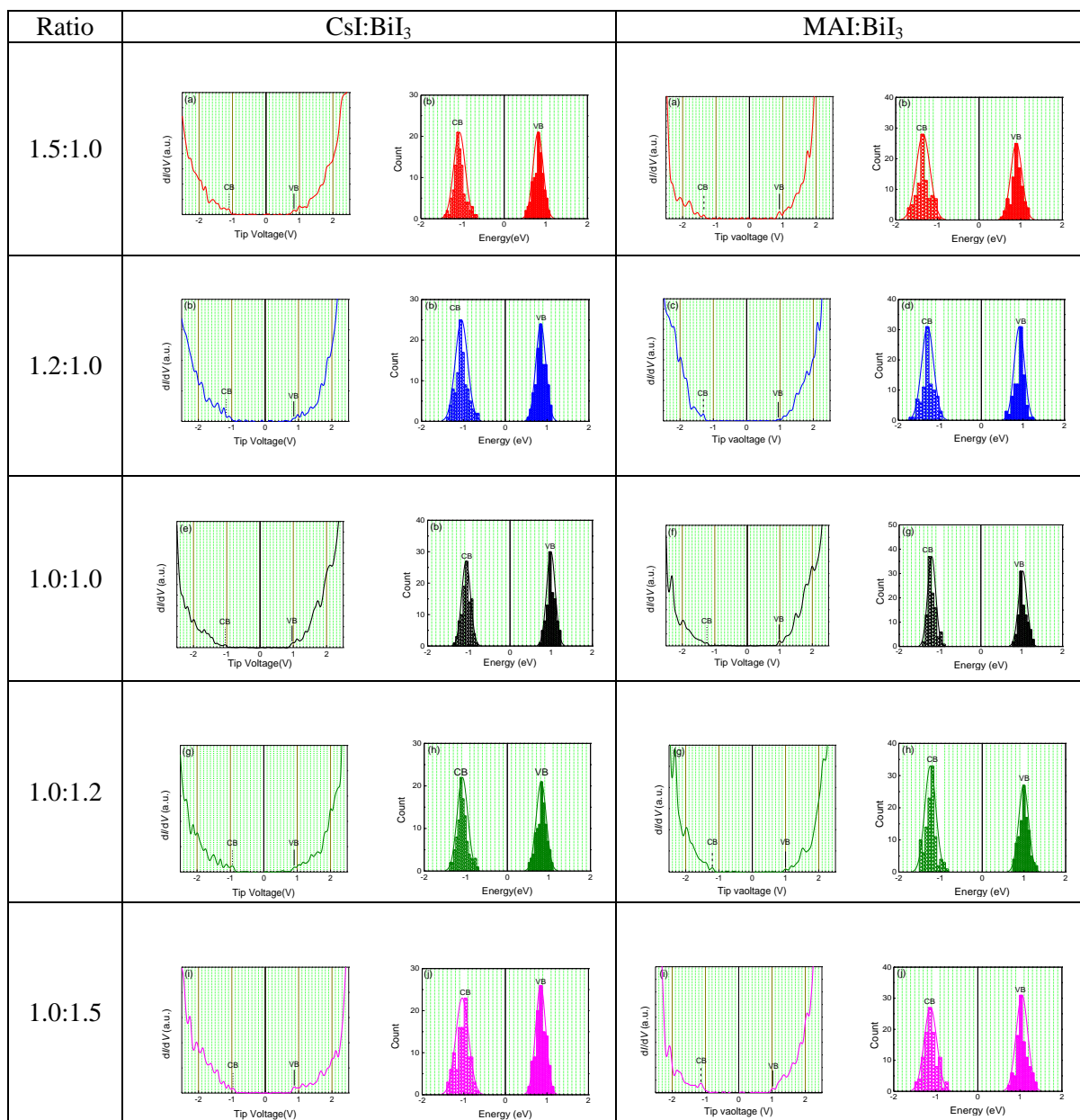


**Fig. S2.** Typical  $dI/dV$  spectra and corresponding histograms of  $\text{Cs}_3\text{Bi}_2\text{I}_9$  and  $\text{MA}_3\text{Bi}_2\text{I}_9$  formed with different precursor-stoichiometries.



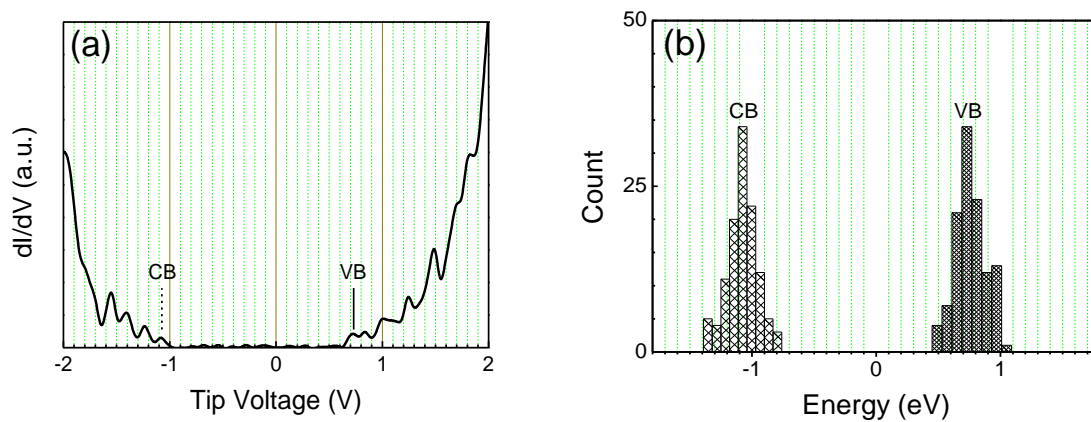


**Fig. S3.** Typical  $dI/dV$  spectrum and corresponding CB and VB energy-histograms of  $\text{BiI}_3$ .

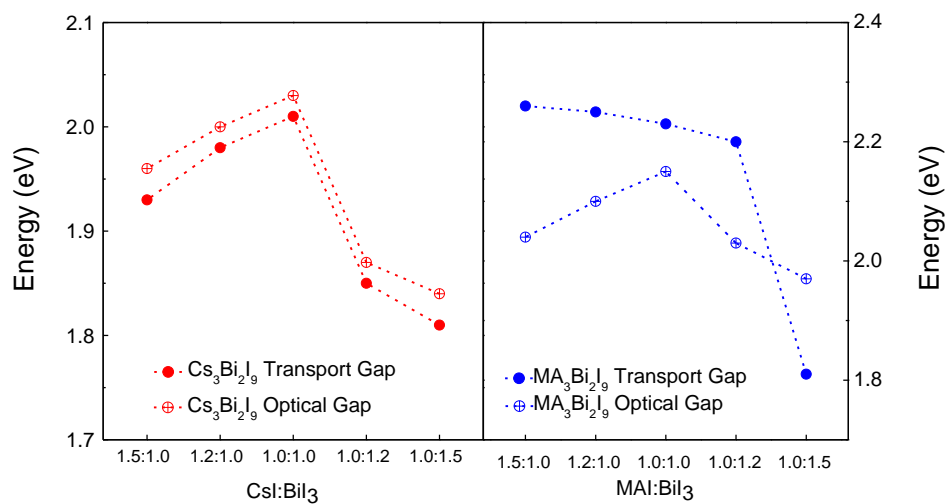


**Fig. S4.** Comparison of transport gap and optical gap in  $\text{Cs}_3\text{Bi}_2\text{I}_9$  and  $\text{MA}_3\text{Bi}_2\text{I}_9$ .

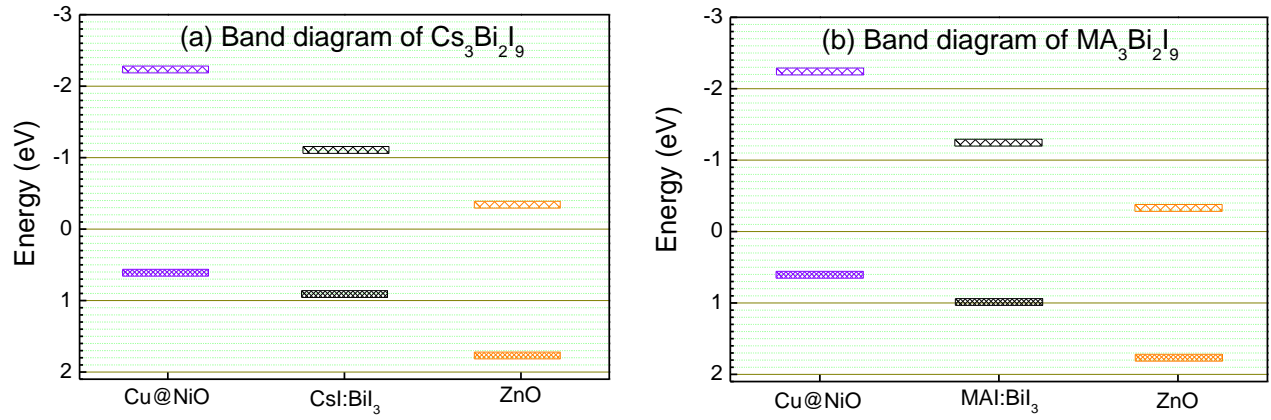


**Fig. S5.** Type-II band alignment of (a) Cu:NiO/Cs<sub>3</sub>Bi<sub>2</sub>I<sub>9</sub>/ZnO and (b) Cu:NiO/MA<sub>3</sub>Bi<sub>2</sub>I<sub>9</sub>/ZnO heterojunctions.

**Table S1**

Photovoltaic parameters of devices based on Cs<sub>3</sub>Bi<sub>2</sub>I<sub>9</sub> and MA<sub>3</sub>Bi<sub>2</sub>I<sub>9</sub>.

Perovskite	Shunt resistance (kΩ)	$V_{OC}$ (V)	$J_{SC}$ (mA/cm <sup>2</sup> )	Fill-Factor (%)	Efficiency (%)
Cs <sub>3</sub> Bi <sub>2</sub> I <sub>9</sub>	0.88	0.51	0.75	30.9	0.12
(CH <sub>3</sub> NH <sub>3</sub> ) <sub>3</sub> Bi <sub>2</sub> I <sub>9</sub>	1.49	0.59	1.4	46.0	0.36

# Sulfur-Vacancy Passivation in Solution-Processed $\text{Sb}_2\text{S}_3$ Thin Films: Influence on Photovoltaic Interfaces

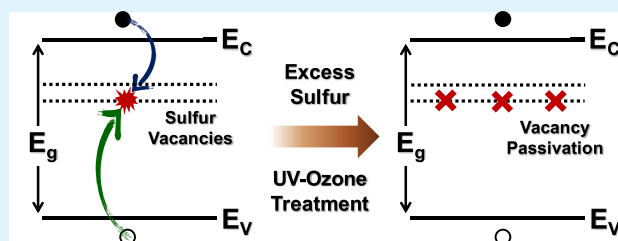
Abhishek Maiti, Soumyo Chatterjee, and Amlan J. Pal\*<sup>✉</sup>

School of Physical Sciences, Indian Association for the Cultivation of Science, Jadavpur, Kolkata 700032, India

## Supporting Information

**ABSTRACT:** We have presented a modified two-step sequential deposition method in forming  $\text{Sb}_2\text{S}_3$  thin films. In contrast to conventional chemical bath deposition (CBD) route, this sequential deposition approach has allowed passivation of sulfur vacancies in  $\text{Sb}_2\text{S}_3$  through a control over precursor stoichiometry (S/Sb ratio) during the film formation. We have made an in-depth characterization of the chalcogenide thin films upon passivation of the vacancies. While a sulfur-deficient composition led to the formation of donor-like sulfur vacancies, a sulfur-rich stoichiometry passivated such vacancies followed by creation of sulfur antisite defects in the chalcogenide. Scanning tunneling spectroscopy and thereby density of states allowed us to locate individual band-energies and their dependence on defect passivation. A strong dependence of optical bandgap and surface morphology of the  $\text{Sb}_2\text{S}_3$  layer on the precursor stoichiometry was evidenced in our study, and an optimized balance between the parameters was estimated for a slightly sulfur-rich composition (S/Sb ratio of 1.2). Interestingly, the photovoltaic parameters of Cu:NiO/ $\text{Sb}_2\text{S}_3$ /PCBM planar heterojunctions excelled at the predicted stoichiometry, yielding a power conversion efficiency of 3.02% along with a significantly high open-circuit voltage of 0.8 V. This effort thus provides new insights into the influence of defect passivation on solar cell characteristics based on solution-processed  $\text{Sb}_2\text{S}_3$  thin films.

**KEYWORDS:** solution-processed  $\text{Sb}_2\text{S}_3$  thin films, defect passivation, band energies, heterojunctions, solar cells



## INTRODUCTION

The necessity for low-cost and environmentally benign materials toward high-efficiency solar cell applications has compelled researchers to explore for newer photovoltaic materials.<sup>1</sup> Despite a tremendous success of organic–inorganic hybrid lead halide perovskites, novel inorganic semiconductors still attract a significant interest owing to their favorable optoelectronic properties.<sup>2</sup> Among these materials, antimony trisulfide ( $\text{Sb}_2\text{S}_3$ ) has emerged as a potential solar energy material due to its earth-abundant and nontoxic constituents along with optimal physical properties, such as a suitable direct bandgap (1.7 eV), high-absorption coefficient ( $10^5 \text{ cm}^{-1}$  at 450 nm), and a decent stable structure.<sup>3–5</sup> Besides, its existence in a single stable phase having a low melting point ( $\sim 550 \text{ }^\circ\text{C}$ ) aids formation of  $\text{Sb}_2\text{S}_3$  thin films in a phase-pure and highly crystalline form.<sup>6</sup> All of these properties make  $\text{Sb}_2\text{S}_3$  a potential candidate toward its use in stable, efficient, and less-expensive photovoltaic devices.<sup>7</sup>

Efforts with  $\text{Sb}_2\text{S}_3$  as a solar energy material have mostly been accounted toward fabrication of solid-state sensitized solar cells having an extremely thin absorber (ETA) architecture.<sup>8,9</sup> The ETA design is principally derived from dye-sensitized solar cell (DSSC) structures, where a thin absorber layer having a thickness of  $\sim 10 \text{ nm}$  is typically deposited onto a mesoporous  $\text{TiO}_2$  scaffold and the pores are subsequently filled with a hole-transport material (HTM), such as P3HT, CuSCN, or spiro-OMeTAD.<sup>10–12</sup> Here P3HT and

spiro-OMeTAD represent poly(3-hexylthiophene), and 2,2',7,7'-tetrakis(*N,N*-di-4-methoxyphenylamino)-9,9'-spirobi-fluorene, respectively. The basic advantage behind realization of such a device structure is faster carrier transfer from the thin absorber layer to the carrier-selective contacts; however, in practice, such benefits are restricted by carrier recombination via trap-assisted tunneling.<sup>13</sup> As a result,  $\text{Sb}_2\text{S}_3$ -based ETA solar cells have so far yielded a power conversion efficiency of  $\sim 7.5\%$ , which is well below the possibility per the Shockley–Queisser efficiency limit.<sup>14</sup> Improper infiltration of pores in ETA solar cells has been a major roadblock toward achieving an improved performance in the solar cells.<sup>15</sup> In this respect, introduction of a planar geometry in such architecture has been projected to be a feasible solution to circumvent the constraint.<sup>16</sup> A compact film having a planar structure not only would reduce the requirement of a large interfacial area for appreciable photocurrent generation, it would moreover prevent interfacial carrier recombination. Indeed, in spite of a lower efficiency, planar geometries have so far yielded a higher open-circuit voltage ( $V_{\text{OC}}$ ) than that in the best performing ETA cells comprised of the same HTM and  $\text{Sb}_2\text{S}_3$  formed through an identical deposition route.<sup>17</sup>

**Received:** October 3, 2019

**Accepted:** December 3, 2019

**Published:** December 3, 2019

Performance of a planar solar cell depends a lot on the quality of the absorber layer. Typically,  $\text{Sb}_2\text{S}_3$  thin films are fabricated by chemical bath deposition (CBD) technique, which is a method elegantly developed by Messina et al.<sup>18</sup> Such a route, although convenient and cost-effective, is unfortunately associated with a number of constraints limiting the performance of devices on the basis of as-grown  $\text{Sb}_2\text{S}_3$  films.<sup>18,19</sup> As an alternative to the CBD method, spin-coating of different antimony and sulfur-containing precursors was proposed to cast  $\text{Sb}_2\text{S}_3$  thin films.<sup>3,20</sup> Such films, when incorporated in a sensitized device structure, have delivered a PCE value of 6.8%.<sup>6</sup> Zheng et al. developed a fast solid-gas reaction process to fabricate  $\text{Sb}_2\text{S}_3$ -sensitized solar cells with a PCE of 6.27%.<sup>21</sup> While most of the efforts in  $\text{Sb}_2\text{S}_3$  solar cells have been carried out in a sensitized architecture, CBD-grown films in most of the planar devices have shown PCE values below 5% which is lower than that in sensitized structures.<sup>22,23</sup> To date, the highest PCE of 5.77% has been reported with films grown by atomic layer deposition (ALD) method; some of the studies have inferred that the inferior performance of  $\text{Sb}_2\text{S}_3$ -based planar heterojunction solar cells could be ascribed to the presence of bulk and surface defects and also a high resistivity in the films limiting the short-circuit current density ( $J_{\text{SC}}$ ) and fill factor (FF) of the devices.<sup>24–26</sup> Hence, to achieve an improved PCE in  $\text{Sb}_2\text{S}_3$  planar heterojunction solar cells, it is important to control the intrinsic defects by tuning sulfur vacancies in the material.

In this direction, we have investigated the influence of sulfur vacancies on photovoltaic properties of antimony trisulfide ( $\text{Sb}_2\text{S}_3$ ) thin films. We have considered a modified sequential deposition approach to fabricate uniform and phase-pure  $\text{Sb}_2\text{S}_3$  thin films; this approach offers not only an alternative to the traditionally used CBD technique but also a precise control over the thickness and composition of the films. Here, we have tailored the sulfur vacancies in the as-grown  $\text{Sb}_2\text{S}_3$  films following a couple of routes: precursor stoichiometry and ultraviolet ozone treatment. By monitoring the shift of band energies through scanning tunneling spectroscopy (STS) and thereof the density of states (DOS) spectra, we aimed to form energy-level-optimized planar heterojunctions solar cells with a high  $V_{\text{OC}}$ .

## ■ EXPERIMENTAL SECTION

**Materials.** Antimony(III) acetate ( $\text{Sb}(\text{CH}_3\text{COO})_3$ , 99.9%) and thiourea ( $\text{SC}(\text{NH}_2)_2$ ), nickel(II) acetate tetrahydrate ( $\text{Ni}(\text{CH}_3\text{COO})_2 \cdot 4\text{H}_2\text{O}$ , 98%), copper(II) chloride dihydrate ( $\text{CuCl}_2 \cdot 2\text{H}_2\text{O}$ , 99.9%), anhydrous *N,N*-dimethylformamide (DMF, 99.8%), dimethyl sulfoxide (DMSO, 99.9%), methanol, and diethanolamine were purchased from Sigma-Aldrich Chemical Co. Phenyl-C61-butyric acid methyl ester (PCBM) (99%) was procured from M/s SES Research, Houston, TX, USA. The materials were used without further purification.

**Fabrication of  $\text{Sb}_2\text{S}_3$  Thin Films through a Two-Step Sequential Deposition Approach.** The  $\text{Sb}_2\text{S}_3$  thin films were deposited following a reported solution-based sequential deposition approach with some modifications.<sup>3</sup> Briefly, antimony acetate and thiourea as cationic and anionic precursors were dissolved in DMF and DMSO, respectively, at 70 °C in a desired stoichiometry. To form  $\text{Sb}_2\text{S}_3$  films, the cationic precursor was first spun on a substrate at 2500 rpm for 30 s followed by a coating of the anionic precursor at an identical spinning condition. The as-deposited films were then subjected to a two-step annealing process: 100 °C for 10 min followed by 300 °C for 20 min. During such an annealing protocol, the as-deposited transparent and colorless films gradually became

yellow and finally a shiny brown while retaining their transparent nature.

In order to control the sulfur content in  $\text{Sb}_2\text{S}_3$  films, the ratio between anionic and cationic precursors was varied between 0.6 and 1.4 in steps of 0.2 in forming  $\text{Sb}_2\text{S}_3$  in a sulfur-deficient and sulfur-rich condition, respectively. In another approach, films formed through stoichiometrically balanced precursors (S/Sb, 1.0) were subjected to UV-ozone (UVO) treatment for 5, 10, 15, or 20 min using a Novascan 4<sup>U</sup>-UV/Ozone System cleaning unit (model PSDP-UV4T).

### Formation of Copper-Doped Nickel Oxide Thin Films.

Copper-doped nickel oxide (Cu:NiO) thin films were cast following a routine sol-gel approach.<sup>27</sup> A precursor solution of an optimized concentration was prepared at room temperature by dissolving 0.4 M  $\text{Ni}(\text{OCOCH}_3)_2$  with 5 at. %  $\text{CuCl}_2$  (as doping agent) in methanol, which acted as the solvent. Upon complete dissolution, diethanolamine was added dropwise to the precursor under a vigorous stirring condition. The color of the solution changed from light green to light blue, implying formation of the respective ammine complex. The resulting solution was further stirred for 1 h and filtered for further use. Suitable substrates were coated with the solution and annealed at 425 °C for 20 min in an ambient condition, leading to thermal decomposition of the ammine complex and formation of crystalline thin films of Cu:NiO.

**Characterization of the Materials.** The materials were characterized through conventional techniques, such as X-ray diffraction (XRD) studies, Raman spectroscopy, X-ray photoelectron spectroscopy (XPS), and optical absorption spectroscopy. The measurements were carried out with a Rigaku Smart Lab X-ray diffractometer (Cu  $K\alpha$  radiation,  $\lambda = 1.54 \text{ \AA}$ ) employed specially for thin films, a Horiba Jobin Yvon Raman triple-grating spectrometer system (model numbeo.r T64000) using 532.0 nm excitation from a diode-pumped solid-state (DPSS) laser, an Omicron XPS instrument (serial no. 0571), and a UV-vis-near-IR spectrophotometer (Cary 5000, Agilent Technologies), respectively. Additionally, band edges of the materials were probed using scanning tunneling spectroscopy (STS) of ultrathin films with a Nanosurf Easyscan2 scanning tunneling microscope (STM) under ambient condition. Highly doped silicon wafers (both n-type and p-type with arsenic and boron as dopants, respectively) having a resistivity of 3–10  $\text{m}\Omega\text{-cm}$  were used as substrates for the studies. Extremely sharp tips were formed through an acute mechanical cut of a Pt/Ir (80:20 (%)) wire having a diameter of 0.25  $\mu\text{m}$ . During approach of the tip, a current of 1 nA was set at a bias of 2.0 V, which was applied to the tip. Morphology of the films was recorded with a JEOL JSM-7500F field emission scanning electron microscope (FE-SEM) and a Nanosurf Easyscan2 atomic force microscope (AFM) in a noncontact mode.

**Fabrication and Characterization of Devices.** While fabricating solar cells, indium tin oxide (ITO) coated glass substrates were cleaned following a standard protocol; they were then subjected to UVO treatment for 20 min. On these treated substrates, an  $\sim 40 \text{ nm}$  thick HTL of Cu:NiO was formed. The HTL-coated ITO substrates were subjected to a very short UVO treatment of around 3 min. They were then transferred to a nitrogen-filled glovebox. The substrates were preheated at 70 °C for 10 min before depositing a layer of  $\text{Sb}_2\text{S}_3$  ( $\sim 120 \text{ nm}$ ) following the two-step sequential deposition process (vide supra). As an electron-transport layer (ETL), PCBM were spun at 3000 rpm for 30 s from a 20 mg/mL solution in chlorobenzene. The layered films were then annealed at 100 °C for 10 min. The device fabrication process was completed by depositing 100 nm thick aluminum strips (orthogonal to the ITO ones) as a top electrode through thermal evaporation in a vacuum chamber ( $10^{-6} \text{ mbar}$ ) fitted inside the glovebox. The active area of the cells was  $10 \text{ mm}^2$ .

The planar heterojunction devices were characterized by recording current-voltage ( $I$ - $V$ ) characteristics under dark and 1 sun illumination conditions using a Keithley 2636A electrometer controlled by LabTracer 2.0 software. The measurements were carried out inside the glovebox, which had both oxygen and moisture content below 0.1 ppm. Contacts with the electrodes were made with pressure-loaded probes. As a source for illumination, a 300 W solar simulator (Newport-Oriel Sol3A) attached with an AM1.5 filter was



used. The simulator was placed outside the glovebox, and the devices were illuminated through a quartz window fitted to the platform of the glovebox. To avoid any contribution from neighboring cells or areas outside the cell, regions outside the device under consideration were covered while recording  $I$ - $V$  characteristics under an illumination condition. A Solartron 1260A impedance analyzer was used to record real and imaginary components of complex impedance as a function of frequency; an ac voltage of 10 mV root-mean-square (RMS) was applied for the impedance measurement with a dc bias of  $V_{OC}$ . Frequency of the test voltage was varied between 1 Hz and 10 MHz, and 10 measurements were made per decade. The external quantum efficiency (EQE) spectrum of the solar cells was recorded with a Horiba Jobin Yvon H20 IR monochromator dispersing the simulated solar illumination; the corresponding photocurrent was measured with a Keithley 486 picoammeter.

## RESULTS AND DISCUSSION

**Importance of Sequential Deposition Approach in Forming  $Sb_2S_3$  Films.** Over the years, CBD technique has been the most common synthesis method to fabricate  $Sb_2S_3$  thin films for photovoltaic applications.<sup>10,18,22</sup> Typically, in the CBD method, a substrate is immersed in a precursor bath to form thin films of non-metallic inorganic semiconductors. The bath contains both cationic and anionic precursors dissolved in a suitable solvent often with additional complexing agent(s) required to improve uniformity and crystallinity of the films, and also in controlling thermodynamics and kinetics of the deposition process.<sup>28</sup> In spite of such measures, CBD-grown  $Sb_2S_3$  films lacked the desired phase purity, since the films contain impurities, such as antimony oxides, hydroxides, or even sulfates.<sup>18,29</sup> Such impurities result in deep traps in  $Sb_2S_3$  films and thereby limit the performance of the respective cells. Moreover, the complex reaction mechanism, which includes heterogeneous nucleation and exponential growth of the films at a low temperature ( $\sim 10$  °C), demands a precise control of processing condition and eventually hinders reproducibility of the process. It should also be noted that a significantly long time ( $\sim 4$  h) is often needed in the CBD approach to obtain an appropriate thickness which may also affect the phase purity and substrate coverage.<sup>30</sup>

In contrast, the sequential deposition process per se through spin-coating is rapid, essentially controls film morphology, and has comparatively easier processability.<sup>3</sup> After sequential deposition of the precursors, formation of thin films occurs during postdeposition annealing. In this work, we have applied a modified sequential deposition process in forming  $Sb_2S_3$  thin films (Figure 1). The postdeposition annealing was done at a mild temperature of 100 °C; at this temperature, thiourea

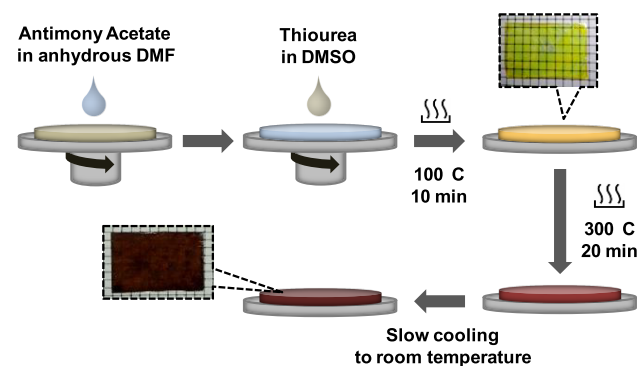


**Figure 1.** Schematic diagram of  $Sb_2S_3$  film fabrication through the sequential deposition approach.

decomposes to generate  $H_2S$  which reacts rapidly with antimony acetate in forming amorphous  $Sb_2S_3$  thin films. The process can in general be noticed through a gradual change in film color from transparent to light yellow and then to dark yellow. Crystallinity of the films was achieved after a further rise of the temperature to 300 °C, changing the film to dark brown in color. Interestingly, the rapid nature of reaction between the precursors effectively prevents formation of impurities, and thus an improved phase purity in  $Sb_2S_3$  thin film is obtained as compared to that in the CBD approach. Such a two-step process additionally offers the liberty to tune the composition by varying the precursor concentrations and the film thickness by the spinning speed. Use of spin-coating technique furthermore improves the degree of surface coverage of the films. It is worth mentioning here that any additional postannealing process, such as sulfuration or selenization, is not necessary in this process, since an excess chalcogen can anyway be introduced in thin films by controlling its content in the precursor.

**Characterization of  $Sb_2S_3$  Thin Films.** Considering the novelty of the film-deposition approach, we first of all aimed to confirm formation of  $Sb_2S_3$  and its phase purity through conventional thin-film characterization methods. In Figure 2, we have presented the results of  $Sb_2S_3$  thin films formed with a balanced precursor stoichiometry (S/Sb, 1.0). The XRD pattern (Figure 2a) shows a series of diffraction peaks at appropriate positions (JCPDS No. 42-1393); the intense peak  $\sim 25^\circ$  matched the diffraction from the (130) plane, which is the preferred orientation for an orthorhombic stibnite structure of  $Sb_2S_3$ .<sup>31</sup> Intensity of the peaks and their narrow full width at half-maxima (fwhm) signify high crystallinity of the material, while the absence of additional peaks implied its phase purity. Raman spectrum of  $Sb_2S_3$  films (Figure 2b) showed the presence of Raman active modes in the form of dominant bands located at 187, 236, 282, and 306  $cm^{-1}$ , which are known to correspond to the orthorhombic phase, alongside a couple of weak ones at 126 and 155  $cm^{-1}$ .<sup>32</sup> The UV-vis-near-IR optical absorption spectrum of  $Sb_2S_3$  thin films has been presented in Figure 2c, which shows a strong absorption over the entire visible region with the absorption onset being located at  $\sim 700$  nm. The bandgap of the thin films has been estimated from the following relation considering  $Sb_2S_3$  as a direct bandgap semiconductor,

$$\alpha hv = C(hv - E_g)^{1/2} \quad (1)$$

where  $\alpha$  is the absorption coefficient,  $hv$  is the photon energy, and  $E_g$  is the energy gap. Extrapolating the linear region of the  $(\alpha hv)^2$  vs  $hv$  plot (inset of Figure 2c), the bandgap of the film at room temperature could be estimated to be around 1.7 eV, which matched well with the reported results.<sup>3</sup>

Valence-state information on  $Sb_2S_3$  was derived from XPS studies. As presented in Figure 3a, the survey spectrum of  $Sb_2S_3$  was dominated by a strong presence of antimony and signatures of sulfur and carbon. The peak at 285.0 eV signifying the presence of carbon in the films can be ascribed to being due to the usual surface contaminations. We have recorded high-resolution spectra of Sb 3d and S 2p (Figure 3b,c). In the spectrum of antimony, two peaks at 528.7 and 537.9 eV corresponded to Sb 3d<sub>5/2</sub> and 3d<sub>3/2</sub> states, respectively. The separation of the Sb 3d doublet was 9.2 eV, indexing a trivalent oxidation state of antimony in the compound.<sup>33</sup> The asymmetric nature of the spectrum showed

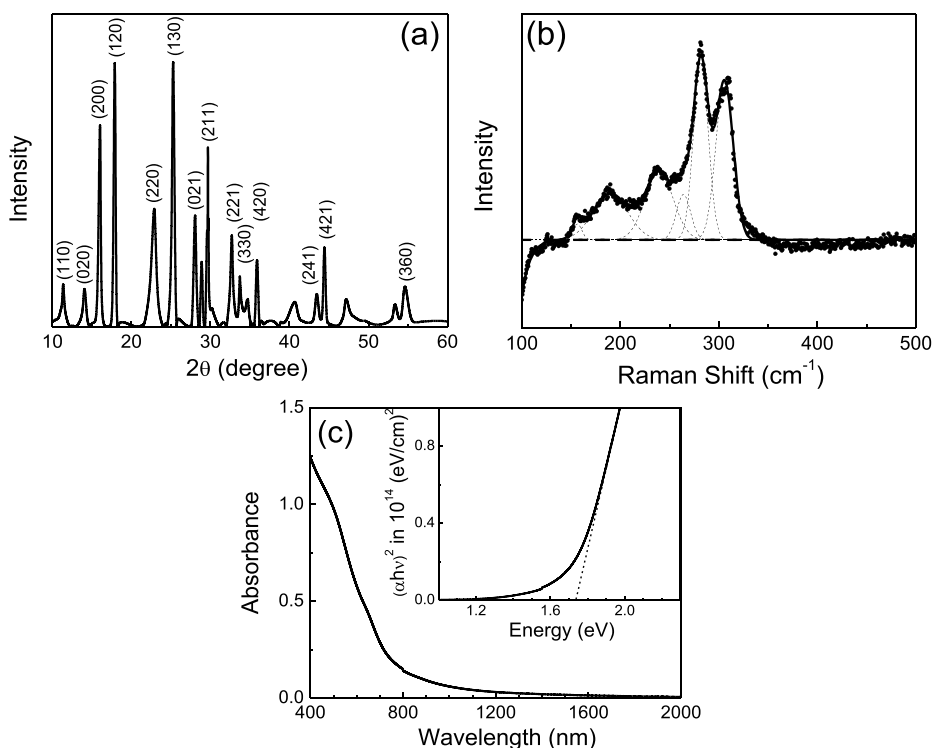


**Figure 2.** (a) XRD pattern, (b) Raman spectrum, and (c) optical absorption spectrum along with the corresponding Tauc plot (inset) of stoichiometric (S/Sb, 1.0)  $\text{Sb}_2\text{S}_3$  thin films.

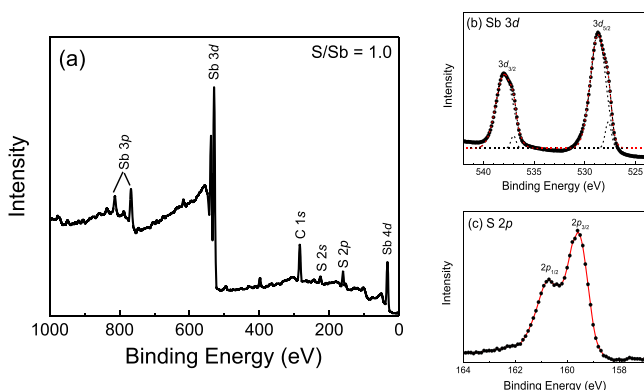


**Figure 3.** (a) Full range XPS spectrum of  $\text{Sb}_2\text{S}_3$  thin films with high-resolution spectra of (b) Sb 3d and (c) S 2p states.

the presence of a couple of feeble shoulder peaks at 527.8 and 537.1 eV corresponding to the  $\text{Sb}^0$  elemental state present in the material.<sup>34</sup> Such a reduction of antimony can be attributed to an ion-induced effect at the time of surface etching and should not be considered as an impurity.<sup>35</sup> The high-resolution spectrum of sulfur showed two overlapped peaks for S  $2p_{3/2}$  and  $2p_{1/2}$  at 159.6 and 160.7 eV, respectively. The S 2p doublet showed an energy separation of 1.1 eV indicating a  $\text{S}^{2-}$  oxidation state in the material.<sup>33</sup> The observed binding energy values were in concurrence with the reported data, reaffirming formation of  $\text{Sb}_2\text{S}_3$  through a solution approach.

**Passivation of Sulfur Vacancies in  $\text{Sb}_2\text{S}_3$  Thin Films.** In a binary chalcogenide compound such as  $\text{Sb}_2\text{S}_3$ , six intrinsic defects may exist: sulfur and antimony vacancies ( $\text{S}_\text{V}$ ,  $\text{Sb}_\text{V}$ ), sulfur and antimony interstitials ( $\text{S}_\text{i}$ ,  $\text{Sb}_\text{i}$ ), and antisite substitutions ( $\text{Sb}_\text{s}$ ,  $\text{Sb}_\text{sb}$ ).<sup>36</sup> Formation energies of the defects depend strongly on the stoichiometry of the precursors.

Conversely, the anisotropic nature of the  $\text{Sb}_2\text{S}_3$  crystal structure and wide distribution of bond lengths also influence defect formation with their energy level location within or outside the gap.<sup>37</sup> It is however well-accepted that, among these defects, the energy level of sulfur vacancies ( $\text{S}_\text{V}$ ) is situated within the gap and thereby affect carrier transport or instill recombination loss in a large manner.<sup>38</sup> Extensive efforts were hence made to develop methods in passivating sulfur vacancies in  $\text{Sb}_2\text{S}_3$  through a range of processes, such as thioacetamide postdeposition treatment,<sup>14</sup> variation of bath temperature in CBD approach,<sup>39</sup> postsulfurization (or selenization),<sup>25</sup> and so forth. However, the methods have always brought a restriction or another limiting their efficacy.

The sequential film-deposition approach provides an opportunity to tailor (passivate) sulfur vacancies in  $\text{Sb}_2\text{S}_3$  thin films. In this endeavor, we have considered two different methods: (1) to vary the relative sulfur content (S/Sb) in the precursors in forming both sulfur-rich and sulfur-deficient thin films and (2) to introduce a postdeposition UV–ozone treatment in suppressing the sulfur vacancies by chemisorption of oxygen atoms on the top surface of the thin films. While the former method is applicable in films formed only through sequential film deposition approach, the latter one has been proved to be more general and effective than the previously reported ones.<sup>40</sup>

**Characteristics of  $\text{Sb}_2\text{S}_3$  Thin Films: Effect of Vacancy Passivation.** In order to tune sulfur vacancies in our  $\text{Sb}_2\text{S}_3$  thin films, we have varied the precursor contents with respect to the stoichiometric condition (S/Sb, 1.0) in forming both sulfur-rich (S/Sb, 1.2 and 1.4) and sulfur-deficient (S/Sb, 0.8 and 0.6) compositions. The elemental composition of  $\text{Sb}_2\text{S}_3$  films was confirmed from EDX analysis (shown in Figure S1 and Table S1 in the Supporting Information). The XRD patterns of all of the vacancy-tuned  $\text{Sb}_2\text{S}_3$  films evidenced a

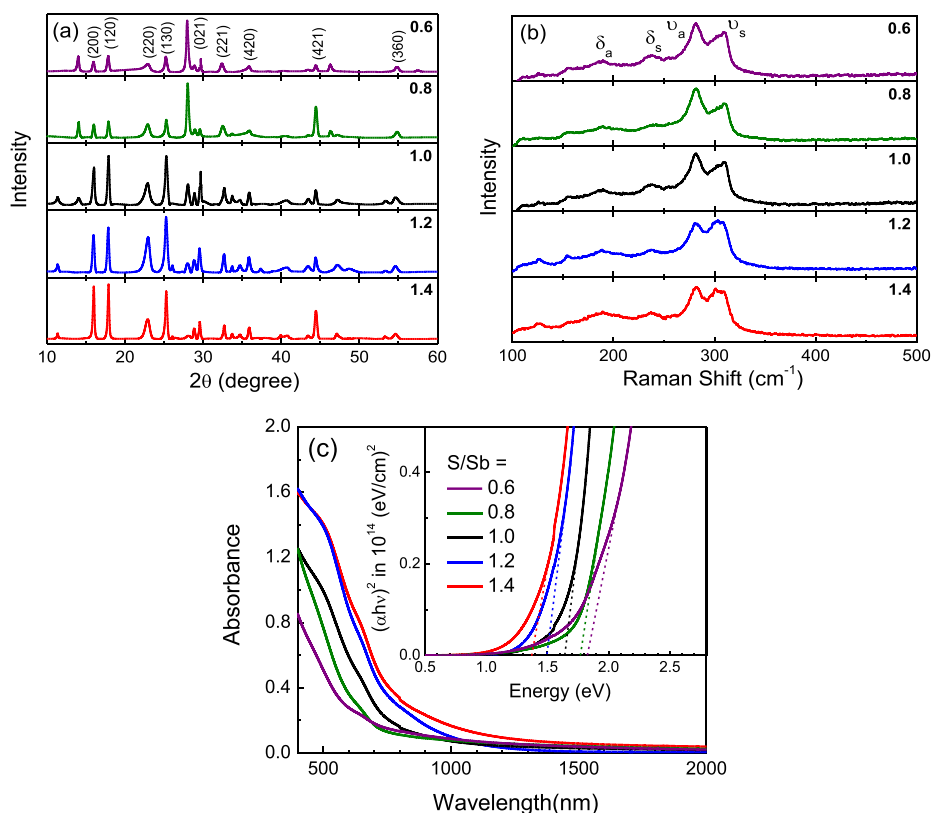


**Figure 4.** (a) XRD patterns, (b) Raman spectra, and (c) optical absorption spectra of vacancy-tailored  $\text{Sb}_2\text{S}_3$  thin films. The inset of panel c shows Tauc plots corresponding to the absorption spectra. Relative sulfur content (S/Sb) in the films has been specified in the legend.

high degree of crystallinity and a preferred orientation along the (130) plane showing continuance of the orthorhombic phase (Figure 4a).<sup>31</sup> The respective grain sizes were estimated by using the Scherrer formula and have been collated in Table S2 in the Supporting Information. The films showed a comparable grain size in the sulfur deficient to stoichiometric composition, whereas a gradual enlargement of the grains in the sulfur-rich conditions was noticed.

We further have characterized the vacancy-tuned  $\text{Sb}_2\text{S}_3$  films by Raman spectroscopy. As presented in Figure 4b, the spectra revealed the presence of dominant Raman bands at 189.6, 237.9, 281.5, and 309.5  $\text{cm}^{-1}$  along with a couple of weak ones at 126 and 155  $\text{cm}^{-1}$ . In order to understand the lattice dynamics of  $\text{Sb}_2\text{S}_3$ , it is important to recall that the  $\text{Sb}_2\text{S}_3$  structure consists of linked  $\text{SbS}_3E$  and  $\text{SbS}_5E$  units, where  $E$  refers to the lone electron pair of antimony atoms. Since, in a simplified view, vibrational modes of chalcogenide compounds are usually explained by considering molecular-like units, so optical phonons of  $\text{Sb}_2\text{S}_3$  can be partially interpreted as appearing solely from  $\text{SbS}_3$  units (without any mention of  $\text{SbS}_5$ ). In  $\text{Sb}_2\text{S}_3$  films formed through conventional techniques, the undistorted  $\text{SbS}_3$  units, which have an ideal trigonal pyramidal ( $C_{3v}$ ) symmetry, give rise to four normal modes of vibration ( $2A_1 + 2E$ ): symmetric stretching  $\nu_s(A_1)$ , antisymmetric stretching  $\nu_a(E)$ , symmetric bending  $\delta_s(A_1)$ , and antisymmetric bending  $\delta_a(E)$ , which are both Raman and infrared active, with  $\nu_s > \nu_a$  and  $\delta_s > \delta_a$  in general consideration. In the recorded Raman spectra of  $\text{Sb}_2\text{S}_3$  thin films (Figure 4b), the band at 281.5  $\text{cm}^{-1}$  hence corresponds to antisymmetric stretching vibrations  $\nu_a(\text{Sb}-\text{S})$ , whereas the band at 309.5  $\text{cm}^{-1}$  should be attributed to symmetric stretching vibrations  $\nu_s(\text{Sb}-\text{S})$ . Similarly, the band at 189.6

and 237.9  $\text{cm}^{-1}$  corresponded to antisymmetric bending vibrations  $\delta_a(\text{S}-\text{Sb}-\text{S})$  and symmetric bending vibrations  $\delta_s(\text{S}-\text{Sb}-\text{S})$ , respectively. In addition, the weak bands at 126 and 155  $\text{cm}^{-1}$  can be attributed to  $A_g$  and  $B_{1g}$  modes of vibration, respectively. The Raman shifts obtained from our measurements are in agreement with the reported values.<sup>41</sup> The spectra are mostly dominated by Raman modes at 281.5 and 309.5  $\text{cm}^{-1}$  corresponding to antisymmetric and symmetric  $\text{Sb}-\text{S}$  stretching vibrations in  $\text{Sb}_2\text{S}_3$ , respectively. A closer inspection of the modes showed that under the influence of precursor stoichiometry, the intensity of the modes changed; the peak corresponding to symmetric stretching gained its intensity with increasing sulfur content in  $\text{Sb}_2\text{S}_3$  (less sulfur vacancies) at the cost of the asymmetric stretching mode. Such a change in the peak intensity has also been explained to be due to the absence of sulfur vacancies leading to shorter  $\text{Sb}-\text{S}$  bonds and vice versa.<sup>41</sup>

When the  $\text{Sb}_2\text{S}_3$  film formed with stoichiometrically balanced precursors (S/Sb, 1.0) was subjected to UV–ozone treatments, suppression of sulfur vacancies took place through chemisorption of oxygen atoms on the surface of the thin films.<sup>42</sup> It is expected that these oxygen atoms formed bonds with antimony and, hence, oxidized the metal into impurity phases such as  $\text{Sb}_2\text{O}_3$ .<sup>7</sup> In the present case, we have varied the treatment time up to 20 min in a step of 5 min; the presence of such impurities has however not been manifested in XRD and Raman studies even in the film exposed for 20 min. It can therefore be assumed that the intense peaks of  $\text{Sb}_2\text{S}_3$  probably have suppressed the oxide signatures. The optical absorption spectra, on the other hand, did not show any marked changes under mild UVO treatment (0–10 min); a shift in the edge of absorption toward the longer wavelength was observed when

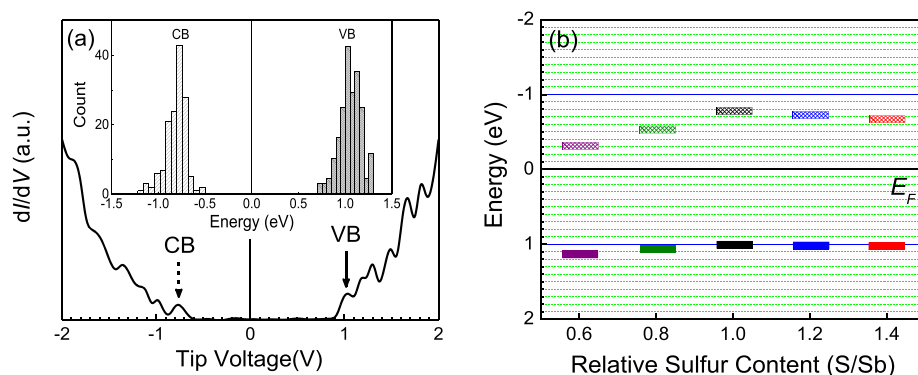


**Figure 5.** (a)  $dI/dV$  spectrum of pristine  $Sb_2S_3$  thin films and (b) band edges of vacancy-tailored  $Sb_2S_3$  thin films. The inset of panel a shows the histogram of the band edges.

the stoichiometric  $Sb_2S_3$  film was treated for 15 min and above (shown in Figure S2a in the [Supporting Information](#)). Such a red shift in the bandgap was also estimated from respective Tauc plots and can be considered to be due to passivation of sulfur vacancies through chemisorption of oxygen atoms (shown in Figure S2b in the [Supporting Information](#)). The evidence of oxygen incorporation in  $Sb_2S_3$  thin films has also been obtained from XPS measurements. Typically, during XPS studies, argon ion bombardment on the sample is carried out to remove traces of oxygen adsorbed from the environment, and as a result, the signature of oxygen can only be obtained if it is incorporated in the bulk of the semiconductor.<sup>43</sup> Interestingly, in the XPS spectra of  $Sb_2S_3$  films with UVO treatment for different lengths of time, the first signature of oxygen could be detected after 15 min of UVO exposure in the form of O 1s peak at a binding energy of 530.9 eV (shown in Figure S3 in the [Supporting Information](#)).

Optical absorption spectra of the vacancy-tailored  $Sb_2S_3$  films having identical thicknesses ( $\sim 110$  nm) were recorded in the UV–vis–near-IR region (Figure 4c); their corresponding Tauc plots have been placed in the inset of the figure. All of the spectra showed a strong absorbance in the visible region; absorbance intensified further with increased sulfur content in the film. Since, in our sequential deposition approach, sulfuration of the antimony precursor is done by  $H_2S$  gas produced by the sulfur precursor thiourea, a lesser amount of thiourea in sulfur-deficient compositions (S/Sb, 0.6 and 0.8) implies an incomplete conversion; a weaker absorbance was hence recorded. With increasing content of thiourea in the precursors, a better conversion was achieved and a higher absorbance was observed in turn. A closer inspection of the spectra in addition showed the presence of a tail extending to the longer wavelength region for sulfur-rich compounds, indicating a reduction of bandgap. The respective Tauc plots (inset of Figure 4c) clearly evidenced bandgap narrowing with increasing sulfur content in the films. In  $Sb_2S_3$ , since both of the band edges are formed by a primary contribution of antimony and sulfur atomic orbitals, its bandgap depends significantly on the Sb–S orbital overlaps, which would vary with a change in the precursor stoichiometry. The optical bandgap of the binary chalcogenide hence becomes dependent on precursor stoichiometry.

Interestingly, the longer wavelength region of the absorption spectra showed the presence of an apparent background absorbance which might have originated from a high surface roughness and thereby scattering of low-energy illumination.<sup>44</sup> It should be noted that, due to a high extinction coefficient of

the material, it is extremely difficult to rule out the presence of any impurities, such as phase residues, solely from optical absorption spectroscopy.

**Band Edges of  $Sb_2S_3$  Films from Scanning Tunneling Spectroscopy.** To study the influence of precursor stoichiometry on the band edges of  $Sb_2S_3$ , we recorded  $dI/dV$  spectra of the semiconductors that in turn provided their energy-dependent density of states (DOS). The DOS spectra provided energies of valence band (VB) and conduction band (CB) of the material in the form of a first peak in either sides of the Fermi energy which was aligned at 0 V. With bias being applied to the tip, the first peak at a positive tip voltage implied withdrawal of electrons from the semiconductor and hence denoted the VB edge of the semiconductor; similarly, the first peak at a negative voltage implied injection of electrons to the CB edge of the material. Since, trap states present within the bandgap also take part in the tunneling process, their signature typically appears nearer to the Fermi energy as compared to the true band edges.<sup>45</sup>

In Figure 5a we have presented a typical  $dI/dV$  spectrum of a  $Sb_2S_3$  film formed with stoichiometrically balanced precursors (S/S, 1.0); spectra of films formed with other stoichiometries have been placed in Figure S4 in the [Supporting Information](#). To compensate for the localized nature of STS measurements, we have recorded  $dI/dV$  spectra at many different locations on each thin film. From each spectrum, we have identified CB and VB edges and summed the energies to form a histogram (insets of Figure 5a and Figure S4 in the [Supporting Information](#)). As evidenced from the  $dI/dV$  spectrum and histogram thereof, the CB edge of the pristine  $Sb_2S_3$  appeared closer to 0 V (Fermi energy) as compared to the VB, inferring an n-type nature of the semiconductor. The measurements have also yielded a transport gap of 1.78 eV, which is a little wider than the optical gap with the energy difference being attributed to the exciton binding energy of the semiconductor. The histogram of the band edges showed that both of the energies have a symmetric distribution. The distribution and a non-intrinsic semiconductor nature observed in pristine  $Sb_2S_3$  films can typically be attributed to the presence of defects or disordered states. It can be suggested that exponentially decaying states were present in the gap (band tails). Such states were speculated to arise mainly from sulfur vacancies which are n-type or donor in nature.<sup>37</sup>

$dI/dV$  characteristics of the vacancy-tuned  $Sb_2S_3$  films showed that with increasing sulfur content from a sulfur-deficient composition (S/Sb, 0.6), the transport gap of  $Sb_2S_3$



widened until the relative sulfur content in the semiconductor reached a stoichiometrically balanced condition (S/Sb, 1.0). Such a blue shift in the transport gap originated due to a shift of the CB edge away from the Fermi energy, while the VB edge remained mostly unaffected under such a variation. In an antimony-rich growth condition, the defect formation is dominated by sulfur vacancies ( $S_V$ ) which are typically formed within the bandgap of the material and near the conduction band leading to a strong n-type electronic conductivity in the semiconductor.<sup>37</sup> Since such midgap defect states also contribute to the tunneling current, the transport gap in STS measurements hence appeared to be narrower than the optical bandgap. With increasing sulfur content in the film, the sulfur vacancies become passivated, thereby widening of the transport gap was recorded. With further increment in sulfur content (S/Sb, 1.2 and 1.4), the bandgap of  $Sb_2S_3$  was found to decrease. Under sulfur abundance, sulfur antisite defects ( $S_{Sb}$ ) dominated, and since such vacancies form also within the bandgap, the transport gap of  $Sb_2S_3$  under a sulfur-rich condition decreased.<sup>37</sup>

Such a change in the nature and position of defect states influenced the type of electronic conductivity in  $Sb_2S_3$  (Figure 5b). Since the intrinsic n-type nature in  $Sb_2S_3$  films originates due to formation of deep-level sulfur vacancies, a sulfur-deficient composition naturally led to the formation of more such vacancies, and thereby a stronger n-type nature was evidenced. In a sulfur-rich condition, on the other hand, passivation of sulfur vacancies and creation of sulfur-antisite defects are expected to take place, thereby compensating the n-type nature.<sup>36</sup> Hence, by varying the precursor stoichiometry, while forming  $Sb_2S_3$  thin films through a sequential-deposition approach, it is possible to tune the type of electronic conductivity of the semiconductor from strong n-type to a mild n-type nature. Energy and fwhm of the band edges and transport gap obtained thereof for different  $Sb_2S_3$  thin films have been collated in Table 1.

**Table 1. Position and FWHM of the Band Edges and Transport Gap Obtained Thereof for Different Relative Sulfur Content in  $Sb_2S_3$  Thin Films**

S/Sb ratio in the precursor	CB with respect to $E_F$		VB with respect to $E_F$		transport gap (eV)	optical bandgap (eV)
	energy (eV)	fwhm (eV)	energy (eV)	fwhm (eV)		
0.6	-0.32	0.60	1.12	0.26	1.43	1.83
0.8	-0.54	0.39	1.07	0.27	1.61	1.76
1.0	-0.77	0.26	1.01	0.27	1.78	1.67
1.2	-0.72	0.32	1.02	0.26	1.74	1.49
1.4	-0.67	0.33	1.02	0.22	1.69	1.37

DOS and histogram of band edges provided further information apart from the VB and CB energies. The histograms could be seen to be distributed over the energy scale due to defect or disordered states. The energy distributions were as such symmetric and Gaussian in nature, and the fwhm of the distribution can be considered to be a measure of defect or disordered states. Interestingly, after tuning the sulfur vacancies, the fwhm of only the CB edge could be seen to be narrowed down, leaving the fwhm of VB mostly unaffected (Table 1). Such a phenomenon can be explained by considering the orbitals involved in the formation

of CB and VB edges of  $Sb_2S_3$ . The CB edge in  $Sb_2S_3$  is known to be formed with antibonding Sb 5p and S 3p states, whereas the VB edge is comprised of bonding Sb 5p, Sb 5s, and S 3p states. Due to the antibonding nature of orbitals in forming the CB edge, its energy has a dominant contribution to the bandgap of  $Sb_2S_3$ <sup>46</sup> and therefore, while the sulfur content was varied in the precursors in forming the films, a shift of the CB edge was more predominant than that of the VB one. The STS results hence deliberate on the change in two band edges along with the transport gap of the material formed under different precursor stoichiometries.

We also studied the influence of UVO treatment on the band edges of  $Sb_2S_3$  thin films (Figure S5a–d in the Supporting Information). Since such a treatment suppressed sulfur vacancies in the semiconductor, the treatment in turn modulated the band edges and transport gap of the binary chalcogenide (Table S3 in the Supporting Information). Typically, due to the presence of sulfur vacancies, stoichiometric  $Sb_2S_3$  shows an n-type conductivity which has been evidenced from the STS measurements. Upon suppression of the sulfur vacancies through UVO treatment, the VB edge appeared closer to 0 V (Fermi energy) as compared to the CB edge, inferring a gradual change in the type of conductivity to a mild p-type (Figure S5e in the Supporting Information). The STS studies hence infer that vacancy engineering in  $Sb_2S_3$  thin films is an effective route in lowering its bandgap. It should be noted here that vacancy-engineered modification in the bandgap and also the type of conductivity have recently been reported to be an effective route in modulating band edges of binary chalcogenides, making them suitable in efficient solar cell applications.<sup>40</sup>

**Surface Morphology of Vacancy-Tailored  $Sb_2S_3$  Thin Films.** Apart from the bandgap, morphology of the absorber layer has a governing role in the performance of planar heterojunction solar cells.<sup>47</sup> A tendency of rapid and uncontrollable crystallization during film formation often leads to a rough and inhomogeneous surface morphology affecting the device performance adversely.<sup>48</sup> Typically, the morphology of metal chalcogenides has been reported to be affected by a change in precursor stoichiometry and also under a prolonged UVO treatment.<sup>49</sup> We therefore recorded AFM images and estimated the RMS roughness of such films to study their surface morphology. In Figure S6a in the Supporting Information, we have presented AFM topographies of  $Sb_2S_3$  thin films formed with different precursor stoichiometries; we have also studied the effect of UVO treatment on  $Sb_2S_3$  thin films formed with stoichiometrically balanced precursors (Figure S6b in the Supporting Information). RMS roughness of the films was estimated from the morphologies using routine software. In Figure 6, we have plotted the roughness alongside the optical bandgap for  $Sb_2S_3$  thin films formed with different precursor stoichiometries and also upon UVO treatment. Morphology of the films could be seen to be affected in sulfur-rich conditions. Such a decline in film morphology under highly sulfur-rich conditions can be ascribed to the presence of a large amount of byproducts (including  $NH_4SCN$ ,  $NH_3$ , and  $HNCS$ ) in the  $Sb_2S_3$  film that originates from an excess amount of thiourea used during film fabrication.<sup>3</sup> Since  $Sb_2S_3$  decomposes in the presence of alkaline materials; existence of  $NH_3$  affects the film morphology under sulfur-rich conditions. A low sulfur content, on the other hand, may help in maintaining an improved film morphology at the cost of incomplete conversion of the

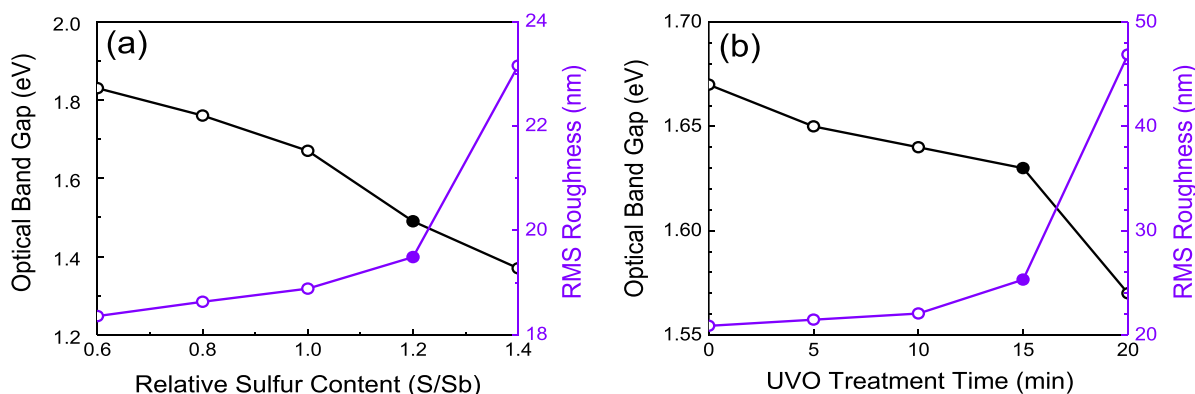


**Figure 6.** Optimization of (a) precursor stoichiometry and (b) UVO treatment time in  $\text{Sb}_2\text{S}_3$  thin films on the basis of optical bandgap and surface roughness.

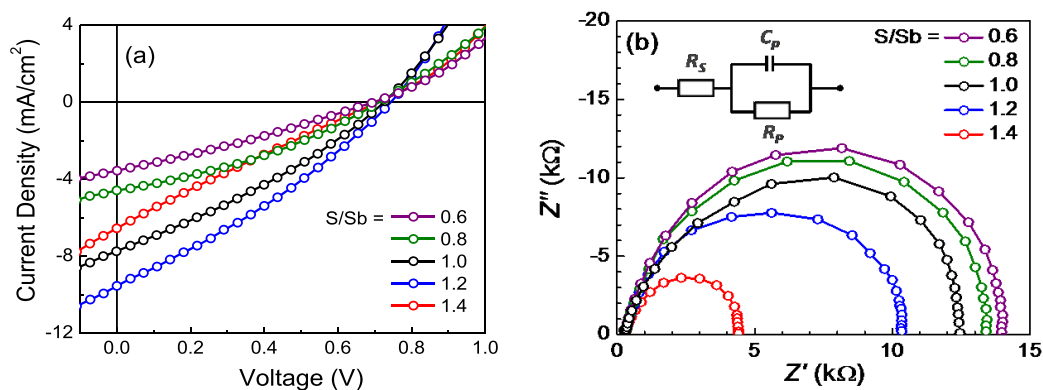


**Figure 7.** (a) Current–voltage characteristics and (b) Nyquist plots of  $\text{Cu:NiO/Sb}_2\text{S}_3/\text{PCBM}$  heterojunctions with different S/Sb ratios under 1 sun illumination. Electrical analogue of the device is shown in the inset of panel b.

**Table 2. Photovoltaic Parameters and Series and Shunt Resistances of  $\text{Cu:NiO/Sb}_2\text{S}_3/\text{PCBM}$  Heterojunctions with Different S/Sb Ratio under 1 Sun Illumination<sup>a</sup>**

S/Sb ratio in the precursor	$J_{\text{SC}}$ ( $\text{mA}/\text{cm}^2$ )	$V_{\text{OC}}$ (V)	fill factor	PCE (%)	$R_{\text{S}}$ ( $\Omega$ )	$R_{\text{P}}$ ( $\text{k}\Omega$ )
0.6	3.55 ( $\pm 0.31$ )	0.70 ( $\pm 0.09$ )	0.28 ( $\pm 0.05$ )	0.69 ( $\pm 0.19$ )	303.8 ( $\pm 0.2$ )	13.9 ( $\pm 0.1$ )
0.8	4.59 ( $\pm 0.36$ )	0.71 ( $\pm 0.11$ )	0.34 ( $\pm 0.06$ )	1.10 ( $\pm 0.21$ )	303.5 ( $\pm 0.1$ )	13.4 ( $\pm 0.2$ )
1.0	7.78 ( $\pm 0.24$ )	0.73 ( $\pm 0.08$ )	0.38 ( $\pm 0.04$ )	2.13 ( $\pm 0.18$ )	302.5 ( $\pm 0.1$ )	12.4 ( $\pm 0.1$ )
1.2	9.61 ( $\pm 0.21$ )	0.74 ( $\pm 0.08$ )	0.40 ( $\pm 0.04$ )	2.84 ( $\pm 0.11$ )	305.7 ( $\pm 0.2$ )	10.3 ( $\pm 0.1$ )
1.4	6.50 ( $\pm 0.30$ )	0.71 ( $\pm 0.10$ )	0.32 ( $\pm 0.05$ )	1.48 ( $\pm 0.16$ )	308.9 ( $\pm 0.2$ )	4.4 ( $\pm 0.1$ )

<sup>a</sup>The values within the parentheses indicate respective standard deviations.

precursors to binary chalcogenides. As can be seen from Figure S6a in the Supporting Information, morphology of the vacancy-tailored  $\text{Sb}_2\text{S}_3$  films degraded in the presence of a high sulfur content (S/Sb, 1.4) in the precursor. The results hence infer that a balance between bandgap and surface morphology is achieved at a relative sulfur content (S/Sb) of 1.2.

Elemental composition of the vacancy-tailored  $\text{Sb}_2\text{S}_3$  thin films was analyzed through EDX measurements. The atomic percent of the elements obtained from such analysis has been placed in Table S1 in the Supporting Information. The analysis evidenced a variation in the composition of the films in accordance to the precursor stoichiometry that in turn supported the degree of control this sequential deposition approach offers.

**Photovoltaic Characteristics.** We then proceeded to study the influence of sulfur-vacancy modification on photovoltaic properties of  $\text{Sb}_2\text{S}_3$  thin films in planar heterojunction

structures having an inverted (p–i–n) geometry. As stated earlier, photovoltaic properties of  $\text{Sb}_2\text{S}_3$  thin films have mostly been studied in a regular (n–i–p) sensitized device structure.<sup>14,20,29</sup> The not-so-impressive photovoltaic performance of  $\text{Sb}_2\text{S}_3$  in such efforts can however be attributed to a high resistivity of the binary chalcogenide that originates from both surface defects and bulk defects of  $\text{Sb}_2\text{S}_3$  thin films.<sup>7</sup> Although, in contrast, devices based on inverted planar heterojunction structures have several advantages, influence of such intrinsic defects in dictating the device performance is more crucial.<sup>17</sup> Hence, we aimed to tune these intrinsic defects in  $\text{Sb}_2\text{S}_3$  thin films by varying the stoichiometry (S/Sb ratio) and studied the respective device performance.

In Figure 7a, we show current–voltage characteristics of vacancy-engineered  $\text{Cu:NiO/Sb}_2\text{S}_3/\text{PCBM}$  planar heterojunction devices under 1 sun illumination; photovoltaic parameters of the respective devices have been presented in Table 2. It should be stated here that we selected  $\text{Cu:NiO}$  as a hole-

selective layer owing to its wide optical bandgap and chemical inertness under ambient condition along with superior conductivity and hole mobility. A comparison of device performance based on such vacancy-tailored  $\text{Sb}_2\text{S}_3$  thin films showed an improvement of all of the photovoltaic parameters upon passivation of sulfur vacancies to a certain limit beyond which it was counterbalanced by a deterioration of film morphology. Due to a decrease in the optical bandgap of  $\text{Sb}_2\text{S}_3$  with vacancy passivation, the  $J_{\text{SC}}$  of the solar cells increased gradually to  $9.61 \text{ mA/cm}^2$  in a sulfur-rich stoichiometry (S/Sb, 1.2). Further increment in sulfur content adversely affected the  $J_{\text{SC}}$  owing to deterioration in the film morphology. The fill factor of the cells also showed evidence of improvement, i.e., a lesser carrier recombination in devices based on defect-passivated  $\text{Sb}_2\text{S}_3$  thin films.

However, the morphological degradation under a high sulfur-rich condition provided carrier recombination pathways and affected the fill factor in an adverse manner. It should be stated here that the  $J_{\text{SC}}$  and fill factor values recorded in our devices were low due to a high resistivity of  $\text{Sb}_2\text{S}_3$  thin films.  $V_{\text{OC}}$  of the cells, on the other hand, was not affected due to passivation of sulfur vacancies in  $\text{Sb}_2\text{S}_3$  thin films. Due to an optimized interface with Cu:NiO and PCBM, the  $\text{Sb}_2\text{S}_3$  layer maintained a type-II band alignment at both the interfaces for all S/Sb ratios leaving the  $V_{\text{OC}}$  of the cells mostly unaffected. It is worth mentioning here that  $V_{\text{OC}}$  in our devices has been higher than that in devices having different architectures and based on the material formed with other solution-processing methods.<sup>3,7,17</sup> Such an improvement can be attributed to the optimization of precursor stoichiometry leading to a balanced optical bandgap and surface morphology of the  $\text{Sb}_2\text{S}_3$  thin films along with band alignment with the carrier-selective contacts. Due to such changes in photovoltaic parameters, PCE of the cells also showed a variation with stoichiometry of the films. The PCE of the cell was optimized to 2.84% at an S/Sb ratio of 1.2; i.e., under a slightly sulfur-rich condition, the  $\text{Sb}_2\text{S}_3$  films showed a better photovoltaic performance. It should be mentioned here that, in a particular batch of device fabrication with an S/Sb ratio of 1.2, PCE of the cells reached 3.02% with a high  $V_{\text{OC}}$  of 0.8 V (Figure S7a in the Supporting Information). The PCE value obtained in our planar heterojunctions is comparable with the reported results on  $\text{Sb}_2\text{S}_3$  solar cells based on CBD grown thin films and/or a sensitized device architecture.<sup>7</sup> To check the reproducibility of the device performance, we have fabricated devices with optimized precursor stoichiometry in batches (at least 20 devices) and characterized them under an identical condition. As can be seen from the histogram of device PCE (Figure S7b in the Supporting Information), the devices routinely yielded a PCE of around 2.8%.

On the other hand, performance of heterojunctions based on UVO-treated stoichiometric  $\text{Sb}_2\text{S}_3$  (S/Sb, 1.0) thin films did not show any change until 10 min of treatment. The parameters started to deteriorate afterward, and the respective  $I$ - $V$  characteristics under 1 sun illumination have been placed in Figure S8 in the Supporting Information. In the same plot, we have placed the  $I$ - $V$  characteristics of an untreated device, and a comparison of the photovoltaic parameters have been presented in Table S4 in the Supporting Information. Clearly, performance of the solar cells degraded in all respects after such an UVO treatment, which can be ascribed to the presence of additional oxide-based impurities in the material. Therefore, although such UVO treatment is an effective approach to

suppress sulfur vacancies in chalcogenides, it may not be a useful route in  $\text{Sb}_2\text{S}_3$  as a mode to improve the solar cell performance.

To obtain further insights on charge-transfer processes in Cu:NiO/ $\text{Sb}_2\text{S}_3$ /PCBM heterojunctions with different S/Sb ratios, we have recorded impedance spectra of the respective solar cells under an illumination condition; Nyquist plots for the devices have been presented in Figure 7b. The plots are dominated by a large distinct semicircle in the low-frequency region which is typically reported for a pn-junction. Such single-arc impedance spectra in the low-frequency region are dictated by charge accumulation and recombination within the active layer and can be fitted to an electrical analogue containing a parallel combination of capacitor-resistor network ( $C_p$ - $R_p$ ) connected in series to another resistor ( $R_s$ ).<sup>50</sup> The parallel and series resistances are typically considered to provide an estimate of layer resistance and interfacial resistance of the device, respectively. When the Nyquist plots were analyzed, a high layer resistance was recorded for the device based on a sulfur-deficient  $\text{Sb}_2\text{S}_3$  layer (S/Sb, 0.6), and as a result a poor device performance was recorded. With increasing sulfur content (S/Sb ratio), the diameter of the arc started to decrease resulting in a reduction in layer resistance ( $R_p$ ), which can be due to formation of shunting pathways through the pinholes present in the film having a poor surface morphology. At a high sulfur content (S/Sb, 1.4) a very low layer resistance was recorded that signifies a high degree of carrier recombination in the respective device. The interfacial resistance ( $R_s$ ), on the other hand, being a measure of the contact resistances in the device, remained mostly unaltered under variation in stoichiometry. The results of impedance spectroscopy were hence in concurrence with the morphological studies and device performance of  $\text{Sb}_2\text{S}_3$  thin films.

To ensure the correctness of our device performance and know the spectral distribution of photocurrent (at 0 V), we have recorded an external quantum efficiency (EQE) spectrum of our champion device (Figure 8). The evolution of the

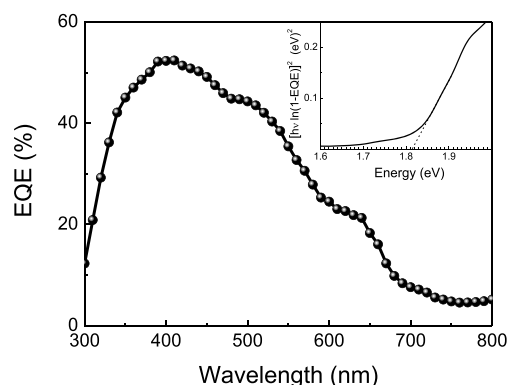


**Figure 8.** EQE spectrum of Cu:NiO/ $\text{Sb}_2\text{S}_3$ /PCBM heterojunction with a S/Sb ratio of 1.2. In the inset, a plot of  $[\hbar\nu \ln(1 - \text{EQE})]^2$  versus  $\hbar\nu$  has been placed to determine the optical bandgap.

photocurrent generation efficiency was similar to the analogous optical absorption spectrum of the respective  $\text{Sb}_2\text{S}_3$  thin film, indicating that excitons generated in the chalcogenide layer primarily contributed to the resultant photocurrent. The photocurrent generation in the champion device was comparable to that of the reported sensitized  $\text{Sb}_2\text{S}_3$  solar cells based on CBD-grown  $\text{Sb}_2\text{S}_3$  thin films. This proves the



effectiveness of using our sequential deposition route for the fabrication of  $\text{Sb}_2\text{S}_3$  thin films for solar cell applications. The  $J_{\text{SC}}$  value was estimated by integrating the overlap of the EQE spectrum with the AM1.5G solar photon flux; the value obtained from EQE spectrum was  $8.68 \text{ mA/cm}^2$ , which was quite close to the  $J_{\text{SC}}$  obtained from the  $I$ - $V$  measurement ( $9.61 \text{ mA/cm}^2$ ). We have more overestimated the optical bandgap from the EQE spectrum as absorption coefficient at a wavelength has a close relationship with the corresponding EQE value. In the inset of Figure 8, we have placed the  $[\ln(1 - \text{EQE})]^2$  vs energy plot; the intercept of the extrapolated linear region with the energy axis provided a bandgap of 1.81 eV for the  $\text{Sb}_2\text{S}_3$  film with S/Sb of 1.2. The value was in fair agreement with the optical bandgap (1.49 eV) estimated from the corresponding optical absorption spectrum. The little wider value of the bandgap obtained from the EQE spectrum can be due to possible light absorption in other active layers of the device as well.

## CONCLUSIONS

In conclusion, we have formed  $\text{Sb}_2\text{S}_3$  thin films through a sequential-deposition technique. As opposed to the traditional chemical bath deposition method, this approach allowed possibilities of sulfur-vacancy passivation through a variation in precursor stoichiometry. Sulfur-deficient precursors generated donor-like sulfur vacancies; sulfur-rich precursors passivated the vacancies and in turn formed sulfur antisite defects in the semiconductor. Optical bandgap of  $\text{Sb}_2\text{S}_3$  thin films could hence be seen to narrow down with increasing sulfur content in the precursor. From the variation of transport gap as obtained from STS studies and thereby DOS spectra, movement of the conduction band (CB) edge has been found to be responsible for the change in bandgap. Due to antibonding nature of the antimony-sulfur orbital overlap in forming the CB edge, this particular band has responded majorly under a variation in the precursor stoichiometry while forming  $\text{Sb}_2\text{S}_3$  thin films. The film-deposition approach in addition offered a control over film morphology. Morphological studies revealed that the decrease in bandgap occurred at an expense of film quality; films with an excess sulfur content showed a high surface roughness. Hence, an optimization of optical bandgap and surface morphology was estimated showing a balance between the two parameters at an S/Sb ratio of 1.2. Interestingly, the photovoltaic parameters of Cu:NiO/ $\text{Sb}_2\text{S}_3$ /PCBM planar heterojunctions excelled at the predicted stoichiometry yielding a power conversion efficiency of 3.02% along with a significantly high open-circuit voltage of 0.8 V.

## ASSOCIATED CONTENT

### Supporting Information

The Supporting Information is available free of charge at <https://pubs.acs.org/doi/10.1021/acsaem.9b01951>.

SEM EDX spectrum (Figure S1); atomic percentage of elements (Table S1); grain sizes (Table S2); optical absorption spectra and respective Tauc plots (Table S3); AFM topographies and  $I$ - $V$  characteristics (Figures S6-S8); photovoltaic parameters of heterojunctions (Table S4) (PDF)

## AUTHOR INFORMATION

### Corresponding Author

\*Tel.: +91-33-24734971. Fax: +91-33-24732805. E-mail: [sspajp@iacs.res.in](mailto:sspajp@iacs.res.in).

### ORCID

Amlan J. Pal: 0000-0002-7651-9779

### Notes

The authors declare no competing financial interest.

## ACKNOWLEDGMENTS

A.J.P. acknowledges the JC Bose National Fellowship (Grant SB/S2/JCB-001/2016) of SERB. A.M. and S.C. acknowledge the DST INSPIRE Fellowship (Grants IF 170922 and IF 140158, respectively).

## REFERENCES

- (1) Lewis, N. S. Toward Cost-Effective Solar Energy Use. *Science* **2007**, *315*, 798–801.
- (2) Giraldo, S.; Jehl, Z.; Placidi, M.; Izquierdo-Roca, V.; Perez-Rodriguez, A.; Saucedo, E. Progress and Perspectives of Thin Film Kesterite Photovoltaic Technology: A Critical Review. *Adv. Mater.* **2019**, *31*, 1806692.
- (3) Zhang, L. J.; Wu, C. Y.; Liu, W. F.; Yang, S. F.; Wang, M. T.; Chen, T.; Zhu, C. F. Sequential Deposition Route to Efficient  $\text{Sb}_2\text{S}_3$  Solar Cells. *J. Mater. Chem. A* **2018**, *6*, 21320–21326.
- (4) Im, S. H.; Lim, C. S.; Chang, J. A.; Lee, Y. H.; Maiti, N.; Kim, H. J.; Nazeeruddin, M. K.; Gratzel, M.; Seok, S. I. Toward Interaction of Sensitizer and Functional Moieties in Hole-Transporting Materials for Efficient Semiconductor-Sensitized Solar Cells. *Nano Lett.* **2011**, *11*, 4789–4793.
- (5) Ma, J. M.; Duan, X. C.; Lian, J. B.; Kim, T.; Peng, P.; Liu, X. D.; Liu, Z. F.; Li, H. B.; Zheng, W. J.  $\text{Sb}_2\text{S}_3$  with Various Nanostructures: Controllable Synthesis, Formation Mechanism, and Electrochemical Performance toward Lithium Storage. *Chem. - Eur. J.* **2010**, *16*, 13210–13217.
- (6) Tang, R. F.; Wang, X. M.; Jiang, C. H.; Li, S.; Jiang, G. S.; Yang, S. F.; Zhu, C. F.; Chen, T. Vacuum Assisted Solution Processing for Highly Efficient  $\text{Sb}_2\text{S}_3$  Solar Cells. *J. Mater. Chem. A* **2018**, *6*, 16322–16327.
- (7) Kondrotas, R.; Chen, C.; Tang, J.  $\text{Sb}_2\text{S}_3$  Solar Cells. *Joule* **2018**, *2*, 857–878.
- (8) Nezu, S.; Larramona, G.; Chone, C.; Jacob, A.; Delatouche, B.; Pere, D.; Moisan, C. Light Soaking and Gas Effect on Nanocrystalline  $\text{TiO}_2/\text{Sb}_2\text{S}_3/\text{CuSCN}$  Photovoltaic Cells following Extremely Thin Absorber Concept. *J. Phys. Chem. C* **2010**, *114*, 6854–6859.
- (9) Zimmermann, E.; Pfadler, T.; Kalb, J.; Dorman, J. A.; Sommer, D.; Hahn, G.; Weickert, J.; Schmidt-Mende, L. Toward High-Efficiency Solution-Processed Planar Heterojunction  $\text{Sb}_2\text{S}_3$  Solar Cells. *Adv. Sci.* **2015**, *2*, 1500059.
- (10) Boix, P. P.; Lee, Y. H.; Fabregat-Santiago, F.; Im, S. H.; Mora-Sero, I.; Bisquert, J.; Seok, S. I. From Flat to Nanostructured Photovoltaics: Balance between Thickness of the Absorber and Charge Screening in Sensitized Solar Cells. *ACS Nano* **2012**, *6*, 873–880.
- (11) Wedemeyer, H.; Michels, J.; Chmielowski, R.; Bourdais, S.; Muto, T.; Sugiura, M.; Dennler, G.; Bachmann, J. Nanocrystalline Solar Cells with an Antimony Sulfide Solid Absorber by Atomic Layer Deposition. *Energy Environ. Sci.* **2013**, *6*, 67–71.
- (12) Moon, S. J.; Itzhaik, Y.; Yum, J. H.; Zakeeruddin, S. M.; Hodes, G.; Gratzel, M.  $\text{Sb}_2\text{S}_3$ -Based Mesoscopic Solar Cell using an Organic Hole Conductor. *J. Phys. Chem. Lett.* **2010**, *1*, 1524–1527.
- (13) Darga, A.; Mencaraglia, D.; Longeaud, C.; Savenije, T. J.; O'Regan, B.; Bourdais, S.; Muto, T.; Delatouche, B.; Dennler, G. On Charge Carrier Recombination in  $\text{Sb}_2\text{S}_3$  and Its Implication for the Performance of Solar Cells. *J. Phys. Chem. C* **2013**, *117*, 20525–20530.

- (14) Choi, Y. C.; Lee, D. U.; Noh, J. H.; Kim, E. K.; Seok, S. I. Highly Improved  $\text{Sb}_2\text{S}_3$  Sensitized-Inorganic-Organic Heterojunction Solar Cells and Quantification of Traps by Deep-Level Transient Spectroscopy. *Adv. Funct. Mater.* **2014**, *24*, 3587–3592.
- (15) Im, S. H.; Kim, H. J.; Rhee, J. H.; Lim, C. S.; Seok, S. I. Performance Improvement of  $\text{Sb}_2\text{S}_3$ -Sensitized Solar Cell by Introducing Hole Buffer Layer in Cobalt Complex Electrolyte. *Energy Environ. Sci.* **2011**, *4*, 2799–2802.
- (16) Jin, X.; Yuan, Y.; Jiang, C. H.; Ju, H. X.; Jiang, G. S.; Liu, W. F.; Zhu, C. F.; Chen, T. Solution Processed  $\text{NiO}_x$  Hole-Transporting Material for All-Inorganic Planar Heterojunction  $\text{Sb}_2\text{S}_3$  Solar Cells. *Sol. Energy Mater. Sol. Cells* **2018**, *185*, 542–548.
- (17) Tang, R. F.; Wang, X. M.; Jiang, C. H.; Li, S.; Liu, W. F.; Ju, H. X.; Yang, S. F.; Zhu, C. F.; Chen, T. *n*-Type Doping of  $\text{Sb}_2\text{S}_3$  Light-Harvesting Films Enabling High-Efficiency Planar Heterojunction Solar Cells. *ACS Appl. Mater. Interfaces* **2018**, *10*, 30314–30321.
- (18) Messina, S.; Nair, M. T. S.; Nair, P. K. Solar Cells with  $\text{Sb}_2\text{S}_3$  Absorber Films. *Thin Solid Films* **2009**, *517*, 2503–2507.
- (19) Maiti, N.; Im, S. H.; Lim, C. S.; Seok, S. I. A Chemical Precursor for Depositing  $\text{Sb}_2\text{S}_3$  onto Mesoporous  $\text{TiO}_2$  Layers in Nonaqueous Media and its Application to Solar Cells. *Dalton Trans.* **2012**, *41*, 11569–11572.
- (20) Choi, Y. C.; Seok, S. I. Efficient  $\text{Sb}_2\text{S}_3$ -Sensitized Solar Cells Via Single-Step Deposition of  $\text{Sb}_2\text{S}_3$  Using S/Sb-Ratio-Controlled  $\text{SbCl}_3$ -Thiourea Complex Solution. *Adv. Funct. Mater.* **2015**, *25*, 2892–2898.
- (21) Zheng, L.; Jiang, K. J.; Huang, J. H.; Zhang, Y.; Bao, B.; Zhou, X. Q.; Wang, H. J.; Guan, B.; Yang, L. M.; Song, Y. L. Solid-State Nanocrystalline Solar Cells with an Antimony Sulfide Absorber Deposited by an in situ Solid-Gas Reaction. *J. Mater. Chem. A* **2017**, *5*, 4791–4796.
- (22) Lei, H. W.; Yang, G.; Guo, Y. X.; Xiong, L. B.; Qin, P. L.; Dai, X.; Zheng, X. L.; Ke, W. J.; Tao, H.; Chen, Z.; Li, B. R.; Fang, G. J. Efficient Planar  $\text{Sb}_2\text{S}_3$  Solar Cells Using a Low-Temperature Solution-Processed Tin Oxide Electron Conductor. *Phys. Chem. Chem. Phys.* **2016**, *18*, 16436–16443.
- (23) Osorio Mayon, Y.; White, T. P.; Wang, R. P.; Yang, Z. Y.; Catchpole, K. R. Evaporated and Solution Deposited Planar  $\text{Sb}_2\text{S}_3$  Solar Cells: A Comparison and its Significance. *Phys. Status Solidi A* **2016**, *213*, 108–113.
- (24) Kim, D. H.; Lee, S. J.; Park, M. S.; Kang, J. K.; Heo, J. H.; Im, S. H.; Sung, S. J. Highly Reproducible Planar  $\text{Sb}_2\text{S}_3$ -Sensitized Solar Cells based on Atomic Layer Deposition. *Nanoscale* **2014**, *6*, 14549–14554.
- (25) Yuan, S. J.; Deng, H.; Yang, X. K.; Hu, C.; Khan, J.; Ye, W. N.; Tang, J.; Song, H. S. Postsurface Selenization for High Performance  $\text{Sb}_2\text{S}_3$  Planar Thin Film Solar Cells. *ACS Photonics* **2017**, *4*, 2862–2870.
- (26) Cardenas, E.; Arato, A.; Perez-Tijerina, E.; Das Roy, T. K.; Castillo, G. A.; Krishnan, B. Carbon-Doped  $\text{Sb}_2\text{S}_3$  Thin Films: Structural, Optical and Electrical Properties. *Sol. Energy Mater. Sol. Cells* **2009**, *93*, 33–36.
- (27) Kim, K. H.; Takahashi, C.; Abe, Y.; Kawamura, M. Effects of Cu Doping on Nickel Oxide Thin Film Prepared by Sol-Gel Solution Process. *Optik* **2014**, *125*, 2899–2901.
- (28) Nair, P. K.; Nair, M. T. S.; García, V. M.; Arenas, O. L.; Peña, A. C. Y.; Ayala, I. T.; Gomezdaza, O.; Sánchez, A.; Campos, J.; Hu, H.; Suárez, R.; Rincón, M. E. Semiconductor Thin Films by Chemical Bath Deposition for Solar Energy Related Applications. *Sol. Energy Mater. Sol. Cells* **1998**, *52*, 313–344.
- (29) Xu, Y. F.; Chen, W. Y.; Hu, L. H.; Pan, X.; Yang, S. F.; Shen, Q.; Zhu, J. Template Deposition of  $\text{Sb}_2\text{S}_3$  for Solid-State Sensitized Solar Cells. *J. Alloys Compd.* **2019**, *784*, 947–953.
- (30) Escorcía-García, J.; Becerra, D.; Nair, M. T. S.; Nair, P. K. Heterojunction  $\text{CdS/Sb}_2\text{S}_3$  Solar Cells using Antimony Sulfide Thin Films Prepared by Thermal Evaporation. *Thin Solid Films* **2014**, *569*, 28–34.
- (31) Escorcía-García, J.; Domínguez-Díaz, M.; Hernández-Granados, A.; Martínez, H. Antimony Sulfide Thin Films Obtained by Chemical Bath Deposition using Tartaric Acid as Complexing Agent. *MRS Advances* **2018**, *3*, 3307–3313.
- (32) Vinayakumar, V.; Hernandez, C. R. O.; Shaji, S.; Avellaneda, D. A.; Martinez, J. A. A.; Krishnan, B. Effects of Rapid Thermal Processing on Chemically Deposited Antimony Sulfide Thin Films. *Mater. Sci. Semicond. Process.* **2018**, *80*, 9–17.
- (33) Wu, Y. L.; Assaud, L.; Krysch, C.; Capon, B.; Detavernier, C.; Santinacci, L.; Bachmann, J. Antimony Sulfide as a Light Absorber in Highly Ordered, Coaxial Nanocylindrical Arrays: Preparation and Integration into a Photovoltaic Device. *J. Mater. Chem. A* **2015**, *3*, 5971–5981.
- (34) Shaji, S.; Garcia, L. V.; Lored, S. L.; Krishnan, B.; Aguilar Martinez, J. A.; Das Roy, T. K.; Avellaneda, D. A. Antimony Sulfide Thin Films Prepared by Laser Assisted Chemical Bath Deposition. *Appl. Surf. Sci.* **2017**, *393*, 369–376.
- (35) Ornelas-Acosta, R. E.; Shaji, S.; Avellaneda, D.; Castillo, G. A.; Das Roy, T. K.; Krishnan, B. Thin Films of Copper Antimony Sulfide: A Photovoltaic Absorber Material. *Mater. Res. Bull.* **2015**, *61*, 215–225.
- (36) Guo, L.; Zhang, B.; Li, S.; Zhang, Q.; Buettner, M.; Li, L.; Qian, X.; Yan, F. Scalable and Efficient  $\text{Sb}_2\text{S}_3$  Thin-Film Solar Cells Fabricated by Close Space Sublimation. *APL Mater.* **2019**, *7*, No. 041105.
- (37) Tumelero, M. A.; Faccio, R.; Pasa, A. A. Unraveling the Native Conduction of Trichalcogenides and Its Ideal Band Alignment for New Photovoltaic Interfaces. *J. Phys. Chem. C* **2016**, *120*, 1390–1399.
- (38) Yin, Y. W.; Wu, C. Y.; Tang, R. F.; Jiang, C. H.; Jiang, G. S.; Liu, W. F.; Chen, T.; Zhu, C. F. Composition Engineering of  $\text{Sb}_2\text{S}_3$  Film Enabling High Performance Solar Cells. *Sci. Bull.* **2019**, *64*, 136–141.
- (39) Messina, S.; Nair, M. T. S.; Nair, P. K. Antimony Sulfide Thin Films in Chemically Deposited Thin Film Photovoltaic Cells. *Thin Solid Films* **2007**, *515*, 5777–5782.
- (40) Peng, B.; Yu, G. N.; Zhao, Y. W.; Xu, Q.; Xing, G. C.; Liu, X. F.; Fu, D. Y.; Liu, B.; Tan, J. R. S.; Tang, W.; Lu, H. P.; Xie, J. L.; Deng, L. J.; Sum, T. C.; Loh, K. P. Achieving Ultrafast Hole Transfer at the Monolayer  $\text{MoS}_2$  and  $\text{CH}_3\text{NH}_3\text{PbI}_3$  Perovskite Interface by Defect Engineering. *ACS Nano* **2016**, *10*, 6383–6391.
- (41) Frost, R. L.; Bahfenne, S.; Keffe, E. C. Raman Spectroscopic Study of the Mineral Gerstleyite  $\text{Na}_2(\text{Sb,As})_8\text{S}_{13}\cdot 2\text{H}_2\text{O}$  and Comparison with Some Heavy-Metal Sulfides. *J. Raman Spectrosc.* **2010**, *41*, 1779–1783.
- (42) Qi, L.; Wang, Y.; Shen, L.; Wu, Y. H. Chemisorption-Induced *n*-Doping of  $\text{MoS}_2$  by Oxygen. *Appl. Phys. Lett.* **2016**, *108*, No. 063103.
- (43) Kaufherr, N.; Lichtman, D. XPS Studies of the Effect of Argon Ion Bombardment on Standard Reference Material 470: Glass K-411. *Surf. Sci.* **1984**, *139*, 347–359.
- (44) Yang, D.; Jang, J. G.; Lim, J.; Lee, J. K.; Kim, S. H.; Hong, J. I. Correlations of Optical Absorption, Charge Trapping, and Surface Roughness of  $\text{TiO}_2$  Photoanode Layer Loaded with Neat Ag-NPs for Efficient Perovskite Solar Cells. *ACS Appl. Mater. Interfaces* **2016**, *8*, 21522–21530.
- (45) Dasgupta, U.; Bera, A.; Pal, A. J. Band Diagram of Heterojunction Solar Cells through Scanning Tunneling Spectroscopy. *ACS Energy Lett.* **2017**, *2*, 582–591.
- (46) Ben Nasr, T.; Maghraoui-Meherzi, H.; Ben Abdallah, H.; Bennaceur, R. Electronic Structure and Optical Properties of  $\text{Sb}_2\text{S}_3$  Crystal. *Phys. B* **2011**, *406*, 287–292.
- (47) Wang, K.; Cheng, J.; Yang, X.; Hu, R.; Fu, L. J.; Huang, J.; Yu, J. S.; Li, L. Enhanced Photovoltaic Properties in  $\text{Sb}_2\text{S}_3$  Planar Heterojunction Solar Cell with a Fast Selenylation Approach. *Nanoscale Res. Lett.* **2018**, *13*, 270.
- (48) Bae, S.; Han, S. J.; Shin, T. J.; Jo, W. H. Two Different Mechanisms of  $\text{CH}_3\text{NH}_3\text{PbI}_3$  Film Formation in One-Step Deposition and its Effect on Photovoltaic Properties of OPV-Type Perovskite Solar Cells. *J. Mater. Chem. A* **2015**, *3*, 23964–23972.

- (49) Ramirez, O.; Ramasamy, P.; Choi, Y. C.; Lee, J. S. Morphology Transformation of Chalcogenide Nanoparticles Triggered by Cation Exchange Reactions. *Chem. Mater.* **2019**, *31*, 268–276.
- (50) Bisquert, J. Theory of the Impedance of Electron Diffusion and Recombination in a Thin Layer. *J. Phys. Chem. B* **2002**, *106*, 325–333.

Supporting Information

# Sulfur-Vacancy Passivation in Solution-Processed $\text{Sb}_2\text{S}_3$ Thin-Films: Influence on Photovoltaic-Interfaces

*Abhishek Maiti, Soumyo Chatterjee, and Amlan J. Pal\**

School of Physical Sciences, Indian Association for the Cultivation of Science, Jadavpur, Kolkata  
700032, India

Corresponding Author

\*Tel.: +91-33-24734971. Fax: +91-33-24732805. E-mail: [sspajp@iacs.res.in](mailto:sspajp@iacs.res.in)

ORCID

Amlan J. Pal: 0000-0002-7651-9779





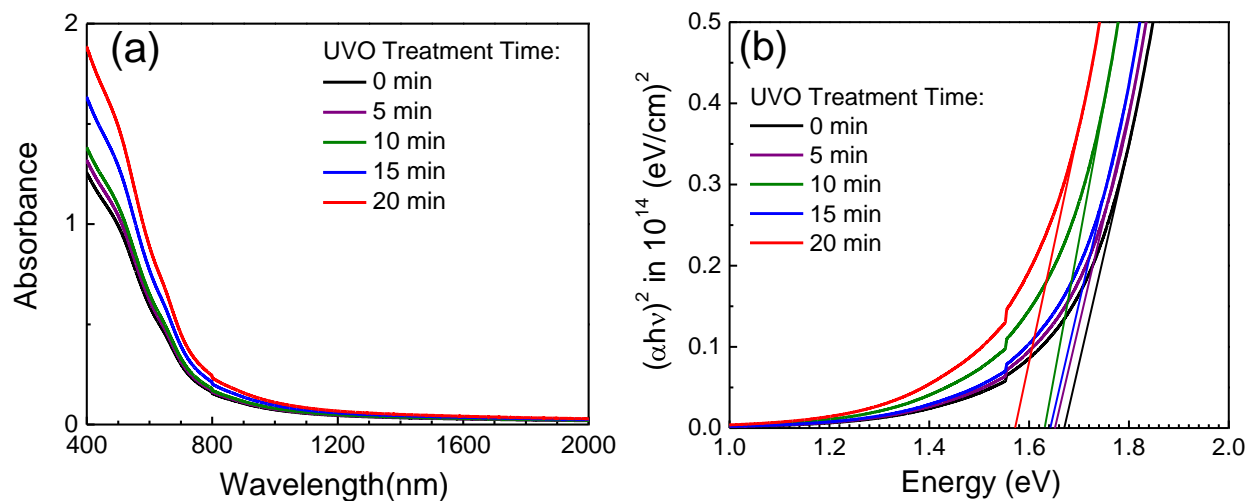


**Figure S2.** (a) Optical absorption spectra and (b) respective Tauc plots of a stoichiometric  $\text{Sb}_2\text{S}_3$  thin-film under different duration of UVO treatment.

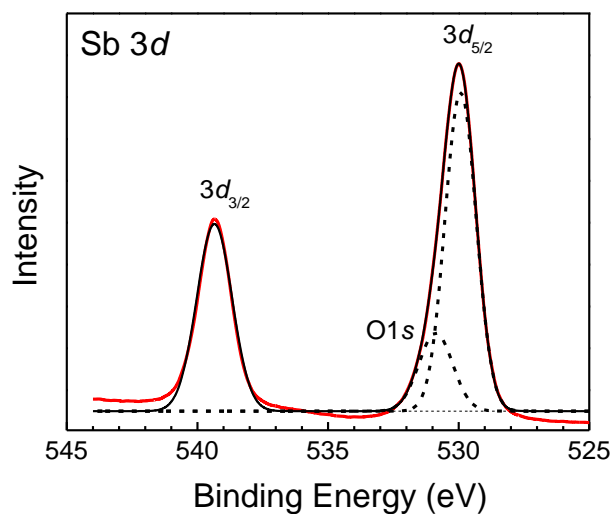


**Figure S3.** High-resolution XPS spectra of Sb 3d and O 1s states for a stoichiometric ( $\text{S/Sb} = 1.0$ )  $\text{Sb}_2\text{S}_3$  thin-film after 15 min of UVO treatment.

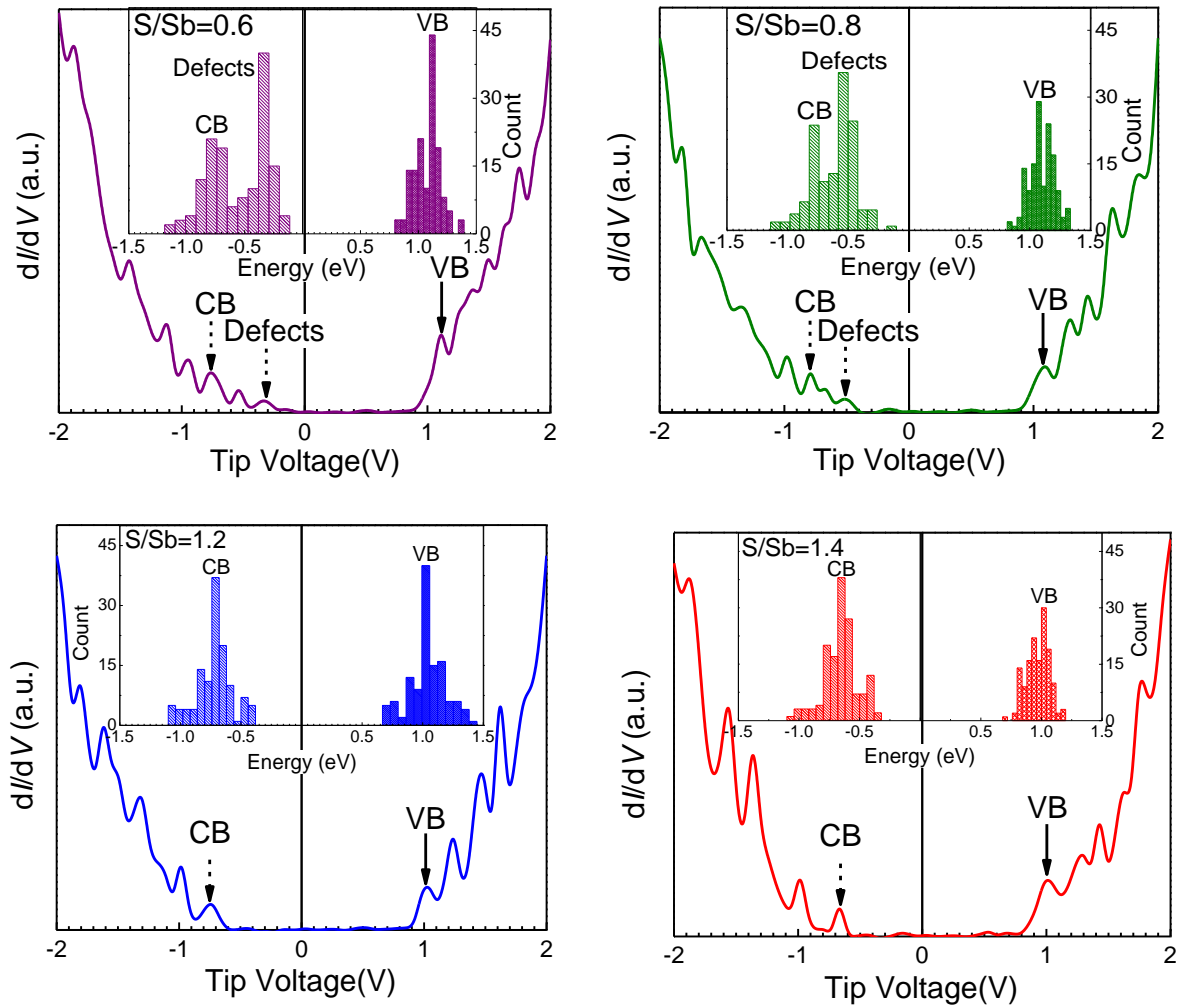


**Figure S4.**  $dI/dV$  spectra of  $Sb_2S_3$  thin-films having different S/Sb ratio as mentioned in legends. Histogram of CB and VB energies is shown in the inset of each figure.

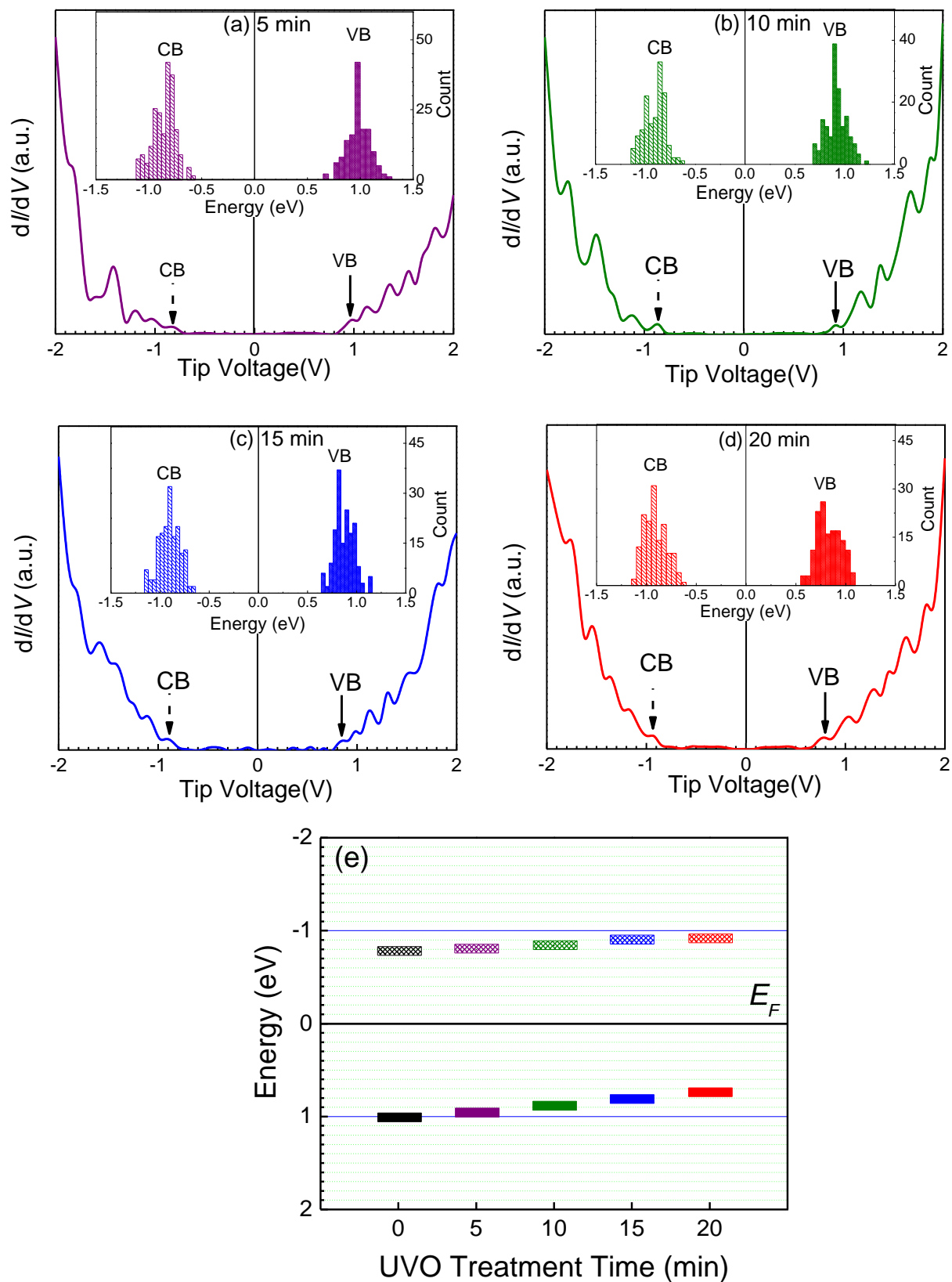


**Figure S5.** (a) - (d)  $dI/dV$  spectra of  $\text{Sb}_2\text{S}_3$  thin-films under different UVO treatment time and (e) influence of treatment time on the band-edges of  $\text{Sb}_2\text{S}_3$  thin-films. Histogram of CB and VB energies is shown in the inset of (a) - (d).

**Table S3.** Band-energies, transport gap, and FWHM of band-edges for  $\text{Sb}_2\text{S}_3$  thin-films under different duration of UVO treatment.

UVO treatment time (min)	Conduction band		Valence band		Transport gap (eV)	Optical gap (eV)
	Energy	FWHM	Energy	FWHM		
	(eV)	(eV)	(eV)	(eV)		
0	-0.77	0.26	1.01	0.27	1.78	1.67
5	-0.80	0.25	0.97	0.26	1.77	1.65
10	-0.84	0.26	0.90	0.25	1.74	1.64
15	-0.89	0.25	0.83	0.25	1.71	1.63
20	-0.93	0.24	0.74	0.25	1.67	1.57

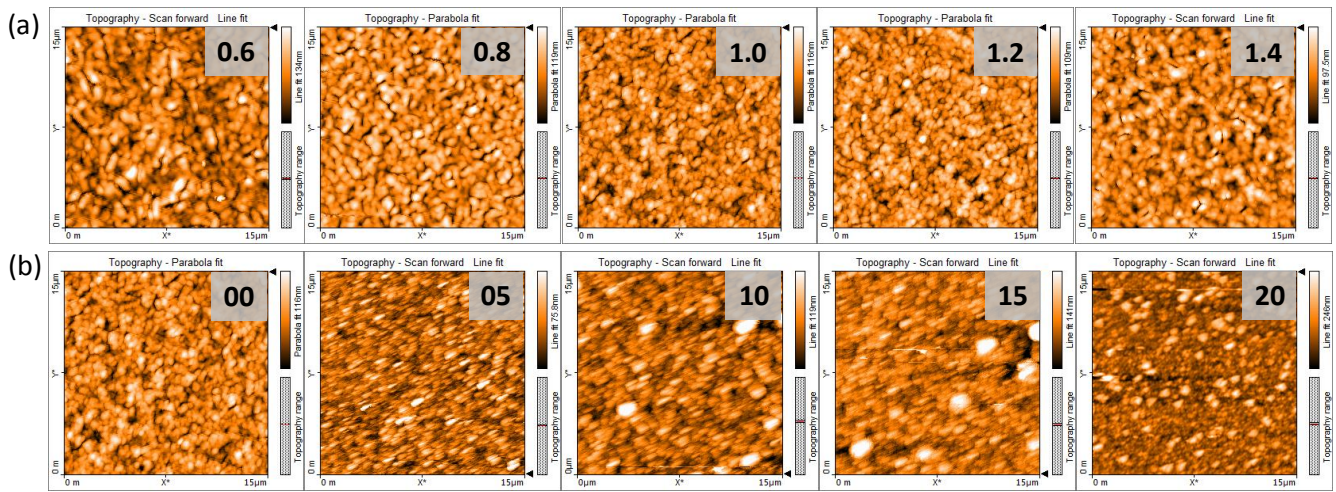


**Figure S6.** AFM topographies of (a)  $\text{Sb}_2\text{S}_3$  films having different precursor stoichiometries and (b) stoichiometric ( $\text{S/Sb} = 1.0$ )  $\text{Sb}_2\text{S}_3$  film under different UVO treatment times as stated in the legends.

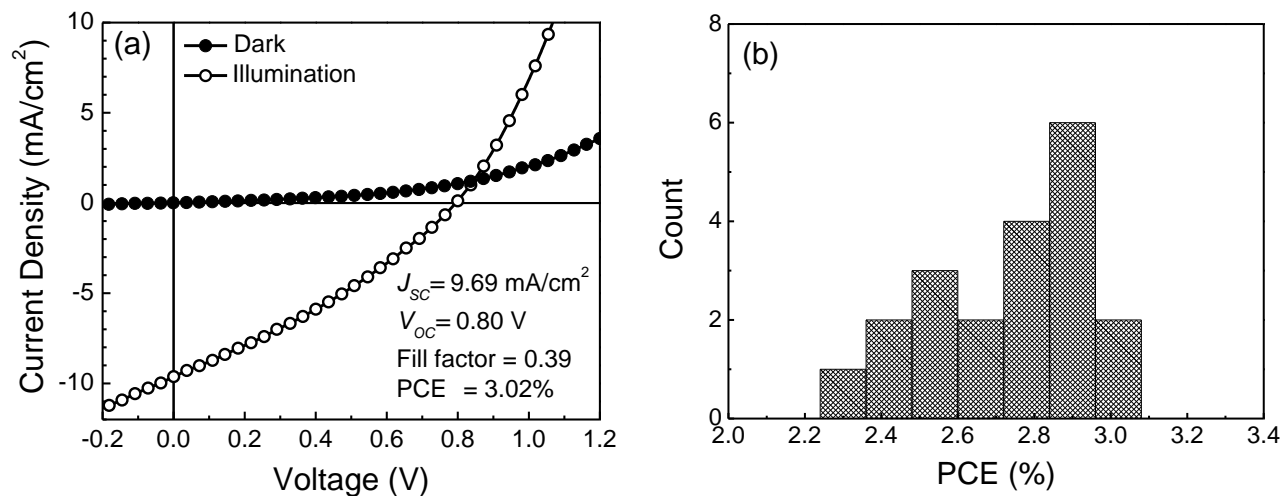


**Figure S7.** (a)  $I$ - $V$  characteristics of best performing Cu:NiO/Sb<sub>2</sub>S<sub>3</sub>/PCBM heterojunction device and (b) histogram of PCE of Cu:NiO/Sb<sub>2</sub>S<sub>3</sub>/PCBM heterojunction devices having optimized S/Sb ratio.

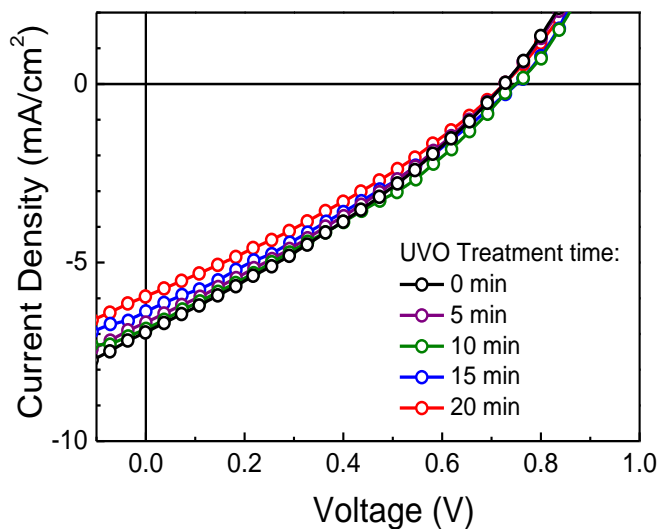


**Figure S8.**  $I$ - $V$  characteristics of Cu:NiO/Sb<sub>2</sub>S<sub>3</sub>/PCBM heterojunctions with different UVO treatment time under 1 sun illumination.

**Table S4.** Photovoltaic parameters of Cu:NiO/Sb<sub>2</sub>S<sub>3</sub>/PCBM heterojunctions with different UVO treatment times under 1 sun illumination.

<b>Treatment time (min)</b>	<b><math>J_{SC}</math> (mA/cm<sup>2</sup>)</b>	<b><math>V_{OC}</math>(V)</b>	<b>Fill factor</b>	<b>PCE (%)</b>
0	7.78	0.73	0.38	2.13
5	7.50	0.73	0.39	2.13
10	7.48	0.74	0.38	2.10
15	7.09	0.74	0.36	1.88
20	6.52	0.72	0.34	1.60

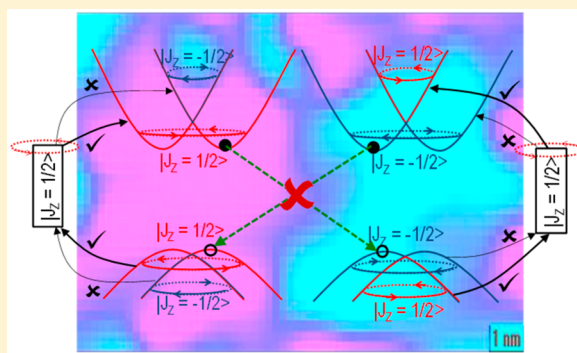
# Rashba Band Splitting in $\text{CH}_3\text{NH}_3\text{PbI}_3$ : An Insight from Spin-Polarized Scanning Tunneling Spectroscopy

Abhishek Maiti,<sup>†</sup> Salma Khatun,<sup>†</sup> and Amlan J. Pal\*<sup>‡</sup>

School of Physical Sciences, Indian Association for the Cultivation of Science, Jadavpur, Kolkata 700032, India

## Supporting Information

**ABSTRACT:** We report an experimental observation of Rashba splitting in methylammonium lead iodide ( $\text{MAPbI}_3$ ). Because of a large spin–orbit coupling parameter in the noncentrosymmetric material, both of the bands were predicted to split having two different spin-textures leading to two different  $Z$ -components of total angular momentum ( $J_z$ ). We use spin-polarized scanning tunneling spectroscopy to probe only one-type of  $J_z$ -matched bands throughout the film;  $dI/dV$  spectra recorded at many different points of a film however allowed us to spot both the Rashba split-levels and also deliberate on their spin-textures. We observe that the bands split in such a manner that the conduction and valence bands closer to the Fermi energy have the same type of spin-textures (a spin-allowed transition model). Still a low recombination rate of photogenerated carriers in  $\text{MAPbI}_3$  has been analyzed by considering Wannier-type excitons, a molecular nature of spin-domains from  $dI/dV$  images, and therefore a spin-forbidden nature of interdomain transition.



**KEYWORDS:** Rashba band splitting, spin-polarized scanning tunneling spectroscopy, spin–orbit coupling in  $\text{CH}_3\text{NH}_3\text{PbI}_3$ , conservation of total angular momentum, spin-forbidden interdomain transition

Although methylammonium lead iodide ( $\text{MAPbI}_3$ ) is well-known for its efficient solar-cell activities,<sup>1–3</sup> it possesses more interesting properties than can be envisaged in a single conventional semiconductor.<sup>4</sup> A suitable bandgap as per Shockley-Queisser limit,<sup>5,6</sup> a high extinction coefficient in the visible wavelength region,<sup>7</sup> a low exciton binding energy for efficient charge separation,<sup>7</sup> an in-built electric dipole arising out of the methylammonium ion presumably facilitating exciton dissociation,<sup>8</sup> a long carrier lifetime,<sup>9–11</sup> a high and ambipolar carrier mobility due to a smaller electron and hole effective masses,<sup>12,13</sup> and so forth are some of the commonly mentioned unique properties of this wonder material. Although such properties are indeed desired in a solar cell material, the most surprising feature of  $\text{MAPbI}_3$  is a low recombination rate of photogenerated carriers.<sup>14–16</sup> The rate is as low as 5 orders of magnitude lower than the predicted Langevin limit despite defects and impurities in  $\text{MAPbI}_3$  that may form in a solution-processed film;<sup>9</sup> this is in a clear contrast to conventional semiconductors in which defects form despite best efforts during the growth process in a best possible environment and act as carrier recombination sites limiting the carrier lifetime and diffusion length.

A low recombination rate of photogenerated carriers in  $\text{MAPbI}_3$  enhancing the carrier lifetime and thereby diffusion length is believed to occur due to Rashba effect.<sup>17,18</sup> The effect drives a spin-splitting leading to a spin-polarization even in a nonmagnetic system like  $\text{MAPbI}_3$ . The effect occurs due to a large spin–orbit coupling (SOC) arising out of high- $Z$

elements (lead and iodine) in the compound along with a lack of centrosymmetry appearing due to a tilted  $\text{PbI}_6$  octahedra and rotating electric dipoles of the organic ions leading to an effective magnetic field and thereby lifting the Kramer's spin-degeneracy of the electrons.<sup>19–21</sup> In the momentum ( $k$ ) space, a  $k$ -dependent spin-splitting of the bands around the band-extrema hence occurs.<sup>22</sup> Splitting for the two bands is however nonidentical resulting in an indirect nature of the bandgap.

Upon photoexcitation, the carriers then reside at band extrema having different points in  $k$ -space. That is, due to a momentum-offset of conduction band (CB) minimum and valence band (VB) maximum, the electrons and holes are in different  $k$ -space; they in-effect find themselves in an indirect bandgap semiconductor and their recombination, which requires a preservation of  $k$ , turns out to be a slow process.<sup>23,24</sup> Regarding the spin-rotation or spin-texture ( $\chi$ ) of the two split-levels, two schools of thought persist among theoreticians: (1) spin-allowed transition model<sup>25</sup> and (2) spin-forbidden transition model.<sup>17</sup> In spin-allowed transition model, CB and VB having a similar type of spin-texture reside closer to the Fermi energy; although recombination of photoexcited carriers is apparently possible due to spin-allowed nature of the transition, a slow recombination is considered to be due to the

**Received:** September 14, 2019

**Revised:** November 27, 2019

**Published:** December 16, 2019



presence of ferroelectric domains, passivation of defects, pressure-driven change of structure, and formation of large polarons.<sup>25,26</sup> In the spin-forbidden transition model, after spin-split the CB and VB closer to the Fermi energy have opposing spin-textures. A recombination between electrons in CB-minimum and holes in VB-maximum is hence a spin-forbidden process leading to a low recombination rate and thereby an enhanced carrier lifetime and a longer diffusion length.<sup>17,18</sup>

So far, a few experimental evidences of the Rashba splitting in a bromide-based perovskite ( $\text{MAPbBr}_3$ ) has been reported from angle-resolved photoemission spectroscopy measurements; the measurement method has provided information on the occupied states only.<sup>27</sup> Giovanni et al. has confirmed the presence of Rashba-split band structures in  $\text{MAPbI}_3$  by using a pump-probe method.<sup>28</sup> There are reports describing nonobservation of Rashba splitting in certain phases of the perovskite as well making the topic under debate.<sup>21,26</sup> A clear experimental evidence of CB-splitting would hence be truly interesting in lead-based hybrid-halide perovskites because the quantum of splitting in the unoccupied states has been predicted to be more than that in the VB.<sup>19,29</sup> Because the bands after Rashba splitting are spin-selective and (due to a strong SOC in the perovskite system) should be viewed in terms of the Z-component of total angular momentum ( $J_z$ ), tunneling of electrons would necessitate conservation of  $J_z$  instead. That is, the tunneling processes in strong SOC systems involve conservation of  $J_z$  in lieu of orbital or spin angular momentum separately.<sup>30–32</sup> We have therefore introduced spin-polarized scanning tunneling spectroscopy (SP-STs), which provides unique opportunities to experimentally probe  $J_z$ -matched Rashba-split bands in  $\text{MAPbI}_3$  and to comment on the spin-states of the two split-levels. Our work may further shed light on the debate and the rationale of a low recombination rate in hybrid halide perovskite materials.

**Formation of  $\text{MAPbI}_3$ .** To confirm formation of  $\text{MAPbI}_3$  in phase-pure form, we have characterized the material through conventional thin-film characterization techniques (Figure S1 in the Supporting Information). The X-ray diffraction (XRD) pattern yielded the characteristic (110) peak of the perovskite at an appropriate position indicating formation of a tetragonal phase at room temperature.<sup>33</sup> The respective optical absorption spectrum similarly showed two dominant and distinct photoinduced peaks located at around 490 and 740 nm which are characteristics of the material synthesized in  $N,N$ -dimethylformamide (DMF) solvent<sup>13</sup> along with a long Urbach tail implying presence of defects.<sup>34</sup> Optical bandgap of the perovskite was estimated from the  $d(\alpha h\nu)^2/d(h\nu)$  versus energy (and Tauc plots); the obtained value of 1.62 (1.52) eV matched well with the reported results.<sup>6</sup> The thin-films were in addition characterized by recording Raman spectroscopy of the compound. A couple of modes in the low-frequency range (70 and 95  $\text{cm}^{-1}$ ) were observed. These are the characteristic modes of the inorganic cage and corresponded to the bending and stretching vibrations of the Pb–I bond, respectively. The bands at 107 and 241  $\text{cm}^{-1}$  similarly could be associated with the vibrations of the  $\text{CH}_3\text{NH}_3^+$  cations and the torsional modes confirming formation of the hybrid halide perovskite in a phase-pure form.<sup>35</sup> X-ray photoelectron spectroscopy (XPS) studies inferred little or no degradation during a quick-transfer to the scanning tunneling microscope (STM) chamber.<sup>36</sup>

**STS of  $\text{MAPbI}_3$  with a Pt/Ir Tip.** In Figure 1a, we have presented typical  $dI/dV$  versus sample voltage plots of the

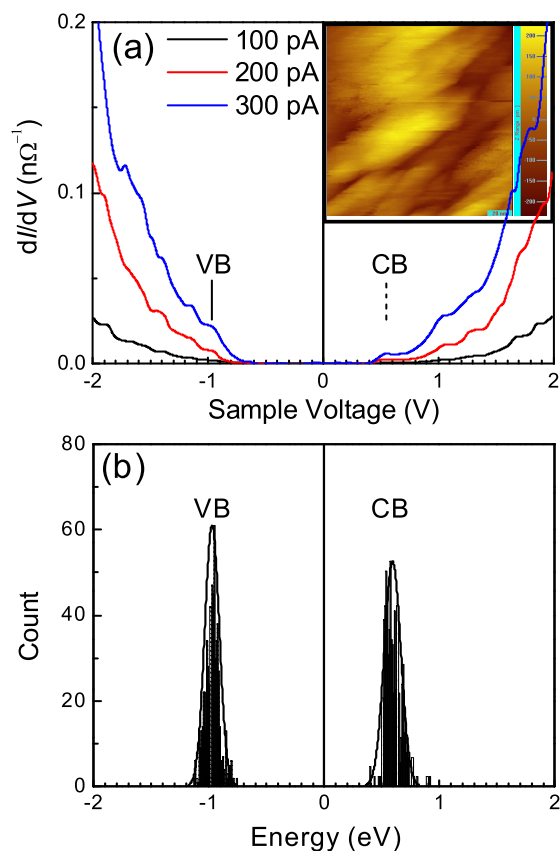


**Figure 1.** (a)  $dI/dV$  spectra of  $\text{MAPbI}_3$  thin-films recorded with a Pt/Ir tip at three tip-approach conditions and (b) histograms of band-energies. Inset of (a) shows a topographic image of the film, whereas the scale bar in the image represents 20 nm, and the height scale of the image is 0.4 nm.

material recorded with a conventional Pt/Ir tip. Plots for three set-points representing different tip-to-sample distances are shown in the figure. Because  $dI/dV$  has a correspondence to the density of states (DOS) spectrum and the bias in the scanning tunneling microscope (STM) was applied to the perovskite with respect to the tip, the first peak in the positive voltage closest to 0 V implied injection of electrons and hence the location of CB. The similar peak in the negative voltage implied withdrawal of electrons and thereby the VB of the semiconductor.<sup>37</sup> Both the peaks are with respect to the Fermi energy ( $E_F$ ) of the semiconductor that is aligned to 0 V. The spectra showed that the CB and VB energies were at 0.57 and 0.96 eV, respectively, away from  $E_F$  leading to a transport gap of 1.53 eV, which matched well with the literature.<sup>6</sup> The band energies tallied the results from films grown through a vacuum deposition method;<sup>38</sup> the energies along with the results from XPS studies imply little contamination during the transfer to the STM chamber. The small variation in the bandgap value was due to some level of arbitrariness in the method of locating a band in different measurements.<sup>39,40</sup> When the band-edges obtained from spectra recorded at different tip-to-sample distances were compared, the CB and VB energies could be found to be independent of the tunneling condition. Subsequent peaks, which appeared in both bias directions of a  $dI/dV$  spectrum, arose due to probing of higher levels. The results hence infer that the range of tip-to-sample separations used in recording STS measurements did not influence the band-edges of the semiconductor.



Because STS is an extremely localized mode of measurement, we have recorded  $dI/dV$  spectra at a large number of points on the films and also at all the three tunnel conditions or tip-to-sample separations. In each of the more than 600  $dI/dV$  spectra, we have identified CB and VB edges to finally draw a histogram of the two band-energies (Figure 1b). The number of bins in a histogram was set to the square root of the measurement-points; the method is commonly termed as a square-root choice. The histograms of band-energies show that the CB was always closer to the Fermi energy than the VB inferring a clear n-type behavior of the perovskite. Such a nature of conductivity in MAPbI<sub>3</sub>, when formed with stoichiometric content of CH<sub>3</sub>NH<sub>3</sub>I and PbI<sub>2</sub>, is in fact known to appear due to iodine-vacancies present in the perovskite; the vacancies can be passivated when the perovskite is formed with PbI<sub>2</sub>-rich precursors.<sup>41–43</sup> The histograms show a symmetric distribution of nearly equal full width at half-maximum (fwhm). It may be stated that band-energies of a semiconductor obtained from  $dI/dV$  spectra as such exhibit a distribution;<sup>44,45</sup> in MAPbI<sub>3</sub>, the histogram of CB and VB-edges may have originated due to presence of grains and grain-boundaries in the solution-cast film (inset of Figure 1a) as well as CH<sub>3</sub>NH<sub>3</sub>I-rich and PbI<sub>2</sub>-rich regions in the ultrathin layer. In the STM topography, we did not achieve an atomic resolution which is observed if a single crystal after an in situ cleaving or films grown through vacuum codeposition method are imaged.<sup>38,46</sup>

**SP-STs of MAPbI<sub>3</sub> with a Chromium-Coated Tip.** We then proceeded to characterize the same film with a chromium-coated antiferromagnetic tip to record SP-STs. In Figure S2a in the Supporting Information, we have presented some topographic images with the spin-polarized tip; the images with a gradual decrease of scale bar evidence grain boundaries and grain interiors in the film as well. With an injection of spin-polarized electrons, the spectroscopy provides unprecedented opportunities to garner information on the spin-texture of the split-bands which may be referred to as bands having  $J_z = +1/2$  and  $J_z = -1/2$ .<sup>47,48</sup> The involvement of  $J_z$  during the tunneling of spin-polarized electrons is because the total angular momentum  $J = L + S$  arising out of a strong spin-orbit interaction term  $L \cdot S$  will have to be the proper eigenvalue at the band-edges;<sup>30–32</sup> the band structure upon Rashba splitting will hence look like the one presented in Figure 2a.<sup>47</sup> Here, a  $J_z = +1/2$  band can be built through ( $L_z = 0$  and  $S_z = +1/2$ ) and ( $L_z = +1$  and  $S_z = -1/2$ ), which can be viewed to possess a particular spin-texture (for example,  $\chi = +1$ ). Similarly, a  $J_z = -1/2$  band can be considered to have formed through ( $L_z = 0$  and  $S_z = -1/2$ ) and ( $L_z = -1$  and  $S_z = +1/2$ ) with another spin-texture ( $\chi = -1$ ). That is, a particular  $J_z$  band (for example,  $J_z = -1/2$ ) is formed through a partial  $S_z = +1/2$  band (red trace) and a part of  $S_z = -1/2$  band (blue trace) in our Figure 2a (left panel).

Because we have had no prior knowledge about the spin-states of the material at the point of measurement and a spin-equilibrium must exist at the macroscopic scale of the film, we have recorded SP-STs at many different points with the chromium-coated antiferromagnetic tip. The large number of  $dI/dV$  spectra could be classified into two broad types; one typical spectrum from each of the two-types of  $dI/dV$  spectra are shown in Figure 2b. When we look for CB and VB energies in the two types of  $dI/dV$  spectra, we observe two sets of bands. The two  $dI/dV$  spectra may apparently imply two different materials in the film. It may however be recalled that

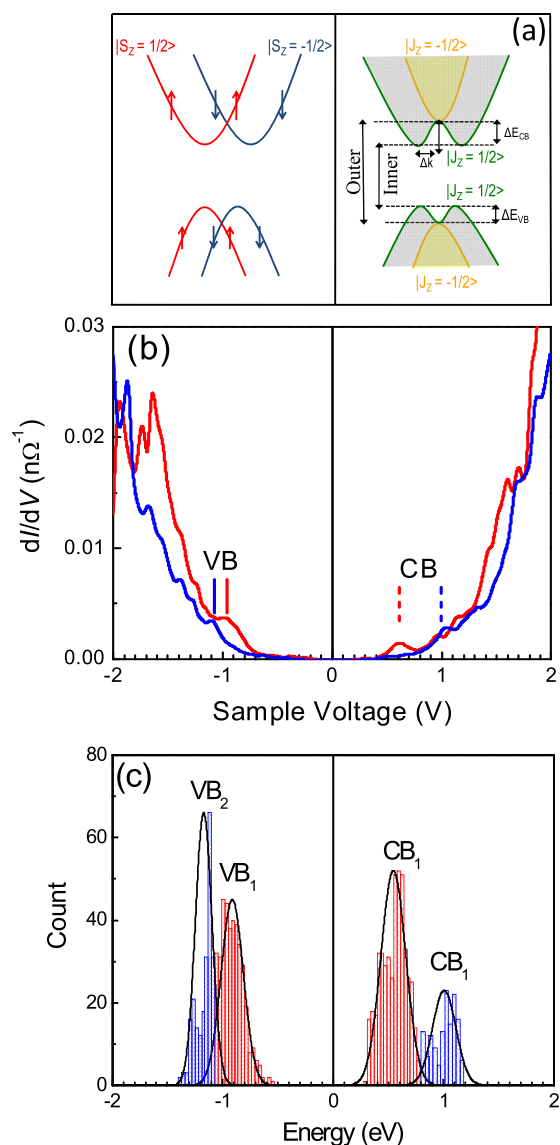


**Figure 2.** (a) Schematic representation of Rashba-split bands considering spin angular momentum (left panel) and total angular momentum (right panel). (b) Two representative  $dI/dV$  spectra of MAPbI<sub>3</sub> thin-films recorded with a chromium-coated antiferromagnetic tip and (c) histogram of band-energies.

the same film yielded only one CB and one VB when probed with a Pt/Ir tip. Therefore, the two sets of bands appearing in SP-STs must be due to the presence of two domains in the films that were invisible by the Pt/Ir tip. The two CB energies arising out of the two types of domains are widely separated (as large as 300 meV); the two VBs are less split. Because each  $dI/dV$  spectrum was recorded in both bias directions at a single sweep, we could correlate CBs and VBs. If we compare the band-edges of a domain with those of the other, we find that both the energies are either nearer (red-trace in Figure 2b) or farther to  $E_F$  (blue trace in Figure 2b). They presumably represent band-energies in the two types of domains. Here also, the tip-to-sample separation was varied by considering different tip-approach conditions (Figure S2b,c in the Supporting Information). When the band-edges were compared in each set, the CB and VB energies could be found to be independent of the tunneling condition.

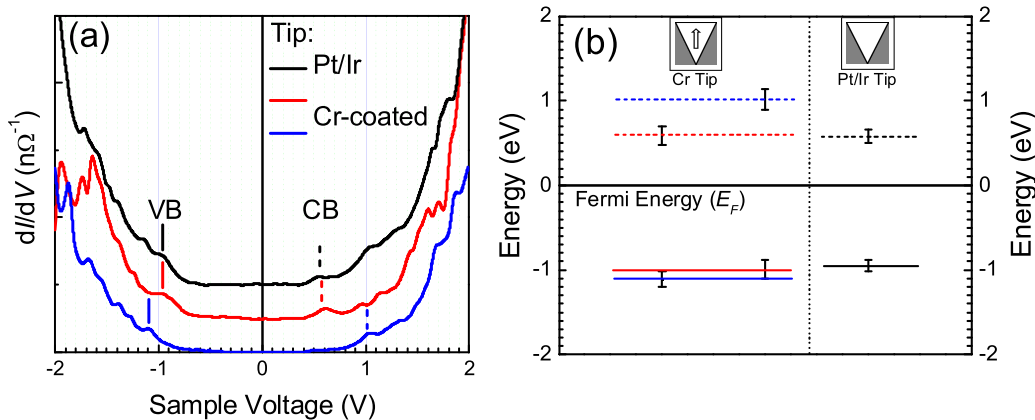


**Figure 3.** (a) Comparison of  $dI/dV$  spectra of MAPbI<sub>3</sub> recorded with a Pt/Ir tip and a chromium-coated antiferromagnetic tip. With the latter tip, the material was probed for matching bands. A Y-offset has been added for clarity of presentation. (b) Band-energies of MAPbI<sub>3</sub> obtained from the  $dI/dV$  spectra and histograms for the two types of STM-tips.

In each of the 600-odd  $dI/dV$  spectra often recorded with different tip-approach conditions of the antiferromagnetic tip, we have identified the CB and VB edges and finally collated the energies in the form of histograms (Figure 2c). The histogram for CB energies could be seen to exhibit two clear peaks. The bands may be marked as CB<sub>1</sub> and CB<sub>2</sub> having energies at 0.60 and 0.99 eV, respectively, away from the Fermi energy. The presence of two peaks in the VB was not as apparent as in the CB; because each  $dI/dV$  spectrum provided the energies in pair, that is, measurement of CB and VB edges are correlated, we could separate out VB<sub>1</sub> and VB<sub>2</sub> corresponding to CB<sub>1</sub> and CB<sub>2</sub>, respectively. We then could draw two distributions in the VB-histogram as well; the separation between the two VBs turned out to be 150 meV. The histograms too infer that CB and VB energies can be either nearer (CB<sub>1</sub> and VB<sub>1</sub>) or farther (CB<sub>2</sub> and VB<sub>2</sub>) to  $E_F$ . That is, the two band-edges split in such a manner that CB<sub>1</sub> and VB<sub>1</sub> are closer to  $E_F$  whereas CB<sub>2</sub> and VB<sub>2</sub> remained away from  $E_F$ .

It may be recalled that the same film when probed with spin-random electrons (Pt/Ir tip) yielded just one CB and VB energies in the histogram. In Figure 3a, we have compared a typical  $dI/dV$  spectrum with a Pt/Ir tip with the two sets of spectra obtained with a chromium-coated antiferromagnetic tip. The band-positions of MAPbI<sub>3</sub> obtained for both the tips have been plotted in Figure 3b in the form of a band diagram. A comparison of the band-edges obtained from the two types of tips show that the CB and VB energies with a Pt/Ir tip matched the inner pair of energies derived with the chromium-coated tip; that is, with the spin-randomness of injected electrons from the Pt/Ir tip, it always probed the CB and VB edges, which had band-energies closer to the  $E_F$  (Figure 3b).

**Origin of Two Pair of Bands in MAPbI<sub>3</sub>: Probing Rashba-Split States through SP-STs.** Appearance of two pairs of band-edges in a MAPbI<sub>3</sub> film under the eye of spin-polarized electrons is indeed an interesting observation. Two pairs of band-edges in a single film infer that two domains based on different spin-textures existed in the thin-film. As such, the perovskite is known to possess a strong spin-orbit coupling (SOC) due to the presence of high-Z elements in the compound. The SOC parameter, in conjunction with a lack of centrosymmetry on a local scale, can lead to an effective magnetic field and thereby lifting of Kramer's spin-degeneracy of the electrons (Rashba effect) leading to band-splitting in

terms of spin-textures.<sup>19–21</sup> It may be stated that spin-textures are in general used for optical transitions and charge carrier dynamics involving excitons and hence both CB and VB energies simultaneously; Z-component of total angular momentum ( $J_z$ ), on the other hand, is considered and should be conserved when only one band (CB or VB) is probed at a time through injection or withdrawal of electrons, respectively.<sup>30–32,47</sup>

In the schematic representation of Rashba-split bands (Figure 4a), we identified them to possess Z-component of total angular momentum  $J_z$  of  $-1/2$  and  $+1/2$  implying a spin-texture  $\chi$  of  $-1$  and  $+1$ , respectively. The splitting in VB was smaller than that of CB; this implies that the VB maximum and CB minimum will be at different positions in the  $k$ -space leading to the formation of an indirect bandgap semiconductor. Here the VB is formed with a major contribution from I(5p) atomic orbital along with minor involvements from Pb(6s) and Pb(6p), whereas the CB arises majorly from Pb(6p) with a small involvement of I(5p) orbital. The CB should therefore undergo a larger Rashba splitting due to a higher Z of lead than that of iodine.<sup>19,29</sup> Also, the CB, which has only a p-character and hence an orbital angular momentum of  $L = 1$ , in conjunction with a spin angular momentum  $S = 1/2$ , is split into two states with  $J = 1/2$  and  $J = 3/2$  carrying two different total angular momenta ( $J$ ). On the other hand, the s-character of lead in forming VB with  $L = 0$  is unaffected due to its unique  $J = 1/2$  value;<sup>19</sup> only the p-character of I(5p) and Pb(6p) orbitals hence contributed to the splitting of VB. That is, by considering the SOC parameter of iodine and involvement of I(5p) orbital in forming the VB, we obtain different  $J$ -values in the VB also. For carrier tunneling, the bottom-most CB ( $J = S = 1/2$ ) and the topmost VB ( $J = S = 1/2$ ), which are doubly degenerate ( $J_z = \pm 1/2$ ),<sup>47,49</sup> will be of relevance in STs and SP-STs studies.

During tunneling of spin-polarized electrons, time-reversal symmetry dictates that the initial and final state of the tunneling process must possess the same orbital and spin angular momentum. Due to a strong SOC parameter in MAPbI<sub>3</sub>, the two parameters are now coupled together leading to a conservation of  $J_z$  in lieu of spin or orbital angular momentum, separately. That is, for a tunneling process to a SOC system, the total angular momentum is conserved instead. A spin-change during a tunneling process while conserving  $J_z$  would have to be absorbed and compensated by

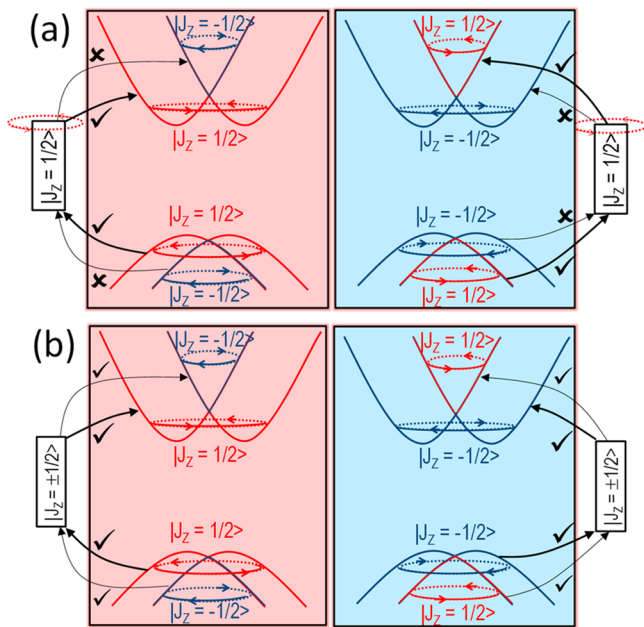


**Figure 4.** (a) Schematic representation of electron-tunneling with a chromium coated tip. Rashba band-splitting in two different domains are shown in the left and the right panels. While red curves represent a  $|J_z = 1/2\rangle$  band, the blue ones refer to the  $|J_z = -1/2\rangle$  band. A chromium-coated tip ( $L_z = 0$  and  $S_z = 1/2$  due to the  $3d^5 4s^1$  electrons) of SP-STM has been considered to inject up-spin electrons with  $|J_z = 1/2\rangle$ . Thick-arrows indicate tunneling of electrons to the  $J_z$ -matched CB-states and from the matched VB-states. Because of conservation of total angular momentum, tunneling of electrons to/from  $J_z$ -mismatched states (thin-arrows) are not allowed. The two-sets of CB and VB-energies hence appeared due to two types of domains. (b) Schematic representation of electron-tunneling with a Pt/Ir tip. Here both thick- and thin-arrows represent allowed transition to the CB and from the VB.

an opposite change in the orbital angular momentum leading to the quantum states of tunneling to possess the same total angular momentum eigenvalue<sup>32</sup> (Table S1 in the Supporting Information). We may recall that electrons from the chromium-coated tip will have only one value  $J_z$  which appears due to spin angular momentum of  $4s^1$  electron ( $L_z = 0$

and  $S_z = 1/2$ );<sup>50</sup> a Pt/Ir tip, on the other hand, will inject both  $J_z = +1/2$  and  $-1/2$  electrons.

Because no magnetic field was applied to the material, a spin-equilibrium must occur even in the microscopic scale of the thin-film. That is, two possible domains would balance their alignment in the film. Rashba-split bands of the two domains have been represented in the two panes of Figure 4a. In each pane, Rashba-split bands have been represented as  $CB_1$  and  $VB_1$  having  $J_z = +1/2$  and  $CB_2$  and  $VB_2$  with  $J_z = -1/2$ . That is, the inner CB and VB levels possessed the same  $J_z$  or spin-textures as proposed in the spin-allowed transition model.<sup>25,26</sup> When a spin-polarized tip was brought close to the material, tunneling of electrons would occur only when their Z-component of total angular momenta ( $J_z$ ) are matched. For example, in a particular domain (left panel of Figure 4a), the spin-polarized tip may probe Rashba-split  $CB_1$  and  $VB_1$  which are closer to the  $E_F$  ( $J_z = +1/2$ ). Similarly, in another domain (right panel of Figure 4a), which is antiparallel to the previous one, the same tip would now probe energy levels of  $CB_2$  and  $VB_2$  (which are farther from the  $E_F$ ) since they now possess  $J_z = +1/2$ . Therefore, when SP-STS measurements were made at many different points, two characteristic  $dI/dV$  spectra were obtained; the spectra in Figure 2a in fact occur out of schematic representations in the left and right panes of Figure 4a.

In Figure 4b, we have presented the schematic representation of electron-tunneling with the Pt/Ir tip. Because the tip can now inject/withdraw both types of electrons, half of the electrons find the same CB/VB levels in the two domains as total angular momentum matched states. The Pt/Ir tip simply probed the CB and VB which are nearer to the  $E_F$ , because such a transition is always allowed for one of the two types of electrons injected from the Pt/Ir tip. We hence obtained only one set of band-energies in the  $dI/dV$  spectra of MAPbI<sub>3</sub> film as the CB minimum and the VB maximum. Energy levels obtained with the Pt/Ir tip matched the energies as seen by spin-polarized electrons in one domain (left panel of Figure 4a). With a ferromagnetic nickel tip, the same quantum of energy-splitting was observed although the relative position of the bands with respect to the Fermi energy were different due to a different work-function of the metal (Figure S3 in the Supporting Information); such a ferromagnetic tip may also

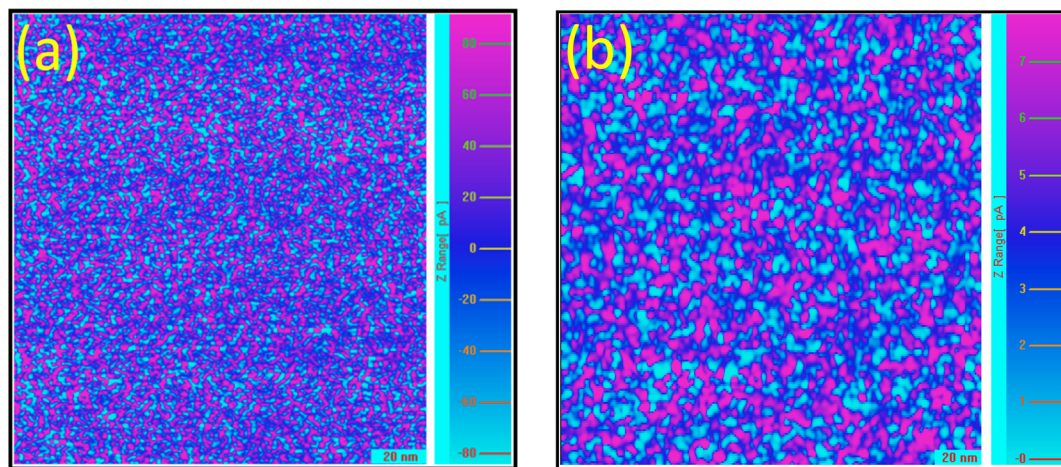


**Figure 5.**  $dI/dV$  images of a MAPbI<sub>3</sub> ultrathin-film recorded (a) with a chromium-coated antiferromagnetic tip to probe the inner and  $J_z$ -matched CB at 0.54 eV and (b) with a Pt/Ir to probe the CB at 0.54 eV from the  $E_F$ .



introduce stray fields influencing electronic-states of the perovskite.<sup>48</sup>

**Spin-Polarized  $dI/dV$  Imaging.** The analysis of probing Rashba-split states in the perovskite was based on the assumption of spin-equilibrium through two possible domains having different spin-states. It will hence be quite interesting to know or view the spin-states of domains in the material. As such, in the  $dI/dV$  images of a film a material is seen from its energy perspective. With SP-STs and the CB of the material having a larger spin-split, we aimed to probe the spin-states in a domain. That is, the chromium-coated antiferromagnetic tip at a suitable (low) voltage would probe only the domains that have a  $J_z$ -matched lower-CB. A spin-polarized  $dI/dV$  image was hence recorded at 0.54 V from  $E_F$ , so that the levels only up to that voltage are probed. At such a voltage, the lower of the two CBs (closer to the  $E_F$ ) could be probed, provided the state has a  $J_z$  matched to that of the spin-polarized electrons; the bias during imaging was kept inadequate, so that the other CB level (away from  $E_F$ ) was never accessed. Neither CB having a mismatched- $J_z$  would be probed. Such an image is shown in Figure 5a. A high DOS in the image (magenta) implied domains whose lower-CB is  $J_z$ -matched to that of the tip (Figure 5a). A low DOS similarly indicated the domains whose lower-CB is forbidden for transition. A magnified view of two domains and its corresponding DOS-profile are shown Figure S4 in the Supporting Information. In the spin-polarized  $dI/dV$  image, we find that the two domains were homogeneously distributed. If we look at the scale bar of the image, we notice that the so-called domains may have molecular dimensions. That is, in a MAPbI<sub>3</sub> film a molecule itself may have formed a spin-domain.

$dI/dV$  images when probed at the VB also yielded domains of molecular dimension (Figure S5 in the Supporting Information). Because of a lower splitting in the VB, the variation in DOS in this image was lower as compared to the image probed at the CB.  $dI/dV$  images recorded with a chromium-coated tip near its Néel temperature, on the other hand, have little contrast (a low variation in DOS) due to (spin)-depolarized nature of the tip in addition to inefficient tunneling process and involvement of the additional thermal energy (Figure S6 in the Supporting Information).

We also have recorded a  $dI/dV$  image with a Pt/Ir tip at a voltage suitable to probe the CB (Figure 5b). With a Pt/Ir tip, a single CB band was available to be probed by the Pt/Ir tip all over the film. As compared to the  $dI/dV$  image with a chromium-coated tip, the image with a Pt/Ir tip looked quite homogeneous when a same vertical scale-bar is imagined. A zoomed DOS-scale in the image (Figure 5b) allowed us to view the little spatial variation of the electronic properties (not spin related) of the sample that is due to grain boundaries and grain interiors, defects, and inhomogeneity in the film. The grain size obtained in the  $dI/dV$  image with Pt/Ir tip was larger than that when probed with chromium-coated tip. This is because domains have almost uniform DOS when energetically seen by the Pt/Ir tip, whereas the spin-state of a molecule is also read by the chromium-coated tip. The STM topographies of the exact same area at which  $dI/dV$  images were recorded are shown in Figure S7 in the Supporting Information. The topographies inferred uniformity of the film-surface. That is, although STM topographies provide only the current-mapping of the surface,  $dI/dV$  images with a spin-polarized tip showed the energy-mapping of the perovskite surface through record of spin-signals as well.

### Rashba Splitting, Interdomain Spin-Forbidden Transition Model, and Implications in Solar Cells.

$dI/dV$  spectra of MAPbI<sub>3</sub> recorded with SP-STs have hence provided an experimental observation of Rashba band splitting in the perovskite. Although lowest of the CB and highest of the VB levels have always a matching spin-texture (spin-allowed transition model), the electrons and holes upon photoexcitation would reside in different  $k$ -space creating an indirect bandgap for recombination. This is because the splitting of the two band-edges were different due to involvement of different elements (and hence SOC parameters) in forming the two band-edges. Because the domains have a size of subnanometer to a couple of nanometers, the quantum of interdomain recombination should be substantial. For an interdomain recombination, electrons of a domain and holes in the neighboring domain would have opposing spin-textures; their radiative recombination would hence be a forbidden process leading to a low recombination rate of photogenerated carriers in MAPbI<sub>3</sub>.<sup>14,15,25</sup>

Electrons and holes upon photoexcitation are quite expected to reside in different molecules/domains. Because both the bands of MAPbI<sub>3</sub> are formed through molecular orbitals of the inorganic moieties, the excitons in the perovskite can be considered to be Wannier type;<sup>51</sup> also, due to a large dielectric constant of the material,<sup>8</sup> electron-hole pair of an exciton would have a weak Coulomb interaction leading the carriers to reside in different molecules. Instead of intramolecular recombination, intermolecular recombination is hence a likely process in MAPbI<sub>3</sub> if it is not a forbidden transition. With both the bands being Rashba-split, and electrons residing at the CB-minimum of a domain and holes at the VB-maximum of a neighboring domain having opposite  $J_z$  values, intermolecular recombination process will hence be a forbidden transition (Figure 6).

On the basis of the observation of splitting in the two bands, it is tempting to comment on carrier transport in perovskite solar cells. In general, the lowest CB and the highest VB are considered for charge transport through a perovskite and in

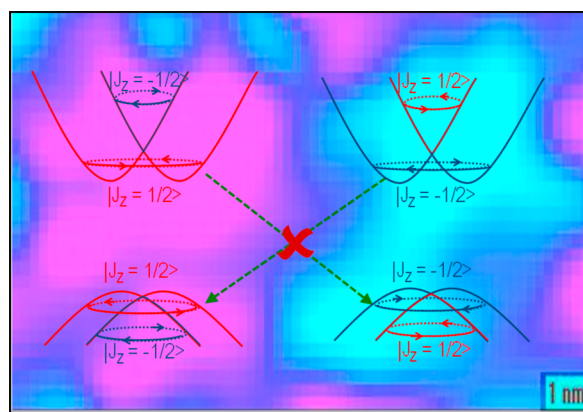


**Figure 6.** A schematic representation of Rashba band splitting in two opposing domains. Upon photoexcitation, electrons and holes reside in different positions in the Brillouin zone creating an indirect bandgap and hence led to a slower intradomain recombination. For interdomain recombination, electrons of a domain and holes of the neighboring domain do have opposing spin-textures in addition; their radiative recombination is hence a forbidden process (as shown by broken-arrows). Background of the schematic representation is an enlarged section of the  $dI/dV$  image (from Figure 5a).

determining the energy-offset with the carrier-transport layers. With the evidence of splitting of the two bands, both the CBs and both the VBs should in fact be considered while ensuring a type-II band-alignment with the electron- and hole-transport layers for a seamless conduction process. Unless one considers both pair of Rashba-split bands in a perovskite like MAPbI<sub>3</sub> for the conduction process, one would leave those levels from the ambit of charge collection.

In conclusion, we have provided a clear experimental observation of Rashba band splitting in MAPbI<sub>3</sub> that has so far been predicted to occur as a result of a strong SOC parameter and a lack of centrosymmetry in the perovskite. We have elegantly used SP-STs which allows tunneling of spin-polarized electrons to/from only the  $J_z$ -matched bands leaving the mismatched ones invisible. We could observe both the Rashba-split bands, since a spin-equilibrium must occur in the microscopic scale of a film; this necessitated a particular band (for example,  $J_z = +1/2$ ) to be closer to the Fermi energy in a domain and away from the Fermi energy in the neighboring domain. With the use spin-polarized tip to probe only the  $J_z$ -matched CB and VB throughout the film, we could view both the  $J_z$ -matched split-levels and deliberate on their relative spin-textures as well. We have observed that the two bands split in such a manner that the CB and VB closer to the Fermi energy have the same type of spin-textures; that is, they follow a spin-allowed transition model for carrier recombination. From  $dI/dV$  images of MAPbI<sub>3</sub>, we estimated the dimension of spin-domains to be molecular in size. With Wannier-type of excitons forming in MAPbI<sub>3</sub> upon photoexcitation, the electron and hole would reside in different molecules/domains enforcing only interdomain recombination; because CB minimum and VB maximum of two neighboring domains have different  $J_z$  values, an interdomain transition becomes a forbidden process leading to a low recombination rate of photogenerated carriers in MAPbI<sub>3</sub>.

**Materials and Methods.** *Materials.* Lead(II) iodide PbI<sub>2</sub> (99%) and *N,N*-dimethylformamide DMF (anhydrous 99.8%) were purchased from Sigma-Aldrich Chemical Co. Methylammonium iodide was purchased from Dyesol Limited. The materials were stored in a nitrogen-filled glovebox with both oxygen and moisture level below 0.1 ppm and were used without further treatment.

*Formation of MAPbI<sub>3</sub> Perovskite Thin-Films.* Thin-films of MAPbI<sub>3</sub> were formed through a conventional solution-process approach following a usual one-step method which is based on codeposition of both the organic and inorganic components. The precursor solution was formed by a thorough mixing of stoichiometric CH<sub>3</sub>NH<sub>3</sub>I and PbI<sub>2</sub> in DMF under an overnight stirring process at 70 °C inside the glovebox. The solution was then spun at 2500 rpm for 30 s on preheated (70 °C) substrates suitable for different measurements. The films were annealed at 100 °C for 20 min while covered with a Petri dish to complete the conversion to the perovskite phase. For STS measurements, ultrathin films were spun at 4000 rpm for 30 s on highly doped Si(111) substrates (arsenic-doped, n-type) having a resistivity of 3–10 mΩ·cm. The one-step method moreover led to limited CH<sub>3</sub>NH<sub>3</sub>I- and PbI<sub>2</sub>-rich regions in the perovskite films. Use of a magnetic substrate was avoided since it is known to induce a substrate-induced exchange splitting and thereby hide a Rashba spin-splitting.<sup>52</sup>

*Thin-Film Characterization.* The thin-films were characterized by X-ray diffraction (XRD) patterns and optical absorption and Raman spectroscopy. The measurements

were conducted with a Rigaku Smart Lab X-ray Diffractometer (Cu K $\alpha$  radiation = 1.5406 Å), UV–vis–NIR spectrophotometer (Cary 5000, Agilent Technologies), and Horiba JobinYvon Raman triple-grating spectrometer system (model number T64000) using 532.0 nm excitation from a diode-pumped solid state (DPSS) laser.

*STS Studies.* STS studies of MAPbI<sub>3</sub> were carried out in an ultrahigh-vacuum scanning tunneling microscope (UHV-STM) with a chamber pressure of  $2 \times 10^{-10}$  Torr. The perovskite films with a thickness of around 10 nm were quickly transferred from the glovebox to the load-lock chamber of the STM; they were transferred to the main chamber following the usual protocol. Extremely sharp STM tips were formed through an acute mechanical cut of the Pt/Ir wire (80%/20%) and were used for the measurement. For spin-polarized STS (SP-STs), chromium-coated (15 nm) silver/gallium (Ag<sub>2</sub>Ga) nanoneedles, coaxial at the tip of a tungsten wire (0.25 mm), were used. Such tips, which were bought from NaugaNeedles LLC., were antiferromagnetic in nature allowing injection of spin-polarized electrons. Temperature of both tips and films were maintained at 80 K during STS studies to enable efficient spin-polarized electron-tunneling process while retaining the noncentrosymmetric phase of the compound.<sup>21</sup> For approach of the tip, a bias of 1.5 V was applied through a feedback-loop; three different currents (100, 200, and 300 pA) were targeted to achieve to obtain different set-points or electron-tunneling conditions. At each set-condition, differential tunnel conductance ( $dI/dV$ ) versus voltage characteristics was recorded with a lock-in amplifier; parameters for the amplifier were 16 mV rms and 1.15 kHz. The dc bias was applied to the substrate with respect to the tip.  $dI/dV$  “images” of the films were recorded through scanning of  $dI/dV$  over a small region; feedback-loop was turned off during the scanning and  $dI/dV$  imaging processes.

## ■ ASSOCIATED CONTENT

### 📄 Supporting Information

The Supporting Information is available free of charge at <https://pubs.acs.org/doi/10.1021/acs.nanolett.9b03800>.

An XRD pattern, optical absorption spectrum along with  $d(\alpha h\nu)^2/d(h\nu)$  versus energy plot, Raman spectrum, SP-STM topographies of MAPbI<sub>3</sub> with a gradual decrease of scale bar,  $dI/dV$  spectra with a chromium-coated tip for three different tip-to-sample distances, two representative  $dI/dV$  spectra of MAPbI<sub>3</sub> thin-films recorded with nickel tip and histogram of band-energies, DOS-profile along a couple of domains,  $dI/dV$  image of a MAPbI<sub>3</sub> ultrathin-film recorded with a chromium-coated tip to probe the inner VB at  $-0.88$  eV, a typical  $dI/dV$  spectrum and a  $dI/dV$  image recorded with a chromium-coated tip near its Néel temperature, and SP-STM topographic map of MAPbI<sub>3</sub> film at the exact same area where  $dI/dV$  images were recorded with chromium-coated tip and Pt/Ir tip (PDF)

## ■ AUTHOR INFORMATION

### Corresponding Author

\*Tel: +91-33-24734971. Fax: +91-33-24732805. E-mail: [sspajp@iacs.res.in](mailto:sspajp@iacs.res.in).

### ORCID

Amlan J. Pal: 0000-0002-7651-9779

## Author Contributions

†A.M. and S.K. made equal contributions to the work.

## Notes

The authors declare no competing financial interest.

## ACKNOWLEDGMENTS

A.J.P. acknowledges the JC Bose National Fellowship of SERB (SB/S2/JCB-001/2016). A.M. and S.K. acknowledge DST INSPIRE Fellowship [IF170922] and CSIR Fellowship No. 09/080(1054)/2017-EMR-I (Roll No. 523092), respectively.

## REFERENCES

- (1) Green, M. A.; Ho-Baillie, A.; Snaith, H. J. *Nat. Photonics* **2014**, *8*, 506–514.
- (2) Park, N. G.; Gratzel, M.; Miyasaka, T.; Zhu, K.; Emery, K. *Nat. Energy* **2016**, *1*, 16152.
- (3) Saliba, M.; Matsui, T.; Domanski, K.; Seo, J. Y.; Ummadisingu, A.; Zakeeruddin, S. M.; Correa-Baena, J. P.; Tress, W. R.; Abate, A.; Hagfeldt, A.; Gratzel, M. *Science* **2016**, *354*, 206–209.
- (4) Manser, J. S.; Christians, J. A.; Kamat, P. V. *Chem. Rev.* **2016**, *116*, 12956–13008.
- (5) Shockley, W.; Queisser, H. J. *J. Appl. Phys.* **1961**, *32*, 510–519.
- (6) Kong, L. P.; Liu, G.; Gong, J.; Hu, Q. Y.; Schaller, R. D.; Dera, P.; Zhang, D. Z.; Liu, Z. X.; Yang, W. G.; Zhu, K.; Tang, Y. Z.; Wang, C. Y.; Wei, S. H.; Xu, T.; Mao, H. K. *Proc. Natl. Acad. Sci. U. S. A.* **2016**, *113*, 8910–8915.
- (7) Galkowski, K.; Mitioglu, A.; Miyata, A.; Plochocka, P.; Portugall, O.; Eperon, G. E.; Wang, J. T. W.; Stergiopoulos, T.; Stranks, S. D.; Snaith, H. J.; Nicholas, R. J. *Energy Environ. Sci.* **2016**, *9*, 962–970.
- (8) Govinda, S.; Kore, B. P.; Bokdam, M.; Mahale, P.; Kumar, A.; Pal, S.; Bhattacharyya, B.; Lahnsteiner, J.; Kresse, G.; Franchini, C.; Pandey, A.; Sarma, D. D. *J. Phys. Chem. Lett.* **2017**, *8*, 4113–4121.
- (9) Wehrenfennig, C.; Eperon, G. E.; Johnston, M. B.; Snaith, H. J.; Herz, L. M. *Adv. Mater.* **2014**, *26*, 1584–1589.
- (10) Eames, C.; Frost, J. M.; Barnes, P. R. F.; O'Regan, B. C.; Walsh, A.; Islam, M. S. *Nat. Commun.* **2015**, *6*, 7497.
- (11) Brenner, T. M.; Egger, D. A.; Kronik, L.; Hodes, G.; Cahen, D. *Nat. Rev. Mater.* **2016**, *1*, 15007.
- (12) Miyata, A.; Mitioglu, A.; Plochocka, P.; Portugall, O.; Wang, J. T. W.; Stranks, S. D.; Snaith, H. J.; Nicholas, R. J. *Nat. Phys.* **2015**, *11*, 582–U94.
- (13) Xing, G. C.; Mathews, N.; Sun, S. Y.; Lim, S. S.; Lam, Y. M.; Gratzel, M.; Mhaisalkar, S.; Sum, T. C. *Science* **2013**, *342*, 344–347.
- (14) Ihly, R.; Dowgiallo, A. M.; Yang, M. J.; Schulz, P.; Stanton, N. J.; Reid, O. G.; Ferguson, A. J.; Zhu, K.; Berry, J. J.; Blackburn, J. L. *Energy Environ. Sci.* **2016**, *9*, 1439–1449.
- (15) Moser, J.-E. *Nat. Mater.* **2017**, *16*, 4–6.
- (16) Zhang, X.; Shen, J. X.; Wang, W. N.; Van de Walle, C. G. *ACS Energy Lett.* **2018**, *3*, 2329–2334.
- (17) Zheng, F.; Tan, L. Z.; Liu, S.; Rappe, A. M. *Nano Lett.* **2015**, *15*, 7794–7800.
- (18) Yu, Z. G. *J. Phys. Chem. Lett.* **2016**, *7*, 3078–3083.
- (19) Kepenekian, M.; Even, J. *J. Phys. Chem. Lett.* **2017**, *8*, 3362–3370.
- (20) Mosconi, E.; Etienne, T.; De Angelis, F. *J. Phys. Chem. Lett.* **2017**, *8*, 2247–2252.
- (21) Frohna, K.; Deshpande, T.; Harter, J.; Peng, W.; Barker, B. A.; Neaton, J. B.; Louie, S. G.; Bakr, O. M.; Hsieh, D.; Bernardi, M. *Nat. Commun.* **2018**, *9*, 1829.
- (22) Kepenekian, M.; Robles, R.; Katan, C.; Saponi, D.; Pedesseau, L.; Even, J. *ACS Nano* **2015**, *9*, 11557–11567.
- (23) Hutter, E. M.; Gelvez-Rueda, M. C.; Osherov, A.; Bulovic, V.; Grozema, F. C.; Stranks, S. D.; Savenije, T. J. *Nat. Mater.* **2017**, *16*, 115–120.
- (24) Kirchartz, T.; Rau, U. *J. Phys. Chem. Lett.* **2017**, *8*, 1265–1271.
- (25) Zhang, X.; Shen, J. X.; Van de Walle, C. G. *J. Phys. Chem. Lett.* **2018**, *9*, 2903–2908.
- (26) Zheng, C.; Yu, S. D.; Rubel, O. *Phys. Rev. Mater.* **2018**, *2*, 114604.
- (27) Niesner, D.; Wilhelm, M.; Levchuk, I.; Osvet, A.; Shrestha, S.; Batentschuk, M.; Brabec, C.; Fauster, T. *Phys. Rev. Lett.* **2016**, *117*, 126401.
- (28) Giovanni, D.; Ma, H.; Chua, J.; Gratzel, M.; Ramesh, R.; Mhaisalkar, S.; Mathews, N.; Sum, T. C. *Nano Lett.* **2015**, *15*, 1553–1558.
- (29) Hu, S. B.; Gao, H.; Qi, Y. T.; Tao, Y. X.; Li, Y. L.; Reimers, J. R.; Bokdam, M.; Franchini, C.; Di Sante, D.; Stroppa, A.; Ren, W. J. *Phys. Chem. C* **2017**, *121*, 23045–23054.
- (30) Chudnovsky, E. M. *Phys. Rev. Lett.* **1994**, *72*, 3433–3436.
- (31) Gennser, U.; Scheinert, M.; Diehl, L.; Tsujino, S.; Borak, A.; Falub, C. V.; Grutzmacher, D.; Weber, A.; Maude, D. K.; Scalari, G.; Campidelli, Y.; Kermarrec, O.; Bensahel, D. *Europhys. Lett.* **2006**, *74*, 882–888.
- (32) Garanin, D. A.; Chudnovsky, E. M. *Phys. Rev. X* **2011**, *1*, No. 011005.
- (33) Weber, O. J.; Charles, B.; Weller, M. T. *J. Mater. Chem. A* **2016**, *4*, 15375–15382.
- (34) Wang, T.; Daiber, B.; Frost, J. M.; Mann, S. A.; Garnett, E. C.; Walsh, A.; Ehrler, B. *Energy Environ. Sci.* **2017**, *10*, 509–515.
- (35) Liang, Z. R.; Zhang, S. H.; Xu, X. Q.; Wang, N.; Wang, J. X.; Wang, X.; Bi, Z. N.; Xu, G.; Yuan, N. Y.; Ding, J. N. *RSC Adv.* **2015**, *5*, 60562–60569.
- (36) Tang, X. F.; Brandl, M.; May, B.; Levchuk, I.; Hou, Y.; Richter, M.; Chen, H. W.; Chen, S.; Kahmann, S.; Osvet, A.; Maier, F.; Steinrueck, H. P.; Hock, R.; Matt, G. J.; Brabec, C. *J. Mater. Chem. A* **2016**, *4*, 15896–15903.
- (37) Dasgupta, U.; Bera, A.; Pal, A. J. *ACS Energy Lett.* **2017**, *2*, 582–591.
- (38) She, L.; Liu, M.; Zhong, D. *ACS Nano* **2016**, *10*, 1126–1131.
- (39) Endres, J.; Egger, D. A.; Kulbak, M.; Kerner, R. A.; Zhao, L.; Silver, S. H.; Hodes, G.; Rand, B. P.; Cahen, D.; Kronik, L.; Kahn, A. *J. Phys. Chem. Lett.* **2016**, *7*, 2722–2729.
- (40) Li, C.; Wei, J.; Sato, M.; Koike, H.; Xie, Z.-Z.; Li, Y.-Q.; Kanai, K.; Kera, S.; Ueno, N.; Tang, J.-X. *ACS Appl. Mater. Interfaces* **2016**, *8*, 11526–11531.
- (41) Kim, J.; Lee, S. H.; Lee, J. H.; Hong, K. H. *J. Phys. Chem. Lett.* **2014**, *5*, 1312–1317.
- (42) Yin, W. J.; Shi, T. T.; Yan, Y. F. *Appl. Phys. Lett.* **2014**, *104*, No. 063903.
- (43) Wang, S.; Sakurai, T.; Wen, W.; Qi, Y. *Adv. Mater. Interfaces* **2018**, *5*, 1800260.
- (44) Marchak, D.; Glozman, D.; Vinshtein, Y.; Jarby, S.; Lereah, Y.; Cheshnovsky, O.; Selzer, Y. *Nano Lett.* **2012**, *12*, 1087–1091.
- (45) Milan, D. C.; Villalvilla, J. M.; Diaz-Garcia, M. A.; Untiedt, C. *Appl. Phys. Lett.* **2013**, *102*, 163307.
- (46) Ohmann, R.; Ono, L. K.; Kim, H.-S.; Lin, H.; Lee, M. V.; Li, Y.; Park, N.-G.; Qi, Y. *J. Am. Chem. Soc.* **2015**, *137*, 16049–16054.
- (47) Myung, C. W.; Javaid, S.; Kim, K. S.; Lee, G. *ACS Energy Lett.* **2018**, *3*, 1294–1300.
- (48) Wiesendanger, R. *Rev. Mod. Phys.* **2009**, *81*, 1495–1550.
- (49) Ping, Y.; Zhang, J. Z. *J. Phys. Chem. Lett.* **2018**, *9*, 6103–6111.
- (50) Oudet, X.; Lochak, G. *J. Magn. Magn. Mater.* **1987**, *65*, 99–122.
- (51) Phuong, L. Q.; Nakaike, Y.; Wakamiya, A.; Kanemitsu, Y. *J. Phys. Chem. Lett.* **2016**, *7*, 4905–4910.
- (52) Warashina, T.; Nurmamat, M.; Miyamoto, K.; Shishidou, T.; Taniguchi, M.; Kimura, A.; Okuda, T. *Phys. Rev. B: Condens. Matter Phys.* **2016**, *94*, 241109.

**Supporting Information**

# Rashba Band Splitting in $\text{CH}_3\text{NH}_3\text{PbI}_3$ : An Insight from Spin-Polarized Scanning Tunneling Spectroscopy

*Abhishek Maiti,<sup>#</sup> Salma Khatun,<sup>#</sup> and Amlan J. Pal<sup>\*</sup>*

School of Physical Sciences, Indian Association for the Cultivation of Science, Jadavpur, Kolkata

700032, India

AUTHOR EMAIL ADDRESS: [sspajp@iacs.res.in](mailto:sspajp@iacs.res.in)



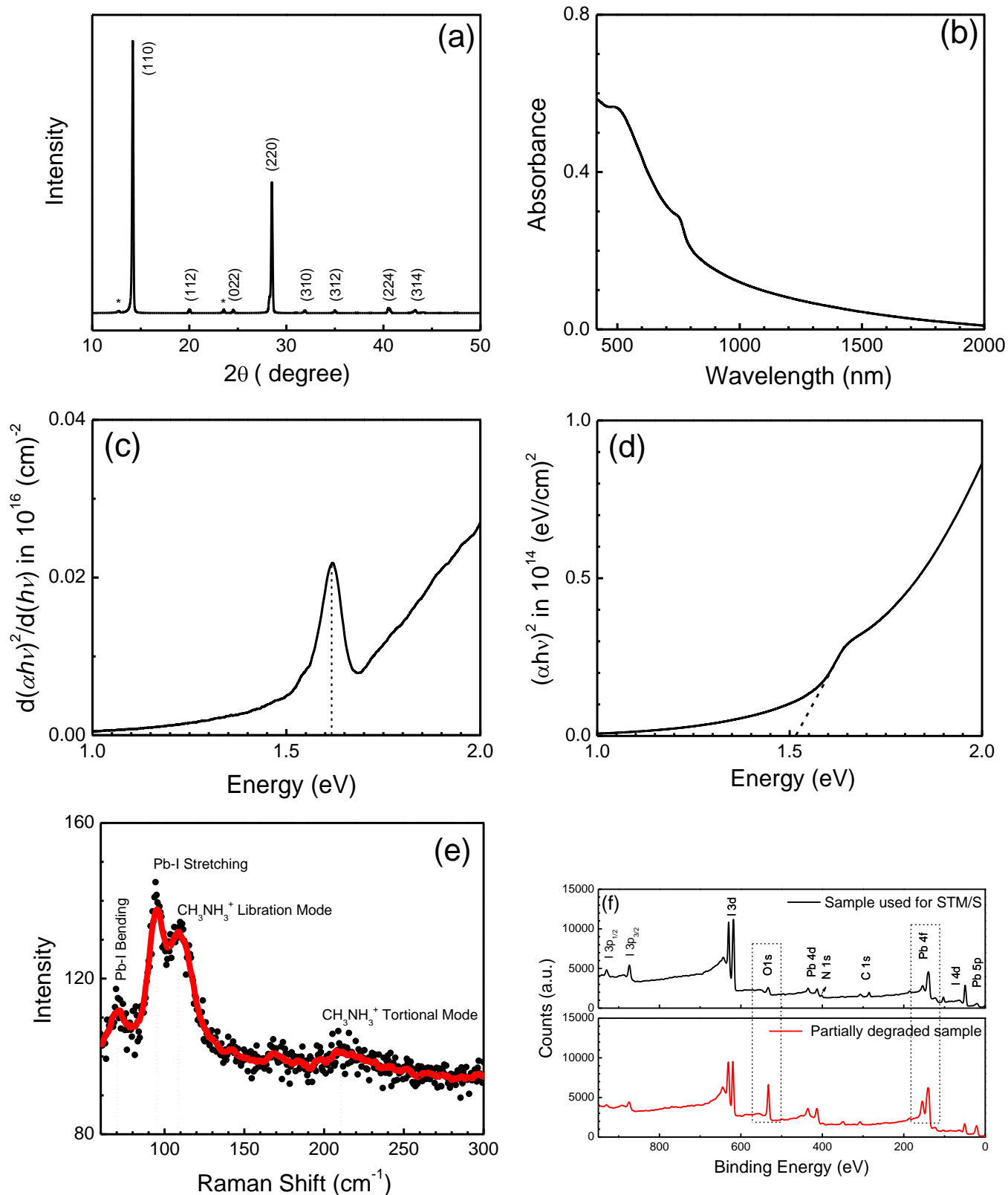


**Figure S1.** (a) XRD pattern, (b) optical absorption spectrum, (c)  $d[(\alpha h\nu)^2]/d(h\nu)$  versus energy plot of the material (d) Tauc plot estimating the optical band gap, (e) Raman spectrum of MAPbI<sub>3</sub> thin-film, and (f) XPS results of two films. In (a), lattice planes have been marked; the asterisks (\*) indicate patterns due to unreacted PbI<sub>2</sub>.



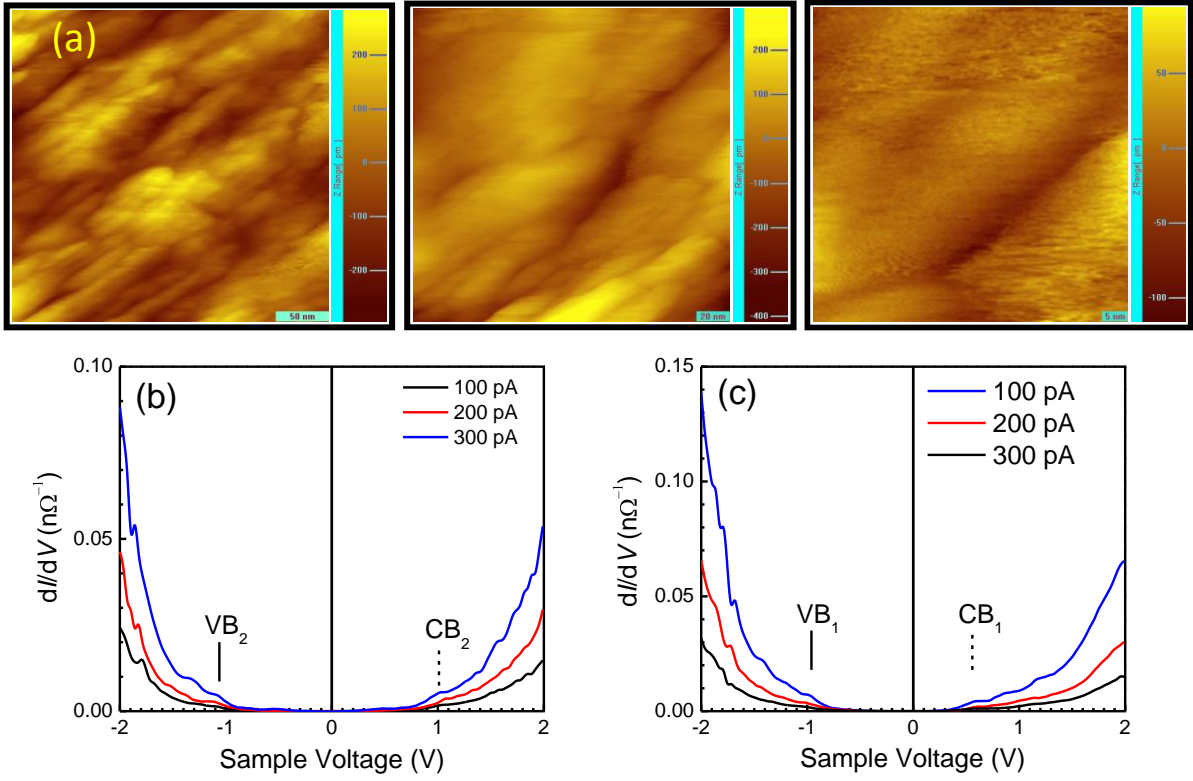


**Figure S2.** (a) SP-STM topographies of MAPbI<sub>3</sub> with a gradual decrease of scale bar. (b-c)  $dI/dV$  spectra with a chromium-coated tip to probe outer and inner pair of bands, respectively, considering three different tip-to-sample distances.

**Table S1.**  $L_z$ ,  $S_z$  and  $J_z$  of states during allowed tunneling processes between a chromium-coated tip and MAPbI<sub>3</sub> through a conservation of total angular momentum.

Tip			Sample			Change during allowed tunneling		
$L_z$	$S_z$	$J_z$	$L_z$	$S_z$	$J_z$	$\Delta L_z$	$\Delta S_z$	$\Delta J_z$
0	+1/2	+1/2	0	+1/2	+1/2	0	0	<b>0</b>
			+1	-1/2	+1/2	+1	-1	<b>0</b>
0	-1/2	-1/2	0	-1/2	-1/2	0	0	<b>0</b>
			-1	+1/2	-1/2	-1	+1	<b>0</b>

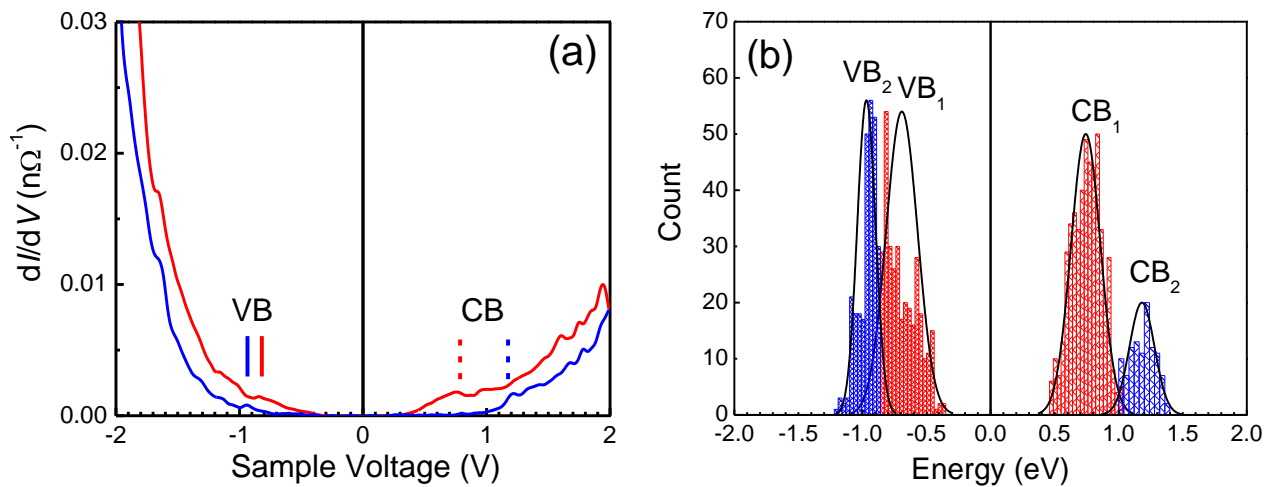


**Figure S3.** (a) Two representative  $dI/dV$  spectra of MAPbI<sub>3</sub> thin-films recorded with nickel tip and (b) histogram of band-energies.

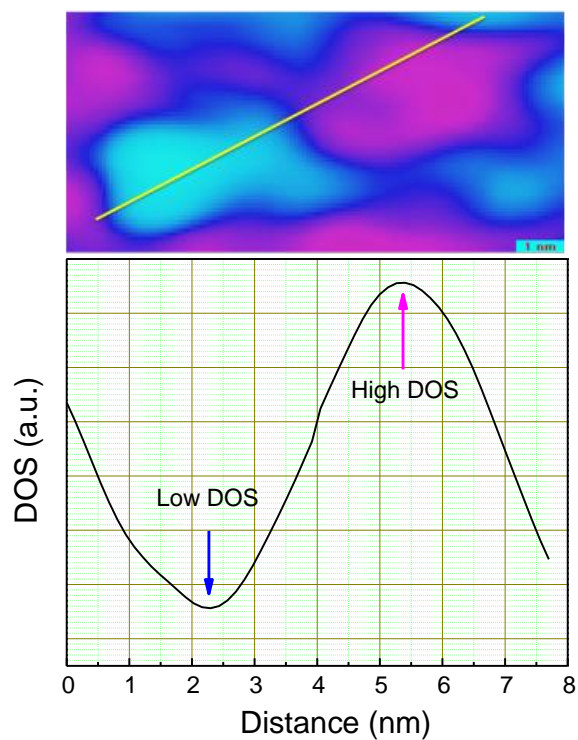


**Figure S4.** A section of  $dI/dV$  image and corresponding DOS-profile along a couple of domains.

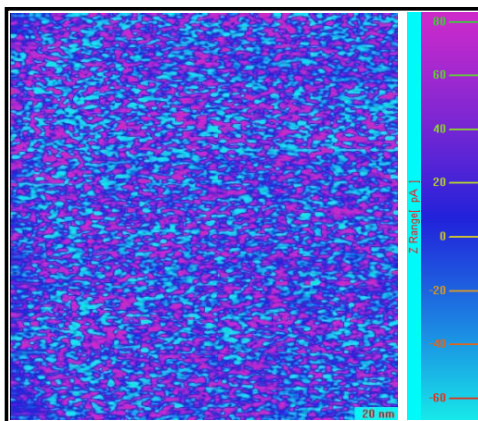


**Figure S5.**  $dI/dV$  images of a  $\text{MAPbI}_3$  ultrathin-film recorded with a chromium-coated tip to probe the inner VB at  $-0.88$  eV.

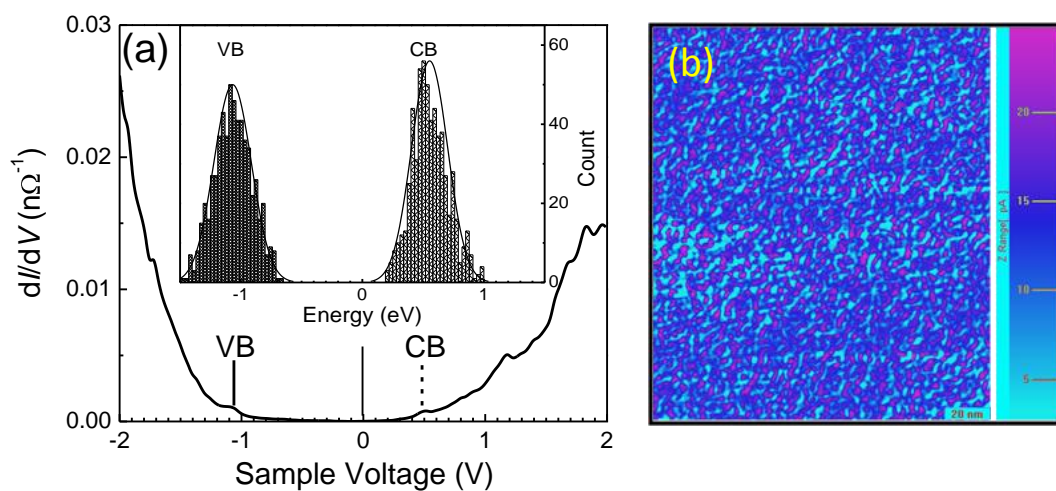


**Figure S6.** (a) A typical  $dI/dV$  spectra of  $\text{MAPbI}_3$  thin-films recorded with a chromium-coated tip near its Néel temperature along with a histogram of band-energies and (b) a  $dI/dV$  image recorded with the tip at  $0.54$  eV.

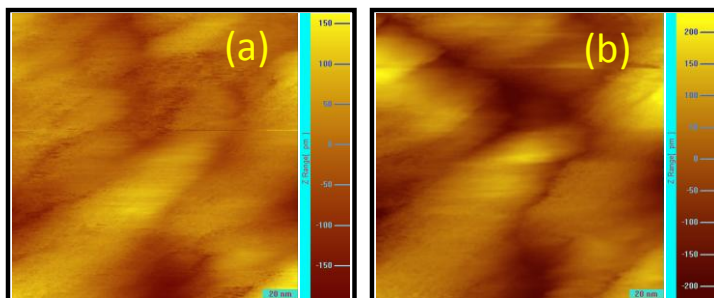


**Figure S7.** SP-STM topographic map of  $\text{MAPbI}_3$  film at the exact same area where  $dI/dV$  images were recorded with (a) chromium-coated tip (Figure 5a) and (b) Pt/Ir tip (Figure 5b).

# Effect of Cation Occupancy Ordering in Double Perovskites To Overcome Hurdles in Carrier Transport: Cs<sub>2</sub>AgBiBr<sub>6</sub> as a Case Study

Published as part of *The Journal of Physical Chemistry virtual special issue "D. D. Sarma Festschrift"*.

Abhishek Maiti and Amlan J. Pal\*

Cite This: *J. Phys. Chem. C* 2021, 125, 16324–16333

Read Online

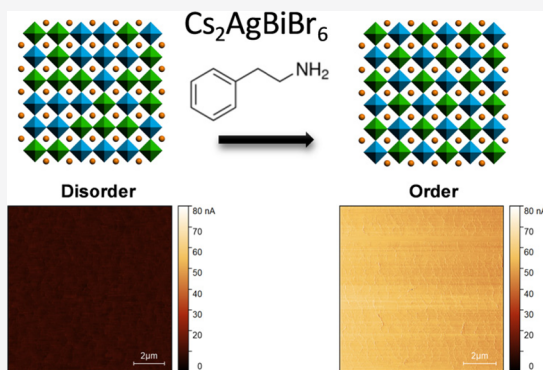
ACCESS |

Metrics & More

Article Recommendations

Supporting Information

**ABSTRACT:** In spite of environmental stability and toxic-free merits, the performance of double perovskite solar cells (Cs<sub>2</sub>AgBiBr<sub>6</sub> to be specific) has not excelled due to their large indirect band gap, low absorption of solar spectrum, and more importantly hurdles in carrier transport processes. A large number of intrinsic defects and self-trapped excitons (STE) appear in the double perovskite due to a disordered arrangement of Ag/Bi octahedra in the perovskite lattice. In this work, we investigate the role of cation ordering in Cs<sub>2</sub>AgBiBr<sub>6</sub> through the use of phenethylammonium bromide (PEABr) in the precursor toward suppression of STEs and deep-level defect states, such as antisite defects of Ag<sup>+</sup>/Bi<sup>3+</sup>, for an improved carrier conduction process. While cation ordering has been verified from X-ray diffraction studies and Raman spectroscopy, a reduction in the defect density and inhibition of STE formation have been witnessed from optical spectroscopy results. The transport gap, obtained from scanning tunneling spectroscopy and density of states spectra thereof, has been found to increase, suggesting the defect states to become suppressed. The effect of cation ordering toward an efficient carrier transport in the ordered lattice of Cs<sub>2</sub>AgBiBr<sub>6</sub> has been demonstrated by Kelvin probe force microscopy and conductive atomic force microscopy. Finally, a fair improvement in photovoltaic parameters was observed in devices based on the ordered double perovskite.



## 1. INTRODUCTION

Lead-free double perovskites have recently emerged as a potential alternative to the hybrid halide perovskite (CH<sub>3</sub>NH<sub>3</sub>PbI<sub>3</sub>) due to their environmental stability and toxic-free merits.<sup>1–4</sup> This new class of double perovskites (elpasolite) is designed through a combinatorial approach by substituting two bivalent lead ions (Pb<sup>2+</sup>) with a monovalent cation and a trivalent cation to balance the overall charge distribution in the compound.<sup>5–7</sup> These double perovskites possess a face-centered cubic rock-salt crystal structure (*Fm* $\bar{3}$ *m* space group) and corner-sharing octahedra of the two cations in alternate. This group of materials has received widespread attention as promising candidates for optoelectronic applications due to the low effective mass of electrons and holes, a decent carrier lifetime, micro-sized grains, high crystallinity, and overall environmental stability.<sup>2,4,8–10</sup>

In the class of lead-free double perovskites, silver–bismuth combination (Cs<sub>2</sub>AgBiBr<sub>6</sub>) with alternate [AgBr<sub>6</sub>]<sup>5–</sup> and [BiBr<sub>6</sub>]<sup>3–</sup> octahedra has received initial importance for solar cell applications. The photovoltaic performance of Cs<sub>2</sub>AgBiBr<sub>6</sub> has however not surpassed (compared to CH<sub>3</sub>NH<sub>3</sub>PbI<sub>3</sub>) primarily due to its large indirect band gap and thereby reduced absorption of visible light and more importantly a correlated effect of low carrier mobility and inefficient carrier

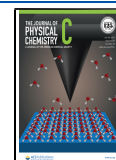
transport through the perovskite lattice.<sup>11,12</sup> Although the band gap can be reduced through material engineering upon introduction of suitable dopants,<sup>13,14</sup> a way to overcome the hurdles in the charge transport process remains a challenge.

In general, cation ordering in double perovskites plays an important role in the emergence of novel electronic and magnetic properties.<sup>15–17</sup> In an ideally ordered Cs<sub>2</sub>AgBiBr<sub>6</sub> double perovskite structure, each [AgBr<sub>6</sub>]<sup>5–</sup> octahedron should be surrounded by six corner-sharing [BiBr<sub>6</sub>]<sup>3–</sup> octahedra and vice versa.<sup>2,18</sup> Due to the solution-based synthesis route of the double perovskite from cation precursors, namely, AgBr and BiBr<sub>3</sub>, formation of a disordered phase with random arrangements of [AgBr<sub>6</sub>]<sup>5–</sup> and [BiBr<sub>6</sub>]<sup>3–</sup> octahedra is inevitable and energetically favorable as well.<sup>19,20</sup> In a disordered lattice, [BiBr<sub>6</sub>]<sup>3–</sup> and [AgBr<sub>6</sub>]<sup>5–</sup> octahedra are located randomly, thus enhancing the electrostatic repulsion between two neighboring

Received: May 29, 2021

Revised: July 4, 2021

Published: July 19, 2021





octahedra locally and thereby distorting the crystalline structure. Under such a situation, due to a strong electron–phonon interaction, the photogenerated charge carriers would be self-trapped at the distorted states arising out from a large Jahn–Teller (JT)-like distortion of the disordered octahedra.<sup>21</sup> Hence, self-trapped excitons (STEs) are formed leading to a poor charge transport in the double perovskite lattice.<sup>20,22</sup> In addition, a disorder in cation occupancies leads to silver at bismuth ( $\text{Ag}_{\text{Bi}}$ ) antisite defects with deep transition levels inside the band gap, providing recombination pathways for photogenerated carriers.<sup>1,23</sup>

In view of this, achieving cation ordering in the lattice of double perovskites would be a promising pathway to suppress formation of STEs and midgap defect states. Through first-principles calculations, Yang et al. proposed that a very high temperature of synthesis can induce better ordering in the lattice;<sup>19</sup> however, such a strategy is almost improbable to be applied in practice. In double perovskite oxides, incorporation of different ligands/polymers as site-selective binders has been followed to achieve spontaneous cation ordering in their thin films (polymer-assisted deposition).<sup>24,25</sup> A similar strategy has been used in double perovskite single crystals ( $\text{Cs}_2\text{AgBiBr}_6$ ) toward control over in situ cation ordering through incorporation of phenethylammonium bromide (PEABr), which has been considered previously for applications in X-ray detectors;<sup>20</sup> with the addition of PEABr in the precursor, a selective coordination between functionalized phenyl and ammonium ions with the two inorganic cations ( $\text{Ag}^+$  and  $\text{Bi}^{3+}$ , respectively) promotes better ordering in the lattice.<sup>20</sup>

With this background information, we have introduced the process of cation ordering in solar cells based on double perovskites. We envisaged that an improved cation ordering in the double perovskite, upon suppression of STE formation and passivation of defect states, would facilitate charge transport and thereby would improve photovoltaic parameters in devices based on the perovskite. While the effect of cation ordering in suppressing STE formation has been investigated by evaluating the Huang–Rhys factor ( $S$ ) as obtained from a combination of electronic absorption spectroscopy, photoluminescence spectroscopy, and Raman spectroscopy, the transport gap obtained from scanning tunneling spectroscopy (STS) and density of states (DOS) spectra evidenced that the ordering process suppressed the formation of deep-level defects.

## 2. MATERIALS AND METHODS

**2.1. Materials.** Cesium bromide ( $\text{CsBr}$ , 99.9%), silver bromide ( $\text{AgBr}$ , 99.9%), bismuth bromide ( $\text{BiBr}_3$ , 99.9%), hydrobromic acid ( $\text{HBr}$ , 48 wt % in water), hydrofluoric acid ( $\text{HF}$ , 48 wt % in water), dimethyl sulfoxide ( $\text{DMSO}$ , 99.9%), 1-phenylethylamine (PEA), anhydrous  $N,N$ -dimethylformamide (DMF, 99.8%), 2-propanol, chlorobenzene (99%), poly(3,4-ethylenedioxythiophene) polystyrene sulfonate (PEDOT:PSS), and bathocuproine (BCP, 96%) were purchased from Sigma-Aldrich Chemical Co. Phenyl-C61-butyric acid methyl ester (PCBM, 99%) was procured from M/s SES Research, Houston, TX. Except  $\text{HBr}$ ,  $\text{HF}$ , PEA, and PEDOT:PSS, rest of the compounds were stored in a nitrogen-filled glove box with both oxygen and moisture levels below 0.1 ppm.

**2.2. Synthesis of Pristine  $\text{Cs}_2\text{AgBiBr}_6$  Crystallites.** A crystalline powder of  $\text{Cs}_2\text{AgBiBr}_6$  was prepared by following a standard procedure as proposed by Igbari et al.<sup>26</sup> In this process, 213 mg of  $\text{CsBr}$ , 94 mg of  $\text{AgBr}$ , and 225 mg of  $\text{BiBr}_3$

(2:1:1) were first dissolved in 20 mL of  $\text{HBr}$ . The solution was stirred in a fume hood at 125 °C for almost 3 h until half of the solvent evaporated. The as-prepared solution was then cooled overnight to room temperature in a dark environment. Orange-colored crystalline powders of  $\text{Cs}_2\text{AgBiBr}_6$  were finally obtained by decanting the excess solution followed by drying in an oven at 50 °C for 24 h.

**2.3. Ordered  $\text{Cs}_2\text{AgBiBr}_6$  Crystallites.** Following a reported procedure,<sup>27</sup> PEABr powder was added to the  $\text{HBr}$  solution of desired concentrations (2, 4, 6, 8, and 10 mol %) and the abovementioned synthesis route was followed.

**2.4. Synthesis of  $\text{PEA}_4\text{AgBiBr}_8$  Crystallites.** This material for control experiments was synthesized through the addition of PEABr,  $\text{AgBr}$ , and  $\text{BiBr}_3$  in 20 mL of  $\text{HBr}$ .

**2.5. Casting of  $\text{Cs}_2\text{AgBiBr}_6$  Thin Films.** The  $\text{Cs}_2\text{AgBiBr}_6$  crystalline powder was dissolved in a stoichiometric (1:1) mixture of DMF and DMSO at 70 °C to form a light-yellow precursor solution (0.8 M), which was spun on properly cleaned substrates inside a glove box at 1000 rpm for 10 s followed by ramping to 3500 rpm for 30 s. An antisolvent treatment was performed by adding 0.5 mL of chlorobenzene on the film at the 20th second of the spin-coating process. After that, the film was rapidly moved to a low-pressure antechamber of the glove box followed by pumping for aging. Finally, the films were annealed for a while (5 min) at an optimized temperature of 280 °C inside the glove box. For STS studies, ultrathin films were cast on highly doped Si(111) substrates (arsenic-doped,  $n$ -type) having a resistivity of 3–10  $\text{m}\Omega\cdot\text{cm}$  at a higher rpm (4500 rpm for 30 s); the silicon substrates were treated with Piranha solution and HF prior to use through a standard protocol for removing contaminants<sup>28</sup> (Warning: Piranha attacks organics, including most plastics. It will react violently with polyethylene and polypropylene tweezers and containers. It will also react violently with organic solvents such as acetone and isopropanol).

**2.6. Characterization of  $\text{Cs}_2\text{AgBiBr}_6$  Thin Films.** X-ray diffraction (XRD) patterns of thin films based on the ordered and disordered double perovskites,  $\text{Cs}_2\text{AgBiBr}_6$ , were recorded with a Rigaku SmartLab X-ray diffractometer (Cu  $K\alpha$  radiation,  $\lambda = 1.54 \text{ \AA}$ ). Raman spectra were recorded with a Horiba Jobin Yvon Raman triple-grating spectrometer system (model number T64000); a diode-pumped solid-state laser with a wavelength of 532.0 nm was used as a source of excitation. Optical absorption and photoluminescence (PL) spectra of the thin films were recorded using a double-beam Shimadzu UV–vis spectrophotometer (UV 2550) and Horiba Jobin Yvon spectrofluorometer (Fluoromax) with a 450 W light source, respectively. X-ray photoelectron spectroscopy (XPS) spectra of the cation-ordered and cation-disordered  $\text{Cs}_2\text{AgBiBr}_6$  were recorded with an X-ray photoelectron spectrometer (Omicron Nanotechnology).

Band edges were determined by STS using a scanning tunneling microscope (STM) (Nanosurf easyScan 2 STM). For such measurements, atomically pointed tips were formed through an oblique cut of a Pt/Ir (80%:20%) wire having a 0.25 mm diameter. As a tip-approach condition, a current of 1 nA was applied at a tip voltage of 2.0 V. Morphology characterization, imaging of the surface potential, and mapping of local conductivity of the films were recorded through atomic force microscopy (AFM), Kelvin probe force microscopy (KPFM), and conducting-AFM (C-AFM) images with a Nanosurf Flex AFM system using NCLR (aluminum-coated), Multi75E-G (Pt/Cr-coated), and PPP-CONTPt (Pt/Ir-

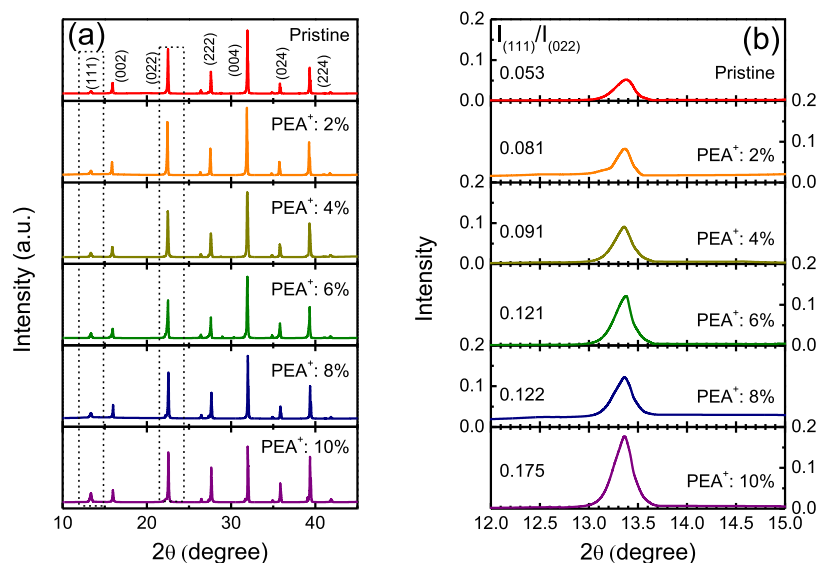


**Figure 1.** (a) Evolution of XRD patterns of  $\text{Cs}_2\text{AgBiBr}_6$  upon addition of  $\text{PEA}^+$ . (b) Peak representing the (111) plane with respect to the intensity of the (022) plane.

coated) cantilever tips, respectively. While the localized conductivity mapping was performed in the contact mode, the other measurements were carried out in the noncontact mode. KPFM studies were carried out in the amplitude-modulated single-pass mode. In the single-pass mode, the cantilever scans over every line while simultaneously recording topography and contact potential difference (CPD); the amplitude of cantilever oscillation was kept small so that the tip remains closer to the surface resulting in better sensitivity and resolution in the KPFM measurements. The work function of the tip was calibrated ( $4.73 \pm 0.01$  eV) with respect to a standard, namely, highly oriented pyrolytic graphite before the measurements.

### 2.7. Fabrication and Characterization of Devices.

Heterojunction solar cells were fabricated on indium tin oxide (ITO)-coated glass substrates, which were first cleaned following a usual procedure and treated with UV–ozone for 20 min. After that, a layer of PEDOT:PSS was spun at 3000 rpm for 60 s followed by annealing at  $150^\circ\text{C}$  to form a hole transport layer (HTL). The substrates were then transferred to the glove box. A layer of the double perovskite was then cast using the previously mentioned film-deposition process. As an electron transport layer (ETL), PCBM was spun at 2500 rpm for 30 s from a stock solution in chlorobenzene (20 mg/mL) and annealed at  $100^\circ\text{C}$ . Finally, an ultrathin film of BCP dissolved in IPA solution (0.5 mg/mL) was cast at 4000 rpm for 30 s as a buffer layer, which was annealed at  $100^\circ\text{C}$ . The process of device fabrication was completed by depositing 100 nm-thick aluminum (Al) strips (orthogonal to the ITO strips) as the top electrode through thermal evaporation in a vacuum chamber ( $10^{-6}$  mbar) fitted to the glove box. The active area of the cells was  $10\text{ mm}^2$ . Current–voltage ( $I$ – $V$ ) characteristics of the sandwiched heterojunction devices were recorded with a Keithley 2636A electrometer under dark and 1 sun illumination conditions. All the measurements were carried out in an inert environment of the glove box. Contacts were made with pressure-loaded gold probes with the respective electrodes. A 300 W solar simulator (Newport Oriol Sol3A) coupled with an AM1.5 filter was used as a source of illumination.

## 3. RESULTS AND DISCUSSION

### 3.1. Introducing Cation Ordering in $\text{Cs}_2\text{AgBiBr}_6$ through $\text{PEA}^+$ Incorporation.

The poor solubility of the silver salt in polar aprotic solutions such as DMF or DMSO has been a major concern to achieve high-quality and phase-pure  $\text{Cs}_2\text{AgBiBr}_6$  perovskite thin films.<sup>18,29</sup> Yang and co-workers have recently developed a new strategy to overcome this drawback;  $\text{Cs}_2\text{AgBiBr}_6$  was first formed in HBr solution followed by spin casting of the compound in a DMF:DMSO solution.<sup>30</sup> Igbari et al. demonstrated the advantages of this method over vacuum deposition for forming phase-pure and near-stoichiometric  $\text{Cs}_2\text{AgBiBr}_6$  thin films.<sup>26</sup> However, during the synthesis of  $\text{Cs}_2\text{AgBiBr}_6$  following the abovementioned methods, formation of disordered arrangements of silver and bismuth octahedra in the perovskite compound and silver at bismuth ( $\text{Ag}_{\text{Bi}}$ ) antisite defects were common and energetically favorable even under an excess HBr-rich growth condition.<sup>31</sup> Such disordered arrangements of  $\text{Ag}^+$  and  $\text{Bi}^{3+}$  in the perovskite compound prompt a large JT-like distortion in the lattice leading to a strong electron–phonon interaction and simultaneous self-trapping of excitons in the distorted  $\text{Cs}_2\text{AgBiBr}_6$ .<sup>20,21,32</sup> Under this circumstance, both generation and transport of charge carriers get impeded resulting in a poor short-circuit current density in solar cells.

In this direction, incorporation of  $\text{PEA}^+$  as ligands during the synthesis can be an effective strategy to promote cation occupancy ordering in the system. According to previous reports, the ligand activity of  $\text{PEA}^+$  can be used to bind  $\text{Ag}^+$ / $\text{Bi}^{3+}$  in a regular arrangement as phenyl and ammonium groups of  $\text{PEA}^+$  possess the ability to make selective coordination with  $\text{Bi}^{3+}$  and  $\text{Ag}^+$ , respectively.<sup>20</sup> To state in the details, the  $\pi$  electron clouds of the phenyl group present in  $\text{PEA}^+$  prefer to form bonds with the  $\sigma^*$  orbital of bismuth halide due to a push electron-induced mechanism; on the other hand, the ammonium group of  $\text{PEA}^+$  bonds with  $\text{Ag}^+$  through a noncovalent intermolecular force to form a  $\text{PEA-AgBr}_2$  complex.<sup>33</sup> Such a preferred linkage occurs since the distance between the phenyl and ammonium groups is about  $6.4\text{ \AA}$  in  $\text{PEA}^+$ , which is similar to the distance between  $\text{Ag}^+$  and  $\text{Bi}^{3+}$  ions in the  $\text{Cs}_2\text{AgBiBr}_6$  lattice ( $6.5\text{ \AA}$ ).<sup>20</sup> Consequently,  $\text{Ag}^+$

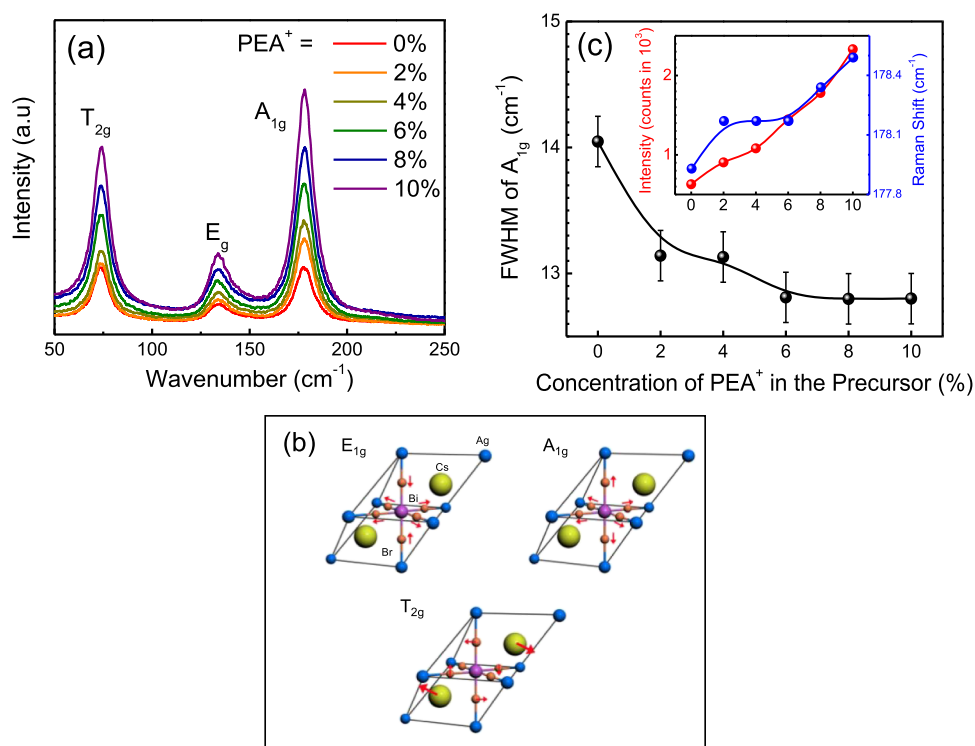


**Figure 2.** (a) Raman spectra of Cs<sub>2</sub>AgBiBr<sub>6</sub> upon addition of different PEA<sup>+</sup> contents. (b) Schematic representation of the Raman modes. (c) Comparison of FWHM of the A<sub>1g</sub> mode as a function of PEA<sup>+</sup> concentration; the inset shows the intensity and Raman shift of the mode.

and Bi<sup>3+</sup> in the lattice would be arranged in a regular fashion through the selective coordination ability of the PEA<sup>+</sup> ligand to finally form an ordered double perovskite phase. However, after the formation of ordered Cs<sub>2</sub>AgBiBr<sub>6</sub>, the ligands would still be attached to the compound with coordinate bonds.<sup>34,35</sup> Upon dissolution of the ordered double perovskite crystals in a DMF/DMSO mixed solvent, as a step for film casting, these PEA<sup>+</sup> ligands would remain in the solution. During the recrystallization process, the ligands would further bind the Ag<sup>+</sup> and Bi<sup>3+</sup> ions to promote ordering. Finally, these PEA<sup>+</sup> ligands would desorb upon annealing at a high temperature (280 °C) leaving an ordered arrangement of Ag/Bi octahedra in the perovskite thin films. It may be stated that the quantity of PEA<sup>+</sup> ligands that can be harvested from the surface may not match the actual feed ratio used during the growth of the crystals. This interesting scientific issue can further be addressed by modeling the reaction kinetics, which is beyond the scope of this work.

**3.2. Structural Characterization to Study Cation Ordering in Cs<sub>2</sub>AgBiBr<sub>6</sub>.** Evaluation of XRD patterns is a straightforward and well-documented approach to quantitatively estimate the cation ordering in a double perovskite.<sup>36</sup> According to the previous report, Cs<sub>2</sub>AgBiBr<sub>6</sub> belongs to the *Fm* $\bar{3}$ *m* space group (FCC);<sup>2</sup> the crystal structure shows that both the (111) and (022) planes do not follow the conventional extinction law. However, in the primary cubic structure, the (111) plane would be extinctive with respect to the extinction law.<sup>36</sup> Under the circumstances, in the case of a complete disorder of Bi<sup>3+</sup> and Ag<sup>+</sup>, the (111) plane can be considered an extinctive one. Hence, evaluation of two superlattice reflections with the adjacent normal lattice reflection, namely, the intensities of the (111) and (022) planes is a straightforward method to study the extent of ordering in the double perovskite; a higher ratio between the

intensities of the (111) and (022) planes, (*I*<sub>111</sub>/*I*<sub>022</sub>), indicates a better ordering of the Ag/Bi octahedra and presence of fewer antisite defects as well.<sup>36</sup> Figure 1a shows the evolution of XRD patterns with an increasing concentration of PEA<sup>+</sup>. As shown in Figure 1b, the intensity of the (111) plane relative to the (022) plane could be seen to increase with an increase of the PEA<sup>+</sup> concentration, supporting an improvement of ordering in silver and bismuth occupancies. The intensity ratio increasing with the PEA<sup>+</sup> concentration is presented in Figure S1 of the Supporting Information. Moreover, the full width at half maximum (FWHM) of the pattern referring the (111) plane could be found to decrease upon an increase in the PEA<sup>+</sup> concentration; such a behavior implies enhanced crystallinity and lesser density of Ag<sub>Bi</sub> defects.<sup>20</sup> The observed change in the XRD patterns of perovskite thin films is consistent with the report on single crystals as well.<sup>20</sup>

It is necessary to mention that doping of PEA<sup>+</sup> in the lattice can be ruled out based on the XRD and XPS studies. Although it stays on the surface of the crystallites through coordination bonds, its presence in the final thin films is unlikely due to the high annealing temperature. In addition, formation of PEA<sup>+</sup>-based lower-dimensional systems at the grain boundaries has also been ruled out.<sup>37</sup> In this direction, we have recorded the XRD patterns of PEA<sub>4</sub>AgBiBr<sub>8</sub> (Figure S2a of the Supporting Information); in the XRD patterns of Cs<sub>2</sub>AgBiBr<sub>6</sub> (Figure 1a), we did not observe any characteristic peaks of PEA<sub>4</sub>AgBiBr<sub>8</sub>, evidencing the absence of PEA<sup>+</sup> in the double perovskite. A similar conclusion can also be drawn from the Raman spectrum of PEA<sub>4</sub>AgBiBr<sub>8</sub> (Figure S2b of the Supporting Information), which has been discussed in a latter section. In addition, no significant change has been observed in the XPS survey spectra (Figure S3a of the Supporting Information) of the ordered and disordered perovskites, confirming the absence of PEA<sup>+</sup> in the ordered lattice. With Cs 3d peaks

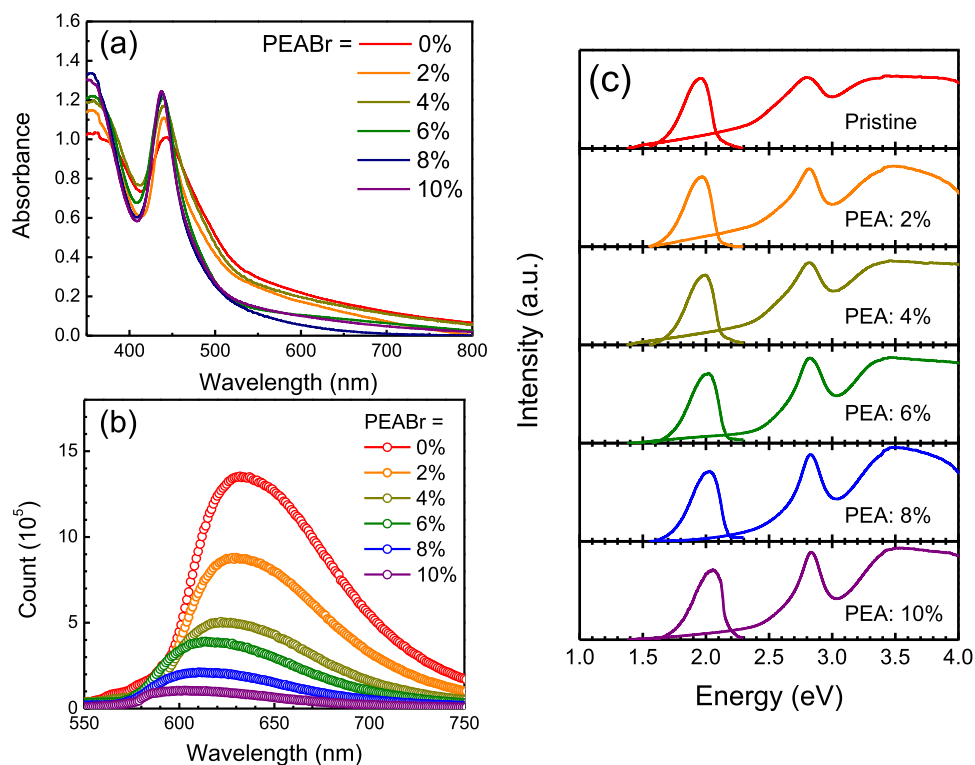


**Figure 3.** Evolution of the (a) absorption and (b) emission spectra. (c) Derivation of Stokes shift as a function of  $\text{PEA}^+$  concentration (with normalized PL spectra).

being intense among others, we have presented the high-resolution spectra of Cs 3d in the ordered and disordered phase of the perovskite; the presence of PEA ions in the films would have affected the binding energies due to a change in the chemical environment. However, the peaks did not show any shift upon cation ordering; this indicated the absence of PEA ions in the thin films (Figure S3b of the Supporting Information).

**3.3. Influence of Cation Ordering on the Raman Mode.** We have studied the Raman modes of the ordered and disordered  $\text{Cs}_2\text{AgBiBr}_6$  (Figure 2a). Along with the investigation of cation ordering, phonon energies can also be calculated from such measurements. The room temperature Raman spectrum of the pristine disordered system was dominated by a peak at  $180\text{ cm}^{-1}$ , which is assigned to a longitudinal optical (LO) phonon mode  $A_{1g}$  coupled with the symmetric stretching vibration of Br around a Bi atom. In addition, two less intense peaks were also observed at  $139$  and  $74\text{ cm}^{-1}$ . The peak at  $139\text{ cm}^{-1}$  is considered as the  $E_g$  mode related to the asymmetric stretching vibrations of Br around a Bi atom. On the other hand, the  $T_{2g}$  mode appearing at  $74\text{ cm}^{-1}$  can be correlated to the scissoring motion of Cs around Br atoms.<sup>38,39</sup> Schematic representations of the vibrations are shown in Figure 2b. Although the influence of  $\text{PEA}^+$ -induced ordering was found to be significant for all the Raman modes, based on conventional practice, we have limited our discussion only to the most intense  $A_{1g}$  mode at  $180\text{ cm}^{-1}$  since energy of the LO phonon was considered for further discussion in a latter section.

Figure 2c shows the intensity, FWHM, and also energy of the peak as a function of  $\text{PEA}^+$  concentration. A sharp increase of the peak intensity and narrowing of the peaks were clearly observed; the figure also shows a little shift of the LO mode

toward a higher energy with an increase in the  $\text{PEA}^+$  concentration. Such an observation has also been found in some other quaternary semiconductor systems (kesterites) supporting the inference of an increasing order in the cation occupancy.<sup>40</sup> We also add that similar to XRD studies, the Raman spectrum of  $\text{Cs}_2\text{AgBiBr}_6$  did not contain any modes of  $\text{PEA}_4\text{AgBiBr}_8$  (Figure S2b of the Supporting Information), confirming the absence of  $\text{PEA}^+$  in the ordered lattice.

**3.4. Optical Characteristics and Suppression of STE Formation in Cation-Ordered  $\text{Cs}_2\text{AgBiBr}_6$ .** We then proceeded to record the optical absorption spectra of the disordered and ordered thin films as a function of  $\text{PEA}^+$  concentration. All the compounds showed a characteristic peak at  $\sim 440\text{ nm}$  confirming the formation of the double perovskite (Figure 3a).<sup>1,11</sup> A little blue shift was observed with increasing  $\text{PEA}^+$  concentration that could be correlated to an enhanced cation ordering in the double perovskite. A similar observation was previously reported in the literature in other semiconductors where the light absorption threshold was significantly higher in an ordered system than that in a disordered one and an increase in the band gap upon a decrease in the defect density was observed.<sup>19,23,41</sup> The optical band gaps of all the compounds were estimated from their Tauc plots (Figure S4 of the Supporting Information). The shrinkage of Urbach energy ( $E_U$ ) also supports the concept of lesser defect concentrations (Figure S5 of the Supporting Information) through an enhanced cation ordering of the Ag/Bi octahedra.<sup>42</sup>

A detailed analysis of STE formation and  $\text{PEA}^+$ -induced cation ordering in the lattice has been carried out from the optical characteristics. The broad PL (Figure 3b) and a large Stokes shift between optical absorption and PL spectra can be considered as characteristic signatures of a disordered double



perovskite (Figure 3c). Formation of STEs due to distortion can intensively constrain exciton dissociation and thereby hinder carrier transport.<sup>20,21</sup> In this section, we have studied the effect of increasing  $\text{Ag}^+/\text{Bi}^{3+}$  cation ordering on reducing formation of STE states as a function of  $\text{PEA}^+$  concentration. The effect of a strong electron–phonon coupling responsible for a large distortion of the crystalline lattice can be quantitatively measured using the Huang–Rhys factor ( $S$ ), which is derived from the following equation<sup>39,43</sup>

$$\text{Stokes shift} = (2S - 1)E_{\text{Phonon}}$$

where  $E_{\text{Phonon}}$  represents the energy of the most intense  $A_{1g}$  mode. As presented in Table 1, the derived value of  $S$  has been

**Table 1. Calculation of Huang–Rhys Factor ( $S$ ) with  $E_{\text{Phonon}} = 22.1 \pm 0.1$  meV as a Function of  $\text{PEA}^+$  Concentration**

$\text{PEA}^+$ concentration	Stokes shift (meV)	Huang–Rhys factor ( $S$ )
0	$840 \pm 5$	$19.6 \pm 0.2$
2	$840 \pm 5$	$19.5 \pm 0.2$
4	$830 \pm 5$	$19.3 \pm 0.2$
6	$810 \pm 5$	$18.8 \pm 0.2$
8	$800 \pm 5$	$18.6 \pm 0.2$
10	$770 \pm 5$	$17.9 \pm 0.2$

found to decrease with an increasing concentration of  $\text{PEA}^+$ . Such lowering of  $S$  can be considered a direct consequence of restricted formation of STEs due to high ordering in cation occupancies.<sup>20</sup>

**3.5. Band Edge and Transport Gap Characterization by STS.** The influence of cation ordering on the band edges of  $\text{Cs}_2\text{AgBiBr}_6$  and thereby their transport gap has been studied by STM/S characterization. The valence band (VB) and conduction band (CB) edges with respect to Fermi energy ( $E_F$ ) of the double perovskite in its disordered and ordered phases could be located from the differential tunnel

conductance spectra ( $dI/dV$ ) or DOS. Since the bias was applied to the tip, the first peak in the positive voltage region of the DOS spectrum closest to 0 V indicated extraction of electrons and hence energy of the VB edge. Likewise, the energy of the first peak in the negative voltage region of the  $dI/dV$  plot implied injection of electrons to the compound and hence location of the CB edge.<sup>23</sup> The characteristic  $dI/dV$  spectra of the disordered and ordered double perovskite compounds are shown in Figure 4a. As STS was employed in an extremely localized mode,  $dI/dV$  spectra were measured at numerous regions on the surface of each ultrathin film. From each of these measurements, VB and CB edges were located to finally obtain a histogram of their energies (Figure S6 of the Supporting Information). The edges obtained from the peaks of histograms inferred  $p$ -type conductivity in the double perovskite as their VB could be found to be closer to  $E_F$  (at 0 V) compared to the relative energy of the CB. Such a  $p$ -type nature of the double perovskite has been previously predicted by considering the presence of acceptor-like silver vacancies ( $V_{\text{Ag}}$ ) and silver at bismuth ( $\text{Ag}_{\text{Bi}}$ ) antisite defects having a low formation energy.<sup>23</sup>

Band edges of the double perovskites can be seen to be heavily influenced by the extent of cation ordering in the compound. Upon formation of a  $\text{PEA}^+$ -induced ordered phase, the VB edge was found to move away from the Fermi energy leading to an increase in the transport gap; the CB edge remained almost unchanged. A much larger change in the VB compared to the CB can be explained by considering the involvement of different atomic orbitals in forming the two bands. In the  $\text{Cs}_2\text{AgBiBr}_6$  double perovskite, the unoccupied CB is generally formed with  $\text{Bi}(6p)$  orbitals, whereas the VB is composed of a mixture of  $\text{Br}(4p)$ ,  $\text{Ag}(4d)$ , and  $\text{Bi}(6p)$  orbitals. A  $\text{PEA}^+$ -induced ordering would hence promote hybridization between the  $\text{Ag}(4d)$  and  $\text{Bi}(6p)$  orbitals leading to a significant increase in the overlap integral and a rise in the occupied VB state without affecting the CB energy.<sup>23,44</sup> The  $p$ -type nature of

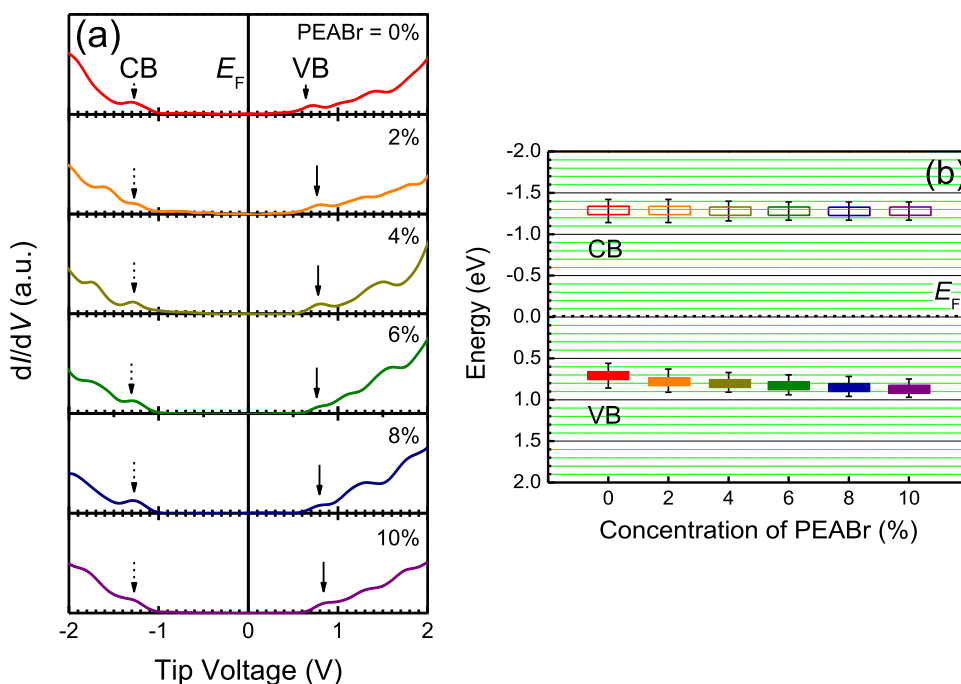


**Figure 4.** (a)  $dI/dV$  versus tip voltage plots. (b) Band edges as a function of  $\text{PEA}^+$  concentration.

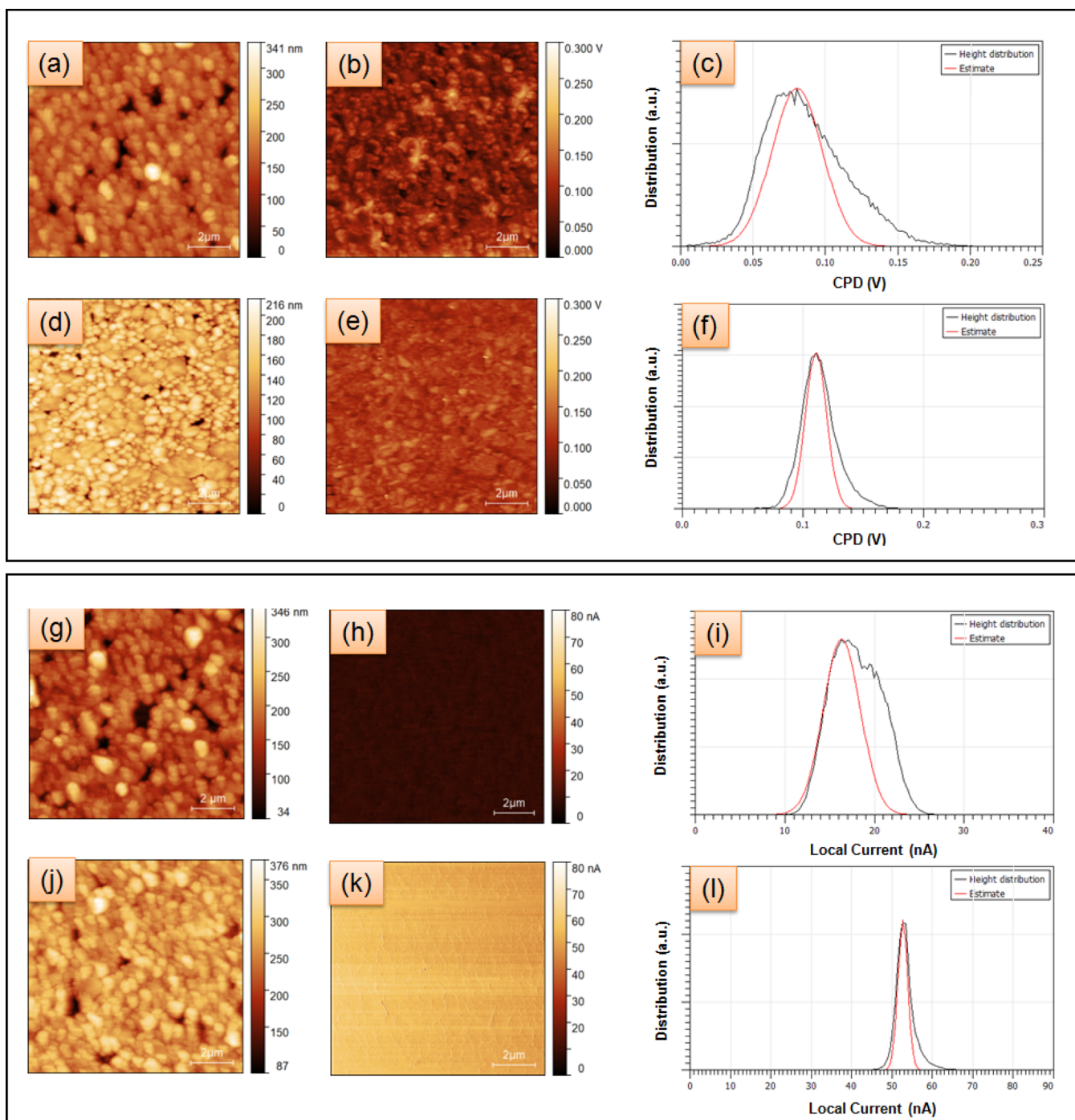


**Figure 5.** Upper panel: (a) topography, (b) CPD map, and (c) statistical distribution of CPD for the disordered  $\text{Cs}_2\text{AgBiBr}_6$  thin films. Such plots for the ordered  $\text{Cs}_2\text{AgBiBr}_6$  films are shown in panels (d–f). Lower panel: (g) topography, (h) local current map, and (i) statistical distribution of local current for the disordered  $\text{Cs}_2\text{AgBiBr}_6$  thin films. Such plots for the ordered  $\text{Cs}_2\text{AgBiBr}_6$  films are shown in panels (j–l).

the disordered double perovskite reduced with an increase in the  $\text{PEA}^+$  concentration in the precursor, suggesting a lesser density of antisite defects in the ordered system (Figure 4b). The transport gap in the ordered double perovskite (similar to the optical band gap) hence increased upon formation of an ordered lattice.

**3.6. Suppressed Formation of Defects and STE: Surface Potential and Local Current Mapping.** To study the role of cation ordering toward an efficient carrier transport process, we further carried out a series of measurements at the local scale. KPFM images were recorded

to measure the surface potential distribution of the disordered and ordered double perovskite films. As such, the surface work function is considered crucial in semiconducting thin films toward optoelectronic applications as it influences the electronic transport by tuning the Fermi energy at the metal–semiconductor interface. To study the role of cation ordering in double perovskite thin films on the transport process, we have mapped the CPD for the disordered and the ordered films under identical experimental conditions. As observed from the CPD map presented in the upper panel of Figure 5 along with topography of the surface, the CPD value

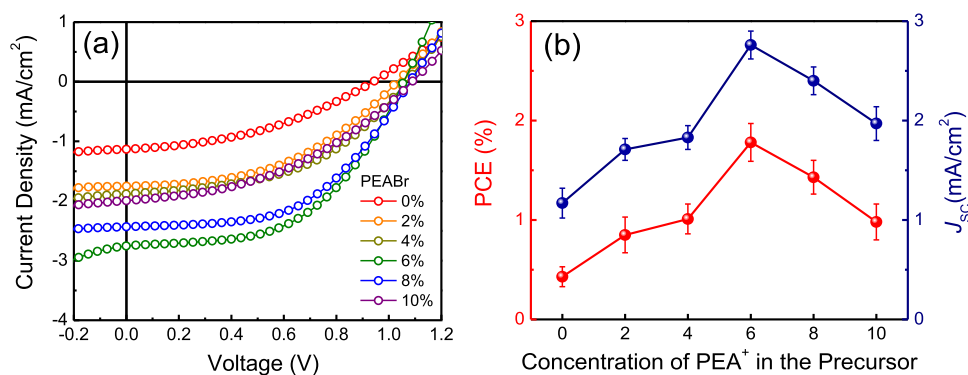


**Figure 6.** (a)  $I$ – $V$  characteristics of PEDOT:PSS/ $\text{Cs}_2\text{AgBiBr}_6$ /PCBM/BCP heterojunctions under 1 sun illumination;  $\text{Cs}_2\text{AgBiBr}_6$  was formed with different  $\text{PEA}^+$  concentrations. (b) Variation of  $J_{\text{SC}}$  and PCE with the  $\text{PEA}^+$  content in the precursor.

increased from  $80 \pm 10$  to  $120 \pm 10$  mV when an ordering developed in the perovskite. A larger CPD value in an ordered perovskite infers extraction and transfer of more charge carriers to the surface due to suppression of STE formation.<sup>45</sup> In other words, fewer defect states on the path of charge transport to electrodes (in the ordered structure) would result in a larger CPD value.<sup>46,47</sup> Since it may be argued that a change in CPD would lead to a shift of Fermi energy itself, the FWHM can be a better suited parameter for probing defect states; a reduction in the FWHM of the surface potential distribution would definitely imply a lesser defect concentration upon cation ordering in the double perovskite.

To study the improvement of charge transport in the ordered perovskite lattice with respect to the disordered one, C-AFM measurements were carried out at the local scale. Identical film thicknesses were considered for the measurements so that a thickness-induced variation in resistance may not prompt a change in the local conductivity; thickness of the two films were identical ( $\sim 150 \pm 5$  nm, Figure S7 of the Supporting Information), as obtained from AFM scratch profile measurements. With a bias voltage of 1.0 V being applied, the resulting current was measured and mapped throughout the surface along with the topography (lower panel of Figure 5). When the current on the surface was analyzed by drawing its distribution, we observed an increase in the average value of local current due to an improvement in the conductivity of the ordered system. Here, the improved conductivity occurred due to lowering of the defect density. The results hence infer an efficient charge transport due to lesser defect densities in the  $\text{Cs}_2\text{AgBiBr}_6$  double perovskite with the cations being ordered in an alternate fashion.

**3.7. Photovoltaic Performance.** We finally proceeded to study the influence of cation ordering on the photovoltaic properties of inverted heterojunction solar cells based on  $\text{Cs}_2\text{AgBiBr}_6$  double perovskite thin films. We fabricated ITO/PEDOT:PSS/ $\text{Cs}_2\text{AgBiBr}_6$ /PCBM/BCP/Al sandwiched heterojunction devices where both the ETL and HTL formed a type-II band alignment with the active material as observed from the STS band diagram (Figure S8 of the Supporting Information). A very thin layer of BCP was formed as a buffer layer to protect the PCBM layer. Figure 6a shows the  $I$ – $V$  characteristics of the heterojunction devices;  $\text{Cs}_2\text{AgBiBr}_6$  in the devices was formed with different concentrations of PEABr in the precursor. Photovoltaic parameters obtained under 1 sun illumination are listed in Table 2. Statistical analysis of each of the photovoltaic parameters was carried out from 20

**Table 2. Photovoltaic Parameters of PEDOT:PSS/ $\text{Cs}_2\text{AgBiBr}_6$ /PCBM/BCP/Al Heterojunctions under 1 Sun Illumination<sup>a</sup>**

PEA <sup>+</sup> concentration (%)	$V_{\text{OC}}$ (V)	$J_{\text{SC}}$ (mA/cm <sup>2</sup> )	fill factor (%)	PCE (%)
0	$0.95 \pm 0.02$	$1.17 \pm 0.15$	$38 \pm 2$	$0.43 \pm 0.10$
2	$1.03 \pm 0.02$	$1.71 \pm 0.11$	$48 \pm 3$	$0.85 \pm 0.18$
4	$1.06 \pm 0.02$	$1.83 \pm 0.12$	$52 \pm 3$	$1.01 \pm 0.15$
6	$1.06 \pm 0.02$	$2.76 \pm 0.14$	$61 \pm 3$	$1.78 \pm 0.19$
8	$1.08 \pm 0.02$	$2.40 \pm 0.14$	$55 \pm 2$	$1.43 \pm 0.17$
10	$1.08 \pm 0.02$	$1.97 \pm 0.17$	$46 \pm 3$	$0.98 \pm 0.18$

<sup>a</sup>PEA<sup>+</sup> concentration for forming  $\text{Cs}_2\text{AgBiBr}_6$  is quoted in the first column.

independent measurements and was presented in a boxcar plot (Figure S9 of the Supporting Information).

As cation ordering in the double perovskite facilitates carrier transport processes by suppressing the STE effect and passivating antisite defects, an improvement in photovoltaic parameters was observed as a function of PEA<sup>+</sup> concentration. An improvement in the open-circuit voltage ( $V_{\text{OC}}$ ) was observed due to an increase in the transport gap and a decrease in defect densities as observed from STS studies. While the increase in  $V_{\text{OC}}$  was from 0.95 to 1.08 V, the increase of short-circuit current density ( $J_{\text{SC}}$ ) was large (from 1.17 to 2.76 mA/cm<sup>2</sup>) leading to a substantial augmentation in PCE from 0.43 to 1.78% with a gradual increase in the PEABr content in the precursor. A further increment in the PEABr concentration (>6%) adversely affected the  $J_{\text{SC}}$  owing to widening of the band gap (Figure 6b). The fill factor of the cells showed evidence of improvement implying a lesser carrier recombination in devices based on ordered  $\text{Cs}_2\text{AgBiBr}_6$  thin films. Hence, as presented in Table 2, the PCE of the cells could be optimized with the PEABr content in the precursor. Although, to the best of our knowledge, this is the highest  $V_{\text{OC}}$  achieved so far in a double perovskite solar cell, the PCE value however remained little low leaving routes for further improvement through appropriate band engineering with carrier transport materials.

## 4. CONCLUSIONS

In conclusion, we have investigated the effect of cation ordering in  $\text{Cs}_2\text{AgBiBr}_6$  double perovskites through incorporation of PEABr in conduction processes. Ordering of the  $[\text{AgBr}_6]^{5-}$  and  $[\text{BiBr}_6]^{3-}$  octahedra in the perovskite occurred



due to a selective coordination between functionalized phenyl and ammonium ions in  $\text{PEA}^+$  with the inorganic  $\text{Ag}^+$  and  $\text{Bi}^{3+}$  ions, respectively. An improvement in the ordering of the two cations (silver and bismuth) was evidenced from XRD studies and Raman spectroscopy. Such an ordering widened the band gap of the perovskite due to a decrease in the  $\text{Ag}_{\text{Bi}}$  antisite defect density and suppression of STEs appearing out of JT-like distortions in the disordered double perovskite. The suppression of STE formation was confirmed on witnessing the shrinkage of the Huang–Rhys factor in the ordered lattice. From STS studies, a lower concentration of defects was observed due to the shift of the VB away from the Fermi energy. Local surface potential and conductivity measurements through KPFM and C-AFM indicated an efficient carrier transport as well in cationic-ordered compounds. Finally, the suppression of STE formation and an efficient carrier transport provided a large improvement in the photovoltaic parameters of devices based on the  $\text{Cs}_2\text{AgBiBr}_6$  double perovskites.

## ■ ASSOCIATED CONTENT

### SI Supporting Information

The Supporting Information is available free of charge at <https://pubs.acs.org/doi/10.1021/acs.jpcc.1c04730>.

Comparison of the intensity of the (111) and (022) planes as a function of  $\text{PEA}^+$  concentration, XRD pattern and Raman spectrum of the  $\text{PEA}_4\text{BiAgBr}_8$  compound, XPS survey spectra of disordered and ordered phases of  $\text{Cs}_2\text{AgBiBr}_6$  thin films, Tauc plot and optical gap of the disordered and ordered double perovskites as a function of  $\text{PEA}^+$  concentration, comparison of Urbach energy ( $E_{\text{U}}$ ) in disordered and ordered phases of the  $\text{Cs}_2\text{AgBiBr}_6$  thin films, histograms of band energies of double perovskites as a function of  $\text{PEA}^+$  concentration, AFM scratch profiles of the double perovskite thin films, band diagram of photovoltaic devices based on thin films of the disordered and ordered double perovskites, and statistical distribution of photovoltaic parameters in different devices (PDF)

## ■ AUTHOR INFORMATION

### Corresponding Author

Amlan J. Pal – School of Physical Sciences, Indian Association for the Cultivation of Science, Kolkata 700032, India; UGC-DAE Consortium for Scientific Research, University Campus, Indore 452001, India; [orcid.org/0000-0002-7651-9779](https://orcid.org/0000-0002-7651-9779); Email: [sspajp@iacs.res.in](mailto:sspajp@iacs.res.in)

### Author

Abhishek Maiti – School of Physical Sciences, Indian Association for the Cultivation of Science, Kolkata 700032, India

Complete contact information is available at: <https://pubs.acs.org/10.1021/acs.jpcc.1c04730>

### Notes

The authors declare no competing financial interest.

## ■ ACKNOWLEDGMENTS

The authors acknowledge Prof. Tarun K. Mandal, School of Chemical Sciences, Indian Association for the Cultivation of Science for rendering his expertise in the synthesis of  $\text{PEABr}$ . A.J.P. acknowledges the JC Bose National Fellowship (SB/S2/

JCB-001/2016) and the Core Research Grant (CRG/2018/000183) of SERB for funding the work. A.M. acknowledges the DST INSPIRE Fellowship [IF170922] for financial assistance.

## ■ REFERENCES

- (1) Greul, E.; Petrus, M. L.; Binek, A.; Docampo, P.; Bein, T. Highly Stable, Phase Pure  $\text{Cs}_2\text{AgBiBr}_6$  Double Perovskite Thin Films for Optoelectronic Applications. *J. Mater. Chem. A* **2017**, *5*, 19972–19981.
- (2) McClure, E. T.; Ball, M. R.; Windl, W.; Woodward, P. M.  $\text{Cs}_2\text{AgBiX}_6$  (X = Br, Cl): New Visible Light Absorbing, Lead-Free Halide Perovskite Semiconductors. *Chem. Mater.* **2016**, *28*, 1348–1354.
- (3) Pan, W.; Wu, H.; Luo, J.; Deng, Z.; Ge, C.; Chen, C.; Jiang, X.; Yin, W. J.; Niu, G.; Zhu, L.; Yin, L.; Zhou, Y.; Xie, Q.; Ke, X.; Sui, M.; Tang, J.  $\text{Cs}_2\text{AgBiBr}_6$  Single-crystal X-ray Detectors with a Low Detection Limit. *Nat. Photonics* **2017**, *11*, 726.
- (4) Slavney, A. H.; Hu, T.; Lindenberg, A. M.; Karunadasa, H. I. A Bismuth-Halide Double Perovskite with Long Carrier Recombination Lifetime for Photovoltaic Applications. *J. Am. Chem. Soc.* **2016**, *138*, 2138–2141.
- (5) Kamat, P. V.; Bisquert, J.; Buriak, J. Lead-Free Perovskite Solar Cells. *ACS Energy Lett.* **2017**, *2*, 904–905.
- (6) Xiao, Z.; Song, Z.; Yan, Y. From Lead Halide Perovskites to Lead-Free Metal Halide Perovskites and Perovskite Derivatives. *Adv. Mater.* **2019**, *31*, No. 1803792.
- (7) Klarbring, J.; Hellman, O.; Abrikosov, I. A.; Simak, S. I. Anharmonicity and Ultralow Thermal Conductivity in Lead-Free Halide Double Perovskites. *Phys. Rev. Lett.* **2020**, *125*, No. 045701.
- (8) Chatterjee, S.; Pal, A. J. Influence of Metal Substitution on Hybrid Halide Perovskites: Towards Lead-free Perovskite Solar Cells. *J. Mater. Chem. A* **2018**, *6*, 3793–3823.
- (9) Nie, R.; Sumukam, R. R.; Reddy, S. H.; Banavoth, M.; Seok, S. I. Lead-free Perovskite Solar Cells Enabled by Hetero-valent Substitutes. *Energy Environ. Sci.* **2020**, *13*, 2363–2385.
- (10) Volonakis, G.; Filip, M. R.; Haghighirad, A. A.; Sakai, N.; Wenger, B.; Snaith, H. J.; Giustino, F. Lead-Free Halide Double Perovskites via Heterovalent Substitution of Noble Metals. *J. Phys. Chem. Lett.* **2016**, *7*, 1254–1259.
- (11) Gao, W.; Ran, C.; Xi, J.; Jiao, B.; Zhang, W.; Wu, M.; Hou, X.; Wu, Z. High-Quality  $\text{Cs}_2\text{AgBiBr}_6$  Double Perovskite Film for Lead-Free Inverted Planar Heterojunction Solar Cells with 2.2% Efficiency. *ChemPhysChem* **2018**, *19*, 1696–1700.
- (12) Savory, C. N.; Walsh, A.; Scanlon, D. O. Can Pb-Free Halide Double Perovskites Support High-Efficiency Solar Cells? *ACS Energy Lett.* **2016**, *1*, 949–955.
- (13) Karmakar, A.; Dodd, M. S.; Agnihotri, S.; Ravera, E.; Michaelis, V. K. Cu(II)-Doped  $\text{Cs}_2\text{SbAgCl}_6$  Double Perovskite: A Lead-Free, Low-Bandgap Material. *Chem. Mater.* **2018**, *30*, 8280–8290.
- (14) Zhang, Z.; Wu, C.; Wang, D.; Liu, G.; Zhang, Q.; Luo, W.; Qi, X.; Guo, X.; Zhang, Y.; Lao, Y.; Qu, B.; Xiao, L.; Chen, Z. Improvement of  $\text{Cs}_2\text{AgBiBr}_6$  Double Perovskite Solar Cell by Rubidium Doping. *Org. Electron.* **2019**, *74*, 204–210.
- (15) Meneghini, C.; Ray, S.; Liscio, F.; Bardelli, F.; Mobilio, S.; Sarma, D. D. Nature of “Disorder” in the Ordered Double Perovskite  $\text{Sr}_2\text{FeMoO}_6$ . *Phys. Rev. Lett.* **2009**, *103*, No. 046403.
- (16) McNally, G. M.; Arévalo-López, A. M.; Guillou, F.; Manuel, P.; Atfield, J. P. Evolution of Cation and Spin Orders in the Double-Double-Double Perovskite Series  $\text{Ca}_x\text{Mn}_{2-x}\text{FeReO}_6$ . *Phys. Rev. Mater.* **2020**, *4*, No. 064408.
- (17) Paul, A.; Birol, T. Cation order control of correlations in double perovskite  $\text{Sr}_2\text{VNbO}_6$ . *Phys. Rev. Res.* **2020**, *2*, No. 033156.
- (18) Kim, J.; Kim, H.; Chandran, M.; Lee, S. C.; Im, S. H.; Hong, K. H. Impacts of Cation Ordering on Bandgap Dispersion of Double Perovskites. *APL Mater.* **2018**, *6*, No. 084903.
- (19) Yang, J.; Zhang, P.; Wei, S.-H. Band Structure Engineering of  $\text{Cs}_2\text{AgBiBr}_6$  Perovskite through Order Disordered Transition: A First-Principle Study. *J. Phys. Chem. Lett.* **2018**, *9*, 31–35.

- (20) Yuan, W.; Niu, G.; Xian, Y.; Wu, H.; Wang, H.; Yin, H.; Liu, P.; Li, W.; Fan, J. In Situ Regulating the Order-Disorder Phase Transition in  $\text{Cs}_2\text{AgBiBr}_6$  Single Crystal toward the Application in an X-Ray Detector. *Adv. Funct. Mater.* **2019**, *29*, No. 1900234.
- (21) Luo, J.; Wang, X.; Li, S.; Liu, J.; Guo, Y.; Niu, G.; Yao, L.; Fu, Y.; Gao, L.; Dong, Q.; Zhao, C.; Leng, M.; Ma, F.; Liang, W.; Wang, L.; Jin, S.; Han, J.; Zhang, L.; Etheridge, J.; Wang, J.; Yan, Y.; Sargent, E. H.; Tang, J. Efficient and Stable Emission of Warm-white Light from Lead-free Halide Double Perovskites. *Nature* **2018**, *563*, 541.
- (22) Longo, G.; Mahesh, S.; Buizza, L. R. V.; Wright, A. D.; Ramadan, A. J.; Abdi-Jalebi, M.; Nayak, P. K.; Herz, L. M.; Snaith, H. J. Understanding the Performance-Limiting Factors of  $\text{Cs}_2\text{AgBiBr}_6$  Double-Perovskite Solar Cells. *ACS Energy Lett.* **2020**, *5*, 2200–2207.
- (23) Maiti, A.; Chatterjee, S.; Peedikakkandy, L.; Pal, A. J. Defects and Their Passivation in Hybrid Halide Perovskites toward Solar Cell Applications. *Sol. RRL* **2020**, *4*, No. 2000505.
- (24) Wang, H.; Gazquez, J.; Frontera, C.; Chisholm, M.; Pomar, A.; Martinez, B.; Mestres, N. Spontaneous Cationic Ordering in Chemical-Solution-Grown  $\text{La}_2\text{CoMnO}_6$  Double Perovskite Thin Films. *NPG Asia Mater.* **2019**, *11*, 44.
- (25) Wang, H.; Frontera, C.; Herrero-Martín, J.; Pomar, A.; Roura, P.; Martínez, B.; Mestres, N. Aqueous Chemical Solution Deposition of Functional Double Perovskite Epitaxial Thin Films. *Chem.-Eur. J.* **2020**, *26*, 9338–9347.
- (26) Igbari, F.; Wang, R.; Wang, Z. K.; Ma, X. J.; Wang, Q.; Wang, K. L.; Zhang, Y.; Liao, L. S.; Yang, Y. Composition Stoichiometry of  $\text{Cs}_2\text{AgBiBr}_6$  Films for Highly Efficient Lead-Free Perovskite Solar Cells. *Nano Lett.* **2019**, *19*, 2066–2073.
- (27) Ban, M.; Zou, Y.; Rivett, J. P. H.; Yang, Y.; Thomas, T. H.; Tan, Y.; Song, T.; Gao, X.; Credgington, D.; Deschler, F.; Sringhaus, H.; Sun, B. Solution-Processed Perovskite Light Emitting Diodes with Efficiency Exceeding 15% through Additive-controlled Nanostructure Tailoring. *Nat. Commun.* **2018**, *9*, 3892.
- (28) Bera, S.; Kolay, J.; Pramanik, P.; Bhattacharyya, A.; Mukhopadhyay, R. Long-Range Solid-State Electron Transport through Ferritin Multilayers. *J. Mater. Chem. C* **2019**, *7*, 9038–9048.
- (29) Kulkarni, A.; Jena, A. K.; Ikegami, M.; Miyasaka, T. Performance Enhancement of  $\text{AgBi}_2\text{I}_7$  Solar Cells by Modulating a Solvent-mediated Adduct and Tuning Remnant  $\text{BiI}_3$  in One-step Crystallization. *Chem. Commun.* **2019**, *55*, 4031–4034.
- (30) Yang, J.; Bao, C.; Ning, W.; Wu, B.; Ji, F.; Yan, Z.; Tao, Y.; Liu, J.; Sum, T.; Bai, S.; Wang, J.; Huang, W.; Zhang, W.; Gao, F. Stable, High-Sensitivity and Fast-Response Photodetectors Based on Lead-Free  $\text{Cs}_2\text{AgBiBr}_6$  Double Perovskite Films. *Adv. Opt. Mater.* **2019**, *7*, No. 1801732.
- (31) Xiao, Z.; Meng, W.; Wang, J.; Yan, Y. Thermodynamic Stability and Defect Chemistry of Bismuth-Based Lead-Free Double Perovskites. *ChemSusChem* **2016**, *9*, 2628–2633.
- (32) Kentsch, R.; Scholz, M.; Horn, J.; Schlettwein, D.; Oum, K.; Lenzer, T. Exciton Dynamics and Electron-Phonon Coupling Affect the Photovoltaic Performance of the  $\text{Cs}_2\text{AgBiBr}_6$  Double Perovskite. *J. Phys. Chem. C* **2018**, *122*, 25940–25947.
- (33) Clegg, W.; Elsegood, M. R. J.; Errington, R. J.; Fisher, G. A.; Norman, N. C. Structure of  $\text{BiBr}_2\text{Ph}$  - A Solid-state Architecture Involving Secondary Bonding and Pi-Pi Interactions. *J. Mater. Chem.* **1994**, *4*, 891–893.
- (34) Heuer-Jungemann, A.; Feliu, N.; Bakaimi, I.; Hamaly, M.; Alkilany, A.; Chakraborty, I.; Masood, A.; Casula, M. F.; Kostopoulou, A.; Oh, E.; et al. The Role of Ligands in the Chemical Synthesis and Applications of Inorganic Nanoparticles. *Chem. Rev.* **2019**, *119*, 4819–4880.
- (35) Wang, T.; Fu, Y.; Jin, L.; Deng, S.; Pan, D.; Dong, L.; Jin, S.; Huang, L. Phenethylammonium Functionalization Enhances Near-Surface Carrier Diffusion in Hybrid Perovskites. *J. Am. Chem. Soc.* **2020**, *142*, 16254–16264.
- (36) Lim, T. W.; Kim, S. D.; Sung, K. D.; Rhyim, Y. M.; Jeon, H.; Yun, J.; Kim, K. H.; Song, K. M.; Lee, S.; Chung, S. Y.; et al. Insights into Cationic Ordering in Re-based Double Perovskite Oxides. *Sci. Rep.* **2016**, *6*, 19746.
- (37) Lee, D.; Yun, J. S.; Kim, J.; Soufiani, A. M.; Chen, S.; Cho, Y.; Deng, X.; Seidel, J.; Lim, S.; Huang, S.; Ho-Baillie, A. W. Y. Passivation of Grain Boundaries by Phenethylammonium in Formamidinium-Methylammonium Lead Halide Perovskite Solar Cells. *ACS Energy Lett.* **2018**, *3*, 647–654.
- (38) Pistor, P.; Meyns, M.; Guc, M.; Wang, H. C.; Marques, M. A. L.; Alcobé, X.; Cabot, A.; Izquierdo-Roca, V. Advanced Raman Spectroscopy of  $\text{Cs}_2\text{AgBiBr}_6$  Double Perovskites and Identification of  $\text{Cs}_3\text{Bi}_2\text{Br}_9$  Secondary Phases. *Scr. Mater.* **2020**, *184*, 24–29.
- (39) Zelewski, S. J.; Urban, J. M.; Surrante, A.; Maude, D. K.; Kuc, A.; Schade, L.; Johnson, R. D.; Dollmann, M.; Nayak, P. K.; Snaith, H. J.; et al. Revealing the Nature of Photoluminescence Emission in the Metal-halide Double Perovskite  $\text{Cs}_2\text{AgBiBr}_6$ . *J. Mater. Chem. C* **2019**, *7*, 8350–8356.
- (40) Rudisch, K.; Davydova, A.; Platzer-Björkman, C.; Scragg, J. The Effect of Stoichiometry on Cu-Zn Ordering Kinetics in  $\text{Cu}_2\text{ZnSnS}_4$  Thin Films. *J. Appl. Phys.* **2018**, *123*, 161558.
- (41) Gao, F.; Zhao, Y.; Zhang, X.; You, J. Recent Progresses on Defect Passivation toward Efficient Perovskite Solar Cells. *Adv. Energy Mater.* **2020**, *10*, No. 1902650.
- (42) Samiee, M.; Joshi, P.; Aidarkhanov, D.; Dalal, V. Measurement of Defect Densities and Urbach Energies of Tail States in  $\text{PTB}_7$  Solar Cells. *Appl. Phys. Lett.* **2014**, *105*, 133511.
- (43) de Jong, M.; Seijo, L.; Meijerink, A.; Rabouw, F. T. Resolving the Ambiguity in the Relation between Stokes Shift and Huang-Rhys Parameter. *Phys. Chem. Chem. Phys.* **2015**, *17*, 16959–16969.
- (44) du, K. Z.; Meng, W.; Wang, X.; Yan, Y.; Mitzi, D. B. Bandgap Engineering of Lead-Free Double Perovskite  $\text{Cs}_2\text{AgBiBr}_6$  through Trivalent Metal Alloying. *Angew. Chem., Int. Ed.* **2017**, *56*, 8158–8162.
- (45) Qi, X.; Tan, F.; Gao, Y.; Wu, T.; Liu, R.; Dong, C.; Yue, G.; Li, S.; Zhang, L. The Effect of Phase Purification on Photovoltaic Performance of Perovskite Solar Cells. *Appl. Phys. Lett.* **2019**, *115*, 192105.
- (46) Yun, J. S.; Ho-Baillie, A.; Huang, S.; Woo, S. H.; Heo, Y.; Seidel, J.; Huang, F.; Cheng, Y. B.; Green, M. A. Benefit of Grain Boundaries in Organic-Inorganic Halide Planar Perovskite Solar Cells. *J. Phys. Chem. Lett.* **2015**, *6*, 875–880.
- (47) Li, J. J.; Ma, J. Y.; Hu, J. S.; Wang, D.; Wan, L. J. Influence of N,N-Dimethylformamide Annealing on the Local Electrical Properties of Organometal Halide Perovskite Solar Cells: an Atomic Force Microscopy Investigation. *ACS Appl. Mater. Interfaces* **2016**, *8*, 26002–26007.

Supporting Information for

Effect of Cation-Occupancy-Ordering in Double  
Perovskites to Overcome Hurdles in Carrier Transport:  
 $\text{Cs}_2\text{AgBiBr}_6$  as a Case Study

Abhishek Maiti<sup>1</sup> and Amlan J. Pal<sup>1,2\*</sup>

<sup>1</sup>*School of Physical Sciences, Indian Association for the Cultivation of Science, Kolkata 700032,  
India*

<sup>2</sup>*UGC-DAE Consortium for Scientific Research, University Campus, Khandwa Road, Indore  
452001, India*

\**E-mail: sspajp@iacs.res.in*

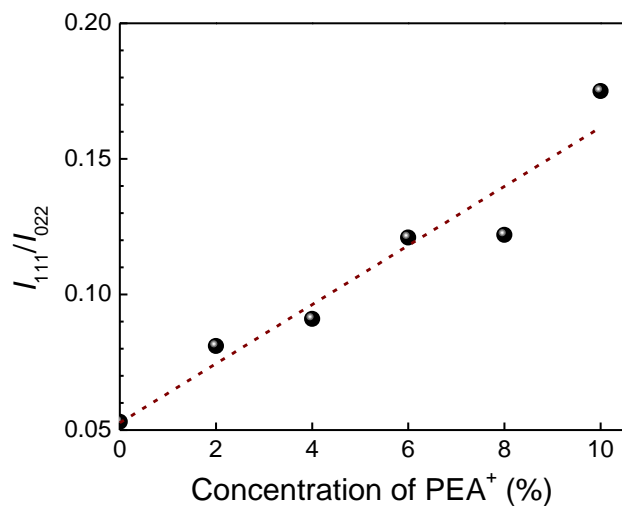


**Figure S1.** Comparison of the intensity of (111) and (022) planes ( $I_{111}/I_{022}$ ) as a function of PEA<sup>+</sup> concentration. An increase in the ratio infers formation of cation-ordering in the lattice.

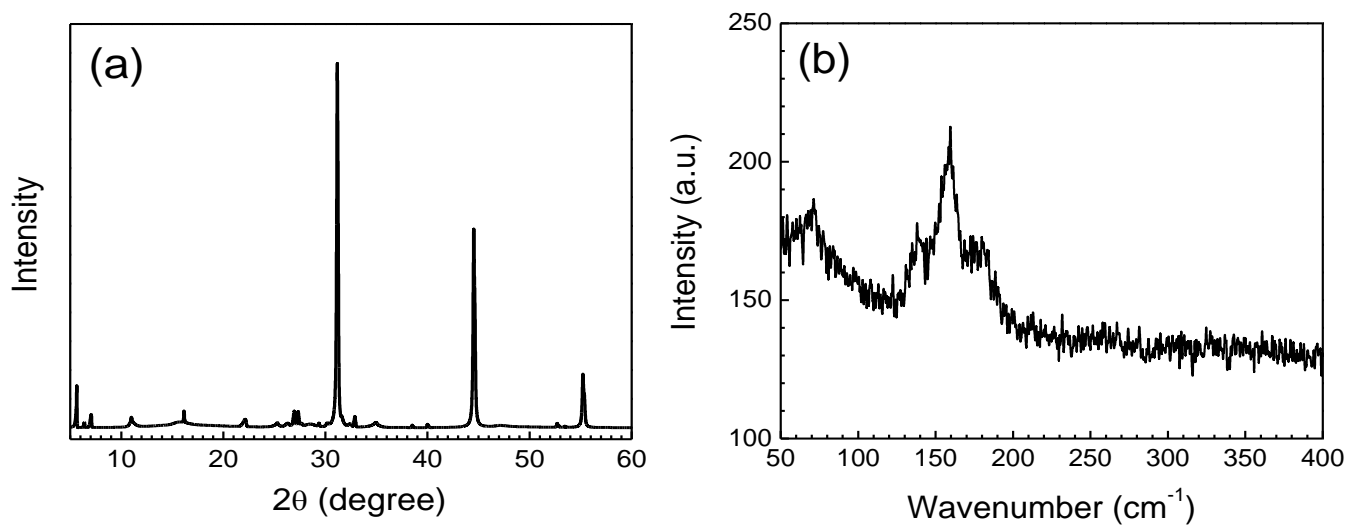


**Figure S2.** (a) XRD pattern and (b) Raman spectrum of PEA<sub>4</sub>BiAgBr<sub>8</sub> compound.

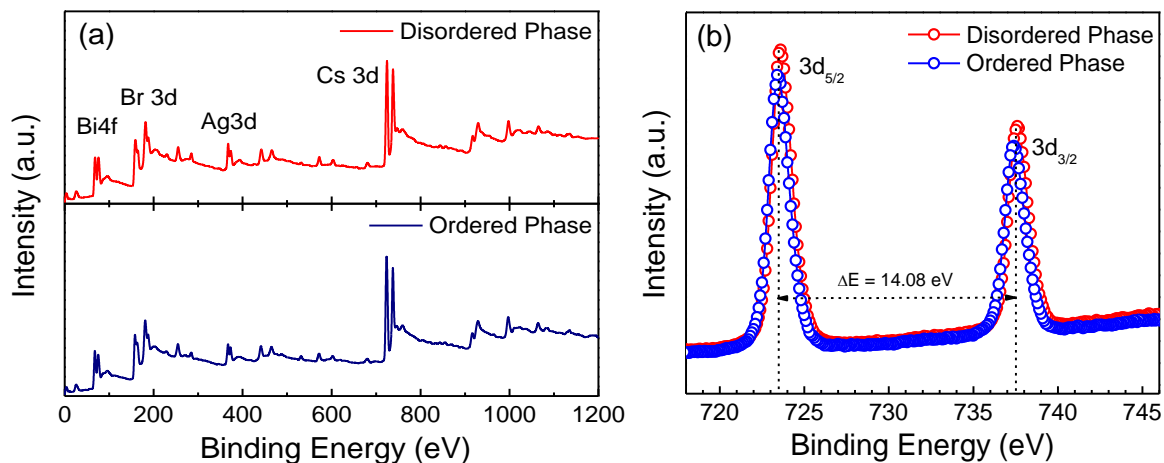


**Figure S3.** (a) XPS survey spectra and (b) comparison of high resolution Cs 3d peaks of pristine disordered- $\text{Cs}_2\text{AgBiBr}_6$  and 6% PEA-induced ordered- $\text{Cs}_2\text{AgBiBr}_6$  double perovskite.

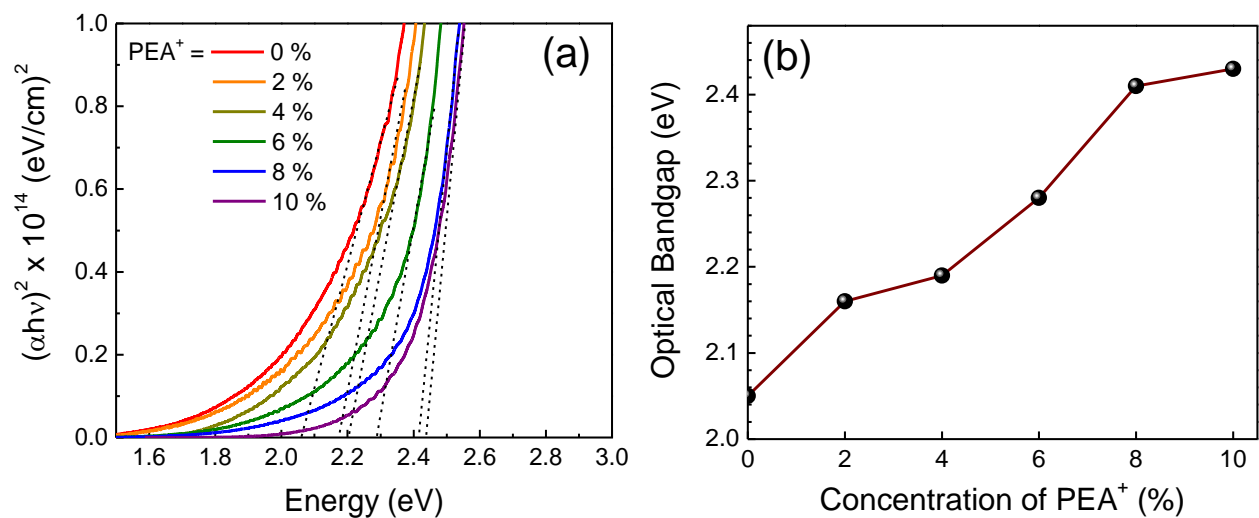


**Figure S4.** (a) Tauc plot and (b) variation of optical gap of the disordered and ordered perovskites as a function of PEA<sup>+</sup> concentration.



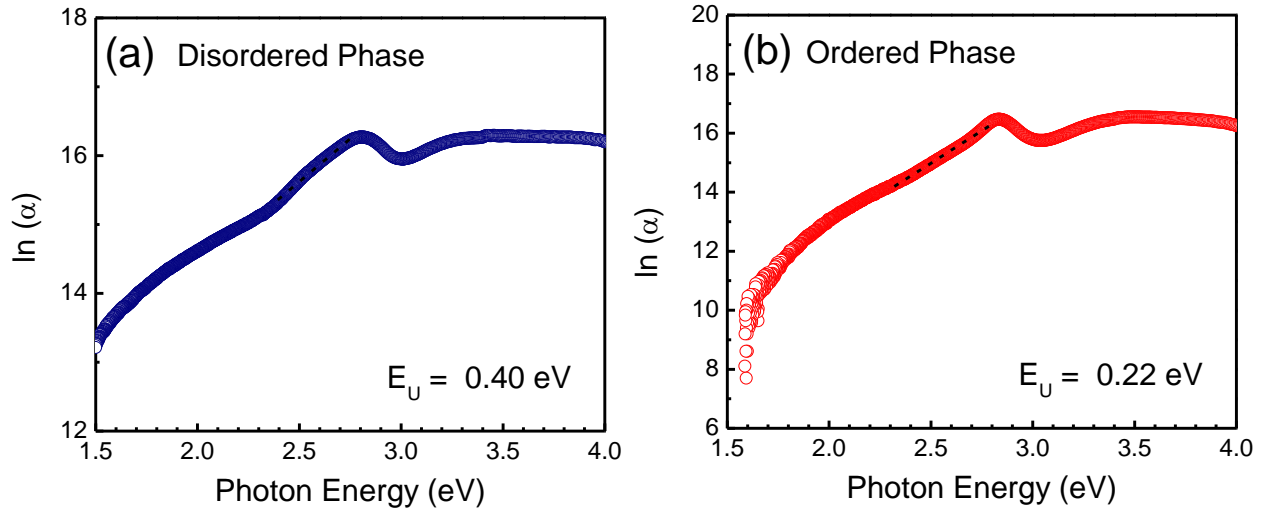


**Figure S5.** Comparison of Urbach energy ( $E_U$ ) in (a) disordered and (b) ordered phase of the  $\text{Cs}_2\text{AgBiBr}_6$  thin-films.

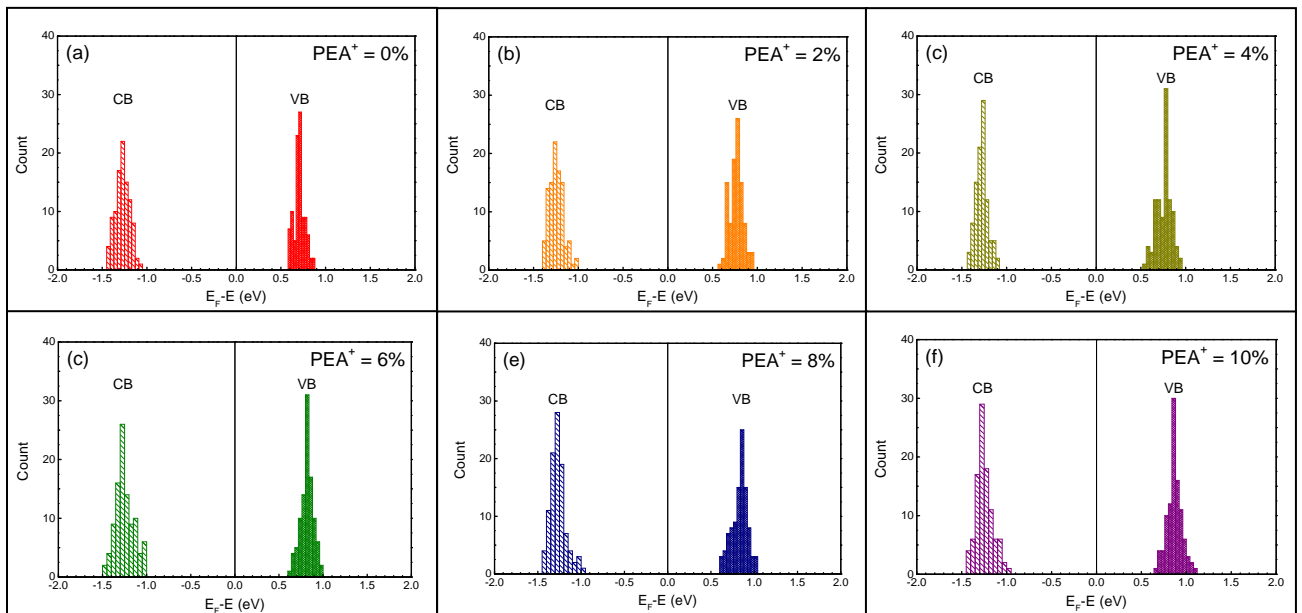


**Figure S6.** Histogram of band-energies of the double perovskites as a function of  $\text{PEA}^+$  concentration (as specified in legends).

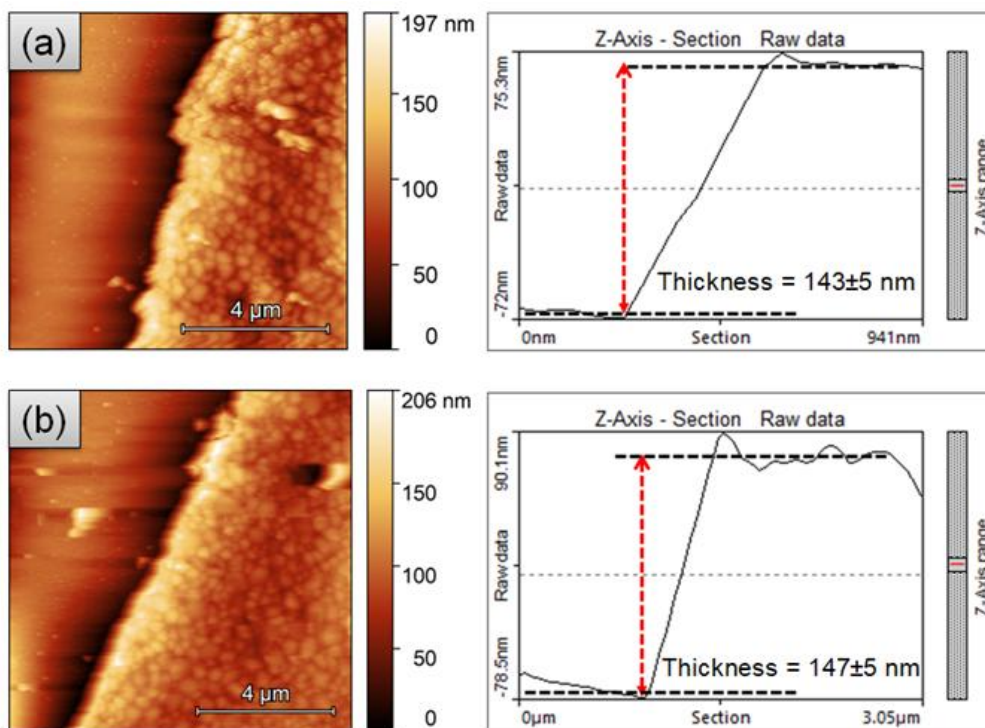


**Figure S7.** AFM scratch profile of (a) disordered and (b) ordered double perovskite thin films.

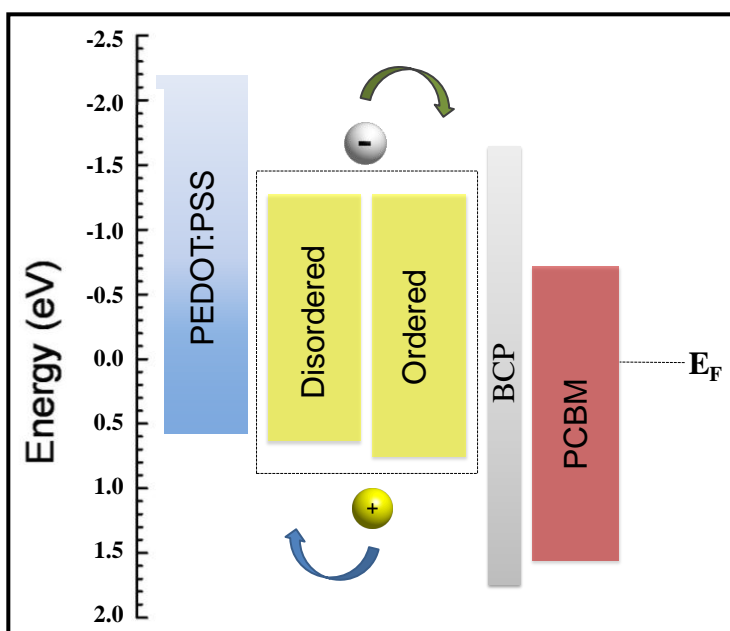


**Figure S8.** Band diagram of ITO / PEDOT:PSS / [disordered/ordered] double perovskite / PCBM / BCP / Al photovoltaic devices.

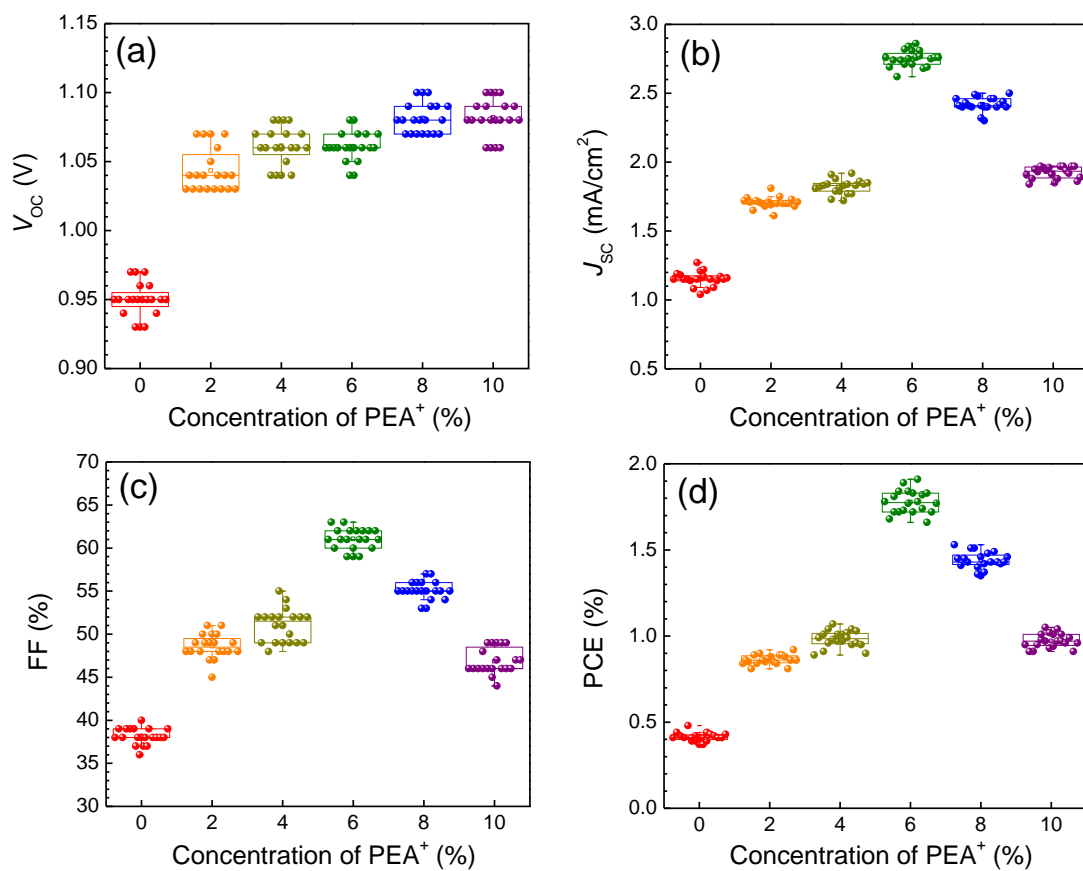


**Figure S9.** Statistical distribution of photovoltaic parameters, such as (a)  $V_{oc}$ , (b)  $J_{sc}$  (c) FF, and (d) PCE of different devices as a function of PEA<sup>+</sup>-concentration.

# Defects and Their Passivation in Hybrid Halide Perovskites toward Solar Cell Applications

Abhishek Maiti, Soumyo Chatterjee, Lekha Peedikakkandy, and Amlan J. Pal\*

The rise of hybrid metal–halide perovskites as potential solar energy materials has revolutionized research on next-generation solar cells. According to recent studies, the rationale behind such success is the rich defect physics of materials. Studies on the origin of different types of prevailing defects, their formation, and mechanism of defect passivation have hence become decisive avenues. Herein, the possible origins of defects and different defect analysis techniques in hybrid halide perovskites are discussed. While initiating the discussion with the archetypal methylammonium lead halide, perovskites beyond the conventional  $ABX_3$  structure are included. In this direction, some major advancements to date on defect formation in the bulk of hybrid halide perovskites, at the grains and grain boundaries, are summarized. Numerous effective methods to passivate the defects and the adverse effect of defects on device efficiency are further highlighted. Hence, the prospect of defect engineering in perovskite materials is pointed toward improving the power conversion efficiency and long-term stability of perovskite solar cells (PSCs). The discussion rightfully addresses that the in-depth exploration of defect engineering is anticipated to have a gigantic impact toward the achievement of predicted efficiency in metal–halide PSCs.

mobility,<sup>[15]</sup> a long carrier diffusion length,<sup>[16]</sup> an extraordinarily high defect tolerance,<sup>[17]</sup> and a low recombination loss,<sup>[18,19]</sup> which have propelled the PCE of solar cells based on the material to reach a record breaking value of 25.2% to date at the lab scale.<sup>[20]</sup> Although a large number of noteworthy developments have taken place in the research field of hybrid halide perovskites since its inception, the material still possesses a couple of major limitations, namely toxicity of lead and long-term ambient stability.<sup>[21,22]</sup> To address these inadequacies, contemporary researches expectedly focused mostly on materials engineering in  $CH_3NH_3PbI_3$ ; in this direction, the substitution of lead by a suitable metal and use of a bulky organic cation at the A-site have shown further promises.<sup>[23,24]</sup> As a consequence, the prototype perovskite,  $CH_3NH_3PbI_3$ , has now become the representative of a large family of analogous compounds appropriate for efficient solar cell applications.


## 1. Introduction

In the present decade, researchers have witnessed an unprecedented success in the arena of materials for solar cells through the introduction of hybrid halide perovskites.<sup>[1–5]</sup> An amazing rise in the power conversion efficiency (PCE) of such perovskite solar cells (PSCs) along with their low fabrication cost has made this class of materials a viable alternative to silicon for commercialization.<sup>[4,6,7]</sup> The most investigated member of this perovskite family is methylammonium lead iodide ( $CH_3NH_3PbI_3$  aka  $MAPbI_3$  aka  $MAPI$ ) which carries the well-known structural formula of  $ABX_3$ . Here, the A-site is usually occupied by an organic or inorganic monovalent cation, the B-site by a divalent lead cation, and the X-site by a halogen.<sup>[1,8,9]</sup> The unprecedented success of  $MAPbI_3$  in solar cell applications is due to a plethora of optimal properties, such as a tunable and appropriate optical bandgap,<sup>[10–12]</sup> a high absorption coefficient,<sup>[13,14]</sup> a high carrier

Besides remarkable advances related to materials engineering in the perovskite, defect physics, being a fundamental issue in device research, has also shared the spotlight significantly over the past few years.<sup>[25,26]</sup> As such, the polycrystalline nature of hybrid halide perovskite materials has made them prone to defects which inevitably put a roadblock toward the improvement of device efficiency.<sup>[27–29]</sup> In solar cell architectures, these defects act as recombination centers in the bulk of the material; in addition, grains and grain boundaries affect carrier transport adversely.<sup>[30–32]</sup> These intrinsic defects can moreover introduce a hysteresis (in the current–voltage characteristics), which remains another area of concern in terms of the reproducibility of device characteristics.<sup>[33–35]</sup>

Considering the significant influence of defects on light absorption, carrier extraction, and carrier transport in a hybrid halide perovskite-based device, it is hence essential to understand them as clearly as possible.<sup>[36–38]</sup> Defect engineering in terms of controlling defect densities in the perovskites is therefore expected to emerge as an important avenue toward the improvement of device efficiency and reach the predicted limit.<sup>[39–41]</sup> In this Review, we have aimed to collate established results on defect formation in the bulk of hybrid halide perovskites and at the interface with carrier transport layers and at grains and grain boundaries as well. Apart from summarizing some major advancement regarding different defect analysis techniques, we have collated a range of defect passivation approaches

A. Maiti, Dr. S. Chatterjee, Dr. L. Peedikakkandy, Prof. A. J. Pal  
School of Physical Sciences  
Indian Association for the Cultivation of Science  
Jadavpur, Kolkata 700032, India  
E-mail: sspajp@iacs.res.in

 The ORCID identification number(s) for the author(s) of this article can be found under <https://doi.org/10.1002/solr.202000505>.

DOI: 10.1002/solr.202000505

toward enhancing the PCEs of solar cells. This Review Article in effect points toward the prospects of defect engineering in perovskite materials to improve the PCE and long-term stability of hybrid halide PSCs.

## 2. Defects in Hybrid Halide Perovskites: An Overview

### 2.1. Origin of Defects and Defect Tolerance

The formation of defects is inevitable in solution-cast polycrystalline materials.<sup>[42]</sup> Most of the halide perovskites are moreover formed through precursor routes in a solution-cast process, making the defects ubiquitous. As such, defects in a semiconductor can either exist in the form of shallow states close to the band edges and thus dope a semiconductor as a p-type or n-type or form deep-level midgap states which act as recombination centers.<sup>[42]</sup> In polycrystalline MAPbI<sub>3</sub> films, electronic properties of the perovskite are greatly influenced by the presence of imperfections, such as intrinsic point defects, Schottky and Frenkel defects, grain boundaries, dislocations, and so forth.<sup>[43]</sup>

Based on the formation type, intrinsic point defects in the bulk of MAPbI<sub>3</sub> are identified as 1) vacancy defects ( $V_{MA}$ ,  $V_{Pb}$ ,  $V_I$ ), which are formed when an ion is absent from its allocated lattice site (MA: methylammonium), 2) interstitial defects ( $MA_i$ ,  $Pb_i$ ,  $I_i$ ), where the ions reside at the interstitial positions of a lattice, and 3) defects arising due to the substitution of an atom with another atom, such as  $MA_{Pb}$  and  $Pb_{MA}$  alongside antisite substitutions, like  $MA_I$ ,  $Pb_I$ ,  $I_{Pb}$ , and  $I_{MA}$  (here  $MA_{Pb}$  represents a defect arising out of MA ion occupying a lead (Pb) site.<sup>[25]</sup> These single-point defects can also appear as pairs, namely Frenkel and Schottky

defects. While Frenkel defects are a combination of a vacancy and an interstitial defect of the same ions, Schottky defects, on the other hand, are formed with cation and anion vacancies.<sup>[43]</sup> It should be kept in mind that a combination of defects can also create dynamic defect states such as edge location (1D) and grain boundary (GB) defects (2D).<sup>[44,45]</sup> In **Figure 1**, we have illustrated all possible point defects in a 3D perovskite lattice ( $ABX_3$ ), where yellow, purple, and blue dots represent the A, B, and X site, respectively, and green dots imply external impurity atoms.<sup>[43]</sup>

A pioneering work in this direction has been conducted by Yin et al. to study the formation energy of all intrinsic defects in the bulk of the prototype MAPbI<sub>3</sub> perovskite.<sup>[25]</sup> Their study revealed low formation energies for  $MA_i$ ,  $V_{Pb}$ ,  $MA_{Pb}$ ,  $I_i$ ,  $V_I$ , and  $V_{MA}$  defects with transition energies being less than 0.05 eV above the valence band maxima (VBM) or below the conduction band minima (CBM) and creating shallow-level traps. Among such possible defects, p-type  $V_{Pb}$ , n-type  $MA_i$ , and n-type  $V_I$  have been identified to be the most-dominant intrinsic defects in the bulk of MAPbI<sub>3</sub> when formed in a CH<sub>3</sub>NH<sub>3</sub>I-rich and PbI<sub>2</sub>-rich stoichiometry, respectively. It is worthy to mention here that it is the balance among all the possible defects that eventually dictates the Fermi energy in MAPbI<sub>3</sub>, depending upon its compositional stoichiometry, and in turn explains the manifestation of bipolar conductivity (both p-type and n-type) observed in the perovskite.<sup>[25,46,47]</sup> In MAPbI<sub>3</sub> perovskite, lead vacancies ( $V_{Pb}$ ) are considered to be the most stable defects and are reported to exist in neutral and doubly negative charged forms.<sup>[25,48]</sup>  $V_{Pb}$  defects in fact form in abundance due to energetically unfavorable antibonding interactions between Pb(s) and I(p) orbitals, leading to the breaking of Pb–I bonds.<sup>[25]</sup> On the other hand, in case of  $MA_i$  defects, the methylammonium

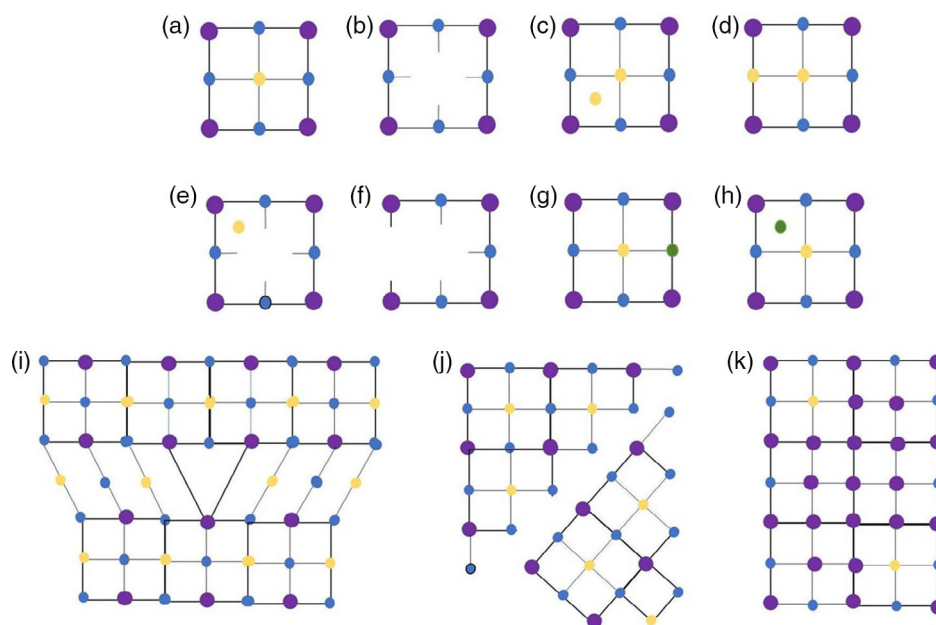


**Figure 1.** a) A perfect perovskite lattice, b) vacancy at the A-site, c) an interstitial defect, d) an antisite substitution (an A-ion occupying an X-site), e) Frenkel defects, f) Schottky defects, g) substitutional impurity, h) interstitial impurity, i) edge dislocation, j) GB, and k) precipitate. Reproduced with permission.<sup>[43]</sup> Copyright 2016, Springer Nature.

cations ( $\text{MA}^+$ ) occupy interstitial positions on the facets of  $\text{PbI}_6$  octahedra; a low formation energy of  $\text{MA}_i$  can be attributed to the weak van der Waals interaction of  $\text{MA}_i$  with  $\text{Pb-I}$  octahedra.<sup>[25]</sup>

An interesting first-principle approach has been reported in the  $\beta$ -phase of  $\text{MAPbI}_3$  toward the evaluation of Frenkel and Schottky defects in hybrid halide perovskites.<sup>[49]</sup> The study estimated the formation energies of such defects and inferred that Schottky defects do not form trap levels inside the bandgap of the perovskite; however, they can still influence the device performance. It is worthy to state here that such an influence of Schottky defects on the performance of  $\text{MAPbI}_3$ -based solar cells has previously been reported through experimental studies.<sup>[27]</sup>

## 2.2. Impact of Defects on Solar Cell Performance

The impact of point defects on the performance of solar cells is quite significant. Such defects can promote deep-level trap states for charge carriers and act as nonradiative recombination centers. Interestingly, such defects can form even in high-quality films, affecting the photovoltaic performance in an adverse manner.<sup>[30–32]</sup> Fortunately, as mentioned earlier, the prototype  $\text{MAPbI}_3$  has shallow defect levels and can be considered to be a defect-tolerant semiconductor.<sup>[50]</sup> This unique property of  $\text{MAPbI}_3$  is beneficial in designing solar cell devices as the possibility of trap-assisted recombination is low under this condition. However, such conclusions are based on first-principle density functional theory (DFT) calculations where periodic boundary conditions are important while studying defect physics. Based on different surface termination conditions, the shallow nature of the defects may disappear especially at the surface. Thus, defects formed at the surface, interface, and even at the grain boundaries can still limit the performance of devices. As the solution-processed perovskite thin films are polycrystalline by nature, the presence of defects at the grain boundaries in the perovskite absorber layer is inevitable and such defects eventually prompts trap-assisted recombination pathways in the otherwise defect-tolerant semiconductor.<sup>[51]</sup> Numerous charged defects can also appear at the absorber layer due to dangling bonds and undercoordinated  $\text{Pb}^{2+}$  defects.<sup>[43]</sup> There are also possibilities of defect migration at the interface between a perovskite and carrier transport layers affecting the efficiency of carrier extraction in turn.<sup>[52,53]</sup> Moreover, it is well reported that defect states in perovskites promote hysteresis in the current–voltage characteristics of the device.<sup>[51]</sup> The stability of such devices based on perovskite materials can therefore have significant dependence on the type and density of defect states.<sup>[28]</sup> According to a couple of recent studies, oxygen and moisture also promote defects in perovskites and thereby accelerate the degradation of respective devices.<sup>[54,55]</sup>

Along with interfacial defects, deep-level defects are also associated with halide perovskite structures. The presence of deep-level trap states in ternary halide perovskites and also in double perovskites and defect-ordered perovskites remains a major point of concern towards the unsatisfactory performance of solar cells based on such absorber materials.<sup>[8,32,56,57]</sup> As opposed to the self-healing property, which limits the density of defect states in  $\text{MAPbI}_3$ , the latter type of perovskites does not show the signature of extensive defect tolerance.<sup>[56,58]</sup>

## 2.3. Different Defect Analysis Techniques

Defect physics in  $\text{MAPbI}_3$  has so far been mostly explored by theoretical and simulation approaches based on DFT.<sup>[25,49,59]</sup> A complex electronic structure of the material has however made such approaches quite nontrivial. It has been observed that different DFT approaches, such as semilocal–functional, hybrid–functional, or exchange–correlation functional on electronic structures, may yield different defect formation energies. The analysis of defects can similarly be influenced by the spin-orbit coupling (SOC) correction term in the material.<sup>[60]</sup> The most accurate investigation regarding the nature and density of defects in  $\text{MAPbI}_3$  can specifically be conducted through DFT approaches in a super-cell structure.<sup>[61]</sup> In this super-cell approach, the calculations have been conventionally carried out by the following equation.

$$\text{DFE}(X)^q = E(X)^q - E(\text{perf}) \sum_i^m n_i \mu_i + q(E_F + V + \Delta V) + E_q \quad (1)$$

where  $E(X)^q$  corresponds to energy of any super-cell having defect state  $X$  in a charge-state of  $q$  and  $E(\text{perf})$  denotes the energy of a perfect super-cell. In Equation (1),  $n$  and  $\mu$  represent the total number and chemical potential, respectively, of the element further added or taken away to the defect free system to form a defect.  $q$  represents the elementary charge of that defect. The term  $q(E_F + V + \Delta V)$  symbolizes energy due to exchange of electrons with Fermi energy of the defective system for any shift in the electrostatic potential ( $\Delta V$ ) due to defects. The last term  $E_q$  denotes long-range coulomb interaction between periodic defects.<sup>[61]</sup>

Molecular dynamics (MD) simulation is another computational method used to study the dynamic and structural properties of metal–halide perovskites.<sup>[62–64]</sup> Theoretical studies as such can provide density of states (DOS), CBM, and VBM energies in a definitive manner and can therefore yield some useful information regarding the relative defect energies in perovskites with possible strategies toward defect engineering.

On the other hand, there are several experimental techniques to determine the defect densities and their influence on optoelectronic properties. We will discuss some of the commonly used techniques in this direction, such as photoluminescence (PL) spectroscopy, photothermal deflection spectroscopy (PDS), confocal fluorescence microscopy (CFM), thermal admittance spectroscopy (TAS), and scanning probe microscopy techniques like conducting atomic force microscopy (c-AFM), Kelvin probe force microscopy (KPFM), and scanning tunneling microscopy (STM).

## 2.4. Theoretical Studies of Defects

Theoretical studies of defect states in  $\text{MAPbI}_3$  have predicted that energy levels of structural defects including iodine and methylammonium vacancies fall within two bands of  $\text{MAPbI}_3$  without altering the bandgap.<sup>[25]</sup> Another study has indicated that the charge imbalance created by methylammonium vacancy is often compensated by an iodine vacancy while retaining the charge



neutrality of the perovskite structure.<sup>[49]</sup> As a result, electronic structures at the band edges are affected minimally with the electronic bandgap being preserved. Although the defect-tolerant nature of the material does not prevent defect formation, it ensures that defects with low formation energies are formed closer to the band edges instead of at the midgap. Such shallow defects hence contribute to overall carrier concentrations instead of deep-level nonradiative intraband trap states.<sup>[45]</sup> Generally, radiative band edge defects are expected to form at very high concentrations; although beneficial for light-emitting diodes (LEDs), it is highly undesirable for solar cell applications. Defect-tolerant studies in other systems such as transition metal dichalcogenides and other semiconductors, as shown in **Figure 2a,b**, indicate that the tendency of a material to form defect states within the bandgap is primarily influenced by the similarity of orbital characters near the conduction and valence bands of semiconductors with antibonding valence band.<sup>[65]</sup> In semiconductors with antibonding VBM, the defect states originating from vacancies/interstitials are not generated inside the bandgap, leading to shallow defect states. Defect tolerance in MAPbI<sub>3</sub> is also attributed to the antibonding character of the VB. The VB of MAPbI<sub>3</sub> comprises contributions from Pb(6s) and I(5p) orbitals whereas the CB is mainly composed of Pb(6p) orbital.<sup>[12]</sup> It can hence be speculated that 3D perovskites having an antibonding character of VBM are very likely to be defect tolerant in the bulk; however, experimental confirmation is yet to be achieved in this regard.

Structural and electronic properties of halide perovskites have been intensively examined using computational methods based on DFT. First-principle calculations based on DFT studies can provide information on the band structure, DOS of conduction and valence band charge densities, etc. In this direction, such computational studies on the defect properties of cubic MAPbI<sub>3</sub> crystals revealed that among such possible defects, p-type V<sub>Pb</sub> and n-type V<sub>I</sub> have been identified to be the most-dominant intrinsic defects in the bulk of MAPbI<sub>3</sub>, having a

CH<sub>3</sub>NH<sub>3</sub>I-rich and PbI<sub>2</sub>-rich stoichiometry, respectively (**Figure 3**).<sup>[25]</sup> The transition energy levels of intrinsic acceptor-type and donor-type defects in MAPbI<sub>3</sub> are shown in **Figure 3a,b** whereas the formation energies of intrinsic point defects at chemical potentials are shown in **Figure 3c–e**. However, more in-depth calculations can be carried out considering different surface terminations during DFT analysis. The concept of the defect-tolerant nature disappears under this circumstance. In case of a thermodynamically stable CH<sub>3</sub>NH<sub>3</sub>I-terminated surface, the most stable defects are identified as a shallow-type V<sub>MA</sub> irrespective of the growth condition. However, in case of I-rich stoichiometry, I<sub>i</sub>-defects may also appear on this surface, which is considered to be located deep within the bandgap. On the other hand, for the same growth condition, a PbI<sub>2</sub>-terminated surface would promote the formation of more I<sub>i</sub>-defects leading to deep-level trap states.<sup>[44]</sup> Furthermore, DFT studies with different halide anions and monovalent cations confirmed that the defect landscape in these hybrid halide perovskites varies with composition; different perovskites have different dominant defects depending on their formation energy and balance among the possible existing defects.<sup>[45]</sup>

In another notable study, DFT with generalized gradient approximation (DFT-GGA) calculations revealed the influence of Frenkel and Schottky defects on MAPbI<sub>3</sub> and inferred that the Schottky defects do not form trap states in the bandgap.<sup>[49]</sup> Similarly, an interesting study on the defect properties of MAPbI<sub>3</sub> through semilocal exchange correlation functionals, such as density functional theory-Perdew–Burke–Ernzerhof (DFT-PBE) calculations, concluded that most of the point defects in MAPbI<sub>3</sub> form shallow states (except I<sub>i</sub> which forms deep-level states) and do not affect the electronic properties of the perovskite.<sup>[66]</sup> However, charge trapping at I<sub>i</sub> is limited by a kinetic barrier, resulting in long carrier diffusion lengths in MAPbI<sub>3</sub>. They also estimated the defect properties in a mixed-halide perovskite, MAPbClI<sub>2</sub>. In comparison with MAPbI<sub>3</sub>, the mixed-halide perovskite has a reduced lattice constant and thereby an increased formation energy of iodine interstitials and hence the reduced possibility of formation of interstitial defects.<sup>[66]</sup> Chlorine incorporation thereby improved recombination lifetime (a longer diffusion length) when compared with pristine MAPbI<sub>3</sub> and yielded a better cell performance in this mixed-halide perovskite and its analogues.<sup>[61,67]</sup> The possible point defects in MAPbI<sub>3</sub> are shown in **Table 1** with their formation energies.

MD simulation is another computational method used to study the dynamic and structural properties of metal–halide perovskites. In MAPbI<sub>3</sub>, such MD simulations have provided vital information regarding the role of iodine vacancies in trapping electrons in the perovskite (**Figure 4a**).<sup>[68]</sup> Similar but independent studies using nonadiabatic MD simulations combined with the time-domain ab initio study have been reported to be effective in studying the role of iodine interstitial defects on hole trapping and recombination rates in MAPbI<sub>3</sub>.<sup>[69]</sup> A faster trapping and release of holes to the valence band through sub-bandgap iodine interstitial states has been evidenced in such studies (**Figure 4b,c**).

Computational methods based on DFT studies have been used to study the formation of defects and its consequences on the

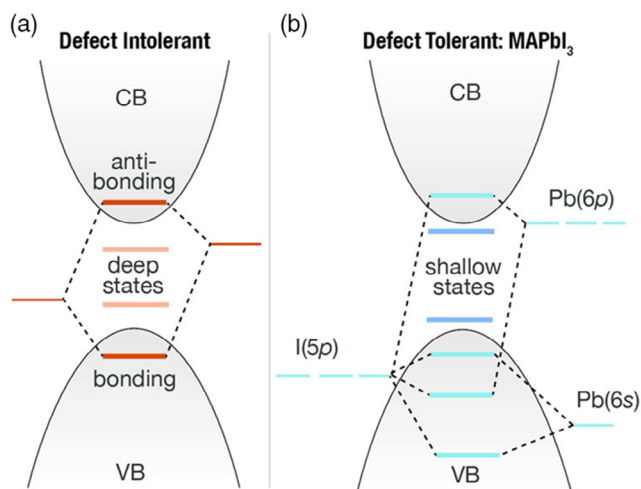


**Figure 2.** Band structures of the a) typical defect-intolerant semiconductor and b) the defect-tolerant (methylammonium lead iodide) perovskite. Reproduced with permission.<sup>[201]</sup> Copyright 2017, American Chemical Society.

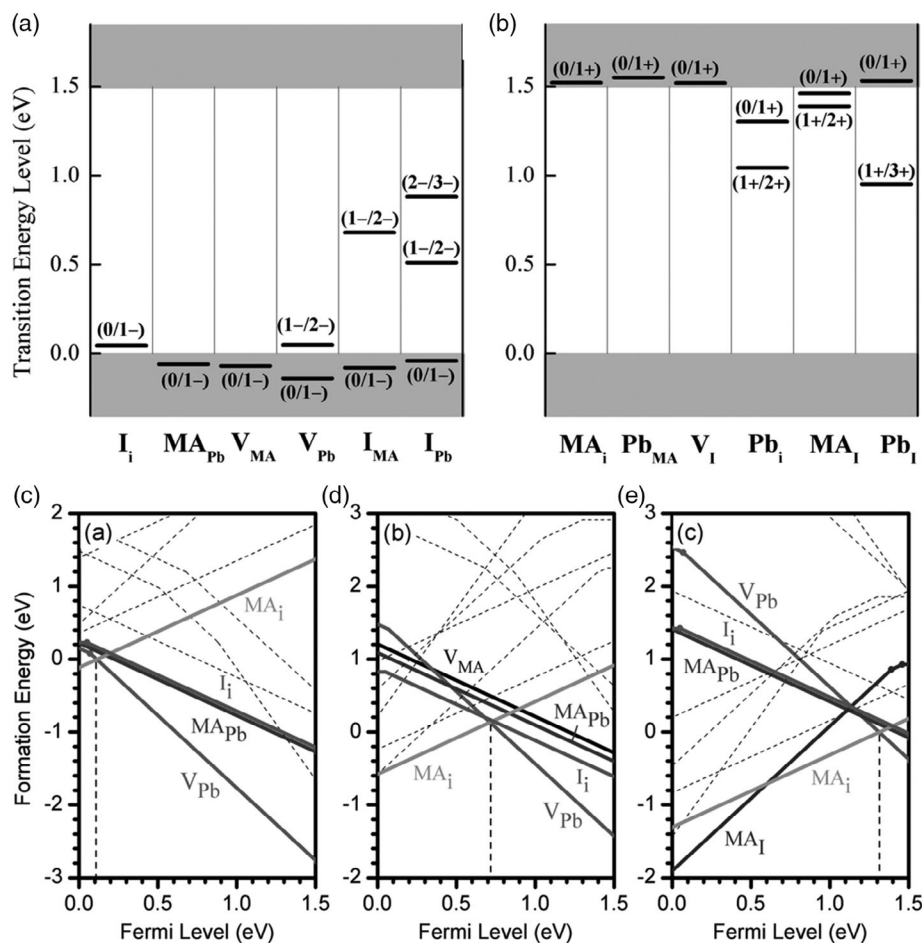


**Figure 3.** The transition energy levels of intrinsic a) acceptor-type and b) donor-type defects in MAPbI<sub>3</sub> and c–e) the formation energies of intrinsic point defects in MAPbI<sub>3</sub> at chemical potentials. In (c–e), defects with much higher formation energies are shown with dashed lines. Reproduced with permission.<sup>[25]</sup> Copyright 2014, AIP Publishing.

**Table 1.** Possible point defects in MAPbI<sub>3</sub> along with their formation energies in electron volt for three different synthesis conditions.<sup>[25]</sup> (The defect states with lowest possible energies have been marked in bold; those defects have the highest possibility of occurrence.)

Synthesis condition	Formation energy and effect on defect states											
	Acceptor like (p-type)						Donor like (n-type)					
	<i>I<sub>i</sub></i>	<i>MA<sub>Pb</sub></i>	<i>V<sub>MA</sub></i>	<i>V<sub>Pb</sub></i>	<i>I<sub>MA</sub></i>	<i>I<sub>Pb</sub></i>	<i>MA<sub>i</sub></i>	<i>Pb<sub>MA</sub></i>	<i>V<sub>I</sub></i>	<i>Pb<sub>i</sub></i>	<i>MA<sub>I</sub></i>	<i>Pb<sub>I</sub></i>
Iodine rich	<b>0.23</b>	<b>0.28</b>	0.81	<b>0.29</b>	1.96	1.53	1.39	2.93	1.87	4.24	3.31	5.54
Stoichiometric	<b>0.83</b>	<b>1.15</b>	<b>1.28</b>	1.62	3.01	3.45	<b>0.93</b>	2.51	1.27	2.91	2.25	3.62
Iodine poor	1.43	1.47	2.01	2.68	4.34	5.10	<b>0.20</b>	1.74	<b>0.67</b>	1.85	0.93	1.97

electronic properties of metal–halide perovskites. Such studies also estimated the influence of external dopants and environmental interactions on the structural and optoelectronic properties of metal–halide perovskites. However, calculations based on DFT studies have some limitations and results may diverge depending on different approximations. Meggiolaro et al. used hybrid DFT, including dispersion corrections and SOC, to

elucidate the changes in the optoelectronic properties of MAPbI<sub>3</sub> on exposure with iodine gas.<sup>[61]</sup> However, methods like semilocal exchange correlation functional, such as the PBE exchange-correlation method, neglect the effect of SOC and self-interaction corrections and thereby provide a room to miscalculate the VB and CB energies and defect levels within the bandgap. The report concluded the use of hybrid methods (local density approximation [LDA] + U + SOC) for the more accurate estimation of defect states and the use of coulomb kernel functions (like HSE06) for shallow defects in MAPbI<sub>3</sub> perovskites.<sup>[61]</sup>

## 2.5. Experimental Evidence of Defects

In the quest of experimental studies on defects in perovskite materials, various optical and scanning probe techniques have been used till date to deal with such defect states. The measurement of the trap-filled voltage in the space-charge-limited current (SCLC) method can be used to obtain the quantitative idea of the intrinsic defect density present in the perovskite.<sup>[70,71]</sup> PL spectroscopy remains an interesting choice in this direction.



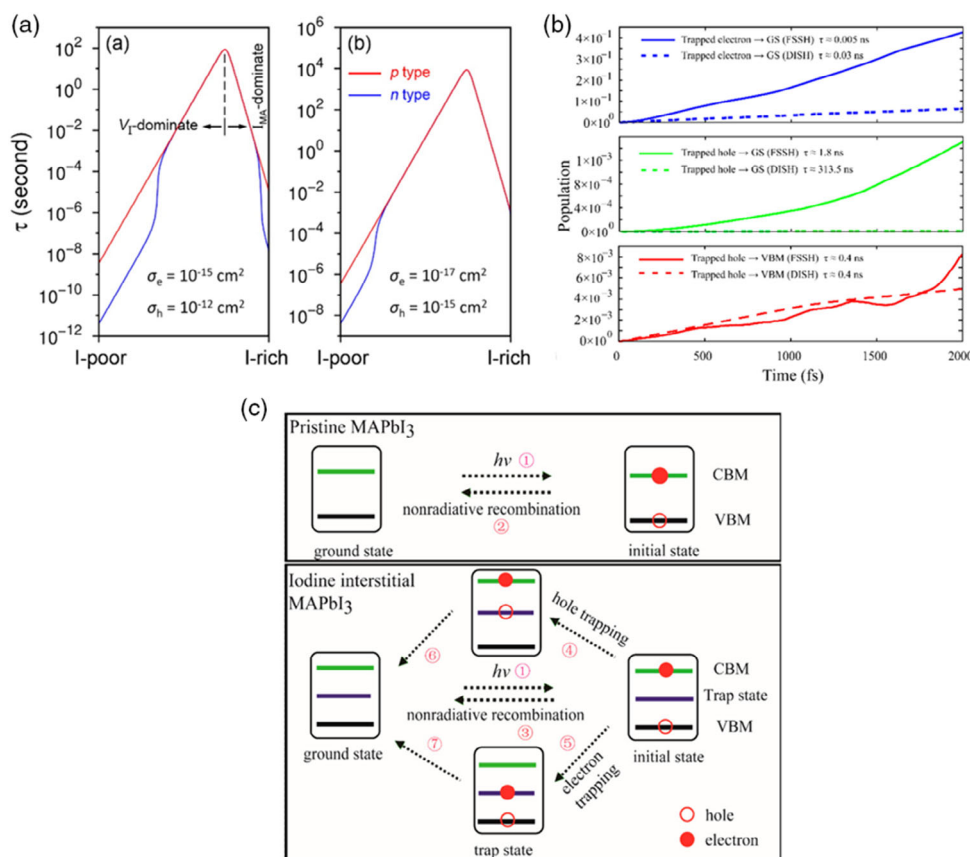


**Figure 4.** a) MD simulations and b) MD simulations combined with time-domain density functional theory to study the role of iodine vacancies in trapping electrons in MAPbI<sub>3</sub> and c) the schematic presentation of the mechanism for electron and hole trapping in MAPbI<sub>3</sub>. a) Reproduced with permission.<sup>[68]</sup> Copyright 2014, American Chemical Society. b) Reproduced with permission.<sup>[69]</sup> Copyright 2017, American Chemical Society.

Steady-state and time-resolved PL (TRPL) spectroscopy have been reported as effective approaches to analyze the density of defects in metal-halide perovskites. Defects usually act as nonradiative recombination sites and quench PL emission; the lifetime of PL emission is also associated with trap density in MAPbI<sub>3</sub>.<sup>[72,73]</sup> Apart from PL, TAS is another novel approach to measure the trap-DOS (t-DOS), which can deliver sufficient information on both the deep and shallow defect states in perovskite thin films.<sup>[74]</sup> PDS is also considered to be an important and sensitive technique to measure any weak absorption near the bandgap, where the information regarding the defect states can be obtained as well. As the fluorescence intensity is inversely proportional to the density of nonradiative defect states, CFM can also be successfully used to examine the defect states in a perovskite thin film.<sup>[75,76]</sup> Scanning probe microscopy (SPM) is also another highly sensitive technique, providing an unprecedented opportunity to probe defect states through its much localized measurement approach.<sup>[77–80]</sup>

### 2.5.1. Space-Charge-Limited Current

When trap states are present in a semiconductor, there is every possibility for injected carriers to become trapped at such states. Now, as the density of the injected carriers increases with an

increase in applied voltage, more and more traps are filled with carriers; the voltage at which all traps are filled is called the trap-filled limit voltage. The measurement of the trap-filled limit voltage in the SCLC model is one of the common and straightforward methods to obtain a rough estimate of defect density in a perovskite material. In this approach, the defect density  $N$  can be estimated using the following equation.

$$N_{\text{defects}} = \frac{2\epsilon\epsilon_0 V_{\text{TFL}}}{eL^2} \quad (2)$$

where  $\epsilon$  and  $\epsilon_0$  imply dielectric constant and vacuum permittivity of the perovskite, respectively,  $V_{\text{TFL}}$  denotes the trap-filled limit voltage,  $e$  is elementary charge, and  $L$  is thickness of the film.<sup>[81]</sup> Following this technique, the approximate value of defect density in polycrystalline perovskite thin films turns out to be  $10^{17}$ – $10^{19}$  m<sup>-3</sup>.<sup>[70,71]</sup>

SCLC measurements can only be carried out in device architectures to detect the electron and hole traps by fabricating electron-only and hole-only devices. However, simultaneous measurements of both types of defects are not possible, yet the SCLC measurements are considered as one of the most widely used methods to characterize defects arising out of grain boundaries, surface or interface defects, and a few bulk point defects (Frenkel defects).<sup>[82]</sup>

### 2.5.2. Time-Resolved Photoluminescence Spectroscopy

PL measurements have a strong correlation with the nonradiative trap states and hence can be recognized as a potential tool to investigate the density of defects in hybrid halide perovskite materials.<sup>[83–85]</sup> When illuminated during PL measurements, a perovskite material absorbs photons and produces e–h pairs. These photogenerated excess carriers can further emit light upon recombination. Now, by changing the excitation intensity, different PL responses can be plotted as a function of pump fluence in a double logarithmic scale. As the carrier dynamics is strongly influenced by intrinsic defects present in the perovskite material, an increment or a decrement of PL intensity at the steady state would imply reduction or enhancement of trap states, respectively. Under this circumstance, an abrupt change in the slope of the curve would be obtained, corresponding to the saturated trap density. The estimation of trap density can be obtained from the following equation<sup>[86]</sup>

$$\eta_{\text{trap}} = \frac{P_{\text{th}}\alpha}{E} \quad (3)$$

where  $P_{\text{th}}$  is the threshold of pump fluence intensity at the saturated defect concentration,  $E$  the energy of photons, and  $\alpha$  is the absorption coefficient. Moreover, the trap density can be obtained by fitting the TRPL data.<sup>[83,84]</sup> The carrier lifetime from TRPL can be expressed as<sup>[87]</sup>

$$\frac{1}{\tau_{\text{total}}} = \frac{1}{\tau_{\text{rad}}} + \frac{1}{\tau_{\text{nonrad}}} \quad (4)$$

where  $\tau_{\text{rad}}$  and  $\tau_{\text{nonrad}}$  denote radiative and nonradiative lifetime respectively. The total lifetime  $\tau_{\text{total}}$  generally depends strongly on the second term,  $\tau_{\text{nonrad}}$ , which is lower of the two lifetimes. Hence, a large effective lifetime infers a less trap-assisted nonradiative recombination and lesser defects. As compared with single crystals, polycrystalline perovskites possess a higher density of defect states, implying the existence of defects at the surface and grain boundaries.<sup>[88]</sup>

Unlike the other defect analysis techniques, PL measurements do not involve any substrate per se. However, as PL emission is only collected by the detector, this technique is associated with surface defects.<sup>[82]</sup>

### 2.5.3. Confocal Fluorescence Microscopy

As the intensity of fluorescence is inversely proportional to the density of nonradiative defect states in a perovskite thin film, CFM can be considered to be one of the significant methods to study the physics of defects in such materials. Here, the absence of fluorescence emission is considered to be a measure of defect states. It provides information on both the bulk and surface defects. It has some specific advantages over TRPL, which provides only an average value across the film.<sup>[75]</sup> CFM provides a unique opportunity to probe the defects even in a particular domain in terms of the microscopic fluorescence mapping process. Here the defects can be viewed in the form of bright and dark domains. In a particular region, bright regions infer the

presence of lesser defects whereas dark regions suggest greater defect densities at a local scale.<sup>[76]</sup>

In one of the pioneering work of its kind, Dequillettes et al. reported an enhanced PL intensity and lifetime in MAPbI<sub>3</sub> films placed in an inert environment.<sup>[89]</sup> They used CFM and time-of-flight secondary ion mass spectrometry (ToF-SIMS) to study MAPbI<sub>3</sub> films under a constant illumination and attributed the increase in PL intensity to be due to the reduced density of trap states in the bulk of the material. ToF-SIMS studies furthermore revealed iodine redistribution in MAPbI<sub>3</sub> films, confirming photoinduced halide migration in MAPbI<sub>3</sub> films. They proposed that such photoinduced iodide migration passivated the iodide interstitials and iodide vacancies, leading to enhancement in the PL emission. They also combined CFM with scanning electron microscopy (SEM) to map the PL decay (**Figure 5**) and explored carrier decay dynamics in perovskite films.<sup>[89]</sup>

It should be noted that this technique is only used to visualize the location of defect states. The types of defects cannot be identified from such measurements. The resolution of the obtained CFM images is also considered as another limitation as the wavelength of excitation light is not comparable with the atomic scale.<sup>[82]</sup>

### 2.5.4. Photothermal Deflection Spectroscopy (PDS)

In absorption spectroscopy, the wavelength dependence of the absorption coefficient at times consists of an exponential part called Urbach tail. Such a “tail” generally appears in poorly crystalline materials and in disordered/amorphous materials, as such materials have some localized states extending within the bandgap.<sup>[90–92]</sup> By applying Urbach’s empirical rule, the Urbach energy can be calculated from the following equation.

$$\alpha = \alpha_0 \exp\left(\frac{h\nu}{E_U}\right) \quad (5)$$

where  $\alpha$  is the absorption coefficient,  $\alpha_0$  is a constant, and  $E_U$  denotes the Urbach energy, which is correlated with the localized states in terms of width of the band tail. To obtain a straight line plot to calculate  $E_U$  from its slope, the equation can be rewritten as

$$\ln \alpha = \ln \alpha_0 + \frac{h\nu}{E_U} \quad (6)$$

In this regard, PDS is a very sensitive technique to measure even a weak absorption near the band edges and provide vital information on the defect states; a lower value of  $E_U$  is an indication of having fewer defect states (**Figure 6a**). Basically,  $E_U$  is an important energetic disorder parameter, a change of which implies the existence of different energetic levels in the perovskite. Zheng and coworkers used hyphosphorous acid (HPA) to passivate metallic lead defects. They have calculated the  $E_U$  using Urbach energy fit to the band edges (**Figure 6b,c**). A lower value of Urbach energy indicates a higher electronic order thereof.<sup>[93]</sup>

It should be kept in mind that the Urbach tail is influenced by the temperature of the material and phonon interactions. Thus, it

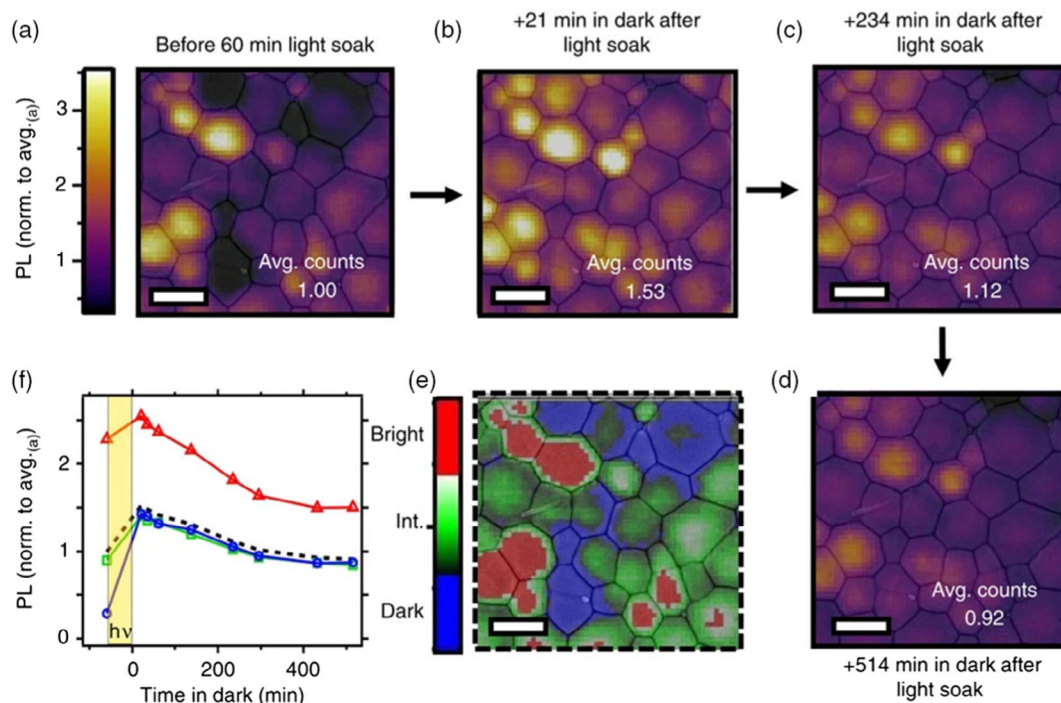


**Figure 5.** Change in PL a) before and b–d) after exposure to simulated sunlight, e) three-color scale image showing dark, intermediate (Int.), and bright regions and f) local PL enhancement and relaxation for dark (blue, enhancement of  $4.9\times$ ), intermediate (green, enhancement of  $1.6\times$ ), and bright (red, enhancement of  $1.1\times$ ) regions. The time ( $t$ ) under illumination is highlighted in yellow and  $t > 0$  shows the local PL relaxation dynamics over the time left in the dark. The dotted black line is the PL relaxation averaged across the whole fluorescence image. Reproduced with permission.<sup>[89]</sup> Copyright 2016, Springer Nature.

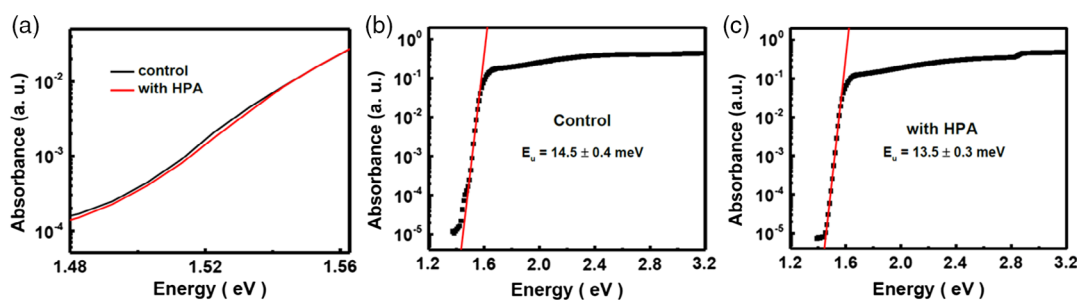


**Figure 6.** a) PDS spectra of the perovskite film processed without and with HPA deposited on quartz substrates and calculation of the Urbach energy " $E_U$ " for the perovskite film processed b) without and c) with HPA. Reproduced with permission.<sup>[93]</sup> Copyright 2015, Springer Nature.

is important to conduct the control experiment at the same temperature.<sup>[82]</sup>

### 2.5.5. Thermal Admittance Spectroscopy

Defect states are sometimes considered as capacitors as the trapping and detrapping nature of defect levels are analogous to the charging and discharging behavior of a capacitor. As a result, if an AC voltage is applied to a device, the admittance of the perovskite system depends on the frequency of the AC voltage. This simple concept is used in TAS that is basically used for the electrical characterization of capacitance and conductance in terms of frequency and temperature in a perovskite to study

the defect levels.<sup>[94,95]</sup> However, due to the temperature dependence, a deep-level trap may sometimes remain unavailable to contribute to the capacitance and conductance at a higher frequency, especially when the emission rate is comparably slower than the frequency.<sup>[74,94]</sup> With an increasing temperature, the rate of emission from the trap increases, resulting in a higher contribution from the defects. In such a scenario, a threshold frequency appears in the form of steps and peaks in the temperature dependence of the conductance plot as a signature of deep-level traps. The temperature of the inflection point for each capacitance versus the temperature plot at a fixed frequency is then drawn in the form of an Arrhenius plot of emission rate versus  $1/kT$ . However, the energy distribution of defect states

can be obtained analytically using the following complex equation.

$$N_t(E_\omega) = -\frac{V_D}{qW_D} \frac{\omega}{kT} \frac{dC}{d\omega} \quad (7)$$

where  $V_D$  and  $W_D$  are the potential barrier and depletion width, respectively,  $\omega$  is the angular frequency,  $C$  the capacitance,  $T$  the temperature, and  $k$  is Boltzmann constant. This effective method can provide information on both shallow and deep defects in perovskite thin films.<sup>[74,95]</sup>

This method has been found to be useful in probing surface or interfacial defects, defects due to grain boundaries, and point defects as well. However, the detection of deep traps near the Fermi energy is not possible due to the dependence of this technique with the trapping–detrapping mechanism.<sup>[82]</sup>

### 2.5.6. Scanning Probe Techniques (c-AFM, KPFM, and STM)

Scanning probe techniques (microscopy) like c-AFM, KPFM, and STM have recently been used to study the electrical properties, band edges, and defect states in hybrid halide perovskites.<sup>[9,32,46,79]</sup> c-AFM which is basically a modified version of AFM, having a conducting tip, can simultaneously measure the local  $I$ – $V$  characteristics along with topographic images. Such  $I$ – $V$  characteristics are generally obtained by applying a voltage in between the perovskite thin film and the tip of c-AFM. In this manner, the conductivity between the tip and the sample is also judged and could be mapped over a section of the film. Now, electronic conductivity can show contrasting behavior at the grain boundaries and interiors. Generally the grain boundaries present in perovskites are insulating in nature with a wider bandgap. Hence, their passivation promotes an increase in local conductivity. Such measurements thus provide unique opportunities to probe the effect of defect passivation by mapping the local conductivity of a semiconducting surface.<sup>[96,97]</sup>

The surface work function of perovskite thin films plays a vital role in optoelectronic devices. The work function which has a key role in the transport mechanism across the Fermi energy can be derived from the surface potential. The distribution function of such a potential (potential has been fitted using Gaussian or Lorentzian function) generally represents the average surface work function,<sup>[98]</sup> which can be obtained from the following equation.

$$eV_{\text{CPD}} = \varphi_{\text{Tip}} - \varphi_{\text{Sample}} \quad (8)$$

where  $V_{\text{CPD}}$  is the contact potential difference (CPD) and  $\varphi_{\text{Tip}}$  and  $\varphi_{\text{Sample}}$  are the work functions of the tip and the sample, respectively. The work function of the tip is derived by scanning a reference or a standard sample like highly oriented pyrolytic graphite (HOPG) or gold. Similar to c-AFM, when the insulating GB defects are passivated, an increase in the CPD would be observed due to the enhancement of the conductivity and accumulation of charges at the surface as well. Hence, a combination of c-AFM and KPFM provides an unprecedented opportunity to confirm the claim of defect passivation in perovskite surfaces.<sup>[78,99]</sup>

STM is another local mode of measurements where the differential tunneling conductance ( $dI/dV$ ) spectra of the

semiconductors can provide the energy-dependent DOS of the perovskite.<sup>[44,100]</sup> The DOS spectra obtained thereof can identify the energies of VBM and CBM of the semiconductor in the form of first peaks in both sides of Fermi energy ( $E_F$ ), which is considered to be aligned at 0 V. When a bias is applied to the tip, the first peak at a positive tip voltage will imply the withdrawal of electrons from the semiconductor and hence indicate the VB edge of the semiconductor; similarly, the first peak at the negative voltage will imply the injection of electrons to the CB edge of the material. As any kind of trap states situated within the bandgap can also contribute in such a tunneling process, their signature will appear nearer  $E_F$  as compared with their true band edges.<sup>[32,44]</sup> The quantitative estimation of the defect states can be predicted from the magnitude of DOS obtained from the  $dI/dV$  spectra. The type of conductivity obtained from such analyses also provides important information on the nature of the defects (donor or acceptor). Similarly, the presence of many different defects can be viewed as a broader distribution of defect state energies in perovskite materials.

KPFM and c-AFM techniques can be useful tools to explore grain boundaries and surface defect states in hybrid perovskites. The setup for such measurements is shown in **Figure 7a**.<sup>[101]</sup> The mapping of the CPD under various laser illumination intensities at a specified wavelength can be measured by KPFM (**Figure 7b**), whereas the current images of MAPbI<sub>3</sub> films under illumination can be recorded through c-AFM measurements (**Figure 7c**).<sup>[102]</sup> Such studies have confirmed that ion migration in polycrystalline perovskite films occurs majorly through grain boundaries and also demonstrated the beneficial effects of the boundaries; the grain boundaries, instead of acting as recombination sites, act as carrier dissociation interfaces that in turn enhance the photocurrent in a device. KPFM has also been used to study the defect-induced band bending at the interface between a perovskite and an electrode.<sup>[99]</sup>

However, it should be kept in mind that a proper electrical tuning of the tip for both c-AFM and KPFM is highly desirable, considering the sensitivity of such measurements. Moreover, in case of c-AFM, the general trend explained earlier is not always true. If a large amount of metal is diffused in the perovskite surface that is natural during the formation of undercoordinated lead defects, the conductivity would decrease after the passivation of such defects.<sup>[78]</sup> Such a phenomenon would also show an opposite trend during KPFM measurements. Upon passivation, the CPD would decrease in a conflicting fashion due to a decrease in the surface conductivity.<sup>[99]</sup>

STM and spectroscopic methods have been used to study the effect of doping on the electronic structure of the bandgap. Ohmann et al. conducted low-temperature STM studies on MAPbBr<sub>3</sub> single crystals and revealed the real-space atomic structure of the perovskite along with local defects and investigated the dislocation lines and surface defects.<sup>[103]</sup> In another study, we have investigated the effect of self-doping in MAPbI<sub>3</sub> and FAPbI<sub>3</sub> perovskites (**Figure 8**) by varying precursor stoichiometry.<sup>[46]</sup> This study demonstrated a gradual shift of the Fermi energy with a change in stoichiometry (from PbI<sub>2</sub>-deficient to PbI<sub>2</sub> rich-conditions), leading to a change in the electronic conductivity of the perovskite from p-type to n-type in nature. A variation in the stoichiometry of the precursor while forming a perovskite film leads to a change in the concentration



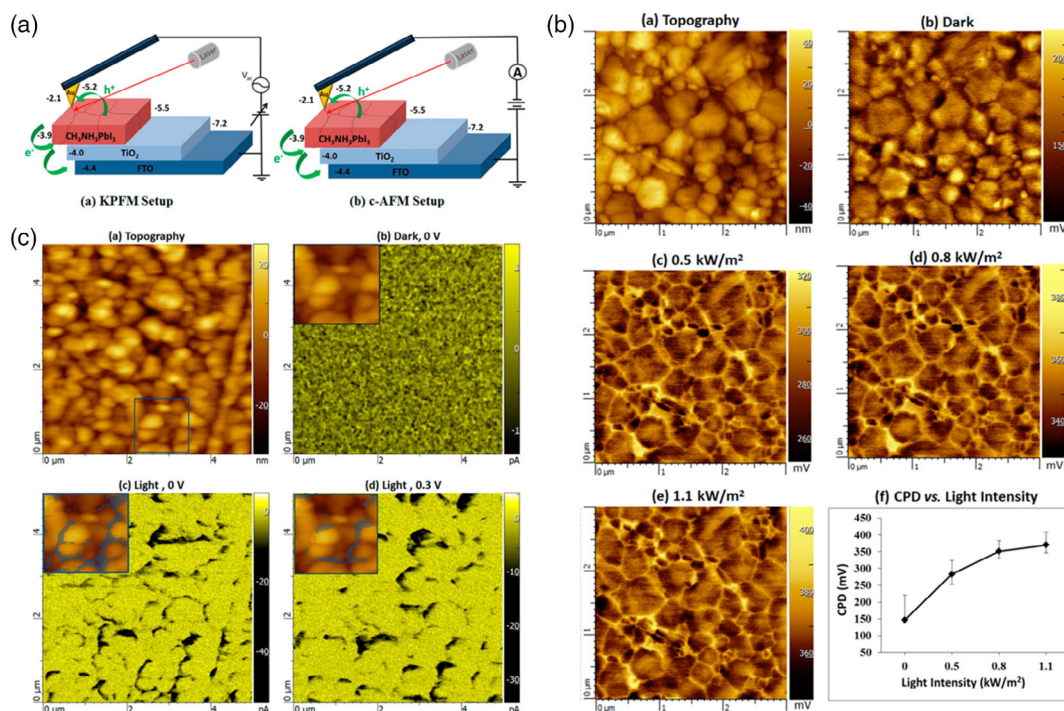


**Figure 7.** a) Illustration of the KPFM and c-AFM setup to explore grain boundaries and surface defect states in hybrid perovskites, respectively. b) Topography map, CPD images taken in the dark, and under various laser illumination intensities at a wavelength of 500 nm, intensity dependence of CPD in MAPbI<sub>3</sub> at a wavelength of 500 nm as measured by KPFM. (c-AFM measurements were carried out on a glass/FTO/TiO<sub>2</sub> structure over an area of 5 μm<sup>2</sup>) c) Topographic image, current image taken in the dark and under illumination at 0 V and under illumination at 0.3 V. Insets in panels (c) show overlaps of the corresponding c-AFM maps and a topography map of the region with a white outline (wavelength and intensity of the illumination were 500 nm and 1.1 kW cm<sup>-2</sup>, respectively.) Reproduced with permission.<sup>[101]</sup> Copyright 2015, American Chemical Society.

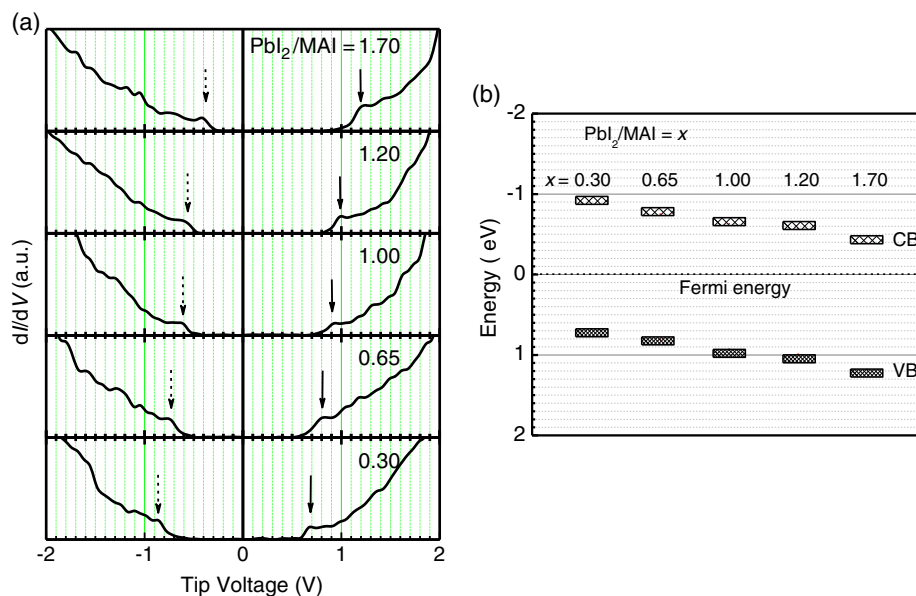


**Figure 8.** a)  $dI/dV$  spectra and b) band diagram of MAPbI<sub>3</sub> films with different PbI<sub>2</sub> and CH<sub>3</sub>NH<sub>3</sub>I (MAI) stoichiometries as mentioned in the legends. Reproduced with permission.<sup>[46]</sup> Copyright 2018, American Chemical Society.

of electrons and holes in the perovskite; in other words, the stoichiometry controls the presence of point defects in the perovskite

in which a low PbI<sub>2</sub>/CH<sub>3</sub>NH<sub>3</sub>I ratio would amount to a PbI<sub>2</sub>-deficient environment, leading to the formation of a large

**Table 2.** Experimental techniques used to probe specific defects.

Technique	Mode of measurement	Sample	Defects probed	Limitations	Ref.
SCLC	Electrical	Electron- or hole-only devices	GB defects, surface defects, interfacial defects, point defects.	Device architecture is needed. Simultaneous measurement of hole and electron traps is not possible.	[81,82]
TRPL	Optical	Solid/liquid/film	Surface defects	Point defects are difficult to probe.	[83,86]
CFM	Optical	Film	–	Only the position of the defects can be probed.	[82,89]
PDS	Optical	Film	Localized point defects	Temperature sensitive	[93]
TAS	Optical	Film	Deep defects, antisite defects, GB defects, surface defects, interfacial defects	Existence of shallow defects is not possible to probe.	[95]
SPM	Electrical	Film	GB defects, surface defects, interfacial defects, point defects	Sensitive in ambient condition. Proper electrical tuning of cantilever and tip is necessary. Energetically mapping of defects is not possible.	[97,103]

number of lead and iodine vacancies. Now, as the formation energy of lead vacancies is much lower than those of the other existing point defects, the former one would dominate and a balance among these existing point defects will mark the Fermi energy for the particular composition of the perovskite (p-type conductivity). Similarly, under a  $\text{CH}_3\text{NH}_3\text{I}$ -deficient environment, that is a  $\text{PbI}_2$ -rich environment, three kinds of point defects were formed in films: lead interstitials, methylammonium vacancies, and iodine vacancies. Among them, iodine vacancy has the least formation energy and a balance among the three defects inferred an n-type behavior in the respective thin film. Thus, studies on the shift in Fermi energy could infer not only the presence of point defects but also the nature and type of defects in hybrid halide perovskites.

We have summarized different experimental defect analysis techniques, as shown in **Table 2**.

### 3. Defect Passivation in $\text{ABX}_3$

As mentioned earlier, the defects states have a detrimental effect on device performance. Hence, the passivation of defects is necessary to boost the PCE of solar cells. In this section, we will discuss different strategies to passivate defect states in perovskites, having a beneficial effect in PSCs. This includes passivation techniques in the perovskite absorber layer through compositional engineering and doping, different surface passivation treatments such as Lewis acid and base treatments, interfacial passivation, and different physical passivation processes.

#### 3.1. Materials Engineering

As stated earlier, one of the wonderful properties of the  $\text{MAPbI}_3$  structure is its defect-tolerant nature. Most of the intrinsic defects in  $\text{MAPbI}_3$  form shallow states close to band edges and do not contribute to the optoelectronic properties of devices based on the material.<sup>[50]</sup> However deep-level defects, grain boundaries, ion migration, and interface defects are reported to adversely affect the stability of the material as well as optoelectronic properties of the devices based on the perovskite. Different passivation techniques have been developed with an aim to

reduce the detrimental effects of defects in the material and improve the stability and performance of  $\text{MAPbI}_3$ -based devices. Various chemical and physical passivation methods have been considered in this respect. Composition engineering in forming mixed-cation (MA, FA, and cesium) and mixed-anion (chloride, bromide, and iodide) perovskites has been reported to be an efficient method to improve performance and stability of perovskite-based devices. The characteristics of high-efficiency solar cells containing such mixed perovskites as the absorber layer have shown that they possess lower defect densities and also have a high defect tolerance. In this regard, the addition of cesium in  $\text{FA}_{0.83}\text{MA}_{0.17}\text{Pb}(\text{I}_{0.83}\text{Br}_{0.17})_3$  has been reported to reduce the defect densities by one order of magnitude.<sup>[104]</sup> The addition of bromides to form mixed-halide perovskites has been reported to transform the deep-level iodide interstitial defect states to shallow defects by shifting their energies closer to the VB. Such treatment can remove metallic lead from the lattice, resulting in an enhancement of carrier lifetime.<sup>[105]</sup>

Metallic lead defects ( $\text{Pb}^0$ ) can originate in  $\text{MAPbI}_3$  films due to a number of possible reasons, such as excitation stresses,<sup>[106]</sup> incomplete reaction or loss of halides during the reaction process,<sup>[107]</sup> contamination to the precursor or solvent, aging stresses,<sup>[45]</sup> and so on. These lead-defects introduce nonradiative pathways, which act as quenching centers of excitons (reduction of PL quantum efficiency), hamper device performance, and also stop the long-term stability of perovskite devices.<sup>[108,109]</sup> The formation of such  $\text{Pb}^0$  defects in  $\text{MAPbX}_3$  can be prevented by increasing the concentration of  $\text{CH}_3\text{NH}_3\text{X}$  in the precursor, that is, through a deliberate  $\text{PbI}_2$ -deficient condition of the reaction, introducing redox-active organic molecules, oxidizing agents, and so forth.<sup>[45]</sup> Zhang et al. reported the passivation of uncoordinated lead ions and iodine vacancies in an all-inorganic perovskite through additional anionic dopants like chloride, which is known to reduce the defect density and also improve the morphology of perovskite crystals.<sup>[110]</sup> It has been reported that even when stoichiometric precursors are used to form  $\text{MAPbI}_3$ , metallic lead remained in the films due to the incomplete reaction or loss of halides during the reaction process. These lead residues introduce nonradiative pathways and quench the PL intensity of the perovskite.<sup>[108]</sup> The formation of metallic lead in  $\text{MAPbX}_3$  can be prevented by increasing the concentration

of methylammonium halide in the precursor, that is, through a deliberate  $\text{PbI}_2$ -deficient condition of the reaction. Zhang et al. reported the passivation of uncoordinated lead ions and iodine vacancies in an all-inorganic perovskite through additional anionic dopants like chloride, which is known to reduce the defect density and also improve the morphology of the perovskite crystal.<sup>[110]</sup>

Nonstoichiometric compositions leading to  $\text{PbI}_2$ -rich and  $\text{PbI}_2$ -poor growth conditions have also been reported to modify the defect states in  $\text{MAPbI}_3$  perovskite. The effect of excess  $\text{PbI}_2$  in the perovskite is controversial; some researchers have inferred that excess iodine has a detrimental effect on perovskite films whereas others have claimed  $\text{PbI}_2$  to act as a defect-passivating agent. A straightforward method in this regard is self-doping, which can be useful for efficient defect passivation in  $\text{MAPbI}_3$ . An addition of excess  $\text{PbI}_2$  was found to be effective to passivate local grains.<sup>[111–113]</sup>  $\text{PbI}_2$ -rich conditions have also been reported to reduce defect densities at the perovskite interfaces and improve the crystallinity of perovskite films, leading to improved efficiencies in  $\text{MAPbI}_3$ -based solar cells. The growth condition with  $\text{PbI}_2$ -poor precursor stoichiometries, in contrast, reduces the deep-level iodine interstitials in  $\text{MAPbI}_3$ , leading to improved PL emission.<sup>[29]</sup> Chen et al. have recently reported an in situ passivation strategy, utilizing excess  $\text{PbI}_2$  to passivate the defects at the perovskite surface and grain boundaries.<sup>[113]</sup> As far as the role of iodine is concerned, the introduction of excess iodine in the precursor solution through the use of  $\text{CH}_3\text{NH}_3\text{I}$ -rich precursors has been reported to reduce deep-level defects. The addition of iodine led to the formation of  $\text{I}_3^-$ , which passivated iodine vacancies.<sup>[45,85]</sup> However, the amount of excess iodine has to be optimized to achieve an optimum performance. We would like to mention here that defect passivation through excess iodine can be accomplished by adding both excess  $\text{CH}_3\text{NH}_3\text{PbI}_3$  and  $\text{PbI}_2$  in the precursor. However, the use of excess  $\text{CH}_3\text{NH}_3\text{PbI}_3$  has been reported to be more beneficial in this regard as the neutralization of negatively charged iodine defects through positively charged  $\text{MA}^+$  forms volatile  $\text{CH}_3\text{NH}_3\text{I}$ , whereas the use of  $\text{Pb}^{2+}$  results in the formation of wide-bandgap  $\text{PbI}_2$  with insulating grain boundaries.<sup>[85]</sup> Such a passivation process effectively improves the stability of PSCs along with boosting the PCE to over 22%.<sup>[85]</sup> In a recent work, Wang et al. reported that antisolvent-washing treatment with excess iodine can be beneficial to enhance the PCE of solar cells, as such a treatment promotes better crystallization and defect passivation of undercoordinated  $\text{Pb}^{2+}$  defects and dangling bonds.<sup>[114]</sup> Inference from work using excess  $\text{PbI}_2$  has remained inconclusive as there are reports of light-induced defect formation in the perovskite synthesized with  $\text{PbI}_2$ -rich precursors.<sup>[115]</sup>

### 3.2. Extrinsic Doping

#### 3.2.1. Inorganic Dopants

Metal-halide perovskites are mostly synthesized through facile solution-based approaches. The addition of inorganic dopants to the reaction mixture is one of the most widely explored methods for external doping and defect passivation. In general, the vast majority of charged defects, such as cation vacancies, halide

vacancies, and antisite defects, is passivated using an additive with the opposite charge. However, this is not true for all the cases as defect passivation can also be conducted, following replacement by similarly charged ions. Although a number of trivalent elements such as bismuth, indium, antimony, gold, etc. have been introduced as dopants in  $\text{MAPbX}_3$  ( $X = \text{I}$  and  $\text{Br}$ ) structures, efforts have mostly resulted in the tuning of electronic structures of the parent perovskite. Among the possible trivalent dopants, bismuth doping has been studied extensively due to multiple aspects of such heterovalent doping. Bismuth has been reported to be an extremely effective means for bandgap tuning (redshift to be specific).<sup>[116]</sup> In addition, at low concentration of doping,  $\text{Bi}^{3+}$  dopants have been found to fill the trap states and improve ionic conductivity of the perovskite; at a higher concentration of doping, they act as nonradiative recombination centers, leading to a transition from bimolecular recombination in pristine  $\text{MAPbX}_3$  perovskites to a dominant trap-assisted monomolecular recombination process.<sup>[117,118]</sup>

Abdi-Jalebi et al. reported doping of  $\text{MAPbI}_3$  with monovalent cations ( $\text{Na}^+$ ,  $\text{Cu}^+$ , and  $\text{Ag}^+$ ) having an ionic radius similar to that of bivalent lead cations. Such heterovalent substitution has led to an improvement in the PCE of solar cells based on doped materials.<sup>[119]</sup> The improved performance upon doping of a monovalent cation has been attributed to a notable decrease in charge transport activation energy through the passivation of  $\text{MA}^+$  vacancies by the filling mechanism and thereby an enhanced electron and hole mobility.<sup>[119]</sup>

Among all the inorganic dopants,  $\text{K}^+$  has been found to be the most suitable candidate, as it can easily accommodate itself in the interstitial position instead of substituting the lead ions. Moreover, it has several useful impacts after the passivation of halide vacancies through immobilizing or the vacancy-filling process, as it can arrest iodine migration and reduce hysteresis in the current–voltage characteristics of solar cell devices.<sup>[120]</sup> Experimentally, passivation of both positive and negative charges in alloyed perovskites has also been achieved through substitution by potassium and rubidium ions. These ions have a smaller effective ionic radius to occupy interstitial sites and surfaces. Such a substitution enhanced the PL emission and charge transport in these doped halide perovskites. In similar studies, Nam et al. reported the incorporation of  $\text{K}^+$ , leading to an improvement in PCE, stability, and the reduction of hysteresis in the current–voltage ( $I$ – $V$ ) characteristics of solar cells.<sup>[121]</sup> Tang et al. studied the effect of various alkali-metal cations on the structural and electronic properties of  $\text{FA}_{0.85}\text{MA}_{0.15}\text{PbBr}_{0.45}\text{I}_{2.55}$ .<sup>[122]</sup> They reported least defects upon  $\text{K}^+$  doping in the perovskite, with an upward shift in both CBM and VBM energies. Such an improvement can be ascribed to the inhibition of iodine ion migration and reduction of bulk and interfacial trap densities by potassium ions, leading to a narrowing of hysteresis in the current–voltage characteristics. With potassium iodide (KI) inclusion in the precursors, Abdi-Jalebi et al. have reported an interesting approach of defect passivation where  $\text{K}^+$  ions could passivate the halide defects in the perovskite absorber layer. A schematic illustration of halide vacancy passivation is shown in **Figure 9a**. In this way, upon an increasing concentration of KI in the precursor, they have reported an improvement in the PCE from 17.3% to 21.5% in devices based on  $(\text{Cs,FA,MA})\text{Pb}(\text{Br}_{0.15}\text{I}_{0.85})_3$  perovskites with a significant increase in the

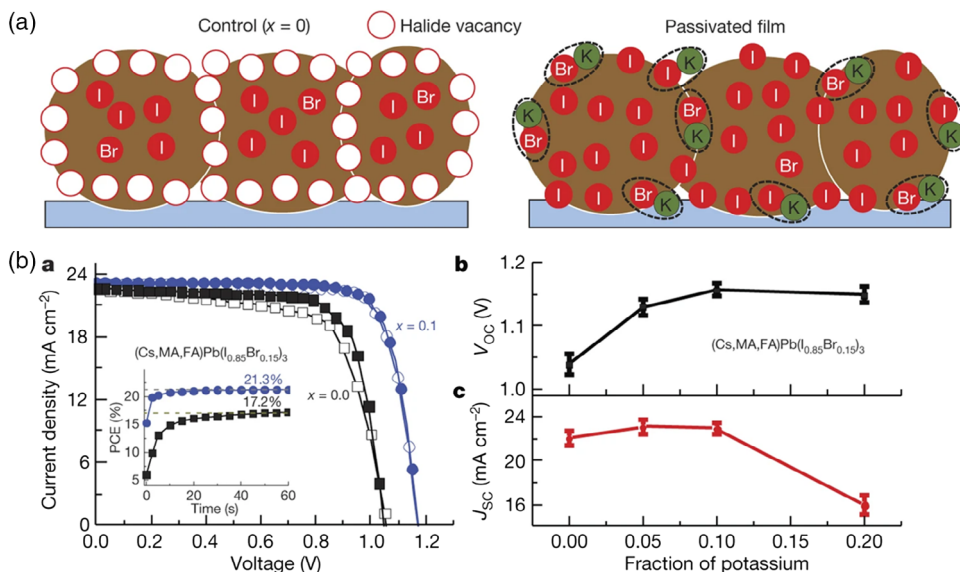


**Figure 9.** a) Schematic representation of the defect passivation process through KI doping and b)  $J$ - $V$  characteristics and variation of short-circuit current density ( $J_{SC}$ ) and open-circuit voltage ( $V_{OC}$ ) with a fraction of potassium in  $(\text{Cs,FA,MA})\text{Pb}(\text{Br}_{0.15}\text{I}_{0.85})_3$ -based solar cells. Reproduced with permission.<sup>[202]</sup> Copyright 2018, Springer Nature.

open-circuit voltage ( $V_{OC}$ ) (Figure 9b). Recently, the incorporation of  $\text{Cs}^+$  and  $\text{K}^+$  has been reported to be effective for obtaining phase-pure and defect-free perovskite absorber layers.<sup>[123]</sup> The incorporation of KI in the precursor is also reported to reduce iodide Frenkel defects in  $\text{MAPbI}_3$ . The dopant metal ions could passivate anionic defects in the perovskite through electrostatic interaction and formation of ionic bonds with negatively charged defects.<sup>[120]</sup> The reduction in the density of defects in  $\text{MAPbI}_3$  has also been achieved through aluminum-ion doping. Such methods effectively reduced the microstrain in the doped  $\text{MAPbI}_3$  crystals, resulting in a reduced hysteresis and an improved PCE in devices based on the doped material.<sup>[124]</sup>

### 3.2.2. Organic Dopants

Passivation of defects can similarly be attempted with a set of organic dopants or additives. Fullerenes (PCBM) can be mixed with the precursors to passivate donor-like Pb-I antisite defects through the formation of coordination bonds in the PCBM-halide complexes.<sup>[45]</sup> Moreover, PCBM can heal iodine-rich trap states and prevent iodide ion migration under the influence of an electric field. The process increased the PCE of respective solar cells by 1.5 times.<sup>[125]</sup> Guanidinium (GA)-based additives in  $\text{MAPbI}_3$  also have passivation capability of ion vacancies, enhancing the carrier lifetime and achieving a high  $V_{OC}$  thereby. It also helps to reduce recombination at the interfaces and provides a protective shield to resist oxygen intrusion. De Marco et al. observed a significant improvement in the PCE from 16.3% to 17.1% by incorporating GA in the precursor solution.<sup>[83]</sup> The addition of the electron-donating polymer, namely PCDTBT, was found to be beneficial to reduce the defects in the perovskite system. Zhang et al. have observed that as compared to a PCE of 13.2% in pristine devices based on mixed-halogen perovskites,

the modified devices with PCDTBT showed an improved efficiency of 16.8%. The lone pair of the polymer combines with the undercoordinated defects and passivates them.<sup>[126]</sup> Many of such organic additives are better categorized as Lewis acid-base passivators and have been explained in a following section. Wang et al. have doped imidazolium (IA) at the A-site of  $\text{ABX}_3$  structure and casted thin films of defect-free perovskite with a compact film morphology. They have observed an increase in carrier lifetime and suppressed ion migration due to the passivation of negatively charged vacancies. In this approach, they became successful to achieve a PCE of 16.0% in an inverted geometry.<sup>[127]</sup> The incorporation of methylammonium (MA)-based additives seems to be effective as well. Apart from an improvement in the PCE of solar cells, MA exerted an additional effect on negatively charged vacancies and antisite defects; the ions via the disproportionation reaction could also counter residual oxidized  $\text{I}_2$ , which stimulated trap states. Interestingly, in such approach, the Pb/I ratio was not disturbed.<sup>[81]</sup>

## 3.3. Surface Passivation

### 3.3.1. Lewis Acid-Base Reaction

Undercoordinated lead and halide ions at the perovskite surface along with dangling surface bonds reduce the stability of the materials and also the efficiency of perovskite-based devices. Lewis acids and bases, which can accept and donate a lone pair of electrons, respectively, are commonly used as a passivating material to reduce the effects of ionic defects in perovskites (Figure 10).<sup>[97,128]</sup>

Derivatives of amines, carboxyl, hydroxyl, carbonyl, and phosphine oxides with a lone pair of electrons are being used to passivate defects in metal-halide perovskites.<sup>[128-130]</sup> The lone pair of electrons on Lewis bases passivates the undercoordinated



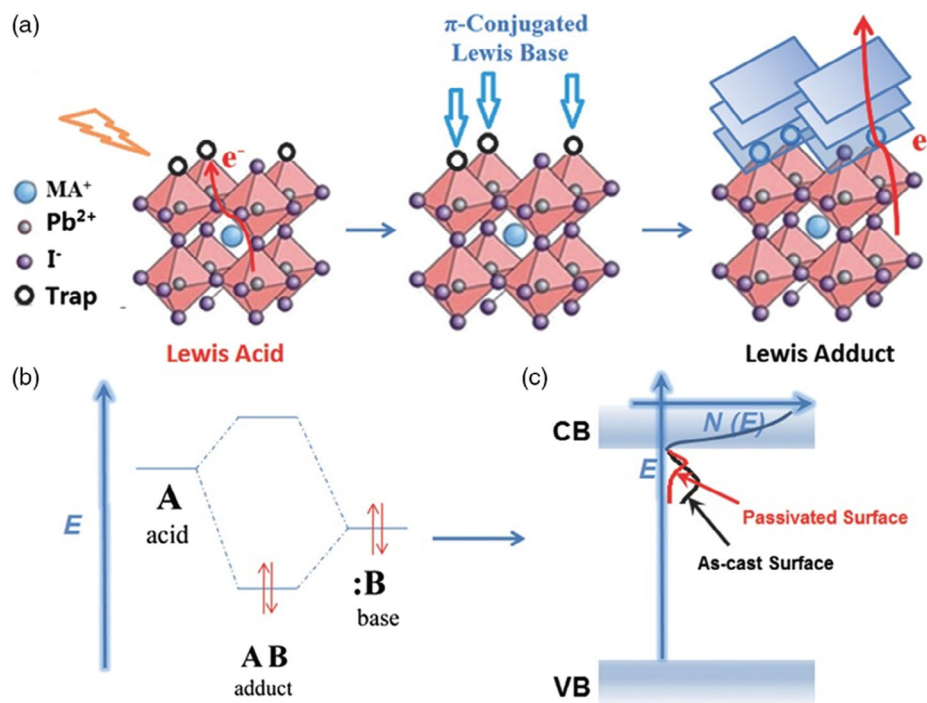


**Figure 10.** a) Schematic illustration of the interaction of  $\pi$ -conjugated Lewis base and lead (Pb), b) formation of a dative covalent bond between two atoms, and c) schematic of passivation of trap states. Reproduced with permission.<sup>[81]</sup> Copyright 2016, John Wiley and Sons.

lead ions by forming coordination with them and thereby improving the optical and electronic properties of such passivated perovskites. Such a Lewis acid–base adduct approach was followed by Park and his group by dissolving the precursors in polar aprotic solvents.<sup>[131]</sup> As polar aprotic solvents bear oxygen, sulfur, or nitrogen, they can act as a Lewis base; the other component of the precursor, namely  $\text{PbI}_2$ , which is known to be a Lewis acid, has a chance to form an adduct by reacting with the Lewis base.<sup>[132]</sup> These Lewis base–Lewis acid adducts between perovskites and solvent groups led to the formation of highly crystalline large grains with improved carrier lifetime. Therefore, it can be noted that the typical route of perovskite precursor preparation is based on dissolving  $\text{PbI}_2$  (Lewis acid) with DMF/DMSO (Lewis base solvent) and supersaturating it to force rapid crystallization.<sup>[133]</sup> In another study, Lee et al. have reported a high efficiency in  $\text{MAPbI}_3$ -based solar cells with urea, a bifunctional Lewis base, which passivated the grain boundaries and initiated grain growth.<sup>[134]</sup> Lin et al., on the other hand, have introduced a layer of  $\pi$ -conjugated Lewis base indene derivative (IDIC) on  $\text{MAPbI}_3$  counter-electrode interfaces. The functional groups ( $\text{C}=\text{O}$  and  $\text{C}\equiv\text{N}$ ) of IDIC strongly interact with the undercoordinated  $\text{Pb}^{2+}$  at the surface and passivate the trap states, reducing the defect densities and improving the charge extraction and carrier transport.<sup>[81]</sup> Similarly Noel et al. showed that sulfur donors of thiophene and nitrogen donors of pyridine could be used for passivating such defects at the surface, followed by an improvement in the solar cell performance.<sup>[128–130]</sup> Graphene is another carbon allotrope used as a defect-passivating material in perovskites. Hadadian et al. reported defect passivation by adding nitrogen-doped graphene in the precursor

solution of perovskites. Here, graphene is reported to reduce nonradiative recombination pathways by passivating positively charged surface defects through the Lewis base property of nitrogen.<sup>[135]</sup> Other 2D materials in this direction include graphene oxide and reduced graphene oxides. Li et al. reported passivation of perovskites with chemically modified graphene oxide and reported an enhancement in the PCE and stability of PSCs. They attributed the passivating effect to be due to an interaction between 4-fluorophenyl function groups of the 2D material with uncoordinated lead ions of the perovskite.<sup>[136]</sup> In this direction, thiophene, pyridine, and EDT have been proven as the most appropriate Lewis bases.<sup>[128–130]</sup> Among them, pyridine has the most powerful impact as it can form the strongest bond at the perovskite surface and passivate undercoordinated  $\text{Pb}^{2+}$  defects.

Similarly, Lewis acids are used to passivate negatively charged undercoordinated halide defects. Carbon allotropes like fullerenes have exhibited excellent electron-transport properties and are reported to improve stability, reduce hysteresis, and improve the PCE of perovskite-based devices.<sup>[51]</sup> Highly electronegative fullerenes exhibit excellent electron-accepting properties. Functionalized fullerenes are reported to bind to uncoordinated atoms of the perovskite surface, passivating the surface defects in the perovskite. Shao et al. reported the use of PCBM as a Lewis acid-passivating material in  $\text{MAPbI}_3$ -based devices.<sup>[51]</sup> They attributed the improvement in device stability as well as solar cell parameters to be due to the passivation of electron-rich defects through PCBM by forming ionic bonding. Here, fullerenes are also reported to passivate Pb–I antisites in perovskites and reduce surface charge recombination pathways, resulting in a narrowed

hysteresis in  $I$ - $V$  characteristics. Similarly, Tian et al. evaluated the effect of functional groups on fullerene derivatives and reported that the addend structure and functionality can influence the passivation ability of perovskites.<sup>[137]</sup> However, although a wide range of fullerene derivatives have been considered for passivating defects in perovskites, the perovskite–fullerene interaction is not yet completely understood. In this direction, IPFB has been reported to be an efficient Lewis acid, which can passivate the undercoordinated  $I^-$  with the formation of supra-molecular halogen bonds.<sup>[129]</sup>

Zang et al. reported the synergistic effect of a Lewis acid and Lewis base dual system; they investigated the effect of bis-PCBM-mixed isomers as a Lewis acid and bromophenyl–thiourea as a Lewis base. They have reported the passivation of deep-level traps as the Lewis acid accepts electrons from Pb–I antisites, whereas the Lewis base passivates the  $Pb^{2+}$  ions.<sup>[138]</sup>

### 3.3.2. Interfacial Passivation

As stated earlier,  $MAPbI_3$  can be considered as a defect-tolerant compound. However, a large number of charged defects may form at the absorber layer surface and also in between material interfaces. As a result, researchers took interest in developing effective passivation methods to reduce such defects. Apart from different postdeposition techniques, two effective methods are considered in this direction.

*Introduction of Passivation Layers:* Introduction of a passivation layer in between the perovskite absorber and the charge transport layer is a common technique to reduce the defect density. This method is somewhat complex but is favourable to achieve high-efficient solar cell devices. Such a passivation layer can be introduced at the interfaces with both the ETL and HTL of solar cell architectures. Depending on the locations of the passivation layer in a device configuration, they are classified and discussed.

To reduce interfacial charge recombination due to surface defects, a few passivation layers are introduced in between the perovskite layer and HTL. In this direction, the most common passivation technique is the addition of MABr and FABr which can act as an intermediate phase to the perovskite  $APbI_{3-x}Br_x$  ( $A = MA$  or  $FA$ ) on top of the perovskite layer.<sup>[72,139]</sup> The excess  $MA^+$  and  $FA^+$  can also passivate defects and compensate the loss due to charged defects arising out of an annealing process. It may be noted that, due to such a treatment, no new perovskites are formed; only a thin layer of the intermediate perovskite phase with a composition gradient is created. Recently, Yao et al. reported the introduction of ethylene amine derivatives with different ligands, which form a capping layer on top of the perovskite, acting as an interfacial passivation layer to boost the efficiency of solar cells.<sup>[140]</sup> Similarly, phenethylammonium iodide containing different functional groups seem to be useful as it creates an ultrathin layer of a 2D perovskite phase, where the electrostatic interaction between the benzene ring of phenethylammonium group and undercoordinated  $Pb^{2+}$  ions increases the efficacy of passivation.<sup>[141]</sup> The introduction of a polymer interlayer, namely polydimethylsiloxane (PDMS) in between the perovskite and HTL, has been found obliging, due to the cross-linking behaviour of the polymer in reducing the interfacial charge recombination.<sup>[142]</sup>

Similarly, the passivation layer can be situated in between the perovskite film and the ETL. Fullerene has been considered to be a very useful passivation agent in this context. A double layer of fullerene can serve as both ETL and an interfacial passivation layer and has been found to be beneficial to reduce the hysteresis in the  $I$ - $V$  characteristics of solar cells.<sup>[51]</sup> Zheng and coworkers recently observed that the undercoordinated  $Pb^{2+}$  can be passivated by the amide group of fullerene derivatives, resulting in a high  $V_{OC}$  in solar cells.<sup>[143]</sup> In this regard, the most powerful agent is certainly quaternary ammonium halides having the zwitterion structure that can passivate both positively and negatively charged defects in the perovskite simultaneously. Zwitterion molecules such as choline chloride can effectively heal both types of defects by their separated positive and negative part to enhance  $V_{OC}$  without losing short-circuit current-density ( $J_{SC}$ ) and fill factor (FF).<sup>[71]</sup> Li and coworkers have reported CsBr to be a suitable candidate for interfacial passivating agents between ETL and the perovskite absorber as the passivating material can reduce the work function of  $TiO_2$  and simultaneously promote uniform crystallization of the perovskite layer to finally suppress the GB defects.<sup>[144]</sup> In this context, poly(methyl methacrylate) (PMMA) has also been used efficiently as a passivation layer which can concurrently reduce the defects originating from dangling bonds at the perovskite- $TiO_2$  interface and shield the  $TiO_2$  layer from oxygen adsorption.<sup>[145]</sup>

Recently, Chen et al. demonstrated the effect of bifacial defect passivation by introducing thiocetic acid which can chemically anchor to the perovskite surface in forming a polymer due to its crosslinking behaviour.<sup>[146]</sup> The polymer layer can passivate the interfacial defects present in between the perovskite and both the charge transport layers. Similarly, Mahmud and coworkers reported a double-sided passivation strategy by incorporating bulky organic cations which form the thin surface layer in both sides of the perovskite in a sandwiched device structure to promote the dual passivation method.<sup>[147]</sup>

*Usage of New Transport Layers:* The defects exist not only in the interfaces between the perovskite and a transport layer but also in the transport materials themselves. In the past few years, many modified charge transport layers are introduced in perovskite solar cells with a reduced defect density.  $TiO_2$  can be considered to be a suitable candidate among all the traditional ETLs in highly efficient solar cell architectures. However, the presence of  $Ti^{3+}$  can serve as defect states and can hinder charge separation at the  $TiO_2$ –perovskite interface.<sup>[53]</sup> In this direction, amine-mediated  $TiO_2$  (AM- $TiO_2$ ),<sup>[148,149]</sup> chlorine-capped  $TiO_2$  ( $TiO_2$ -Cl),<sup>[150]</sup> and defective- $TiO_2$ <sup>[144]</sup> have been introduced. They were found to be beneficial to heal the defects in the parent  $TiO_2$  compound. Moreover, the application of such modified compounds in solar cell devices has been found to be better than that of  $TiO_2$ . Similarly,  $SnO_2$ , which is commonly used as an ETL, is benign in defect states due to  $Sn^{4+}$ . Recently, Jung et al. have used  $SnO_2$ –KCl composite as an ETL and observed an increase in the PCE of perovskite solar cells. Such an improvement has been explained in terms of defect passivation in the  $SnO_2$  layer.<sup>[151]</sup> Passivating defects in a HTL has also been considered to be a major approach to promote the PCE of perovskite solar cells. As such, the most commonly used HTL, spiro-OMeTAD, is responsible for the degradation of perovskite solar cells due to its inherent defects. Passivation of defects in spiro-OMeTAD

through doping is however costly.<sup>[152]</sup> Moreover, this compound has little role in passivating defects of the perovskite layer. Numerous HTLs have therefore been introduced to encounter these issues; copper phthalocyanine (CuPc) and conjugated polymers such as PCDTBT can be useful to passivate the defects in a HTL.<sup>[153,154]</sup>

### 3.3.3. Physical Passivation Methods

Apart from chemical modifications of a perovskite structure, physical treatments of perovskite films can also reduce defect density and improve the performance of perovskite-based devices. In this section, we have discussed a few physical passivation methods to passivate the defects in perovskites. These techniques are simpler and more straightforward as compared with chemical modification processes. Moreover, the methods are almost independent of the choice of perovskite material and device configuration.

**Light:** One such example is light-induced passivation of defects in perovskites. Photons have dual effects on the defect states; they can heal defects and at the same time can create new defect states.<sup>[155]</sup> Dequilette et al. reported photoinduced enhancement in PL emission in perovskite thin films.<sup>[89]</sup> They attributed this enhancement to be due to an order of magnitude reduction in the trap density of perovskite layers. They proposed that under illumination, photoexcited electrons passivated the surface vacancies, leading to a change in the internal electric field prompting iodide migration. The iodide migration fills up vacancies and reduces the density of defect states and thereby nonradiative recombination pathways, improving PL emission from the perovskite crystals. In another report, Mosconi et al. reported light-induced annihilation of  $(V_I)^+/(I_I)^-$  Frenkel defect pairs in MAPbI<sub>3</sub> thin films.<sup>[156]</sup> However, there is a limitation of this approach as defect healing can only be facilitated through the low migration energy of iodine-related defects only.

**Heat:** Defect states generally appear due to the loss of periodicity in the crystal lattice during synthesis through solution process. Application of heat can recover the periodicity as such perturbation can rearrange lattice and also improve the film quality. In addition, the organic cation ( $MA^+$  or  $FA^+$ ) is evaporated during the annealing of the film, making the perovskite into a PbI<sub>2</sub>-rich one, which can further passivate the defects at the surface; advantages of such self-passivation methods have been discussed previously. However, optimization of the annealing temperature is very much important as pinholes are generated at higher temperatures, which can increase the defect density further. In this regard, a thermal treatment for 10–30 min at 150 °C has been found to be suitable for MA- and/or FA-based perovskite materials.

**Hot Casting:** Similar to the thermal treatment technique, hot casting method also possesses unprecedented opportunities in passivating surface and GB defects. Unlike thermal annealing, in a hot casting method, heat is applied during the spin casting method. Hot casting of perovskite films improves crystallite size and reduces trap states at the surface and bulk defects as well. It may be recalled that defects can be associated with pinholes, surface roughness, and grain size of the perovskite layer.<sup>[157]</sup> It has been found that such technique is capable of growing

mm-sized grains which are highly desirable for the large-scale production of perovskite solar cells.

**Vacuum and Solvent-Assisted Annealing:** Li et al. reported the vacuum-assisted annealing of perovskite films for the effective removal of volatile degradation byproducts and to improve crystallization in perovskites, leading to a higher PCE in solar cells.<sup>[158]</sup> In another study, Xiao et al. reported the solvent-assisted annealing of perovskites under dimethyl formamide (DMF) vapor. The schematic diagram of such a solvent-assisted annealing process is shown in **Figure 11a**. They reported an improvement in the crystallization of MAPbI<sub>3</sub> and PCE of devices; solvent-annealed films yielded crystallites as large as 1 μm, which were observed from SEM images, as compared with 260 nm crystallites obtained upon a usual thermal-annealing process (**Figure 11b**).<sup>[74]</sup>

**Antisolvent-Assisted Crystallization:** The application of the antisolvent during spin coating process is another mostly used technique to increase crystallization which further reduces the defect density. However, proper selection of the antisolvent toward perovskite film fabrication is crucial in this regard as some of the chemical groups present in antisolvent may affect perovskite formation. In general, antisolvents with low boiling point, high vapor pressure, and good polarity are suitable in this method.<sup>[159]</sup> Similarly, antisolvent vapor such as alcohol and dichloromethane (DCM) can also be used widely to prepare large-grain perovskite thin films.<sup>[160]</sup>

### 3.3.4. 3D Perovskites Passivated by 2D Perovskites

2D perovskites have recently witnessed an enormous progress in terms of stability due to an effective protection by hydrophobic organic spacer cations.<sup>[161]</sup> However, due to their large optical bandgap and anisotropic and inefficient charge transport caused by such long organic spacer cations, the PCE of solar cells based on pure 2D perovskites is still inferior as compared with their parent 3D analogues.<sup>[162]</sup> Hence, the application of the pure 2D Ruddlesden–Popper or Dion–Jacobson phase in solar cell structures and defect physics in such systems has not gained momentum as compared with double or triple perovskites. However, the hybridization of 2D and 3D perovskites is turning to be a promising pathway.<sup>[161,163]</sup> Recently, a desired stability of 2D perovskite has been combined with the superior light-harvesting properties of 3D perovskites to fabricate highly efficient solar cells having long environmental stability simultaneously. In this section, the significant role of 2D perovskites, either as an additive or as a passivation layer, has been discussed. In this context, the Ruddlesden–Popper  $(RNH_3)_2(A)_{n-1}BX_{3n+1}$  phase of the perovskite has been the focus.<sup>[162]</sup> 2D perovskites have recently been found to offer dual roles, as it can protect a MAPbI<sub>3</sub> layer from thermal degradation and can prevent ion migration as well.<sup>[164]</sup> In this direction, the reaction of a long-chain organic spacer, namely butylammonium (BA) with MAPbI<sub>3</sub>, has been found to passivate defects; the defective surface of the 3D perovskite can be healed by the 2D counterpart yielding a PCE of 22.5% in MAPbI<sub>3</sub>-based devices.<sup>[164]</sup> Similarly, Wang et al. have recently introduced BA in a 3D perovskite to form  $(BA)_x(FA_{0.83}Cs_{0.17})_{1-x}Pb(I_{0.6}Br_{0.4})_3$ ; it has been observed that the 2D phase was helpful to enhance the

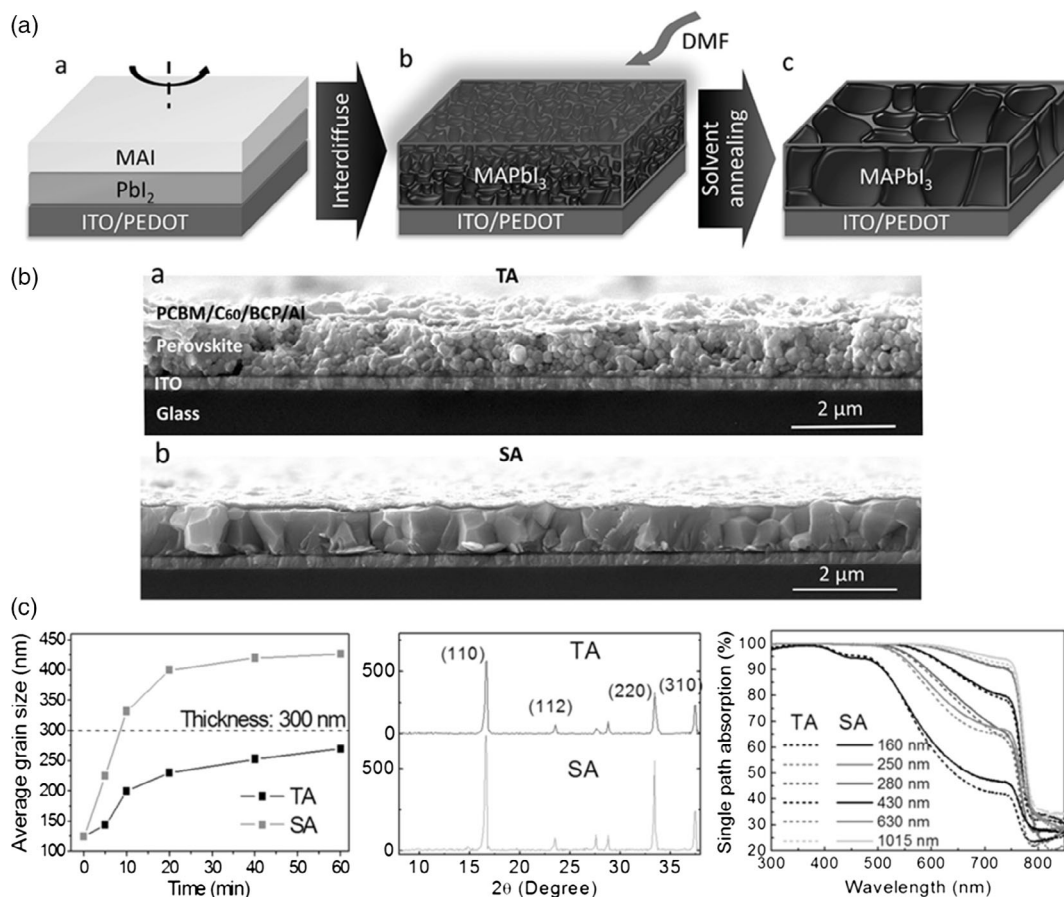


**Figure 11.** a) Schematic representation of solvent-assisted thermal annealing and b,c) its effects on perovskite films. Reproduced with permission.<sup>[74]</sup> Copyright 2014, John Wiley and Sons.

crystallinity by reducing crystal defects and suppressing nonradiative recombination pathways.<sup>[165]</sup> The use of alkylammonium halide has led to the formation of 2D–3D hybrid perovskites with the 2D perovskite passivating the defects of 3D ones.<sup>[166]</sup> The 2D–3D-heterostructured perovskites thus showed an enormous promise in the fabrication of gradient perovskite films. Yao et al. recently reported the incorporation of similar bulky cation-containing ethylene amine ligands which can create an ultrathin layer of 2D perovskite at both sides of a 3D perovskite to heal the defects at grain boundaries.<sup>[140]</sup>

In Table 3, we have summarized different types of commonly used defect passivation approaches in  $\text{APbX}_3$ .

## 4. Defects in Perovskites Beyond $\text{ABX}_3$ and Their Passivation

### 4.1. Perovskites Beyond $\text{ABX}_3$

To address the toxicity of lead in perovskite materials for solar cells, focus has always been toward lead substitution in  $\text{MAPbI}_3$  with suitable elements having isoelectronic configurations ( $s^2p^0$ ), which is often believed to be one of the major factors in achieving superior optoelectronic properties in the

material.<sup>[8,167,168]</sup> Through combinatorial approaches, trivalent metal-based ternary perovskites ( $\text{A}_3\text{B}_2\text{X}_9$ ) and double perovskites in the form  $\text{A}_2\text{B}'\text{B}''\text{X}_6$ , where  $\text{B}'$  and  $\text{B}''$  are monovalent and trivalent metals, respectively, have been considered.<sup>[169]</sup> Unfortunately, the photovoltaic performances of such classes of materials remained inferior as compared with the parent perovskite,  $\text{MAPbI}_3$ . The photovoltaic performance of such systems did not excel primarily due to a wider bandgap of 2 eV and above.<sup>[170]</sup> The truncated efficiency of these perovskites is also closely related to defect physics in the materials. The presence of deep-level defects in those ternary and double perovskites has been considered to be one of the major roadblocks against achieving high-efficiency solar cells. Understanding the origin of defects and defect passivation techniques in these systems has remained crucial for further advancement toward improving the performance of devices based on such perovskites.

### 4.2. Defects in Double Perovskites

Double perovskites are considered to be a stable and less-toxic alternative to  $\text{MAPbI}_3$  and its derivatives. In a double-perovskite structure, the bivalent lead ion is replaced by a combination of heterovalent cation(s), leading to formation of  $\text{A}_2\text{M(I)M(III)X}_6$  or



**Table 3.** Different defect engineering approaches used in APbX<sub>3</sub>-based perovskite devices.

Defect-passivation technique	Passivating agent	Target defect	Mechanism	Perovskite system	Heterojunction	J <sub>SC</sub> [mA/cm <sup>2</sup> ]	V <sub>OC</sub> [V]	FF	PCE [%]	Ref.	
Compositional engineering	Cs	Ion vacancy	Filling	FA <sub>0.85</sub> MA <sub>0.1</sub> Cs <sub>0.05</sub> PbI <sub>2</sub> Br <sub>0.3</sub>	c-TiO <sub>2</sub> /mp-TiO <sub>2</sub> /perovskite/Spiro-OMeTAD	22.00	1.13	0.77	19.10	[104]	
	In situ PbI <sub>2</sub>	Halide vacancy	Strain relaxation	(FAPbI <sub>3</sub> ) <sub>1-x</sub> (MAPbBr <sub>3</sub> ) <sub>x</sub>	SnO <sub>2</sub> /perovskite/Spiro-OMeTAD	23.36	1.06	0.78	19.55	[187]	
	I <sub>2</sub> /IPA	Halide vacancy	Filling	MAFAPbI <sub>3-x</sub> Br <sub>x</sub>	bl-TiO <sub>2</sub> /mp-TiO <sub>2</sub> /perovskite/Spiro-OMeTAD	25.00	1.10	0.80	22.10	[85]	
	I <sub>2</sub> /antisolvent washing	Halide vacancy	Filling	MAPbI <sub>3</sub>	TiO <sub>2</sub> /MAPbI <sub>3</sub> /Spiro-OMeTAD	22.39	1.17	0.79	21.33	[114]	
Inorganic Doping	Na <sup>+</sup>	MA vacancy	Substitutional filling	MAPbI <sub>3</sub>	c-TiO <sub>2</sub> /mp-TiO <sub>2</sub> /perovskite/Spiro-OMeTAD	22.97	0.90	0.73	15.14	[119]	
	Ag <sup>+</sup>	MA vacancy	Substitutional filling	MAPbI <sub>3</sub>	c-TiO <sub>2</sub> /mp-TiO <sub>2</sub> /perovskite/Spiro-OMeTAD	19.24	1.02	0.71	14.18	[119]	
	Cu <sup>+</sup>	MA vacancy	Substitutional filling	MAPbI <sub>3</sub>	c-TiO <sub>2</sub> /mp-TiO <sub>2</sub> /perovskite/Spiro-OMeTAD	21.81	0.99	0.72	15.25	[119]	
	K <sup>+</sup>	MA vacancy	Substitutional filling	MA <sub>0.15</sub> FA <sub>0.85</sub> Pb(I <sub>0.85</sub> Br <sub>0.15</sub> )	c-TiO <sub>2</sub> /mp-TiO <sub>2</sub> /perovskite/Spiro-OMeTAD	22.92	1.15	0.77	20.55	[122]	
	Al <sup>3+</sup>	MA vacancy	Substitutional filling	MAPbI <sub>3</sub>	poly-TPD/perovskite/PCBM/BCP	22.40	1.10	0.77	19.10	[124]	
	KI	MA and halide vacancy	Filling and immobilizing	(Cs,FA,MA) <sub>0.9</sub> K <sub>0.1</sub> Pb(I <sub>0.85</sub> Br <sub>0.15</sub> ) <sub>3</sub>	bl-TiO <sub>2</sub> /mp-TiO <sub>2</sub> /perovskite/Spiro-OMeTAD	23.20	1.17	0.79	21.50	[202]	
Organic Additive	GA	Ion vacancy	Vacancy filling	MAPbI <sub>3</sub> Cl <sub>3-x</sub>	TiO <sub>2</sub> /perovskite/Spiro-OMeTAD	21.24	1.07	0.75	17.13	[83]	
	F4TCNQ	Metallic lead	Coordinate bonding	MAPbI <sub>3</sub>	NiO <sub>x</sub> /perovskite/PCBM/BCP	19.57	1.06	0.80	16.60	[157]	
	MA/EtOH	Cation vacancy	Filling, Ostwald ripening	MAPbI <sub>3</sub>	SnO <sub>2</sub> /perovskite/Spiro-OMeTAD	22.98	1.13	0.77	20.02	[81]	
	IA	Cation vacancy	Substitutional filling	MA <sub>1-x</sub> IA <sub>x</sub> PbI <sub>3</sub>	PTAA/perovskite/PC <sub>61</sub> BM/BCP	20.07	1.03	0.80	16.03	[127]	
	Zinc porphyrin	Undercoordinated Pb <sup>2+</sup>	Coordinate bonding	Cs,FA,MA perovskite	SnO <sub>2</sub> /perovskite with YD <sub>2</sub> -O-C <sub>8</sub> /Spiro-OMeTAD	24.4	1.05	0.80	20.50	[203]	
	Lewis acid base reaction	IPFB	Undercoordinated I <sup>-</sup>	Halogen bonding	MAPbI <sub>3</sub> Cl <sub>3-x</sub>	bl-TiO <sub>2</sub> /mp-Al <sub>2</sub> O <sub>3</sub> /perovskite/Spiro-OMeTAD	23.38	1.06	0.67	15.70	[129]
		Pyridine	Undercoordinated Pb <sup>2+</sup>	Coordinate bonding	MAPbI <sub>3</sub>	bl-TiO <sub>2</sub> /perovskite/Spiro-OMeTAD	22.00	1.15	0.73	18.50	[204]
IDIC		Undercoordinated Pb <sup>2+</sup>	Coordinate bonding	MAPbI <sub>3</sub>	PTAA/perovskite/IDIC/C <sub>60</sub> /BCP	22.96	1.11	0.76	19.50	[205]	
DTA		Undercoordinated Pb <sup>2+</sup>	Coordinate bonding	MAPbI <sub>3-x</sub> Cl <sub>x</sub>	PTAA/perovskite/DTA/C <sub>60</sub> /BCP	22.50	1.17	0.81	21.45	[206]	
Passivation Layer between perovskite and HTL	FABr	Ion vacancy	Grain modulation	FAPbBr <sub>3-x</sub> I <sub>x</sub>	bl-TiO <sub>2</sub> /mp-TiO <sub>2</sub> /Spiro-OMeTAD	23.18	1.16	0.79	21.31	[139]	
	PDMS	Ion migration	GB passivation	MAPbI <sub>3</sub>	SnO <sub>2</sub> /MAPbI <sub>3</sub> /PDMS/CuSCN	23.9	1.02	0.78	19.04	[142]	
	Fullerene derivative	PbI <sub>3</sub> <sup>-</sup> antisite (at GB)	Coordinate bonding	MAPbI <sub>3</sub>	NiO <sub>x</sub> /perovskite/fullerene derivative/PCBM/Ag	22.04	1.02	0.78	17.63	[143]	
	Ethylene amine capping layer	I <sup>-</sup> vacancy	Hydrogen bonding	MAPbI <sub>3</sub>	TiO <sub>2</sub> /LD perovskite/3D perovskite/LD perovskite/Spiro-OMeTAD	22.77	1.06	0.75	18.09	[140]	
	Phenethyl ammonium iodide	I <sup>-</sup> vacancy	Vacancy filling	(FAPbI <sub>3</sub> ) <sub>1-x</sub> (MAPbBr <sub>3-y</sub> Cl <sub>y</sub> ) <sub>x</sub>	SnO <sub>2</sub> /perovskite/Spiro-OMeTAD	25.04	1.18	0.77	22.98	[141]	
	PEAI	I <sup>-</sup> vacancy	Filling	FA <sub>1-x</sub> MA <sub>x</sub> PbI <sub>3</sub>	SnO <sub>2</sub> /perovskite/PEAI/Spiro-OMeTAD	24.90	1.16	0.81	23.56	[163]	

**Table 3.** Continued.

Defect-passivation technique	Passivating agent	Target defect	Mechanism	Perovskite system	Heterojunction	$J_{sc}$ [mA/cm <sup>2</sup> ]	$V_{oc}$ [V]	FF	PCE [%]	Ref.
Passivation Layer between perovskite and ETL	QAHs (Zwitterion)	Ion vacancy	Hydrogen bonding and electrostatic interaction	FA <sub>0.85</sub> MA <sub>0.15</sub> Pb(1 <sub>0.85</sub> Br <sub>0.15</sub> ) <sub>3</sub>	PTAA/perovskite/C <sub>60</sub> /BCP	23.70	1.14	0.78	21.00	[71]
	PTAA	Ion migration	GB passivation	MAPbI <sub>3-x</sub> Cl <sub>x</sub>	PTAA-modified PEDOT:PSS/perovskite/PCBM	21.58	1.07	0.82	19.04	[207]
	PMMA	I <sup>-</sup> vacancy	Coordinate bonding	Cs <sub>0.07</sub> Rb <sub>0.03</sub> FA <sub>0.765</sub> MA <sub>0.135</sub> PbI <sub>2.55</sub> Br <sub>0.45</sub>	In-doped TiO <sub>x</sub> /mp-TiO <sub>2</sub> /perovskite/Spiro-OMeTAD	23.20	1.16	0.76	20.40	[145]
Dual layer passivation	Thioctic acid	Pb <sup>2+</sup> , Ti <sup>4+</sup>	Coordinate bonding	MAPbI <sub>3</sub>	compact TiO <sub>2</sub> /MAPbI <sub>3</sub> -poly TA/Spiro-OMeTAD	23.48	1.14	0.76	20.40	[146]
	n-BAI	Ion migration	Physical barrier	Cs <sub>0.07</sub> Rb <sub>0.03</sub> FA <sub>0.765</sub> MA <sub>0.135</sub> PbI <sub>2.55</sub> Br <sub>0.45</sub>	compact-mp TiO <sub>2</sub> /PMM:PCBM/n-BAI/perovskite/n-BAI/Spiro-OMeTAD	23.94	1.20	0.79	22.77	[147]
Passivation in transport layer	Defective TiO <sub>2</sub>	Ion migration	Ionic bonding, GB passivation	MAPbI <sub>3-x</sub> Br <sub>x</sub>	defective TiO <sub>2</sub> /perovskite/Spiro-OMeTAD	23.11	1.06	0.78	19.0	[144]
	TiO <sub>2</sub> -Cl	Ion migration	GB passivation	FA <sub>0.85</sub> MA <sub>0.15</sub> PbI <sub>2.55</sub> Br <sub>0.45</sub>	TiO <sub>2</sub> -Cl/perovskite/Spiro-OMeTAD	21.70	1.17	0.79	20.10	[150]
	SnO <sub>2</sub> -KCl	Ion migration	GB passivation	(FAPbI <sub>3</sub> ) <sub>0.95</sub> (MAPbBr <sub>3</sub> ) <sub>0.05</sub>	SnO <sub>2</sub> -KCl/perovskite/Spiro-OMeTAD	24.2	1.137	0.81	22.20	[151]
	PCDTBT	Ion migration	GB passivation	MAPbI <sub>3</sub>	TiO <sub>2</sub> /PCBM/perovskite/PCDTBT/MoO <sub>3</sub>	22.20	1.14	0.80	19.10	[154]
3D perovskites passivated by 2D perovskites	BA	Ion migration	GB passivation	BA <sub>2</sub> PbI <sub>4</sub> /MAPbI <sub>3</sub>	PTAA/perovskite/PCBM/C <sub>60</sub> /BCP	22.49	1.11	0.78	19.56	[164]
Physical passivation	Heat	Halide vacancy, Ion migration	Strain relaxation, GB passivation	MAPbI <sub>3</sub>	PEDOT:PSS/perovskite/PCBM/BCP	21.10	0.91	0.81	15.60	[74]
	VASP	Ion migration	GB passivation	FA <sub>0.81</sub> MA <sub>0.15</sub> PbI <sub>2.55</sub> Br <sub>0.45</sub>	bl-TiO <sub>2</sub> /mp-TiO <sub>2</sub> /perovskite/Spiro-OMeTAD	23.99	1.07	0.80	20.47	[158]

A<sub>2</sub>M(IV)X<sub>6</sub>.<sup>[171]</sup> In the former class of compounds, two bivalent lead ions are replaced by one monovalent and one trivalent ion; in A<sub>2</sub>M(IV)X<sub>6</sub>, the two lead ions are replaced by a tetravalent ion and a vacancy site renaming the compound as a vacancy-ordered halide double perovskite.<sup>[172,173]</sup> Possible structures of a multitude of halide double-perovskite materials have been theoretically predicted. Only a few of them could however be synthesized successfully and a fewer have shown promising results for application in optoelectronic devices. In general, double perovskites are reported to possess a superior stability under ambient conditions.<sup>[174]</sup>

#### 4.2.1. Defect Analysis

Among vacancy-modulated double perovskites, Cs<sub>2</sub>SnX<sub>6</sub> and cesium hexabromopalladate(IV) (Cs<sub>2</sub>PdBr<sub>6</sub>) have been reported to exhibit an enhanced stability and interesting optoelectronic properties.<sup>[175]</sup> Cs<sub>2</sub>NaBiI<sub>6</sub>-based solar cells with excellent stability and reproducibility have also been reported.<sup>[176]</sup> Double perovskites like Cs<sub>2</sub>NaBiCl<sub>6</sub>, Cs<sub>2</sub>KBiCl<sub>6</sub>, and (CH<sub>3</sub>NH<sub>3</sub>)<sub>2</sub>AgBiBr<sub>6</sub> were reported to possess a wide bandgap in the 2–3 eV range.<sup>[8,170,177]</sup> Within the group of methylammonium-based double perovskites, (CH<sub>3</sub>NH<sub>3</sub>)<sub>2</sub>SnI<sub>6</sub> has been proposed to possess an optimal

bandgap for solar cell applications; evidence of solar cell fabrication with the material is still absent presumably due to its inferior film quality. In a Ti(IV)-based vacancy-ordered bromide double-perovskite (Cs<sub>2</sub>TiBr<sub>6</sub>), a solar cell efficiency of 3.3% has been reported.<sup>[178,179]</sup>

Optoelectronic properties of double perovskites are significantly affected by defects in the crystals. Theoretical calculations were carried out to estimate defect formation energies and identify dominant defects in double-perovskite systems. DFT calculations were used to estimate band structures and defects in the Cs<sub>2</sub>AgBiX<sub>6</sub> class of double perovskites.<sup>[180,181]</sup> The VBM of Cs<sub>2</sub>AgBiBr<sub>6</sub> could be seen to provide major contributions from antibonding states of Br(4*p*) and Ag(4*d*) orbitals; Bi(6*s*) lies below the VBM with no significant contributions. The CBM, on the other hand, consists of Bi(6*p*) with minor contributions from Ag(5*p*) and Br(4*p*) orbitals. With the VBM located at X-point and CBM at L-point of momentum space, Cs<sub>2</sub>AgBiBr<sub>6</sub> turned out to be an indirect-bandgap semiconductor.<sup>[180,181]</sup>

Filip et al. and Xiao et al.<sup>[180,181]</sup> in fact calculated formation energies of 20 possible intrinsic defects in Cs<sub>2</sub>AgBiBr<sub>6</sub> system: four vacancies (V<sub>Cs</sub>, V<sub>Ag</sub>, V<sub>Bi</sub>, and V<sub>Br</sub>), four interstitials (Cs<sub>i</sub>, Ag<sub>i</sub>, Bi<sub>i</sub>, and Br<sub>i</sub>), six cation-on-cation antisites (Cs<sub>Ag</sub>, Cs<sub>Bi</sub>, Ag<sub>Cs</sub>, Ag<sub>Bi</sub>, Bi<sub>Cs</sub>, and Bi<sub>Ag</sub>), three cation-on-anion antisites (Cs<sub>Br</sub>, Ag<sub>Br</sub>, and Bi<sub>Br</sub>), and three anion-on-cation antisites (Br<sub>Cs</sub>, Br<sub>Ag</sub>, and

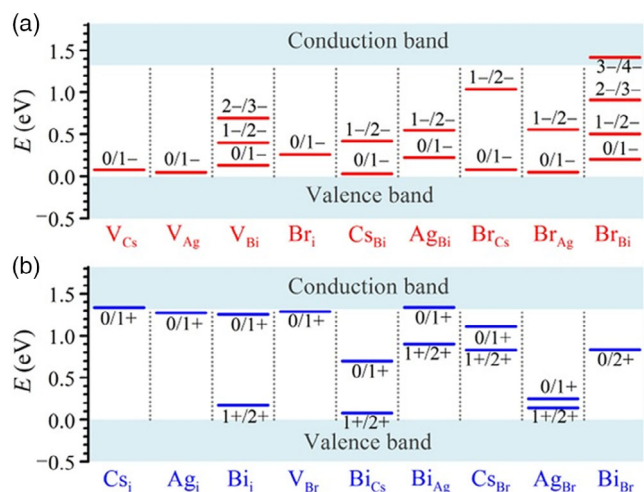


**Figure 12.** Calculated transition energy levels for intrinsic a) acceptor-type and b) donor-type defects in  $\text{Cs}_2\text{AgBiBr}_6$ . Reproduced with permission.<sup>[181]</sup> Copyright 2016, John Wiley and Sons.

$\text{Br}_{\text{Bi}}$ ). Defect formation energies of these defects are shown in **Figure 12**. Among these defects, four vacancy defects have low formation energies, affecting optoelectronic properties of the double-perovskite.  $V_{\text{Ag}}$  is reported to possess the lowest enthalpy of formation; it hence appears as a shallow defect above VBM. The shallow nature of  $V_{\text{Ag}}$  is attributed to a strong antibonding coupling between  $\text{Ag}(4d)$  and  $\text{Br}(4p)$  orbitals, which push the VBM to a higher energy level turning the  $V_{\text{Ag}}$  level to become further shallow.  $V_{\text{Bi}}$  on the other hand exhibits a deep transition level. Among the 12 antisites,  $\text{Ag}_{\text{Bi}}$  and  $\text{Bi}_{\text{Ag}}$  have relatively low formation energies. Other intrinsic defects with high formation energies do not influence the optical and electrical properties of  $\text{Cs}_2\text{AgBiBr}_6$ .

Xu et al. and Volonakis et al. independently investigated  $\text{Cs}_2\text{AgInX}_6$  compounds using DFT calculations.<sup>[182,183]</sup> In **Figure 13**, the electronic band structures of such double perovskites have been presented as obtained from first-principle calculations along with the projected DOS. Unlike Ag–Bi systems, Ag–In-based double perovskites exhibit a direct bandgap. This is due to the fact that the VBM of  $\text{Cs}_2\text{AgInX}_6$  (X: Cl, Br) has a minimal contribution from  $\text{In}(5s)$  orbitals and is mainly formed by the hybridization between  $\text{Ag}(4d)$  and  $X(p)$  orbitals. They estimated that  $\text{Ag}_i$  and  $V_{\text{Br}}$  possessed the lowest defect formation energy and acted as shallow donors enforcing intrinsic  $n$ -type conductivity in  $\text{Cs}_2\text{AgInBr}_6$ . Overall, although lead-free-halide double perovskites have emerged as promising materials for application in various optoelectronic devices, the performance of double-perovskite-based devices is far below their theoretically predicted values. Understanding the origin of defects and suitable defect passivation techniques is hence crucial for further advancement toward improving the performance of such perovskite-based devices.<sup>[182,183]</sup>

#### 4.2.2. Defect Passivation

Luo et al. have reported that doping of  $\text{Cs}_2\text{AgInCl}_6$  with sodium ions partly prevents the forbidden transitions in the double perovskite and thereby improves the PL quantum yield (PLQY) to  $\approx 80\%$  as compared with the QY of 0.1% in pristine  $\text{Cs}_2\text{AgInCl}_6$ .<sup>[184]</sup> The pristine material exhibits a broad-band white light emission. As per their work,  $\text{Na}^+$  doping alters the orbital nature of trapped excitons, breaking the partly forbidden transitions; this reduces electronic dimensionality, leading to radiative recombination of self-trapped excitons and improving the PL in doped samples.<sup>[184]</sup>

Using first-principle calculations, Xu et al. have investigated the formation of deep-level defect states arising from grain

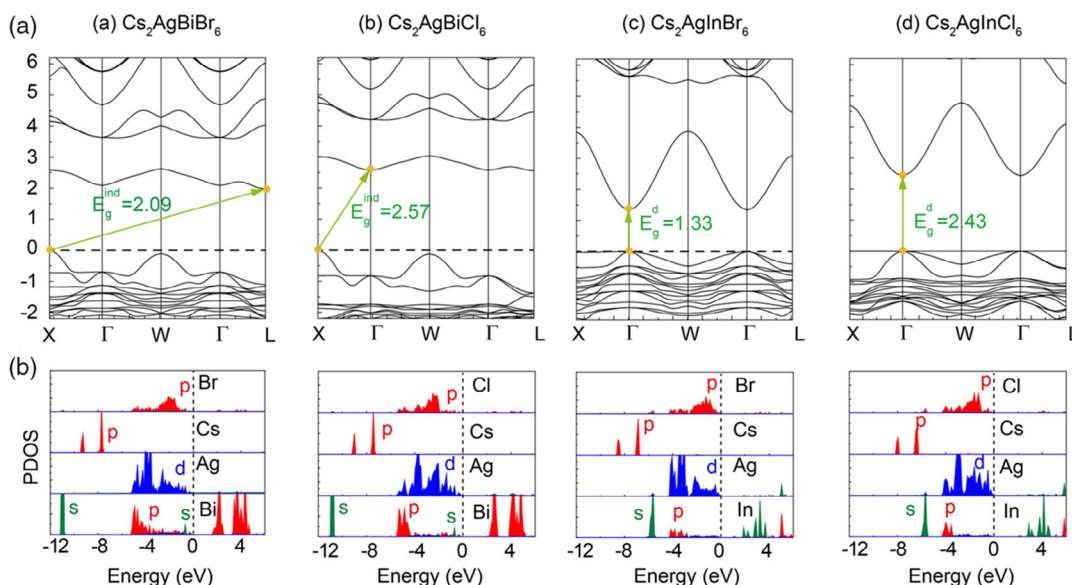


**Figure 13.** a) Comparison of HSE + SOC calculated electronic band structures and orbital-projected DOS for  $\text{Cs}_2\text{AgBiBr}_6$ ,  $\text{Cs}_2\text{AgBiCl}_6$ ,  $\text{Cs}_2\text{AgInBr}_6$ , and  $\text{Cs}_2\text{AgInCl}_6$  and b) the projected DOS of  $s$ ,  $p$ ,  $d$  orbitals which are colored in green, red, and blue, respectively. Reproduced with permission.<sup>[182]</sup> Copyright 2017, American Chemical Society.

boundaries in  $\text{Cs}_2\text{AgInCl}_6$  and  $\text{Cs}_2\text{AgBiCl}_6$ .<sup>[185]</sup> The electronic band structure at a particular GB namely  $\Sigma 5(310)$  shows the presence of deep-level defect states at the grain boundaries which can adversely affect the performance of double-perovskite-based devices. They have observed that through doping of  $\text{Cs}_2\text{AgInCl}_6$  with  $\text{Cl}_i$  (chloride interstitial defect) and  $\text{In}_{\text{Ag}}$  (indium at silver sites) defects, deep-level states arising from grain boundaries can be passivated through modification of electronic structures (Figure 14a). With a schematic diagram (Figure 14b), they have shown that upon  $\text{Cl}_i$  doping, the S1 GB defect states move closer to VBM. Similarly the  $\text{In}_{\text{Ag}}$  anti-bonding states push S1 and S2 states closer to CBM. The combined effect of  $\text{Cl}_i$  and  $\text{In}_{\text{Ag}}$  defect segregation at the grain boundaries removes the defect states from the band gap. Similar observation was reported on  $\text{Cs}_2\text{AgBiCl}_6$  crystals upon  $\text{Cl}_i$  doping. Their study indicated that spontaneous segregation of defects at grain boundaries could be used as a method to eliminate deep-level defect states.<sup>[185]</sup>

Nandha et al. have reported  $\text{Mn}^{2+}$ -induced luminescence from  $\text{Cs}_2\text{AgInCl}_6$ . This material is absorbed in the UV region and transfers the energy to  $d$ -orbital electrons of manganese ions occupying the lattice sites.<sup>[186]</sup> De-excitation from the  $\text{Mn}(d)$  levels leads to PL in the red region. In a somewhat similar report, Chen et al. have reported  $\text{Yb}^{3+}$ -induced near-infrared emission in addition to the trap-state visible region PL in  $\text{Cs}_2\text{AgBiX}_6$ .<sup>[187]</sup> They have found that doping of  $\text{Yb}^{3+}$  can be useful to remove the deep-level defect states situated within the bandgap, resulting in an increase in the PLQY. By controlling the dopant

concentration, they have tuned the emission profile and dynamics of photon relaxation (Figure 15). Furthermore, they have reported that their synthesis approach is also suitable to yield dopant-induced luminescence from  $\text{Cs}_2\text{AgBiX}_6$ . In another article,  $\text{Ce}^{3+}$  doping in  $\text{Cs}_2\text{SnI}_6$ , which is a vacancy-modulated double perovskite, has resulted in improving PL emission. Here, the  $\text{Ce}^{3+}$  ions have introduced  $(\text{Ce}^{3+}\text{Sn}^{4+}+\text{V}_{\text{Cl}})$  and  $(\text{Sn}^{2+}\text{Sn}^{4+}+\text{V}_{\text{Cl}})$  defects, promoting radiative recombination pathways and thereby increasing the PL intensity.<sup>[188]</sup>

Tran et al. have shown that doping of  $\text{Cs}_2\text{AgInCl}_6$  with antimony ions converts direct bandgap of pristine  $\text{Cs}_2\text{AgInCl}_6$  to an indirect one. They have reported that the CBM, which was initially composed of  $s$ -orbitals, forms with  $p$ -orbitals upon an increase in antimony content; this in turn decreases the bandgap and results in an indirect-bandgap semiconductor.<sup>[189]</sup> On the other hand, Slavney et al. have reported band-edge reconstruction in  $\text{Cs}_2\text{AgBiBr}_6$  by doping with tantalum ions ( $\text{Tl}^+$ ). They have observed that  $\text{Tl}^+$  ions at lower doping concentrations reduce the bandgap of the material by  $\approx 0.6$  eV; at higher contents of  $\text{Tl}^+$  ions, the nature of bandgap turns to a direct one.<sup>[190]</sup> Similarly, the report of Karmakar et al. on  $\text{Cu}^{2+}$ -doped  $\text{Cs}_2\text{SbAgCl}_6$  double perovskites has evidenced a significant reduction in the bandgap (from 2.6 to 1.0 eV).<sup>[191]</sup> They have inferred that the incorporation  $3d^9$  orbitals of  $\text{Cu}^{2+}$  near the VBM of  $\text{Cs}_2\text{SbAgCl}_6$  has led to the reduction of bandgap while retaining the 3D structure of the double perovskite.<sup>[191]</sup>

The elimination of ion migration in  $\text{Cs}_2\text{AgBiBr}_6$  polycrystalline films has been reported through deposition of  $\text{BiOBr}$

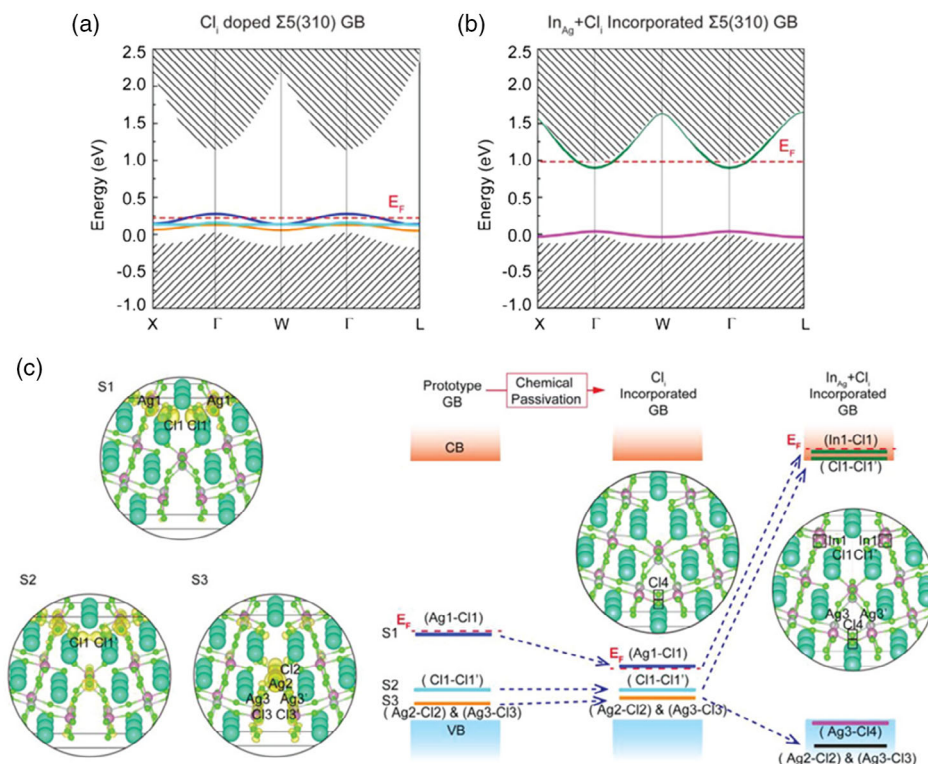


**Figure 14.** a) Calculated band structures of  $\text{Cs}_2\text{AgInCl}_6$  with  $\Sigma 5(310)$  (representation of a particular GB) GB after  $\text{Cl}_i$  and  $\text{In}_{\text{Ag}} + \text{Cl}_i$  incorporation and b) schematic diagram of the  $\text{Cl}_i$  and  $\text{In}_{\text{Ag}} + \text{Cl}_i$  incorporation at the GB in  $\text{Cs}_2\text{AgInCl}_6$  to eliminate the deep defect states within the bandgap. Reproduced with permission.<sup>[185]</sup> Copyright 2019, John Wiley and Sons.



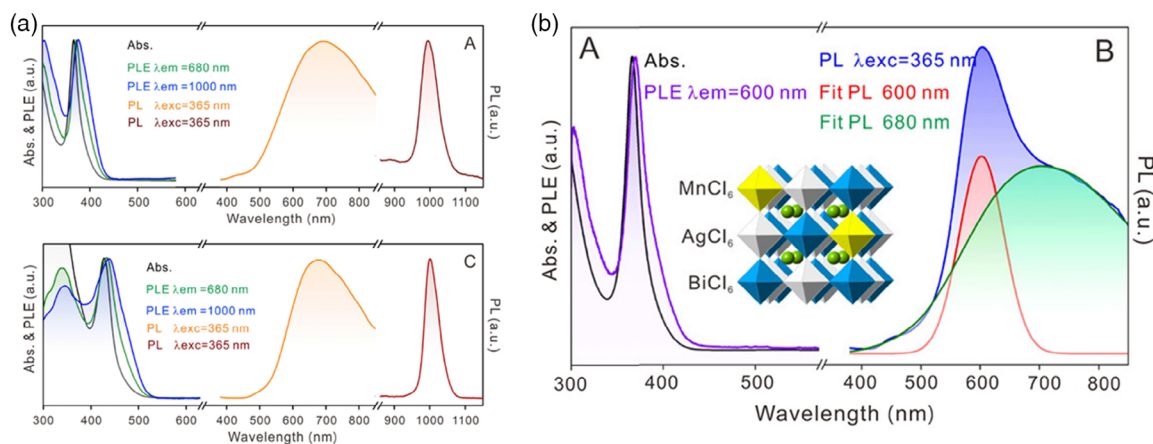


**Figure 15.** a) Absorption and PL spectra of Yb-doped  $\text{Cs}_2\text{AgBiX}_6$  ( $X = \text{Cl}^-$ ,  $\text{Br}^-$ ) and b) Mn-doped  $\text{Cs}_2\text{AgBiCl}_6$  double-perovskite nanocrystals. Reproduced with permission.<sup>[187]</sup> Copyright 2019, American Chemical Society.

passivating layer. Due to a fair degree of lattice matching with the double perovskite, the  $\text{BiOBr}$  layer aided defect passivation, inhibited ion migration, and hence improved X-ray detection ability of the double perovskite.<sup>[192]</sup>

Till date,  $\text{Cs}_2\text{AgBiBr}_6$  has been one of the most-successfully used double perovskites in the fabrication of thin-film solar cells. A poor morphology of  $\text{Cs}_2\text{AgBiBr}_6$  films with large crystallites and pinholes has been stated to be one of the major reasons toward resulting in ill-performed devices. Recently, Wu and coworkers have reported an antisolvent and postannealing treatment of  $\text{Cs}_2\text{AgBiBr}_6$  that can arguably enhance the crystal quality and PCE of the solar cells.<sup>[193]</sup> Another facile strategy has been reported of late for passivating the defects by introducing an N719 dye interlayer in a solar cell architecture.<sup>[194]</sup>

#### 4.3. Defects in Ternary Halide Perovskites (Triple Perovskites)

An optimistic avenue to achieve lead-free halide perovskites can also be imagined in a structure like  $\text{A}_3\text{M}_2\text{X}_9$  with layers of metal-halide bioctahedral being connected through a monovalent cation. As stated earlier, the ternary halide perovskites, which are frequently termed defect-ordered perovskites, have been considered through a combinatorial approach of a bivalent-metal-based  $\text{AMX}_3$  perovskite; in  $\text{A}_3\text{M}_2\text{X}_9$ , a section of the metal site ( $M$ ) is swapped by vacancies.<sup>[195]</sup> Structures like  $\text{A}_3\text{M}_2\text{X}_9$  with metal-halide  $\text{MX}_6$  octahedral layers have hence been envisaged considering  $\text{Bi}^{3+}$  or  $\text{Sb}^{3+}$  in the metal site and methylammonium ( $\text{MA}^+$ ), formamidinium ( $\text{FA}^+$ ), cyclohexyl ammonium, imidazolium,  $\text{K}^+$ ,  $\text{Rb}^+$ , or  $\text{NH}_4^+$  as the singly protonated cation (A-site) which plug the voids between the layers.<sup>[8,196]</sup> Depending upon the growth condition, this type of perovskite can result either in 1) a 0D hexagonal close-packed structure having isolated face-sharing  $\text{MX}_6$  octahedra instead of a 3D corner-sharing octahedra or 2) a 2D defect perovskite with corrugated double layers of corner-sharing  $\text{MX}_6$  octahedra. The advantages of these lead-free perovskites are their low toxicity and a better air stability than the prototype  $\text{CH}_3\text{NH}_3\text{PbI}_3$ . However, device performance of perovskites has not shone mostly due to a large bandgap of the order of 2 eV or more, resulting in a low efficiency ( $\eta$ ) as per the

Shockley–Queisser limit.<sup>[195,197]</sup> Also, due to an absence of a 3D framework through corner-shared  $\text{PbI}_6$  octahedra, carrier mobility in these perovskites is also low, resulting in a reduced efficiency in devices based on such 0D systems. The abovementioned issues have recently been addressed through band engineering of the materials. It remains important to gather information about bulk and interfacial defects which unavoidably form during the band engineering and also during film formation toward device fabrication. Defect states having energies outside the gap do not in general pose a serious concern in device performance; deep-level defects existing inside the bandgap, on the other hand, adversely affect the materials' optoelectronic properties as the defect sites can act as trapping or recombination centers hindering efficient carrier conduction. Identification and more importantly passivation of these defects in  $\text{A}_3\text{M}_2\text{X}_9$  perovskites are hence enormously essential to work toward increasing  $\eta$  in  $\text{A}_3\text{M}_2\text{X}_9$ -based solar cells.<sup>[32,56,198]</sup>

##### 4.3.1. Defect Analysis

The most popular members of this series can be classified as bismuth-based and antimony-based perovskites with methylammonium or cesium at the A-site:  $(\text{CH}_3\text{NH}_3)_3\text{Bi}_2\text{I}_9$ ,  $\text{Cs}_3\text{Bi}_2\text{I}_9$ ,  $(\text{CH}_3\text{NH}_3)_3\text{Sb}_2\text{I}_9$ , and  $\text{Cs}_3\text{Sb}_2\text{I}_9$ . In general, the singly protonated cation ( $\text{CH}_3\text{NH}_3^+$  or  $\text{Cs}^+$ ) has little impact on determining the band edges, while they can participate in creating deep- or shallow-levels traps in the material.<sup>[56]</sup> As there are few reports on determination of defect states in this class of perovskite, we have made some discussion in this respect.

**First-Principle Calculations:** First-principle calculations have been reported as an interesting approach to obtain insights into defect states in the  $\text{A}_3\text{B}_2\text{X}_9$  perovskite system. Although mathematical calculations for MA-based ternary perovskite systems are still unavailable in the literature, some valuable information about defect states in cesium-based perovskite could be found. Ghosh et al. have provided first-principle calculations in  $\text{Cs}_3\text{Bi}_2\text{I}_9$  and observed the presence of deep-level defect states in the material.<sup>[56]</sup> They have classified possible point defects broadly into two types: acceptor like and donor like. By

considering different stoichiometries of the compound, they have inferred that the occurrence of defect states depends on the growth condition or stoichiometry of the precursors. While acceptor-like defects originate due to cation vacancies ( $V_{Cs}$ ,  $V_{Bi}$ ), iodine interstitials ( $I_i$ ), Cs on Bi substitutions ( $Cs_{Bi}$ ), and antisite substitutions, specifically iodide on cation ( $I_{Cs}$ ,  $I_{Bi}$ ), donor-like defects originate from iodine vacancies ( $V_i$ ), cation interstitials ( $Cs_i$ ,  $Bi_i$ ), Bi-on-Cs substitutions ( $Bi_{Cs}$ ), and cation-on-iodide antisite substitutions ( $Cs_i$ ,  $Bi_i$ ). Depending on the stoichiometry of the precursors, that is the growth condition, different defects prevail and become responsible for poor photovoltaic performance as well (Figure 16a,b).

In their work, Saparov et al. have also carried out band structure calculations in the  $Cs_3Sb_2I_9$  system.<sup>[199]</sup> In a similar fashion, they have considered different growth conditions by varying the precursor stoichiometry and determined formation energies of different defect states (Figure 16c,d). The possible defects in  $Cs_3Sb_2I_9$  were found to be cation vacancies ( $V_{Cs}$ ,  $V_{Sb}$ ), iodine interstitials ( $I_i$ ), Cs-on-Sb substitutions ( $Cs_{Sb}$ ), and antisite substitutions, namely iodide on cation ( $I_{Cs}$ ,  $I_{Sb}$ ), iodine vacancies ( $V_i$ ), cation interstitials ( $Cs_i$ ,  $Sb_i$ ), Sb-on-Cs substitutions ( $Sb_{Cs}$ ), and cation-on-iodide antisite substitutions ( $Cs_i$ ,  $Sb_i$ ).

First-principle calculations in determining defect states in methylammonium-based ternary perovskite systems are still inadequate, presumably due to the complexity of the structure.<sup>[56]</sup>

*Experimental Evidences:* As such, there is no clear experimental evidence to probe the defect states exactly in an  $A_3B_2X_9$  perovskites. Our group has made an endeavor through scanning tunneling spectroscopy (STS) in probing the presence of defect states in a ternary halide perovskite.<sup>[32]</sup> We have studied the role of defect states on the band edges of  $A_3Bi_2I_9$  ( $A = Cs^+$  and  $CH_3NH_3^+$ ). A range of different precursor stoichiometries were considered to achieve different reaction environments. Depending on the growth condition, different types of defects could be seen to form that affect the band energies of the materials. The band edges were determined from differential tunnel conductance ( $dI/dV$ ) spectra (Figure 17a), which have a correspondence to the DOS of the material under study. The STS results have shown that the Fermi energy of the materials was always closer to the VBM than the CBM, showing a p-type nature of the perovskites, as obtained from a large number of measurements and drawn of energy-level histograms (Figure 17b). A nonintrinsic nature of the perovskite semiconductor, even when formed with stoichiometric precursors, implies the presence of point defects in such materials. Theoretical calculations have also inferred the presence of possible point defects; the defects were classified into acceptor like and donor like, as also described in the previous section. The STS studies evidenced a p-type nature of conductivity in the perovskite material irrespective of the compound being formed in a  $BiI_3$ -rich or a  $CsI$ -rich (or a  $CH_3NH_3I$ -rich) environment

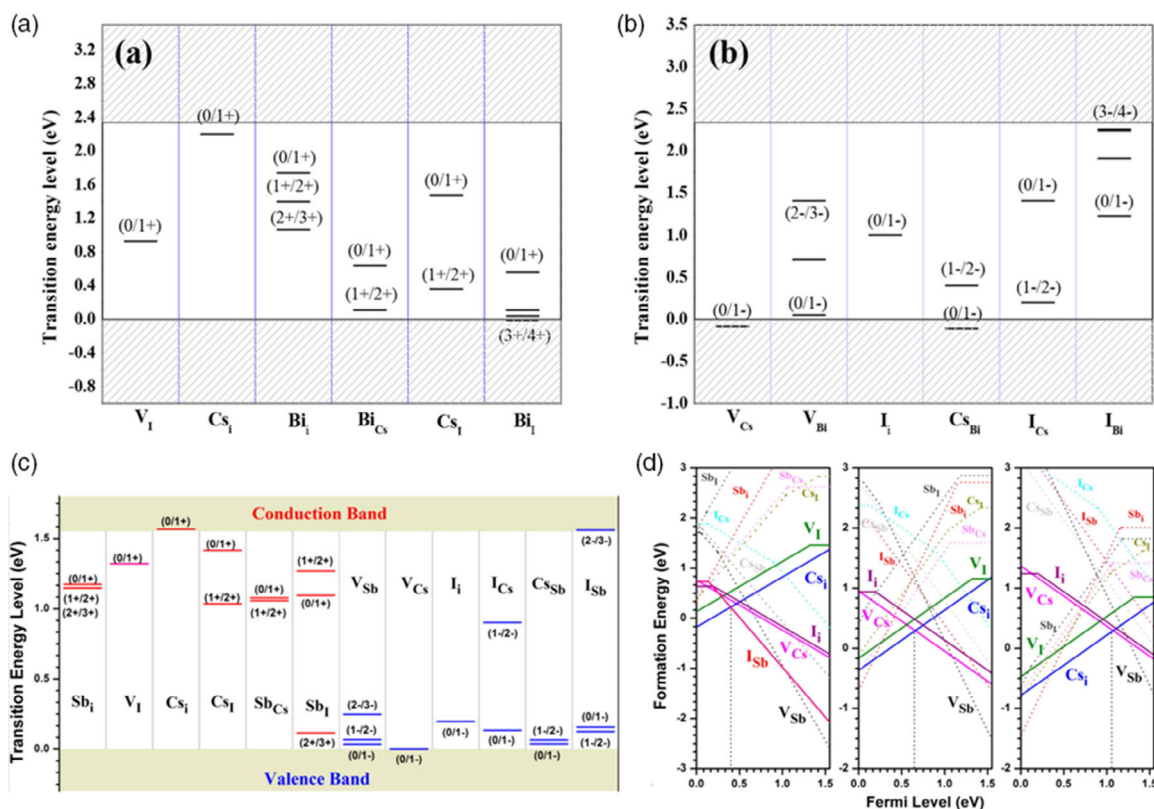


**Figure 16.** Transition energy levels of intrinsic a) donor-type and b) acceptor-type defects. c) GGA-calculated transition energy levels of the acceptor- (blue lines) and donor- (red lines) level formation energies of intrinsic point defects and d) chemical potentials at different growth conditions (I rich/Sb poor, moderate, and I poor/Sb rich, respectively) in  $Cs_3Sb_2I_9$  perovskite. Reproduced with permission.<sup>[56]</sup> Copyright 2017. American Chemical Society. Reproduced with permission.<sup>[199]</sup> Copyright 2014. American Chemical Society.

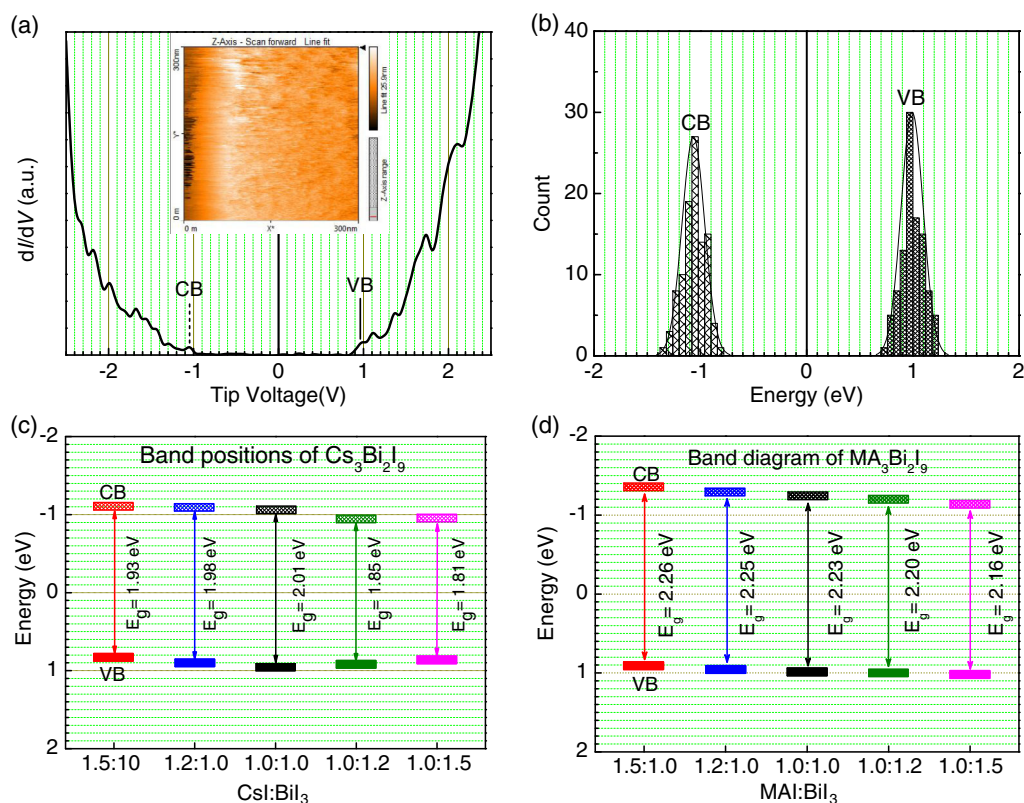


**Figure 17.** a) Typical  $dI/dV$  spectrum and b) the respective histogram of CB and VB energies of stoichiometric (1:1)  $\text{Cs}_3\text{Bi}_2\text{I}_9$  perovskite thin films, c) band positions of  $\text{Cs}_3\text{Bi}_2\text{I}_9$  formed with different stoichiometric ratios of the precursors, namely CsI and BiI<sub>3</sub>, and d) Band positions of  $\text{MA}_3\text{Bi}_2\text{I}_9$  formed with different stoichiometric ratios of the precursors, namely MAI and BiI<sub>3</sub>. Inset of (a) shows the topography of the stoichiometric  $\text{Cs}_3\text{Bi}_2\text{I}_9$  perovskite thin film. Reproduced with permission.<sup>[32]</sup> Copyright 2019, Elsevier.

(Figure 17c). Interestingly, a lowering of the bandgap was achieved in  $\text{Cs}_3\text{Bi}_2\text{I}_9$  formed with a CsI-rich condition, implying the formation of  $\text{Cs}_{\text{Bi}}$  vacancies in addition to other acceptor-like vacancies, such as  $\text{I}_{\text{Bi}}$  and  $\text{V}_{\text{Bi}}$  with formation energies being a little higher than that of  $\text{Cs}_{\text{Bi}}$  in the perovskites. With the support of theoretical calculations, we could also confirm the presence of  $\text{V}_{\text{I}}$  defects in the perovskite formed in a BiI<sub>3</sub>-rich condition. In the methylammonium-based perovskite,  $(\text{CH}_3\text{NH}_3)_3\text{Bi}_2\text{I}_9$ , the bandgap did not respond upon a variation of precursor stoichiometry (Figure 17d); it has therefore been concluded that the defects present in methylammonium-based perovskites ( $\text{MA}_3\text{B}_2\text{X}_9$ ) have shallow energy levels.

#### 4.3.2. Defect Passivation

Due to the deep-level nature of defects in a system like  $\text{A}_3\text{Bi}_2\text{X}_9$ , defect passivation is naturally extremely important. An efficient manner of defect passivation is however sparse. Among the few available reports, the research group of Matthews has provided a route of deep-level defect suppression in the  $\text{Cs}_3\text{Bi}_2\text{I}_9$  system using excess BiI<sub>3</sub> in the precursor solution.<sup>[198]</sup> They have observed an improvement in the photovoltaic parameters which have been correlated with the passivation of intrinsic defects or some structural disorders. In support of their inference, they have characterized  $\text{Cs}_3\text{Bi}_2\text{I}_9$  for PL and cathodoluminescence

(CL) spectroscopies (Figure 18a). Both the spectroscopic results suggested an enhancement in the emission intensity with the addition of excess BiI<sub>3</sub> in the precursor, suppressing the formation of secondary phases (Figure 18b). They have also confirmed such conclusions from transient absorption (TA) spectroscopy (Figure 18c) and carrier decay dynamics (Figure 18d). The enhancement of PL intensity was hence correlated with the passivation of trap states which were present in  $\text{Cs}_3\text{Bi}_2\text{I}_9$  and acted as nonradiative channels for decay of carriers.

In  $\text{A}_3\text{M}_2\text{X}_9$  lead-free perovskite systems, Cl passivation has been reported to be an effective avenue to boost the performance of LEDs and solar cells based on such perovskites.<sup>[200]</sup> In our research group, we have introduced a new route of defect passivation by incorporating chloride in the  $\text{MA}_3\text{Sb}_2\text{I}_9$  perovskite system.<sup>[80]</sup> Apart from defect passivation, a phase transformation could be observed to have occurred in  $\text{MA}_3\text{Sb}_2\text{I}_9$  during the transformation from a 0D dimer phase to a 2D-layered phase upon chloride incorporation. STS studies suggested a major change in band energies due to the phase transformation process. Along with defect passivation, we have also observed a contracting nature of the local surface potential distribution as probed through KPFM (Figure 19a). With local conductivity measurement by c-AFM, we could infer that the conductivity of the antimony halide perovskite system increased upon the passivation of defects upon chlorine incorporation (Figure 19b).

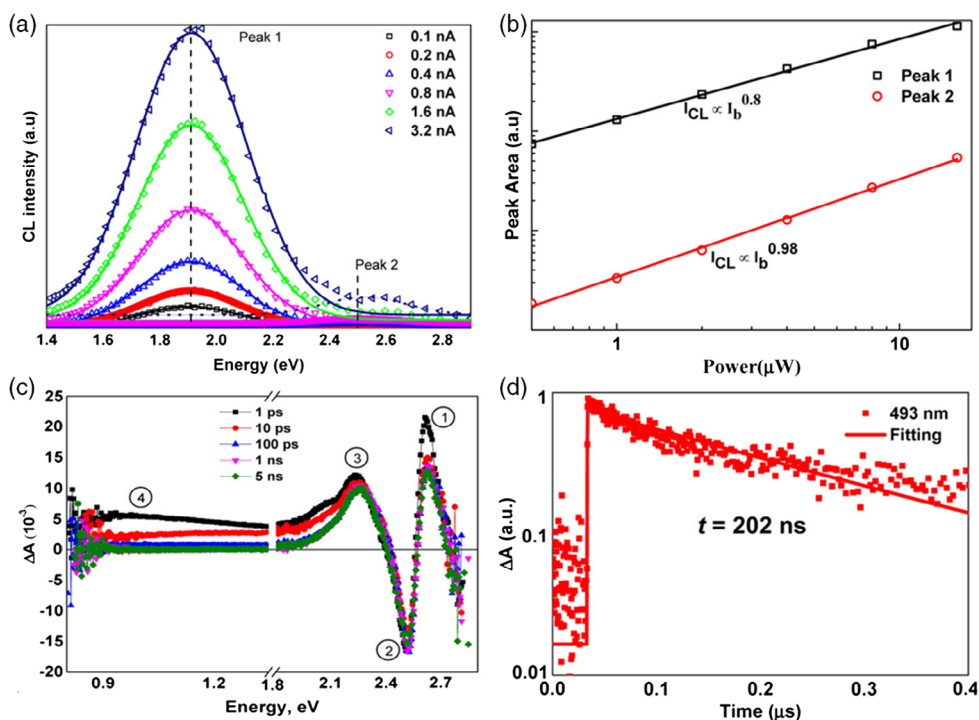


**Figure 18.** a) Gaussian fitting of CL spectra of  $\text{Cs}_3\text{Bi}_2\text{I}_9$  thin films at different electron beam currents ( $I_b$ ), b) power-law fits of CL peak area against different electron beam powers, c) TA spectra of  $\text{Cs}_3\text{Bi}_2\text{I}_9$  thin films for different time delays under 400 nm excitation, and d) carrier decay dynamics of the same at 493 nm. Reproduced with permission.<sup>[198]</sup> Copyright 2018, American Chemical Society.

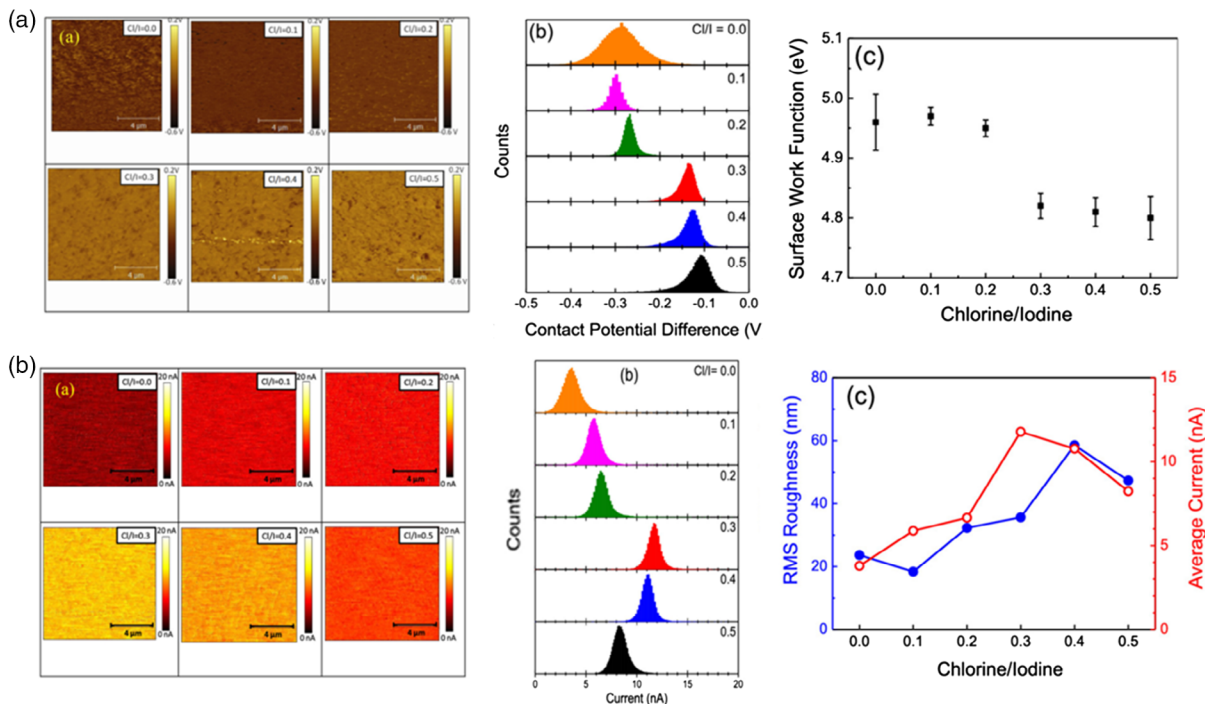


**Figure 19.** a) Contact potential images, distribution of CPD, and average surface work function of  $\text{MA}_3\text{Sb}_2\text{Cl}_x\text{I}_{9-x}$  with a range of chlorine-to-iodine (Cl/I) ratios. b) Conductivity mapping, distribution of current at 1.0 V, and a comparison between root mean square roughness (from AFM topographies) and average current of  $\text{MA}_3\text{Sb}_2\text{Cl}_x\text{I}_{9-x}$  with a range of chlorine-to-iodine (Cl/I) ratios. Reproduced with permission.<sup>[80]</sup> Copyright 2019, American Chemical Society.



**Table 4.** Major defects and passivating agents used for defect engineering in perovskites beyond ABX<sub>3</sub>.

Perovskite	Major defects	Passivating agents	Ref.
Cs <sub>2</sub> AgBiBr <sub>6</sub>	V <sub>Cs</sub> , V <sub>Ag</sub> , V <sub>Bi</sub> , V <sub>Br</sub> , Cs <sub>i</sub> , Ag <sub>i</sub> , Bi <sub>i</sub> , Br <sub>i</sub> , Cs <sub>Ag</sub> , Cs <sub>Bi</sub> , Ag <sub>Cs</sub> , Ag <sub>Bi</sub> , Bi <sub>Cs</sub> , Bi <sub>Ag</sub> , Cs <sub>Br</sub> , Ag <sub>Br</sub> , Bi <sub>Br</sub> , Br <sub>Cs</sub> , Br <sub>Ag</sub> , and Br <sub>Bi</sub> .	Mn <sup>2+</sup> Yb <sup>2+</sup> doping	[180,181,186, 188,190–192]
(MA) <sub>2</sub> AgBiBr <sub>6</sub>	No report	–	–
Cs <sub>2</sub> NaBiI <sub>6</sub>	No report	–	–
Cs <sub>2</sub> KBiCl <sub>6</sub>	No report	–	–
Cs <sub>2</sub> NaBiCl <sub>6</sub>	No report	–	–
Cs <sub>2</sub> AgInCl <sub>6</sub>	V <sub>Cs</sub> , V <sub>Ag</sub> , V <sub>In</sub> , V <sub>Cl</sub> , Cs <sub>i</sub> , Ag <sub>i</sub> , In <sub>i</sub> , Br <sub>i</sub> , Cs <sub>Ag</sub> , Cs <sub>In</sub> , Ag <sub>Cs</sub> , Ag <sub>In</sub> , In <sub>Cs</sub> , In <sub>Ag</sub> , Cs <sub>Cl</sub> , Ag <sub>Cl</sub> , In <sub>Br</sub> , Cl <sub>Cs</sub> , Cl <sub>Ag</sub> , and Cl <sub>In</sub> .	Na <sup>+</sup> , Mn <sup>2+</sup> doping, Cl incorporation	[182,183]
Cs <sub>2</sub> SnI <sub>6</sub>	V <sub>Cs</sub> , V <sub>Sn</sub> , V <sub>I</sub> , Cs <sub>i</sub> , Sn <sub>i</sub> , I <sub>i</sub> , Cs <sub>Sn</sub> , Sn <sub>Cs</sub> , Cs <sub>I</sub> , Sn <sub>I</sub> , I <sub>Cs</sub> , I <sub>Sn</sub>	No report	[208]
Cs <sub>2</sub> TiBr <sub>6</sub>	V <sub>Cs</sub> , V <sub>Ti</sub> , V <sub>Br</sub> , Cs <sub>i</sub> , Ti <sub>i</sub> , Br <sub>i</sub> , Cs <sub>Br</sub> , Ti <sub>Cs</sub> , Cs <sub>Ti</sub> , Ti <sub>Br</sub> , Br <sub>Cs</sub> , I <sub>Ti</sub>	I incorporation	[179]
Cs <sub>3</sub> Bi <sub>2</sub> I <sub>9</sub>	Cs <sub>Bi</sub> , I <sub>Bi</sub> , V <sub>Bi</sub> , V <sub>I</sub>	Excess BiI <sub>3</sub>	[56,198]
Cs <sub>3</sub> Sb <sub>2</sub> I <sub>9</sub>	V <sub>Cs</sub> , V <sub>Sb</sub> , I <sub>i</sub> , Cs <sub>Sb</sub> , Cs <sub>i</sub> , Cs <sub>I</sub> , Sb <sub>i</sub> , I <sub>Cs</sub> , I <sub>Sb</sub> , Sb <sub>Cs</sub> , S <sub>Bi</sub>	Cl incorporation	[80]
MA <sub>3</sub> Sb <sub>2</sub> I <sub>9</sub>	No report	–	–
MA <sub>3</sub> Bi <sub>2</sub> I <sub>9</sub>	No report	–	–

The defect landscape and passivating agents used for defect engineering in perovskites beyond ABX<sub>3</sub> are shown in Table 4.

## 5. Conclusion and Future Outlook

Hybrid halide perovskites offer enormous potential toward the development of next-generation solar cells. Though an outstanding progress has been witnessed over the past decade in improving the efficiency of such perovskite solar cells, there are still some gaps toward the commercialization of technology. The prevailing challenges of perovskite solar cells in terms of device performance and long-term stability are fundamentally governed by defect physics; hence, defect engineering has now become a crucial aspect in optimizing the performance of perovskite solar cells. In this Review, we have discussed about the ensemble of defects, their possible origins, a host of defect analysis techniques, and effective methods to passivate the defects in prototype solar cells based on methylammonium lead halide and its derivatives. In our discussion, we have also highlighted the limitations of existing methods while investigating the origin of defects.

In this context, the recently developed “super-cell” approach has been considered to be an effective method toward addressing the limitations of first-principle calculations. Considering some recent developments, we have identified some cutting-edge experimental techniques in probing the defects at the local scale and the defects’ function in restraining device performance and prompting device degradation. These defects have been found to promote nonradiative recombination in perovskite solar cells that

in turn limit V<sub>OC</sub>, amplify hysteresis phenomena, and hamper carrier transport besides affecting long-term device stability. A combination of different techniques, such as scanning probe microscopy, transient measurements, and ultrafast carrier dynamics at the nanoscale have been found to be appropriate in investigating defect physics in terms of their nature, concentration, and local response. Based on the understanding, we have considered passivation of defects as the next proficient strategy; we have expanded our discussion on different approaches to passivate the defects in the bulk, on the surface, and at grains and grain boundaries. We have summarized some pioneering material-engineering approaches to passivate the defects and thoroughly discussed their role in understanding the nature, density, and distribution of such defects in perovskite materials and devices. A detailed discussion on the effectiveness of some experimental approaches such as compositional tuning, engineering of charge transport layers, and introduction of interfaces in reducing defect-assisted nonradiative recombination in solar cells to improve the V<sub>OC</sub> of the devices has also been presented.

We expect that such materials and device engineering can be effective in suppressing the ion migration, reducing photocurrent hysteresis, and improving the long-term device stability. Furthermore, we believe that interfacial engineering by manipulating the surfaces and GBs with passivating agents can be highly effective in reducing the recombination centers and can improve the carrier transport process and also enhance the device performance. In this context, we have argued the necessity of developing a proper band alignment between charge transport layers and the perovskite absorber as a smart approach to minimize the defect density and promote facile charge transport. A few new routes, such as fabrication of single-crystalline thin films with fewer defects and grain boundaries, design of new molecules as passivation layers, and new charge transport layers to fully passivate the defects on the surface and/or at GBs, have also been discussed in this Review. Our discussion has rightfully addressed how the study of defects in ABX<sub>3</sub> and beyond the prototype perovskite is essential for the commercialization of perovskite solar cells. On a broader note, it is expected that the solar cell efficiency would further increase toward the theoretically predicted limit upon addressing the prevailing issues with defects through defect engineering and post-treatment techniques.

## Acknowledgements

A.J.P. acknowledges the JC Bose National Fellowship of SERB (SB/S2/JCB-001/2016). A.M. and L.P. acknowledge DST INSPIRE Fellowship [IF170922] and SERB National Post-Doctoral fellowship (PDF/2017/001243), respectively.

## Conflict of Interest

The authors declare no conflict of interest.

## Keywords

defect engineering, defect passivation, device efficiencies, defect states, hybrid halide perovskites, origin of defects

Received: August 21, 2020  
Revised: October 28, 2020  
Published online: November 10, 2020

- [1] A. Kojima, K. Teshima, Y. Shirai, T. Miyasaka, *J. Am. Chem. Soc.* **2009**, *131*, 6050.
- [2] A. K. Jena, A. Kulkarni, T. Miyasaka, *Chem. Rev.* **2019**, *119*, 3036.
- [3] M. A. Green, A. Ho-Baillie, H. J. Snaith, *Nat. Photonics* **2014**, *8*, 506.
- [4] N. G. Park, M. Gratzel, T. Miyasaka, K. Zhu, K. Emery, *Nat. Energy* **2016**, *1*, 16152.
- [5] Q. Jiang, Z. N. Chu, P. Y. Wang, X. L. Yang, H. Liu, Y. Wang, Z. G. Yin, J. L. Wu, X. W. Zhang, J. B. You, *Adv. Mater.* **2017**, *29*, 1703852.
- [6] L. B. Qiu, L. K. Ono, Y. B. Qi, *Mater. Today Energy* **2018**, *7*, 169.
- [7] A. J. Pal, *Curr. Sci.* **2019**, *116*, 714.
- [8] S. Chatterjee, A. J. Pal, *J. Mater. Chem. A* **2018**, *6*, 3793.
- [9] S. Chatterjee, A. J. Pal, *J. Phys. Chem. C* **2016**, *120*, 1428.
- [10] S. Khatun, A. Maiti, A. J. Pal, *Appl. Phys. Lett.* **2020**, *116*, 012104.
- [11] S. Bonomi, I. Tredici, B. Albini, P. Galinetto, A. Rizzo, A. Listorti, U. A. Tamburini, L. Malavasi, *Chem. Commun.* **2018**, *54*, 13212.
- [12] R. Prasanna, A. Gold-Parker, T. Leijtens, B. Conings, A. Babayigit, H. G. Boyen, M. F. Toney, M. D. McGehee, *J. Am. Chem. Soc.* **2017**, *139*, 11117.
- [13] C. Redondo-Obispo, I. Suarez, S. J. Quesada, T. S. Ripolles, J. P. Martinez-Pastor, A. L. Alvarez, A. de Andres, C. Coia, *J. Phys. Chem. Lett.* **2020**, *11*, 2188.
- [14] H. Fujiwara, M. Kato, M. Tamakoshi, T. Miyadera, M. Chikamatsu, *Phys. Status Solidi A* **2018**, *215*, 1700730.
- [15] L. M. Herz, *ACS Energy Lett.* **2017**, *2*, 1539.
- [16] G. W. P. Adhyaksa, L. W. Veldhuizen, Y. H. Kuang, S. Brittman, R. E. I. Schropp, E. C. Garnett, *Chem. Mater.* **2016**, *28*, 5259.
- [17] D. Meggiolaro, S. G. Motti, E. Mosconi, A. J. Barker, J. Ball, C. A. R. Perini, F. Deschler, A. Petrozza, F. De Angelis, *Energy Environ. Sci.* **2018**, *11*, 702.
- [18] A. Maiti, S. Khatun, A. J. Pal, *Nano Lett.* **2020**, *20*, 292.
- [19] M. B. Johnston, L. M. Herz, *Accounts Chem. Res.* **2016**, *49*, 146.
- [20] NREL Chart, <https://www.nrel.gov/pv/cell-efficiency.html>.
- [21] D. Wang, M. Wright, N. K. Elumalai, A. Uddin, *Sol. Energy Mater. Sol. Cells* **2016**, *147*, 255.
- [22] Q. Wali, F. J. Iftikhar, M. E. Khan, A. Ullah, Y. Iqbal, R. Jose, *Org. Electron.* **2020**, *78*, 105590.
- [23] M. Saliba, T. Matsui, K. Domanski, J. Y. Seo, A. Ummadisingu, S. M. Zakeeruddin, J. P. Correa-Baena, W. R. Tress, A. Abate, A. Hagfeldt, M. Gratzel, *Science* **2016**, *354*, 206.
- [24] C. Dong, Z. K. Wang, L. S. Liao, *Energy Technol.* **2020**, *8*, 1900804.
- [25] W. J. Yin, T. T. Shi, Y. F. Yan, *Appl. Phys. Lett.* **2014**, *104*, 063903.
- [26] A. Kalam, A. G. Al-Sehemi, A. Mahapatra, D. Verma, S. Trivedi, M. K. Pandey, *Mater. Res. Express* **2019**, *6*, 105510.
- [27] B. W. Li, V. Ferguson, S. R. P. Silva, W. Zhang, *Adv. Mater. Interfaces* **2018**, *5*, 1800326.
- [28] S. P. Dunfield, L. Bliss, F. Zhang, J. M. Luther, K. Zhu, M. van Hest, M. O. Reese, J. J. Berry, *Adv. Energy Mater.* **2020**, *10*, 1904054.
- [29] F. Wang, S. Bai, W. Tress, A. Hagfeldt, F. Gao, *npj Flex. Electron.* **2018**, *2*, 22.
- [30] E. Aydin, M. De Bastiani, S. De Wolf, *Adv. Mater.* **2019**, *31*, 1900428.
- [31] A. Maiti, S. Chatterjee, A. J. Pal, *ACS Appl. Energy Mater.* **2020**, *3*, 810.
- [32] A. Maiti, G. Paul, H. Bhunia, A. J. Pal, *Sol. Energy Mater. Sol. Cells* **2019**, *200*, 109941.
- [33] D. H. Kong, N. G. Park, *Adv. Mater.* **2019**, *31*, 1805214.
- [34] D. A. Jacobs, Y. L. Wu, H. P. Shen, C. Barugkin, F. J. Beck, T. P. White, K. Weber, K. R. Catchpole, *Phys. Chem. Chem. Phys.* **2017**, *19*, 3094.
- [35] W. Chen, K. Sun, C. Y. Ma, C. Q. Leng, J. H. Fua, L. J. Hu, M. Li, M. Wang, Z. G. Zang, X. S. Tang, H. F. Shi, S. R. Lu, *Org. Electron.* **2018**, *58*, 283.
- [36] W. Li, R. Long, J. F. Tang, O. V. Prezhdo, *J. Phys. Chem. Lett.* **2019**, *10*, 3788.
- [37] J. Kim, C. H. Chung, K. H. Hong, *Phys. Chem. Chem. Phys.* **2016**, *18*, 27143.
- [38] Y. M. Lee, I. Maeng, J. Park, M. Song, J. H. Yun, M. C. Jung, M. Nakamura, *Front. Energy Res.* **2018**, *6*, 128.
- [39] D. Y. Luo, R. Su, W. Zhang, Q. H. Gong, R. Zhu, *Nat. Rev. Mater.* **2020**, *5*, 44.
- [40] R. Brakkee, R. M. Williams, *Appl. Sci. Basel* **2020**, *10*, 3061.
- [41] M. Stolterfoht, C. M. Wolff, Y. Amir, A. Paulke, L. Perdigon-Toro, P. Caprioglio, D. Neher, *Energy Environ. Sci.* **2017**, *10*, 1530.
- [42] H. J. Queisser, E. E. Haller, *Science* **1998**, *281*, 945.
- [43] J. M. Ball, A. Petrozza, *Nat. Energy* **2016**, *1*, 16149.
- [44] L. B. Qiu, S. S. He, L. K. Ono, Y. B. Qi, *Adv. Energy Mater.* **2020**, *10*, 1902726.
- [45] X. Zhou, W. J. Qi, J. L. Li, J. Cheng, Y. M. Li, J. S. Luo, M. J. Ko, Y. L. Li, Y. Zhao, X. D. Zhang, *Sol. RRL* **2020**, *4*, 2000308.
- [46] G. Paul, S. Chatterjee, H. Bhunia, A. J. Pal, *J. Phys. Chem. C* **2018**, *122*, 20194.
- [47] Q. Wang, Y. C. Shao, H. P. Xie, L. Lyu, X. L. Liu, Y. L. Gao, J. S. Huang, *Appl. Phys. Lett.* **2014**, *105*, 163508.
- [48] A. Buin, P. Pietsch, J. X. Xu, O. Voznyy, A. H. Ip, R. Comin, E. H. Sargent, *Nano Lett.* **2014**, *14*, 6281.
- [49] J. Kim, S. H. Lee, J. H. Lee, K. H. Hong, *J. Phys. Chem. Lett.* **2014**, *5*, 1312.
- [50] K. X. Steirer, P. Schulz, G. Teeter, V. Stevanovic, M. Yang, K. Zhu, J. J. Berry, *ACS Energy Lett.* **2016**, *1*, 360.
- [51] Y. H. Shao, Z. G. Xiao, C. Bi, Y. B. Yuan, J. S. Huang, *Nat. Commun.* **2014**, *5*, 5784.
- [52] G. C. Xing, B. Wu, S. Chen, J. Chua, N. Yantara, S. Mhaisalkar, N. Mathews, T. C. Sum, *Small* **2015**, *11*, 3606.
- [53] J. M. Azpiroz, E. Mosconi, J. Bisquert, F. De Angelis, *Energy Environ. Sci.* **2015**, *8*, 2118.
- [54] Y. X. Ouyang, L. Shi, Q. Li, J. L. Wang, *Small Methods* **2019**, *3*, 1900154.
- [55] J. Bisquert, E. J. Juarez-Perez, *J. Phys. Chem. Lett.* **2019**, *10*, 5889.
- [56] B. Ghosh, S. Chakraborty, H. Wei, C. Guet, S. Z. Li, S. Mhaisalkar, N. Mathews, *J. Phys. Chem. C* **2017**, *121*, 17062.
- [57] L. Schade, A. D. Wright, R. D. Johnson, M. Dollmann, B. Wenger, P. K. Nayak, D. Prabhakaran, L. M. Herz, R. Nicholas, H. J. Snaith, P. G. Radaelli, *ACS Energy Lett.* **2019**, *4*, 299.
- [58] J. Berry, T. Buonassisi, D. A. Egger, G. Hodes, L. Kronik, Y. L. Loo, I. Lubomirsky, S. R. Marder, Y. Mastai, J. S. Miller, D. B. Mitzi, Y. Paz, A. M. Rappe, I. Riess, B. Rybtchinski, O. Stafsudd, V. Stevanovic, M. F. Toney, D. Zitoun, A. Kahn, D. Ginley, D. Cahen, *Adv. Mater.* **2015**, *27*, 5102.
- [59] W. J. Yin, J. H. Yang, J. Kang, Y. F. Yan, S. H. Wei, *J. Mater. Chem. A* **2015**, *3*, 8926.
- [60] X. Wu, F. Y. Kang, W. H. Duan, J. Li, *Prog. Nat. Sci.* **2019**, *29*, 247.
- [61] D. Meggiolaro, F. De Angelis, *ACS Energy Lett.* **2018**, *3*, 2206.
- [62] E. Mosconi, J. M. Azpiroz, F. De Angelis, *Chem. Mater.* **2015**, *27*, 4885.
- [63] G. Zhou, W. Chu, O. V. Prezhdo, *ACS Energy Lett.* **2020**, *5*, 1930.
- [64] L. Zhang, M. G. Ju, W. Z. Liang, *Phys. Chem. Chem. Phys.* **2016**, *18*, 23174.
- [65] A. Zakutayev, C. M. Caskey, A. N. Fioretti, D. S. Ginley, J. Vidal, V. Stevanovic, E. Tea, S. Lany, *J. Phys. Chem. Lett.* **2014**, *5*, 1117.
- [66] Y. Wang, T. Gould, J. F. Dobson, H. M. Zhang, H. G. Yang, X. D. Yao, H. J. Zhao, *Phys. Chem. Chem. Phys.* **2014**, *16*, 1424.
- [67] S. D. Stranks, G. E. Eperon, G. Grancini, C. Menelaou, M. J. P. Alcocer, T. Leijtens, L. M. Herz, A. Petrozza, H. J. Snaith, *Science* **2013**, *342*, 341.

- [68] M. L. Agiorgousis, Y. Y. Sun, H. Zeng, S. B. Zhang, *J. Am. Chem. Soc.* **2014**, *136*, 14570.
- [69] W. Li, J. Liu, F. Q. Bai, H. X. Zhang, O. V. Prezhdo, *ACS Energy Lett.* **2017**, *2*, 1270.
- [70] T. M. Brenner, D. A. Egger, L. Kronik, G. Hodes, D. Cahen, *Nat. Rev. Mater.* **2016**, *1*, 15007.
- [71] X. P. Zheng, B. Chen, J. Dai, Y. J. Fang, Y. Bai, Y. Z. Lin, H. T. Wei, X. C. Zeng, J. S. Huang, *Nat. Energy* **2017**, *2*, 17102.
- [72] G. F. Han, T. M. Koh, S. S. Lim, T. W. Goh, X. T. Guo, S. W. Leow, R. Begum, T. C. Sum, N. Mathews, S. Mhaisalkar, *ACS Appl. Mater. Interfaces* **2017**, *9*, 21292.
- [73] Y. X. Tian, A. Merdasa, E. Unger, M. Abdellah, K. B. Zheng, S. McKibbin, A. Mikkelsen, T. Pullerits, A. Yartsev, V. Sundstrom, I. G. Scheblykin, *J. Phys. Chem. Lett.* **2015**, *6*, 4171.
- [74] Z. G. Xiao, Q. F. Dong, C. Bi, Y. C. Shao, Y. B. Yuan, J. S. Huang, *Adv. Mater.* **2014**, *26*, 6503.
- [75] O. D. Lavrentovich, *Characterization of Materials* (Ed: E. N. Kaufmann), John Wiley & Sons, Inc., Hoboken, NJ **2012**, p. 1.
- [76] B. H. Wang, K. Y. Wong, S. F. Yang, T. Chen, *J. Mater. Chem. A* **2016**, *4*, 3806.
- [77] J. Y. Ma, J. Ding, H. J. Yan, D. Wang, J. S. Hu, *ACS Appl. Mater. Interfaces* **2019**, *11*, 21627.
- [78] H. N. Si, S. C. Zhang, S. F. Ma, Z. H. Xiong, A. Kausar, Q. L. Liao, Z. Zhang, A. Sattar, Z. Kang, Y. Zhang, *Adv. Energy Mater.* **2020**, *10*, 1903922.
- [79] S. Paramanik, S. Chatterjee, A. J. Pal, *ACS Appl. Electron. Mater.* **2020**, *2*, 1395.
- [80] G. Paul, A. J. Pal, *J. Phys. Chem. C* **2019**, *123*, 13500.
- [81] Z. H. Liu, J. N. Hu, H. Y. Jiao, L. Li, G. H. J. Zheng, Y. H. Chen, Y. Huang, Q. Zhang, C. Shen, Q. Chen, H. P. Zhou, *Adv. Mater.* **2017**, *29*, 1606774.
- [82] X. X. Chen, S. J. Cheng, L. Xiao, H. D. Sun, *J. Phys. D Appl. Phys.* **2020**, *53*, 373001.
- [83] N. De Marco, H. P. Zhou, Q. Chen, P. Y. Sun, Z. H. Liu, L. Meng, E. P. Yao, Y. S. Liu, A. Schiffer, Y. Yang, *Nano Lett.* **2016**, *16*, 1009.
- [84] Q. F. Dong, Y. J. Fang, Y. C. Shao, P. Mulligan, J. Qiu, L. Cao, J. S. Huang, *Science* **2015**, *347*, 967.
- [85] W. S. Yang, B. W. Park, E. H. Jung, N. J. Jeon, Y. C. Kim, D. U. Lee, S. S. Shin, J. Seo, E. K. Kim, J. H. Noh, S. I. Seok, *Science* **2017**, *356*, 1376.
- [86] F. Yuan, Z. X. Wu, H. Dong, J. Xi, K. Xi, G. Divitin, B. Jiao, X. Hou, S. F. Wang, Q. H. Gong, *J. Phys. Chem. C* **2017**, *121*, 15318.
- [87] V. D'Innocenzo, A. R. S. Kandada, M. De Bastiani, M. Gandini, A. Petrozza, *J. Am. Chem. Soc.* **2014**, *136*, 17730.
- [88] P. Fassel, Y. Zakharko, L. M. Falk, K. P. Goetz, F. Paulus, A. D. Taylor, J. Zaumseil, Y. Vaynzof, *J. Mater. Chem. C* **2019**, *7*, 5285.
- [89] D. W. Dequillettes, W. Zhang, V. M. Burlakov, D. J. Graham, T. Leijtens, A. Oshero, V. Bulovic, H. J. Snaith, D. S. Ginger, S. D. Stranks, *Nat. Commun.* **2016**, *7*, 11683.
- [90] L. M. Pazos-Outon, T. P. Xiao, E. Yablonovitch, *J. Phys. Chem. Lett.* **2018**, *9*, 1703.
- [91] A. D. Wright, R. L. Milot, G. E. Eperon, H. J. Snaith, M. B. Johnston, L. M. Herz, *Adv. Funct. Mater.* **2017**, *27*, 1700860.
- [92] M. Ledinsky, T. Schonfeldova, J. Holovsky, E. Aydin, Z. Hajkova, L. Landova, N. Neykova, A. Fejfar, S. De Wolf, *J. Phys. Chem. Lett.* **2019**, *10*, 1368.
- [93] W. Zhang, S. Pathak, N. Sakai, T. Stergiopoulos, P. K. Nayak, N. K. Noel, A. A. Haghghirad, V. M. Burlakov, D. W. deQuillettes, A. Sadhanala, W. Z. Li, L. D. Wang, D. S. Ginger, R. H. Friend, H. J. Snaith, *Nat. Commun.* **2015**, *6*, 10030.
- [94] S. Wang, P. Kaienburg, B. Klingebiel, D. Schillings, T. Kirchartz, *J. Phys. Chem. C* **2018**, *122*, 9795.
- [95] N. Liu, Q. Du, G. Z. Yin, P. F. Liu, L. Li, H. P. Xie, C. Zhu, Y. J. Li, H. P. Zhou, W. B. Zhang, Q. Chen, *J. Mater. Chem. A* **2018**, *6*, 6806.
- [96] C. Hanmandlu, S. Swamy, A. Shing, H. A. Chen, C. C. Liu, C. S. Lai, A. Mohapatra, C. W. Pao, P. L. Chen, C. W. Chu, *J. Mater. Chem. A* **2020**, *8*, 5263.
- [97] C. X. Ran, J. T. Xu, W. Y. Gao, C. M. Huang, S. X. Dou, *Chem. Soc. Rev.* **2018**, *47*, 4581.
- [98] W. Melitz, J. Shen, A. C. Kummel, S. Lee, *Surf. Sci. Rep.* **2011**, *66*, 1.
- [99] J. J. Li, J. Y. Ma, Q. Q. Ge, J. S. Hu, D. Wang, L. J. Wan, *ACS Appl. Mater. Interfaces* **2015**, *7*, 28518.
- [100] U. Dasgupta, A. Bera, A. J. Pal, *ACS Energy Lett.* **2017**, *2*, 582.
- [101] J. S. Yun, A. Ho-Baillie, S. J. Huang, S. H. Woo, Y. Heo, J. Seidel, F. Z. Huang, Y. B. Cheng, M. A. Green, *J. Phys. Chem. Lett.* **2015**, *6*, 875.
- [102] Y. C. Shao, Y. J. Fang, T. Li, Q. Wang, Q. F. Dong, Y. H. Deng, Y. B. Yuan, H. T. Wei, M. Y. Wang, A. Gruverman, J. Shieida, J. S. Huang, *Energy Environ. Sci.* **2016**, *9*, 1752.
- [103] R. Ohmann, L. K. Ono, H. S. Kim, H. P. Lin, M. V. Lee, Y. Y. Li, N. G. Park, Y. B. Qi, *J. Am. Chem. Soc.* **2015**, *137*, 16049.
- [104] M. Saliba, T. Matsui, J. Y. Seo, K. Domanski, J. P. Correa-Baena, M. K. Nazeeruddin, S. M. Zakeeruddin, W. Tress, A. Abate, A. Hagfeldt, M. Gratzel, *Energy Environ. Sci.* **2016**, *9*, 1989.
- [105] H. C. Cho, S. H. Jeong, M. H. Park, Y. H. Kim, C. Wolf, C. L. Lee, J. H. Heo, A. Sadhanala, N. Myoung, S. Yoo, S. H. Im, R. H. Friend, T. W. Lee, *Science* **2015**, *350*, 1222.
- [106] L. G. Wang, H. P. Zhou, J. N. Hu, B. L. Huang, M. Z. Sun, B. W. Dong, G. H. J. Zheng, Y. Huang, Y. H. Chen, L. Li, Z. Q. Xu, N. X. Li, Z. Liu, Q. Chen, L. D. Sun, C. H. Yan, *Science* **2019**, *363*, 265.
- [107] R. Lindblad, D. Q. Bi, B. W. Park, J. Oscarsson, M. Gorgoi, H. Siegbahn, M. Odelius, E. M. J. Johansson, H. Rensmo, *J. Phys. Chem. Lett.* **2014**, *5*, 648.
- [108] G. Sadoughi, D. E. Starr, E. Handick, S. D. Stranks, M. Gorgoi, R. G. Wilks, M. Bar, H. J. Snaith, *ACS Appl. Mater. Interfaces* **2015**, *7*, 13440.
- [109] C. G. Bischak, C. L. Hetherington, H. Wu, S. Aloni, D. F. Ogletree, D. T. Limmer, N. S. Ginsberg, *Nano Lett.* **2017**, *17*, 1028.
- [110] X. Y. Zhang, L. N. Li, Z. H. Sun, J. H. Luo, *Chem. Soc. Rev.* **2019**, *48*, 517.
- [111] F. Z. Liu, Q. Dong, M. K. Wong, A. B. Djuricic, A. N. Ng, Z. W. Ren, Q. Shen, C. Surya, W. K. Chan, J. Wang, A. M. C. Ng, C. Z. Liao, H. K. Li, K. M. Shih, C. R. Wei, H. M. Su, J. F. Dai, *Adv. Energy Mater.* **2016**, *6*, 1502206.
- [112] B. W. Park, N. Kedem, M. Kulbak, D. Y. Lee, W. S. Yang, N. J. Jeon, J. Seo, G. Kim, K. J. Kim, T. J. Shin, G. Hodes, D. Cahen, S. I. Seok, *Nat. Commun.* **2018**, *9*, 3301.
- [113] Y. C. Chen, Q. Meng, Y. Y. Xiao, X. B. Zhang, J. J. Sun, C. B. Han, H. L. Gao, Y. Z. Zhang, Y. Lu, H. Yan, *ACS Appl. Mater. Interfaces* **2019**, *11*, 44101.
- [114] F. Y. Wang, M. F. Yang, S. Yang, X. Qu, L. L. Yang, L. Fan, J. H. Yang, F. Rosei, *Nano Energy* **2020**, *67*, 104224.
- [115] J. Holovsky, A. P. Amalathas, L. Landova, B. Dzurak, B. Conrad, M. Ledinsky, Z. Hajkova, O. Pop-Georgievski, J. Svoboda, T. C. J. Yang, Q. Jeangros, *ACS Energy Lett.* **2019**, *4*, 3011.
- [116] O. A. Lozhkina, A. A. Murashkina, V. V. Shilovskikh, Y. V. Kapitonov, V. K. Ryabchuk, A. V. Emeline, T. Miyasaka, *J. Phys. Chem. Lett.* **2018**, *9*, 5408.
- [117] P. K. Nayak, M. Sendner, B. Wenger, Z. P. Wang, K. Sharma, A. J. Ramadan, R. Lovrincic, A. Pucci, P. K. Madhu, H. J. Snaith, *J. Am. Chem. Soc.* **2018**, *140*, 574.
- [118] R. Meng, G. B. Wu, J. Y. Zhou, H. Q. Zhou, H. H. Fang, M. A. Loi, Y. Zhang, *Chem. Eur. J.* **2019**, *25*, 5480.

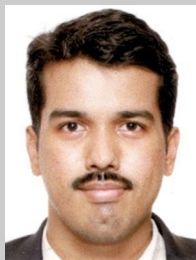
- [119] M. Abdi-Jalebi, M. I. Dar, A. Sadhanala, S. P. Senanayak, M. Gratzel, R. H. Friend, *J. Vis. Exp.* **2017**, 121, e55307.
- [120] D. Y. Son, S. G. Kim, J. Y. Seo, S. H. Lee, H. Shin, D. Lee, N. G. Park, *J. Am. Chem. Soc.* **2018**, 140, 1358.
- [121] J. K. Nam, S. U. Chai, W. Cha, Y. J. Choi, W. Kim, M. S. Jung, J. Kwon, D. Kim, J. H. Park, *Nano Lett.* **2017**, 17, 2028.
- [122] Z. G. Tang, S. Uchida, T. Bessho, T. Kinoshita, H. B. Wang, F. Awai, R. Jono, M. M. Maitani, J. Nakazaki, T. Kubo, H. Segawa, *Nano Energy* **2018**, 45, 184.
- [123] M.-C. Tang, Y. Fan, D. Barrit, R. Li, H. X. Dang, S. Zhang, T. J. Magnanelli, N. V. Nguyen, E. J. Heilweil, C. A. Hacker, D.-M. Smilgies, K. Zhao, A. Amassian, T. D. Anthopoulos, *Sol. RRL* **2020**, 4, 2000272.
- [124] J. T. W. Wang, Z. P. Wang, S. Pathak, W. Zhang, D. W. deQuilettes, F. Wisnivesky-Rocca-Rivarola, J. Huang, P. K. Nayak, J. B. Patel, H. A. M. Yusof, Y. Vaynzof, R. Zhu, I. Ramirez, J. Zhang, C. Ducati, C. Grovenor, M. B. Johnston, D. S. Ginger, R. J. Nicholas, H. J. Snaith, *Energy Environ. Sci.* **2016**, 9, 2892.
- [125] J. Xu, A. Buin, A. H. Ip, W. Li, O. Voznyy, R. Comin, M. J. Yuan, S. Jeon, Z. J. Ning, J. J. McDowell, P. Kanjanaboos, J. P. Sun, X. Z. Lan, L. N. Quan, D. H. Kim, I. G. Hill, P. Maksymovych, E. H. Sargent, *Nat. Commun.* **2015**, 6, 7081.
- [126] C. C. Zhang, M. Li, Z. K. Wang, Y. R. Jiang, H. R. Liu, Y. G. Yang, X. Y. Gao, H. Ma, *J. Mater. Chem. A* **2017**, 5, 2572.
- [127] Y. Wang, Y. Yang, D. W. Han, Q. F. Yang, Q. Yuan, H. Y. Li, D. Y. Zhou, L. Feng, *Sol. Energy Mater. Sol. Cells* **2020**, 212, 110553.
- [128] N. K. Noel, A. Abate, S. D. Stranks, E. S. Parrott, V. M. Burlakov, A. Goriely, H. J. Snaith, *ACS Nano* **2014**, 8, 9815.
- [129] A. Abate, M. Saliba, D. J. Hollman, S. D. Stranks, K. Wojciechowski, R. Avolio, G. Grancini, A. Petrozza, H. J. Snaith, *Nano Lett.* **2014**, 14, 3247.
- [130] R. J. Stewart, C. Grieco, A. V. Larsen, J. J. Maier, J. B. Asbury, *J. Phys. Chem. Lett.* **2016**, 7, 1148.
- [131] J. W. Lee, H. S. Kim, N. G. Park, *Accounts Chem. Res.* **2016**, 49, 311.
- [132] L. F. Zhu, Y. Z. Xu, P. P. Zhang, J. J. Shi, Y. H. Zhao, H. Y. Zhang, J. H. Wu, Y. H. Luo, D. M. Li, Q. B. Meng, *J. Mater. Chem. A* **2017**, 5, 20874.
- [133] X. B. Cao, C. L. Li, L. L. Zhi, Y. H. Li, X. Cui, Y. W. Yao, L. J. Ci, J. Q. Wei, *J. Mater. Chem. A* **2017**, 5, 8416.
- [134] J. W. Lee, S. H. Bae, Y. T. Hsieh, N. De Marco, M. K. Wang, P. Y. Sun, Y. Yang, *Chem* **2017**, 3, 290.
- [135] M. Hadadian, J. P. Correa-Baena, E. K. Goharshadi, A. Ummadisingu, J. Y. Seo, J. S. Luo, S. Gholipour, S. M. Zakeeruddin, M. Saliba, A. Abate, M. Gratzel, A. Hagfeldt, *Adv. Mater.* **2016**, 28, 8681.
- [136] H. Li, L. M. Tao, F. H. Huang, Q. Sun, X. J. Zhao, J. B. Han, Y. Shen, M. K. Wang, *ACS Appl. Mater. Interfaces* **2017**, 9, 38967.
- [137] C. B. Tian, E. Castro, G. Betancourt-Solis, Z. Nan, O. Fernandez-Delgado, S. Jankuru, L. Echegoyen, *New J. Chem.* **2018**, 42, 2896.
- [138] F. Zhang, D. Q. Bi, N. Pellet, C. X. Xiao, Z. Li, J. J. Berry, S. M. Zakeeruddin, K. Zhu, M. Gratzel, *Energy Environ. Sci.* **2018**, 11, 3480.
- [139] K. T. Cho, S. Paek, G. Grancini, C. Roldan-Carmona, P. Gao, Y. H. Lee, M. K. Nazeeruddin, *Energy Environ. Sci.* **2017**, 10, 621.
- [140] D. S. Yao, X. Mao, X. X. Wang, Y. Yang, M. T. Hoang, A. J. Du, E. R. Waclawik, G. J. Wilson, H. X. Wang, *J. Power Sources* **2020**, 463, 228210.
- [141] J. Zhuang, P. Mao, Y. G. Luan, X. H. Yi, Z. Y. Tu, Y. Y. Zhang, Y. P. Yi, Y. Z. Wei, N. L. Chen, T. Lin, F. Y. Wang, C. Li, J. Z. Wang, *ACS Energy Lett.* **2019**, 4, 2913.
- [142] J. Kim, Y. Lee, A. J. Yun, B. Gil, B. Park, *ACS Appl. Mater. Interfaces* **2019**, 11, 46818.
- [143] T. Zheng, L. S. Fan, H. Zhou, Y. Zhao, B. Jin, R. F. Peng, *ACS Appl. Mater. Interfaces* **2020**, 12, 24747.
- [144] Y. B. Li, J. K. Cooper, W. J. Liu, C. M. Sutter-Fella, M. Amani, J. W. Beeman, A. Javey, J. W. Ager, Y. Liu, F. M. Toma, I. D. Sharp, *Nat. Commun.* **2016**, 7, 12446.
- [145] W. G. Kong, T. Ding, G. Bi, H. Z. Wu, *Phys. Chem. Chem. Phys.* **2016**, 18, 12626.
- [146] H. Chen, T. Liu, P. Zhou, S. Li, J. Ren, H. C. He, J. S. Wang, N. Wang, S. J. Guo, *Adv. Mater.* **2020**, 32, 1905661.
- [147] M. A. Mahmud, T. Duong, Y. T. Yin, H. T. Pham, D. Walter, J. Peng, Y. L. Wu, L. Li, H. P. Shen, N. D. Wu, N. Mozaffari, G. Andersson, K. R. Catchpole, K. J. Weber, T. P. White, *Adv. Funct. Mater.* **2020**, 30, 1907962.
- [148] H. Back, G. Kim, J. Kim, J. Kong, T. K. Kim, H. Kang, H. Kim, J. Lee, S. Lee, K. Lee, *Energy Environ. Sci.* **2016**, 9, 1258.
- [149] S. K. Pathak, A. Abate, P. Ruckdeschel, B. Roose, K. C. Godel, Y. Vaynzof, A. Santhala, S. I. Watanabe, D. J. Hollman, N. Noel, A. Sepe, U. Wiesner, R. Friend, H. J. Snaith, U. Steiner, *Adv. Funct. Mater.* **2014**, 24, 6046.
- [150] H. R. Tan, A. Jain, O. Voznyy, X. Z. Lan, F. P. G. de Arquer, J. Z. Fan, R. Quintero-Bermudez, M. J. Yuan, B. Zhang, Y. C. Zhao, F. J. Fan, P. C. Li, L. N. Quan, Y. B. Zhao, Z. H. Lu, Z. Y. Yang, S. Hoogland, E. H. Sargent, *Science* **2017**, 355, 722.
- [151] E. D. Jung, A. K. Harit, D. H. Kim, C. H. Jang, J. H. Park, S. Cho, M. H. Song, H. Y. Woo, *Adv. Mater.* **2020**, 32, 2002333.
- [152] Z. Yu, L. C. Sun, *Adv. Energy Mater.* **2015**, 5, 1500213.
- [153] F. G. Zhang, X. C. Yang, M. Cheng, W. H. Wang, L. C. Sun, *Nano Energy* **2016**, 20, 108.
- [154] F. L. Cai, J. L. Cai, L. Y. Yang, W. Li, R. S. Gurney, H. N. Yi, A. Iraqi, D. Liu, T. Wang, *Nano Energy* **2018**, 45, 28.
- [155] H. H. Fang, F. Wang, S. Adjokatse, N. Zhao, M. A. Loi, *Adv. Funct. Mater.* **2016**, 26, 4653.
- [156] E. Mosconi, D. Meggiolaro, H. J. Snaith, S. D. Stranks, F. De Angelis, *Energy Environ. Sci.* **2016**, 9, 3180.
- [157] C. Liu, Z. Q. Huang, X. T. Hu, X. C. Meng, L. Q. Huang, J. Xiong, L. C. Tan, Y. W. Chen, *ACS Appl. Mater. Interfaces* **2018**, 10, 1909.
- [158] X. Li, D. Q. Bi, C. Y. Yi, J. D. Decoppet, J. S. Luo, S. M. Zakeeruddin, A. Hagfeldt, M. Gratzel, *Science* **2016**, 353, 58.
- [159] J. Li, R. H. Yang, L. C. Que, Y. F. Wang, F. Wang, J. Wu, S. B. Li, *J. Mater. Res.* **2019**, 34, 2416.
- [160] D. Shi, V. Adinolfi, R. Comin, M. J. Yuan, E. Alarousu, A. Buin, Y. Chen, S. Hoogland, A. Rothenberger, K. Katsiev, Y. Losovyj, X. Zhang, P. A. Dowben, O. F. Mohammed, E. H. Sargent, O. M. Bakr, *Science* **2015**, 347, 519.
- [161] I. C. Smith, E. T. Hoke, D. Solis-Ibarra, M. D. McGehee, H. I. Karunadasa, *Angew. Chem., Int. Ed.* **2014**, 53, 11232.
- [162] C. C. Stoumpos, D. H. Cao, D. J. Clark, J. Young, J. M. Rondinelli, J. I. Jang, J. T. Hupp, M. G. Kanatzidis, *Chem. Mater.* **2016**, 28, 2852.
- [163] Q. Jiang, Y. Zhao, X. W. Zhang, X. L. Yang, Y. Chen, Z. M. Chu, Q. F. Ye, X. X. Li, Z. G. Yin, J. B. You, *Nat. Photonics* **2019**, 13, 460.
- [164] Y. Lin, Y. Bai, Y. J. Fang, Z. L. Chen, S. Yang, X. P. Zheng, S. Tang, Y. Liu, J. J. Zhao, J. S. Huang, *J. Phys. Chem. Lett.* **2018**, 9, 654.
- [165] Z. P. Wang, Q. Q. Lin, F. P. Chmiel, N. Sakai, L. M. Herz, H. J. Snaith, *Nat. Energy* **2017**, 2, 17135.
- [166] T. M. Koh, V. Shanmugam, X. T. Guo, S. S. Lim, O. Filonik, E. M. Herzig, P. Muller-Buschbaum, V. Swamy, S. T. Chien, S. G. Mhaisalkar, N. Mathews, *J. Mater. Chem. A* **2018**, 6, 2122.
- [167] P. K. Kung, M. H. Li, P. Y. Lin, J. Y. Jhang, M. Pantaler, D. C. Lupascu, G. Grancini, P. Chen, *Sol. RRL* **2020**, 4, 1900306.
- [168] Z. W. Xiao, Z. N. Song, Y. F. Yan, *Adv. Mater.* **2019**, 31, 1803792.
- [169] H. Yin, Y. M. Xian, Y. L. Zhang, W. Z. Li, J. D. Fan, *Sol. RRL* **2019**, 3, 1900148.



- [170] F. X. Ji, J. Klarbring, F. Wang, W. H. Ning, L. Q. Wang, C. Y. Yin, J. S. M. Figueroa, C. K. Christensen, M. Etter, T. Ederth, L. C. Sun, S. I. Simak, I. A. Abrikosov, F. Gao, *Angew. Chem., Int. Ed.* **2020**, *59*, 15191.
- [171] S. Khalfin, Y. Bekenstein, *Nanoscale* **2019**, *11*, 8665.
- [172] E. Lopez-Fraguas, S. Masi, I. Mora-Sero, *ACS Appl. Energy Mater.* **2019**, *2*, 8381.
- [173] N. R. Xiao, Y. H. Tang, Y. L. Qiu, D. D. Liu, K. F. Wang, *Sol. Energy* **2020**, *204*, 429.
- [174] E. Greul, M. L. Petrus, A. Binek, P. Docampo, T. Bein, *J. Mater. Chem. A* **2017**, *5*, 19972.
- [175] N. Sakai, A. A. Haghighirad, M. R. Filip, P. K. Nayak, S. Nayak, A. Ramadan, Z. P. Wang, F. Giustino, H. J. Snaith, *J. Am. Chem. Soc.* **2017**, *139*, 6030.
- [176] C. Zhang, L. G. Gao, S. Teo, Z. L. Guo, Z. H. Xu, S. Zhao, T. L. Ma, *Sustainable Energy Fuels* **2018**, *2*, 2419.
- [177] J. C. Dahl, W. T. Osowiecki, Y. Cai, J. K. Swabeck, Y. Bekenstein, M. Asta, E. M. Chan, A. P. Alivisatos, *Chem. Mater.* **2019**, *31*, 3134.
- [178] M. Chen, M. G. Ju, A. D. Carl, Y. X. Zong, R. L. Grimm, J. J. Gu, X. C. Zeng, Y. Y. Zhou, N. P. Padtare, *Joule* **2018**, *2*, 558.
- [179] J. Euvrard, X. M. Wang, T. Y. Li, Y. F. Yan, D. B. Mitzi, *J. Mater. Chem. A* **2020**, *8*, 4049.
- [180] M. R. Filip, X. L. Liu, A. Miglio, G. Hautier, F. Giustino, *J. Phys. Chem. C* **2018**, *122*, 158.
- [181] Z. W. Xiao, W. W. Meng, J. B. Wang, Y. F. Yan, *ChemSusChem* **2016**, *9*, 2628.
- [182] J. Xu, J. B. Liu, B. X. Liu, B. Huang, *J. Phys. Chem. Lett.* **2017**, *8*, 4391.
- [183] G. Volonakis, A. A. Haghighirad, R. L. Milot, W. H. Sio, M. R. Filip, B. Wenger, M. B. Johnston, L. M. Herz, H. J. Snaith, F. Giustino, *J. Phys. Chem. Lett.* **2017**, *8*, 772.
- [184] J. J. Luo, X. M. Wang, S. R. Li, J. Liu, Y. M. Guo, G. D. Niu, L. Yao, Y. H. Fu, L. Gao, Q. S. Dong, C. Y. Zhao, M. Y. Leng, F. S. Ma, W. X. Liang, L. D. Wang, S. Y. Jin, J. B. Han, L. J. Zhang, J. Etheridge, J. B. Wang, Y. F. Yan, E. H. Sargent, J. Tang, *Nature* **2018**, *563*, 541.
- [185] J. Xu, J. B. Liu, B. X. Liu, J. F. Wang, B. Huang, *Adv. Funct. Mater.* **2019**, *29*, 1805870.
- [186] K. N. Nandha, A. Nag, *Chem. Commun.* **2018**, *54*, 5205.
- [187] N. Chen, T. Cai, W. H. Li, K. Hills-Kimball, H. J. Yang, M. D. Que, Y. Nagaoka, Z. Y. Liu, D. Yang, A. G. Dong, C. Y. Xu, R. Zia, O. Chen, *ACS Appl. Mater. Interfaces* **2019**, *11*, 16855.
- [188] H. D. Zhang, L. D. Zhu, J. Cheng, L. Chen, C. Q. Liu, S. L. Yuan, *Materials* **2019**, *12*, 1501.
- [189] T. T. Tran, J. R. Panella, J. R. Chamorro, J. R. Morey, T. M. McQueen, *Mater. Horizons* **2017**, *4*, 688.
- [190] A. H. Slavney, L. Leppert, D. Bartsaghi, A. Gold-Parker, M. F. Toney, T. J. Savenije, J. B. Neaton, H. I. Karunadasa, *J. Am. Chem. Soc.* **2017**, *139*, 5015.
- [191] A. Karmakar, M. S. Dodd, S. Agnihotri, E. Ravera, V. K. Michaelis, *Chem. Mater.* **2018**, *30*, 8280.
- [192] B. Yang, W. C. Pan, H. D. Wu, G. D. Niu, J. H. Yuan, K. H. Xue, L. X. Yin, X. Y. Du, X. S. Miao, X. Q. Yang, Q. G. Xie, J. Tang, *Nat. Commun.* **2019**, *10*, 1989.
- [193] W. Y. Gao, C. X. Ran, J. Xi, B. Jiao, W. W. Zhang, M. C. Wu, X. Hou, Z. X. Wu, *ChemPhysChem* **2018**, *19*, 1696.
- [194] X. Q. Yang, Y. H. Chen, P. Y. Liu, H. M. Xiang, W. Wang, R. Ran, W. Zhou, Z. P. Shao, *Adv. Funct. Mater.* **2020**, *30*, 2001557.
- [195] B. W. Park, B. Philippe, X. L. Zhang, H. Rensmo, G. Boschloo, E. M. J. Johansson, *Adv. Mater.* **2015**, *27*, 6806.
- [196] P. C. Harikesh, H. K. Mulmudi, B. Ghosh, T. W. Goh, Y. T. Teng, K. Thirumal, M. Lockrey, K. Weber, T. M. Koh, S. Z. Li, S. Mhaisalkar, N. Mathews, *Chem. Mater.* **2016**, *28*, 7496.
- [197] K. M. Boopathi, P. Karuppuswamy, A. Singh, C. Hanmandlu, L. Lin, S. A. Abbas, C. C. Chang, P. C. Wang, G. Li, C. W. Chu, *J. Mater. Chem. A* **2017**, *5*, 20843.
- [198] B. Ghosh, B. Wu, H. K. Mulmudi, C. Guet, K. Weber, T. C. Sum, S. Mhaisalkar, N. Mathews, *ACS Appl. Mater. Interfaces* **2018**, *10*, 35000.
- [199] B. Saparov, F. Hong, J. P. Sun, H. S. Duan, W. W. Meng, S. Cameron, I. G. Hill, Y. F. Yan, D. B. Mitzi, *Chem. Mater.* **2015**, *27*, 5622.
- [200] M. Y. Leng, Y. Yang, Z. W. Chen, W. R. Gao, J. Zhang, G. D. Niu, D. B. Li, H. S. Song, J. B. Zhang, S. Jin, J. Tang, *Nano Lett.* **2018**, *18*, 6076.
- [201] R. E. Brandt, J. R. Poindexter, P. Gorai, R. C. Kurchin, R. L. Z. Hoyer, L. Nienhaus, M. W. B. Wilson, J. A. Polizzotti, R. Sereika, R. Zaltauskas, L. C. Lee, J. L. MacManus-Driscoll, M. Bawendi, V. Stevanovic, T. Buonassisi, *Chem. Mater.* **2017**, *29*, 4667.
- [202] M. Abdi-Jalebi, Z. Andaji-Garmaroudi, S. Cacovich, C. Stavrakas, B. Philippe, J. M. Richter, M. Alsari, E. P. Booker, E. M. Hutter, A. J. Pearson, S. Lilliu, T. J. Savenije, H. Rensmo, G. Divitini, C. Ducati, R. H. Friend, S. D. Stranks, *Nature* **2018**, *555*, 497.
- [203] Y. Zhou, H. Zhong, J. H. Han, M. Q. Tai, X. W. Yin, M. H. Zhang, Z. Y. Wu, H. Lin, *J. Mater. Chem. A* **2019**, *7*, 26334.
- [204] S. M. Jain, Z. Qiu, L. Haggman, M. Mirmohades, M. B. Johansson, T. Edvinsson, G. Boschloo, *Energy Environ. Sci.* **2016**, *9*, 3770.
- [205] Y. Z. Lin, L. Shen, J. Dai, Y. H. Deng, Y. Wu, Y. Bai, X. P. Zheng, J. Y. Wang, Y. J. Fang, H. T. Wei, W. Ma, X. C. Zeng, X. W. Zhan, J. S. Huang, *Adv. Mater.* **2017**, *29*, 1604545.
- [206] K. Chen, J. N. Wu, Y. A. Wang, Q. Guo, Q. Y. Chen, T. T. Cao, X. Guo, Y. Zhou, N. Chen, M. J. Zhang, Y. F. Li, *J. Mater. Chem. A* **2019**, *7*, 21140.
- [207] M. Wang, H. X. Wang, W. Li, X. F. Hu, K. Sun, Z. G. Zang, *J. Mater. Chem. A* **2019**, *7*, 26421.
- [208] Z. W. Xiao, Y. Y. Zhou, H. Hosono, T. Kamiya, *Phys. Chem. Chem. Phys.* **2015**, *17*, 18900.



**Abhishek Maiti** is a graduate student (senior research fellow) under DST-INSPIRE Fellowship Scheme of DST, Government of India, in the School of Physical Sciences at Indian Association for the Cultivation of Science (IACS), Kolkata, India. In 2017, he received his M.Sc. in physics from Jadavpur University, Kolkata. His current research focuses on the understanding of band structures, defects, and localized carrier transport of halide perovskite thin films and nanostructures through scanning probe microscopy.



**Soumyo Chatterjee** is a postdoctoral fellow at Indian Association for the Cultivation of Science (IACS), Kolkata, India. He received his M.Sc and Ph.D. in physics in 2013 and 2019, respectively, from University of Calcutta, Kolkata. His research focuses on thin-film formation of inorganic semiconductors and hybrid halide perovskites, fabrication and characterization of optoelectronic devices, and nonvolatile resistive-switching memories.



**Lekha Peedikakkandy** received her Master's degree in chemistry from University of Calicut, Malappuram, India, and Ph.D. from Indian Institute of Technology. Bombay, India. She did this work during her stay at Indian Association for the Cultivation of Science (IACS), Kolkata, as a National Postdoctoral Fellow of SERB (SERB-NPDF). Her research interest includes optoelectronic materials, dye-sensitized solar cells, perovskite solar cells, and synthesis of nanomaterials.



**Amlan J. Pal** is a JC Bose National Fellow and Professor at the School of Physical Sciences, Indian Association for the Cultivation of Science (IACS), Kolkata, India. He received M.Sc. and Ph.D. in physics from University of Calcutta and Jadavpur University, respectively. His research interests include materials engineering, leading to organic electronics, solar cells based on organic and inorganic semiconductors, hybrid halide perovskites, 2D transitional metal dichalcogenides, scanning tunneling spectroscopy, organic spintronics, and so forth.

REPORT ON PROGRESS

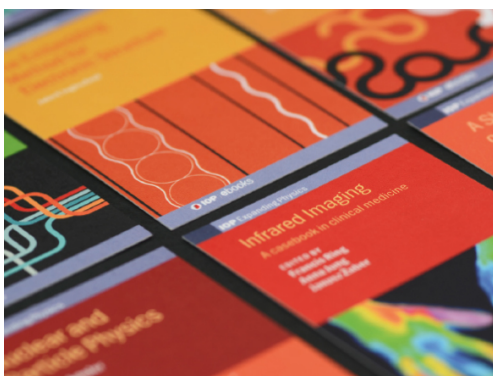
## Carrier recombination in $\text{CH}_3\text{NH}_3\text{PbI}_3$ : why is it a slow process?

To cite this article: Abhishek Maiti and Amlan J Pal 2022 *Rep. Prog. Phys.* **85** 024501

View the [article online](#) for updates and enhancements.

### You may also like

- [Modeling hybrid perovskites by molecular dynamics](#)  
Alessandro Mattoni, Alessio Filippetti and Claudia Caddeo
- [Operational stability of perovskite light emitting diodes](#)  
Qi Dong, Lei Lei, Juliana Mendes et al.
- [Surface morphological, optical and electrical characterization of methylammonium lead bromide perovskite \( \$\text{CH}\_3\text{NH}\_3\text{PbBr}\_3\$ \) thin film](#)  
Jyoti Chaudhary, Shaily Choudhary, Chandra Mohan Singh Negi et al.



**IOP | ebooks™**

Bringing together innovative digital publishing with leading authors from the global scientific community.

Start exploring the collection—download the first chapter of every title for free.

## Report on Progress

# Carrier recombination in $\text{CH}_3\text{NH}_3\text{PbI}_3$ : why is it a slow process?

Abhishek Maiti<sup>1</sup> and Amlan J Pal<sup>1,2,\*</sup> <sup>1</sup> School of Physical Sciences, Indian Association for the Cultivation of Science, Jadavpur, Kolkata 700032, India<sup>2</sup> UGC-DAE Consortium for Scientific Research, University Campus, Khandwa Road, Indore 452001, IndiaE-mail: [sspajp@iacs.res.in](mailto:sspajp@iacs.res.in)

Received 4 September 2021, revised 25 December 2021

Accepted for publication 17 January 2022

Published 17 February 2022

**Abstract**

In methylammonium lead iodide ( $\text{MAPbI}_3$ ), a slow recombination process of photogenerated carriers has often been considered to be the most intriguing property of the material resulting in high-efficiency perovskite solar cells. In spite of intense research over a decade or so, a complete understanding of carrier recombination dynamics in  $\text{MAPbI}_3$  has remained inconclusive. In this regard, several microscopic processes have been proposed so far in order to explain the slow recombination pathways (both radiative and non-radiative), such as the existence of shallow defects, a weak electron–phonon coupling, presence of ferroelectric domains, screening of band-edge charges through the formation of polarons, occurrence of the Rashba splitting in the band(s), and photon-recycling in the material. Based on the up-to-date findings, we have critically assessed each of these proposals/models to shed light on the origin of a slow recombination process in  $\text{MAPbI}_3$ . In this review, we have presented the interplay between the mechanisms and our views/perspectives in determining the likely processes, which may dictate the recombination dynamics in the material. We have also deliberated on their interdependences in decoupling contributions of different recombination processes.

Keywords: methylammonium lead iodide, slow recombination process, defect tolerance, ferroelectric domains, polaron formation, Rashba band splitting, photon recycling

(Some figures may appear in colour only in the online journal)

**Contents**

1. Introduction	2	3.1.2. A weak electron–phonon coupling: interaction of carriers with lattice	5
2. Unique structure of $\text{MAPbI}_3$ : role of the organic moiety in the slow recombination	3	3.2. Radiative recombinations	8
3. Different microscopic origins of slow recombination in $\text{MAPbI}_3$	4	3.2.1. Presence of ferroelectric domains	8
3.1. Non-radiative recombinations	4	3.2.2. Formation of polarons: screening of band-edge charges	9
3.1.1. Defect tolerance: presence of shallow defects	5	3.2.3. Rashba band splitting: spin-forbidden inter-domain transition	13
		3.2.4. Photon-recycling	14
		3.3. Auger recombination	15

\* Author to whom any correspondence should be addressed.  
Corresponding editor: Dr Horst-Guenter Rubahn.

4. Interplay between the propositions: a few open questions	15
5. Conclusions	17
Acknowledgments	18
References	18

## 1. Introduction

Since the successful use of methylammonium lead iodide ( $\text{CH}_3\text{NH}_3\text{PbI}_3$  aka MAPbI<sub>3</sub>) as absorber material in photovoltaic devices, a lot of research activities has been witnessed in the field of hybrid halide perovskite solar cells [1, 2]. Superior photovoltaic performance of the wonder material has been attributed to many unique properties of the perovskite, such as solution-processability [3, 4] structural stability [5], tunable bandgap [6, 7], a high extinction coefficient, a low exciton binding energy [8], high mobility [9], defect tolerance [10], and, most importantly, a low recombination loss of photogenerated carriers resulting in a long carrier lifetime and a large carrier diffusion length in the materials [11–17]. Due to a balanced combination of these material-properties, this compound has emerged as a viable alternative to silicon solar cells [2, 4]. During the last few years, the success of this perovskite material has triggered a lot of research to address the origin of these unique properties [2, 18]. Though, all of the above-mentioned properties have contributed toward the success of the absorber in achieving high-efficiency solar cells, one of the most unique properties of the compound is its very slow recombination process of photogenerated charge carriers [13, 16, 17]. It may be recalled that a slow recombination process in conventional semiconductors such as silicon and GaAs has led to an extended lifetime of photoexcited charge carriers and hence a superior power conversion efficiency in solar cells.

In general, recombination dynamics in a semiconductor material is governed by the following recombination rate equation:

$$-\frac{dn}{dt} = k_1n + k_2n^2 + k_3n^3, \quad (1)$$

where,  $k_1$ ,  $k_2$ , and  $k_3$  denote first, second, and third order rate-constants representing non-radiative trap-assisted recombination, radiative band-to-band recombination, and non-radiative Auger recombination, respectively [19, 20]. Here,  $n$  signifies the carrier density which generally decides the dominating term of equation (1). In view of this, carrier-lifetime is generally defined as a characteristic time-constant obtained from an exponential decay process which is actually the limiting term in equation (1). As an example, when the density of photogenerated carriers is small enough, the term  $k_1$  dominates and carrier-lifetime is designated as non-radiative [21]. However, in high-quality well-passivated films of MAPbI<sub>3</sub> that can be easily cast due to the current development of the field [22, 23], the recombination dynamics can rather be considered as a complex phenomenon governed by different events. The higher-order Auger recombination term can be neglected in MAPbI<sub>3</sub> for simplicity, because such a recombination is in

general observed in highly-doped compounds with a large carrier density ( $n > 10^{18} \text{ cm}^{-3}$ ) [20, 21, 24–26]. Such a higher value of  $n$  in MAPbI<sub>3</sub> is further restricted by the availability of solar irradiation on earth. The two recombination terms associated with  $k_1$  ( $n < 10^{15} \text{ cm}^{-3}$ ) and  $k_2$  ( $n > 10^{15} \text{ cm}^{-3}$ ) thus strongly influence the average lifetime (of photogenerated charge carriers) in MAPbI<sub>3</sub> [20, 27].

Before we proceed to deliberate on the slow recombination process in this unique material, it is imperative to state comparison with respect to that of a conventional inorganic semiconductor (silicon). In this regard, a comparison of an effective bulk lifetime as a function of excess carrier density can be considered to be a customary approach in observing a critical difference between the recombination processes in the two semiconductors (equation (1)) [20, 21, 28]. Such comparative studies reveal that the average lifetime in MAPbI<sub>3</sub> ( $\sim \mu\text{s}$ ) is comparatively lower than that in crystalline silicon ( $\sim \text{ms}$ ) at a typical carrier density of  $10^{15}$ – $10^{16} \text{ cm}^{-3}$  and at a particular surface velocity ( $S = 10 \text{ cm s}^{-1}$ ) [29]. However, the internal quantum efficiency in MAPbI<sub>3</sub> is still far higher (close to the radiative limit) than that in silicon solar cells at an identical condition. This mismatch appears primarily due to a direct nature of bandgap and the absence of higher-order Auger recombination term in the recombination dynamics of MAPbI<sub>3</sub>. In crystalline silicon, most of the losses appear due to the Auger effect; on the other hand, since MAPbI<sub>3</sub> does not suffer losses from Auger recombination, the recombination loss in MAPbI<sub>3</sub> thin-films can be considered to be slow (in comparison to silicon) in spite of possessing a comparatively faster bulk lifetime of photogenerated carriers with respect to the inorganic semiconductor [29, 30].

Also, recombination dynamics of a semiconductor compound possessing low mobility of charge carriers (as in MAPbI<sub>3</sub>) has often been explained in the framework of the Langevin model [20, 28]. Notwithstanding that the model is an idealistic concept and a difference in the experimental parameters may affect the calculated electron–hole recombination process, the recombination rate in MAPbI<sub>3</sub> was reported to be five orders of magnitude lower than the Langevin limit [12]. Such a non-Langevin nature of recombination in MAPbI<sub>3</sub> inspired us to search for an insight into the underlying recombination dynamics in the material. In addition, some of the transport parameters such as carrier mobility, lifetime, and diffusion length could be found to be self-inconsistent; such parameters have made the material more intriguing than ever. A remarkably long carrier lifetime ( $\tau \geq 1 \mu\text{s}$ ) and a large carrier diffusion length ( $L_D \geq 5 \mu\text{m}$ ) have been observed in polycrystalline thin-films of MAPbI<sub>3</sub> despite possessing moderate mobility ( $\mu \approx 1$ – $100 \text{ cm}^2 \text{ V}^{-1} \text{ s}^{-1}$ ), which is significantly lower than that of other conventional semiconductors, such as GaAs ( $\mu \approx 500 \text{ cm}^2 \text{ V}^{-1} \text{ s}^{-1}$ ). A high carrier lifetime and a long diffusion length in the materials are also intriguing considering omnipresent defects in its thin films, which were formed though a crude solution-cast method [9, 11, 12, 31]. It is sometimes argued that the cross-section of trapping and recombination are lower in this compound than those in other semiconductors for a given concentration of defects leading to a long carrier-lifetime in MAPbI<sub>3</sub> [30].



On the other hand, the rate of carrier scattering even in disordered films has been found to be negligible as observed from temperature-dependent studies of carrier mobility ( $\mu \propto T^{-3/2}$ ), terahertz (THz) spectroscopy, and microwave conductivity measurements [13, 28, 31, 32]. These results imply that photogenerated charge-carriers in MAPbI<sub>3</sub> are protected by some means from recombination and scattering with defects or longitudinal optical phonons leading to a remarkably long carrier-lifetime and diffusion-length as well [13, 20, 21, 33].

When we look back at the two recombination terms associated with MAPbI<sub>3</sub>, we find that several microscopic origins dealing with  $k_1$  and  $k_2$  have been proposed for the low recombination dynamics. The primary mechanisms are: (1) defect-tolerant nature of the material [10, 20, 34], (2) weak electron–phonon coupling [35–38], (3) presence of ferroelectric domains [39–41], (4) formation of polarons and screening of band-edge charges [13, 16], (5) Rashba splitting in both bands [17, 42–44], and (6) photon recycling [27, 45]. While some of the mechanisms apply to non-radiative recombinations, some are effective to radiation processes. After years of rigorous research, there still remained some inherent limitations and inconsistencies in these abovementioned models. A decoupling of their relative contributions is yet to be formulated for a complete understanding of the carrier recombination phenomenon.

In this focused review, we have summarized the major processes proposed for the radiative and non-radiative recombination pathways to date and critically assessed implications of each of the processes to further shed light on the origin of a low recombination loss in the compound. We have also described the interplay between these well-explored mechanisms to bring out mutual exclusiveness due to interdependencies. Such analysis would help the research community to identify the factor(s) which influence the recombination dynamics most. We have inferred that the slow recombination process is influenced more or less by different atomistic pathways based on different internal and external conditions, such as carrier density and temperature, respectively. Finally, we aim toward a better understanding of a high carrier lifetime and a long diffusion length in achieving a slow recombination process. Such an analysis would provide an outline in screening newer perovskite compounds toward their use as solar cells, both computationally and experimentally.

## 2. Unique structure of MAPbI<sub>3</sub>: role of the organic moiety in the slow recombination

In this section, we have discussed the possible roles of the organic moiety (CH<sub>3</sub>NH<sub>3</sub><sup>+</sup> or MA cation) behind the slow recombination dynamics in MAPbI<sub>3</sub> by revisiting the unique structure of the compound. Through intense research over a decade, it is now well-established that MAPbI<sub>3</sub> belongs to a series of ABX<sub>3</sub> perovskite structure where *A* is a monovalent methylammonium cation, *B* stands for a bivalent metal cation (Pb<sup>2+</sup>), and *X* represents a halogen (I<sup>-</sup>). The lead-site is six-fold coordinated by iodides to form the PbI<sub>6</sub> octahedra and finally a 3D corner-sharing network with MA<sup>+</sup> at the center [1, 2]. The hybrid crystal structure (figure 1) of the material

is quite unique and can be considered as two interpenetrating sub-lattices: the inorganic PbI<sub>6</sub> octahedra and the organic MA<sup>+</sup>. Now, since the valence band (VB) and conduction band (CB) are formed through an overlap of atomic orbitals [46] associated solely with the PbI<sub>6</sub> lattice [5], charge transport occurs primarily through the inorganic sub-lattice, while the organic (MA<sup>+</sup>) sub-lattice possessing a strong electric-dipole acts as a medium and thereby controls the electrostatic background experienced by the charge carriers [13].

With a few exceptions, most of the experimental studies confirm the superiority of organic–inorganic hybrid perovskites over all-inorganic ones in terms of efficient charge transport and efficiency [47, 48]. A longer carrier lifetime and carrier diffusion length have also been observed in hybrid halide systems as compared to the all-inorganic ones [49]. We have summarized such transport parameters for some typical perovskite systems in table 1 confirming that a combined dynamics of both inorganic and organic sub-lattices is important while explaining the slow recombination process of photogenerated carriers in hybrid-halide perovskite solar cells.

In this connection, it is customary to mention that MAPbI<sub>3</sub> holds three primary structural phases at three different temperature regions [5, 53–55]. The atomistic origin of carrier dynamics behind a low recombination loss can be strongly influenced by a temperature-dependent structural change arising out of these phase transitions. While proceeding toward a low temperature, the phases are termed as: (1) cubic *Pm-3m* phase above 330 K, (2) a body-centered tetragonal *I4/mcm* phase in between 330 and 160 K, and finally (3) an orthorhombic *Pnma* phase below 160 K [5, 53–55]. During the phase transitions, the dominant structural change is the rotation of the organic cation along with an influence on the dynamics of PbI<sub>6</sub> octahedra in terms of an order-disorder transition. The structural dynamics of the organic and inorganic sub-lattices are reported to be complementary to each other. At a low temperature, the rotation of the *A* cation is frozen while the PbI<sub>6</sub> octahedra continue to revolve. At higher temperatures, the situation becomes opposite with the rotation of *A* cation being activated keeping the PbI<sub>6</sub> octahedra rigid [5, 53–55]. Such a structural orientation of the compound in effect governs some of the aforementioned processes which will be discussed in a latter section.

While the actual role of the organic cation is yet to be fully understood, its presence in MAPbI<sub>3</sub> has been experimentally demonstrated to be crucial in explaining most of the proposed mechanisms of slow carrier-recombination. An impeded mono-molecular non-radiative recombination has been explained in terms of the soft nature of the compound which is associated with the organic cation [35, 36]. Similarly, a range of propositions explaining the bi-molecular radiative recombination have pointed toward the association of the organic moiety. First of all, as per the ferroelectric domain theory, alignment of the organic cation forms such domains which separate photogenerated electron–hole pairs and slow down the recombination process [39–41]. Polarons, as the second example, are inferred to have formed with the assistance of organic cations when they re-orient themselves to screen the carriers and protect them from scattering by defects (and

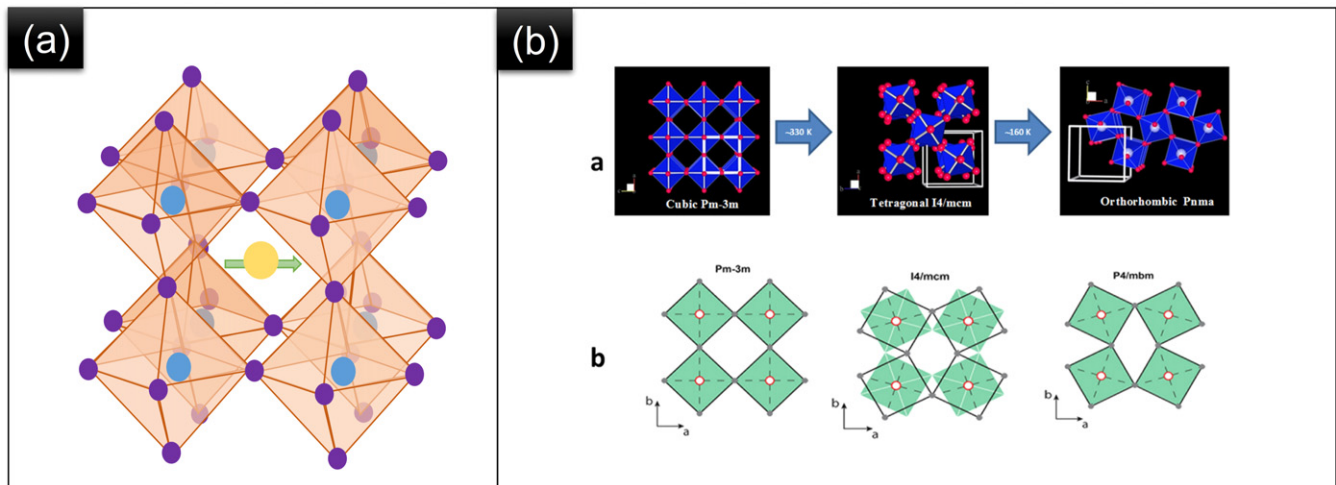


**Figure 1.** (a) Schematic representation of the MAPbI<sub>3</sub> structure. The purple, blue and yellow colors denote I, Pb, and MA moiety, respectively. The arrow points to the direction of the dipole moment of the organic cation. (b) Schematic illustration of the temperature-dependent structural phase transition in the compound at >330 K, in between 330 and 160 K, and below 160 K, respectively. Reprinted by permission from Springer Nature Customer Service Centre GmbH: Springer. Sci. Rep. [5] (c) 2016.

**Table 1.** Comparison of average lifetime and diffusion length of photogenerated carriers for different perovskite systems.

Compound	Average lifetime ( $\mu\text{s}$ )	Diffusion length ( $\mu\text{m}$ )	References
MAPbI <sub>3</sub>	5.0–15.0	10.0–40.0	[9, 11–14, 16, 31, 32, 50, 51]
FAPbI <sub>3</sub>	1.0–2.0	5.0–20.0	[16, 52]
CsPbI <sub>3</sub>	0.1–0.2	0.1–0.5	[15, 47–49]

thereby a longer lifetime) [13, 51]. Thirdly, in the conjecture of Rashba splitting, the necessary electric field responsible to break the centrosymmetry originates from the organic cation resulting in a splitting of both the bands having different spins and leading to an indirect bandgap and a long carrier lifetime [17, 42, 56]. The hypothesis of photon recycling is however independent of the choice of the A-site cation [27, 45].

### 3. Different microscopic origins of slow recombination in MAPbI<sub>3</sub>

As mentioned above, the unique recombination dynamics in MAPbI<sub>3</sub> does not appear due to any solitary process; it is rather a complex phenomenon with the involvement of different atomistic and microscopic incidents coupled with various radiative and non-radiative terms in the rate equation (equation (1)). In the following sections, we will discuss different mechanisms that would lead to a low recombination loss through radiative and non-radiative decay processes.

#### 3.1. Non-radiative recombinations

Ease of solution-processability has been considered to be the major rationale toward the success of halide perovskites as an absorber layer in solar cells [3, 4]. In such solution-processed film-formation techniques, especially in ‘soft’ materials (hardness <1 GPa) like MAPbI<sub>3</sub>, the presence of defects and imperfections should be ubiquitous as the periodic crystal lattice

would suffer disorders and have grain-boundaries as well during the growth process [57, 58]. These defects are well-known to form recombination centers responsible for non-radiative Shockley–Read–Hall (SRH) recombination pathways and significantly influence the total recombination dynamics. In this process, an electron (hole) can be trapped at the recombination center and attracted by a hole (electron) for recombination. The non-radiative process with the generation of phonons (instead of photons) would result in a significant heat loss [57, 59, 60]. Hence, a fast non-radiative recombination process would lead to a low open-circuit voltage ( $V_{\text{OC}}$ ) and a poor fill-factor (FF), which are not desirable in forming state-of-the-art thin-film solar cells [61]. Surprisingly, it has been found that non-radiative recombinations of electrons and holes in MAPbI<sub>3</sub> are *not* accelerated by point-defects omnipresent in the bulk of the compound [62]. Although non-radiative recombination in the bulk of MAPbI<sub>3</sub> may amount to 90% of the total loss, a long non-radiative lifetime ( $\mu\text{s}$ ) can still be achievable due to a very slow non-radiative recombination process in the compound. In comparison, high-quality GaAs, which yields a PLQY as high as 96%, exhibits a fast non-radiative lifetime (ns). Here PLQY represents photoluminescence quantum yield. This qualitative comparison shows that trap-assisted recombination in MAPbI<sub>3</sub> is characteristically a slow process. The splitting of quasi-Fermi level in MAPbI<sub>3</sub> is hence closest to the thermodynamic limit; the  $V_{\text{OC}}$  could hence reach the theoretical-limit possible in the compound [63].

Till now, two different microscopic processes have been envisaged behind the long non-radiative lifetime in MAPbI<sub>3</sub>:

(i) defect tolerant nature of the material and (ii) a weak electron–phonon coupling [37, 62, 64]. In the following, we have made a detailed discussion on these two processes.

**3.1.1. Defect tolerance: presence of shallow defects.** Among all the proposed models of impeded SRH non-radiative recombination processes, the initial and well-accepted one is the defect tolerant nature of the compound [10, 46, 65]. It is believed that due to their shallow nature, defect-states are benign in MAPbI<sub>3</sub> as compared to other inorganic materials resulting in a longer non-radiative lifetime as obtained from decay dynamics of photoluminescence (PL) spectroscopy [21, 29, 30]. According to first-principle density functional theory (DFT) calculations, intrinsic point-defects are less likely to form within the bandgap; they are rather estimated to be located near the band-edges due to their shallow nature which may be considered as the origin of defect-tolerance in this compound [34, 46]. Experimentally, it has been shown through scanning tunneling spectroscopy (STS) that although MAPbI<sub>3</sub> is prone to possess a large density of point-defects, such as metal-vacancies and iodine-vacancies (depending on the stoichiometry of the precursors or the growth condition), the defects have no impact to the electronic bandgap and thereby other functional properties of the material [65].

In order to understand the defect-tolerant nature of the compound, it is essential to know the details of band-formation in the material. The VB and CB in MAPbI<sub>3</sub> are formed with two pairs of overlapping molecular orbitals: while the VB is formed with Pb-6s and I-5p antibonding orbitals, the CB is composed of Pb-6p and I-5p bonding orbitals [46, 65]. In this scaffold, 5p-orbitals of iodide will be held loosely bound to the nucleus due to a weak electronegative nature; a weaker interaction is therefore expected with the metal p orbitals. Hence, due to a strong interaction between orbitals of the two building-block elements, I and Pb, the anti-bonding orbital (CB-edge) will be stabilized and the bonding one (VB-edge) will be destabilized. As a result, the vacancies developed in the perovskite would form shallow levels near the band-edges with a significantly less tendency to be formed within the bandgap [65]. These shallow defects are hence not capable to trap charge carriers effectively. Unlike deep-level defects, which as such promote non-radiative recombination sites for charge carriers, the shallow defects in MAPbI<sub>3</sub> can be considered ‘inert’ offering a little adverse impact on the carrier diffusion length and lifetime. However, it should be remembered that such an assumption is only valid for point-defects presented in the bulk of the perovskite. DFT calculations considering different surface terminations have recently revealed the presence of deep-level iodine-interstitials at the surface of the perovskite [66].

In a recent study, Chu *et al* explored the breakdown of SRH theory of non-radiative recombination through *ab initio* non-adiabatic molecular dynamics calculations due to the defect-tolerant nature of the compound [62]. The overall non-radiative recombination pathways are a combination of the two processes as shown in figure 2(a) where a photogenerated hole (electron) trapped by defects can either relax back to the VB (CB) as soon as the thermal fluctuation overcomes the

energy barrier or recombine with an electron (hole) through hopping to CB (VB). However, in MAPbI<sub>3</sub> they did not find a significant change in non-radiative recombination rate even after considering different defect-mediated recombination pathways when compared to the defect-free pristine compound (figures 2(b)–(d)). They envisioned that due to the soft nature of the compound, photogenerated carriers can couple with low-frequency phonons which would appreciably reduce the non-adiabatic coupling further. They also argued that such a soft nature of the inorganic sub-lattice is crucial for the aforementioned defect-tolerant nature of the compound [62]. Such a deviation of SRH recombination is also evidenced in the case of all-inorganic perovskites (CsPbI<sub>3</sub>) where the point defects are not so harmful [67]. Hence, these findings strongly support the theory of a slow dissipation to heat energy due to a defect tolerant nature of the compound resulting in a low recombination loss of photogenerated carriers [62, 67]. However, as a critical evaluation of these results, we find an unusual consideration of bi-molecular non-radiative recombination in first principle calculations (because an electron and a hole are assumed to be sitting in very close proximity). The feasibility of such a process in reality (1 Sun) however remains under strong speculation.

In spite of explaining a high non-radiative lifetime ( $\tau \sim 1 \mu\text{s}$ ), the theory of defect tolerance contains a few inconsistencies as well. This conjecture fails to explain a comparatively high recombination rate in all-inorganic CsPbI<sub>3</sub> and also in FAPbI<sub>3</sub> where the lifetime of photogenerated carriers is comparably reduced in spite of being defect-tolerant [15, 47–49]. Moreover, measurement of non-radiative carrier lifetime through space-charge limited current analysis, deep level transient spectroscopy, and thermal admittance spectroscopy may have some limitations, since the phenomenon of ion-migration can strongly influence the lifetime calculation [10, 21, 34, 46]. In addition, the recently-exhibited tail-states of these shallow defects can excite multiple trapping and de-trapping sites which can further control the recombination dynamics as well [68]. The over-simplicity of this concept ignoring the presence of surface-defects are considered to be responsible for its failure in explaining such a complex phenomenon [69]. In addition, the chemical and physical nature of the defect-states, both at the bulk and at the surface, and also the static- and dynamic defects are yet to be explored to gain more in-depth insights.

**3.1.2. A weak electron–phonon coupling: interaction of carriers with lattice.** Charge-carrier dynamics are also affected by lattice vibrations and the resultant electron–phonon coupling in MAPbI<sub>3</sub> due to a comparatively soft nature of the material [13, 33, 35, 38, 70]. In addition, temperature-dependent mobility studies also support a strong dependence of carrier transport on the quanta of lattice vibration, that is phonons [32]. The electron–phonon coupling or interaction of electrons (holes) with crystal lattice has been explained in the literature by two models: acoustic phonons and optical phonons. The interaction between charge carriers and acoustic phonons has been elucidated by a deformation-potential scattering model, where, due



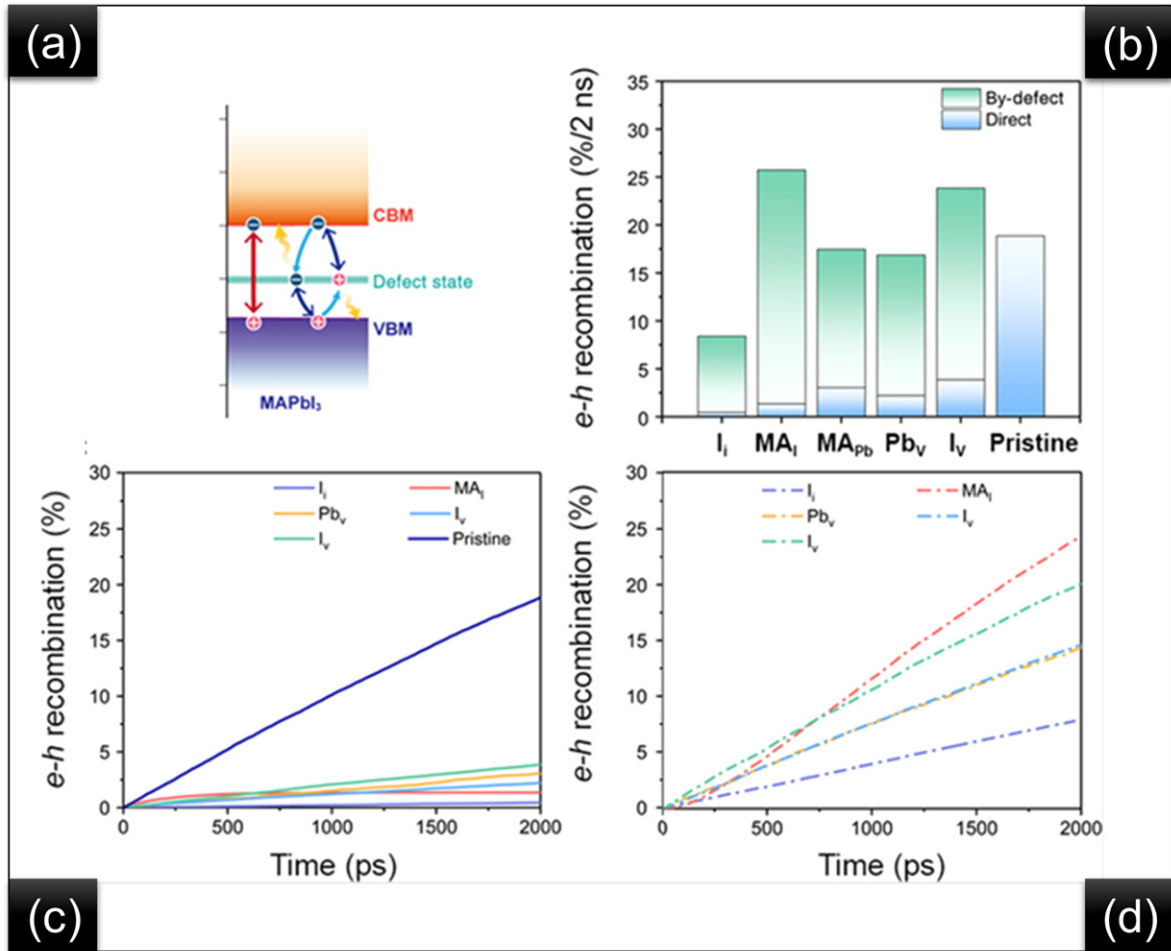


**Figure 2.** (a) Schematic representation of the trap-assisted non-radiative recombination process. (b) Comparison of electron–hole recombination rate for different ‘defective’ perovskites as compared to the pristine. (c) and (d) Time-dependent electron–hole (e–h) recombination rate for different defect pathways; the direct and by-defect e–h recombined percentage are shown in (c) and (d), respectively. From [62]. Reprinted with permission from AAAS.

to lattice vibrations, the atoms are displaced from their equilibrium position resulting in a structural distortion and thereby a change in the band structure [38, 71]. On the other hand, optical phonons produce an electric field and hence a polarization in the lattice to couple the charge carriers as governed by a Frölich-type interaction [28, 72]. It has been found that while acoustic phonons may affect charge transports primarily at low temperatures, optical phonons (longitudinal) mostly influence the overall charge carrier recombination dynamics in MAPbI<sub>3</sub> [20, 32, 33]. Many-body theoretical simulations have revealed that three low-frequency phonon modes, namely, Pb–I–Pb bending, MA-cation displacement, and Pb–I stretching modes are in particular responsible for the (slow) non-radiative recombination process in MAPbI<sub>3</sub> (figure 3(a)) [73]. Low energy of the phonon modes significantly balances the energy loss through multi-phonon emissions slowing down the recombination process. An in-depth understanding of the phenomenon has been demonstrated by Kirchartz *et al* by consid-

ering the non-radiative recombination as a transition of electrons in the CB to a trap-state inside the bandgap (figure 3(b)). The parabolas correspond to two vibrational energy eigen-surfaces where a transition between these two states signifies an overlap between the wave functions of the two parabolas. Generally, such an overlap of wave-functions governs the rate of transition and can be quantified by the Huang–Rhys factor which is inversely proportional to the energy of the phonon modes [37]. As described earlier, since the primary phonon modes in MAPbI<sub>3</sub> possess low energy eigenvalues, the Huang–Rhys factor will be high and the probability of transition between the parabolas will decrease accordingly lowering the non-radiative recombination process in the compound. This classic textbook concept has also been experimentally verified by Kirchartz *et al* (figure 3(c)) [37]; the Huang–Rhys factor was found to decrease with higher phonon energies. Such an observation strongly infers that due to the presence of low-energy phonon modes, the Huang–Rhys factor would

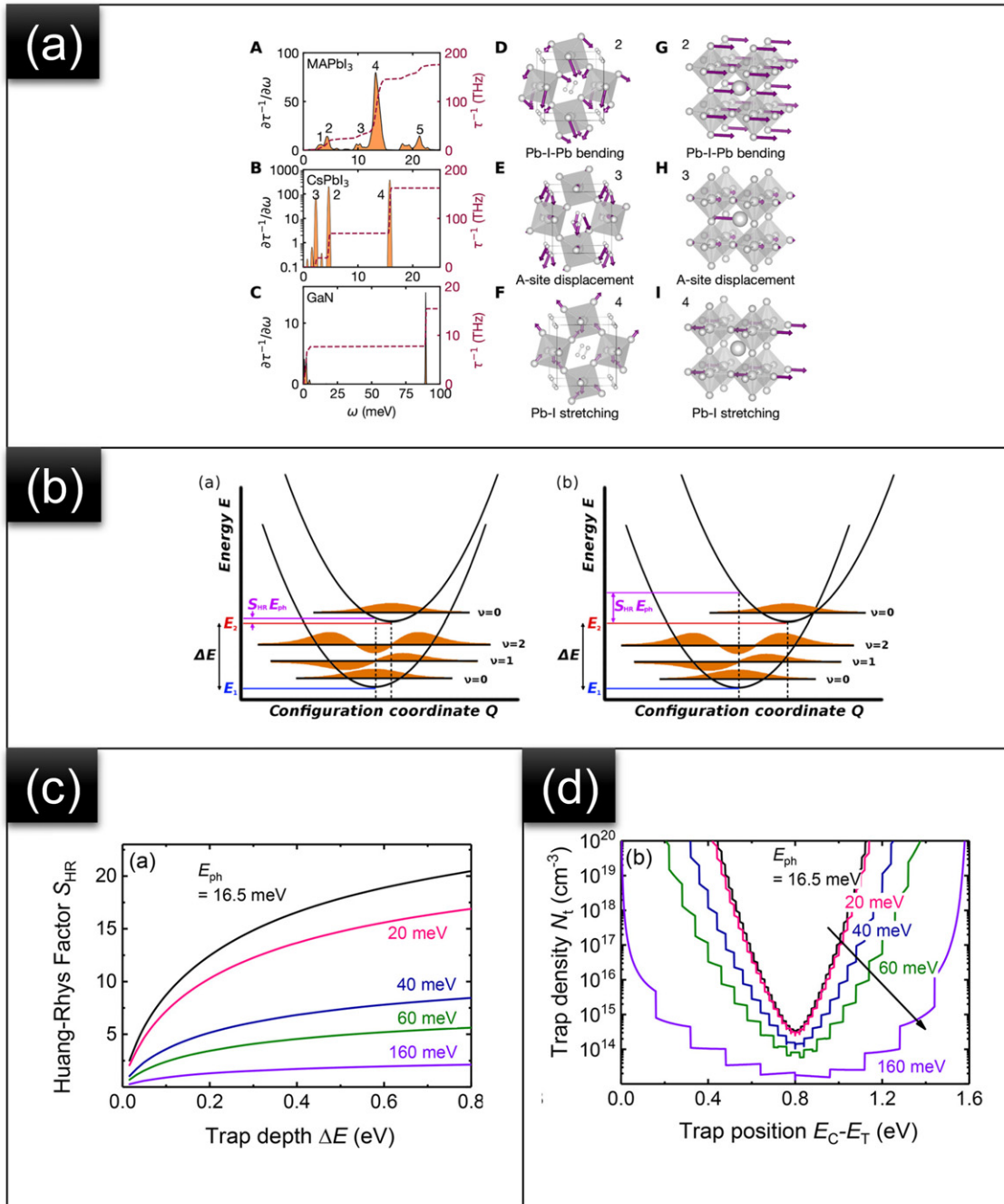


**Figure 3.** (a) Different low energy phonon modes in MAPbI<sub>3</sub> and their contribution toward carrier dynamics through spectral decomposition. A comparison of these phonon modes with other conventional semiconductors is also shown. Reprinted with permission from [73]. Copyright (2019) American Chemical Society. (b) A schematic representation of two configurations with a small and a large Huang–Rhys factor,  $S_{HR}$ . The energy eigenvalues of the two vibrational eigenstates are presented as  $E_1$  and  $E_2$  respectively.  $E_{ph}$  represents the energy of emitted optical phonon modes and  $\nu$  is the vibrational quantum number. (c) Variation of the Huang Rhys factor as a function of trap depth for different phonon energies. (d) Trap density versus trap position as a function of different phonon energies. (b)–(d) Reprinted with permission from [37]. Copyright (2018) American Chemical Society.

possess a high value. As a result, the non-radiative recombination process in MAPbI<sub>3</sub> would further be slowed down. It has also been shown that the presence of low energy phonon modes would lead to a shift of defect-states toward the band-edges (figure 3(d)) and hence result in a further slowing down of the recombination process.

Although, a non-radiative lifetime in the bulk of MAPbI<sub>3</sub> is appeared to be high, it is sometimes argued that ‘deactivation’ of non-radiative defect channels is not an intrinsic property of the perovskite. Non-radiative defect states are as such inevitable in metal halide perovskites in inducing a fast trapping process; however, due to advancements in the film-

formation process, a variety of defect passivation strategies reduced the density of defect states in the compounds leading to a high PLQY at a moderate excitation density [22, 23]. In other words, the ‘deactivation’ of non-radiative defect channels is not a self-occurring process.

Although, the non-radiative recombination loss in the bulk of MAPbI<sub>3</sub> is appeared to be minimum, it is still inevitable in solar cell architectures, that is, at the interfaces of an absorber and charge transport layers, due to physiochemical-interaction-induced structural faults and distortions [66]. We may hence conclude that defect engineering, surface passivation, proper alignment of energy levels, and tuning the splitting of the quasi-Fermi levels at the junctions are some of the vital routes to further minimize the non-radiative recombination at the interfaces between MAPbI<sub>3</sub> and electron/hole transport layers [58, 74].

### 3.2. Radiative recombinations

Carrier-lifetime in MAPbI<sub>3</sub> is also governed by radiative band-to-band recombination processes in the van Roosbroeck–Shockley framework [20, 21]. In this section, different propositions in the framework of radiative recombination, such as (i) presence of ferroelectric domains [39–41], (ii) formation of polarons and thereby screening of band-edge charges [13, 16], (iii) Rashba splitting in both bands [17, 42–44], and (iv) photon recycling [27, 45] have been discussed that may contribute to the radiative rate constant  $k_2$  in MAPbI<sub>3</sub> and slow down the overall recombination process.

**3.2.1. Presence of ferroelectric domains.** Slow radiative recombination in MAPbI<sub>3</sub> can be explained by considering the presence of ferroelectric domains in the material. As stated earlier, MAPbI<sub>3</sub> at room temperature retains a tetragonal phase with  $I4/mcm$  space group which is likely to possess a ferroelectric nature due to the presence of polarizable organic cation MA<sup>+</sup> [5, 41, 75]. The existence of ferroelectric domains was first predicted by Kanatzidis and co-workers in their pioneering work [76]. They observed an anomalous hysteresis behavior in the current–voltage ( $I$ – $V$ ) characteristics of MAPbI<sub>3</sub> single crystals through a conventional four-probe method. Although this behavior was explained by considering the presence of ferroelectric domains in the material, a more direct and perceiving evidence of such nanoscale domains was provided by Kutes *et al* through piezo force microscopy (PFM) (figures 4(a) and (b)) to ‘see’ the ferroelectric domains locally and to probe their responses as well [75].

In the scheme of PFM, an AC-electric field was applied to the conducting tip in contact with the surface of a MAPbI<sub>3</sub> thin film. Since, ferroelectric compounds are also piezoelectric in nature, the local region of the film having contact with the conducting probe would also yield mechanical vibrations which could be detected simultaneously during the scanning; the phase difference between the AC-signal and piezo actuation was used to investigate the orientations of ferroelectric domains and the position of the domain walls was revealed from the amplitude [75].

The origin of ferroelectricity in MAPbI<sub>3</sub> has been explained by considering the existence of spontaneous electric polarization which originates from a continuous breaking of the crystal centrosymmetry in absence of an inversion center. Figures 4(c) and (d) schematically illustrate the possible schematic orientations of the molecular dipoles, in which the existence of MA<sup>+</sup> with a molecular dipole moment of 2.3 D at the center of the perovskite cage also introduces the possibility of orientational disorder and polarization [39].

In this framework, such a strong lattice polarization can expand the photogenerated carrier separation and thereby enhancing the carrier lifetime and diffusion length. The mechanism of carrier separation in the ferroelectric domain framework has been schematically presented in figure 5(a); the scenario, which is analogous to conventional  $p$ – $n$  junctions, has been proposed by Frost *et al* [39]. In a photovoltaic device based on conventional semiconductors, charge carriers are generally separated by an electric field of a  $p$ – $n$  junction. Similarly, in the concept of the ferroelectric domain, the built-in electric field of ferroelectric domains is responsible for the separation of photogenerated charge carriers. The probability of carrier recombination depends on the size of ferroelectric domains. Although the typical size of such domains is in the nanometer scales, the probability of recombination during diffusion to the electrodes is reduced since the separated carriers in the ferroelectric compound can now easily diffuse through domain boundaries; this is in contrast to the charge transports upon separation of carriers in conventional heterojunctions. A ‘build-up’ of charge carriers of a particular type was suggested along with peaks and troughs in the electric potential originated from the local dipole-ordering [39]. In this manner, a ‘ferroelectric highway’ was hypothesized along which a particular carrier (electron/hole) can diffuse toward the respective electrodes, unhindered by carriers of opposite charge (hole/electron) and leading to a low recombination loss.

In this regard, the role of domain walls acting as ‘segregated channels’ for unimpeded motions of charge carriers was demonstrated by Liu *et al* [41]. They proposed charged domain-walls (CDWs) and uncharged domain-walls (UCDWs) in between two ferroelectric domains. The role of CDWs is much more significant as electrons favor to diffuse through head-to-head CDWs while holes prefer to travel through tail-to-tail CDWs. Hence, under the influence of an electric field, electrons and holes are expected to move through different CDWs reducing the possibility of recombination. Role of UCDWs is however different in recombination dynamics. Such domain walls act as dipole layers and provide significant potential steps augmenting carrier separation and thereby increasing carrier diffusion length in hybrid halide perovskites (figure 5(b)).

Despite the success of the concept of ferroelectric domains while explaining slow recombination in MAPbI<sub>3</sub>, certain inherent discrepancies have remained in the mechanism. Chen *et al* ruled out the existence of these domains at higher temperatures [16]. First-principle calculations suggest that the alignment of MA<sup>+</sup> dipole strongly depends on temperature. While a low temperature favors a complete alignment of the dipoles and the formation of large ferroelectric domains, an



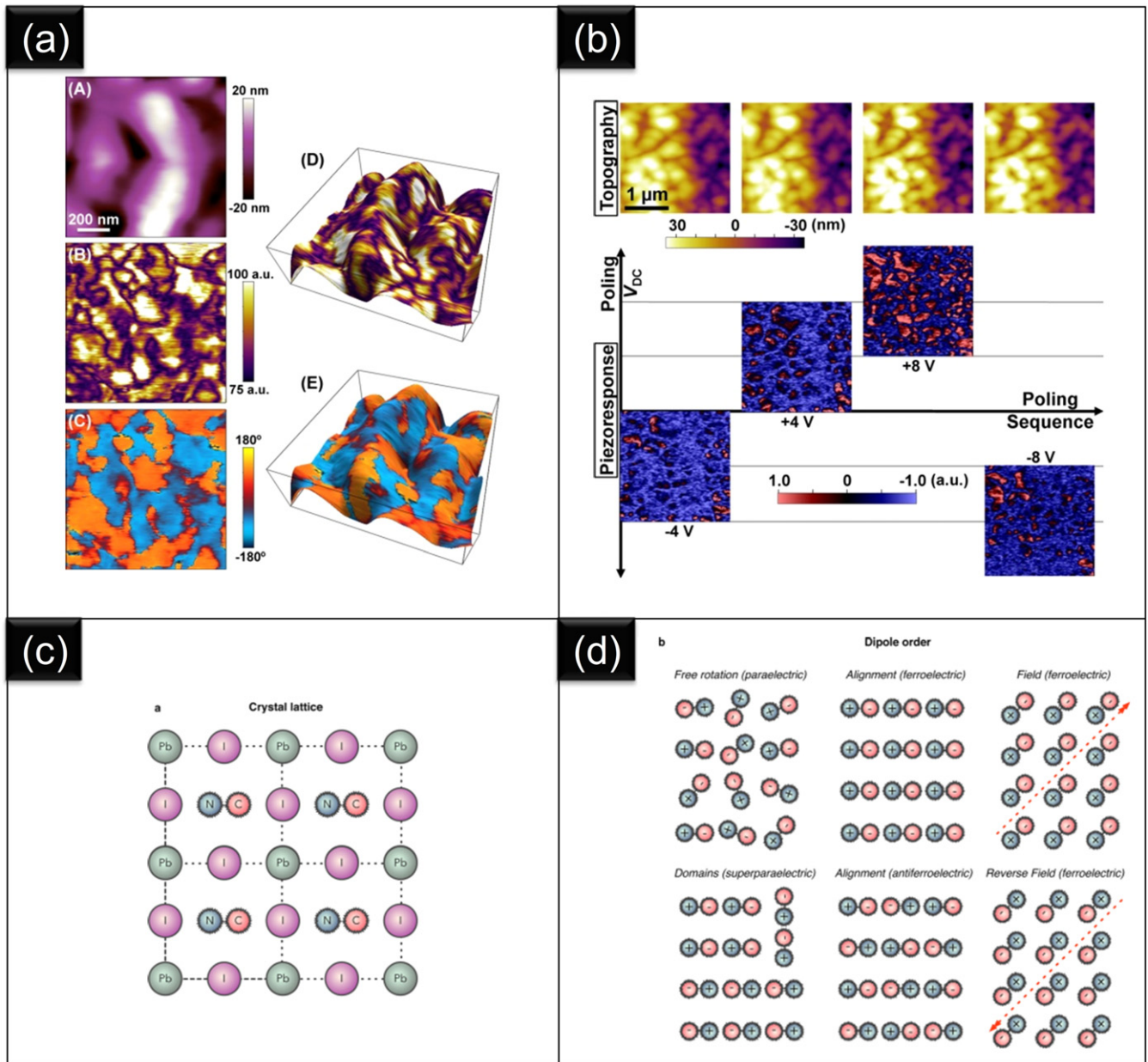


**Figure 4.** (a) AFM and PFM images of the MAPbI<sub>3</sub> thin-films with AFM topography, PFM amplitude, PFM phase, superimposed topography amplitude, and phase. (b) Four AFM topography images (top row) of a single  $2.5 \times 2.5 \mu\text{m}^2$  area, with simultaneously acquired corresponding PFM images beneath mapping the piezoresponse, each after scanned DC poling at the biases indicated evincing partial, reversible ferroelectric domain switching. (a) and (b) Reprinted with permission from [75]. Copyright (2014) American Chemical Society. (c) A schematic 2D-view of the MAPbI<sub>3</sub> crystal structures and (d) the possible orientations of molecular dipoles within the lattice responsible to different ordering. (c) and (d) Reprinted with permission from [39]. Copyright (2014) American Chemical Society.

increase in temperature leads to disordered dipoles and eventually small domains (figures 5(c)–(f)) [40]. As a consequence, ferroelectric domains are expected to disappear at high temperatures enabling faster recombination of photogenerated carriers. However, experimental observations showed rather an opposite effect: an increase in carrier lifetime with increasing temperature [16, 32, 51, 77]. Hence, in the light of temperature-dependent results, the theory of ferroelectric domain formation in MAPbI<sub>3</sub> fails to explain the slow radiative recombination of photogenerated carriers at higher temperatures.

**3.2.2. Formation of polarons: screening of band-edge charges.** The puzzle of slow radiative band-to-band recombination in MAPbI<sub>3</sub> was aimed to solve by considering the conjecture of polaron formation and screening of charges [13, 16]. Polarons are quasi-particles that describe the interaction between electrons (holes) and lattice. In general, when electrons (holes) move in a lattice, they can be trapped within the potential-well appearing due to displacement of neighboring atoms. A combination of a self-trapped electron (hole) and the ‘pattern of atomic displacement’ is considered as a polaron, which can move from one place to another

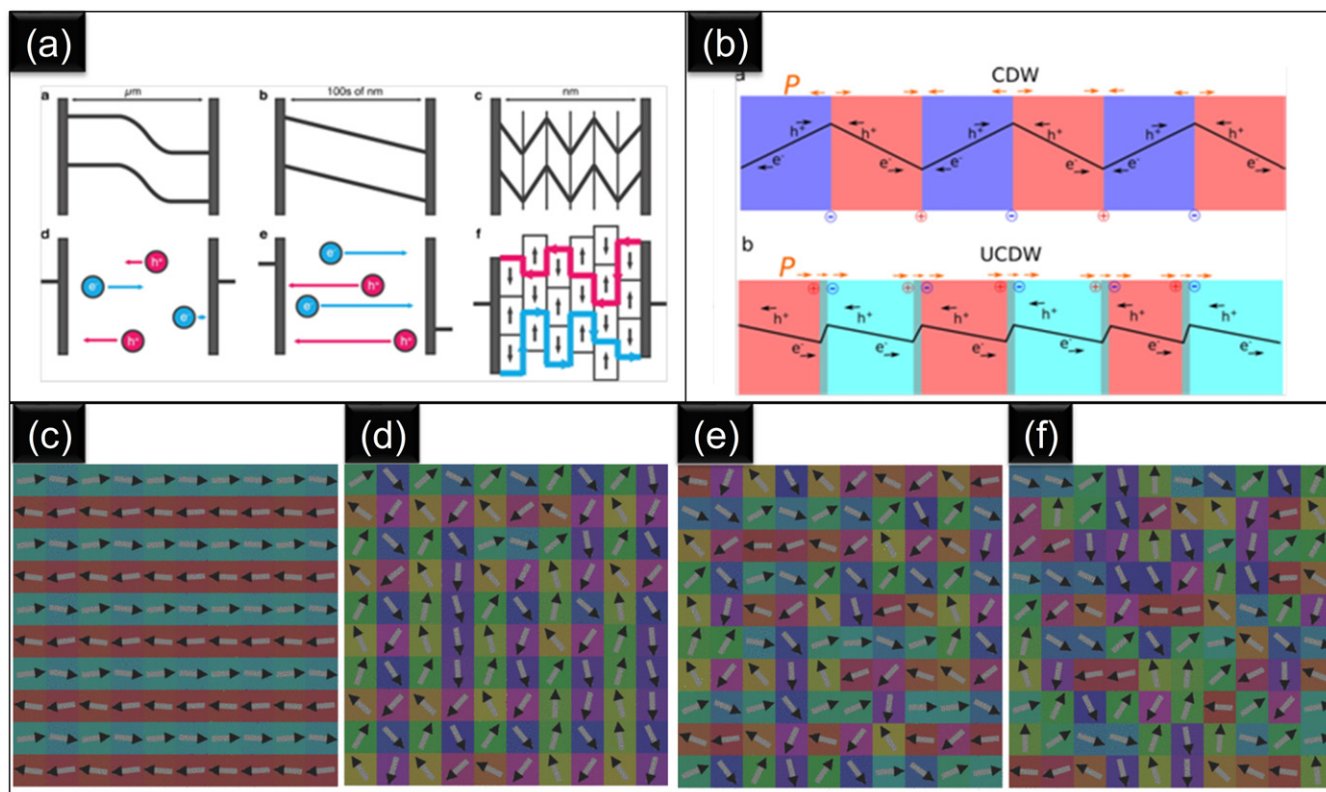


**Figure 5.** (a) A schematic illustration of a built-in potential in a  $p$ - $n$  junction, single, and multi-domain ferroelectric film, along with the electron and hole separation pathways respectively. Reprinted with permission from [39]. Copyright (2014) American Chemical Society. (b) A schematic representation of the electrostatic potential step where electron and hole separate in the periodic array of CDWs and UCDWs. Reprinted with permission from [41]. Copyright (2015) American Chemical Society. (c)–(f) Methylammonium dipole alignment as a function of temperature. Low-temperature results in complete alignment and large domains, while disorder with increasing temperature leading to small domains, eventually results in completely disordered dipoles in the high-temperature limit ((c): 0 K, (d): 100 K, (e): 300 K, and (f): 1000 K). Reproduced from [40]. CC BY 4.0.

through lattice distortion [13, 33]. In particular, polarons are usually observed in various polar solids such as metal oxides, ionic crystals, and ferroelectric materials [21, 33]. The formation of polarons in  $\text{MAPbI}_3$  has been reported by Park *et al* in their pioneering work through a combination of transient absorption spectroscopy, time-domain Raman spectroscopy, and DFT studies [78]. Furthermore, a series of first-principle calculations also supported the existence of polarons in  $\text{MAPbI}_3$  [13, 33, 79].

Polarons are generally classified into two categories based on the nature of their spatial distribution [33, 79–81]. When the charge carriers are localized over multiple number of lattice sites, it is portrayed as a large polaron; on the other hand, if it is localized over a limited number of lattice sites or a few bond-lengths, the notion of small polaron is generally considered [82]. The basic nature of polaronic transport through a crystal lattice is different in the two cases. According to the Boltzmann transport model, the motion of large polarons is described as coherent transport along with high mobility, large momentum, and minimum scattering as a consequence of their large effective mass [79, 80]. Small polarons, on the other hand, are associated with incoherent transport with a large of scattering cross-section [13, 33]. The polaron physics in  $\text{MAPbI}_3$  has revealed that only large polarons are responsible

for a slow electron–hole recombination process by reducing the bimolecular rate constant  $k_2$  [13, 33]. Small polarons do not play any role in this regard; its presence is rather hypothesized to be detrimental for efficient charge extraction [83].

Recent studies propose that the formation of large polarons may also be governed by dynamically-disordered MA dipoles. As stated earlier, MA moieties in hybrid perovskites can be easily rotated and aligned locally; the dipole moment hence generates an irregular local potential landscape at the nanoscale [13, 33, 51, 79]. According to a pioneering work of Chen *et al*, movement of charge carriers through the perovskite lattice can induce re-ordering of the MA dipoles and hence a local orientational rearrangement (figure 6(a)) leading to the formation of large dipolar polarons [51]. Under the state of affairs, electrons (holes) reside in the inorganic  $\text{PbI}_6$  sub-lattice while a polarization cloud rests in the organic MA sub-lattice. A combined motion of MA cations has been predicted to screen the Coulomb potential of an electron–hole and to promote charge carrier separation. Hence, a ‘recombination’ effectively denotes recombination of two oppositely charged polarons; the enhanced effective mass of large polarons along with a small recombination cross-section in effect provides a protective shield against both recombination and scattering with phonons and hence results in slow recombination [51].

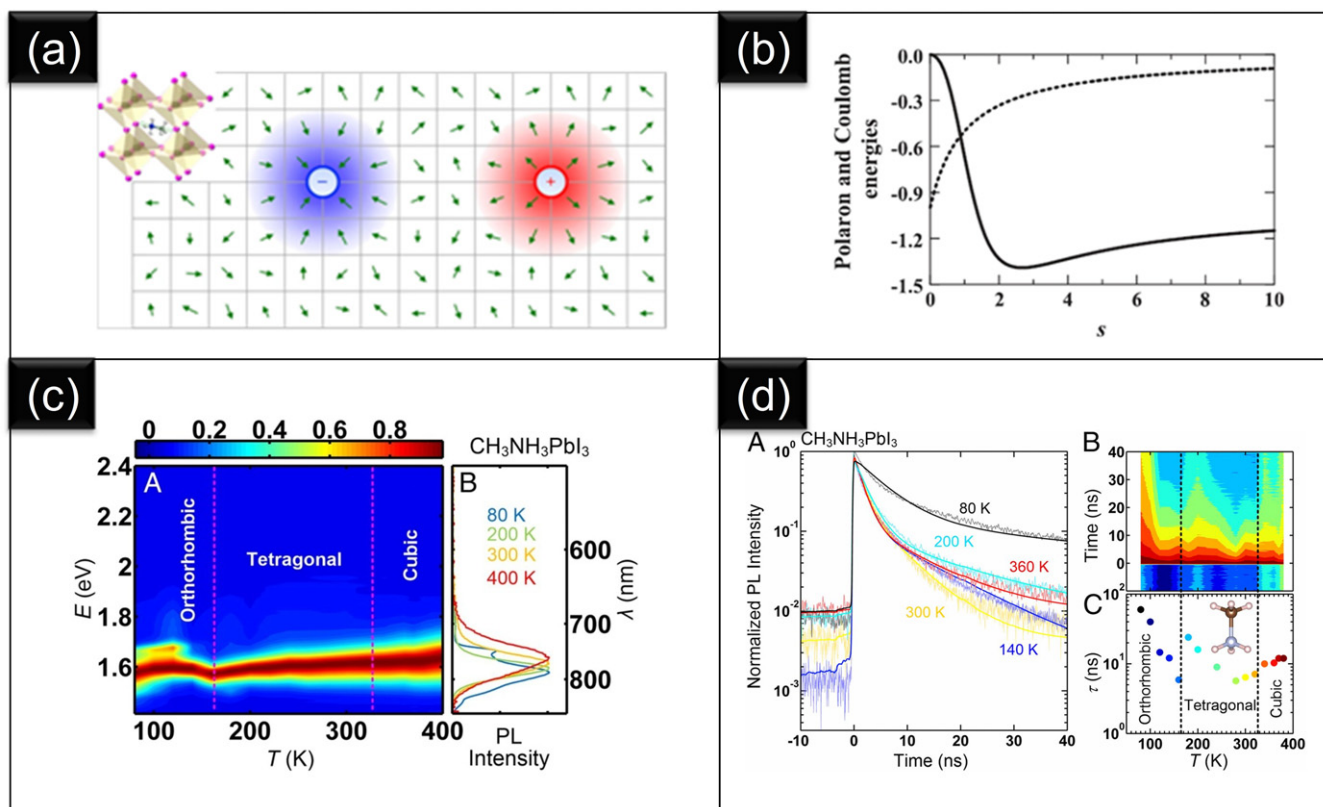


**Figure 6.** (a) Formation of dipolar polarons in MAPbI<sub>3</sub>. Charge carriers can induce rotational reorganization of the surrounding CH<sub>3</sub>NH<sub>3</sub> dipoles (green arrows) leading to the formation of dipolar polarons. Reproduced from [51]. CC BY 4.0. (b) Antagonism between long-range Coulomb interaction and a short-range repulsive force as a function of inter-polaron separation. Reprinted from [84], with the permission of AIP Publishing. (c) Time-averaged PL spectra of MAPbI<sub>3</sub> with a color contour map of the data and the PL data in 1D plot at four different temperatures: 80, 200, 300, and 400 K. (d) TRPL spectra of MAPbI<sub>3</sub> at 80, 140, 200, 300, and 360 K, a color contour map of all the temperature, and the resulting lifetimes relevant to the band-edge as a function of temperature. Reproduced with permission from [16].

An in-depth and comprehensive understanding of the delayed bi-molecular radiative recombination process in the framework of polaron formation has been envisaged recently in the perovskite [21, 33, 84]. It may be noted that in the event of recombination between oppositely charged polarons, the long-range attractive Coulomb interaction must be counterbalanced by a repulsive force. Unlike other conventional charge carriers, large polarons generally travel slowly as their movement is coupled with displacement patterns of the lattice or ions accountable for their formation through self-trapping. When two oppositely-charged large electron- and hole-polarons move toward each other, constructive interference occurs between the displacement patterns. In case of self-trapping at a small distance, the electronic charge carriers overlap with each other and this constructive interference of the displacement patterns produces a strong short-range repulsive force. Due to a large static displacement in the compound, the repulsion between the two oppositely charged polarons even overcome the long-range Coulomb force leading to a reduction of  $k_2$  and thereby the recombination rate. In figure 6(b), the antagonism between the long-range Coulomb interaction and a short-range repulsive force has been demonstrated as a function of inter-polaron separation. Due to the overlap or interference of displacement patterns (black curve) of two

oppositely charged polarons, an increase in the net polaron energy is observed overcoming the long-range Coulomb interaction (dotted curve) [84].

Additionally, as observed in figure 6(b), the asymmetry in the net energy of polarons suggests that a further decrement of the recombination rate is also possible, if the inter-polaron distance can be increased by some external perturbation such as temperature. Such a prediction has been verified in another breakthrough work where the role of polarons behind the temperature-dependent recombination-dynamics in MAPbI<sub>3</sub> was experimentally verified through variable temperature band-edge time-resolved photoluminescence spectroscopy (TRPL) [16]. A rise in carrier lifetime was observed with an increasing temperature as governed by a change in rotational entropy (figures 6(c) and (d)). Such a sudden increase in carrier lifetime would not have occurred due to changes in the electronic structure only. The phenomenon was described as a transformation of the system into another phase with a higher rotational entropy due to the well-known structural phase transition in MAPbI<sub>3</sub> [5, 16]. At higher temperatures, due to higher rotational entropy, the effective screening by the organic moiety increases proportionally allowing the formation of more polarons to further slow down the recombination process.



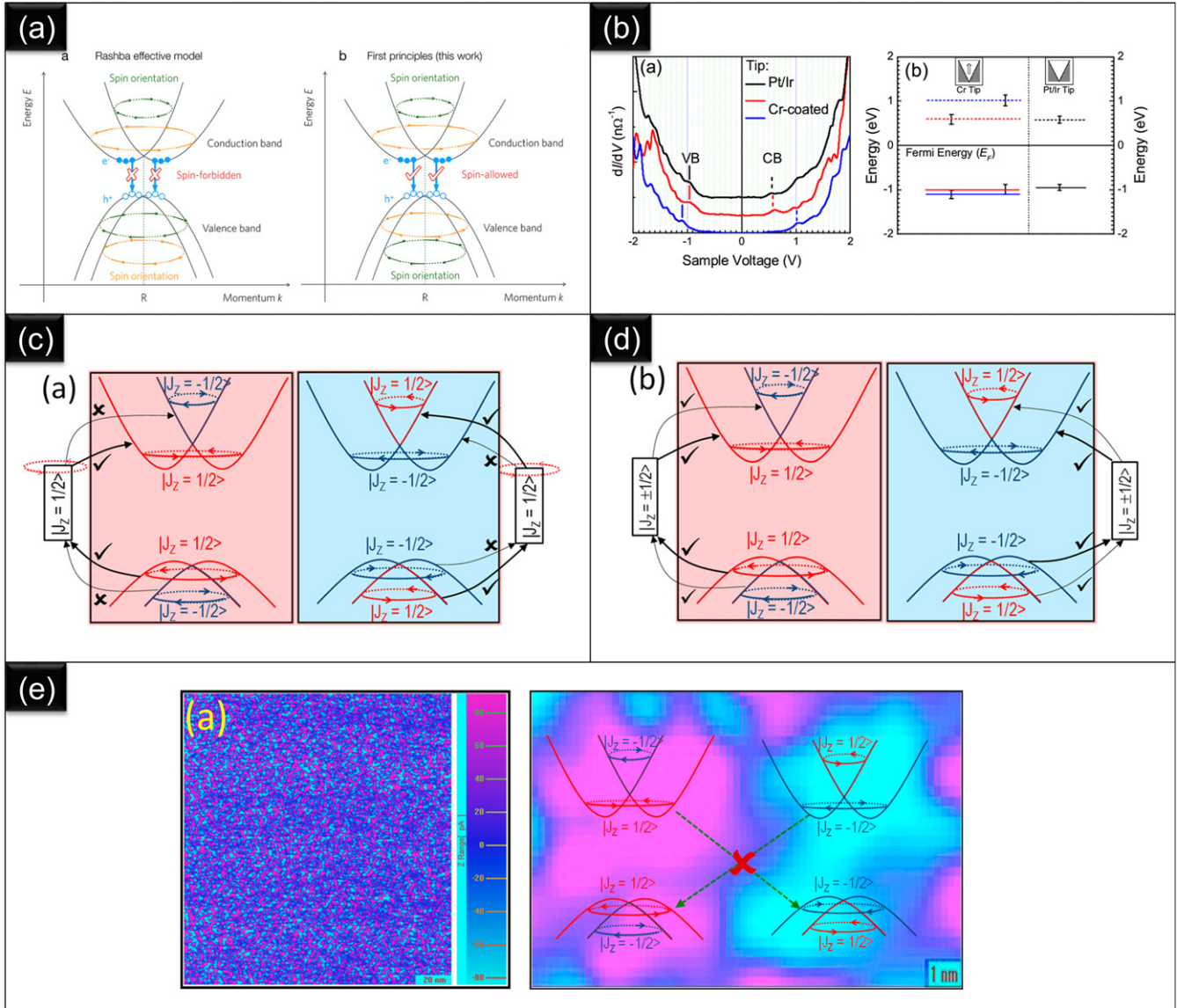


**Figure 7.** (a) Schematic representation of the spin-forbidden transition model and spin-allowed transition model as obtained from first-principle calculations. Reprinted with permission from [44]. Copyright (2018) American Chemical Society. (b) Evaluation of  $dI/dV$  spectra of MAPbI<sub>3</sub> recorded with a platinum/iridium (Pt/Ir) tip and a chromium-coated antiferromagnetic tip, band diagram of MAPbI<sub>3</sub> obtained from the  $dI/dV$  spectra, and histograms for the two types of STM-tips. (c) Schematic illustration of the spin-polarized tunneling process with a chromium coated tip. The Rashba band splitting in two different domains are shown in the left and the right sections. Red curves represent a  $|J_z = 1/2\rangle$  band and blue curves refer to the  $|J_z = -1/2\rangle$  band. A chromium-coated tip has been considered to inject up-spin electrons with  $|J_z = 1/2\rangle$ . Thick-arrows designate tunneling of electrons to the  $J_z$ -matched CB states and from the matched VB states. Tunneling of electrons to/from  $J_z$ -mismatched states (thin-arrows) are not allowed due to conservation of total angular momentum. The two sets of CB- and VB-energies thus appeared due to two types of domains. (d) Schematic representation of electron-tunneling with a Pt/Ir tip. Here both thick and thin arrows denote the allowed transition to the CB and from the VB. (e)  $dI/dV$  images of the MAPbI<sub>3</sub> film recorded with a chromium-coated antiferromagnetic tip to probe molecular size spin-domains and schematic representation of the spin forbidden interdomain recombination process. Reprinted with permission from [17]. Copyright (2020) American Chemical Society.

In a sense, the polaron theory may appear much more consistent than the postulation of ferroelectric domains as it can explain the long lifetime of carriers at high temperatures [16]. However, there are still some open questions, which have to be addressed experimentally, such as effective mass, binding energy, and coherence length of polarons. As mentioned earlier, along with large polarons, the presence of small polarons is also inevitable; such polarons have been

considered to be responsible for the degradation of the compound [13, 33]. The stability of large polarons is also hindered by the small ones [70]. Recently, it has also been explored that the formation of polarons may induce Jahn–Teller distortion in the perovskite octahedra due to a coupling of the soft structure of the compound and excess charge pool that can be detrimental for the photostability of the material [33].

All these studies infer that polaron engineering is highly desired in achieving a balance between a long carrier lifetime and photostability. In this regard, tunability of the size of polarons has been explored recently by Zhou *et al.*, who proposed an interesting avenue in terms of transforming a small polaron into a large one by controlling the delocalization through cation mixing [70]. The dynamic disorder of both inorganic and organic sub-lattices may also be considered for polaron-engineering as it can be influenced easily by steric interaction and temperature effects [79]. In addition, some open questions, such as the interaction between *A*-site cation and inorganic sub-lattice, still remain while accepting the model of polaron formation. According to early studies, polaron formation was explained with the aid of only the organic moiety [33, 51]. However, Zhu and co-workers have observed that the formation of polaron primarily occurs in the sub-picosecond time scale which is much faster than the rotation of the organic cation (several picoseconds) [80, 85]. This theory hence further raises a question on the necessity of an organic moiety in the perovskite while achieving superior photovoltaic performance. However, polaron formation time, which remained faster in the organic–inorganic hybrid perovskite (0.3 ps) than in an all-inorganic one (0.7 ps), has remained a key parameter behind a large diffusion length in the hybrid perovskite [86, 87]. They (Angelis and co-workers) have moreover considered a disorder in the organic moiety toward the polaron hopping process and thereby achieving a larger diffusion length of the photogenerated carriers [87]. Hence, the role of *A*-site cation in terms of polaron formation and explaining a high carrier lifetime and diffusion length has still remained quite important.

**3.2.3. Rashba band splitting: spin-forbidden inter-domain transition.** The most interesting theory of the bi-molecular recombination process in MAPbI<sub>3</sub> is certainly the occurrence of Rashba band-splitting [17, 42, 43, 56]. The presence of heavy elements (high *Z*) such as lead and iodine induces a strong spin–orbit coupling (SOC) parameter in the compound. Additionally, due to tilted PbI<sub>6</sub> octahedra and a rotation of the organic cation, a lack of centrosymmetry is manifested in the compound [56]. Under this scenario, the system realizes an effective magnetic field which further lifts the spin-degeneracy of the electrons and results in a splitting of both CB and VB bands in momentum space [43]. The photogenerated carriers in the momentum space thus find themselves effectively in an indirect bandgap environment due to a non-identical nature of splitting in the two bands and hence become long-lived [17, 42]. Although the occurrence of Rashba splitting in MAPbI<sub>3</sub> may be well-accepted by the research community, many theoreticians have discarded its role behind the band-to-band recombination process [44]. The degree of inconsistency in the Rashba splitting theory may appear to be larger than other propositions discussed so far. However, in previous work with spin-polarized scanning tunneling spectroscopy (SP-STS), a strong possibility of Rashba band-splitting has been justified for the slow electron–hole recombination process by considering spin-forbidden inter-domain transitions [17].

So far, various computational methods have been extensively applied to investigate the splitting parameter along with the spin texture of the bands by considering different static and dynamic structures of MAPbI<sub>3</sub> [17, 42–44, 56]. In addition, a few experimental studies also strongly support the occurrence of the Rashba effect in the compound. A significant effort regarding the experimental observation of Rashba spin-splitting has been demonstrated by Giovanni and co-workers through spin-dependent circularly polarized pump–probe experiments [88]. Neisner *et al.* presented a direct observation of the split in VBs from angle-resolved photoemission spectroscopy measurements [89]. In this direction, the report on the observation of Rashba splitting in both the bands from SP-STS provides a complete band-picture in MAPbI<sub>3</sub> [17].

The topic of Rashba splitting in MAPbI<sub>3</sub> remained in discussion with two opposing models of spin-texture in the split-bands being existed in the literature [44]. A group of theoreticians envisaged a spin-forbidden transition model while the other group believed in a spin-allowed transition model (figure 7(a)). In the first model, the spin-textures of the inner CB and VB (closer to the Fermi energy,  $E_F$ ) are opposite in nature. Recombination between the electrons (in CB-minimum) and holes (in VB-maximum) is therefore not allowed due to the spin-forbidden nature of the process leading to a low recombination loss of photogenerated carriers [42]. Such a possibility was ruled out by the other group of scientists; in their spin-allowed transition model, the inner bands (closer to  $E_F$ ) upon Rashba split have similar spin-textures resulting in spin-allowed recombination process [44].

Considering the opposing models proposed theoretically, we have experimentally determined the spin-textures of the two split-levels through SP-STS, simultaneously [17]. With a nonmagnetic Pt/Ir tip, tunneling conductance ( $dI/dV$ ) spectra of MAPbI<sub>3</sub> provided the usual band gap even when measured at different positions of the film [65]. A narrow variation in the two energy levels appeared due to local inhomogeneity in the film causing defect-states. Interestingly, when measurements were carried out with a chromium-coated spin-polarized antiferromagnetic tip, two completely different sets of spectra were observed; two typical spectra are shown in figure 7(b) with blue and red curves. The spin polarized band-positions (Rashba-split bands) obtained from these two sets of  $dI/dV$  spectra infers that the CB and VB can be either nearer (CB<sub>1</sub> and VB<sub>1</sub>) or farther (CB<sub>2</sub> and VB<sub>2</sub>) to the  $E_F$ . This shows that the splitting of the two band-edges occurs in such a manner that CB<sub>1</sub> and VB<sub>1</sub> (possessing analogous spin-states) are either closer to  $E_F$  or remained away from  $E_F$  (CB<sub>2</sub> and VB<sub>2</sub>). This observation suggests that MAPbI<sub>3</sub> follows a spin-allowed model of recombination. A schematic representation of spin-polarized tunneling (through a chromium-coated tip) as compared to spin-independent tunneling (through Pt/Ir tip) has been presented in figures 7(c) and (d).

In figure 7(e), we have provided a typical  $dI/dV$  image of an ultrathin-film of MAPbI<sub>3</sub> recorded with a chromium-coated tip. While recording  $dI/dV$  images, a material is viewed from the energy perceptible [17, 66]; a relatively higher DOS in the image implies domains whose lower CB is  $J_Z$ -allowed



with respect to the tip (figure 7(e)). Here  $J_z$  represents the  $Z$ -component of total angular momentum. Similarly, a low DOS indicates those domains whose lower-CB is forbidden for tunneling from the spin-polarized tip. Homogeneously distributed domains could be seen vividly in the  $dI/dV$  image. Interestingly, the size of the domains observed in spin-polarized  $dI/dV$  images had molecular dimensions.

These experimental results delivered a clear observation of Rashba band splitting in MAPbI<sub>3</sub> for both the bands, *simultaneously*. The spin-polarized band structure of the materials, as revealed from SP-STs, evidences that the CB-minimum and the VB-maximum possess a similar type of spin texture and supports the spin-allowed transition model. Apparently, it seems that carrier recombination is reasonably possible due to the spin-allowed nature of recombination between the CB-minimum and the VB maximum. However, the slow recombination of rate can still be explained despite of the above-mentioned observation. In MAPbI<sub>3</sub>, due to the presence of a large dielectric constant of the compound and hence a weak Coulomb interaction of the carriers, the excitons are considered as Wannier type [90], where an electron–hole pair resides in different molecules. Under this situation, intermolecular recombination is the most likely process instead of intramolecular recombination as described by Rappe and co-workers [42]. Interestingly, due to the spin-forbidden nature of such a transition, electron–hole recombination is not possible as shown in figure 7(e) (right panel).

A spin-forbidden nature of interdomain recombination can reasonably explain the long carrier lifetime along with a large carrier diffusion length in MAPbI<sub>3</sub>. This model is also capable of explaining the longer carrier lifetime at relatively higher temperatures. According to the reports of Niesner and co-workers, temperature-induced structural fluctuations promote a dynamical symmetry-breaking resulting in an enhanced splitting [89]. Unlike ferroelectric domains, which disappear at higher temperatures, there is no possibility of the spin-domains to vanish at higher temperatures. However, STS is unable to detect such domains under this condition due to the inefficient electron tunneling process involved in the measurements [17]. Any other spin-polarized optical spectroscopic technique may further shed light on the occurrence of the Rashba effect at higher temperatures. Furthermore, this theory is equally capable to explain a shorter lifetime and diffusion length of photogenerated carriers in all-inorganic perovskites as the Rashba splitting is comparatively weaker in such systems [91]. In any case, to establish the acceptance of this model over the polaron model, experimental verification of spin-forbidden and spin-allowed recombination of photogenerated carriers is desirable with and without Rashba splitting respectively, through suitable spectroscopic and/or optical measurements. We conclude with a disclaimer that Rashba splitting is associated with the surface or very close to the surface rather than the bulk of the material.

**3.2.4. Photon-recycling.** MAPbI<sub>3</sub> possesses more interesting properties that can be envisaged in a single semiconductor material. As stated earlier, this material possesses a long bimolecular carrier lifetime and a high radiative recombination

yield at the same time [11, 27, 28, 45, 50]. Such a combination of properties is indeed unique for a semiconductor to excel in optoelectronic applications. This unique combination has raised the possibility of photon-recycling in the compound [27, 45]. According to this model, absorption and emission of photons occur repeatedly during the transport process. Photon-recycling generally occurs when a semiconductor exhibits a few prerequisite properties, such as a high absorption coefficient, strong PL, and a small Stokes shift. In a pioneering work in this direction, the role of photon-recycling was reported revealing that any photoexcited state in the perovskite material is associated with multiple absorption-emission events before recombination [27]. While confocal optical microscopy was employed to study the spatial distribution of emission, photothermal deflection spectroscopy was used to investigate the absorption process. Both these results were combined to probe the photon distribution traveling through the film.

According to this model, the typical distance a carrier can travel is not limited by the conventional notion of carrier diffusion length. After radiative recombination, a photon is emitted and reabsorbed to create another electron–hole pair (figure 8(a)). In other words, as long as the recombination process is radiative, photogenerated carriers can roam through the perovskite essentially in presence of photons in the film. The radiative recombination rate-constant  $k_2$  can thus be strongly influenced due to simultaneous regeneration of carriers inside the compound. However, the event of photon-recycling depends strongly on a predetermined factor called ‘escape probability’ which generally governs how long a photon would remain inside the film/device. In the light of this, the well-known rate equation (equation (1)) can be modified to:

$$-\frac{dn}{dt} = k_1n + k_2^{\text{ext}}n^2 + k_3n^3 = k_1n + P_{\text{esc}}k_2^{\text{int}}n^2 + k_3n^3, \quad (2)$$

where the total external radiative recombination rate constant is obtained by multiplying the internal rate constant with the escape probability [20]. The escape probability is usually expected to be low ( $\sim 5\%$ ) due to a high refractive index of the compound [20]. As a result, a reduction of  $k_2^{\text{ext}}$  would occur in contrast to a higher  $k_2^{\text{int}}$  leading to an impeded electron–hole radiative recombination [92]. In this regard, a textured film has additional advantages over a planar film as the light will depart only at the second interface. Due to multiple internal reflections in a textured film, the reverberation of light in the active layer is possible for a longer time (figure 8(b)) [45].

This theory opens up a new direction in the charge carrier recombination process and moreover successfully explains interesting speculation of recombination. Generally, slow recombination is not expected in materials with strong absorption properties. It may be noted that  $k_2$  does not match well with the theoretical predictions based on the principle of detailed balance since a strong absorption coefficient would lead to large radiative recombination [21]. However, considering the effect of photon recycling, the order of  $k_2$  matches well as expected from the reciprocity theorem [27].

Deceptively, this model does not consider the significance of the organic cation. It must be remembered that the efficiency of all-inorganic perovskite (CsPbI<sub>3</sub>) solar cells is far

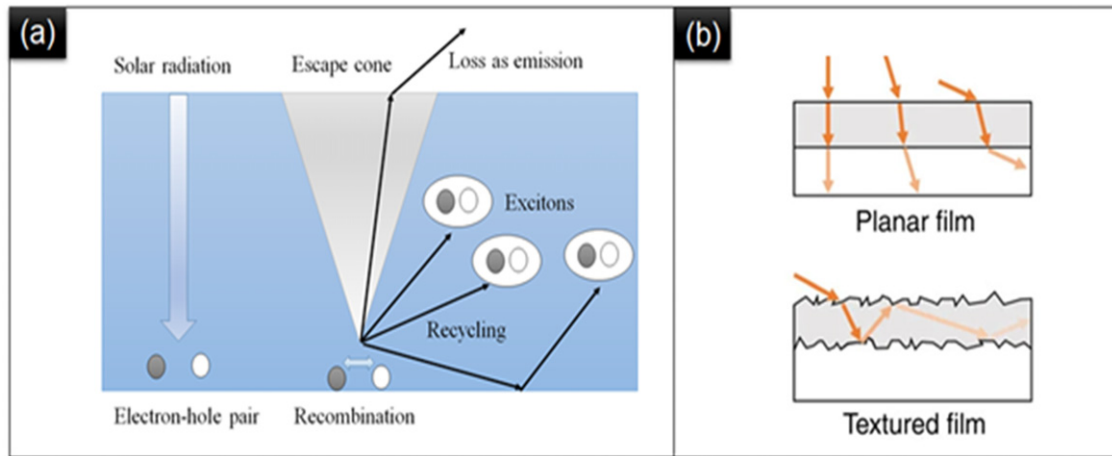


**Figure 8.** (a) Schematic representation of the photon recycling process. (b) Advantage of textured film over a planar film for photon recycling. In the case of textured film, the escape probability reduces further due to multiple internal reflections. Reproduced from [45]. CC BY 4.0.

below than that of organic–inorganic hybrid ones [15, 47–49]. A similar scenario has been observed for carrier lifetime and carrier diffusion length as presented earlier in table 1. In view of this, the model apparently fails at this moment to explain the superior transport properties of hybrid perovskites over the inorganic ones. It may also be noted that photon recycling can have significant importance when PLQY of the material is close to unity. As the PLQY in MAPbI<sub>3</sub> is low, the explanation of slow recombination in MAPbI<sub>3</sub> under the framework of photon recycling has still remained a matter of concern to the research community [30]. However, it is believed that this mechanism is really intriguing and deserves further study.

### 3.3. Auger recombination

Auger effect is a non-radiative process in which a third charge carrier is created due to recombination between an electron–hole pair [20, 21, 25, 26]. In such a tri-molecular process, the newly created electron (hole) go away to a higher excited state and finally decay through the emission of phonons (figure 9(a)) [26]. Based on the nature of the third charge carrier, the process can be classified into two categories: in the case of an electron, the process is termed as e–e–h Auger recombination; on the other hand, if it is a hole, the procedure is envisaged as h–e–h process [25, 26]. As stated earlier, the higher-order Auger term in the rate equation only appears at higher carrier concentrations ( $n > 10^{18} \text{ cm}^{-3}$ ). In perovskite solar cells,  $n$  is restricted by the availability of solar irradiation on earth. However, considering the application of perovskites in solid-state light-emitting devices, Auger recombination offers a significant role in the recombination dynamics as these operations demand a higher  $n$  through carrier injecting layers [25].

In a recent study, Shen *et al* explored the interdependence of the Auger process with Rashba splitting [25]. Due to a strong SOC, the parameter  $\mathbf{J}$  can possess different values from  $\mathbf{L} + \mathbf{S}$  to  $\mathbf{L} - \mathbf{S}$ . Considering the  $p$  ( $\mathbf{L} = 1$ ) characteristic of CB, it may originally split into many higher-order states. Auger recombination lifetime can be enhanced by such a unique band structure due to a splitting in the  $\mathbf{k}$ -space. In figure 9(b), a

schematic illustration has been presented to show the involvement of higher order CBs. A comparatively higher-order of magnitude of the Auger coefficient has been due to the transitions from all the CBs (figure 9(c)) [25].

## 4. Interplay between the propositions: a few open questions

In spite of intense research over the years, the determination of different rate constants through theoretical and experimental approaches remained inconclusive. Such an observation supports the existence of multiple recombination pathways in limiting the recombination rate [20, 21]. Similarly, based on the above discussion, we envisage that the slow recombination process in MAPbI<sub>3</sub> is governed by different microscopic processes. In this regard, we discuss the interplay between the propositions to decouple the relative contribution of the individual processes and identify the foremost process(s) involved in MAPbI<sub>3</sub>. In this direction, on the basis of theoretical frameworks and experimental observations achieved to date, we note that a higher-order Auger recombination is less probable in MAPbI<sub>3</sub> until charge carriers are injected externally with a high density; our discussion has been limited to only trap-assisted non-radiative and band-to-band radiative recombination processes only [25].

Due to the defect tolerant nature and weak electron–phonon coupling in the compound, non-radiative recombination is comparatively slower than that in other conventional semiconductors [10, 37]. However, after critical analysis we believe these two processes are not mutually exclusive; they are rather interrelated. Recently, the origin of defect tolerance in MAPbI<sub>3</sub> has been explained by a coupling between photogenerated electron and low-frequency phonons [62]. In this frame of reference, the apparent exclusiveness of these two processes can hence be removed. However, in MAPbI<sub>3</sub> most of the non-radiative recombination occurs at the surface and interface of the perovskite with the carrier-transport layers. In this regard, different post-processing techniques and suitable

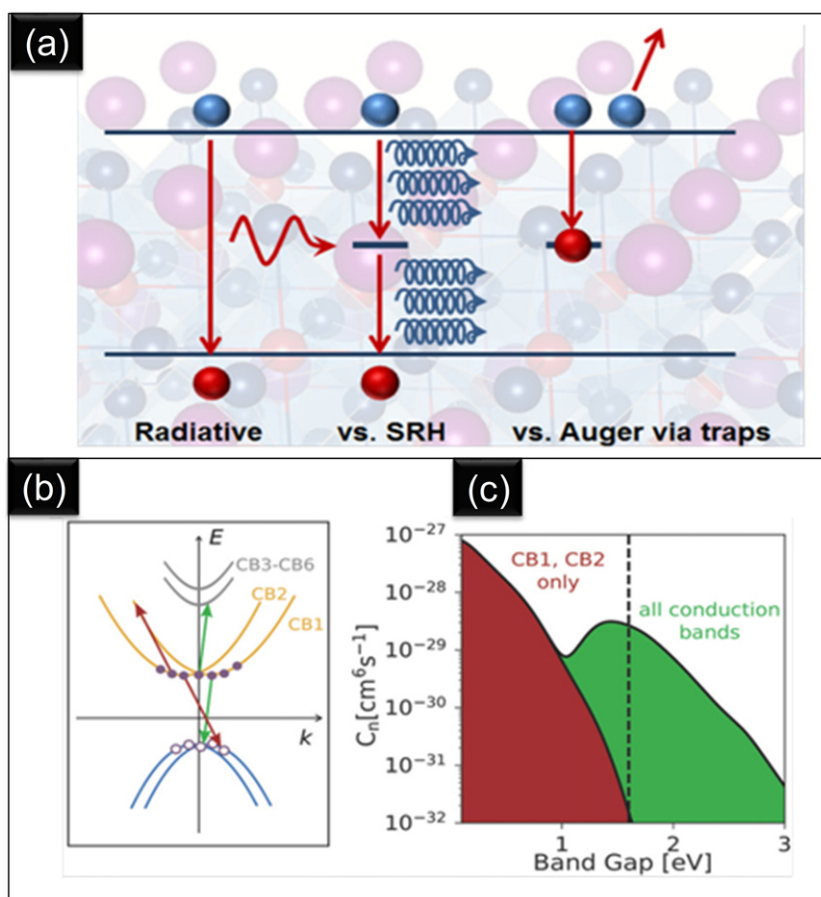


**Figure 9.** (a) Schematic representation of the Auger recombination process. Reprinted with permission from [26]. Copyright (2018) American Chemical Society. (b) Role of Rashba split CB and possible transition pathways in Auger recombination. (c) Calculated Auger coefficient as a function of bandgap considering different transition pathways through higher-order CBs. [25] John Wiley & Sons. © 2018 WILEY-VCH Verlag GmbH & Co. KGaA, Weinheim.

choice of transport layers are possible routes in achieving a low recombination loss. For example, antisolvent-induced crystallization, hot-casting, vacuum- and solvent-assisted annealing, and Lewis acid–base adduct approaches as different post-processing techniques are possible routes in achieving a low recombination loss. Similarly, the introduction of a passivation layer and/or a passivating layer with an appropriate band-alignment at the interfaces with the perovskite and acting as a charge-transport layer as well are being considered to achieve a low recombination loss in a device further. It may be noted that a proper microscopic origin of non-radiative recombination is not fully documented in the literature making the topic unclear till now.

On the other hand, a critical analysis of different microscopic hypotheses associated with band-to-band recombination is challenging in order to converge on their relative contributions. In this direction, we have tried to look for similarities between these different recombination pathways. In table 2, we have summarized some of the common parameters that are associated with different proposed radiative recombination processes. The research community would be greatly benefited if more pieces of evidence are inferred through both theoretical and experimental work to unravel all these models and

finally arrive at a conclusion regarding the dominating process involved in the radiative recombination process.

However, based on the current understanding, it seems that trap-assisted non-radiative recombination in  $\text{MAPbI}_3$  is less probable at low temperatures since the defect-states would be energetically inactive at such an experimental condition [32, 52]. Among the radiative recombination pathways, we find that charge carrier dynamics in  $\text{MAPbI}_3$  at a very low temperature is mostly influenced by ferroelectric domains [39, 40]. Under these state-of-affairs, due to the centrosymmetry of the crystal structure, a static Rashba band splitting is less probable; a dynamic Rashba effect is however still possible to influence the recombination dynamics at low temperatures [17, 42, 43, 56]. Similarly, polaron formations will also cease at low temperatures as the coupling between lattice and photogenerated carriers are favorable only at high temperatures [33, 51, 79, 80, 93]. With an increase in temperature, the ferroelectric domains would disappear due to a disorder of the system [40]. Interestingly, such a disorder, on the other hand, is favorable for the formation of polarons. Moreover, an increase in temperature is reported to be suitable to break the centrosymmetry in the compound due to a fast re-orientation of the MA cation [56]. Therefore, at room temperature, the dominant process must be either Rashba band splitting or polaron formation.

**Table 2.** Common parameters associated with different radiative recombination processes.

Proposed models	Necessity of organic moiety	Role of dipole moment	Large dielectric constant	Polarizability of lattice	Centrosymmetry in the structure	Ability to explain temperature-dependent recombination rate
Ferroelectric domains	✓	✓	✓	✓	✓	x
Large polarons	✓	✓	✓	✓	x	x
Rashba effect	✓	✓	✓	x	✓	x
Photon recycling	x	?	?	?	x	?

Recently, Kim *et al* reported a ferroelectric switching behavior of the Rashba split bands with an external electric field [94]. This effort unlocks the possibility of coupling between Rashba bands and ferroelectric polarization. It is highly possible that at high temperatures, the ferroelectric domains are converted into ‘Rashba spin-domains’ as visualized in the spin-forbidden interdomain transition model [17]. In this regard, further studies can open a new direction in the rationale of the slow recombination process in the compound. However, a correlation of the large polaron model with Rashba band-splitting or the concept of ferroelectric domain seems to be less likely. Based on the current understanding, the formation of polarons appears to be a completely independent phenomenon toward explaining a slow recombination process; a couple of reports have correlated the band-tails with polaron formation in order to explain the limitation of non-radiative recombination through the defect-tolerant nature of the material [21, 33].

The possibility of simultaneous Rashba splitting and polaron formation cannot be overruled at all. As such, all charge carriers are not involved in the formation of polarons; the remaining ones can be influenced by the Rashba contribution of spin-forbidden recombination. Further spectroscopic measurements are needed in this regard to monitoring the superiority and/or interdependence of these two processes. In addition, it should be remembered that Rashba band splitting is associated to the surface and thus most probably its impact is less in the bulk of the perovskite. Hence, at the higher temperatures, we can predict that the low recombination is governed by Rashba band splitting at the surface and polaron dynamics at the interior of the compound.

The possibility of photon recycling also deserves sizable speculations as it is not well-explored yet. The apparent contradiction of theoretically and experimentally determined rate constant ( $k_2$ ) has recently been explained under this framework. Moreover, considering a high PLQY and a long radiative lifetime simultaneously, such a possibility has gained an essential impact [27, 45]. This unique combination of slow recombination and a strong absorption at room temperature is not explicable in other conjectures of slow radiative recombination, such as the Rashba effect and polaron formation. It is likely that as long as photons stay in the compound, photon recycling is a dominating process; the probability of other prevailing processes turns high when the photons escape the device. At low carrier densities ( $n < 10^{14} \text{ cm}^{-3}$ ), the photon-recycling process does not offer any significant role.

## 5. Conclusions

After rigorous investigations over a long decade, a thorough understanding of low recombination loss (of photogenerated carriers) leading to prolonged carrier lifetime and a large carrier diffusion length is still unclear to researchers working in the field of perovskite solar cells. In this regard, this review provides an account of different well-investigated propositions of carrier recombination in MAPbI<sub>3</sub> associated with both radiative and non-radiative pathways. We have discussed their limitations in terms of their inability in explaining certain experimental results and critically assessed the inconsistencies in some of the proposed models. On the basis of such an assessment, we have tried to recognize which factor(s) governs the recombination dynamics most. First of all, we infer that a slow non-radiative SRH recombination appears due to either the defect tolerant nature of the compound or a weak electron–phonon coupling in the lattice; they are in fair agreement with the multiphonon theoretical framework as well. We also have evaluated the interrelation between these two processes and concluded that they are not mutually exclusive.

We have discussed the radiative band-to-band recombination in light of several microscopic and atomistic origins such as ferroelectric domain theory, polaronic transport, Rashba band splitting, and the photon recycling process. Our discussion revealed that the radiative recombination in MAPbI<sub>3</sub> strongly depends on external perturbations such as temperature. At low temperatures, the appearance of ferroelectric domains is likely to be responsible for a long carrier lifetime and thereby a large diffusion length. On the other hand, with increasing temperature, such domains start to disappear. In this situation, Rashba splitting and/or polaron transport become the influencing process behind a low recombination loss of photogenerated carriers in MAPbI<sub>3</sub>. Regardless of current advancement in the understanding of the recombination dynamics and transport process through these two models, more innovative spectroscopic as well as optical measurements are necessary to establish the feasibility of a few phenomena, such as spin-forbidden inter-domain recombination process and direct observation of polaronic transport at the nanoscale. In this direction, we have critically evaluated the possibility of simultaneous contribution from the Rashba effect and polaron dynamics in controlling the slow recombination process at the surface and interior, respectively. The effect of different perturbations and complex interactions on these



abovementioned processes are yet to be explored at the atomic level. We also noted that the carrier density was also crucial in determining the tangible radiative recombination pathways. Although, at a low carrier density ( $10^{16} \text{ cm}^{-3}$ ), the model of Rashba splitting or polaron formations are highly plausible, the contribution of photon-recycling becomes significant at a higher concentration of charge carriers and for a textured film with a low escape probability. This model recently gained sufficient interest among the perovskite community as the apparent discrepancy of  $k_2$  can be corrected under this framework. At this moment, though the model of photon-recycling apparently fails to explain the superior transport properties of organic–inorganic hybrid perovskites over the inorganic ones, we believe that this mechanism is really intriguing and definitely deserves further attention.

We hereby conclude that one should envision newer pathways to control the recombination dynamics further. In order to eliminate most of the parasitic non-radiative SRH recombination centers, additional material engineering is required to achieve high-quality perovskite films. Similarly, pathways in slowing down the radiative recombination should be considered. In this direction, ferroelectric domain engineering by different poling processes should be a quick approach to increase the radiative lifetime at low temperatures. On the other hand, Rashba band splitting can be tuned by manipulating the crystal symmetry and the content of heavy atoms (lead and iodine) through suitable doping elements. Photon management can in principle be considered as an effective approach to tune efficient light-extraction and light-trapping schemes through matching of refractive index and geometry of the perovskite with the substrates. Moreover, all these approaches should also be applied to other perovskites in order to identify materials with a slow recombination process and thereby yielding a high efficiency in solar cells.

## Acknowledgments

AJP acknowledges JC Bose National Fellowship (JBR/2021/000001) and Core Research Grant (CRG/2018/000183) of SERB. AM acknowledges DST INSPIRE Fellowship [IF170922].

## Data availability statement

No new data were created or analysed in this study.

## ORCID iDs

Amlan J Pal  <https://orcid.org/0000-0002-7651-9779>

## References

- [1] Kojima A, Teshima K, Shirai Y and Miyasaka T 2009 Organometal halide perovskites as visible-light sensitizers for photovoltaic cells *J. Am. Chem. Soc.* **131** 6050–1
- [2] Jena A K, Kulkarni A and Miyasaka T 2019 Halide perovskite photovoltaics: background, status, and future prospects *Chem. Rev.* **119** 3036–103
- [3] Heo J H, Lee M H, Han H J, Patil B R, Yu J S and Im S H 2016 Highly efficient low temperature solution processable planar type  $\text{CH}_3\text{NH}_3\text{PbI}_3$  perovskite flexible solar cells *J. Mater. Chem. A* **4** 1572–8
- [4] Wang P, Wu Y H, Cai B, Ma Q S, Zheng X J and Zhang W H 2019 Solution-processable perovskite solar cells toward commercialization: progress and challenges *Adv. Funct. Mater.* **29** 1807661
- [5] Whitfield P S, Herron N, Guise W E, Page K, Cheng Y Q, Milas I and Crawford M K 2016 Structures, phase transitions and tricritical behavior of the hybrid perovskite methylammonium lead iodide *Sci. Rep.* **6** 35685
- [6] Unger E L, Kegelmann L, Suchan K, Sorell D, Korte L and Albrecht S 2017 Roadmap and roadblocks for the band gap tunability of metal halide perovskites *J. Mater. Chem. A* **5** 11401–9
- [7] Khatun S, Maiti A and Pal A J 2020 Bowing of transport gap in hybrid halide perovskite alloys ( $\text{CH}_3\text{NH}_3\text{Sn}_{1-x}\text{Pb}_x\text{I}_3$ ): which band is responsible? *Appl. Phys. Lett.* **116** 012104
- [8] Galkowski K *et al* 2016 Determination of the exciton binding energy and effective masses for methylammonium and formamidinium lead tri-halide perovskite semiconductors *Energy Environ. Sci.* **9** 962–70
- [9] Brenner T M, Egger D A, Rappe A M, Kronik L, Hodes G and Cahen D 2015 Are mobilities in hybrid organic–inorganic halide perovskites actually ‘high’? *J. Phys. Chem. Lett.* **6** 4754–7
- [10] Steirer K X, Schulz P, Teeter G, Stevanovic V, Yang M, Zhu K and Berry J J 2016 Defect tolerance in methylammonium lead triiodide perovskite *ACS Energy Lett.* **1** 360–6
- [11] Stranks S D, Eperon G E, Grancini G, Menelaou C, Alcocer M J P, Leijtens T, Herz L M, Petrozza A and Snaith H J 2013 Electron–hole diffusion lengths exceeding 1 micrometer in an organometal trihalide perovskite absorber *Science* **342** 341–4
- [12] Wehrenfennig C, Liu M Z, Snaith H J, Johnston M B and Herz L M 2014 Charge-carrier dynamics in vapour-deposited films of the organolead halide perovskite  $\text{CH}_3\text{NH}_3\text{PbI}_{3-x}\text{Cl}_x$  *Energy Environ. Sci.* **7** 2269–75
- [13] Zhu X Y and Podzorov V 2015 Charge carriers in hybrid organic–inorganic lead halide perovskites might be protected as large polarons *J. Phys. Chem. Lett.* **6** 4758–61
- [14] Dong Q F, Fang Y J, Shao Y C, Mulligan P, Qiu J, Cao L and Huang J S 2015 Electron–hole diffusion lengths  $> 175 \mu\text{m}$  in solution-grown  $\text{CH}_3\text{NH}_3\text{PbI}_3$  single crystals *Science* **347** 967–70
- [15] Hutter E M, Sutton R J, Chandrashekar S, Abdi-Jalebi M, Stranks S D, Snaith H J and Sayenije T J 2017 Vapour-deposited cesium lead iodide perovskites: microsecond charge carrier lifetimes and enhanced photovoltaic performance *ACS Energy Lett.* **2** 1901–8
- [16] Chen T R *et al* 2017 Origin of long lifetime of band-edge charge carriers in organic–inorganic lead iodide perovskites *Proc. Natl Acad. Sci. USA* **114** 7519–24
- [17] Maiti A, Khatun S and Pal A J 2020 Rashba band splitting in  $\text{CH}_3\text{NH}_3\text{PbI}_3$ : an insight from spin polarized scanning tunneling spectroscopy *Nano Lett.* **20** 292–9
- [18] Wang K, Yang D, Wu C C, Sanghadasa M and Priya S 2019 Recent progress in fundamental understanding of halide perovskite semiconductors *Prog. Mater. Sci.* **106** 100580
- [19] Manser J S and Kamat P V 2014 Band filling with free charge carriers in organometal halide perovskites *Nat. Photon.* **8** 737–43
- [20] Johnston M B and Herz L M 2016 Hybrid perovskites for photovoltaics: charge-carrier recombination, diffusion, and radiative efficiencies *Acc. Chem. Res.* **49** 146–54

- [21] deQuilettes D W, Frohna K, Emin D, Kirchartz T, Bulovic V, Ginger D S and Stranks S D 2019 Charge-carrier recombination in halide perovskites *Chem. Rev.* **119** 11007–19
- [22] Braly I L, deQuilettes D W, Pazos-Outon L M, Burke S, Ziffer M E, Ginger D S and Hillhouse H W 2018 Hybrid perovskite films approaching the radiative limit with over 90% photoluminescence quantum efficiency *Nat. Photon.* **12** 355–61
- [23] Xu W D *et al* 2019 Rational molecular passivation for high-performance perovskite light-emitting diodes *Nat. Photon.* **13** 418–24
- [24] Stranks S D 2017 Nonradiative losses in metal halide perovskites *ACS Energy Lett.* **2** 1515–25
- [25] Shen J-X, Zhang X, Das S, Kioupakis E and Van de Walle C G 2018 Unexpectedly strong Auger recombination in halide perovskites *Adv. Energy Mater.* **8** 1801027
- [26] Staub F, Rau U and Kirchartz T 2018 Statistics of the Auger recombination of electrons and holes via defect levels in the band gap—application to lead-halide perovskites *ACS Omega* **3** 8009–16
- [27] Pazos-Outon L M *et al* 2016 Photon recycling in lead iodide perovskite solar cells *Science* **351** 1430–3
- [28] Herz L M 2017 Charge-carrier mobilities in metal halide perovskites: fundamental mechanisms and limits *ACS Energy Lett.* **2** 1539–48
- [29] Kirchartz T, Kruckemeier L and Unger E L 2018 Research update: recombination and open-circuit voltage in lead-halide perovskites *APL Mater.* **6** 100702
- [30] Kirchartz T, Marquez J A, Stolterfoht M and Unold T 2020 Photoluminescence-based characterization of halide perovskites for photovoltaics *Adv. Energy Mater.* **10** 1904134
- [31] Oga H, Saeki A, Ogomi Y, Hayase S and Seki S 2014 Improved understanding of the electronic and energetic landscapes of perovskite solar cells: high local charge carrier mobility, reduced recombination, and extremely shallow traps *J. Am. Chem. Soc.* **136** 13818–25
- [32] Milot R L, Eperon G E, Snaith H J, Johnston M B and Herz L M 2015 Temperature-dependent charge-carrier dynamics in  $\text{CH}_3\text{NH}_3\text{PbI}_3$  perovskite thin films *Adv. Funct. Mater.* **25** 6218–27
- [33] Ghosh D, Welch E, Neukirch A J, Zakhidov A and Tretiak S 2020 Polarons in halide perovskites: a perspective *J. Phys. Chem. Lett.* **11** 3271–86
- [34] Brandt R E *et al* 2017 Searching for ‘defect-tolerant’ photovoltaic materials: combined theoretical and experimental screening *Chem. Mater.* **29** 4667–74
- [35] Wright A D, Verdi C, Milot R L, Eperon G E, Perez-Osorio M A, Snaith H J, Giustino F, Johnston M B and Herz L M 2016 Electron–phonon coupling in hybrid lead halide perovskites *Nat. Commun.* **7** 11755
- [36] Zhao T Q, Shi W, Xi J Y, Wang D and Shuai Z G 2016 Intrinsic and extrinsic charge transport in  $\text{CH}_3\text{NH}_3\text{PbI}_3$  perovskites predicted from first-principles *Sci. Rep.* **6** 19968
- [37] Kirchartz T, Markvart T, Rau U and Egger D A 2018 Impact of small phonon energies on the charge-carrier lifetimes in metal-halide perovskites *J. Phys. Chem. Lett.* **9** 939–46
- [38] Motta C and Sanvito S 2018 Electron–phonon coupling and polaron mobility in hybrid perovskites from first principles *J. Phys. Chem. C* **122** 1361–6
- [39] Frost J M, Butler K T, Brivio F, Hendon C H, van Schilfgaarde M and Walsh A 2014 Atomistic origins of high-performance in hybrid halide perovskite solar cells *Nano Lett.* **14** 2584–90
- [40] Frost J M, Butler K T and Walsh A 2014 Molecular ferroelectric contributions to anomalous hysteresis in hybrid perovskite solar cells *APL Mater.* **2** 081506
- [41] Liu S, Zheng F, Koocher N Z, Takenaka H, Wang F G and Rappe A M 2015 Ferroelectric domain wall induced band gap reduction and charge separation in organometal halide perovskites *J. Phys. Chem. Lett.* **6** 693–9
- [42] Zheng F, Tan L Z, Liu S and Rappe A M 2015 Rashba spin–orbit coupling enhanced carrier lifetime in  $\text{CH}_3\text{NH}_3\text{PbI}_3$  *Nano Lett.* **15** 7794–800
- [43] Myung C W, Javaid S, Kim K S and Lee G 2018 Rashba–Dresselhaus effect in inorganic/organic lead iodide perovskite interfaces *ACS Energy Lett.* **3** 1294–300
- [44] Zhang X, Shen J X and Van de Walle C G 2018 Three-dimensional spin texture in hybrid perovskites and its impact on optical transitions *J. Phys. Chem. Lett.* **9** 2903–8
- [45] Richter J M *et al* 2016 Enhancing photoluminescence yields in lead halide perovskites by photon recycling and light out-coupling *Nat. Commun.* **7** 13941
- [46] Yin W J, Shi T T and Yan Y F 2014 Unusual defect physics in  $\text{CH}_3\text{NH}_3\text{PbI}_3$  perovskite solar cell absorber *Appl. Phys. Lett.* **104** 063903
- [47] Wang K, Jin Z W, Liang L, Bian H, Bai D L, Wang H R, Zhang J R, Wang Q and Liu S Z 2018 All-inorganic cesium lead iodide perovskite solar cells with stabilized efficiency beyond 15% *Nat. Commun.* **9** 4544
- [48] Lau C F J, Wang Z P, Sakai N, Zheng J H, Liao C H, Green M, Huang S J, Snaith H J and Ho-Baillie A 2019 Fabrication of efficient and stable  $\text{CsPbI}_3$  perovskite solar cells through cation exchange process *Adv. Energy Mater.* **9** 1901685
- [49] Shi J, Wang Y and Zhao Y 2019 Inorganic  $\text{CsPbI}_3$  perovskites toward high-efficiency photovoltaics *Energy Environ. Mater.* **2** 73–8
- [50] Adhyaksa G W P, Veldhuizen L W, Kuang Y H, Brittman S, Schropp R E I and Garnett E C 2016 Carrier diffusion lengths in hybrid perovskites: processing, composition, aging, and surface passivation effects *Chem. Mater.* **28** 5259–63
- [51] Chen Y *et al* 2016 Extended carrier lifetimes and diffusion in hybrid perovskites revealed by Hall effect and photoconductivity measurements *Nat. Commun.* **7** 12253
- [52] Gelvez-Rueda M C, Renaud N and Grozema F C 2017 Temperature dependent charge carrier dynamics in formamidinium lead iodide perovskite *J. Phys. Chem. C* **121** 23392–7
- [53] Brivio F *et al* 2015 Lattice dynamics and vibrational spectra of the orthorhombic, tetragonal, and cubic phases of methylammonium lead iodide *Phys. Rev. B* **92** 144308
- [54] Weller M T, Weber O J, Henry P F, Di Pumpo A M and Hansen T C 2015 Complete structure and cation orientation in the perovskite photovoltaic methylammonium lead iodide between 100 and 352 K *Chem. Commun.* **51** 4180–3
- [55] Khatun S, Maiti A, Das G and Pal A J 2020 Role of individual bands in the unusual temperature-dependent band gap of methylammonium lead iodide *J. Phys. Chem. C* **124** 19841–8
- [56] Kepenekian M and Even J 2017 Rashba and Dresselhaus couplings in halide perovskites: accomplishments and opportunities for spintronics and spin–orbitronics *J. Phys. Chem. Lett.* **8** 3362–70
- [57] Buin A, Pietsch P, Xu J X, Voznyy O, Ip A H, Comin R and Sargent E H 2014 Materials processing routes to trap-free halide perovskites *Nano Lett.* **14** 6281–6
- [58] Akin S, Arora N, Zakeeruddin S M, Gratzel M, Friend R H and Dar M I 2020 New strategies for defect passivation in high-efficiency perovskite solar cells *Adv. Energy Mater.* **10** 1903090
- [59] Maiti A, Paul G, Bhunia H and Pal A J 2019 Band-edges of bismuth-based ternary halide perovskites  $\text{A}_3\text{Bi}_2\text{I}_9$  through scanning tunneling spectroscopy vis-a-vis impact of defects in limiting the performance of solar cells *Sol. Energy Mater. Sol. Cells* **200** 109941
- [60] Maiti A, Chatterjee S and Pal A J 2020 Sulfur-vacancy passivation in solution-processed  $\text{Sb}_2\text{S}_3$  thin films: influence on photovoltaic interfaces *ACS Appl. Energy Mater.* **3** 810–21

- [61] Wu N D *et al* 2017 Identifying the cause of voltage and fill factor losses in perovskite solar cells by using luminescence measurements *Energy Technol.* **5** 1827–35
- [62] Chu W B, Zheng Q J, Prezhdo O V, Zhao J and Saidi W A 2020 Low-frequency lattice phonons in halide perovskites explain high defect tolerance toward electron–hole recombination *Sci. Adv.* **6** eaaw7453
- [63] Guo D Y, Caselli V M, Hutter E M and Savenije T J 2019 Comparing the calculated Fermi level splitting with the open-circuit voltage in various perovskite cells *ACS Energy Lett.* **4** 855–60
- [64] Wolff C M, Caprioglio P, Stolterfoht M and Neher D 2019 Nonradiative recombination in perovskite solar cells: the role of interfaces *Adv. Mater.* **31** 1902762
- [65] Paul G, Chatterjee S, Bhunia H and Pal A J 2018 Self-doping Maiti is a graduate student (Senior Research Fellow) under DST-INSPIRE of conductivity through scanning tunneling spectroscopy *J. Phys. Chem. C* **122** 20194–9
- [66] Qiu L B, He S S, Ono L K and Qi Y B 2020 Progress of surface science studies on ABX<sub>3</sub> based metal halide perovskite solar cells *Adv. Energy Mater.* **10** 1902726
- [67] Chu W B, Saidi W A, Zhao J and Prezhdo O V 2020 Soft lattice and defect covalency rationalize tolerance of b-CsPbI<sub>3</sub> perovskite solar cells to native defects *Angew. Chem., Int. Ed.* **59** 6435–41
- [68] Wright A D, Milot R L, Eperon G E, Snaith H J, Johnston M B and Herz L M 2017 Band-tail recombination in hybrid lead iodide perovskite *Adv. Funct. Mater.* **27** 1700860
- [69] Mehdizadeh-Rad H and Singh J 2019 Influence of urbach energy, temperature, and longitudinal position in the active layer on carrier diffusion length in perovskite solar cells *ChemPhysChem* **20** 2712–7
- [70] Zhou L J *et al* 2019 Cation alloying delocalizes polarons in lead halide perovskites *J. Phys. Chem. Lett.* **10** 3516–24
- [71] Karakus M, Jensen S A, D'Angelo F, Turchinovich D, Bonn M and Canovas E 2015 Phonon–electron scattering limits free charge mobility in methylammonium lead iodide perovskites *J. Phys. Chem. Lett.* **6** 4991–6
- [72] Davies C L *et al* 2018 Bimolecular recombination in methylammonium lead triiodide perovskite is an inverse absorption process *Nat. Commun.* **9** 293
- [73] Ponce S, Schlipf M and Giustino F 2019 Origin of low carrier mobilities in halide perovskites *ACS Energy Lett.* **4** 456–63
- [74] Zheng X P, Chen B, Dai J, Fang Y J, Bai Y, Lin Y Z, Wei H T, Zeng X C and Huang J S 2017 Defect passivation in hybrid perovskite solar cells using quaternary ammonium halide anions and cations *Nat. Energy* **2** 17102
- [75] Kutes Y, Ye L H, Zhou Y Y, Pang S P, Huey B D and Padture N P 2014 Direct observation of ferroelectric domains in solution-processed CH<sub>3</sub>NH<sub>3</sub>PbI<sub>3</sub> perovskite thin films *J. Phys. Chem. Lett.* **5** 3335–9
- [76] Stoumpos C C, Malliakas C D and Kanatzidis M G 2013 Semiconducting tin and lead iodide perovskites with organic cations: phase transitions, high mobilities, and near-infrared photoluminescent properties *Inorg. Chem.* **52** 9019–38
- [77] Savenije T J *et al* 2014 Thermally activated exciton dissociation and recombination control the carrier dynamics in organometal halide perovskite *J. Phys. Chem. Lett.* **5** 2189–94
- [78] Park M *et al* 2018 Excited-state vibrational dynamics toward the polaron in methylammonium lead iodide perovskite *Nat. Commun.* **9** 2525
- [79] Zheng F and Wang L W 2019 Large polaron formation and its effect on electron transport in hybrid perovskites *Energy Environ. Sci.* **12** 1219–30
- [80] Miyata K, Meggiolaro D, Trinh M T, Joshi P P, Mosconi E, Jones S C, De Angelis F and Zhu X Y 2017 Large polarons in lead halide perovskites *Sci. Adv.* **3** e1701217
- [81] Mahata A, Meggiolaro D and De Angelis F 2019 From large to small polarons in lead, tin, and mixed lead–tin halide perovskites *J. Phys. Chem. Lett.* **10** 1790–8
- [82] Feynman R P 1955 Slow electrons in a polar crystal *Phys. Rev.* **97** 660–5
- [83] Zheng K B *et al* 2016 Direct experimental evidence for photoinduced strong-coupling polarons in organolead halide perovskite nanoparticles *J. Phys. Chem. Lett.* **7** 4535–9
- [84] Emin D 2018 Barrier to recombination of oppositely charged large polarons *J. Appl. Phys.* **123** 055105
- [85] Kubicki D J, Prochowicz D, Hofstetter A, Pechy P, Zakeeruddin S M, Gratzel M and Emsley L 2017 Cation dynamics in mixed-cation (MA)<sub>x</sub>(FA)<sub>1-x</sub>PbI<sub>3</sub> hybrid perovskites from solid-state NMR *J. Am. Chem. Soc.* **139** 10055–61
- [86] Ambrosio F, Wiktor J, De Angelis F and Pasquarello A 2018 Origin of low electron–hole recombination rate in metal halide perovskites *Energy Environ. Sci.* **11** 101–5
- [87] Ambrosio F, Meggiolaro D, Mosconi E and De Angelis F 2019 Charge localization, stabilization, and hopping in lead halide perovskites: competition between polaron stabilization and cation disorder *ACS Energy Lett.* **4** 2013–20
- [88] Giovanni D, Ma H, Chua J, Gratzel M, Ramesh R, Mhaisalkar S, Mathews N and Sum T C 2015 Highly spin-polarized carrier dynamics and ultra large photoinduced magnetization in CH<sub>3</sub>NH<sub>3</sub>PbI<sub>3</sub> perovskite thin films *Nano Lett.* **15** 1553–8
- [89] Niesner D, Wilhelm M, Levchuk I, Osvet A, Shrestha S, Batentschuk M, Brabec C and Fauster T 2016 Giant Rashba splitting in CH<sub>3</sub>NH<sub>3</sub>PbBr<sub>3</sub> organic–inorganic perovskite *Phys. Rev. Lett.* **117** 126401
- [90] Phuong L Q, Nakaike Y, Wakamiya A and Kanemitsu Y 2016 Free excitons and exciton–phonon coupling in CH<sub>3</sub>NH<sub>3</sub>PbI<sub>3</sub> single crystals revealed by photocurrent and photoluminescence measurements at low temperatures *J. Phys. Chem. Lett.* **7** 4905–10
- [91] Hu S B *et al* 2017 Dipole order in halide perovskites: polarization and Rashba band splittings *J. Phys. Chem. C* **121** 23045–54
- [92] Crothers T W, Milot R L, Patel J B, Parrott E S, Schlipf J, Muller-Buschbaum P, Johnston M B and Herz L M 2017 Photon reabsorption masks intrinsic bimolecular charge-carrier recombination in CH<sub>3</sub>NH<sub>3</sub>PbI<sub>3</sub> perovskite *Nano Lett.* **17** 5782–9
- [93] Neukirch A J *et al* 2016 Polaron stabilization by cooperative lattice distortion and cation rotations in hybrid perovskite materials *Nano Lett.* **16** 3809–16
- [94] Kim M, Im J, Freeman A J, Ihm J and Jin H 2014 Switchable  $S = 1/2$  and  $J = 1/2$  Rashba bands in ferroelectric halide perovskites *Proc. Natl Acad. Sci.* **111** 6900–4



**Abhishek Maiti** is a graduate student (Senior Research Fellow) under DST-INSPIRE Fellowship scheme of DST, Government of India, in the School of Physical Sciences at Indian Association for the Cultivation of Science, Kolkata, India. In 2017, he received his MSc degree in Physics from Jadavpur University, Kolkata. Of late, he has been awarded with Newton Bhabha PhD Placements Programme 2020–21. His current research focuses on understanding of optical and electronic properties of halide perovskite through scanning probe techniques. In addition, he is also involved in the design and development of lead-free perovskite solar cells with the aid of photophysics.



**Amlan J Pal** is currently the director at UGC-DAE Consortium for Scientific Research, Indore. He is also a Professor and a JC Bose National Fellow in the School of Physical Sciences, Indian Association for the Cultivation of Science, Kolkata, India. He received the MSc degree in physics from University of Calcutta and PhD from Jadavpur University. His research interests include device physics, ultrahigh vacuum scanning tunneling spectroscopy, and materials engineering leading to organic electronics, solar cells based on organic/inorganic semiconductors and hybrid halide perovskites, organic spintronics, and so forth.